Advances in Experimental Medicine and Biology 1355

Xunbin Wei
Bobo Gu *Editors*

Optical Imaging in Human Disease and Biological Research

Springer

Advances in Experimental Medicine and Biology

Volume 1355

Advances in Experimental Medicine and Biology provides a platform for scientific contributions in the main disciplines of the biomedicine and the life sciences. This series publishes thematic volumes on contemporary research in the areas of microbiology, immunology, neurosciences, biochemistry, biomedical engineering, genetics, physiology, and cancer research. Covering emerging topics and techniques in basic and clinical science, it brings together clinicians and researchers from various fields.

Advances in Experimental Medicine and Biology has been publishing exceptional works in the field for over 40 years, and is indexed in SCOPUS, Medline (PubMed), Journal Citation Reports/Science Edition, Science Citation Index Expanded (SciSearch, Web of Science), EMBASE, BIOSIS, Reaxys, EMBiology, the Chemical Abstracts Service (CAS), and Pathway Studio.

2019 Impact Factor: 2.450 5 Year Impact Factor: 2.324

More information about this series at http://www.springer.com/series/5584

Xunbin Wei • Bobo Gu
Editors

Optical Imaging in Human Disease and Biological Research

Springer

Editors
Xunbin Wei
State Key Laboratory of Oncogenes and Related Genes
Shanghai Cancer Institute, Med-X Research Institute and School of Biomedical Engineering, Shanghai Jiao Tong University
Shanghai, China

Biomedical Engineering Department
Peking University
Beijing, China

Bobo Gu
School of Biomedical Engineering
Shanghai Jiao Tong University
Shanghai, China

ISSN 0065-2598 ISSN 2214-8019 (electronic)
Advances in Experimental Medicine and Biology
ISBN 978-981-15-7626-3 ISBN 978-981-15-7627-0 (eBook)
https://doi.org/10.1007/978-981-15-7627-0

This Springer imprint is published by the registered company Springer Nature Singapore Pte Ltd.
The registered company address is: 152 Beach Road, #21-01/04 Gateway East, Singapore 189721, Singapore

Introduction

Recently, imaging has become an indispensable tool in biological research, clinical trials, medical practice, etc. Thus, there has been an explosion in the development of novel technologies to image molecules, organelles, organs, and biological processes, which provide the necessary biological information for disease diagnostics. In the past four decades, there has been a huge increase in emerging imaging technologies and their applications in human diseases diagnostics, including magnetic resonance imaging, X-ray computed tomography, nuclear tomographic imaging, etc. Noninvasive imaging with photons is an intriguing avenue to extract the interested biological information. When light travels through the tissue, the biological information can be obtained from the absorption, scattering, fluorescence, ultrasonic waves, and other specific parameters. Fluorescence imaging, which utilizes fluorescence dyes or proteins as labels for molecular processes or structures, can provide location, morphology, and dynamics of specimens. Due to its sensitivity, inherent biological safety, and relative ease of use, fluorescence imaging becomes the most widely used and mature imaging method. Raman imaging, including surface-enhanced Raman scattering and coherent anti-stokes Raman scattering here, can provide high-resolution noninvasive molecular analysis of biological samples and has a breakthrough potential for dissection of molecular composition at a single cellular organelle level. Raman imaging relies on the inelastic scattering, i.e., Raman scattering, of light, and the photon frequency will be shifted up or down when interacting with specific molecular vibrations. Raman imaging can provide chemical fingerprints of cells, tissues, or organs, and label-free, nondestructive, chemically selective and spatially resolved analysis. However, the penetration depth of photons is limited by the scattering of tissue. Fortunately, photons in the tissue can be converted into ultrasonic waves, which are scattered much less. Absorption of photons by specimens thermoelastically induces the pressure waves by photoacoustic effect, and then photoacoustic image is created by detecting the induced pressure wave. This emerging technology overcomes the high degree of scattering of photons in biological tissue by virtue of photoacoustic effect and subsequently provides multiscale images of living biological structures ranging from organelles to organs. To construct the 3D images, optical coherence tomography (OCT) technology is explored since the early 1980s. OCT based on low-coherence interferometry synthesizes the cross-sectional images from a series of laterally adjacent depth

scans. Its specific advantages are the high depth and transversal resolution. Depending on the properties of light source, OCT can achieve sub-micrometer resolution with the development of laser technology. Due to the diffraction (Abbe's) limitation, the resolution of current optical imaging technologies is limited to 200–350 nm. To see details of smaller things, super-resolution imaging methods, including stimulated emission depletion, photoactivated localization, and stochastic optical reconstruction, were proposed and demonstrated. Currently, its resolution can reach 5 nm, which is an extremely important step forward in the optical imaging of molecular structures. In addition, optical imaging methods can also provide the information about biological processes such as cancer metastasis. Combining the fluorescence or/and photoacoustic imaging methods, in vivo imaging flow cytometer can track the circulating tumor cells in real time. According to different biological environment, these optical imaging methods can be selected to provide important biological information for human diseases diagnostics. This book will introduce the basic principle of these optical imaging technologies and focus on the human disease diagnostics using these optical imaging methods. It is intended to attract and provide researchers with different background with necessary information and the latest trend in this area of optical imaging in diseases diagnostics. Finally it will hopefully promote further development of optical imaging methods and expand optical imaging to a wide range of disease diagnostics.

The original version of the book was revised: Volume number has been updated. The correction to this chapter is available at https://doi.org/10.1007/978-981-15-7627-0_14

Contents

Fundamentals of Optical Imaging

1

Liyun Lin, Pengfei Jiang, Zhouzhou Bao, Wen Pang, Shihui Ding, Ming-Jie Yin, Pengcheng Li, and Bobo Gu

1.1 Introduction

The development of medical imaging from X-ray imaging to computer-assisted tomography (CT), to ultrasound imaging, and to magnetic resonance imaging (MRI) has promoted the technical revolution, enabling improvements in the healthcare quality. The medical imaging technologies mentioned above provide many distinguished advantages, but they also suffer from some limitations, e.g., most of these methods are functional and anatomical imaging, and the specimen are mainly limited to tissue or organ levels. In order to obtain the biological information at the cellular and even molecular levels, which can offer early-stage information of disease, especially cancer, optical imaging method is rapidly developed and has been one of standard research tools for diagnosis of human diseases [1–3]. Optical

Liyun Lin, Pengfei Jiang, and Zhouzhou Bao contributed equally to this work.

L. Lin · P. Jiang · W. Pang · S. Ding · B. Gu (✉)
School of Biomedical Engineering, Shanghai Jiao Tong University, Shanghai, China
e-mail: bobogu@sjtu.edu.cn

Z. Bao
Department of Obstetrics and Gynecology, Ren Ji Hospital, School of Medicine, Shanghai Jiao Tong University, Shanghai, China

Shanghai Key Laboratory of Gynecologic Oncology, Ren Ji Hospital, School of Medicine, Shanghai Jiao Tong University, Shanghai, China

M.-J. Yin
Beijing Key Laboratory for Green Catalysis and Separation, College of Environmental and Energy Engineering, Beijing University of Technology, Beijing, China

P. Li
Britton Chance Center of Biomedical Photonics, Wuhan National Laboratory for Optoelectronics, Huazhong University of Science and Technology, Wuhan, China

X. Wei, B. Gu (eds.), *Optical Imaging in Human Disease and Biological Research*, Advances in Experimental Medicine and Biology 1355,
https://doi.org/10.1007/978-981-15-7627-0_1

imaging exploits the optical property variation including absorption, scattering, reflection, and fluorescence [4], to observe the specimen, such as cells, tissues, organs, and even entire live objects. As compared with the conventional medical imaging methods, optical imaging is more powerful in many fields including [1]: (1) optical imaging has better biosafety since the excitation source is light that is non-ionizing radiation; (2) imaging size scale from a few tens of nanometer (super-resolution imaging that beyond the diffraction limit) to macroscopic objects; (3) multi-dimensional imaging using one or several of transmission, reflection, scattering, absorption, fluorescence, and spectroscopic information, combined with other medical imaging methods; (4) imaging of in vitro, in vivo, and ex vivo specimens; (5) providing biological dynamics information, biochemical information, etc.; (6) high sensitivity and selectivity at molecular level.

Various optical imaging modalities and wide application scope make optical imaging field extremely rich and broad. It means that optical imaging is also a realm of forefront research worldwide, thus newly developed optical imaging technologies, improved instruments, and new biomedical applications are constantly emerging. So various optical microscopy, including fluorescence microscopy [5], confocal microscopy [6], multiphoton microscopy [7], super-resolution microscopy [8–10], etc., are currently in wide usage. With the rapid development of optical technology and fluorophore, e.g., far-red emissive fluorophore [11] and fluorophore with aggregation-induced emission feature [12], optical microscopy could further obtain various advantages. It is worth to note that the biosafety of newly developed nanomaterials is still the concern [13, 14]. Optical tomography, including optical coherence tomography (OCT) [15] and diffuse optical tomography (DOT) [16], could create the volumetric model of a specimen by reconstructing images. Due to the availability of highly specific optical probes, whole-animal and even patient-based optical imaging technologies have been proposed and demonstrated [17].

This chapter will first introduce the basic concept of optical imaging, which is followed by the main mechanism of light-matter interactions, including absorption, scattering, fluorescence, etc., in biological tissue. It is worth to note that these optical properties not only could be used as the imaging contrast but also affect the imaging quality. And then the working principle of various light microscopy and optical tomography technologies will be presented with their main features and bioimaging applications. Finally, the chapter would discuss the challenges and perspectives of these optical imaging methods for further development in the near future.

1.2 Basic Concept of Optical Imaging

A number of optical phenomena, including absorption, scattering, fluorescence, etc., have been used to form contrast for optical imaging or improve the optical imaging quality. It is necessary to introduce these light-matter interactions in biological tissue.

1.3 Absorption and Fluorescence

The absorbed energy would be released by radiative and non-radiative pathways once photon is absorbed by matter. For the non-radiative pathway, the energy of incident light would be transformed to the thermal energy. The absorption induced thermal distribution could provide the imaging contrast, enabling thermal imaging [18]. Meanwhile, the absorbed energy is turned into heat, leading to the transient thermoelastic expansion and subsequently ultrasonic emission, then photoacoustic imaging is enabled [19]. However, absorption can also lower the penetration depth of optical imaging technologies. The biological sample has strong absorption in visible light, so near-infrared (NIR) light is utilized to enhance imaging depth [20]. The radiative pathway could induce the emission of fluorescence or phosphorescence [1]. Normally, radiative and non-radiative processes take place sequentially or simultaneously, so the emitted photon undergoes the Stokes shift (or has a longer wavelength/lower energy as compared with the absorbed photon), which could be explained using the energy states and relaxation pathways of molecule, i.e., the Jablonski diagrams, as shown in Fig. 1.1. In practice, the electronic states of one molecule possesses various related vibrational energy levels. Once absorbing one photon, the molecule is excited from one of these vibrational levels S_0 to the excited single state S_1 or S_2. Molecule in the exited state can be relaxed to the S_0 state by various ways including radiative and non-radiative pathways, which are described as solid and dashed lines in Fig. 1.1, respectively. Fluorescence is the fast emission process of energy by a direct relaxation from the lowest vibration state of S_1 to S_0. The process typically occurs within nanosecond scale, meanwhile the excited state lifetime depends on its immediate environment. Thus the image of the morphology could be constructed by fluorescence lifetime imaging microscopy (FLIM)

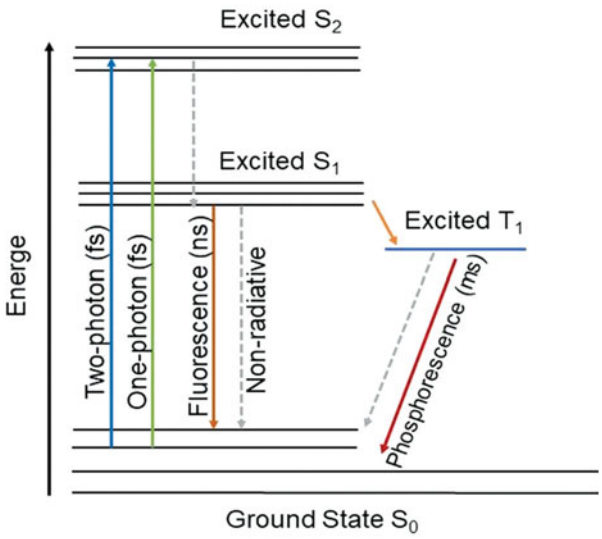

Fig. 1.1 Jablonski diagram. The characteristics and mutual relationship of molecule physical processes when molecules absorb photons and dissipate energy back to the ground state. (Adapted with permission from Ref. [5]. Copyright 2005 Springer Nature)

technology [21], which will be introduced in Chap. 4 in detail. If the molecule experiences the spin conversion, it can be transferred to triplet state T_1 via intersystem crossing (ISC). The subsequent radiation is very slow and within the time scale of millisecond, the emitted signal is known as phosphorescence. In the relaxation process from T_1 to S_0, the energy could be transferred to the ambient oxygen and result in reactive oxygen species (ROS), which is the main mechanism of photodynamic therapy (PDT) [22, 23]. For imaging purpose, fluorescence is employed and other processes that lower the quantum efficiency including non-radiative process, phosphorescence, etc. should be minimized as much as possible. Fluorescence resonance energy transfer (FRET) can suppress the emission of the donor when the molecules are close enough to each other, and this process could provide the position information of the molecules at the nanoscale, enabling bioimaging and biosensing [24].

It is well known that the standard fluorescence microscopy utilizes the fluorescence to generate an image for study of organic or inorganic substance. Normally, the substance absorbs short wavelength light and emits long wavelength light due to the non-radiative loss. In contrast, in multiphoton fluorescence microscopy, multiphotons with lower energy are absorbed concurrently and the fluorescent substance emits shorter wavelength fluorescence.

1.4 Scattering and Multiple Scattering

When propagating in matter, light will interact with matter and suffer from scattering, wherein some forms of radiation such as sound and light are forced to deviate from the straight pathway due to the localized non-uniformity in the matter [25]. Here, the scattering of light refers to the elastic and inelastic scattering, which includes Rayleigh scattering, Mie scattering and Raman scattering, Brillouin scattering, respectively.

Elastic scattering means that the wavelength/energy of the scattered light is not changed. The scattering process can be described that the scatterer experiences the oscillating polarization due to the light, and the resulted polarization induces the light radiation in all directions, leading to attenuated incident light accordingly. Rayleigh scattering is the main elastic scattering of light by particles much smaller than the wavelength of radiation [26]. Here, the particles could be individual atoms or molecules. The intensity of scattering is proportional to the fourth power of the optical frequency, or with the inverse fourth power of the wavelength. Thus, near-infrared (NIR) light is utilized to lower the scattering and subsequently enhance the penetration depth for optical imaging. Once the wavelength of incident light is similar to or smaller than the particles size, Mie theory should be applied for scattering analysis. In contrast to Rayleigh scattering, the Mie scattering intensity does not depend that much on the optical wavelength [27].

While in the inelastic scattering process, some of the energy of the incident light would be lost or increased. Raman scattering is the most common inelastic scattering in optical imaging field [28, 29]. Typically, the molecules are endowed with a higher

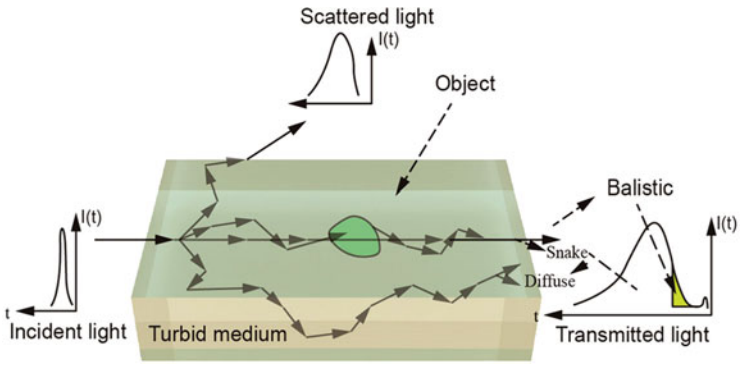

Fig. 1.2 Light propagates through a turbid medium. (Adapted with permission from Ref. [1]. Copyright 2003 WILEY-VCH)

energy due to the change of vibration and rotation states, and correspondingly the energy of scattered light is lowered. Raman spectroscopy, which can be used to measure the vibrational modes of molecules, usually provides structural fingerprint spectra to identify molecules. Actually, the Raman scattering is extremely weak (approximately one in ten million). Some enhancement methods have been adopted to amplify Raman signals. Surface-enhanced Raman scattering (SERS) is the most common technique that enhances Raman scattering by adsorbing molecules on metal surface or nanostructures [30, 31]. The enhancement factor can reach as much as 10^{10} to 10^{11}, enabling single molecule detection. The scattered light could also obtain anti-Stokes components with increased energy if the molecules are initially excited. More information about Raman imaging will be described in Chap. 9.

When light is scattered only one time by the particles, it refers to single scattering. Generally, the light would be scattered many times since there are various particles in the transmission media. It means light undergoes multiple scattering inevitably when propagating in the matter. The main difference is that single scattering is treated as random phenomenon, while multiple scattering can be treated as a more deterministic process since various scattering events tend to average out [25], which thus can be modeled well with diffusion theory.

As shown in Fig. 1.2, when light travels through a highly scattering medium, the transmitted light consists of three parts: unscattered (or coherently scattered), weakly scattered, and multiple scattered light. The coherently scattered light, also named as ballistic photons, propagates along the incident pathway and thus carries the maximum information of the transmitted medium. One portion of scattered light, but still in the transmission orientation, is named as snake photons and also carries significant information of the scattering medium. To use ballistic and snake photon for imaging, most of the diffuse photons, which suffer from multiple scattering, have to be discriminated.

1.5 Optical Propagation in Tissue

The main limitation of optical imaging penetration depth and resolution is ascribed to the optical characteristics of tissue since there are various substructures and boundaries in cells. Both scattering and absorption could attenuate the propagated light in accordance with Lambert-Beers law: $I(z) = I_0 \exp(-\mu z)$. Meanwhile, the scattering (μ_s) and absorption (μ_a) parameters with the physical units of cm^{-1} or mm^{-1} are adopted to describe the scattering and absorption, respectively, and the mean free path L_s and L_a is related to the reciprocal value of these coefficients.

Tissue is highly absorptive for visible light ($\mu_a \gg 1\ cm^{-1}$, $L_a < 1$ cm) due to the rich absorbing medium in cells, e.g., cytochromes and hemoglobin. While in the wavelength range from 600 to 900 nm, i.e., NIR wavelength range, light can penetrate tissues up to several centimeters (μ_a is less than 0.5 cm^{-1} and can reach 0.1 cm^{-1}) [32]. The good penetration depth in NIR wavelength range stimulates the exploration of NIR fluorescent molecules, which is difficult to synthesize and also less efficient. Another solution to excite fluorescent molecules in NIR wavelength range is the utilization of nonlinear optical excitation [33], including multiphoton excitation, harmonic generation, etc.

However, the main problem for optical imaging using visible light is scattering instead of absorption. The scattering coefficient (μ_s) is approximately around 100 cm^{-1}, which is approximately four orders of magnitude larger than μ_a, so the total mean free path is just 0.1 mm. Thus, optical imaging using visible light is limited to thin sections or shallow depth. The optical properties of blood and penetration depth of light are shown in Fig. 1.3.

1.6 Overview of Optical Imaging

Various optical characteristics are used to construct the imaging contrast. According to the type of detected photon, i.e., coherently scattered and diffuse photons, the optical imaging methods could be classified. Since the coherently scattered photons could carry the maximum information of the inside composition of tissue, coherently scattered photons based optical imaging methods, including confocal imaging, fluorescence imaging, multiphoton imaging, etc., could obtain the imaging directly using the detected photons. While the diffuse photon, which should be discriminated from coherently scattered photons when performing optical imaging, carries very limited information and can't perform optical imaging directly, so post-processing (mainly algorithm) has to be adopted to reconstruct the imaging, this kind of optical imaging methods include diffuse optical tomography (DOT), etc. More details of these technologies of optical imaging will be introduced in the next section.

Most optical imaging systems require at least three basic essential factors: light source to excite the specimen, filter to remove the background signal, and photon detector to obtain signal. Light source can be distinguished by their output wavelength, bandwidth, power, etc. Lamps, LEDs, and lasers are the common used light source for optical imaging. To improve the signal-to-noise ratio (SNR) and

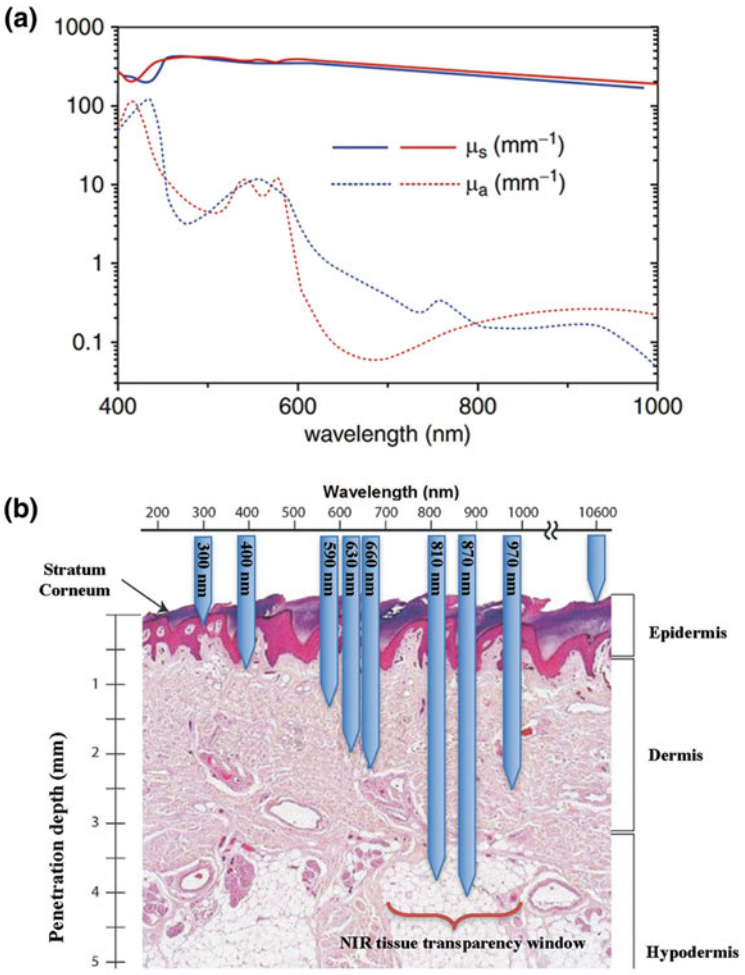

Fig. 1.3 (**a**) Optical properties of blood. Scattering coefficient μ_s and absorption coefficient μ_a of oxygenated (red) and deoxygenated (blue) whole blood [34] (adapted with permission from Ref. [2]; copyright 2014 Springer Nature); (**b**) The penetration depth of light with different wavelengths in tissue [35]. (Adapted with permission from Ref. [35]. Copyright 2010 WILEY-VCH)

subsequently imaging quality, the background signal including excitation light, autofluorescence, should be efficiently eliminated. Considering that the emission intensity is usually weak and wavelength is close to the excitation, filters should be selected carefully by the transmission spectra. Long-pass, short-pass, band-pass, or notch filters with appropriate optical density (OD, defined as the ratio of transmitted to original light intensity) will be used according to the practical optical imaging systems. When selecting photon detectors, the channel number (single channel or

multichannel), detection dynamic (commonly expressed in bits), sensitivity, and resolution should be considered.

1.7 Standard Optical Microscopy

As shown in Fig. 1.4, a compound optical microscopy [36], which consists of a combination of lenses and uses light to generate a magnified image of specimen projected onto the retina or imaging device, is the basic and widely used optical imaging method. Here, the term compound refers to that the combination of objectives and the eyepiece (or ocular) work together to generate the final magnified image, meanwhile, the final magnification equals to the product of the magnifying power of the objective lens and that of the eyepiece.

It is well known that objective lens and condenser lens are the key components in forming images. The objective lens could collect diffracted light by specimen and generate a magnified real image at intermediate image plane near the eyepiece or oculars once the specimen is illuminated by the focused light using the condenser lens. Actually, the achievable resolution depends on the objective lens and on the illumination. Illumination is one critical factor to determine the performance of optical microscopy. It is critical to achieve that the focus point and size of emitted light should be adjusted to locate at the front aperture of the condenser and match the specimen field diameter of the employed objective lens, respectively. One of the

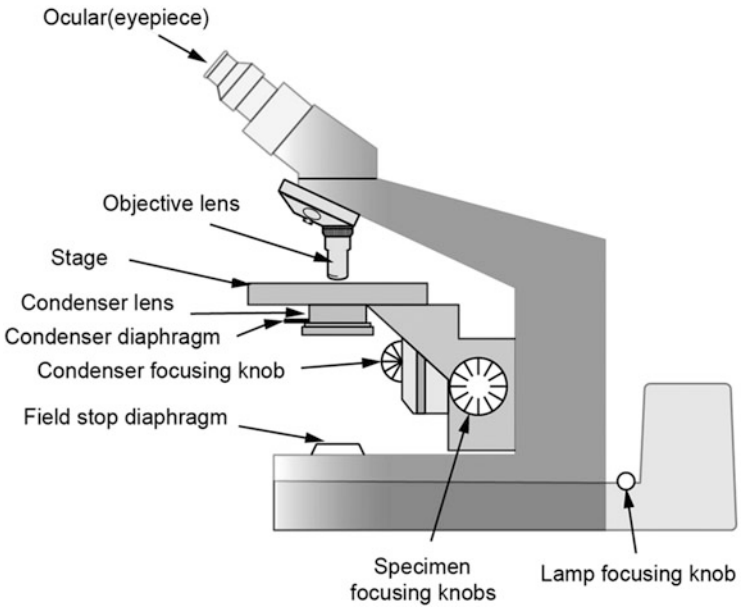

Fig. 1.4 The compound light microscopy. (Adapted with permission from Ref. [36]. Copyright 2001 WILEY-VCH)

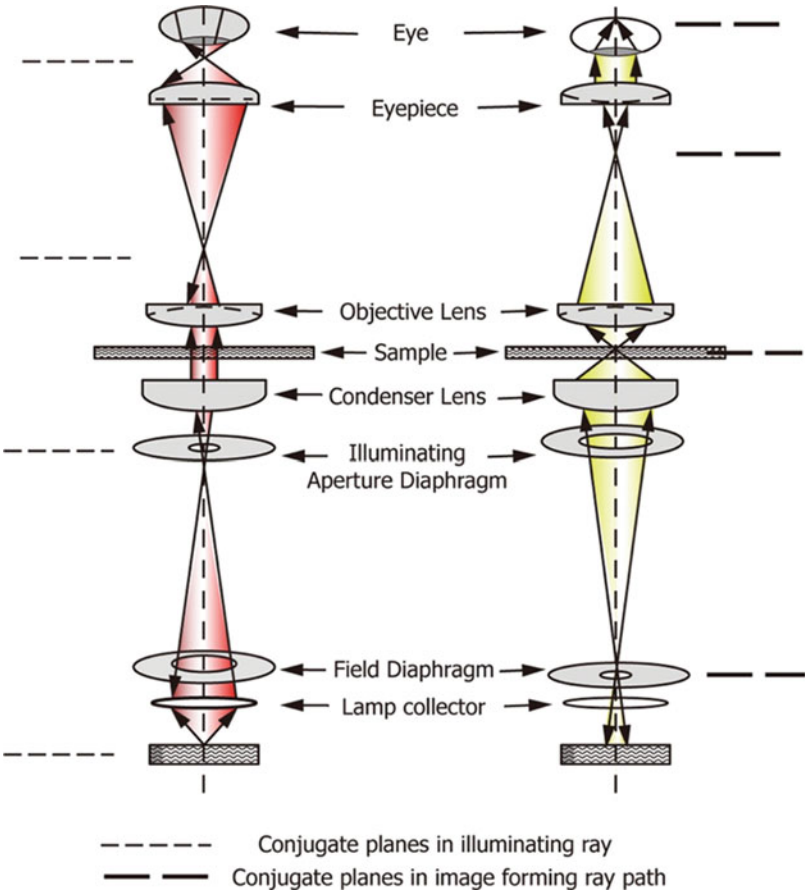

Fig. 1.5 Schematic design for Kohler illumination. (Adapted with permission from Ref. [36]. Copyright 2001 WILEY-VCH)

most common used illumination systems is the Kohler illumination, which could fulfill these requirements and provide a uniform illumination field. Furthermore, to achieve the best resolution, light with the widest available cone should be used to illuminate the specimen. As shown in Fig. 1.5, the specimen is illuminated uniformly with a widest available light cone in the Kohler illumination scheme. The light pathways, displayed in Fig. 1.5, schematically represent the light rays of specimen illuminating and image-forming. The illuminating light rays generate the images of the filament at the plane of the condenser aperture diaphragm, the rear focal plane of the objective lens, and the eye point of the eyepiece. All planes mentioned above are named as conjugate planes of illuminating light rays, which means that image focused on one plane is automatically focused on all other conjugate planes. Meanwhile the conjugate planes of image-forming light rays are consisted of field diaphragm, the plane of the sample, the plane of intermediate image, and the eye's

retina (or other imaging device). It allows to independently control the angle and intensity, at which the specimen is illuminated.

The definition of optical resolution is the shortest distance between two distinguishable points on a specimen. As mentioned above, the resolution is related directly to the cone of light from the specimen to the objective, meanwhile, the resolution is also limited due to the diffraction limit. The resolution is determined by Rayleigh's criterion [37]: $d = 0.61\lambda/\mathrm{NA}$, where d is the resolution, NA is the numerical aperture (NA) of the objective, describing its ability to gather light. $\mathrm{NA} = n \sin(\theta)$, here n refers to the medium refractive index, θ refers to the maximum angle at which the light could be gathered by the objective. The larger the cone of light entering the objective, the larger its NA. One way to further increase NA is to increase n by using the immersion medium with higher refractive index (e.g., oil) as compared with air. It is worth to note that the high NA objectives would decrease the working distance. Therefore, the resolution can be increased by increasing NA or choosing shorter wavelength, but UV light is harmful for biological samples. In order to further increase the resolution and break the diffraction limit, the concept of super-resolution imaging was proposed and demonstrated, more details will be described in Chap. 2.

1.8 Fluorescence Microscopy

In contrast to other optical microscopy based on the object-related characteristics including absorption, optical path differences, phase gradients, birefringence, etc., fluorescence microscopy is an optical microscopy that uses fluorescence to study the properties of specimen, enabling observe the distribution of a single molecular species and even detect individual fluorescent molecules. Meanwhile, the fluorescence microscopy, including a simple setup like epifluorescence microscopy or a complicated design like confocal microscopy, could use optical sectioning to improve the resolution. To use fluorescence microscopy for biomedical study, one can utilize the endogenous fluorescence (autofluorescence) or label the specimen with the suitable molecule.

Light with the specific wavelength illuminated the specimen, and the fluorophores absorbed light, inducing the emission of the fluorescent signal. To achieve the fluorescence image with high SNR, the illuminating light is separated from the much weak fluorescent signal by filter. In fluorescence microscopy, the typical components include light source, excitation and emission filters, and dichroic mirror (or dichroic beam-splitter). The filters and dichroic mirror should be chosen carefully to match the spectral characteristics of the used fluorophores.

The fluorescence microscopy is widely utilized nowadays, e.g., epifluorescence microscopy, wherein the excitation light passes through the same objective that gathers the fluorescence signal for imaging, is frequently used in life science. As shown in Fig. 1.6, the specimen is illuminated by the excitation light via the objective, the excited fluorescence is subsequently collected by the same objective, which should have higher NA for better resolution. Since most of the excitation light

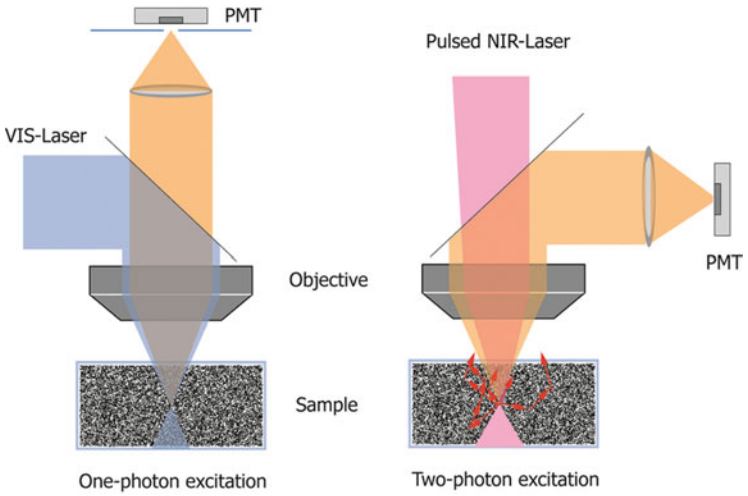

Fig. 1.6 Fluorescence microscopy based on one-photon (left) and two-photon (right) excitation. (Adapted with permission from Ref. [2]. Copyright 2014 Springer Nature)

either excites the fluorophores or transmits through the specimen, the reflected excitation light collected by the objective lens is very limited, enabling the high SNR of fluorescence images. The dichroic beam-splitter transmits fluorescence signal to the eyepiece or detector, but reflects the remaining excitation light. With the advance of fluorophores [38], which can specifically target the cellular different compositions or probe the processes of ion channel, the fluorescence microscopy plays more and more important role in biology [39].

1.9 Confocal Microscopy

In the conventional wide-field microscopy, the image of specimens is the stack of the clear image from the in-focus region and blurred images of all out-of-focus regions. This effect has no significant influence on the imaging quality of thin samples. However, for the thick specimens imaging, especially for the in vivo imaging, the generated image by conventional wide-field microscopy is mainly composed of optical information from out-of-focus region, lowering the contrast of the in-focus signal and deteriorating the image quality.

Confocal microscopy, most frequently named laser confocal scanning microscopy (LCSM) or confocal laser scanning microscopy (CLSM), provides a strategy to overcome this problem by introducing a spatial pinhole to prevent all defocused light from blurring the images [40]. Confocal microscopy could reconstruct the high-quality three-dimensional structures of the specimen via capturing various two-dimensional images generated at different depths in the specimen, making it an extremely valuable tool in life and biological science.

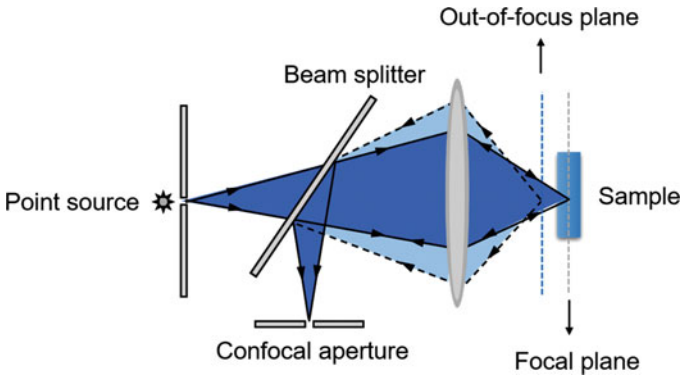

Fig. 1.7 Working principle of confocal microscopy. (Adapted with permission from Ref. [41]. Copyright 2006 Springer)

The operating principle of confocal microscopy is described in Fig. 1.7. In contrast to the conventional wide-field microscopy, in which the specimens are evenly excited by the light source meantime and all the excited fluorescence is collected simultaneously, the confocal microscopy utilizes a pinhole located in one optically conjugated plane in front of the detector to block all out-of-focus signal. Thus, the generated image is composed of in-focus optical information, indicating that confocal image is fundamentally an optical section of the specimens. Moreover, the resolution of confocal microscopy is much higher than that of wide-field microscopy since only fluorescence signal emitted from the focal point can be detected. However, most of the excited fluorescence signal are blocked by pinhole, the intensity of detected signal is significantly decreased, thus long exposure or sensitive detector (e.g., photomultiplier tube (PMT) or avalanche photodiode) has to be adopted.

As described above, only one point of specimen located within the focal plane can be imaged at one time. The focused spot has to be swept across the whole specimen, either by scanning the laser beam in a raster mode with galvanometer mirrors [42] or by moving the sample stage [43], to reconstruct the structure of specimen with confocal microscopy.

The stage scanning with fixed laser beam eliminates the lens induced aberrations. Nevertheless, any motion of the specimens could cause vibration and distortion, deteriorating imaging resolution and quality. Therefore, beam scanning with galvanometer mirrors is more appropriate for biological imaging. While for three-dimensional image constructions [44], piezoelectric platform or stepper motor has to be adopted to move the sample stage vertically and consequently alter the focal plane. The vertical resolution is related to the thickness of the focal plane and can approach the limit of resolution theoretically. Actually, it depends on multiple factors, such as specimen property, wavelength, and number aperture.

Confocal microscopy enables direct, noninvasive sectioning of intact, thick, living specimens as well as improved lateral resolution, making it powerful tool for biological applications.

1.10 Multiphoton Microscopy

It is well known that visible light has very limited penetration depth in biological tissue, NIR light provides a strategy to increase the bioimaging depth, and NIR light based multiphoton microscopy attracted much interest from both academic and industrial fields recent years.

Multiphoton absorption, which is a typical nonlinear absorption process [33, 45], refers to the simultaneous absorption of two or more photons. Two-photon/three-photon absorption corresponds to a third-order/fifth-order nonlinear process, which is described by the third-order/fifth-order nonlinear optical susceptibility $\chi^{(3)}/\chi^{(5)}$. And the absorption capability is described by two-photon/three-photon absorption cross-section. The optical transition of multiphoton absorption, which is related to the square/cubic of light intensity for two-photon/three-photon absorption, is totally different from the linear absorption. Thus, the highly focused laser beam with high peak power is of great importance for multiphoton absorption process. The common light source for multiphoton excitation is femtoseconds laser, which can provide high peak power and low average power due to its ultra-short pulse. The unique features of femtoseconds laser enable nonlinear optics process and avoid laser induced thermal damage for biological samples. It is worth to note that the simultaneous absorption of multiple photons, i.e., multiphoton absorption is different from the up-conversion process, in which multiple photons are absorbed sequentially by rare-earth ions and each sequential step is a linear process [46]. With the rapid development of high-power pulsed lasers and functional materials with large two-photon/three-photon absorption cross-section, multiphoton absorption is receiving much attention for both academic and technological applications.

The typical application of multiphoton absorption in biological field is multiphoton microscopy, which is regarded as a good choice for imaging of living, intact biological samples on the scales from molecular level to the whole organisms [47, 48]. Multiphoton microscopy has many inherent advantages including improved penetration depth and reduced photodamage, which is the direct result of employing NIR femtosecond lasers.

In multiphoton microscopy, the fluorophore is excited by the femtosecond laser and the excited fluorescence is detected to form a fluorescence image. Multiphoton microscopies including two-photon and three-photon microscopies [47, 48] have been applied for bioimaging applications. As compared with two-photon microscopy, the three-photon microscopy can obtain better imaging depth, but its requirements of laser source and detector are much higher than that of two-photon microscopy. Two-photon microscopy is more feasible and promising for practical bioimaging applications. In two-photon microscopy, the high-power pulsed laser beam is tightly focused for two-photon excitation, and the defocused region has

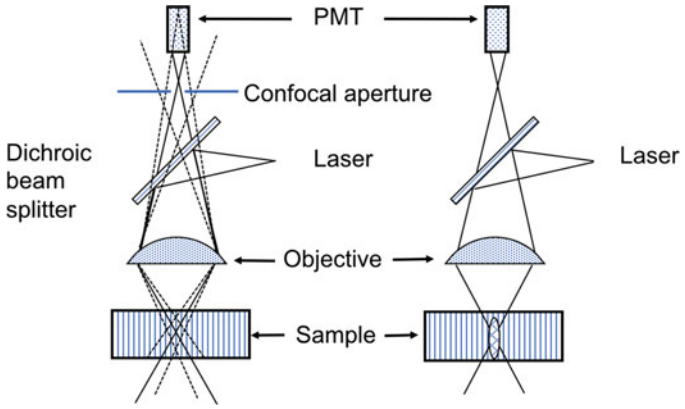

Fig. 1.8 Confocal and multiphoton imaging. (Adapted with permission from Ref. [45]. Copyright 2008 American Chemical Society)

much less possibility to be excited due to the nonlinear optics characteristics. This process efficiently eliminates the defocused fluorescence, which exists inevitably in single-photon excitation process without the confocal aperture, as shown in Fig. 1.8. Two-photon microscopy inherently possesses optical sectioning capability without additional confocal aperture. Meanwhile, two-photon microscopy can significantly improve the photobleaching issue as only the focused point can be excited. Moreover, as compared with UV-visible light excitation in common microscopy, NIR light excitation in two-photon microscopy has much deeper penetration depth due to its less scattering and absorption in biological tissue. The viability of biological samples can be improved and more scans can be performed to construct the three-dimensional images since the UV light is eliminated efficiently. In addition to the photodamage and imaging depth, resolution is another factor to evaluate the performance of microscopy. As discussed earlier in this chapter, the objective lens and the diffraction limit by the specimen determine the imaging resolution. As compared with conventional confocal microscopy, multiphoton microscopy theoretically should possess worse resolution since the significantly longer wavelength is used. However, the achieved resolution is also influenced by other factors like out-of-focus fluorescence. Generally, the main advantages of multiphoton microscopy are not improved resolution but others described above. As compared with the conventional laser scanning microscopy in optical system, only few optical elements need to be changed in the multiphoton microscopy.

1.11 Super-Resolution Microscopy

As described above, the fluorescence microscopy is widely used to observe the detailed information in biological samples. However, the conventional fluorescence microscopy suffers from low spatial resolution due to the diffraction limit. The

lateral and axial resolution can reach about 200–300 nm and 500–700 nm, respectively, which is comparable or larger than the subcellular structures. In order to study more details in the subcellular domain, various super-resolution microscopy techniques have been proposed and demonstrated in recent years, including stimulated emission depletion (STED) microscopy [49], stochastic optical reconstruction microscopy (STORM) [50], saturated structured-illumination microscopy (SSIM) [51], photoactivated localization microscopy (PALM) [52], etc. In 2014, Eric Betzig, Stefan W. Hell, and William E. Moerner were awarded the Nobel Prize in Chemistry for their contributions to super-resolution fluorescence microscopy. The mechanism of STED microscopy will be briefly introduced in this section, and more details about other super-resolution microscopy techniques will be discussed in Chap. 2.

STED microscopy is one typical super-resolution technique. The concept of STED microscopy was first proposed by S. W. Hell and J. Wichmann in 1994 [49], and was first experimentally demonstrated by S. W. Hell and T. Klar in 1999 [53, 54]. STED microscopy utilizes another laser (called STED laser) to alter the fluorescence emission of fluorescent molecule out of the excitation center. This process is achieved by stimulated emission, which is the process by which an incident photon with specific frequency interacts with an excited atomic electron, inducing it to drop to a lower energy and emit a new photon with the same characteristic as the incident photon, including phase, frequency, polarization, and direction. This process is totally different from the spontaneous emission, in which the emitted photon has random features in phase, frequencey, polarization and direction. In conventional fluorescence microscopy, the emitted fluorescence is spontaneous one. Spontaneous emission can be interrupted before the photon is released under the STED laser excitation. The excited electron is forced to relax to a higher vibration state than that in fluorescence transition process, making the emitted photon red-shift. This shift could differentiate the two types of photons, i.e., stimulated and spontaneous one.

STED achieves super-resolution by depleting fluorescence signal around the focal point, leaving the center focal point to emit fluorescence as shown in Fig. 1.9. Point spread function (PSF) refers to the three-dimensional intensity distribution of the image of a point object and its size determines the resolution of the microscopy. In order to sharpen PSF and yield better resolution, the STED laser should have a pattern with zero intensity at the center and non-zero intensity at the periphery. The phase mask is inserted in light path to modify the pattern of STED laser, and the widely used STED pattern is donut-shaped as shown in Fig. 1.9. However, it is difficult to achieve super-resolution imaging with STED alone since the pattern of laser is also restricted by the diffraction too. In order to achieve optical super-resolution, one strategy is to utilize the nonlinear dependence of the depleted population on the STED laser intensity. When the STED laser intensity exceeds one certain threshold, all spontaneous emission is suppressed. With further increment of STED laser power, the saturated depletion region further expands without any strong influence on the focal point. As a result, only the fluorescence signal from a very small region around the focal point can be successfully captured for imaging. It is

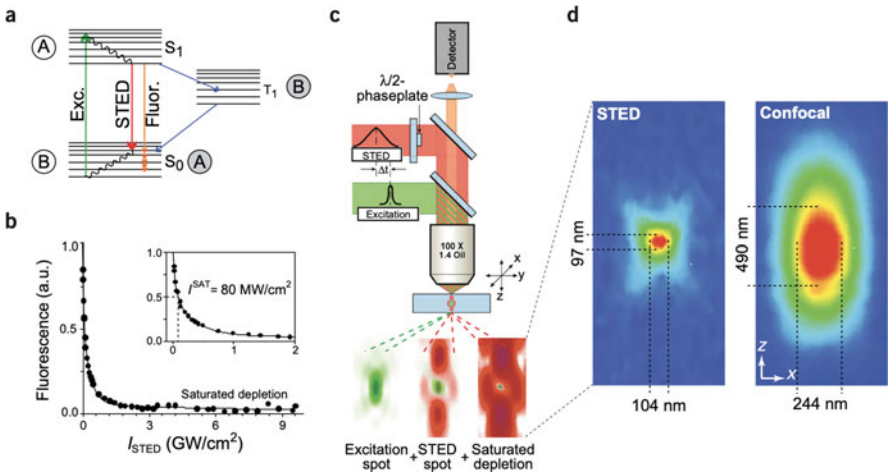

Fig. 1.9 Physical conditions, setup, and typical focal spot for STED. (**a**) Energy diagram of an organic fluorophore. (**b**) Saturated depletion of the S_1 with increasing STED pulse intensity ISTED. (**c**) Sketch of a point-scanning STED microscope. (**d**) Fluorescent spot in the STED and in the confocal microscope. (Adapted with permission from Ref. [54]. Copyright 2003 Springer Nature)

worth to note that the region size is restricted to the actual power level of STED laser rather than the light diffraction. Currently, the achieved resolution is normally about 30–80 nm [55].

1.12 Optical Coherence Tomography

Optical coherence tomography (OCT) is an emerging technology that has been clinically used in a broad range, such as ophthalmology and dentistry. Combined with catheters and endoscopes, OCT can perform high-resolution and real-time intraluminal imaging of organs [56, 57], making it a powerful imaging technology for medical diagnostics. Similar to ultrasound imaging using ultrasound scattered from specific tissues for imaging, OCT is also a reflection imaging technique, except that it utilizes scattered light instead of scattered ultrasound for imaging.

The basic operation principle of OCT is the low-coherent interferometry. As shown in Fig. 1.10, light is divided into two arms, i.e., sample arm in which the sample information is achieved and reference arm, and then the reflected light from sample and mirror are combined together, forming the interference pattern if the optical path difference between the two arms is within the coherence length. A-Scan, a scanning method by scanning the reference arm, can obtain the reflectivity profile of the sample, which is related to the spatial dimensions and position of structure to be imaged. The cross-section tomography, i.e., B-scan, can be obtained by laterally scanning sample arm. In conventional low-coherent interferometry, interference occurs over several meters. In OCT, interference occurs within micrometers when

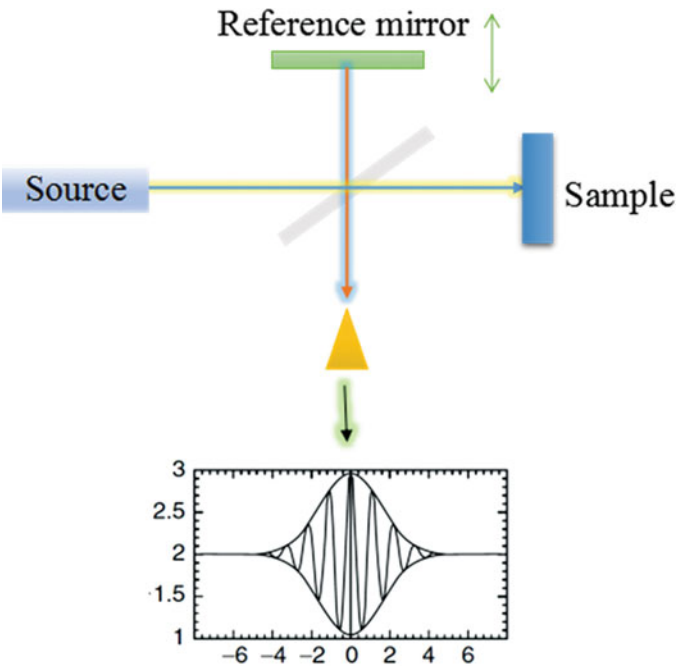

Fig. 1.10 The working principle of time-domain OCT

using broad-band light source like super-luminescent diodes, short-pulsed laser, etc. The axial resolution of OCT depends on the coherent length of light source. The shorter the coherent length, the better the axial resolution. The employed broad-band light source efficiently shortens the coherent length and subsequently increases the resolution. This OCT technique mentioned above is time-domain OCT, and many other OCT techniques like frequency domain OCT, spatially encoded frequency domain OCT, time encoded frequency domain OCT, etc. will be introduced in Chap. 10.

1.13 Diffuse Optical Tomography

The ballistic or snake photons, which can be captured by optical microscopy or OCT described above, are rare in thick biological tissue and only suitable for thin biological tissue imaging. NIR diffuse optical tomography (DOT), an imaging method utilizing scattered photons, can image thick biological tissue. DOT utilizes a finite set of measurements of transmitted light between point pairs on the specimen surface to reconstruct a transverse slice or even a three-dimensional volume of the specimen. The diffusive-photon-based image reconstruction needs special algorithms, and various algorithms for DOT based on the technique of inverse problem have been developed. Moreover, utilization of fluorescence markers could

substantially improve the SNR. Since 1990s [58], DOT, which is mainly composed of a series of light sources and detectors around the skull, has been used to humans and neonates as a powerful diagnostic tool. Based on tomography reconstruction, the hemodynamic response in the cerebral cortex can be obtained with millimeter resolution [59].

1.14 Other Imaging Modalities

In addition to the widely used bioimaging modalities mentioned above, various new techniques have also proposed and demonstrated for bioimaging applications.

Fluorescence lifetime imaging microscopy, i.e., FLIM, could map the spatial lifetime distribution of the fluorophore within a specimen. As compared with the conventional fluorescence microscopy, the utilization of fluorescence lifetime as the imaging contrast possesses a lot of advantages. More details about FLIM will be introduced in Chap. 4.

Nonlinear optical effects such as multiphoton absorption can be utilized as the imaging contrast for microscopic studies. The nonlinear optical imaging methods provide various advantages, e.g., precise spatial selection due to the higher-order dependence on the excitation intensity. Second-harmonic microscopy [60], which is based on the nonlinear optical effect named second-harmonic generation (SHG), can obtain contrasts from SHG signal (exactly half the wavelength or double frequency of the incident light) variations in a specimen under excitation. Intense laser light and non-centrosymmetric molecular structure are required to produce SHG signal for imaging [61]. While for third-harmonic microscopy [62], the contrast signal, i.e., third-harmonic generation (THG) signal, is exactly one-third the wavelength or triple frequency of the incident light. In contrast to SHG, THG can be observed both in bulk and at surfaces without any requirement on molecular symmetry. Since harmonic generation doesn't involve any light absorption, there is no any thermal damage or photobleaching on specimen when performing imaging if the wavelength of incident light is selected outside of the absorption band.

The Raman imaging is unique and powerful imaging method to obtain details on the molecular level based on the Raman spectrum of the sample, which can show the vibration mode of molecules. Thus Raman imaging can provide structural fingerprints, enabling to distinguish different molecules including biomolecules. The Raman images of the specimens can be interrogated from the complete spectra, which is measured at each pixel of the specimen. More details about Raman imaging will be introduced in Chap. 9. Unlike Raman spectroscopy, coherent anti-Stokes Raman scattering (CARS) addresses the molecular vibrations using multiple photons, and then generates a coherent signal for imaging [63]. In CARS system, two laser beams (ω_p and ω_s) interact in the sample to generate an anti-Stokes optical output ($\omega_{AS} = 2\omega_p - \omega_s$) in the phase-matched direction. And CARS signal is resonantly enhanced if $\omega_p - \omega_s$ is in accord with the frequency of a Raman active molecular vibration, making that CARS signal is orders of magnitude stronger than spontaneous Raman emission.

Photoacoustic imaging, which is based on the photoacoustic effect, is also used for various biomedical applications. The laser pulses are delivered to the specimen, then part of the photons are absorbed and converted to heat and subsequently induce the thermoelastic expansion and ultrasonic emission for imaging. Thus photoacoustic image can be constructed by detecting and analyzing those generated ultrasonic waves [19]. More details of photoacoustic imaging will be introduced in Chap. 8.

1.15 Conclusion and Perspective

In this fundamental chapter, a number of the main physical and optical mechanisms that make up the foundation of modern optical imaging techniques were introduced. Following the basic concept of biomedical photonics such as absorption, scattering, and fluorescence, the working mechanisms of conventional optical microscopy (including fluorescence microscopy, confocal microscopy, super-resolution microscopy, etc.) and optical tomography (including optical coherence tomography and diffuse optical tomography) were introduced. Finally, other imaging modalities were briefly presented. Moreover, the typical applications of these emerging optical imaging were also covered.

Current optical imaging techniques have shown great potential for imaging from subcellular structures to human beings with real-time, high-resolution and noninvasive features. With the development of new technologies and theranostics requirements, future optical imaging should have new features: (1). Multifunctional imaging. Each imaging technique, with its own unique characteristics, can offer certain biological information. To obtain the comprehensive information of the biological sample or process, a combination of two or more imaging methods is necessary. Thus, integration of several imaging techniques, i.e., multi-modal imaging technologies are evolving and innovative works; (2). Super-resolution imaging. Though still in its infancy, super-resolution microscopy has exhibited great potential in the study of structures and processes related to living organisms. It is urgent to develop fast super-resolution microscopy with a large field of view. (3). Combination microscopy. Another significant achievement of optical imaging is the integration of near-field and far-field techniques to increase the dynamic range, enabling to switch between near-field and the far-field modes and achieve high resolution in small-area and large-area images in far-field. (4). Miniaturized microscopy. Most of commercial optical microscopies are desktop instruments. To meet clinical diagnosis requirements, it is of great importance to miniaturize these optical microscopies. Recently, a two-photon microscope with fast high-resolution and miniaturized characteristic was proposed and demonstrated to record neuronal activities for several hours at the level of spines in mice [64].

Acknowledgments This work was supported by the Natural Science Foundation of China (61805135), Pujiang Talents Program (18PJ1405100), the National Key Research and

Development Program of China (2019YFC1604604), and Shanghai Jiao Tong University (ZH2018QNA43).

References

1. Prasad PN (2003) Introduction to biophotonics. Wiley-Interscience, Hoboken, NJ
2. Scheffold F (2014) Optical imaging of neocortical dynamics. Springer, New York, NY
3. Schulz RB, Semmler W (2008) Molecular imaging I. Springer, New York, NY
4. Niemz MH (2004) Laser-tissue interactions: fundamentals and applications. Springer, Berlin; New York, NY
5. Lichtman JW, Conchello JA (2005) Fluorescence microscopy. Nat Methods 2(12):910–919
6. Pawley JB (2006) Handbook of biological confocal microscopy. Springer, New York, NY
7. Zipfel WR, Williams RM, Webb WW (2003) Nonlinear magic: multiphoton microscopy in the biosciences. Nat Biotechnol 21(11):1368–1376
8. Hell SW (2015) Nanoscopy with focused light (nobel lecture). Angew Chem Int Edit 54 (28):8054–8066
9. Betzig E (2015) Single molecules, cells, and super-resolution optics (nobel lecture). Angew Chem Int Edit 54(28):8034–8053
10. Moerner WE (2015) Nobel lecture: single-molecule spectroscopy, imaging, and photocontrol: foundations for super-resolution microscopy. Rev Mod Phys 87(4):1183–1112
11. Yuan L, Lin WY, Zheng KB, He LW, Huang WM (2013) Far-red to near infrared analyte-responsive fluorescent probes based on organic fluorophore platforms for fluorescence imaging. Chem Soc Rev 42(2):622–661
12. Mei J, Leung NLC, Kwok RTK, Lam JWY, Tang BZ (2015) Aggregation-induced emission: together we shine, united we soar! Chem Rev 115(21):11718–11740
13. Yong KT, Law WC, Hu R, Ye L, Liu LW, Swihart MT, Prasad PN (2013) Nanotoxicity assessment of quantum dots: from cellular to primate studies. Chem Soc Rev 42(3):1236–1250
14. Yin F, Gu B, Li JX, Panwar N, Liu Y, Li ZG, Yong KY, Tang BZ (2019) In vitro anticancer activity of aiegens. Biomater Sci 7(9):3855–3865
15. Fercher AF, Drexler W, Hitzenberger CK, Lasser T (2003) Optical coherence tomography - principles and applications. Rep Prog Phys 66(2):239–233
16. Hoshi Y, Yamada Y (2016) Overview of diffuse optical tomography and its clinical applications. J Biomed Opt 21(9):091312
17. Hoffman RM, Yang M (2006) Whole-body imaging with fluorescent proteins. Nat Protoc 1 (3):1429–1438
18. Vollmer M, Möllmann K-P (2017) Infrared thermal imaging: fundamentals, research and applications. John Wiley & Sons, New York, NY
19. Wang LHV, Hu S (2012) Photoacoustic tomography: in vivo imaging from organelles to organs. Science 335(6075):1458–1462
20. Gu B, Yong KT, Liu B (2018) Strategies to overcome the limitations of aiegens in biomedical applications. Small Methods 2(9):1700392
21. Bastiaens PIH, Squire A (1999) Fluorescence lifetime imaging microscopy: spatial resolution of biochemical processes in the cell. Trends Cell Biol 9(2):48–52
22. Dolmans DEJGJ, Fukumura D, Jain RK (2003) Photodynamic therapy for cancer. Nat Rev Cancer 3(5):380–387
23. Gu B, Wu WB, Xu GX, Feng GX, Yin F, Chong PHJ, Qu JL, Yong KT, Liu B (2017) Precise two-photon photodynamic therapy using an efficient photosensitizer with aggregation-induced emission characteristics. Adv Mater 29(28):1701076
24. Sekar RB, Periasamy A (2003) Fluorescence resonance energy transfer (fret) microscopy imaging of live cell protein localizations. J Cell Biol 160(5):629–633
25. Luan F, Gu B, Gomes ASL, Yong KT, Wen SC, Prasad PN (2015) Lasing in nanocomposite random media. Nano Today 10(2):168–192

26. Shen YC, Qian F, Lu ZH (2001) Real-time detection of pulsed laser energy by photoacoustic technique and its application in hyper-rayleigh scattering studies. Prog Nat Sci 11:S233–SS36
27. Saidi IS, Jacques SL, Tittel FK (1995) Mie and rayleigh modeling of visible-light scattering in neonatal skin. Appl Opt 34(31):7410–7418
28. Saar BG, Freudiger CW, Reichman J, Stanley CM, Holtom GR, Xie XS (2010) Video-rate molecular imaging in vivo with stimulated raman scattering. Science 330(6009):1368–1370
29. Kuzmin AN, Pliss A, Lim CK, Heo J, Kim S, Rzhevskii A, Gu B, Yong KT, Wen SC, Prasad PN (2016) Resonance raman probes for organelle-specific labeling in live cells. Sci Rep 6 (1):1–9
30. Campion A, Kambhampati P (1998) Surface-enhanced raman scattering. Chem Soc Rev 27 (4):241–250
31. Yuan YF, Lin YN, Gu B, Panwar N, Tjin SC, Song J, Qu JL, Yong KT (2017) Optical trapping-assisted sers platform for chemical and biosensing applications: design perspectives. Coord Chem Rev 339:138–152
32. Weissleder R, Ntziachristos V (2003) Shedding light onto live molecular targets. Nat Med 9 (1):123–128
33. Gu B, Zhao CJ, Baev A, Yong KT, Wen SC, Prasad PN (2016) Molecular nonlinear optics: recent advances and applications. Adv Opt Photon 8(2):328–369
34. Faber DJ, Aalders MCG, Mik EG, Hooper BA, van Gemert MJC, van Leeuwen TG (2004) Oxygen saturation-dependent absorption and scattering of blood. Phys Rev Lett 93(2):028102
35. Barolet D, Boucher A (2010) Radiant near infrared light emitting diode exposure as skin preparation to enhance photodynamic therapy inflammatory type acne treatment outcome. Lasers Surg Med 42(2):171–178
36. Murphy DB (2001) Fundamentals of light microscopy and electronic imaging. Wiley-Liss, New York, NY
37. Born M, Wolf E (2013) Principles of optics: electromagnetic theory of propagation, interference and diffraction of light. Elsevier, Amsterdam
38. Hong GS, Antaris AL, Dai HJ (2017) Near-infrared fluorophores for biomedical imaging. Nat Biomed Eng 1(1):1–22
39. Yuste R (2005) Fluorescence microscopy today. Nat Methods 2(12):902–904
40. Marvin M (1961) Google patents
41. Pawley J (2006) Handbook of biological confocal microscopy. Springer Science & Business Media, New York, NY
42. Brakenhoff GJ (1979) Imaging modes in confocal scanning light microscopy (CSLM). J Microsc 117(2):233–242
43. Wilson T, Gannaway J, Johnson P (1980) A scanning optical microscope for the inspection of semiconductor materials and devices. J Microsc 118(3):309–314
44. Gu M (1996) Principles of three dimensional imaging in confocal microscopes. World Scientific, Singapore
45. He GS, Tan LS, Zheng Q, Prasad PN (2008) Multiphoton absorbing materials: molecular designs, characterizations, and applications. Chem Rev 108(4):1245–1230
46. Chen GY, Qju HL, Prasad PN, Chen XY (2014) Upconversion nanoparticles: design, nanochemistry, and applications in theranostics. Chem Rev 114(10):5161–5114
47. Helmchen F, Denk W (2005) Deep tissue two-photon microscopy. Nat Methods 2(12):932–940
48. Horton NG, Wang K, Kobat D, Clark CG, Wise FW, Schaffer CB, Xu C (2013) In vivo three-photon microscopy of subcortical structures within an intact mouse brain. Nat Photonics 7 (3):205–209
49. Hell SW, Wichmann J (1994) Breaking the diffraction resolution limit by stimulated emission: stimulated-emission-depletion fluorescence microscopy. Opt Lett 19(11):780–782
50. Rust MJ, Bates M, Zhuang XW (2006) Sub-diffraction-limit imaging by stochastic optical reconstruction microscopy (storm). Nat Methods 3(10):793–795

51. Gustafsson MGL (2005) Nonlinear structured-illumination microscopy: wide-field fluorescence imaging with theoretically unlimited resolution. Proc Natl Acad Sci U S A 102 (37):13081–13086
52. Hess ST, Girirajan TPK, Mason MD (2006) Ultra-high resolution imaging by fluorescence photoactivation localization microscopy. Biophys J 91(11):4258–4272
53. Klar TA, Hell SW (1999) Subdiffraction resolution in far-field fluorescence microscopy. Opt Lett 24(14):954–956
54. Hell SW (2003) Toward fluorescence nanoscopy. Nat Biotechnol 21(11):1347–1355
55. Huang B, Bates M, Zhuang XW (2009) Super-resolution fluorescence microscopy. Annu Rev Biochem 78:993–1016
56. Tearney GJ, Brezinski ME, Bouma BE, Boppart SA, Pitris C, Southern JF, Fujimoto JG (1997) In vivo endoscopic optical. Biopsy with optical coherence tomography. Science 276 (5321):2037–2039
57. Drexler W, Morgner U, Ghanta RK, Kartner FX, Schuman JS, Fujimoto JG (2001) Ultrahigh-resolution ophthalmic optical coherence tomography. Nat Med 7(4):502–507
58. Arridge SR, Schweiger M, Hiraoka M, Delpy DT (1993) A finite element approach for modeling photon transport in tissue. Med Phys 20:299–309
59. Koizumi H, Yamamoto T, Maki A, Yamashita Y, Sato H, Kawaguchi H, Ichikawa N (2003) Optical topography: practical problems and new applications. Appl Opt 42(16):3054–3062
60. Campagnola PJ, Loew LM (2003) Second-harmonic imaging microscopy for visualizing biomolecular arrays in cells, tissues and organisms. Nat Biotechnol 21(11):1356–1360
61. Gu B, Pliss A, Kuzmin AN, Baev A, Ohulchanskyy TY, Damasco JA, Yong KT, Wen SC, Prasad PN (2016) In-situ second harmonic generation by cancer cell targeting zno nanocrystals to effect photodynamic action in subcellular space. Biomaterials 104:78–86
62. Yelin D, Silberberg Y (1999) Laser scanning third-harmonic-generation microscopy in biology. Opt Express 5(8):169–175
63. Cheng JX, Xie XS (2004) Coherent anti-stokes raman scattering microscopy: instrumentation, theory, and applications. J Phys Chem B 108(3):827–840
64. Zong WJ, Wu RL, Li ML, Hu YH, Li YJ, Li JH, Rong H, Wu HT, Xu YY, Lu Y et al (2017) Fast high-resolution miniature two-photon microscopy for brain imaging in freely behaving mice. Nat Methods 14(7):713–719

Super-resolution Microscopy for Biological Imaging

2

Zhigang Yang, Soham Samanta, Wei Yan, Bin Yu, and Junle Qu

2.1 Introduction

Optical microscopy, especially confocal laser scanning microscopy, has been developed as a powerful tool in biomedical imaging [1–3]. In recent years, it has attracted a lot of attentions from the scientific communities with diverse research interests. Over the past decades, it has been widely utilized for realizing the deep biological insights of specific interactions in living systems with reasonable spatio-temporal resolution. Since optical microscopy can provide more suitable *spatial* and *temporal* resolutions to attain real-time dynamic imaging compared to other microscopic techniques like optical coherence tomography (OCT), positron emission tomography (PET), magnetic resonance imaging (MRI), and electron microscopy, it has garnered additional considerations from the researchers (Fig. 2.1).

The unperturbed and non-invasive nature of the traditional optical microscopy has made it an obvious choice for diverse bio-imaging applications [3–6]. In conventional fluorescence microscopy, fluorescence emission is mainly collected by the objective lens of a microscope. Since optical resolution in conventional light microscope is plagued with light diffraction, its best attainable resolution has been limited to half of the light wavelength being applied. It means that using visible light, even a precise wide field microscope with high numerical aperture can only reach a resolution of ~200 nm (known as Abbe's law) [7]. In 1873, Ernst Abbe defined the "diffraction limit" as a major liability in the use of conventional microscopy. It implied that the resolution of an optical microscope is fundamentally limited, not by the quality of the instrument, but owing to the diffraction of light. For an ideally

Z. Yang · S. Samanta · W. Yan · B. Yu · J. Qu (✉)
Center for Biomedical Phonics, College of Physics and Optoelectronic Engineering, Shenzhen University, Shenzhen, China
e-mail: jlqu@szu.edu.cn

X. Wei, B. Gu (eds.), *Optical Imaging in Human Disease and Biological Research*, Advances in Experimental Medicine and Biology 1355,
https://doi.org/10.1007/978-981-15-7627-0_2

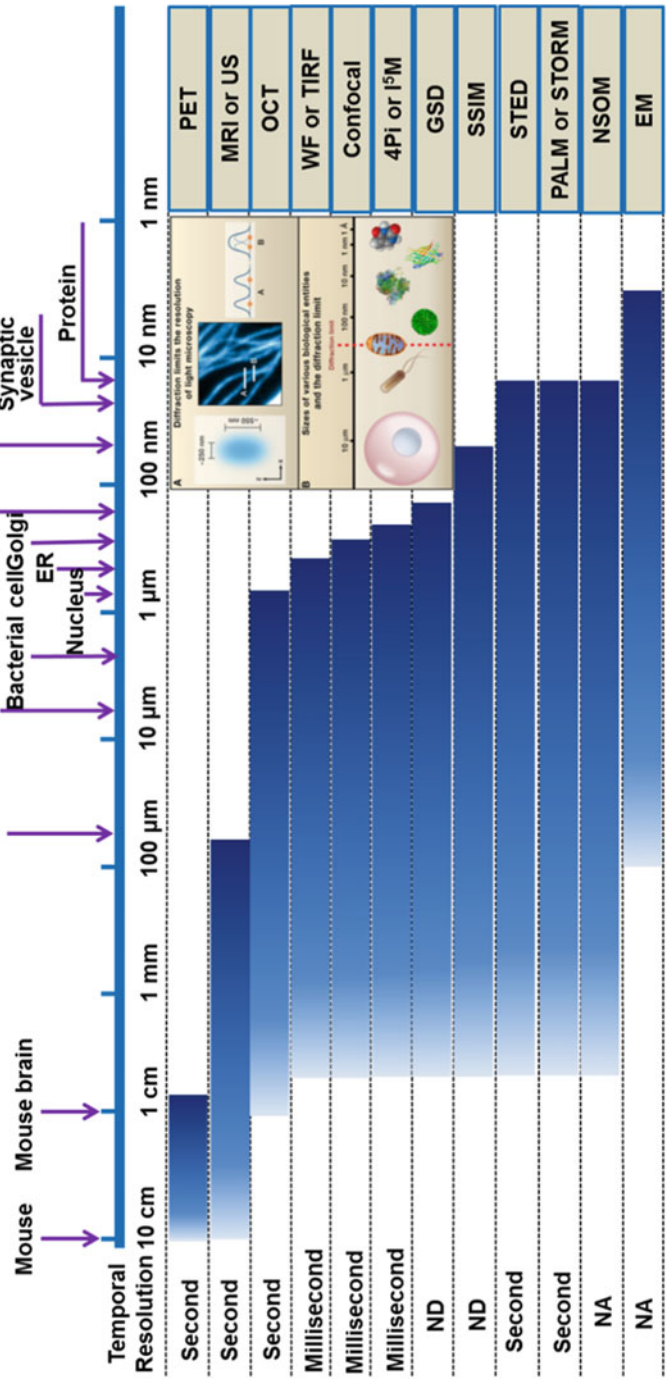

Fig. 2.1 Comparison of the spatial and temporal resolutions of biological imaging techniques (Adapted with the permission from Ref. [2] © (2008) Macmillan Publishers Ltd.)

constructed microscope, the resolution, d, is associated with the wavelength (λ) of light, and the numerical aperture (NA) of the objective lens by the equation $d = \lambda/2\text{NA}$. For a microscope operating in air, the numerical aperture is limited to 1, and the resolution cannot be better than about 0.5λ, although some improvements in resolution can be achieved by imaging in immersion media of higher refractive index. Thus, owing to the limitation of spatial resolution, various fundamental processes of chemical biology occurring inside living cells with range from tens to hundreds of nanometers and within few millisecond timescales are difficult to be resolved by conventional light microscopy. Along these lines, new fluorescent imaging approaches equipped for breaking this apparently impenetrable fence for resolving complex machineries laying in biological structures at less than 200 nm are in high demand. To improve the resolution and quality of the images by overcoming the optical diffraction limit, different SRM techniques (Table 2.1) have been developed in recent years based on various principles.

Pioneering new microscopy techniques that break the diffraction barrier has remained a hot research topic for decades. Development of SRM techniques is complemented by advancements in designing newer fluorescent probes. The 2014 Nobel Prize in chemistry was awarded jointly to Eric Betzig, Stefan W. Hell, and William E. Moerner for their contributions to the development of super-resolved fluorescence microscopy. Since then, SRM has grabbed the limelight. In recent decades, the study of subcellular organelles using SRM has attracted a huge amount of interest and provided the scope for understanding the functions of subcellular organelles through a different perspective. This chapter quickly summarizes the important features of different SRM techniques (Table 2.1) for advanced biological imaging.

2.2 Scanning Near-Field Optical Microscopy and Far-Field Optical Super-resolution Microscopy

To understand the origin of diffraction limit, a slightly simplified model of light scattering by an object can be considered. Basically, upon light illumination, the structures having size greater than "d" scatter light into waves which can be captured by an optical microscope when propagating away from the object. On the contrary, the light scattered by the structures in the object with size smaller than "d" predominantly results in the evanescent waves that are found to be localized in the vicinity of the object which exponentially decay away. Even though these evanescent waves contain fine structural information about the object, they cannot be collected by a conventional microscope to form a proper sub-wavelength resolution image. Therefore, devising new methods to capture these evanescent waves from the near-field of the sample can be a convenient way to form a super-resolved image. Placing a recording medium in direct contact with the object to be imaged is considered as the simplest approach to utilize the evanescent waves for imaging and the procedure is better known as contact printing or contact lithography. Most probably in 1820s this process was first introduced by Joseph-Nicéphore Niépce to reproduce photographic

Table 2.1 A glimpse of the different super-resolution imaging techniques, devised for biological studies

Super-resolution imaging				
Techniques		Important features	Advantages	Shortcomings
PSF Engineering	STED	An extra laser (STED laser) is used for depletion process	Very high spatial resolution (~20 nm); fast acquisition	Intense STED laser causes photodamage to live cells, tissues and fluorophores
	GSD	Uses triplet state or other metastable state as fluorescent 'off' state	High spatial resolution; avoid use of STED laser	Longer acquisition time, high laser power, not suitable for live cell studies
	RESOLFT	Cocktail of various microscopy techniques (STED, GSD)	High-resolution image	Scarcity of dedicated fluorophores
Single Molecule Localization Microscopy	STORM	Photoblinking or photoswitching properties of fluorophores	Very high spatial resolution; Better localization precision	Longer acquisition time, use of external STORM buffer
	PALM	Photoconvertible or photoactivatable fluorophores	Compatible with fluorescent proteins; High resolution	Lesser photon yield
	SOFI	SMLM with certain relaxation	Relaxation in probe selection, afford inadequate photoswitching	Complex computational set up, lesser spatial resolution
	PAINT	Alternative stochastic super-resolution imaging	Can use transient fluorescent dyes, circumvent photobleaching	Slow acquisition
Frequency Domain Processing	SIM	Flexibility in sample preparation	Relaxation in choosing fluorescent probes	Fundamental restraint to achieve ultra-high spatial resolution (~20 nm)
			Advantages of a traditional confocal microscope with much higher spatial resolution	

images, even though achieving sub-wavelength resolution was not the objective. In 1928, for the first time, Synge detected evanescent waves but it was not realized as an imaging technique until the emergence of scanning near-field optical microscopy (SNOM) in 1984. The SNOM was developed with a scanning tip passing over a

surface in the near field, and the detection signal was collected from the light transmitted through a sub-wavelength hole [8]. The imaging resolution is dependent not on the wavelength of light, but on the tip aperture size and distance from the sample. Therefore, the small tip used in scanning mode is a key factor to determine the imaging resolution in SNOM. Even though, SNOM can achieve very high resolution beyond diffraction limit in the lateral direction, there are certain difficulties in maintaining a constant and very close distance between the tip and sample, which is crucial for this imaging. Therefore, it needs advanced feedback mechanisms.

The development of many far-field SRM techniques has allowed the researchers to study the biological ultra-fine structures at nanoscale level. Usually, these methods are highly dependent on the choice of appropriate fluorescent probes wherein the conversion between a fluorescent "on" state and "off" state is attained by certain photophysical or photochemical mechanisms. These photophysical or photochemical conversions take place either at spatially well-defined regions of the sample or by detecting the photo-switchable single molecules in a stochastic manner. The fluorescent probes for super-resolution fluorescence microscopy require many additional specialized qualities compared to the conventional imaging techniques in terms of brightness, photostability, and photo-switching credentials. Such constraints have not only spurred the need to design new dedicated fluorescent probes for super-resolution imaging but also led to many improvisations of the SRM techniques like acquiring multicolor data. Several innovative ways have been introduced to successfully demonstrate the multicolor super-resolution fluorescence imaging. For example, fluorophores with different fluorescence activation wavelengths, and well-separated emission spectra, or the fluorophores with overlapping emission spectra but capable of exhibiting ratiometric imaging response, have been employed to successfully achieve multicolor super-resolution imaging. Multicolor super-resolution imaging also has been recently accomplished by taking advantage of other spectral properties of the fluorophores such as fluorescence lifetime.

In this context, it is important to discuss the main working principle of different SRM techniques along with their contemporary applications in biological studies to assess the current status and future scope.

2.3 Point Spread Function Engineering Super-resolution Microscopy

In diffraction-limited confocal microscope, the resolution depends on the size of the illumination spot, commonly termed as the point spread function (PSF). Substantial enhancements in both resolution and contrast could be achieved if the effective PSF is made sharper by engineering some new techniques [9]. This PSF engineering constitutes to be an effective way to break the diffraction limit and has been conveniently applied in nanoscopic techniques like STED. STED nanoscopy

might be considered as an extension of confocal laser scanning microscopy (CLSM) with certain advancements.

2.3.1 Stimulated Emission Depletion (STED) Microscopy

Initially, STED microscopy, as an advanced imaging technique, was theoretically proposed in 1994 and experimentally performed later [10, 11]. In principle, two laser beams are needed to carry out super-resolution imaging studies using STED method [11, 12]. One pulsed laser beam is used to transfer fluorescent dyes to the excited states, generating a fluorescent spot owing to optical diffraction; and the second one (called STED laser) with larger pulse width, actually producing a doughnut-shape spot, is employed to selectively deactivate the fluorescent dyes lying in the overlapping region of excitation and STED laser spots (called depletion process). Typically, the doughnut-shaped STED beam selectively suppresses fluorescence photon emission in the periphery of the excitation beam to preferably ensure almost zero-intensity at the center. Figure 2.2 represents a simplified illustration of the STED imaging. Undoubtedly, in STED, the depletion laser power is an important factor to determine the imaging resolution. In practice, first, the excitation laser pulse is applied, followed by an immediate STED pulse. However, there are instances of using STED pulses without continuous wave lasers. Moreover, to feature a zero-intensity spot that basically coincides with the excitation focal spot, the STED pulse can be properly modified.

In this advanced optical microscopic technique, especially for the biological samples, selecting apposite fluorescent dyes with excellent nonlinear response is another determining factor to achieving better spatial resolution (Fig. 2.2). Basically, all the fluorophores around the focal excitation spot need to be in their fluorescent "off" state to attain an exceptionally high resolution, since the stimulated emission rate has a nonlinear dependence on the intensity of the STED beam (Fig. 2.2). To retrieve the high-resolution images, the focal spot is then scanned across the object. Theoretically, the full-width-at-half maximum (FWHM) of the PSF at the excitation

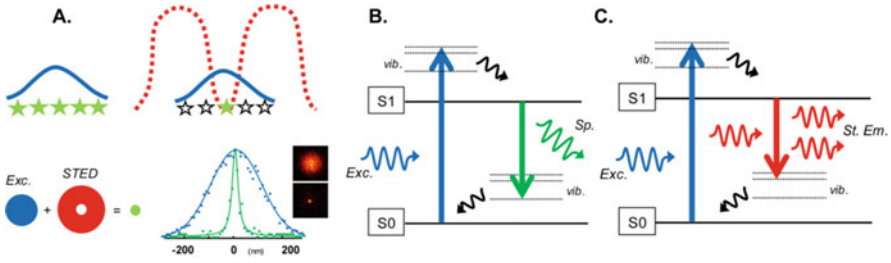

Fig. 2.2 Working principle of STED microscopy. (**a**) Simplified working principle of STED; (**b**, **c**) Schematic representation of the electronic states involved in STED imaging from a simplified Jablonski diagram. (Adapted with the permission from Ref. [11] © (2017) American Chemical Society)

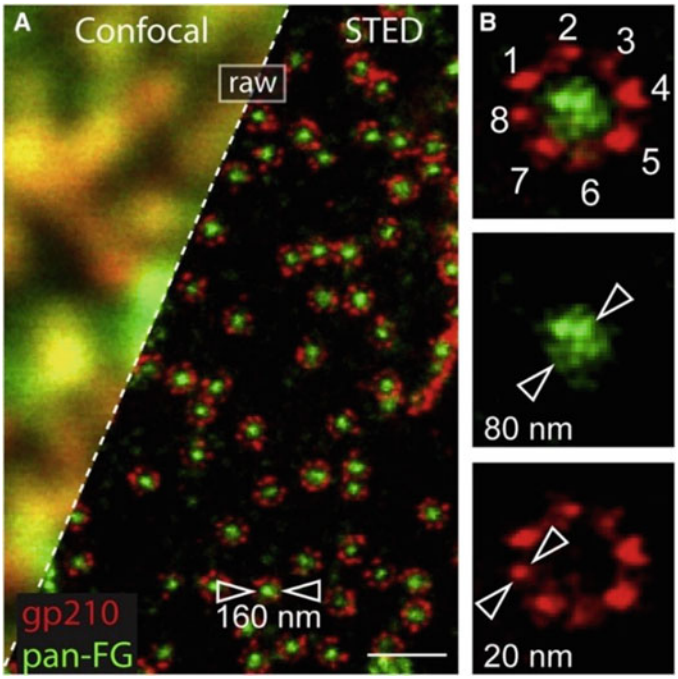

Fig. 2.3 Fluorescence imaging of protein complexes with a STED microscope. (**a**) Confocal and STED imaging of immunolabeled subunits in amphibian nuclear pore complex. (**b**) Individual nuclear pore complex image showing eight antibody-labeled gp210 homodimers with super-high resolution. (Adapted with the permission from Ref. [13] © (2013) Cell Press)

focal spot can be compressed by increasing the intensity of the STED pulses as presented in Eq. (2.1).

$$\Delta r = \frac{\Delta}{\sqrt{1 + I_{\max}/I_S}} \tag{2.1}$$

where Δr is the lateral resolution, Δ represents the FWHM of the diffraction-limited PSF, $I_{\max}$ is the peak intensity of the STED laser, and I_S stands for the threshold intensity needed in order to achieve saturated emission depletion.

The STED microscopy can provide a lateral resolution of 10–80 nm and a longitudinal resolution of 30–600 nm with high imaging speeds (Fig. 2.3) [13]. These abilities of the STED nanoscopy stimulated its increasing contribution in visualizing and understanding many complex biological structures (Fig. 2.3) and dynamic functions in a plethora of cell and tissue types at nanoscale level. However, for live cell STED imaging, use of intense laser could be detrimental as it can cause severe photodamage to the live cells, tissues, and even the used fluorophores. Moreover, use of intense STED laser beam is likely to accelerate the photobleaching process of fluorophores which may impede the long-term STED imaging. Therefore,

optimizing the STED laser power is crucial to achieve a successful good quality STED image.

Minimizing the STED Laser Power

Usually, two major strategies can be followed to achieve successful STED imaging with reduced STED laser power. Developing novel STED imaging techniques such as adaptive optics STED [14, 15], phasor plot STED [16], and digitally enhanced STED [17] is one of the prominent approaches that can offer the scope of lowering the depletion power during the acquisition of STED images. The other significant method to minimize the STED laser power basically relies upon the development of new dedicated STED probes/fluorophores with better photostability and lower saturation intensity (I_S). Recently, perovskite quantum dots [18], carbon dots [19], organosilicon nanohybrids [20], and lanthanide-doped up-conversion nanoparticles (UCNPs) [21, 22] have been successfully employed to demonstrate STED imaging with very low STED laser power. Typically, these new fluorescent materials contain superior photostability and much lower saturation intensity (I_S) compared to the traditional STED probes. For example, UCNPs can offer saturation intensity which is about two orders of magnitude lower than those of traditional STED probes. However, use of such new probes for live biological STED imaging application is still very scarce compared to the traditional probes.

2.3.2 Ground State Depletion (GSD) Microscopy

Unlike the STED microscopy, GSD mainly uses the triplet state T_1 or another metastable dark states of a fluorophore as the "Off" state and the singlet state as the "On" state. A high energy excitation laser is used to excite the probes so that the electrons bombarded with the photons undergo "spin-flip" and the probes mainly could go to the triplet state or metastable dark state from the singlet excited state. However, the fluorescent probes then come back to the ground state stochastically and endure numerous transitions from photon emitting excited to ground state before reaching to the dark triplet state (non-emissive or very weakly emissive). The individual fluorophores can be then spatially separated temporarily from the adjacent fluorophores as only a less number of fluorophores could emit at a time. Therefore, to circumvent the diffraction limit, GSD follows the principle of reducing the number of fluorophores emitting concomitantly, rather than using an extra depletion laser as in the case of STED. However, it should be highlighted that thousands of photons need to be collected for several minutes to construct a complete GSD image, since only a subset of fluorophores are allowed to emit at a time in GSD. Use of high laser power and a comparatively longer acquisition time restrict the use of this SRM method in dynamic live cell studies and it is only better implemented in fixed cell studies. The fluorophores used in GSD are generally less photostable than STED which cannot attain the saturation of the triplet state easily [11, 23]. The GSD microscopy can considerably enlarge the conceptual range and the applicability of

far-field optical SRM in near future with the advancement in designing new fluorophores.

2.3.3 Reversible Saturable Optical Fluorescence Transitions (RESOLFT)

A cocktail of various optical fluorescence microscopy techniques to achieve very high resolution is popularly termed with the acronym RESOLFT which basically stands for REversible Saturable OpticaL Fluorescence Transitions. As mentioned earlier, conventional microscopy techniques cannot surpass diffraction limit. To overcome this diffraction barrier, the fluorescent molecules are temporarily switched to a state in RESOLFT wherein they cannot generate fluorescence signal upon light illumination. Basically, more generalized principle of STED and GSD microscopy are used in the RESOLFT [24]. For a chosen fluorescent probe, saturated optical transition (depletion) between the different states is crucial in far-field microscopy to obtain the nanoscale resolution using RESOLFT. The fluorescent molecules having at least two distinguishable states, in which reversible switching between the two states is conceivable, can be utilized in RESOLFT. At least one of such transitions is required to be induced by light irradiation.

If a simple model is considered, wherein the bright fluorescent state of the probe is denoted as A and the dark state without fluorescent signal is signified as B, then one of the transitions between A→B can be induced by laser light. In RESOLFT, the specimen is illuminated inhomogeneously so that at one position the illumination intensity becomes very small, virtually reaching at zero under ideal conditions. In such condition the dark state B of the probe molecules is unattainable and the molecules remain entirely in the bright state. In this setup, the molecules lingering in the bright state can approach a smaller area than the conventional diffraction limit upon increasing the intensity of transition light. Therefore, all the detected signals correspond only to the probe molecules remaining in the minimum illumination intensity point. Subsequently, a high-resolution image with sub-diffraction resolution can be constructed by scanning the whole sample across the surface.

The reversible transition of the fluorescent molecules from B to A can be reached either spontaneously or by inducing light of different wavelength. During the scanning process, the fluorescent probes need to switch reversibly several times in order to exist in A or B state. In addition, reversal of the bright and the dark states in the A→B model could also be utilized to obtain RESOLFT image, which is commonly defined as negative RESOLFT image.

2.4 Single-Molecule Localization Microscopy

In conventional fluorescence microscopy, biological samples are selectively labeled with the fluorescent tags/molecules, either by fusing the fluorescent proteins genetically with the genes of interest or by linking it to the antibodies as in

immunohistochemistry. Typically, more concentrated fluorophores result in the fluorescence image with enhanced contrast. To visualize a single fluorophore under a microscope (or even under the naked eye), the number of photons emitted must be sufficiently high, whereas the background needs to be low enough at the same time. The two-dimensional image of a point source observed under a microscope is an extended spot, corresponding to the Airy disk (a section of the point spread function) of the imaging system. Two closely spaced entities labeled with two fluorophores are difficult to identify individually because of the limitation posed by the diffraction of light. This is quantified by Abbe's criterion, stating that the minimal distance that allows resolving two point sources is given by

$$d = \lambda/2\mathrm{NA} \tag{2.2}$$

where λ is the wavelength of the fluorescent emission and NA is the numerical aperture of the microscope.

The theoretical resolution limit at the shortest practical excitation wavelength is around 150 nm in the lateral dimension and approaching 400 nm in the axial dimension (if using an objective having a numerical aperture of 1.40 and the excitation wavelength is 400 nm).

However, it is possible to overcome the diffraction limit if the emissions from the two neighboring fluorescent molecules are made distinguishable by identifying the individual photons coming from each of the two fluorophores. Once a set of photons from a specific molecule is collected, it forms a diffraction-limited spot in the image plane of the microscope. The center of this spot can be found by fitting the observed emission profile to a known geometrical function, typically a Gaussian function in two dimensions. The error that is made in localizing the center of a point emitter scales to a first approximation as the inverse square root of the number of emitted photons, and if enough photons are collected it is easy to obtain a localization error much smaller than the original point spread function. Multiple closely spaced emitters are indistinguishable. The position of a point source can be recovered only if the photons emitted have been identified from those arising from the neighboring molecules.

The basic principle of every single-molecule localization microscopy (SMLM) technique including both PALM and STORM is to determine the localization of single fluorophores with high precision [25–28]. This can be achieved by switching the individual fluorescent molecules between the ON and OFF states sequentially rather than concomitantly (Fig. 2.4). Essentially most of fluorescent dyes remain in the dark state except a sparse number of molecules which exist in the switch ON state in each cycle. Subsequently, a lot of positional coordinates are collected through many cycles which basically signify the position of individual fluorescent molecules, used to label the sample. Superimposition of the collected frames from different switching cycles can be used to construct a super-resolution image computationally. Both PALM and STORM approaches can be used to achieve higher spatial resolution of 10–40 nm in lateral direction and 10–50 nm in longitudinal directions, even though the photon collections in these techniques require much more time than other

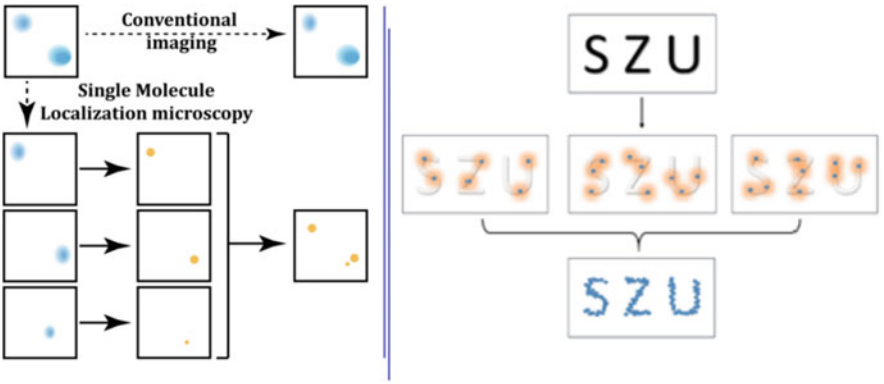

Fig. 2.4 Basic principle and simplified schematic image reconstruction process of SMLM-based super-resolution imaging. (Reproduced with the permission from Ref. [39] © (2018) Elsevier)

imaging methods. Ultimately, the quality of an SMLM image depends extensively on the localization precision wherein the number of detected photons per single fluorophore signifies the localization precision [27]. Each SMLM-based SRM technique follows a unique photo-switching process of the fluorescent probes even though the basic concept of all the SMLM techniques remain very similar.

Reconstruction of the Super-resolution Image in SMLM

SMLM imaging can also be greatly influenced by the image reconstruction process, since the super-resolution image is basically reconstructed from the thousands or even tens of thousands of collected original images. The use of suitable reconstruction algorithm can have an imperative impact on the quality of super-resolution image and the speed of data processing. Generally, the spatio-temporal resolution of the super-resolution images for every SMLM technique is determined by the single-molecule localization accuracy and speed of SMLM. Improving the location density, accuracy, and speed of SMLM is the key from the technological point of view to successfully utilize it in the dynamic live cell super-resolution imaging. In this regard, a variety of two-dimensional (2D) high-density SMLM [28–32] techniques have been developed recently to improve the temporal resolution of SMLM while ensuring the localization accuracy. However, for the three-dimensional (3D) SMLM system, due to the axial extension of the PSF, the 3D PSF images of the fluorescent molecules experience greater similarity and larger overlapping area, which require a higher-order localization algorithm to be resolved. In order to solve this problem and improve the 3D SMLM density, the high-density 2D SMLM algorithm is combined with axial localization methods such as astigmatism, double helix point spread function (DH-PSF), and multifocal plane imaging to achieve high-density fluorescent molecular localization in 3-dimensions [33–36].

2.4.1 (Direct) Stochastic Optical Reconstruction Microscopy (STORM)

STORM has emerged as one of the most promising SMLM technique and contributed enormously in studying the insights of cellular and molecular biology with remarkable resolution beyond the diffraction limit. Determining the precise positions of the fluorescent labels in a sample is crucial in this method which comprises multiple cycles. In these cycles, fluorophores go through repetitive activation, imaging, and deactivation perpetually. Basically, different subset of single fluorophores is activated stochastically at a time which plays a crucial role in determining the precise positions of the fluorophores. Repetition of this process and then plotting the image spots obtained in each cycle together result in a complete STORM image (Fig. 2.4) [37–41]. The resolution of the STORM image does not depend on the diffraction limit; instead, it directly relies upon the localization precision and the localization density. Therefore, the number of photons collected and the number of fluorophores used to label the sample are the most important factors which determine the resolution of the STORM image.

It is important to note that only when a subset of fluorescent dyes becomes fluorescent, the acquisition of imaging data is conceivable. It is essential to control the photophysical behavior of fluorophores to achieve better imaging quality in all SRM. In STORM, it is obligatory for the fluorophores to exhibit at least two stable and selectively distinguishable states, comprising fluorescent "ON" and "OFF" states, to be utilized in the imaging applications. In addition, the fluorophores need to spend a suitable time in each state so that the useful information can be acquired. Therefore, suitable choice of fluorescent probes is the key to achieving successful STORM imaging with exceptionally high resolution. Common difficulties encountered during the construction of STORM image can be dodged by using proper organic fluorescent probes. Therefore, there is a huge scope for developing excellent newer fluorophores with excellent photophysical and photochemical properties for advanced STORM imaging. In recent years, a lot of STORM fluorescent probes have been reported such as Alexa647, Rhodamine derivatives, etc. [39].

Of late, instead of common two (excitation and activation) laser beams, a single laser beam was introduced to modulate the photoblinking of a single fluorophore; wherein the use of this improvised photo-switching process has been termed as direct STORM (dSTORM). Chemical additives, mostly the redox buffer systems are used to tune the switching behavior of several fluorophores in STORM. However, use of such imaging buffers must be curbed to utilize it in long-term live cell STORM imaging as it imposes toxicity concerns.

In recent time, STORM imaging has been implemented to realize many complex biological issues at nanoscale level where conventional microscopy failed. For instances, the structure of functional telomeres (Fig. 2.5) were studied in details using the STORM imaging which revealed that for the formation and maintenance of t-loops the shelterin protein component TRF2 plays the central role [42]. In near future, this microscopic technique could be employed more extensively with the development of advanced fluorescent probes.

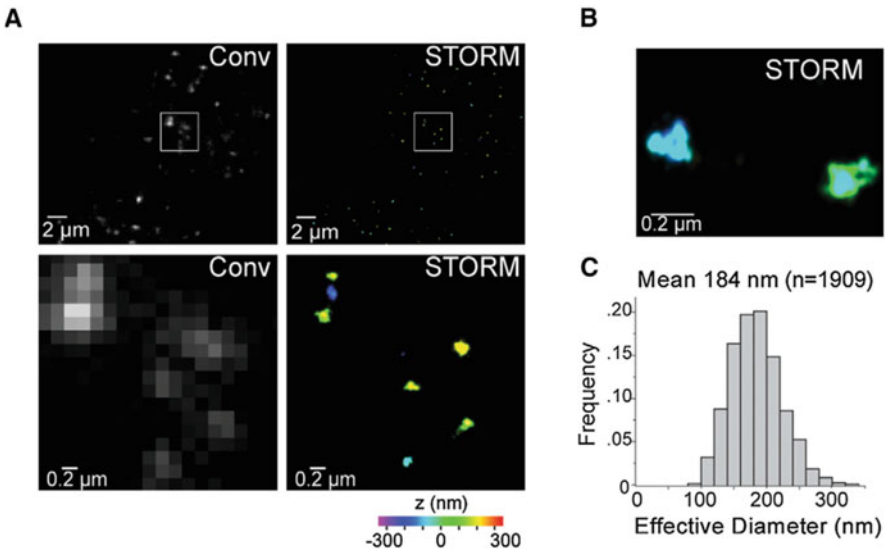

Fig. 2.5 Super-resolution imaging of telomeres in intact mouse embryo fibroblasts (MEFs) using STORM. (**a**) Comparison of conventional (Conv) and 3D-STORM (STORM) images of MEF telomeres. (**b**) Enlarged area of 3D-STORM image showing two telomeres. (**c**) Distribution of the effective diameter of the telomere signals. (Ref. [42] © (2013) Elsevier Inc.)

2.4.2 Photo-Activated Localization Microscopy (PALM/FPALM)

Photo-activated localization microscopy (PALM) was initially proposed by E. Betzig in 2006. PALM was developed as an advanced biophysical imaging method largely prompted by the discovery of photo-converting fluorescent proteins with controllable photochromism, such as photo-activatable GFP. Basically, it is a typical single-molecule localization microscopy technique. The photoconvertible or photo-activatable fluorophores (both FPs and organic fluorophores) which render photoactivation at least once before getting photobleached can be potentially eligible for PALM/FPALM [43]. A large number of organic fluorophores and fluorescent proteins have been recently reported for successful PALM imaging [44, 45]. Some of them are compatible with live cell imaging and could be potentially utilized for dynamic live cell SRM studies. Other reports of such fluorescent probes for PALM/FPALM that can allow faster acquisition or denser labeling are also very important for advanced bio-imaging applications in future.

The light-induced photochromism of the selected fluorophores could be utilized as a promising method to distinguish the neighboring molecules by capturing their individual fluorescent emissions with time. In PALM, stochastically sparse subsets of fluorophores can be turned-on with the excitation light of a specific wavelength. Therefore, the molecules in a subset can be individually photo-activated and imaged according to their spectra. In PALM, the spontaneous photobleaching process of the activated fluorophores is exploited to avoid the simultaneous accumulation of the

active fluorophores in the sample, which would otherwise lead to a diffraction-limited image. However, in this regard, reversible switching between a fluorescent on-state and a dark off-state of a dye is utilized in STORM.

Comparing PALM with STORM
PALM and STORM both share a common fundamental principle of SMLM, and hence, these two techniques are intertwined in many reports. Still, there are some basic technical differences between these two. In PALM, photoactivation of the single fluorophore is crucial. Before the activated molecule gets photobleached, continuous emission is desirable in PALM for a limited interval of time. However, in STORM, stochastic photoblinking of the organic fluorophores are exploited to find out the precise location of neighboring single molecules. Therefore, robust blinking between the fluorescent and dark states is very crucial and the probability of distinguishing two neighboring fluorophores depends profoundly on the blinking property. In comparison with PALM, STORM can offer better scope for obtaining the precise localization of single molecules as it deals with higher photon yield from the activated single fluorophores owing to the perpetual reactivation of the same molecule [43, 46].

2.4.3 Super-resolution Optical Fluctuation Imaging (SOFI)

SOFI is a fluorescence fluctuation-based technique that can afford some relaxation in the photo-switching of the probe at the expense of more complex computational setup and mathematical calculations. The location of the single fluorescent molecule in SMLM is represented by the point spread function (PSF) centroid position. In SMLM techniques like STORM and PALM, precise location of the isolated fluorophores is determined by finding the position of PSF centers. However, lack of proper fluorophores with adequate activation and deactivation or photo-switching behavior could impede these SMLM experiments in many occasions. Super-resolution optical fluctuation imaging (SOFI) has been developed as an alternative SMLM technique which can afford much more relaxation in the requirements for the photo-switching kinetics. The fluorophores with reversible stochastic and independent intensity fluctuations which might result in the overlapping of images can also be implemented in SOFI [47]. Even if there is inadequate on-off switching or not so prominent intensity fluctuations, it is still possible to construct SOFI image. Therefore, SOFI does not have any obligation to controlling the photo-switching and/or photoactivation behavior of a fluorescent probe for long time. However, the chosen fluorophores for SOFI imaging still need to be capable of cycling between fluorescent on/off states or at least two distinguishable fluorescent states with different fluorescence intensities. Hypothetically, a very high resolution of image can be expected from a SOFI imaging. However, in practice there are very limited uses of this SRM method in biology till date. Several issues such as noise and non-uniform brightness of the sample can have an adverse impact on image quality and sometimes use of a higher-order model can be restricted. There are very few examples of

live cell SOFI imaging with extremely high resolution. In ultra-fine structural analysis of biological samples, SOFI lags behind STORM and PALM as it cannot improve resolution markedly. Still in near future there is a possibility to broaden the scope of utilizing this SRM technique for biological application.

2.4.4 Points Accumulation for Imaging in Nanoscale Topography (PAINT)

Points accumulation for imaging in nanoscale topography (PAINT) is theoretically a single-molecule localization method, first developed by Sharonov and Hochstraser in 2006 [48]. Originally, it was developed as an alternative stochastic super-resolution imaging strategy depending on the stochastic adsorption/absorption and photobleaching/desorption of the fluorescent molecule.

Nile red dye was first used to successfully achieve super-resolution PAINT images of cell membranes and artificial lipid vesicles [48]. Microenvironment sensitive Nile red dye is non-fluorescent in aqueous medium and it becomes fluorescent upon interacting with hydrophobic environment such as artificial lipid vesicles and cell membranes. The small concentration of the dye at the nanomolar level can be used to adjust the sorption rate of the molecules to the diffraction-limited area in the millisecond region. Unlike the conventional labeling strategies wherein the fixed fluorophores are used to label the target molecules, freely diffusing fluorescent dyes transiently interacting with the sample can be utilized in PAINT. The stochastic binding of single dye molecules to an immobilized target can be spatially and temporally resolved under a typical wide field fluorescence microscope. Each dye molecule is photobleached and returned to the dark field before the next dye molecule comes into play.

Therefore, the PAINT is able to achieve both the super-resolved image of the fixed target and the dynamic binding kinetics of diffusing molecules in the solution to the target by maintaining a balance between the dye adsorption/absorption and photobleaching/desorption rates. This balance can be estimated with stochastic statistical principles. And this super-resolution nanoscopy can be further extended to regular dyes termed as DNA-PAINT when the dynamic binding and unbinding of a dye-labeled DNA probe to a fixed DNA origami is applied for the stochastic single-molecule imaging [49]. DNA-PAINT is no longer limited to the environment-sensitive dyes and can measure both the adsorption and the desorption kinetics of the probes to the target. The method utilizes the camera blurring effect of moving dyes. When a regular dye is diffusing in the solution, its image on a typical CCD camera is blurred because of its relatively fast-moving speed and the relatively long camera exposure time which contribute to the fluorescence background. However, when the dye binds to a fixed target, the dye stops moving and a clear point spread function can be taken by the camera, which could be termed as (motion blur) mbPAINT [50]. Improvement of the temporal resolution was further (20 times) achieved using a rotational phase mask placed in the Fourier plane during data acquisition and that could resolve the distorted point spread function, containing the

temporal information. The method was named as Super Temporal-Resolved Microscopy (STReM) [51].

2.5 Structured Illumination Microscopy (SIM)

Structured illumination microscopy (SIM) is one of the most prominent SRM techniques that has been universally implemented to address plethora of biological issues [52, 53]. It mainly exploits frequency domain processing method to circumvent the diffraction limit wherein the enhanced spatial resolution can be attained by collecting data from frequency space outside the observable region. The main advantage of SIM is its flexibility in sample preparation for vast biological application. The samples/probes, prepared for standard fluorescence microscopic studies can be used in SIM without much difficulty. Interestingly, SIM also can be used for multicolor super-resolution imaging. Efficient use of the available photon is one of the best qualities in SIM, wherein the sensitive imaging cameras can collect and detect photons with high efficacy ensuring the use of minimum excitation power. This can be advantageous to curb the phototoxicity concerns in biological samples for live cell SIM imaging studies. However, some issues should be considered carefully in SIM to improve imaging quality. For instances, Fourier transform used to characterize the point spread function (PSF) of the microscope is crucial for the image reconstruction process. During the whole imaging process, minimizing the sample drift, mechanical drift of the microscope, and vibrations is important to eloquently reconstruct SIM images with minimal artifacts. Chromatic aberrations in multicolor process and spherical aberration are the major causes resulting in typical optical artifacts. Finally, photobleaching caused by the continuous exposure could lead to the reduction of the signal-to-noise ratio.

Phototoxicity of the fluorophores remained as the main concern for the implementation of SIM imaging in live cell specimen. Highly fluorescent and photostable probes with organelle-specific localization are anticipated to increase the imaging duration for long-term imaging. It should be highlighted that the SIM nanoscopy deals with sophisticated computational procedure that is very difficult to adjust swiftly all the time. To reconstruct the SIM images from limited photon budgets, denoising algorithms can be used. However, improved signal-to-noise ratio (SNR) often may compromise the attainable spatial resolution. Moreover, unlike the STORM and STED, ultra-high spatial resolution (~20 nm) can never be achieved using this technique because of the fundamental restraint (~100 nm).

Apart from the technical complexity in the image reconstruction process, the other major disadvantage of the classic SIM is its sensitivity to the optical aberrations and out-of-focus background fluorescence. These drawbacks cannot be avoided in thicker biological samples and eventually lead to the limited imaging depth. To overcome these problems, spot-scanning SIM [54], also recognized as the image scanning microscopy (ISM) [55] was introduced, that can achieve improved spatial resolution likewise the classic SIM without hampering the SNR and sensitivity. Therefore, the 3D super-resolution (SR) imaging of thicker specimens becomes

feasible using the spot-scanning SIM. The key modification in the spot-scanning SIM is the use of the array detector instead of the point detector as employed in case of confocal microscopy. Each detector pixel then can serve as an independent point detector with the pixel size representing an almost closed confocal pinhole and records an independent super-resolution image of the scanning focused spot with different viewing angles. However, there is apparently no loss of light because all the collected fluorescence will hit somewhere on the array detector. Then, a final SR image can be obtained by pixel reassignment. According to the different pixel reassignment methods, there are two different implementations of ISM technology [56]. One is based on the method of digital pixel reassignment, such as multifocal structured illumination microscopy (MSIM) [57], and confocal spinning-disk-based ISM (CSD-ISM) [58]; the other is based on optical pixel reassignment methods, such as instant SIM (iSIM) [59, 60], RE-scan confocal microscopy (RCM) [61], and optical photon reassignment microscopy (OPRA) [62]. In computer-based pixel reassignment ISM, the performance of ISM and especially its multi-spot scanning variants, such as MSIM, depends strongly on the accuracy of the reference positions of the multiple excitation foci. These coordinates are crucial for the reconstruction algorithm. A related method, multiple measurement vector (MMV) model-based sparse Bayesian learning (MSBL) algorithm [63] does not need to estimate a reference measurement but treats the reconstruction process as an MMV signal reconstruction problem, which simplifies the reconstruction process and ensures best resolution enhancement for a given MSIM data. To improve the image acquisition speed and spatial resolution of ISM, MSIM using helical phase engineering (MSIMH) [64] has been shown to provide decent 3D imaging with a higher resolution along the z-axis if the label density along the optical axis is sparse.

Due to its technical simplicity, versatility, and robustness, spot-scanning SIM technology can be easily compatible with many other microscopy techniques such as multi-photon fluorescence microscopy and florescence lifetime microscopy. So, spot-scanning SIM could offer all the known advantages of a traditional confocal microscope with twice the spatial resolution and higher contrast. Moreover, because of its high depth penetration, spot-scanning SIM also has the potential to image the thicker samples and live tissue.

2.6 Conclusions and Future Prospects

Super-resolution microscopy has laid down the foundation of developing the next generation biomedicine in coming days by providing the opportunity of studying the unknown details of the intracellular dynamics at nanoscale level. Especially, the detailed precise understanding of the organelle specific biological events, occurring in the subcellular context, can open the scope of answering many unknown aspects of biology pertaining to critical physiological disorders. Therefore, it is very important to sum up the recent advancement in developing various types of SRM methods to assess their prospects in advanced biological imaging. Moreover, outlining the plus points and shortcomings of different SRM mechanisms can provide the lids to

outline the future direction of this field. This chapter includes all these aspects very briefly to provide the readers a compact status report on the use of SRM in biological imaging.

In near future, a marked progress can be envisaged in designing newer small molecule fluorescent probes for advanced super-resolution imaging studies. For instances, developing new small molecule based STED fluorophores that can work with extremely low laser power could become revolutionary in unraveling many unknown aspects of live cell dynamics at nanoscale level. Similarly, designing newer spontaneously blinking fluorophores has the potential to broaden the scope of utilizing STORM imaging in complex living biological models.

Acknowledgements We thank all our colleagues for their dedicated efforts to advance the field of optical microscopy and its applications in biology and medicine. While this chapter has focused on the more narrowly defined topic of super-resolution microscopy, we acknowledge that a more comprehensive review and inclusion of more results was not practical due to length limitations. This chapter was prepared with support in part from the National Natural Science Foundation of China (61525503/61875131); Guangdong Natural Science Foundation Innovation Team (2014A030312008). Additional information can be found at: https://bpg.szu.edu.cn/#/plat/mainPage.

References

1. Wegner KD, Hildebrandt N (2015) Quantum dots: bright and versatile in vitro and in vivo fluorescence imaging biosensors. Chem Soc Rev 44:4792–4834
2. Peng H-S, Chiu DT (2015) Soft fluorescent nanomaterials for biological and biomedical imaging. Chem Soc Rev 44:4699–4722
3. Yuan L, Lin W, Zheng K, He L, Huang W (2013) Far-red to near infrared analyte-responsive fluorescent probes based on organic fluorophore platforms for fluorescence imaging. Chem Soc Rev 42:622–661
4. Kolemen S, Akkaya EU (2018) Reaction-based BODIPY probes for selective bio-imaging. Coord Chem Rev 354:121–134
5. Kikuchi K (2010) Design, synthesis and biological application of chemical probes for bio-imaging. Chem Soc Rev 39:2048–2053
6. Qian X, Xu Z (2015) Fluorescence imaging of metal ions implicated in diseases. Chem Soc Rev 44:4487–4449
7. Ernst A (1873) Über einen neuen Beleuchtungsapparat am Mikroskop (About a new illumination apparatus to the microscope). Arch Mikrosk Anat 9:469–480. (in German, Bonn: Verlag von Max Cohen & Sohn)
8. Betzig E, Trautman JK (1992) Near-field optics - microscopy, spectroscopy, and surface modification beyond the diffraction limit. Science 257:189–195
9. Fang Y, Kuang C, Ma Y, Wang Y, Liu X (2015) Resolution and contrast enhancements of optical microscope based on point spread function engineering. Front Optoelectronics 8:152–162
10. Hell SW, Wichmann J (1994) Breaking the diffraction resolution limit by stimulated emission: stimulated-emission-depletion fluorescence microscopy. Opt Lett 19:780–782
11. Blom H, Widengren J (2017) Stimulated emission depletion microscopy. Chem Rev 117:7377–7427
12. Klar TA, Hell SW (1999) Subdiffraction resolution in far-field fluorescence microscopy. Opt Lett 24:954–956

13. Göttfert F, Wurm CA, Mueller V, Berning S, Cordes VC, Honigmann A, Hell SW (2013) Coaligned dual-channel STED nanoscopy and molecular diffusion analysis at 20 nm resolution. Biophys J 105:L01–L03
14. Yan W, Yang YL, Tan Y, Chen X, Li Y, Qu JL, Ye T (2017) Coherent optical adaptive technique improves the spatial resolution of STED microscopy in thick samples. Photonics Res 5:176–181
15. Wang LW, Yan W, Li RZ, Weng XY, Zhang J, Yang ZG, Liu LW, Qu JL (2018) Aberration correction for improving the image quality in STED microscopy using the genetic Algorithm. Nanophotonics 7:1971–1980
16. Wang LW, Chen BL, Yan W, Yang ZG, Peng X, Lin DY, Weng XY, Ye T, Qu JL (2018) Resolution improvement in STED super-resolution microscopy at low power using a phasor plot approach. Nanoscale 10:16252–16260
17. Wang LW, Chen Y, Peng X, Zhang J, Wang JL, Liu LW, Yang Z, Yan W, Qu JL (2020) Ultralow power demand in fluorescence nanoscopy with digitally enhanced stimulated emission depletion. Nanophotonics 9:831. https://doi.org/10.1515/nanoph-2019-0475
18. Ye S, Yan W, Zhao MJ, Peng X, Song J, Qu JL (2018) Low-saturation-intensity, high-photostability, and high-resolution STED nanoscopy assisted by $CsPbBr_3$ quantum dots. Adv Mater 30:201800167
19. Li H, Ye S, Guo JQ, Wang HB, Yan W, Song J, Qu JL (2019) Biocompatible carbon dots with low-saturation-intensity and high photobleaching-resistance for STED nanoscopy imaging of the nucleolus and tunneling nanotubes in living cells. Nano Res 12:3075–3084
20. Liang LL, Yan W, Qin X, Peng X, Feng H, Wang Y, Zhu ZY, Liu LM, Han Y, Xu QH, Qu JL, Liu XG (2020) Designing sub-2 nm organosilica nanohybrids for far-field super-resolution imaging. Angew Chem 7:746–751
21. Liu YJ, Lu YQ, Yang XS, Zheng XL, Wen SH, Wang F, Vidal X, Zhao JB, Liu DM, Zhou ZG, Ma CS, Zhou JJ, Pipe JA, Xi P, Jin DY (2017) Amplified stimulated emission in upconversion nanoparticles for super-resolution nanoscopy. Nature 543:229–233
22. Zhan QQ, Liu HC, Wang BJ, Wu QS, Pu R, Zhou C, Huang BR, Peng XY, Agren H, He S (2017) Achieving high-efficiency emission depletion nanoscopy by employing cross relaxation in upconversion nanoparticles. Nat Commun 8:1058
23. Yang Z, Sharma A, Qi J, Peng X, Lee DY, Hu R, Lin D, Qu J, Kim JS (2016) Super-resolution fluorescent materials: an insight into design and bioimaging applications. Chem Soc Rev 45:4651–4667
24. Hoyera P, de Medeiros G, Balázs B, Norlin N, Besir C, Hanne J, Kräusslich H-G, Engelhardt J, Sahl SJ, Hell SW, Hufnagel L (2016) Breaking the diffraction limit of light-sheet fluorescence microscopy by RESOLFT. Proc Natl Acad Sci U S A 113:3442–3446
25. Li H, Vaughan JC (2018) Switchable fluorophores for single-molecule localization microscopy. Chem Rev 118:9412–9454
26. Liu Z, Lavis LD, Betzig E (2015) Imaging live-cell dynamics and structure at the single-molecule level. Mol Cell 58:644–659
27. Sauer M, Heilemann M (2017) Single-molecule localization microscopy in eukaryotes. Chem Rev 117:7478–7509
28. Sage D, Kirshner H, Pengo T et al (2015) Quantitative evaluation of software packages for single-molecule localization microscopy. Nat. Methods 12:717–724
29. Quyang W, Aristov A, Lelek M et al (2018) Deep learning massively accelerates super-resolution localization microscopy. Nat Biotechnol 36:460–468
30. Yu B, Chen DN, Qu JL, Niu HB (2011) Fast Fourier-domain localization algorithm of single-molecule with nanometer precision. Opt Lett 36:4317–4319
31. Wu JJ, Li SW, Zhang SW, Lin DY, Yu B, Qu JL (2018) Fast analysis method for stochastic optical reconstruction microscopy using multiple measurement vector model sparse Bayesian learning. Opt Lett 43:3977–3980

32. Zhang SW, Wu JJ, Chen DN, Li SW, Yu B, Qu JL (2019) Fast frequency-domain compressed sensing analysis for high-density super-resolution imaging using orthogonal matching pursuit. IEEE Photonics J 11:6900108
33. Babcock H, Sigal Y, Zhuang X (2012) A high-density 3D localization algorithm for stochastic optical reconstruction microscopy. Opt Nanoscopy 1:6
34. Gu L, Sheng Y, Chen Y et al (2014) High-density 3D single molecular analysis based on compressed sensing. Biophys J 106:2443–2449
35. Shuang B, Wang W, Shen H et al (2016) Generalized recovery algorithm for 3D super-resolution microscopy using rotating point spread functions. Sci Rep 6:30826
36. Min J, Holden SJ, Carlini L et al (2014) 3D high-density localization microscopy using hybrid astigmatic/biplane imaging and sparse image reconstruction. Opt Express 5:3935–3948
37. Stennett EMS, Ciuba MA, Levitus M (2014) Photophysical processes in single molecule organic fluorescent probes. Chem Soc Rev 43:1057–1075
38. Allen JR, Silfies JS, Schwartz SA, Davidson MW. Single-molecule super-resolution imaging. https://www.microscopyu.com/techniques/super-resolution/single-molecule-super-resolution-imaging
39. Samanta S, Gong W, Li W, Sharma A, Shim I, Zhang W, Das P, Pan W, Liu L, Yang Z, Qu J, Kim JS (2019) Organic fluorescent probes for stochastic optical reconstruction microscopy (STORM): recent highlights and future possibilities. Coord Chem Rev 380:17–34
40. Rust MJ, Bates M, Zhuang XW (2006) Sub-diffraction-limit imaging by stochastic optical reconstruction microscopy (STORM). Nat Methods 3:793–795
41. Bates M, Jones SA, Zhuang X (2013) Stochastic optical reconstruction microscopy (STORM): a method for superresolution fluorescence imaging. Cold Spring Harb Protoc 2013:498. https://doi.org/10.1101/pdb.top075143
42. Doksani Y, Wu JY, de Lange T, Zhuang X (2013) Super-resolution fluorescence imaging of telomeres reveals TRF2-dependent T-loop formation. Cell 135:345–356
43. Samanta S, He Y, Sharma A, Kim J, Pan W, Yang Z, Li J, Yan W, Liu L, Qu J, Kim JS (2019) Fluorescent probes for nanoscopic imaging of mitochondria. Chem 5:1–30
44. Hess ST, Girirajan TPK, Mason MD (2006) Ultra-high-resolution imaging by fluorescence photoactivation localization microscopy. Biophys J 91:4258–4272
45. Brown TA, Fetter RD, Tkachuk AN, Clayton DA (2010) Approaches toward super-resolution fluorescence imaging of mitochondrial proteins using PALM. Methods 51:458–463
46. Dempsey GT, Vaughan JC, Chen KH, Bates M, Zhuang X (2011) Evaluation of fluorophores for optimal performance in localization-based super-resolution imaging. Nat Methods 8:1027–1036
47. Geissbuehler S, Dellagiacoma C, Lasser T (2011) Comparison between SOFI and STORM. Biomed Opt Express 2:408–420
48. Sharonov A, Hochstrasser RM (2006) Wide-field subdiffraction imaging by accumulated binding of diffusing probes. Proc Natl Acad Sci U S A 103:18911–18916
49. Schnitzbauer J, Strauss MT, Schlichthaerle T, Schueder F, Jungmann R (2017) Super-resolution microscopy with DNA-PAINT. Nat Protoc 12:1198–1228
50. Chen J, Bremauntz A, Kisley L, Shuang B, Landes CF (2013) Super-resolution mbPAINT for Optical Localization Of Single-Stranded DNA. ACS Appl Mater Interfaces 5:9338–9343
51. Wang W, Shen H, Shuang B, Hoener BS, Tauzin LJ, Moringo NA, Kelly KF, Landes CF (2016) Super temporal-resolved microscopy (STReM). J Phys Chem Lett 7:4524–4529
52. Heintzmann R, Huser T (2017) Super-resolution structured illumination microscopy. Chem Rev 117:13890–13908
53. Hirano Y, Matsuda A, Hiraoka Y (2015) Recent advancements in structured-illumination microscopy toward live-cell imaging. Microscopy 64:237–249
54. Sheppard CJR (1988) Super-resolution in confocal imaging. Optik 80:53–54
55. Muller CB, Enderlein J (2010) Image scanning microscopy. Phys Rev Lett 104:198101
56. Gregor I, Enderlein J (2019) Image scanning microscopy. Curr Opin Chem Biol 51:74–83

57. York AG, Parekh SH, Dalle ND et al (2012) Resolution doubling in live, multicellular organisms via multifocal structured illumination microscopy. Nat Methods 9:749–754
58. Olaf S, Christoph P, Michaela C et al (2013) Resolution doubling in fluorescence microscopy with confocal spinning-disk image scanning microscopy. Proc Natl Acad Sci U S A 110:21000–21005
59. York AG, Chandris P, Nogare DD et al (2013) Instant super-resolution imaging in live cells and embryos via analog image processing. Nat Methods 10:1122–1126
60. Winter PW, York AG, Nogare DD et al (2014) Two-photon instant structured illumination microscopy improves the depth penetration of super-resolution imaging in thick scattering samples. Optica 1:181–191
61. Luca GMRD, Breedijk RMP, Brandt RAJ et al (2013) Re-scan confocal microscopy: scanning twice for better resolution. Biomed Opt Express 4:2644–2656
62. Roth S, Sheppard CJ, Wang K et al (2013) Optical photon reassignment microscopy (OPRA). Opt Nanoscopy 2:1–6
63. Wu J, Li SW, Cao HQ et al (2018) Resolution improvement of multifocal structured illumination microscopy with sparse Bayesian learning algorithm. Opt Express 26:31430–31438
64. Li SW, Wu JJ, Li H et al (2018) Rapid 3D image scanning microscopy with multi-spot excitation and double-helix point spread function detection. Opt Express 26:23585–23593

Two-Photon Fluorescence Imaging

3

Fan Feng, Heng Mao, Aimin Wang, and Liangyi Chen

3.1 Introduction

Two-photon fluorescence microscopy (TPM) is laser scanning microscopy that locally excites a fluorophore based on two-photon absorption. Currently, TPM is a powerful tool for noninvasive observation of the structure and functional activity of cells and organs with subcellular resolution in intact tissue or live animals in vivo due to its excellent penetration and optical sectioning ability.

TPM has been used in various applications. Neurologists use TPM to monitor synapses, axons, dendrites, spines, neural activity, and neuronal networks. Under different stimuli, e.g., touch, food, electricity, and visual patterns, animals respond with behaviors accompanied by functional neural spikes and structural change [1–5]. Hence, specific behaviors are linked to specific neural responses. These linkages provide essential information that may indicate how the neural system processes information that comes from the outside world and activates the commands that come from inside the individual neural system. TPM plays an extremely important role as a tool in neuroscience. In addition, TPM is used to observe how the immune

F. Feng
Center for Bioinformatics, School of Life Sciences, Peking University, Beijing, China
e-mail: ffeng@pku.edu.cn

H. Mao
School of Mathematical Sciences, Peking University, Beijing, China

A. Wang
Department of Electronics, Peking University, Beijing, China

L. Chen (✉)
State Key Laboratory of Membrane Biology, Beijing Key Laboratory of Cardiometabolic Molecular Medicine, Institute of Molecular Medicine, Peking University, Beijing, China
e-mail: lychen@pku.edu.cn

X. Wei, B. Gu (eds.), *Optical Imaging in Human Disease and Biological Research*, Advances in Experimental Medicine and Biology 1355,
https://doi.org/10.1007/978-981-15-7627-0_3

system responds to antigens [6–9], vascular disease [10, 11], the function of cancer cells and tumor movement [12], and plant cell growth [13] and in drug discovery [14].

In this chapter, we review the principle, system, and characteristics of two-photon microscopy and then address some issues in two-photon microscopy and the latest progress. Finally, miniature two-photon microscopy is introduced.

3.2 Two-Photon Absorption and Two-Photon Microscopy

In 1929, at the Institute for Theoretical Physics, Gottingen, Maria Göppert-Mayer investigated the quantum possibility of two photons being absorbed by one molecule simultaneously [15]. However, the possibility of two-photon absorption is extremely low and requires a tremendously high peak light intensity to implement a demonstration. Not until 1961 did Kaiser and Garrett achieve the first two-photon absorption in an experiment not long after the invention of the laser by Maiman in May 1960 [16]. In 1990, Denk and Strickler and Webb combined two-photon absorption with laser scanning confocal fluorescence microscopy with unprecedented capabilities [17]. Since then, two-photon microscopy equipped with pico- or femtosecond-pulsed, high-power lasers has become a standard tool in biology and medicine for three-dimensional high-contrast, high-resolution, fast imaging.

As illustrated in Fig. 3.1a, a fluorophore molecule is excited by one photon to a high-energy state. After a very short time stayed in this state, via nonradiative relaxation, the fluorophore transfers to the ground state with emission of a fluorescence photon in nanoseconds. Due to the relaxation energy loss, the excitation photon has more energy than the emission photon; in other words, the wavelength of the excitation light is shorter than that of the emission light. The intensity of the emission fluorescence is linearly proportional to the intensity of the excitation laser for one-photon excitation.

If the energy of one photon is insufficient for exciting the fluorophore to the excited state, then excitation and emission will not occur. However, if the energy of two photons is sufficient, then excitation may occur. For an easier understanding, we can assume that one power-insufficient photon pushes the fluorophore to a virtual state that lasts a very short time. During this period, if this in-a-virtual-state fluorophore encounters another power-insufficient photon and the energy of the two photons is sufficient for excitation, then excitation may occur, as shown in Fig. 3.1a. The intensity of the emission fluorescence is proportional to the excitation laser intensity squared for two-photon excitation. The probability of two-photon excitation for different molecules is denoted by the cross-section with units of GM (Göppert-Mayer) or 10^{-50} cm^4 s/photon. For instance, the two-photon excitation cross-section of EGFP (Clontech) at a wavelength of 927 nm approximately equals 39×10^{-50} cm^4 s/photon. Due to this very low probability, two-photon absorption is rare and hard to observe. To improve the two-photon absorption, one way is to use a bright marker with a higher two-photon cross-section and an appropriate wavelength for illumination. Another way is to focus the laser spatially and temporally to form a

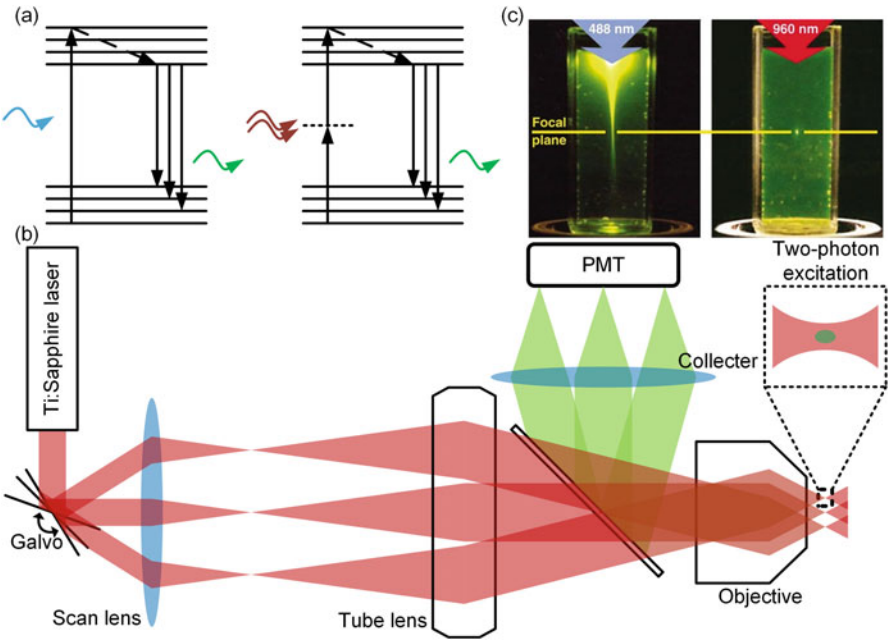

Fig. 3.1 Two-photon excitation and two-photon microscope. (**a**) Illustration of one-photon excitation and two-photon excitation. (**b**) Two-photon microscope system. (**c**) Images of (**a**) one-photon fluorescence and two-photon fluorescence. (Reprinted with permission from [18])

denser photon flux. Practically, a high-NA (numerical aperture) objective is used to tightly focus lasers to spatially increase the density of photons. In the meantime, a pulsed laser is used to temporally increase the density of photons.

A typical two-photon microscope system is shown in Fig. 3.1b, composed of a Ti:sapphire laser, a galvomirror, an objective, and a photomultiplier tube (PMT). The pulsed laser spot is scanned by the galvomirrors on the sample plane, and the fluorescence is collected and then projected onto the PMT due to its sensitivity. Then, the signal recorded by the PMT is reorganized into a temporal sequence to form an image.

For instance, a mode-locked Ti:sapphire laser with a repetition rate of 80 MHz, a pulse duration of ~100 fs, and an average power of 50 mW is used for two-photon microscopy due to its stability and flexibility, which is pumped by a 532 nm laser and generates a 700–1300 nm pulsed laser.

A scanner, usually a two-axis galvomirror or acousto-optic deflector (AOD), redirects the laser spot to different lateral positions on the specimen plane. For volumetric imaging, an axial scanning mechanism is needed, usually using a piezo, electrically tunable lens (ETL), spatial light modulator (SLM), tunable acoustic gradient index of refraction lens (TAG), or remote focusing. There are different scanning strategies, such as scanning the specimen line by line or target by target.

The most commonly used line-by-line scanning produces sufficient sampling with a limited imaging speed. The higher-speed target-by-target imaging only scans some fixed places determined based on previous scanning of the brain area to localize the individual neurons [19].

The detector in two-photon microscopy should be highly sensitive due to the scarcity of two-photon fluorescence. PMTs and avalanche photodiodes (APDs) are widely used in low-photon detection. A PMT uses multiple external amplifiers to boost one electron up to millions with a short response time of nearly 1 ns.

One advantage of TPM is the optical sectioning ability. As illustrated above, two-photon absorption is difficult, and only the area near the laser foci has sufficient photons for efficient two-photon excitation, so the collected fluorescence only comes from the focal areas as illustrated in Fig. 3.1c. Hence, no sufficient TPM excitation occurs at regions away from the foci, which leads to less photobleaching and phototoxicity. This optical sectioning ability is very similar to that in one-photon confocal microscopy but originates from two-photon excitation without a pinhole. With optical sectioning ability, TPM provides a high signal-to-noise ratio image with satisfactory contrast for general cases.

Another advantage of TPM is its long penetration depth into a sample. In fact, inhomogeneous biological tissue scatters light, resulting in degraded confinement of the excitation photon density and imaging contrast. Rayleigh scattering, which dominates the scattering, is inversely proportional to the wavelength, and the wavelength of the infrared light used in TPM is longer than that of the visible light used in conventional one-photon microscopy, e.g., confocal microscopy. In addition, the longer wavelength excitation light in two-photon imaging compared to that in one-photon imaging is less absorbed by water, which is the principal component of biological tissue. These two major characteristics allow the excitation of infrared light in TPM to go deeper. This property is crucial for applications that require a deep penetration depth.

Therefore, TPM is particularly suitable for imaging targets buried at a great depth in thick and scattering tissue in vivo and in situ, e.g., for imaging neurons under the cortex. In addition, photobleaching and phototoxicity are not the prime considerations for the photon budget due to the light efficiency. However, the thermal damage induced by linear absorption should be considered. The safe limitations are reported to be 2–5 $mW/\mu m^2$ for the average power and 0.025–0.06 $nJ/\mu m^2$ for the pulse energy density [20, 21].

In neuroscience, a visual stimulus, e.g., a rotated raster pattern, a virtual reality scenario, or an LED signal, is vital to discover the linkage and relationship between the behavior and neuronal response for a type of experiment. However, most of the light sources in one-photon microscopy are visible to the animal including zebrafish, which raises the question of whether the neurons are responding to the visual stimulation pattern or simply to the one-photon laser source of excitation. In contrast, the infrared light source in two-photon microscopy is invisible, which excludes the possibility of light source interference.

Due to the presence of an inhomogeneous refractive index and tissue scattering, the excitation light is often distorted, and it is difficult to focus light efficiently. The

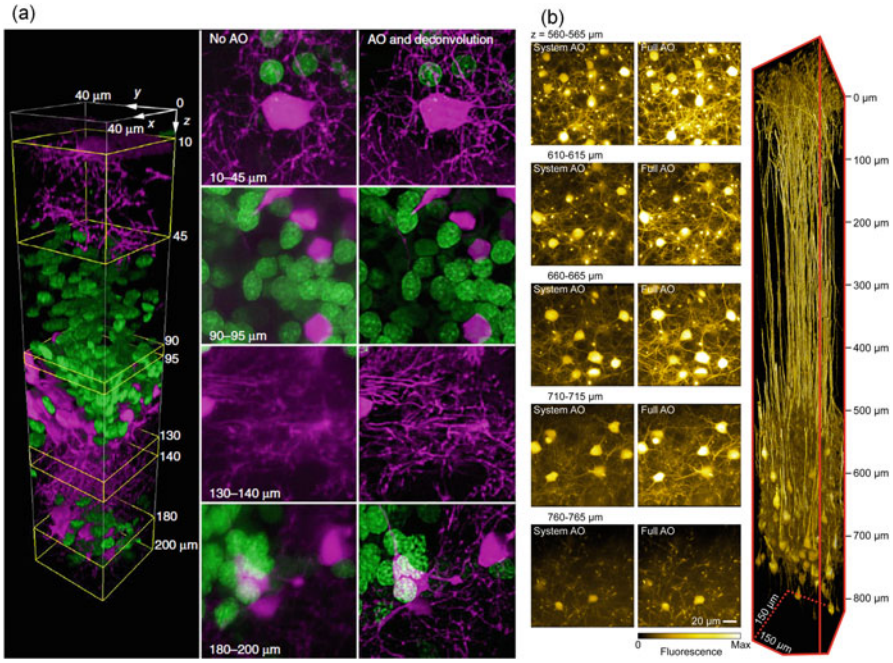

Fig. 3.2 TPM-based AO-assisted confocal and TPM. (**a**) Two-color confocal imaging of oligodendrocytes (magenta) and neuronal nuclei (green) without and with TPM-based AO technique (reprinted with permission from [23]). (**b**) The TPM three-dimensional image stack and images at different depths from in vivo imaging of neurons in a 150 × 150 × 810μm^3 volume of vS1 cortex with System AO and Full AO corrections. (Reprinted with permission from [26])

distorted point spread function (PSF) reduces the photon intensity, leading to a dramatic decrease in the signal until the signal is completely submerged in the noise at a certain depth. Adaptive optics (AO) system is usually used for dealing with this situation. After retrieving or reconstructing the sample-induced wavefront, a compensation wavefront is applied in the system by using an active optical component, e.g., a spatial light modulator or a deformable mirror, to cancel the perturbation [22–25]. In addition, the two-photon excitation fluorescence can also be used as a guide for another imaging model as shown in Fig. 3.2a, b. In 2018, the Betzig group at Janelia Research Campus [26] reported a system combined lattice light sheet and TPM-based AO. The fluorescence of TPM is sent to a Shack–Hartmann wavefront sensor to reconstruct the wavefront of a local area, and the excitation and emission paths are both compensated for to fully explore the power of the lattice light sheet.

3.3 Challenges in Two-Photon Microscopy

Generally, a microscope with a large volumetric field of view (FOV), long-term imaging, and high spatial and temporal resolution is always welcomed by the biological community. However, it is very hard to improve one parameter without comprising the others. Hence, trading off one parameter for another with optimization to approach the hardware limitations, e.g., detector pixel readout rate, becomes important to meet the requirements of different biological applications.

3.3.1 Speed of Imaging Acquisition

One major drawback of scanning-form microscopy is the imaging speed limitation. By using a scanning device, e.g., galvomirrors, the laser foci travel the region of interest (ROI) point by point in the entire FOV. To obtain an acceptable fluorescence intensity, the integral time of the detector should be long enough to receive multiple fluorescence photons. Typically, TPM produces an effective pixel rate of 12 MHz when using a laser source with a repetition rate of 80 MHz; in other words, fluorescence with almost 5–6 pulses produces one pixel.

Many techniques have been developed to address this issue in recent decades. In 2005, the Chris Xu group [27] at Cornell University reported the spatial and temporal focusing (TeFo) technique to reduce background for better penetration. An optical grating is used to form a "rainbow" beam with parallel beams linearly displaced by wavelength. Every spectrum component is spatially focused but not well overlapped, which increases the axial confinement of photons. TeFo provides an example for illustrating how to modulate the PSF spatially and temporally.

Based on TeFo, the Vaziri group [28] in 2016 at Rockefeller University demonstrated one-pulse-per-voxel excitation (Fig. 3.3d) by the sculpted PSF technique to achieve a fast volume rate and a large volume (3–6 Hz, $0.5 \times 0.5 \times 0.5\ mm^3$) with single-cell resolution. The PSF is reshaped with axial confinement and lateral extension using TeFo (sculpted PSF $\sim 5 \times 5 \times 10 \mu m^3$, Gaussian PSF $\sim 5 \times 5 \times 70 \mu m^3$) to excite minimal voxels and resolve the target as illustrated in Fig. 3.3a. Note that the repetition rate of the laser in this scenario is relatively low (4.1 MHz) to increase the photon flux in one pulse. The sculpted PSF provides a conceptual framework for fast, large-volume imaging by slightly compromising the spatial resolution.

In 1998, the Stefan Hell group [29] drew the first schematic of spatial multiplexing for multiphoton microscopy. A rotating microlens disk is used to spatially separate the laser to form multiple foci for excitation as illustrated in Fig. 3.3b, resulting in a 40–100-fold imaging speed increase. However, the energy of individual foci decreases dramatically, which is harmful to the signal-to-noise ratio (SNR) and penetration. In 2007, W. Amir et al. [30] presented a temporal multiplex multiphoton microscope. The two laser sources consisted of two interplaced pulse trains directed to different planes of the sample, and the actual

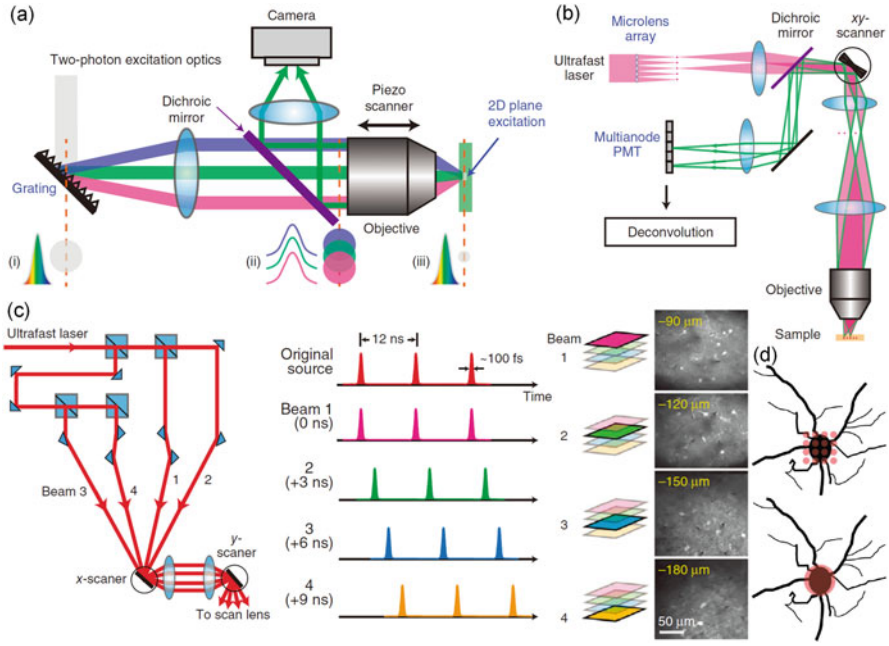

Fig. 3.3 Spatial and temporal focusing and complexing. (**a**) Schematic of temporal focusing based sculpted PSF technique, temporal and spatial cross-section profiles of the laser beam impinging on the grating, back focal plane and focal plane of the objective. (**b**) Multifocal spatial complexing using a microlens array. (**c**) Multi-pulses temporal complexing (reprinted with permission from [1]). (**d**) Comparison of diffraction-limited PSF-based sampling and sculpted PSF-based sampling. (Reprinted with permission from [28])

distribution was obtained by demultiplexing the recorded signal. This method provides the concept that the pulse can be reordered and separated (Fig. 3.3c).

A milestone was reached by the Vaziri group in 2019 [31] by combining spatiotemporal multiplexing, PSF sculpting, and remote scanning techniques. On the one hand, a grating is applied to deliberately disperse the light by wavelength and then form a point spread function axially confined and laterally extended. Then, the imaging speed is improved by reducing the lateral sampling. The key to successfully achieving PSF sculpting is using a low-repetition-rate laser and PSF axial confinement to ensure sufficient photon intensity. On the other hand, the pulse is divided into multiple light paths to obtain different temporal delays and then directed along with different spatial directions with a customized mirror. The spatiotemporal multiplexing provides a flexible configuration for specific imaging requirements. By combining PSF sculpting and spatiotemporal multiplexing in two-photon/three-photon microscopy, this hybrid strategy (HyMS) builds an integrated, conceptual framework to accommodate the need for high-speed (16.7 Hz, $0.69 \times 0.675 \times 0.6$ mm^3, TPM) and large-volume (5.1 Hz, $1 \times 1 \times 0.6$ mm^3,

TPM) imaging acquisition with single-cell resolution. Under this condition, the spatial resolution is compromised for a higher imaging speed and a larger volume scale, but still sufficient to resolve single neurons.

The pixel acquisition speed of HyMS approaches the PMT limit, and the pixels are distributed regularly in the ROI. Neurons only occupy a small space in the brain cortex, and some of the sampling pixels do not provide a neuronal signal. Thus, unique techniques have been developed in neuroscience. Typically, three-dimensional random-access multiphoton fluorescence microscopy (RAMP) [32] takes full advantage of *prior* biological knowledge. RAMP uses laser focus raster scanning of one neuron and then redirects the laser foci to another neuron for scanning as shown in Fig. 3.4a. Later, in 2019, the Chris Xu group presented an adaptive excitation source (AES) that allows the laser foci to be suppressed in the blank areas and emerge in the neuronal areas [19] as illustrated in Fig. 3.4b. The occupied areas of neurons were obtained from a previous measurement with complete raster scanning and its ROI information. The laser blocking strategy tremendously reduced the average power compared to the regular scheme, which is important for longitudinal neuroimaging with less thermal damage. Specifically, the average number of photons for each neuron is 7 times higher, and the average power is almost 4.5 times lower (30 Hz, 0.7 × 0.7 mm^2, 18 mW, TPM). The combination of RAMP and AES may further improve the imaging speed and efficiency.

Recently, unprecedented ultrafast TPM was reported by joint efforts between the Tsia group at the University of Hong Kong and the Ji group at the University of California, Berkeley [34]. A module consisting of a pair of nearly parallel mirrors, called free-space angular-chirp-enhanced delay (FACED), is used to divide one light pulse into 80 pulses that are temporally and spatially separated, enabling horizontal image sampling as illustrated in Fig. 3.4d. Then, another galvomirror is used to perform vertical sampling, which means that the speed of this galvomirror determines the image acquisition speed. Using FACED-TPM, neuronal imaging up to 3000 Hz (80 × 1200 pixels, 50 × 250μm^2) has been observed, which is sufficient for monitoring some transient activity. In this situation, the pixel acquisition rate reaches the PMT hardware limitation.

For large volumetric imaging, e.g., mesoscale, the imaging speed is far behind the requirement. Recently, the Ji group combined the Bessel beam module and a mesoscope for sparsely labeled neuron imaging, resulting in dozens of times improvement in speed by avoiding axial scanning [33] as illustrated in Fig. 3.4c. The Bessel beam module reshapes the Gaussian foci to Bessel foci with an elongated axial distribution. Unlike the Gaussian focus scanning strategy (0.06 Hz, 307 images, 301 × 405 × 612μm^3), the fluorescence obtained by lateral scanning of Bessel foci (3.2 Hz, 6 images, 301 × 405 × 612μm^3) provides information with an axial extension without actual physical axial scanning. Additionally, the core of Bessel foci is smaller than that of Gaussian foci, and the lateral resolution when using a Bessel beam is better than that when using Gaussian foci. As the Bessel beam is axially elongated, the photon density is compromised, the signal-to-background ratio (SNR) of the image is degraded, and the penetration depth may become a problem.

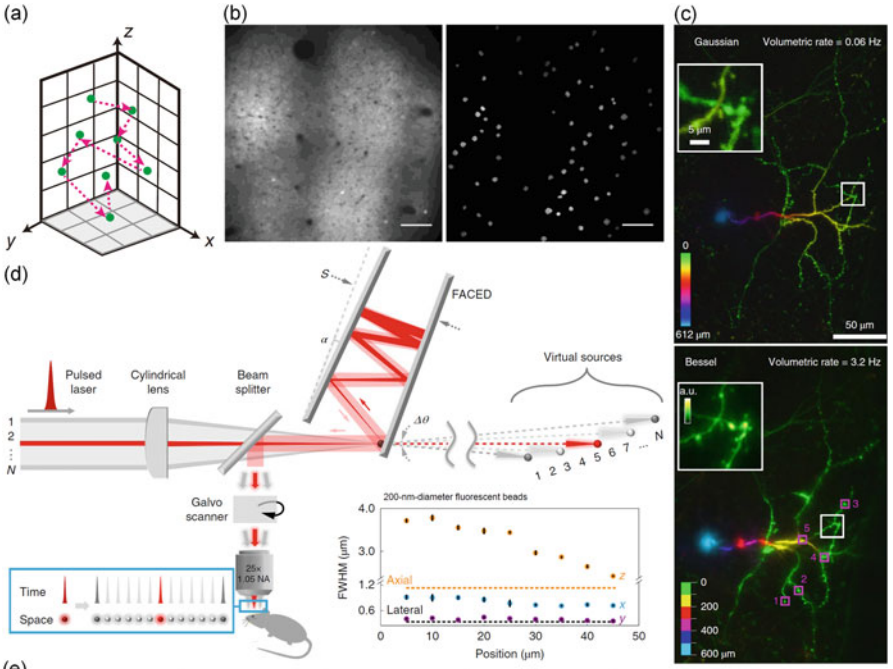

	i)	ii)	iii)	iv)	v)
# stripes	9	1	7	9	4
# lines / stripe	3500	1024	1750	500	512
Area (mm²)	4.4 x 5.4	0.6 x 0.6	4.4 x 4.2	6.3 x 5.4	4 x .6 x .6
Pixel size (µm²)	1.2 x 1.3	0.6 x 0.6	2.4 x 2.6	12 x 13	1.2 x 1.2
Frame rate (Hz)	0.7	21	1.9	4.3	9.5

Fig. 3.4 Conditional fast TPM. (**a**) Custom scanning in three-dimensional random-access multi-photon photon microscopy (reprinted with permission from [1]). (**b**) Comparison of TPM of the structural image of neurons located at 750µm beneath the dura without and with adaptive excitation source at the same location in an awake mouse. Scale bars, 100µm (reprinted with permission from [19]). (**c**) Maximum intensity projection of Gaussian and Bessel module in volumetric functional imaging neurons with synaptic resolution in awake mice (reprinted with permission from [33]). (**d**) FACED reshapes the pulsed light sheet to spatially separated and temporally delayed foci at the focal plane of an objective with slightly compromised resolution on direction *x* and *z* (reprinted with permission from [34]). (**e**) Example of optimized imaging parameters for the TPM with different imaging acquisition speeds and FOV. (Reprinted from [35] with permission by the Creative Commons Attribution License)

3.3.2 Volumetric Field of View

Due to the scanning form of TPM, the volumetric FOV and the imaging speed can be easily traded off with each other for different scan patterns. As illustrated in Fig. 3.4e, the traveling of laser foci requires more time for scanning a larger FOV. A TPM with optimized parameters for different applications was demonstrated by Karel Svoboda at Janelia Research Campus. For example, TPM imaging with 1024×1024 pixels, a 0.6×0.6 mm^2 area, and a 0.6×0.6μm^2 pixel size achieves a frame rate of 21, whereas the imaging consisting of seven stripes each with 1750×1750 pixels, a 4.4×4.2 mm^2 area, and a 2.4×2.6μm^2 pixel size achieves a frame rate of 1.9 [35]. For an imaging stack, TPM with $752 \times 1125 \times 307$ pixels, a $0.301 \times 0.45 \times 0.612$ mm^3 area, and a $0.4 \times 0.4 \times 2$μm^3 pixel size will only have a frame rate of 0.06 [33].

3.3.3 Imaging Depth

As mentioned above, TPM has good depth penetration. Generally, the depth of TPM used in imaging the mouse brain is almost 0.6–0.7 mm with good SNR [19, 31, 33]. Advanced TPM equipped with the AO system achieved near-diffraction-limited imaging up to 850μm below the pia in awake mice as shown above in Fig. 3.2c [25]. Masashi Kondo et al. [36] performed functional imaging of the prefrontal cortex and hippocampus up to 1.2 mm by using a red indicator with a longer wavelength laser source in TPM, which suffers less scattering and absorption. Longer penetration (1.2 mm) with a green indicator would require three-photon excitation with a longer wavelength [31, 37].

3.4 Miniature Two-Photon Microscopy

For the neuroscience community, the idealized scene is that brain imaging is performed while the animal is free of constraints. However, this working condition cannot be achieved by using conventional bulky benchtop TPM. Therefore, miniaturized microscopy mounted on the head of the animal provides an acceptable scheme for both neuroscientists and microscopists. This section will briefly introduce the history of miniature one- and two-photon fluorescence microscopy and present current miniature two-photon microscopy techniques. Usually, a miniature microscope consists of three parts: headpiece, benchtop package, and connector. This cutting-edge headpiece only retains necessary components, like objective, scanner, and structural parts, to maintain this part lightweight and small. The miniature objective is often a gradient index lens (GRIN), a fiber bundle, or a customized miniature objective. Moreover, microelectromechanical systems (MEMS) scanner would be used here, instead of galvomirror in benchtop TPM. The connector transmitted the emission fluorescence and excitation laser bidirectionally to and from a standard benchtop microscope. In 2006, Carl Petersen group

of Ecole Polytechnique Federale de Lausanne used a custom 3 × 3 mm fiber bundle manufactured by Schott Fiber Optics containing 300 × 300 individual fibers as the objective and the connector to visualize dynamics in the barrel cortex of freely moving mice with a voltage-sensitive dye, resulting in an imaging speed of 500 frames per second, a spatial resolution of 200 μm [38]. Furthermore, Matthew Larkum group of the University of Bern combined the GRIN objective and fiberoptic cable with a prism reflecting light horizontally at 90° resulting in a perpendicular view to record dendritic Ca signals in the apical tuft of L5 pyramidal neurons in 2007 [39]. In 2008, Mark Schnitzer group of the Stanford University described a miniaturized 1.1 g epifluorescence microscope providing a high lateral resolution up to 2.8–3.9 μm and a high acquisition speed of 100 Hz, but with only 50–100 mm depth limitation [40]. In 2010, the Fritjof Helmchen group of the University of Zurich reported a miniaturized wide-field microscope incorporated with light-sheet illumination, with a lateral resolution of 3.2 μm and a superior axial resolution of 5.1 μm and superior imaging contrast [41].

In 2011, the Mark Schnitzer group introduced a miniature (1.9 g) integrated fluorescence microscope [42]. Core components, like CMOS camera and light-emitting diode, are mass-producible parts, therefore easily accessible. This microscope enabled high-speed cellular imaging across 0.5 mm areas of a lateral resolution of 2.5 μm inactive mice and allowed concurrent tracking of Ca spiking in >206 Purkinje neurons across nine cerebellar microzones. The epi-illumination one-photon microscope is short of optical sectioning capability, resulting in poor SNR and degraded resolution in deep tissue. Typically, this microscope only promises reliable imaging quality in superficial layers with limited penetration depth (100 μm).

It is worth mentioning that light-field microscopy showed great potential in three-dimensional imaging with unparalleled acquisition speed [43]. By using a microlens array, the light intensity with different spatial and direction is simultaneously recorded. In 2018, the Alipasha Vaziri group presented a miniature light-field microscope capable of capturing neuronal network activity within a large volume of 700 × 600 × 360 μm at 16 Hz, capturing the dynamics of 810 neurons in the hippocampus [44]. Still, this light-field microscopy compromised the spatial resolution of 15 μm, insufficient to identify densely distributed neurons.

Until this point, all connectors in miniature microscopes are an entity, like fibers or wires, for transmitted fluorescence and laser bidirectionally. Nevertheless, the physical cables may be messily entangled and infeasible for socially interacting complex behavioral paradigms. In 2019, Giovanni Barbera group of the National Institute on Drug Abuse of NIH developed a wireless miniature microscope, including a light source, lens, and camera, which allows recording activities from hundreds of medium spiny neurons at a single-cell resolution [45]. This 3.9 g microscope used an LED for excitation, an onboard field-programmable gate array (FPGA) for control, and Micro SD Card for data storage, which is powered by a 3.8 g rechargeable LiPo battery. Nonetheless, continuous long-term imaging for more than >28 min by this miniature microscope will not be expected due to the limited battery energy supply.

Table 3.1 Summary of current miniature two-photon microscopy techniques

	FHIRM-TPM	Denk group 2001	Helmchen group 2008	Kerr group 2009	Schnitzer group 2009
Resolution (μm)	*XY*: 0.65/*Z*: 3.3	–	0.98/7.68	1	1.3/10.3
Maximum field of view (μm^2)	130 × 130	65 × 65	200 × 200	250 × 250	100 × 295
Maximum speed (Hz)	40 (256 × 256)	2 (128 × 128)	8 (512 × 512)	8.2 (64 × 64)	4 (400 × 135)
Scanning mechanism	MEMS scan	Fiber scan	Fiber scan	Fiber scan	MEMS scan
Weight	2.15 g	25 g	0.6 g	5.5 g	2.9 g
Excitation wavelength	920 nm	820–850 nm	812 nm	925 nm	790–810 nm
Pulse width after the objective	~100 fs	100 fs (10 mW)/1 ps (180 mW)	100 fs	1.8 ps	~110 fs
Laser power after the objective	10–25 mW	Not shown	~150–200 mW	100–150 mW	27 mW
Free-moving experiment	Mouse	Rat	Not shown	Rat	Not shown
GFP/GCaMP imaging	Capable	Not capable	Not capable	Low efficiency	Not capable

Nowadays, the camera-based miniature one-photon microscopy is technically mature and robust, shown in Table 3.1. Especially, open-source projects, e.g., UCLA Miniscope [46, 47], Finchscope [47], CHEndoscope [48], and MiniScope [49], contributed to this field and made the wide-field one-photon microscope more accessible, economical, and practical. Consequently, more and more neuroscientists conduct brain research based on miniature microscopy. In 2016, Alcino Silva group of UCLA used the miniature microscopy in Ref. [42] to image active CA1 neurons during each context exploration and found more overlap between the neural ensembles encoding B and C, spaced 5 h apart, than between the neural ensembles encoding A and C, spaced 7 days apart [47]. In 2019, Yang Dan group of the University of California, Berkeley, found two subpopulations of galaninergic neurons in the dorsomedial hypothalamus with distinct axon projections and opposing roles in regulating the switch between rapid eye movement (REM) and non-REM (NREM) sleep [50]. Furthermore, the miniature one-photon microscopy was also used in revealing the regulation mechanism of anxiety [51] and fear [52].

As for the miniature two-photon microscope, one significant difference from the one-photon microscope is the illumination source. The excitation light source for a two-photon microscope is a high-power pulsed laser as mentioned above, which is expensive and bulky. Therefore, there are three challenges for miniaturizing two-

photon microscopy: (1) delivering femtosecond pulsed laser to a live brain with high quality, (2) fast and accurate scanning the laser foci without disturbing the animal, and (3) efficiently collecting the fluorescence. Besides, the two-photon microscope is more sensitive to motion artifacts caused by the heart beating due to optical sectioning and higher spatial resolution compared to the one-photon microscope, which confers an additional challenge.

To the best of our knowledge, Winfried Denk group of Bell Laboratories reported the first miniature two-photon microscope carried by an adult rat in 2001 [53]. A flexible tether containing electrical wires and single-mode optical fibers connects the bulky excitation laser of 820–850 nm wavelength with optical setup and the head-mountable microscope. The headpiece is 7.5 cm long and 25 g in weight. The compactable and lightweight, resonant flexural vibrations of the fiber tip as scanning mechanism results in an imaging speed of 2 Hz and a FOV of 65 × 65 μm. Moreover, a miniature PMT was installed in the headpiece for fluorescence detection. Despite the grating pair being used for dispersive compensation, an accumulated nonlinear phase shift in the silica fiber core cannot be fully compensated, resulting in the broadened pulse and low imaging SNR. To solve this problem, Fritjof Helmchen group used a hollow-core photonic crystal fiber for efficient delivery of near-IR femtosecond laser pulses at 812 nm [54]. Well-designed periodic air-silica arrays in photonic crystal fiber (PCF) confine light energy in the air core at a certain wavelength range. This microscope achieved a lateral resolution of 1 μm and axial of 8 μm at frame rates of 25 Hz with a field-of-view of up to 200 μm while the device has 1 mm dimensions and the headpiece weighs only 0.6 g. Therefore, intensity-dependent nonlinear effects are solved due to the air-guiding property of photonic crystal fiber [55]. In 2009, Mark Schnitzer group presented a 2.9 g miniature two-photon microscope based on a MEMS scanning mirror at 560 Hz resonance which is much faster than fiber-tip scanning [56].

In 2017, Heping Chen group of the Peking University developed a fast high-resolution, miniature two-photon microscope (FHIRM-TPM) with a 2.15 g head-piece weight and 150 × 150 μm FOV [57] as shown in Fig. 3.5 and Table 3.1. At first, an HC-920 that delivered 920 nm femtosecond laser pulses with minimum dispersive distortion is custom designed and produced for exciting GFPs and GCaMPs, the most commonly used fluorescent markers and typical Ca^{2+} indicators. Secondly, a custom 0.8 NA micro-objective theoretically provided lateral 0.64 μm and axial 3.35 μm resolution. Thirdly, a MEMS scanner enabled 40 Hz temporal resolution at 256 × 256 pixels sampling. Finally, a new type of supple fiber bundle (SFB) was used for fluorescence collection instead of multimode polymer fibers [56] or fusion-type fiber bundles. The SFB is composed of 800 optical fibers and fused it to a 1.5-mm-diameter cylinder at either end while keeping it loose and flexible between the ends. By implementing independent-rotatable connectors attached to the optical and electrical lines, SFB minimizes stress, e.g., torque and tension, on the animal without compromising the photon collection efficiency. By combining these techniques, FHIRM-TPM provides near-diffraction-limit resolution and contrast in freely moving animals, comparable to those of benchtop TPM. In 2021, FHIRM-TPM 2.0 was presented to support an FOV of 420 × 420 × 180 μm and a working

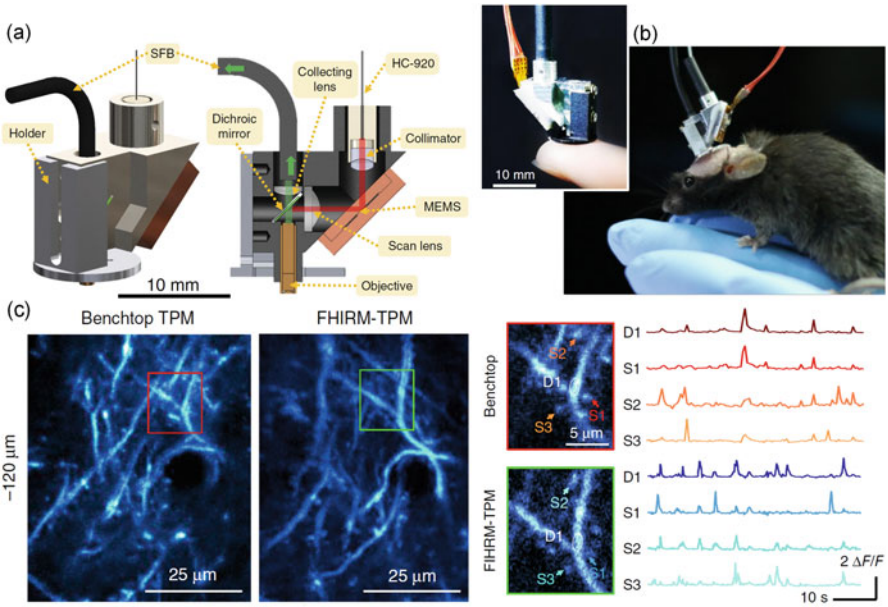

Fig. 3.5 FHIRM-TPM. (**a**) Optical components and mechanical assembly of the miniature microscope. (**b**) Photographs of a FHIRM-TPM on a fingertip and mounted to the head of a mouse. (**c**) Ca^{2+} signals imaging by FHIRM-TPM from dendrites and spines of a mouse expressing GCaMP6f. (Reprinted with permission from [57])

distance of 1 mm in water, and axial scanning by integrating a fast electrically tunable lens (ETL) [58]. FHIRM-TPM series demonstrates its abilities in resolving brain activity at the single synapse and dendrite levels in tail suspension, stepping down from an elevated platform, and social interaction, which has proven its robustness and broad applicability.

3.5 Conclusions and Future Prospects

1. Depending on the biological applications, different directions have been explored to push the spatial, temporal, imaging depth, and FOV of the two-photon microscopy, respectively.
2. Miniature two-photon microscopy poses the latest frontier to achieve high-resolution imaging in freely behaving animals.

References

1. Yang W, Yuste R (2017) In vivo imaging of neural activity. Nat Methods 14(4):349–359
2. Stosiek C et al (2003) In vivo two-photon calcium imaging of neuronal networks. Proc Natl Acad Sci U S A 100(12):7319–7324
3. Svoboda K, Tank DW, Denk W (1996) Direct measurement of coupling between dendritic spines and shafts. Science 272(5262):716–719
4. Svoboda K, Yasuda R (2006) Principles of two-photon excitation microscopy and its applications to neuroscience. Neuron 50(6):823–839
5. Ohki K et al (2005) Functional imaging with cellular resolution reveals precise micro-architecture in visual cortex. Nature 433(7026):597–603
6. Rossi B, Constantin G (2016) Live imaging of immune responses in experimental models of multiple sclerosis. Front Immunol 7:506
7. Miller MJ et al (2002) Two-photon imaging of lymphocyte motility and antigen response in intact lymph node. Science 296(5574):1869–1873
8. Schwickert TA et al (2007) In vivo imaging of germinal centres reveals a dynamic open structure. Nature 446(7131):83–87
9. Lindquist RL et al (2004) Visualizing dendritic cell networks in vivo. Nat Immunol 5 (12):1243–1250
10. Yoon J-H, Jeong Y (2019) In vivo imaging for neurovascular disease research. Arch Pharm Res 42(3):263–273
11. Mulligan SJ, MacVicar BA (2004) Calcium transients in astrocyte endfeet cause cerebrovascular constrictions. Nature 431(7005):195–199
12. Imamura T, Saitou T, Kawakami R (2018) In vivo optical imaging of cancer cell function and tumor microenvironment. Cancer Sci 109(4):912–918
13. Grossmann G et al (2018) Green light for quantitative live-cell imaging in plants. J Cell Sci 131 (2):jcs209270
14. Vinegoni C et al (2019) Fluorescence anisotropy imaging in drug discovery. Adv Drug Deliv Rev 151:262–288
15. Göppert M (1929) Über die Wahrscheinlichkeit des Zusammenwirkens zweier Lichtquanten in einem Elementarakt. Naturwissenschaften 17(48):932–932
16. Maiman TH (1960) Stimulated optical radiation in ruby. Nature 187(4736):493–494
17. Denk W, Strickler JH, Webb WW (1990) Two-photon laser scanning fluorescence microscopy. Science 248(4951):73–76
18. Zipfel WR, Williams RM, Webb WW (2003) Nonlinear magic: multiphoton microscopy in the biosciences. Nat Biotechnol 21(11):1368–1376
19. Li B et al (2020) An adaptive excitation source for high-speed multiphoton microscopy. Nat Methods 17(2):163–166
20. König K et al (1997) Cellular response to near-infrared femtosecond laser pulses in two-photon microscopes. Opt Lett 22(2):135–136
21. Hopt A, Neher E (2001) Highly nonlinear photodamage in two-photon fluorescence microscopy. Biophys J 80(4):2029–2036
22. Sinefeld D et al (2015) Adaptive optics in multiphoton microscopy: comparison of two, three and four photon fluorescence. Opt Express 23(24):31472–31483
23. Wang K et al (2014) Rapid adaptive optical recovery of optimal resolution over large volumes. Nat Methods 11(6):625–618
24. Wang K et al (2015) Direct wavefront sensing for high-resolution in vivo imaging in scattering tissue. Nat Commun 6:7276
25. Liu R et al (2019) Direct wavefront sensing enables functional imaging of infragranular axons and spines. Nat Methods 16(7):615
26. Liu TL et al (2018) Observing the cell in its native state: imaging subcellular dynamics in multicellular organisms. Science 360(6386):284

27. Zhu GH et al (2005) Simultaneous spatial and temporal focusing of femtosecond pulses. Opt Express 13(6):2153–2159
28. Prevedel R et al (2016) Fast volumetric calcium imaging across multiple cortical layers using sculpted light. Nat Methods 13(12):1021–1028
29. Bewersdorf J, Pick R, Hell SW (1998) Multifocal multiphoton microscopy. Opt Lett 23 (9):655–657
30. Amir W et al (2007) Simultaneous imaging of multiple focal planes using a two-photon scanning microscope. Opt Lett 32(12):1731–1733
31. Weisenburger S et al (2019) Volumetric Ca2+ imaging in the mouse brain using hybrid multiplexed sculpted light microscopy. Cell 177:1050
32. Katona G et al (2012) Fast two-photon in vivo imaging with three-dimensional random-access scanning in large tissue volumes. Nat Methods 9(2):201–208
33. Lu R et al (2020) Rapid mesoscale volumetric imaging of neural activity with synaptic resolution. Nat Methods 17(3):291–294
34. Wu JL et al (2020) Kilohertz two-photon fluorescence microscopy imaging of neural activity in vivo. Nat Methods 17:287
35. Sofroniew NJ et al (2016) A large field of view two-photon mesoscope with subcellular resolution for in vivo imaging. elife 5:e14472
36. Kondo M et al (2017) Two-photon calcium imaging of the medial prefrontal cortex and hippocampus without cortical invasion. elife 6:e26839
37. Wang TY et al (2020) Quantitative analysis of 1300-nm three-photon calcium imaging in the mouse brain. elife 9:22
38. Ferezou I, Bolea S, Petersen CC (2006) Visualizing the cortical representation of whisker touch: voltage-sensitive dye imaging in freely moving mice. Neuron 50(4):617–629
39. Murayama M et al (2007) Fiberoptic system for recording dendritic calcium signals in layer 5 neocortical pyramidal cells in freely moving rats. J Neurophysiol 98(3):1791–1805
40. Flusberg BA et al (2008) High-speed, miniaturized fluorescence microscopy in freely moving mice. Nat Methods 5(11):935–938
41. Engelbrecht CJ, Voigt F, Helmchen F (2010) Miniaturized selective plane illumination microscopy for high-contrast in vivo fluorescence imaging. Opt Lett 35(9):1413–1415
42. Ghosh KK et al (2011) Miniaturized integration of a fluorescence microscope. Nat Methods 8 (10):871–878
43. Prevedel R et al (2014) Simultaneous whole-animal 3D imaging of neuronal activity using light-field microscopy. Nat Methods 11(7):727–U161
44. Skocek O et al (2018) High-speed volumetric imaging of neuronal activity in freely moving rodents. Nat Methods 15(6):429
45. Barbera G et al (2019) A wireless miniScope for deep brain imaging in freely moving mice. J Neurosci Methods 323:56–60
46. Dussaux C et al (2018) Fast confocal fluorescence imaging in freely behaving mice. Sci Rep 8 (1):16262
47. Cai DJ et al (2016) A shared neural ensemble links distinct contextual memories encoded close in time. Nature 534(7605):115–118
48. Liberti WA et al (2017) An open source, wireless capable miniature microscope system. J Neural Eng 14(4):045001
49. Zhang L et al (2019) Miniscope GRIN lens system for calcium imaging of neuronal activity from deep brain structures in behaving animals. Curr Protoc Neurosci 86(1):e56
50. Chen KS et al (2018) A hypothalamic switch for REM and non-REM sleep. Neuron 97 (5):1168–1176.e4
51. Jimenez JC et al (2018) Anxiety cells in a hippocampal-hypothalamic circuit. Neuron 97 (3):670–683.e6
52. Campos CA et al (2018) Encoding of danger by parabrachial CGRP neurons. Nature 555 (7698):617–622

53. Helmchen F et al (2001) A miniature head-mounted two-photon microscope: high-resolution brain imaging in freely moving animals. Neuron 31(6):903–912
54. Engelbrecht CJ et al (2008) Ultra-compact fiber-optic two-photon microscope for functional fluorescence imaging in vivo. Opt Express 16(8):5556–5564
55. Flusberg BA et al (2005) Fiber-optic fluorescence imaging. Nat Methods 2(12):941–950
56. Piyawattanametha W et al (2009) In vivo brain imaging using a portable 2.9 g two-photon microscope based on a microelectromechanical systems scanning mirror. Opt Lett 34 (15):2309–2311
57. Zong W et al (2017) Fast high-resolution miniature two-photon microscopy for brain imaging in freely behaving mice. Nat Methods 14(7):713–719
58. Zong WJ et al (2021) Miniature two-photon microscopy for enlarged field-of-view, multi-plane and long-term brain imaging. Nat Methods 18(1):46. 18(2):220

Two-Photon Phosphorescence Lifetime Microscopy

4

Nastaran Abbasizadeh and Joel A. Spencer

4.1 Background

Due to the central role of oxygen in several physiological and pathological conditions, different strategies have been developed over the years to enable the quantitative or semi-quantitative measurement of oxygen in the blood and tissues. These strategies include approaches such as electron paramagnetic resonance (EPR), nitroimidazole (e.g., pimonidazole) adduct staining, microelectrodes, and optical sensors [5–7]. Although EPR has provided some signs of progress towards measuring free radicals and oxygen in biological systems, its usage in human subjects is challenging due to complex instrumentation (e.g., the need for magnets with a large air gap and adequate homogeneity in the magnetic-field), probe administration (placing an exogenous probe in the desired location), and regulatory issues for human applications (e.g., obtaining approval for indefinite embedding of the probes in the tissue) [8–11]. Nitroimidazoles can be used to determine whether cells have been in hypoxia (below ~10 mmHg), but they provide an indirect measurement of hypoxia and can only be used for a single timepoint measurement due to the destructive biopsy required for tissue preparation and measurement [12–14]. Alternatively, Clark-type electrodes, devised by Leland Clark in 1953, can provide robust and quantitative oxygen tension measurements in the whole blood and tissue [15]. As an electrochemical sensor, Clark-type electrodes have shown several advantages over other sensors such as good stability and high reproducibility, but they can also suffer from limitations like oxygen consumption and needle

N. Abbasizadeh · J. A. Spencer (✉)
Department of Bioengineering, University of California Merced, Merced, CA, USA

NSF-CREST Center for Cellular and Biomolecular Machines and the Health Science Research Institute, University of California Merced, Merced, CA, USA
e-mail: joel.spencer@ucmerced.edu

X. Wei, B. Gu (eds.), *Optical Imaging in Human Disease and Biological Research*, Advances in Experimental Medicine and Biology 1355,
https://doi.org/10.1007/978-981-15-7627-0_4

sensor-induced damage to the tissue [16–18]. Optical techniques, such as phosphorescence lifetime quenching microscopy, can provide fast, quantitative oxygen sensing non-invasively in living biological samples without oxygen consumption, making it an optimal alternative to the methods described above [18]. Furthermore, phosphorescence lifetime quenching measurements do not show the luminophore concentration-dependency associated with intensity measurements. This is especially important in the context of measuring oxygen tension inside tissues and cells with heterogeneous distributions of probes and depth-dependent signal loss that can invalidate intensity-based measurements. 2PLM is a relatively new version of phosphorescence lifetime quenching microscopy for non-invasive sensing of the partial pressure of oxygen (pO_2) with high spatial and temporal resolution.

Historically, "optical sensing" of oxygen was initiated with the Kautsky and Hirsch work in the 1930s in which they reported the quenching of phosphorescence in traces of oxygen. In this experiment, they monitored room temperature phosphorescence of dyes immobilized on silica gel and observed light emission only when there was no oxygen present [19]. This method was later used by Pringsheim et al. [20] to measure oxygen production as low as 5×10^{-8} cm^3 at atmospheric pressure per minute [20]. In 1968, Bergman introduced a prototype of a complete optical system that comprised all the components of the modern optical sensor, including a miniature UV emitting glow lamp, a UV transmitting filter, a fluoranthene disk, a UV absorbing filter, and a cadmium sulfide photoconductive cell responded to nitrogen [21].

Peterson et al. [22] proposed an oxygen flow visualization (imaging) technique by spraying and then imaging the oxygen stream on a silica gel thin-layer chromatography plate covered by absorbing dyes. They introduced this technique as a new method to study the oxygen flow over airfoil shapes or the behavior of fluidic devices [22].

A breakthrough was realized when the group of David Wilson reported a new phosphorescence lifetime technique for measuring oxygen tension in biological samples based on oxygen-dependent quenching of metalloporphyrin probes [23]. This technique can be thought of as the single-photon analog to 2PLM and serves as the foundation for it. The Wilson group and other groups used this technique to measure pO_2 in perfused tissues [24], tumors [25], single capillaries [26], and many other applications uncovering new details about how oxygen delivery and consumption occurs in vivo. Most of this work was performed before two-photon excitation techniques were widely available, however.

The theoretical basis for two-photon excitation was first presented about 90 years ago in 1931 by Maria Göppert-Mayer [27]. In her doctoral dissertation she rightly predicted the phenomenon of two-photon absorption, but it was not until 1990 that two-photon excited microscopy became a reality. Denk et al. [28] reported the seminal work on two-photon excited fluorescence for laser scanning microscopy (LSM) with ultrafast pulsed lasers and opened a new window for nonlinear microscopy in biological samples [28, 29]. In the mid-2000s, two-photon excitation was finally applied successfully to phosphorescence lifetime measurement of oxygen in vivo [30]. 2PLM benefits from the use of near-infrared (NIR) excitation

wavelengths for two-photon excitation, where optical scattering and absorption is reduced in biological samples. Use of this NIR "optical window" typically leads to reduced photodamage and higher depth of penetration compared to single-photon excitation at visible wavelengths [31]. The possibility of widespread use of 2PLM gained traction later in 2008 when Finikova et al. reported an antenna-core probe to address the very low two-photon absorption (2PA) cross sections in the early generations of oxygen probes built around Pt or Pd metalloporphyrins [32]. Their technique, which they called two-photon laser scanning microscopy, made it possible to reliably image microvasculature and tissue oxygenation with high spatial resolution in live animals. Today, researchers are still designing novel high-performance 2PA phosphorescent probes to broaden the range of possible biomedical applications [33].

The patent from the Webb group and the publication in the journal Science in 1990 provided the first proof to the biological community that multiphoton excitation microscopy was a viable option for the imaging of biological systems [28]. 2PLM, as a new branch of this technique, facilitates direct insight into the tissue microenvironment by mapping oxygenation. The application of 2PLM to biomedical imaging and sensing has resulted in many critical experimental findings, especially on the role of oxygen in several physiological and pathological conditions.

4.2 Fundamentals of 2PLM

Developing optical imaging techniques like 2PLM that feature high spatial resolution while providing quantitative information about key microenvironmental factors such as oxygen can provide answers to some of the most important and challenging biomedical questions. To effectively apply 2PLM for biological studies, however, it is crucial to understand the components, mechanisms, and recent instrumentation development enabling this method.

4.2.1 Molecular Underpinnings of Phosphorescence Quenching

When electronic excitation of a molecule occurs from the absorption of a photon, the energy can dissipate via several mechanisms (Fig. 4.1). For many luminophores used in biological samples, the electronic transition from the ground state (S_0) to the singlet excited state (S_1) can occur via one- or two-photon absorption (Fig. 4.1) [34]. Two-photon excitation occurs from the simultaneous absorption of two lower-energy, higher-frequency photons, with a combined energy that matches the S_0 to S_1 energy differential (Fig. 4.1) [35]. Upon excitation to S_1, energy can be immediately lost through non-radiative vibrational relaxation to the lowest mode of S_1. From S_1, two major deactivation pathways are possible that result in emission: fluorescence in which energy is released directly from S_1 in the form of a photon while the molecule returns to S_0, and phosphorescence in which the molecule undergoes intersystem

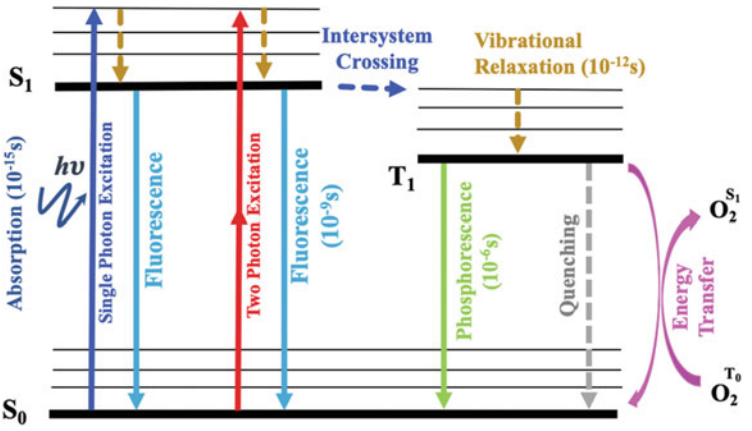

Fig. 4.1 Jablonski energy diagram highlighting some of the potential radiative and non-radiative deactivation pathways following light absorption by a model phosphor. Single-photon and two-photon excitation are shown as blue (UV-Visible wavelengths) and red (NIR wavelengths) arrows, respectively. Quenching of the triplet state (T_1) by bimolecular oxygen (O_2 T_0) results in the production of singlet oxygen (O_2 S_1) and the regeneration of the ground state phosphor (S_0)

crossing (via a change in electron spin from paired to unpaired) to the triplet excited state (T_1) before releasing energy in the form of a photon as the molecule returns to S_0 [34, 36]. Collisional quenching of T_1 by neighboring molecules or molecular structures can cause the T_1 to S_0 transition without emission of a photon. The effect of phosphorescence quenching by a single quencher [Q] results in a decrease in phosphorescence intensity and lifetime following the Stern–Volmer relationship:

$$I_0/I = \tau_0/\tau = 1 + K_q \times \tau_0 \times [Q], \tag{4.1}$$

where I_0 and τ_0 are the intensity and lifetime of phosphorescence emission in the absence of quencher, respectively, I and τ are the intensity and lifetime at a specific concentration of quencher [Q], respectively, and K_q is the quenching constant [37–39]. Bimolecular oxygen (O_2) is one of the most potent dynamic quenchers in physiologically relevant conditions resulting in very efficient quenching of most phosphors [19]. This dynamic quenching can be exploited to quantitatively measure pO_2 since the average lifetime of phosphorescent emission depends directly on the pO_2 in the environment surrounding an excited phosphor according to Eq. (4.1). When quenching occurs, energy is transferred from T_1 to triplet biomolecular oxygen converting it to highly reactive singlet oxygen (Fig. 4.1) [19, 40]. Singlet oxygen, as a by-product of the quenching process, and its derivatives (reactive oxygen species or ROS) are highly reactive molecules that can efficiently react with nearby biological molecules resulting in undesirable phototoxicity as a potential side-effect of 2PLM [34, 41]. Advantageously, the inherent two-photon absorption mechanism of 2PLM prevents singlet oxygen production outside of the focus, thereby minimizing the total singlet oxygen typically produced by several orders

of magnitude compared to single-photon phosphorescence lifetime microscopy. Nevertheless, singlet oxygen production via triplet state quenching can be used constructively as in the case of photodynamic therapy, a promising antitumor strategy in mainstream cancer treatment [42, 43].

4.2.2 Experimental Setup of 2PLM for Oxygen Sensing

Many of the modern 2PLM systems are composed of semi-independent imaging and sensing arms or sequentially acquired imaging and sensing modes that share the same optical path [33, 44–47]. The imaging mode provides the user with a way to visualize the area of interest based on fluorescence emission with a high frame rate. This fast imaging approach is beneficial for many in vivo experiments since the region of interest must be identified in a relatively short time (e.g., while the animal is under anesthesia). The sensing mode provides excitation/emission cycles for phosphorescence lifetime measurement typically on a pixel by pixel basis and is often very slow ($\sim 10^3$ to 10^6 slower) relative to the imaging mode [48–50]. This slow speed can be attributed to the difference in natural lifetimes of fluorescence (typically ~1–10 ns) and phosphorescence (typically ~1–100μs) and the low quantum yield of phosphorescence (often <0.1 at physiological oxygen tension) compared to fluorescence (often >0.2). The phosphorescence emission is typically too slow and too dim to be useful for image formation in intravital measurements.

For certain oxygen sensing probes (e.g., Pt meso-tetraarylporphyrin-coumarin-343 [PtP-C343]), two-photon absorption occurs via two-photon antenna chromophores embedded in the molecule that can then transfer the energy via fluorescence resonance energy transfer (FRET) to the core metalloporphyrin for oxygen quenching [32]. In this type of probe, the contrast for imaging and lifetime sensing can originate from the same molecule [32]. The drawback of such a dual-purpose probe is that the fluorescence emission overlaps with blue-green wavelengths often reserved for molecular reporters based on fluorescent proteins (e.g., CFP/GFP/YFP). We encountered this issue when using PtP-C343 for oxygen measurements in the bone marrow of knock-in mice with GFP-labeled endogenous hematopoietic stem cells (HSCs) [51]. The relatively weak GFP-HSC reporter was overshadowed by the strong fluorescence emission of the PtP-C343. We overcame this challenge by switching to a two-photon excitable probe (Pt-G4), generously provided by Dr. Sergei Vinogradov, that gave no detectable background fluorescence in the GFP emission band.

As observed in Fig. 4.2, 2PLM images are generated by *x-y* raster scanning of a femtosecond pulsed laser (e.g., titanium sapphire laser) using fast-scanning mirror combinations (e.g., polygon/galvanometer or dual galvanometer scanners) that provide lateral focal-point positioning. Dichroic mirrors (for cases where the imaging excitation wavelength and lifetime measurement excitation wavelength are different) and polarizing beam splitters are commonly used for splitting and/or combining the imaging and sensing arms of a 2PLM system (Fig. 4.2). Phosphorescence lifetime measurements are typically acquired in the time domain whereby an excitation gate

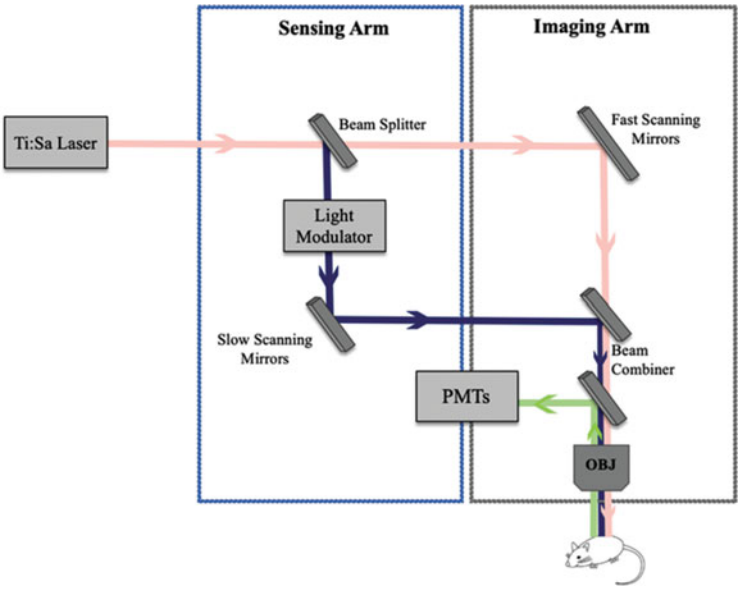

Fig. 4.2 Generalized microscope setup for 2PLM. For imaging, light from a Titanium Sapphire laser (Ti:Sa) is scanned by fast-scanning mirrors and focused onto the sample by an objective lens (Obj). For phosphorescence sensing, the light is gated by a light modulator and directed by a slow-scanning mirror through the objective lens onto the sample. The fluorescence is collected by a standard photo-multiplier tube (PMT) while the phosphorescence is captured by a photon-counting PMT module to be saved for later processing

consisting of tens to hundreds of individual laser pulses is created by passing the laser through an electro-optic modulator (EOM) or an acoustic-optic modulator (AOM). The modulated beam is directed laterally by slow-scanning mirrors and focused by an objective lens to excite the sample. The resulting phosphorescence emission decay is collected by a very sensitive detector (usually a photon-counting Photo-Multiplier Tube [PMT]) and synchronized to the excitation gate so that the photon arrival times can be measured relative to the excitation gate. Due to very low signal, hundreds to sometimes thousands of excitation/emission cycles are collected for each focal point in the sample, and a histogram of arrival times is generated until an acceptable (~20–25) signal-to-noise ratio (SNR) is achieved [32]. To determine the phosphorescence lifetime, the phosphorescence intensity decay histogram is fitted with an exponential decay function to calculate the phosphorescence lifetime. This lifetime is then compared against a calibration plot obtained from independent in vitro oxygen titration experiments to convert the lifetime value to pO_2 [32].

For a relatively low-light level technique such as 2PLM, considerations need to be made about how to handle the collected photon signal in a manner that maximizes SNR. This is especially important when considering that the accuracy of the calculated lifetime (and subsequent measurement of oxygen tension) is directly dependent on the SNR of the collected signal. The most common method of choice

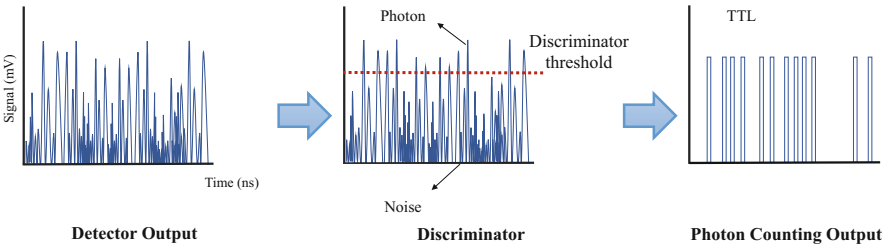

Fig. 4.3 Single-Photon Counting (SPC) diagram. The raw detector electronic output is filtered by a discriminator that rejects electronic peaks below an empirically defined threshold and converts peaks above the threshold to individual TTL outputs for recording by a computer

in 2PLM is single-photon counting (SPC). SPC can refer to several different techniques that have in common the goal of recognizing true photonic signal while rejecting electronic noise [52, 53]. Conceptually, SPC can be thought of as an electronic filtering technique based on an empirically defined threshold (Fig. 4.3). PMTs used for 2PLM are capable of detecting a single photon but they suffer from significant dark current (or dark counts) from the dynode amplification process. SPC enables much of this noise to be filtered out since noise peaks originating from dynodes within the PMT are typically weaker than what is generated by a photon striking the photocathode. In SPC, the raw detector output is filtered through a discriminator with an adjustable threshold that is preselected empirically based on the peak SNR of the specific detector (Fig. 4.3) [52]. Electronic peaks above the threshold are considered "true" photon peaks and are digitized with transistor-transistor logic (TTL) (or similar digital logic with high noise immunity) and recorded by a computer with a data acquisition card. Any peaks below the threshold are rejected which includes most of the dark current (Fig. 4.3). SPC does not reject background signal from ambient light or endogenous luminescence of the sample, so care should be taken in eliminating signal from those sources separately.

4.2.3 Improvements for 2PLM

4.2.3.1 Time Acquisition and Lifetime Improvement

Although 2PLM systems have brought a lot of benefits for oxygen sensing in tissue, due to long triplet lifetimes and low photon count rates relative to 2-photon excited fluorescence, the temporal function of conventional 2PLMs is limited, especially when considering fast-moving cells (e.g., activated T cells) or motion artifacts (e.g., breathing and heart beat) in live animals [54]. In principle, frame rates in phosphorescence lifetime microscopy can be enhanced by implementing gated cameras, or frequency-domain spatial multiplexing, although these techniques can suffer from poor depth resolution [55, 56]. S. S. Howard et al. [56] experimentally demonstrated a parallel-excitation/parallel-collection MPM–PLIM system [56]. In their adaptive optics system, multiphoton laser scanning microscopy was integrated with custom

reflection-based spatial light modulators as an adaptive beam shaping technique to form a linear array of point sources that are modulated by different frequencies [56]. They reported that in comparison with conventional configurations, the designed microscopy improves the pixel rate by 100 times while simultaneously acquiring intensity images and phosphorescence lifetime at depth [56]. In 2019, M. Rytelewski et al. developed a "Fast" Scanning Two-photon Phosphorescence Lifetime Imaging Microscope (FaST-PLIM) that differs from the conventional 2PLM in the signal accumulation approach and also unitary acquisition design [54]. Each pixel in FaST-PLIM receives only one excitation/emission cycle gate before the next pixel is excited. They decreased the decay measurement period for each cycle since full recovery of the phosphor to ground state is not required for accurate measurement with this unitary acquisition regime. With this increased acquisition speed, they succeeded to directly observe and investigate the relationship between fast-moving T-lymphocytes and local oxygen concentration in tumors [54]. They found that T-lymphocyte motility was significantly decreased in regions of hypoxia within the mouse bone marrow [54].

4.2.3.2 Saturation Effects

In two-photon excited microscopy, the probability of TPA depends on the square of the excitation intensity and is limited to the diffraction limited focal volume [57]. At very high excitation intensities, however, due to saturation effects of the excited state the quadratic dependence is lost. When this occurs, a fraction of neighboring molecules outside of the laser focus enter S_1, expanding the excitation volume and thus degrading the resolution and efficiency of excitation [58]. For biomedical researchers using fluorescence microscopy, saturation effects are rarely observed since high excitation powers are usually avoided due to negative biological effects.

When considering two-photon excited phosphorescence, however, saturation is common since the lifetime of T_1 can be $>10^4$ times longer lived than S_1. Each subsequent pulse of an ultrafast optical oscillator (e.g., Ti:Sa laser) operating at 80 MHz repetition rate can pump an increasing number of S_0 molecules into the T_1 state before a significant fraction of them can relax to S_0 resulting in a population inversion. When saturation occurs, the efficiency of each subsequent laser pulses decreases, and the spatial resolution of the measurement degrades. In order to obtain a detectable phosphorescent signal, working in the saturation regime is often unavoidable for in vivo 2PLM. Popular metalloporphyrin probes used for 2PLM are known to have very low two-photon absorption cross sections and very low quantum yields of phosphorescence [59].

One obvious solution to avoid saturation effects is to minimize the average excitation power. A multiple foci approach can be employed, where power is distributed over several foci to minimize the saturation effects of any individual focal volume [60]. Another option to minimize saturation effects is focus shaping. We previously employed a focus shaping technique where the laser beam was scanned across a 100μm slit that was conjugated to the focus in the sample (Fig. 4.4a) [44]. This elegant technique generates an excitation gate while also scanning the focused beam in the sample by a few micrometers laterally during

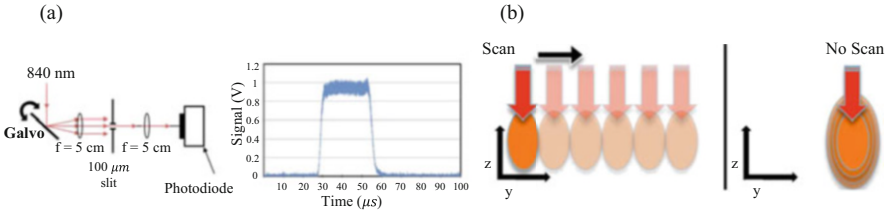

Fig. 4.4 (**a**) Schematic setup of the scanned slit and its excitation pulse graph indicating how the galvanometer scans the focused beam across a slit to form the excitation gate. In experiment mode, the photodiode is removed so that the light can pass through the rest of the system to illuminate the sample (not shown). (**b**) Comparison of scanning across a slit vs. a stationary focused beam. The focal volume increases and resolution decreases with each subsequent excitation pulse during the excitation gate [61]

the ~10–40μm excitation gate (Fig. 4.4a) [44, 61]. Unlike stationary beams which increase the focal volume and decrease resolution (especially in the *z*-axis) with each subsequent laser pulse of the excitation gate, scanning across a slit minimizes saturation effects, leading to more efficient use of laser power and better retention of axial resolution (Fig. 4.4b).

4.2.3.3 Phosphorescent Probe Design

Optimizing the phosphorescent probe design by selecting molecules with a high quantum yield of phosphorescence and a strong 2PA cross section are key to improving the SNR in 2PLM and increasing the acquisition speed [62]. To date, metalloporphyrin molecules have been considered as the best phosphorescent oxygen sensitive probes [32, 63]. What distinguishes these molecules from other probes is their high sensitivity to the physiological range of pO_2, high stability at room temperature or 37 °C, their potential to be chemically modified to diminish the effect of external factors like pH or protein binding, and above all, relatively good phosphorescent quantum yields [63–65]. Originally, three main groups of metalloporphyrins were created for phosphorescence lifetime measurement: unmodified metalloporphyrins, polyglutamate dendrimer metalloporphyrins, and polyarylglycine dendrimer metalloporphyrins surrounded by long polyethylene glycol (PEG) residues [64, 65]. One of the main limitations of the first two groups is the dependency on albumin binding for sensitivity in the physiological range of pO_2. Since the albumin concentration is ~600μM in blood, some fraction of molecules remain unbound making the interpretation inaccurate and unreliable [63–66]. Decoration of the third generation of probes with PEG prevents binding to biological molecules such as albumin, thereby making them more reliable even in the presence of biomacromolecules [32, 63]. Furthermore, the lack of binding to biomolecules makes them good candidates for extravascular measurement if they can be delivered to the interstitial space [65]. Most oxygen sensor probes synthesized since then have been designed with a similar architecture to the third-generation probes. Among proposed oxygen probes [67], PtP-C343 was the first practical two-photon absorbing oxygen probe to have been widely applied in different biological applications

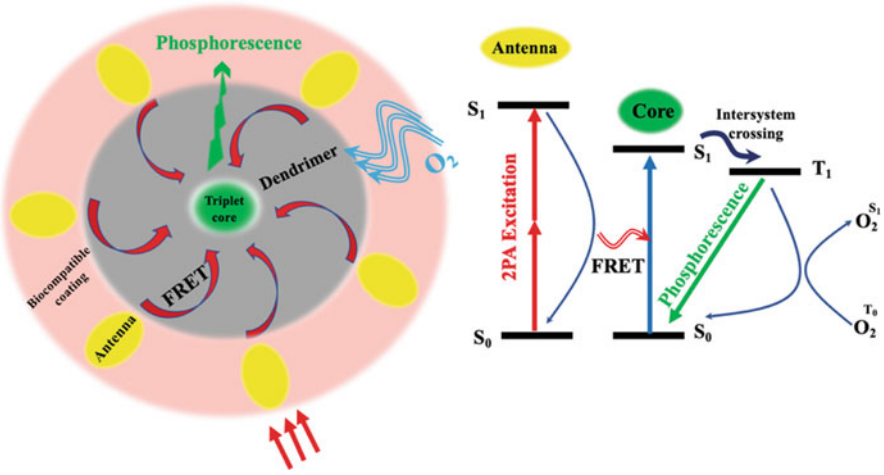

Fig. 4.5 Schematic and energy diagram of 2PA antennae probes. Two-photon energy (Red arrows) is absorbed by several 2P-antenna chromophores (Yellow ovals) and transferred to the metalloporphyrin-core (Green oval) via FRET. When the excited phosphorescent probes are exposed to oxygen (Blue arrow), energy from the triplet state (T_1) is quenched by triplet oxygen

[44, 45, 59]. Due to the very low two-photon absorption cross section of the core metalloporphyrin, PtP-C343 relies on coumarin-343 moieties to act as two-photon antennae that transfer the absorbed energy to the core metalloporphyrin via FRET [32]. The generalized schematic of 2PA antennae oxygen probes like PtP-C343 is shown in Fig. 4.5 [24].

2PA antennae probes have complex chemical structures and require strict fine tuning of the distance between the antenna chromophores and the core porphyrin. Small deviation in the distance can significantly reduce the probe's emissivity and degrade imaging performance. Recently, scientists in the group of Dr. Sergei Vinogradov reported Oxyphor 2P as a new direct two-photon excitable oxygen probe. The single chromophore has intrinsically high quantum yield and 2PA cross section rendering it 50–60 times brighter than previous metalloporphyrin oxygen sensors [30]. Because Oxyphor 2P is not an antennae probe, it overcomes limitations associated with core-antenna 2PA probes. Breakthroughs in design, such as the 50–60× increase in signal, open up new possibilities for faster oxygen sensing techniques and potentially 3D oxygen mapping at a reasonable frame rate [33].

4.3 Oxygen Measurement by 2PLM

In humans, the brain is responsible for ~25% and 20% of the glucose-derived energy consumption and net oxygen consumption, respectively, while it comprises just 2% of the body weight [68]. Providing a sufficient oxygen supply through a highly specialized vascular system is essential for maintenance of healthy brain function.

Table 4.1 An overview of in vivo 2PLM pO_2 measurements

Probe location	Probe name	Application	References
Brain of anesthetized animals	PtP-C343	Mapping of pO_2 in blood vessels and tissue at steady state and during various stimulations or occlusions to understand oxygen delivery and consumption.	[32, 45, 59, 72–77]
	Oxyphor 2P	Synthesis of Oxyphor 2P as a new 2PA probe for cortical oxygen measurement	[33]
Brain of awake animals	PtP-C343, Oxyphor 2P	Mapping of pO_2 in awake animals to study brain oxygenation within the cortex.	[46, 47, 78–82]
Bone marrow	PtP-C343, PtTCHP-C307, Pt-G4	Direct in vivo measurements of pO_2 in the bone marrow and hematopoietic stem cell niche in normal and diseased states.	[44, 54, 55, 67, 83]
Retina	Pt(II) tetra phthalimidoporphyrin	In vivo depth-resolved imaging of pO_2 in the retinal capillary plexus.	[84]
Tumor (Bone marrow)	PtP-C343	FaST-PLIM system to investigate the dependency of T-lymphocyte motility on oxygen distribution in tumors.	[54, 83]

Today a growing list of human disorders including Alzheimer's disease (AD) [69], Parkinson's disease (PD) [70], and Huntington's disease (HD) [71] are found to be associated with deficiencies in tissue oxygen or cerebrovascular dysfunctions. For this reason, there has been an increased focus on studying the dynamics of cerebral oxygen delivery and consumption to better understand the role that oxygen plays in normal and diseased states of the brain.

The introduction of PtP-C343 as the first practical two-photon phosphorescent nanoprobe by the Vinogradov team in 2008 serves as a milestone for oxygen mapping via 2PLM and has led to an interest in applying 2PLM to understand the fundamental role of oxygen in a variety of tissues and contexts in vivo (Table 4.1) [32]. PtP-C343 provides a significant improvement over previous probes in terms of 2PA cross section, measurement depth in tissue, and the minimization of singlet oxygen production [30]. Using PtP-C343 for the first time, Finikova et al. reported a combination of phosphorescence quenching with two-photon laser scanning microscopy (2PLSM) that enable them to record high-resolution images of oxygen distributions in heterogeneously oxygenated glass pipettes and cells [32]. Following PtP-C343 synthesis, Sakadzic et al. used the 2PLM technique to demonstrate in vivo two-photon pO_2 measurements with high resolution, depth of penetration up to 250μm, and low probe concentration in living rodent cortical tissue and microvasculature [59].

In 2011, Devor et al. reported the dependence of cerebral tissue oxygen changes on the baseline pO_2 level and stimulus duration when evoked by sensory stimulation. They found that in tissue sites that are at the low baseline pO_2, constant stimulation

won't overshoot the oxygen tension from the baseline to a high pO_2 level. In contrast, during stimulus-evoked activation, transient decreases occur during the "initial dip" and "poststimulus undershoot." Their results suggest the elevated pO_2 in blood during the hemodynamic response functions to maintain the oxygen tension at normal levels for tissue sites far from the blood vessels [72]. Parpaleix et al. [73] then showed the initial dip in pO_2 at the level of capillaries during odor stimulation and reported that oxygen dynamics in cerebral capillaries reflects neuronal activity. They also investigated the range to which erythrocyte-associated transients (EATs) reflect the neuronal activity. Based on their results, at rest the pO_2 between two EAT is closer to the real physiological pO_2 in the neuropil relative to reported pO_2 from EAT peaks [73]. In another related experiment, the Lecoq group [74] mapped oxygen in various vascular compartments and showed the existence of diffusion-based arterio-venous shunts. Their study also showed that at the site of synaptic transmission, odor evokes a pO_2 increase in vasculature which is preceded by an initial dip in the neuropil [74].

Sakadžić et al. [75] incorporated a two-photon microscopy (TPM) and Doppler optical coherence tomography (OCT) imaging setup and demonstrated that precapillary arterioles and low-branching-order capillaries are responsible for supplying most of the oxygen to the cortical tissue at baseline, while high-branching-order capillaries serve as a buffer to secure enough oxygen, especially during high oxygen consumption or low blood flow conditions [75]. The results of their study provide valuable information for the interpretation of fMRI data and may help inform the development of improved fMRI techniques. In another project, using TPM and Doppler OCT, Moeini et al. (2020) quantified the cerebral pO_2 and blood flow in awake mice during forced treadmill exercise to investigate the relationship between cerebral tissue oxygenation, capillary flow, and exercise intensity. Their study showed that compared to rest, cerebral pO_2 and perfusion increase during running at 5 m/min. At faster speeds (10 and 15 m/min), however, arteriolar and capillary blood flow decreases while tissue oxygenation remains unchanged likely due to autoregulation and an increase in RBC linear density [81].

Using 2PLM, Sakadžić et al. [45] succeeded to map the periarteriolar tissue pO_2 in the brain and fit the changes of oxygen tension with the Krogh cylinder model of oxygen diffusion to estimate the cerebral metabolic rate of oxygen ($CMRO_2$) [45]. Estimation of $CMRO_2$ is a valuable but challenging task that requires complex multimodal imaging and mathematical modeling. $CMRO_2$ interpretations are used for analysis of brain function and diagnosis of cortical pathological conditions, so the invention of new approaches for simplifying its calculations may lead to a better understanding of the metabolic rate of oxygen in the brain under various conditions.

Lyons et al. [78] used awake mice to study the cortical oxygenation with 2PLM and PtP-C343. They reported that isoflurane enhances the capillary RBC flow and thus leads to positive error in brain oxygenation measurements. To reduce the anesthetic effect, they studied the cerebral pO_2 for the first time in an unstressed, awake mouse through a cranial window and reported accurate values of pO_2 close to the physiological conditions in the vasculature and interstitium of mouse cerebral grey matter. Since accurate measurement of the oxygen tension is critical for

investigating neural interactions and diseases associated with them, their work can provide standard values for other researchers to investigate neural processes and model brain metabolism [78]. The same group also reported that imaging through a cranial window with a water immersion objective at room temperature lowers the brain temperature, decreases cerebral blood flow, and can invalidate pO_2 measurements based on phosphorescence lifetime. They demonstrated that although postsurgical decrease of brain temperature returns to normal after a couple of days, imaging with a water immersion objective reduces the temperature again by 2–3 °C. To eliminate this effect, they found that a dry objective or heated water immersion objective can diminish the temperature fluctuation and produced more accurate results [79]. In aged awake mice, Moeini et al. [46] studied age-associated alternations in brain oxygenation within the barrel cortex. Using awake mice was key for this experiment since anesthesia might affect physiological and hemodynamic parameters correlated with aging leading to a false interpretation of the results. They reported that aging is accompanied by lower pO_2 in cerebral arterioles and venules, lower cerebral tissue pO_2, and more spatial heterogeneities in the distribution of oxygen in tissue. The detection of hypoxic micro-pockets and a significant decrease in brain oxygenation with aging is an important finding that has important implications for neurodegenerative diseases and cognition decline in elderly people [46].

Kazmi et al. [76] designed an experiment in which they mapped changes in intravascular oxygen tension of the brain before and after occlusion by exploiting real-time Laser Speckle Contrast Imaging (LSCI) to guide the occlusion process and 2PLM techniques to measure the pO_2. This study helped to underline the role of vascular networking on pre- and post-occlusion oxygenation [76].

Using 2PLM, K. Kisler et al. [77] confirmed the key role of pericytes in the regulation of cerebral blood flow (CBF) in response to stimuli [77]. They reported that in pericyte-deficient mice, following neuronal stimuli there was a decrease in CBF that, in turn, caused neurovascular uncoupling and reduced oxygen supply to the brain. Given that pericytes are degraded in Alzheimer's disease, knowing the mechanism for how the dysfunction of these cells affects the brain may help lead to the development of better diagnosis and treatment of neurologic disorders.

On a different note, Q. Zhang et al. [80] took advantage of polarography, spectroscopy, and 2PLM techniques to measure oxygen levels in the cortex of awake mice during locomotion and found that locomotion considerably enhances brain oxygenation, specifically in the olfactory bulb, frontal cortex sites and regions that are more engaged in locomotion [80].

Recently, significant progress was made on probe design for 2PLM oxygen sensing. In 2019, Esipova et al. [33] introduced a new two-photon oxygen probe, Oxyphor 2P, with 50–60 times brighter signal than all previous metalloporphyrin probes used for oxygen sensing. To validate its performance for longitudinal measurement and quantitative imaging of pathological states, they measured tissue oxygenation for 4 days after induction of a single-capillary micro-stroke in the cortex [33]. Due to its high signal, Oxyphor 2P has the potential of being employed with 2PLM to determine the tissue metabolic states in a variety of biomedical

contexts. In 2020, Kritchenkov et al. synthesized new oxygen probes based on iridium (Ir) complexes with high quantum yields around 13–15%. They found these probes had relatively short lifetimes in the range of 1–2.5 μs which is advantageous for fast data acquisition during real-time oxygen sensing [85]. Combining advances in applying 2PLM to awake animals with the advances in Oxyphor 2P synthesis, Li et al. [47] measured the absolute intravascular pO_2 in an large number of arterioles, venules, and capillaries (6544 vascular segments vs. <100 capillaries in Lyons et al. study), as well as RBC-pO_2, InterRBC-pO_2, EAT, and RBC flow properties in capillaries across layers I–V (Max depth 600 mm vs. ~410 mm from Lyons et al. [78]). Their results revealed that the intracapillary resistance to oxygen delivery, the RBC flux, and oxygenation heterogeneity are higher in upper cortical layers compared to the deeper regions while in Layer IV, where oxygen consumption is the maximum, the oxygen extraction fraction is enhanced [47]. These detailed findings provide deep insights into layer-dependent oxygen delivery and consumption in the brain. Consistent with this study, Sencan et al. (2020) used Oxyphor 2P to show that in response to sensory stimulation, alterations in intravascular pO_2 are conserved across cortical layers I–IV. In contrast to the previous reports performed in anesthetized animals they showed that there is no "initial dip" of intravascular oxygen tension in awake mice following sensory stimulation. In addition, they found O_2 saturation increases more in the venules compared to arteries [82].

While 2PLM oxygen sensing in the brain is an extremely important avenue of investigation, there remains significant opportunities for applying 2PLM to understand the role of oxygen in other biological contexts. For example, we performed the first direct in vivo measurements of local oxygen tension in the bone marrow and hematopoietic stem cell niche of live mice using PtP-C343 and Pt-G4 [44, 51]. We uncovered heterogeneities in local pO_2, with the lowest pO_2 found in deeper perisinusoidal regions and less hypoxic areas closer to the endosteal region [44]. We found that endogenous hematopoietic stem and progenitor cells do not reside in the most hypoxic regions of the bone marrow at steady state [51]. When the bone marrow was altered by radiation and chemotherapy, however, we discovered a significant increase in pO_2, pointing to the role of stress in altering the stem cell metabolic microenvironment [44].

In collaboration with the Vinogradov lab in 2014, we presented a new probe, PtTCHP-C307, which was designed to overcome limitations of PtP-C343 by providing improvements in phosphorescence quantum yield, efficiency of the antenna-core energy transfer, improved signal dynamic range, and minimized quenching of the phosphorescence by electron transfer [67]. PtTCHP-C307 performance was validated in vivo by acquiring pO_2 measurement through the intact mouse skull into the bone marrow as previously described but with minor improvement in signal intensity [44, 67]. In another bone marrow study, Rytelewski et al. [54] developed a novel imaging regimen (FaST-PLIM) which is able to map tissue oxygenation in vivo at cellular resolution while enabling the capture of cellular dynamics. In this study they established FaST-PLIM to directly visualize the relationship between local oxygen concentrations and T-lymphocyte (T cell) motility in

tumors and found the motility of T cells depends on the local oxygen concentration. This study introduced the FaST-PLIM system as a potentially valuable tool for oxygen sensing in a wide range of biological studies where acquisition time is important [54]. In 2020, using this new optical system they studied extracellular oxygen concentrations in a model of leukemia. They used intracellular hypoxia measurement with pimonidazole in combination with 2PLM to couple the extracellular oxygen levels to intracellular hypoxia at different stages of the B-cell acute lymphocytic leukemia (B-ALL). They discovered that during the initial and intermediate disease stages due to expansion of vascular network, pO_2 increases externally while intracellular hypoxic is still present. In end stage disease, they observed that high cellularity and metabolic demands of the tumor cells led to increased intracellular hypoxia and a shift in the external hyperoxia to a noticeable pO_2 reduction [83].

2PLM oxygen sensing has also been applied in other contexts. For example, Schilling et al. [86] developed an implantable polymeric mesh including PtP-C343 which was capable of supporting bone marrow stromal cell growth and differentiation. Designed electrospun fibers were applied to report oxygen levels with high spatial resolution during bone regeneration in real time. Their new carriage system for probe delivery showed promise for overcoming the common limitations like accumulation in the interstitial space over time due to leaky vasculature or the lack of distribution in tissues that have not yet been vascularized [86]. 2PLM oxygen sensing has also been applied for the first time to the retina in vivo. Sencan et al. [84] reported absolute pO_2 measurements in the superficial, intermediate, and deep retinal microvascular plexus under both normoxia and hyperoxia [84]. The authors hope that implementing 2PLM for pO_2 measurement in retinal microvasculature will lay a foundation for additional studies on the physiology of retinal disorders.

4.4 Conclusion

2-photon phosphorescence lifetime microscopy (2PLM), as a robust nonlinear optical microscopy technique, has received a lot of attention recently due to its potential for quantitative pO_2 imaging in tissue with high spatial resolution. In this chapter, we provided background on the development of 2PLM, discussed the most common oxygen sensing measurement methods and concepts, and explained the general principles and optical configurations of a 2PLM system. We discussed the key characteristics and strategies for improvement of the technique and presented an overview of how 2PLM has been used for oxygen sensing in biological applications to improve our understanding of the basic biology underlying several areas of human health.

2PLM has the potential to help answer some of the most challenging and important questions related to the role of oxygen in biology and medicine. Even though 2PLM has become the premier tool for studying oxygen in vivo, it is still relegated to a small subset of specialists due to the cost and expertise required to build a 2PLM system and the expertise required to synthesize the phosphor probes.

Therefore, significant hurdles remain to the widespread availability of this technique for the broader scientific community. Nevertheless, with new developments in both the instrumentation and the phosphor probe design, there is hope that even these hurdles will be overcome.

References

1. Chelushkin PS, Tunik SP (2019) Phosphorescence lifetime imaging (PLIM): state of the art and perspectives. In: Yamanouchi K, Tunik S, Makarov V (eds) Progress in photon science, vol 119. Springer International Publishing, Cham, pp 109–128
2. Shcheslavskiy I, Neubauer A, Bukowiecki R, Dinter F, Becker W (2016) Combined fluorescence and phosphorescence lifetime imaging. Appl Phys Lett 108(9):091111. https://doi.org/10.1063/1.4943265
3. McGown LB, Nithipatikom K (2000) Molecular fluorescence and phosphorescence. Appl Spectrosc Rev 35(4):353–393. https://doi.org/10.1081/ASR-100101229
4. Yamanouchi K, Tunik S, Makarov V (eds) (2019) Progress in photon science: recent advances, vol 119. Springer International Publishing, Cham
5. Clerici WJ, Hensley K, DiMartino DL, Butterfield DA (1996) Direct detection of ototoxicant-induced reactive oxygen species generation in cochlear explants. Hear Res 98(1–2):116–124. https://doi.org/10.1016/0378-5955(96)00075-5.
6. Kizaka-Kondoh S, Konse-Nagasawa H (2009) Significance of nitroimidazole compounds and hypoxia-inducible factor-1 for imaging tumor hypoxia. Cancer Sci 100(8):1366–1373. https://doi.org/10.1111/j.1349-7006.2009.01195.x
7. Papkovsky DB (2004) Methods in optical oxygen sensing: protocols and critical analyses. In: Methods in enzymology, vol 381. Elsevier, Amsterdam, pp 715–735
8. Swartz HM, Walczak T (1998) Developing in vivo EPR oximetry for clinical use. In: Hudetz AG, Bruley DF (eds) Oxygen transport to tissue XX, vol 454. Springer, Boston, MA, pp 243–252
9. International Society on Oxygen Transport to Tissue, Takahashi E, Bruley DF (2010) Oxygen transport to tissue XXXI. Springer, New York, NY
10. Swartz HM et al (2004) Clinical applications of EPR: overview and perspectives. NMR Biomed 17(5):335–351. https://doi.org/10.1002/nbm.911.
11. Swartz HM et al (2014) Clinical EPR. Acad Radiol 21(2):197–206. https://doi.org/10.1016/j.acra.2013.10.011.
12. Schafer R, Gmitro AF (2015) Dynamic oxygenation measurements using a phosphorescent coating within a mammary window chamber mouse model. Biomed Opt Express 6(2):639. https://doi.org/10.1364/BOE.6.000639.
13. Raleigh JA, Chou S-C, Arteel GE, Horsman MR (1999) Comparisons among pimonidazole binding, oxygen electrode measurements, and radiation response in C3H mouse tumors. Radiat Res 151(5):580. https://doi.org/10.2307/3580034.
14. Chitneni SK, Palmer GM, Zalutsky MR, Dewhirst MW (Feb. 2011) Molecular imaging of hypoxia. J Nucl Med 52(2):165–168. https://doi.org/10.2967/jnumed.110.075663
15. Clark LC, Wolf R, Granger D, Taylor Z (Sep. 1953) Continuous recording of blood oxygen tensions by polarography. J Appl Physiol 6(3):189–193. https://doi.org/10.1152/jappl.1953.6.3.189
16. Niazi A (2016) Real time measurement of oxygen by integrating a clark sensor with low cost printed circuit board technology and solid electrolyte membrane. University of Birmingham, Birmingham, p 138
17. Shell JR, LaRochelle EP, Bruza P, Gunn JR, Jarvis LA, Gladstone DJ (2019) Comparison of phosphorescent agents for noninvasive sensing of tumor oxygenation via Cherenkov-excited luminescence imaging. J Biomed Opt 24(03):1. https://doi.org/10.1117/1.JBO.24.3.036001.

18. Wolfbeis OS (2015) Luminescent sensing and imaging of oxygen: fierce competition to the Clark electrode. BioEssays 37(8):921–928. https://doi.org/10.1002/bies.201500002
19. Kautsky H (1939) Quenching of luminescence by oxygen. Trans Faraday Soc 35:216. https://doi.org/10.1039/tf9393500216
20. Pollack M, Pringsheim P, Terwoord D (1944) A method for determining small quantities of oxygen. J Chem Phys 12(7):295–299. https://doi.org/10.1063/1.1723942
21. Bergman I (1968) Rapid-response Atmospheric oxygen monitor based on fluorescence quenching. Nature 218(5139):396–396. https://doi.org/10.1038/218396a0
22. Peterson JI, Fitzgerald RV (1980) New technique of surface flow visualization based on oxygen quenching of fluorescence. Rev Sci Instrum 51(5):670–671. https://doi.org/10.1063/1.1136277
23. Vanderkooi JM, Wilson DF (1986) A new method for measuring oxygen concentration in biological systems. In: Longmuir IS (ed) Oxygen transport to tissue VIII, vol 200. Springer, Boston, MA, pp 189–193
24. Rumsey WL, Vanderkooi JM, Wilson DF (1988) Imaging of phosphorescence: a novel method for measuring oxygen distribution in perfused tissue. Sci New Ser 241(4873):1649–1651
25. Dewhirst MW et al (1999) Quantification of longitudinal tissue pO2 gradients in window chamber tumours: impact on tumour hypoxia. Br J Cancer 79(11–12):1717–1722. https://doi.org/10.1038/sj.bjc.6690273.
26. Zheng L, Golub AS, Pittman RN (1996) Determination of PO2 and its heterogeneity in single capillaries. Am J Physiol Heart Circ Physiol 271(1):H365–H372. https://doi.org/10.1152/ajpheart.1996.271.1.H365
27. Göppert-Mayer M (1931) Über Elementarakte mit zwei Quantensprüngen. Ann Phys 401 (3):273–294. https://doi.org/10.1002/andp.19314010303
28. Denk W, Strickler J, Webb W (1990) Two-photon laser scanning fluorescence microscopy. Science 248(4951):73–76. https://doi.org/10.1126/science.2321027
29. So PTC, Dong CY, Masters BR, Berland KM (2000) Two-photon excitation fluorescence microscopy. Annu Rev Biomed Eng 2:399
30. Estrada AD, Ponticorvo A, Ford TN, Dunn AK (2008) Microvascular oxygen quantification using two-photon microscopy. Opt Lett 33(10):1038. https://doi.org/10.1364/OL.33.001038.
31. Briñas RP, Troxler T, Hochstrasser RM, Vinogradov SA (2005) Phosphorescent oxygen sensor with dendritic protection and two-photon absorbing antenna. J Am Chem Soc 127 (33):11851–11862. https://doi.org/10.1021/ja052947c
32. Finikova OS et al (2008) Oxygen microscopy by two-photon-excited phosphorescence. ChemPhysChem 9(12):1673–1679. https://doi.org/10.1002/cphc.200800296
33. Esipova TV, Barrett MJP, Erlebach E, Masunov AE, Weber B, Vinogradov SA (2019) Oxyphor 2P: a high-performance probe for deep-tissue longitudinal oxygen imaging. Cell Metab 29 (3):736–744.e7. https://doi.org/10.1016/j.cmet.2018.12.022
34. Lichtman JW, Conchello J-A (2005) Fluorescence microscopy. Nat Methods 2(12):910–919. https://doi.org/10.1038/nmeth817
35. Terenziani F, Katan C, Badaeva E, Tretiak S, Blanchard-Desce M (2008) Enhanced two-photon absorption of organic chromophores: theoretical and experimental assessments. Adv Mater 20 (24):4641–4678. https://doi.org/10.1002/adma.200800402
36. Jaffe HH, Miller AL (1966) The fates of electronic excitation energy. J Chem Educ 43(9):469. https://doi.org/10.1021/ed043p469.
37. Evale BG, Hanagodimath SM (2010) Static and dynamic quenching of biologically active coumarin derivative by aniline in benzene–acetonitrile mixtures. J Lumin 130(8):1330–1337. https://doi.org/10.1016/j.jlumin.2010.03.011.
38. Laws WR, Contino PB (1992) [21] Fluorescence quenching studies: analysis of nonlinear Stern-Volmer data. In: Methods in enzymology, vol 210. Elsevier, Amsterdam, pp 448–463
39. Fraiji LK, Hayes DM, Werner TC (1992) Static and dynamic fluorescence quenching experiments for the physical chemistry laboratory. J Chem Educ 69(5):424. https://doi.org/10.1021/ed069p424.

40. Quaranta M, Borisov SM, Klimant I (2012) Indicators for optical oxygen sensors. Bioanal Rev 4(2–4):115–157. https://doi.org/10.1007/s12566-012-0032-y
41. Schweitzer C, Schmidt R (2003) Physical mechanisms of generation and deactivation of singlet oxygen. Chem Rev 103(5):1685–1758. https://doi.org/10.1021/cr010371d
42. Agostinis P et al (2011) Photodynamic therapy of cancer: an update. CA Cancer J Clin 61 (4):250–281. https://doi.org/10.3322/caac.20114
43. Ho AH-P (2017) Handbook of photonics for biomedical engineering, 1st edn. Springer, New York, NY
44. Spencer JA et al (2014) Direct measurement of local oxygen concentration in the bone marrow of live animals. Nature 508(7495):269–273. https://doi.org/10.1038/nature13034.
45. Sakadžic S et al (2016) Two-photon microscopy measurement of cerebral metabolic rate of oxygen using periarteriolar oxygen concentration gradients. Neurophotonics 3(4):045005. https://doi.org/10.1117/1.NPh.3.4.045005.
46. Moeini M et al (2018) Compromised microvascular oxygen delivery increases brain tissue vulnerability with age. Sci Rep 8(1):8219. https://doi.org/10.1038/s41598-018-26543-w.
47. Li B et al (2019) More homogeneous capillary flow and oxygenation in deeper cortical layers correlate with increased oxygen extraction. elife 8:e42299. https://doi.org/10.7554/eLife.42299
48. Redondo CS et al (2017) Interplay of fluorescence and phosphorescence in organic biluminescent emitters. J Phys Chem C 121(27):14946
49. Baggaley E, Weinstein JA, Williams JAG (2014) Time-resolved emission imaging microscopy using phosphorescent metal complexes: taking FLIM and PLIM to new lengths. In: Lo KK-W (ed) Luminescent and photoactive transition metal complexes as biomolecular probes and cellular reagents, vol 165. Springer, Berlin, pp 205–256
50. Choi H et al (2012) 3D-resolved fluorescence and phosphorescence lifetime imaging using temporal focusing wide-field two-photon excitation. Opt Express 20(24):26219. https://doi.org/10.1364/OE.20.026219.
51. Christodoulou C et al (2020) Live-animal imaging of native haematopoietic stem and progenitor cells. Nature 578(7794):278–283. https://doi.org/10.1038/s41586-020-1971-z.
52. Becker W (2005) Advanced time-correlated single photon counting techniques. Springer, New York, NY
53. Jiménez-Banzo A, Ragàs X, Kapusta P, Nonell S (2008) Time-resolved methods in biophysics. 7. Photon counting vs. analog time-resolved singlet oxygen phosphorescence detection. Photochem Photobiol Sci 7(9):1003. https://doi.org/10.1039/b804333g
54. Rytelewski M et al (2019) Merger of dynamic two-photon and phosphorescence lifetime microscopy reveals dependence of lymphocyte motility on oxygen in solid and hematological tumors. J Immunother Cancer 7(1):78. https://doi.org/10.1186/s40425-019-0543-y.
55. Fricke M, Nielsen T (2005) Two-dimensional imaging without scanning by multifocal multiphoton microscopy. Appl Opt 44(15):2984. https://doi.org/10.1364/AO.44.002984.
56. Howard SS, Straub A, Horton NG, Kobat D, Xu C (2013) Frequency-multiplexed in vivo multiphoton phosphorescence lifetime microscopy. Nat Photonics 7(1):33–37. https://doi.org/10.1038/nphoton.2012.307
57. Denk W, Piston DW, Webb WW (1995) Two-photon molecular excitation in laser-scanning microscopy. In: Pawley JB (ed) Handbook of biological confocal microscopy. Springer, Boston, MA, pp 445–458
58. Larson DR (2003) Water-soluble quantum dots for multiphoton fluorescence imaging in vivo. Science 300(5624):1434–1436. https://doi.org/10.1126/science.1083780
59. Sakadžić S et al (2010) Two-photon high-resolution measurement of partial pressure of oxygen in cerebral vasculature and tissue. Nat Methods 7(9):755–759. https://doi.org/10.1038/nmeth.1490.
60. Fittinghoff DN, Wiseman PW, Squier JA (2000) Widefield multiphoton and temporally decorrelated multifocal multiphoton microscopy. Opt Express 7(8):273. https://doi.org/10.1364/OE.7.000273.

61. Spencer JA (2012) Characterization of bone marrow intravascular pO_2 by 2-photon phosphorescence quenching method. Doctoral Dissertation. Retrieved from ProQuest Dissertations and Theses (Accession Order No. AAT 3541737)
62. Lebedev AY, Cheprakov AV, Sakadžić S, Boas DA, Wilson DF, Vinogradov SA (2009) Dendritic phosphorescent probes for oxygen imaging in biological systems. ACS Appl Mater Interfaces 1(6):1292–1304. https://doi.org/10.1021/am9001698
63. Esipova TV, Karagodov A, Miller J, Wilson DF, Busch TM, Vinogradov SA (2011) Two new 'protected' oxyphors for biological oximetry: properties and application in tumor imaging. Anal Chem 83(22):8756–8765. https://doi.org/10.1021/ac2022234
64. Dunphy I, Vinogradov SA, Wilson DF (2002) Oxyphor R2 and G2: phosphors for measuring oxygen by oxygen-dependent quenching of phosphorescence. Anal Biochem 310:191
65. Wilson DF, Lee WMF, Makonnen S, Finikova O, Apreleva S, Vinogradov SA (2006) Oxygen pressures in the interstitial space and their relationship to those in the blood plasma in resting skeletal muscle. J Appl Physiol 101(6):1648–1656. https://doi.org/10.1152/japplphysiol.00394.2006
66. Lo L-W, Koch CJ, Wilson DF (1996) Calibration of oxygen-dependent quenching of the phosphorescence of Pd-meso-tetra (4-carboxyphenyl) porphine: a phosphor with general application for measuring oxygen concentration in biological systems. Anal Biochem 236 (1):153–160. https://doi.org/10.1006/abio.1996.0144
67. Roussakis E, Spencer JA, Lin CP, Vinogradov SA (2014) Two-photon antenna-core oxygen probe with enhanced performance. Anal Chem 86(12):5937–5945. https://doi.org/10.1021/ac501028m
68. Zlokovic BV (2011) Neurovascular pathways to neurodegeneration in Alzheimer's disease and other disorders. Nat Rev Neurosci 12(12):723–738. https://doi.org/10.1038/nrn3114
69. Montagne A, Zhao Z, Zlokovic BV (2017) Alzheimer's disease: a matter of blood–brain barrier dysfunction? J Exp Med 214(11):3151–3169. https://doi.org/10.1084/jem.20171406
70. Al-Bachari S, Vidyasagar R, Emsley HC, Parkes LM (2017) Structural and physiological neurovascular changes in idiopathic Parkinson's disease and its clinical phenotypes. J Cereb Blood Flow Metab 37(10):3409–3421. https://doi.org/10.1177/0271678X16688919
71. Lim RG et al (2017) Huntington's disease iPSC-derived brain microvascular endothelial cells reveal WNT-mediated angiogenic and blood-brain barrier deficits. Cell Rep 19(7):1365–1377. https://doi.org/10.1016/j.celrep.2017.04.021.
72. Devor A et al (2011) 'Overshoot' of O2 is required to maintain baseline tissue oxygenation at locations distal to blood vessels. J Neurosci 31(38):13676–13681. https://doi.org/10.1523/JNEUROSCI.1968-11.2011
73. Parpaleix A, Houssen YG, Charpak S (2013) Imaging local neuronal activity by monitoring PO2 transients in capillaries. Nat Med 19(2):241–246. https://doi.org/10.1038/nm.3059
74. Lecoq J et al (2011) Simultaneous two-photon imaging of oxygen and blood flow in deep cerebral vessels. Nat Med 17(7):893–898. https://doi.org/10.1038/nm.2394.
75. Sakadžić S et al (2014) Large arteriolar component of oxygen delivery implies a safe margin of oxygen supply to cerebral tissue. Nat Commun 5(1):5734. https://doi.org/10.1038/ncomms6734.
76. Kazmi SMS et al (2013) Three-dimensional mapping of oxygen tension in cortical arterioles before and after occlusion. Biomed Opt Express 4(7):1061. https://doi.org/10.1364/BOE.4.001061.
77. Kisler K et al (2017) Pericyte degeneration leads to neurovascular uncoupling and limits oxygen supply to brain. Nat Neurosci 20(3):406–416. https://doi.org/10.1038/nn.4489.
78. Lyons DG, Parpaleix A, Roche M, Charpak S (2016) Mapping oxygen concentration in the awake mouse brain. elife 5:e12024. https://doi.org/10.7554/eLife.12024
79. Roche M, Chaigneau E, Rungta RL, Boido D, Weber B, Charpak S (2019) In vivo imaging with a water immersion objective affects brain temperature, blood flow and oxygenation. elife 8: e47324. https://doi.org/10.7554/eLife.47324

80. Zhang Q et al (2019) Cerebral oxygenation during locomotion is modulated by respiration. Neuroscience. https://doi.org/10.1101/639419
81. Moeini M, Cloutier-Tremblay C, Lu X et al (2020) Cerebral tissue pO_2 response to treadmill exercise in awake mice. Sci Rep 10:13358. https://doi.org/10.1038/s41598-020-70413-3
82. Şencan İ, Esipova T, Kılıç K, Li B, Desjardins M, Yaseen MA, Wang H, Porter JE, Kura S, Fu B, Secomb TW, Boas DA, Vinogradov SA, Devor A, Sakadžić S (2020) Optical measurement of microvascular oxygenation and blood flow responses in awake mouse cortex during functional activation. J Cereb Blood Flow Metab. https://doi.org/10.1177/0271678X20928011
83. Rytelewski M, Harutyunyan K, Baran N, Mallampati S, Zal MA, Cavazos A, Butler JM, Konoplev S, El Khatib M, Plunkett S, Marszalek JR, Andreeff M, Zal T, Konopleva M (2020) Inhibition of oxidative phosphorylation reverses bone marrow hypoxia visualized in imageable syngeneic B-ALL mouse model. Front Oncol 10:991. https://doi.org/10.3389/fonc.2020.00991
84. Şencan I et al (2018) Two-photon phosphorescence lifetime microscopy of retinal capillary plexus oxygenation in mice. J Biomed Opt 23(12):1. https://doi.org/10.1117/1.JBO.23.12.126501
85. Kritchenkov IS, Elistratova AA, Sokolov VV, Chelushkin PS, Shirmanova MV, Lukina MM, Dudenkova VV, Shcheslavskiy VI, Kalinina S, Reeß K, Rück A, Tunik SP (2020) A biocompatible phosphorescent Ir(iii) oxygen sensor functionalized with oligo(ethylene glycol) groups: synthesis, photophysics and application in PLIM experiments. New J Chem 44(25):10459–10471. https://doi.org/10.1039/D0NJ01405B
86. Schilling K et al (2019) Electrospun fiber mesh for high-resolution measurements of oxygen tension in cranial bone defect repair. ACS Appl Mater Interfaces 11(37):33548–33558. https://doi.org/10.1021/acsami.9b08341.

Whole-Body Fluorescence Imaging in the Near-Infrared Window

5

Guangcun Chen, Chunyan Li, Yejun Zhang, and Qiangbin Wang

5.1 Introduction

In vivo fluorescence imaging has generated great interest among researchers and physicians due to its great potential applications in both fundamental research and clinical practice [1–3]. In general, in vivo fluorescence imaging requires specific fluorophores for tissue labeling, an excitation (Ex) light source to excite the fluorophore, and a light detector to gain emission (Em) signals (Fig. 5.1a). By labeling the structure and molecular processes with specific fluorophores, fluorescence imaging can provide the anatomy and multiple physiological and pathological information of tissues and organs [1, 4–6]. Due to its intrinsic imaging characteristic, fluorescence imaging has shown numerous advantages as compared with other imaging modalities (computed tomography, magnetic resonance imaging, etc.), such as inherent biological safety, high resolution, quantitative sensitivity, multiple optical channels, and ease of use. Thus, it has become a promising methodology for whole-body imaging and has been widely used in investigating the fundamental biological phenomena, disease diagnosis, imaging-guided surgery treatment, efficacy evaluation, and so forth [1–7].

Despite the numerous advantages, the traditional in vivo fluorescence imaging (400–650 nm) still faces several critical challenges, such as its poor tissue penetration depth, the autofluorescence of mammalian tissues, and so forth [1, 6–8]. For in vivo fluorescence imaging, the applied excitation light has to travel through the

G. Chen · C. Li · Y. Zhang · Q. Wang (✉)
CAS Key Laboratory of Nano-Bio Interface, Suzhou Key Laboratory of Functional Molecular Imaging Technology, Division of Nanobiomedicine and i-Lab, CAS Center for Excellence in Brain Science, Suzhou Institute of Nano-Tech and Nano-Bionics, Chinese Academy of Sciences, Suzhou, China
e-mail: qbwang2008@sinano.ac.cn

X. Wei, B. Gu (eds.), *Optical Imaging in Human Disease and Biological Research*, Advances in Experimental Medicine and Biology 1355,
https://doi.org/10.1007/978-981-15-7627-0_5

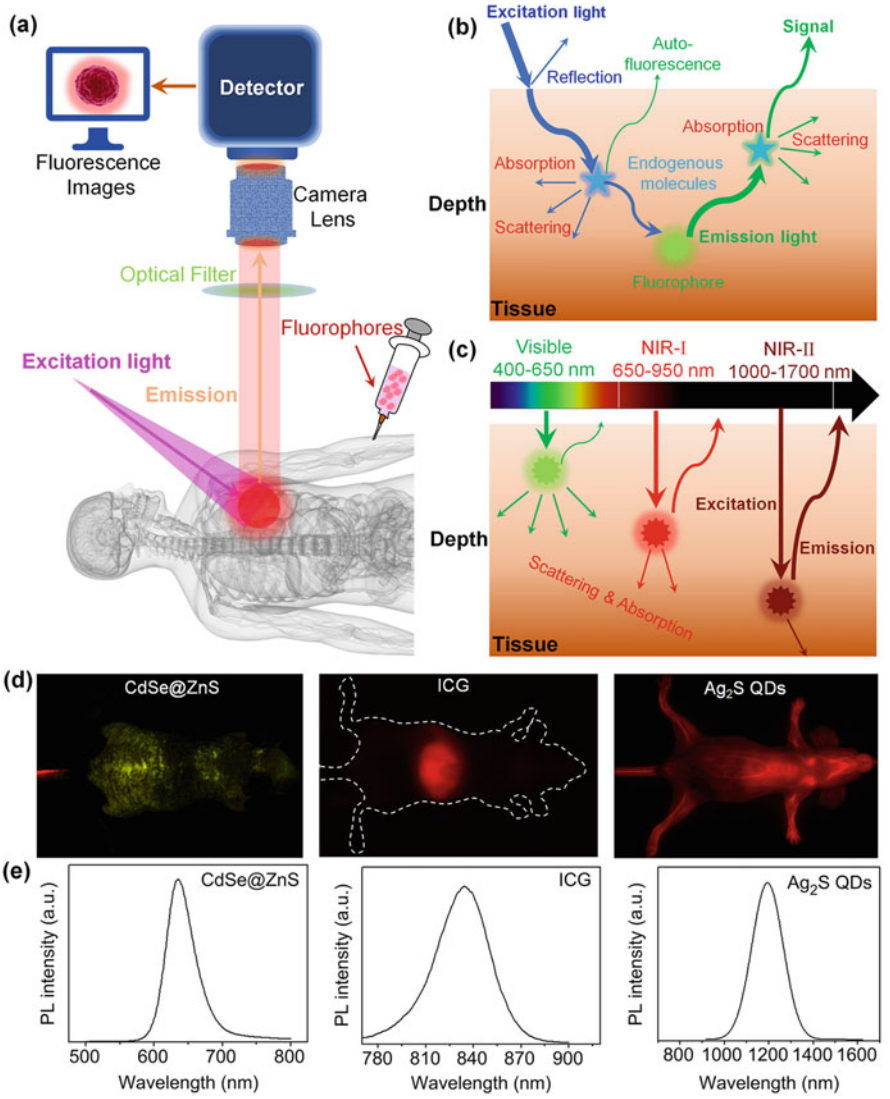

Fig. 5.1 The principles of in vivo fluorescence imaging and the interaction between light and biological tissues. (**a**) Schematic illustration of the whole-body fluorescence imaging. (**b**) The reflection, absorption, scattering, and emission of light in tissue. (**c**) Schematic illustration of the difference of fluorescence imaging in the visible (400–650 nm), the first NIR (NIR-I, 650–950 nm), and the second NIR (NIR-II, 1000–1700 nm) windows. The tissue penetration depth of light increases with the increase of wavelength of light, while the absorption and scattering of light decrease with the increase of wavelength of light. (**d**) Whole-body fluorescence images of nude mice after intravenous injection of CdSe@ZnS QDs (visible), ICG (NIR-I), or Ag_2S QDs (NIR-II), respectively. (**e**) The photoluminescence spectra of CdSe@ZnS QDs (emission peak at 635 nm), ICG (emission peak at 835 nm), and Ag_2S QDs (emission peak at 1200 nm). (Reproduced with permission [10]. Copyright 2014, Elsevier)

biological tissue to excite the fluorescent labels, and the emitted light from each fluorophore also has to travel through the biological tissue to reach the external detector. During the traveling of light in tissues, photons will be absorbed and scattered by the surrounding biomolecules (such as lipid, fat, protein, and water), resulting in the attenuation of the light signal proportional to the depth of the interested target in tissues (Fig. 5.1b). Due to the signal attenuation coupled with the interference from tissue autofluorescence, the imaging resolution and contrast of traditional in vivo fluorescence imaging will dramatically decrease with increasing tissue depths, thus hampering the applications of traditional fluorescence imaging in in vivo imaging. In the past few decades, the deep understanding of the interactions between light and the biological tissues has great aided the development of in vivo fluorescence imaging modalities in the first near-infrared (NIR-I, 650–950 nm) and second near-infrared windows (NIR-II, 1000–1700 nm), which enables researchers to peer deeper into biological tissues to visualize anatomical or functional features of tissues because of the reduced light scattering, absorption, and autofluorescence of tissues in the NIR imaging window [1, 5–9] (Fig. 5.1c).

First, it has found that the degree of scattering ($\mu s'$) for most tissues (including skin, muscle, mucous tissue, subcutaneous tissue, cranial bone, and brain tissue) follows an inversely proportional wavelength relationship, suggesting the reduced scattering at longer wavelengths [1, 8, 9]. Second, photons emitted from NIR fluorophores (650–1700 nm) have lower energy than the visible fluorophores (400–650 nm). The low energy significantly reduces the reaction activity of these NIR photons with most biological tissues, thereby reducing the light absorbance in the NIR window. However, it is also worth noting that there is a water overtone absorbance peak in the wavelength range of 1400–1500 nm, which wavelength range should be avoided during in vivo imaging. Third, autofluorescence spectra of heart, spleen, and liver tissue under excitation with 808 nm light shows that the autofluorescence of tissues also can be significantly eliminated in imaging windows with longer wavelength. And the autofluorescence of tissues is almost absence in the >1500 nm NIR window [1, 8]. In an example of whole-body fluorescence imaging by using CdSe@ZnS quantum dots (CdSe@ZnS QDs, emission peak at 635 nm), indocyanine green (ICG, emission peak at 835 nm), and Ag_2S QDs (emission peak at 1200 nm), it was found that the red signal of CdSe@ZnS QDs was hardly detected in vivo and the green-yellow autofluorescence signal was strong in the visible imaging window [10]. For fluorescence imaging in the NIR window, the liver was clearly observed by using ICG and the whole-body blood vessel was clearly visualized by using Ag_2S QDs with minimal autofluorescence interference (Fig. 5.1d, e).

All the above researches have suggested the fluorescence imaging in the NIR window (650–1700 nm) has numerous advantages as compared with the visible window (400–650 nm), including the reduced light scattering, minimal absorption, and minimal autofluorescence interference [1, 5, 8, 10]. In particular, fluorescence imaging in the second NIR window (NIR-II, 1000–1700 nm) can offer an ideal spatiotemporal resolution in deep tissue imaging, which has inspired researchers to develop new NIR fluorescent probes, imaging systems for NIR-II imaging. In this

chapter, the primary NIR fluorescent probes and their applications for whole-body fluorescence imaging, clinical applications and future prospects of NIR fluorescence imaging are systematically summarized and discussed.

5.2 NIR Fluorophores for In Vivo Fluorescence Imaging

Nowadays, several classes of NIR fluorophore have been developed to afford deep tissue fluorescence imaging with high signal-to-background ratio (SBR), including organic fluorophores and inorganic fluorophores (Table 5.1). And many efforts have been devoted to develop NIR fluorophores with more favorable spectral properties, higher quantum efficiency, and better biocompatibility, such as organic dyes and nanoparticles (NPs), single-walled carbon nanotubes (SWCNTs), rare-earth doped NPs (RE NPs), QDs, and so forth [2, 11–13]. Herein, the development, properties, and biomedical applications of commonly used NIR fluorophores are introduced and discussed.

5.2.1 Organic Fluorophores

Organic fluorophores generally include small-molecule dyes and organic NPs. Small-molecule dyes commonly can be fast cleared with scarce retention in the reticuloendothelial system after injection and imaging, making then high promise for clinical applications. Nowadays, many NIR-I small-molecule dyes are commercially available for both fundamental researches and clinical applications. For example, indocyanine green (ICG; emission ~800 nm) and methylene blue (MB; emission ~700 nm) have been approved by The US Food and Drug Administration (FDA) for clinical use for several decades [14–16]. IRDye800cW and Zwitterionic cyanine dyes are being tested in the Phase 1 clinical trials [17–20]. Recently, a series of NIR-II organic fluorophores also have been developed for in vivo imaging, including CH1055, IR-1061, etc. [3, 21, 22]. These NIR-II organic fluorophores usually contain a donor-acceptor-donor structure. By rationally designing the chemical structure of organic fluorophores to regulate the energy gap between the highest occupied molecular orbital (HOMO) and the lowest unoccupied molecular orbital (LUMO), the emission wavelength of the fluorophores can be tuned from NIR-I to NIR-II.

Organic NP is another type of organic fluorophore that has several advantages as compared with small-molecule dyes. For example, small-molecule dyes can be complexed with biomolecule or polymers to form organic NPs. Thus, the fluorescent yield, water solubility, and biocompatibility of these molecule dyes can be significantly improved to favor their biomedical applications [3, 23–27]. Another type of organic NP is semiconducting polymer-based NP (SPNP). By regulating the bandgap of SPNPs, various emission wavelengths in the NIR window can be obtained [28–30]. For example, Hong et al. synthesized a pDA dot through a copolymerization reaction of 1-(4,6-dibromo-3-fluorothieno [3,4-b]thiophen-2-yl)

Table 5.1 Typical fluorophores emitting in the NIR-I and NIR-II window for whole-body fluorescence imaging in fundamental researches and clinical applications

Type	Fluorophores	Properties	Quantum yields	Biomedical Applications	Ref.
Organic probes	MB	Ex: 665 nm, Em: 686 nm	9.6%	Cardiac perfusion, coronary angiography	[14]
	ICG	Ex: 807 nm Em: 822 nm	9.3%	Cardiac perfusion, tumor surgery, blood vessel imaging, lymph node mapping	[14, 16, 69]
	IRDye800cW	Ex: 665 nm, Em: 686 nm	12%	Surgical navigation in head and neck cancer	[18, 19]
	IRX	Ex: 680 nm, 808 nm, Em: 775–808 nm, 1061 nm	0.5–0.65%, 1.8%	Imaging sentinel lymph nodes, tumor imaging	[13, 23, 26]
	Zwitterionic cyanine dyes	Ex: 772 nm, Em: 788 nm	15.1%	Image-guided surgery	[17, 20]
	CH1055	Ex: 808 nm, Em: 1055 nm	0.03%	Vessel and lymph node imaging, image-guided surgery	[21]
	IR-E1	Ex: 808 nm, Em: 1071 nm	0.7%	Dynamic brain imaging	[61]
	CX dyes	Ex: 808 nm, Em: 883 nm, 981 nm, 1089 nm	0.66–0.091%	Lymphatic imaging, in vivo detection of endogenous $ONOO^-$ in the livers	[22]
	IR-FGP	Ex: 745 nm, Em: 1050 nm	0.19%	Brain tissue imaging	[25]
	CH-4T	Ex: 808 nm, Em: 1055 nm	0.1%	Real-time vessel imaging, lymph node imaging	[24]
	BODIPY	Ex: 649 nm, Em: 723 nm	100%	Tumor imaging, Alzheimer's disease imaging	[27]
	pDA	Ex: 808 nm Em: 900–1400 nm	1.7%	Ultrafast blood flow imaging	[28]
	Conjugated polymer NPs	Ex: 998 nm, Em: 1156 nm	0.1%	Imaging of cerebral vasculatures	[30]
	NIR-I emitting AIE dots	Ex: 500 nm, Em: 720 nm	/	Mapping of Aβ deposition in AD model	[33]
	NIR-II emitting AIE dots	Ex: 630 nm, Em: 810–1200 nm	13.9%	Vessel imaging, tumor imaging	[32]

(continued)

Table 5.1 (continued)

Type	Fluorophores	Properties	Quantum yields	Biomedical Applications	Ref.
Inorganic probes	CdTe QDs	Ex: 775 nm Em: 800 nm, 850 nm	13%, 45%	Cell tracking, tumor imaging, lymph node mapping	[34–36]
	Ag_2S QDs	Ex: 808 nm Em: 1200 nm	15.5%	Stem cell tracking, tumor detection, lymph node mapping, blood flow imaging, image-guided surgery	[10, 37, 38, 76]
	Ag_2Se QDs	Ex: 808 nm, Em: 820 nm, 1300 nm	1–3.09%	Blood vessel imaging, whole-body imaging	[39, 40]
	PbS QDs	Ex: 808 nm, Em: 1300 nm	17.3%	Stem cell tracking, tumor imaging, blood flow imaging	[41–43]
	SWCNTs	Ex: 808 nm, Em: 1000–1800 nm multiband	0.4%	Real-time vessel imaging, lymph node imaging, tumor imaging	[55–57]
	Up-conversion Re NPs	Ex: 980 nm, Em: 808 nm	/	Cell tracking, tumor imaging	[51, 52]
	Down-conversion Re NPs	Ex: 808 nm, Em: 1185–1525 nm	/	Imaging of inflammation, brain vessel imaging	[50, 53, 54]
	Au nanoclusters	Ex: 710 nm, Em: 830 nm	0.7%	Imaging kidney dysfunction	[58]

nonan-1-one and 2,6-bis(trimethyltin)-4,8-bis (2-ethylhexyloxy)benzo[1,2-b;3,4-b0]difuran. Because of the narrow bandgap of the pDA dot, a NIR emission (900–1400 nm) was obtained [28].

The third type of crucial organic NP is aggregation-induced emission (AIE) dots, which was first reported by Prof. Tang from the Hong Kong University of Science and Technology [31–33]. Because the brightness of these fluorophores can be distinctly enhanced in their aggregation form, the SBR as well as the sensitivity of in vivo fluorescence imaging will be significantly enhanced by using these fluorophores. Thus, they have been widely used in numerous biomedical researches, such as cancer diagnosis, vascular imaging, cell tracking, etc.

5.2.2 Inorganic Fluorophore

The current available inorganic fluorophores include QDs, RE NPs, SWCNTs, metal nanoclusters, and so forth.

QDs are a class of fluorescent nanocrystals with long fluorescence lifetime, high photostability, high quantum yield, tunable emission properties. Nowadays, NIR-emitting QDs generally include Group II–VI QDs (CdTe) [34–36], Group I–VI QDs (Ag_2S, Ag_2Se, Ag_2Te) [37–40], Group IV–VI QDs (PbS, PbSe, PbTe) [41–43], Group II–VI QDs (HgS, HgTe) [44], Group III–V QDs (InAs, InP) [45], Group I–III–VI QDs ($CuInS_2$, $CuInSe_2$, $AgInSe_2$) [46], and Group IV QDs (Si and Ge NPs) [47]. Based on the "quantum confinement effect," the confinement of electron movement in the nanocrystals enables those semiconductor nanocrystals emitting strong fluorescence. And the emission wavelength of QDs is generally determined by their bandgap energy. Therefore, a QD having a larger size typically possesses a smaller bandgap energy and emits at longer wavelength than its smaller form. Because of their unique light-emitting properties, QDs have been extensively used in biomedical imaging research, including cell labeling and tracking, cancer diagnosis and therapy, vascular imaging, and so forth [4, 12, 48, 49].

RE NPs generally contain an inorganic crystalline host matrix (e.g., $NaYF_4$, CaF_2) and the embedded lanthanide ions (La, Ho, Pr, Tm, Er, Lu, etc.) [50–54]. The RE NPs can be excited by a NIR laser (808 or 980 nm) and emit at visible (400–650 nm) or NIR (650–1700 nm) windows, and their emission properties are primarily dependent on the doped lanthanide ions. Based on different luminescence principles, RE NPs can be divided into up-conversion nanoprobes and down-conversion nanoprobes. RE NP-based up-conversion probes can consecutively absorb two or more photons and emit a single higher energy photon through the anti-Stokes shift process [51, 52]. For example, Zhao et al. developed a (α-$NaYbF_4$:Tm^{3+})/CaF_2 up-conversion probes, which possess a strong NIR emission at 800 nm when excited with a 980 nm NIR laser diode [51]. The RE NP-based down-conversion probes generally can emit at NIR-II window (1000–1700 nm) when excited by an 808 or 980 nm NIR laser diode through the Stokes shift process [50, 53, 54]. For example, Naczynski et al. developed a RE NP with a $NaYF_4$ shell and a $NaYF_4$ Yb:Ln-doped core. The NIR-II emission wavelength of the RE NPs can be precisely tuned from 1185 to 1525 nm by doping Ho, Pr, Tm, or Er in the $NaYF_4$ core, respectively [50]. Due to the excellent optical properties of both NIR excitation and NIR emission, RE NP has been proved to be an ideal probe for in vivo fluorescence imaging with high biocompatibility, high photochemical stability, and extremely low background autofluorescence.

SWCNTs are the first NIR-II fluorophore that developed for intravital fluorescence imaging. Due to the van Hove transitions across bandgaps, SWCNTs always have multiband emission peak ranging from 1000 to 1800 nm when excited by an 808 nm NIR laser diode [55–57]. And the emission wavelength of SWCNTs can be tuned by changing the diameter of the nanotube and the chiral angle. In 2009, Dai group from Stanford University firstly synthesized a phospholipid-polyethylene glycol complex functionalized SWCNT for whole-body NIR fluorescence imaging

in mice [57]. After that, SWCNTs had been extensively used for multiple bioimaging research, such as the internal organs imaging, blood vessel imaging, lymph node imaging, tumor imaging, etc.

In addition to QDs, RE NPs, and SWCNTs, a series of other inorganic NPs with NIR emission properties also have been developed for in vivo fluorescence imaging, including gold NPs, silica NPs, persistent luminescent NPs, etc. [58, 59]. For instance, Yu et al. developed a renal-clearable luminescent gold NP (Excitation: 710 nm, Emission: 830 nm) for kidney dysfunction imaging [58]. Biffi et al. synthesized a multimodal silica NPs fluorescence emission at 720 and 860 nm for labeling and imaging MDA-MB-231 cells [59]. With the breakthrough development of NIR fluorophores over the past several decades, in vivo NIR fluorescence imaging has begun to play an increasingly important role in both basic biomedical researches and clinical practices. Herein, the applications of NIR fluorescence imaging in whole-body vascular system imaging, precision cancer theranostics, and stem cell-based regenerative medicine were systematically introduced and discussed.

5.3 NIR Fluorescence Imaging for Whole-Body Vascular System Imaging

Because of its high spatial and temporal resolution, NIR fluorescence imaging has been proven to be an excellent method for blood vascular system imaging, lymphatic imaging, blood flow monitoring, and vascular-related disease research [2, 10, 14, 55]. In particular, the recently developed NIR-II imaging has distinctly advanced both the sensitivity and spatiotemporal resolution of whole-body vascular and lymphatic imaging [10, 55].

5.3.1 Whole-Body Blood Vessel and Blood Flow Imaging

The vascular system, also called the circulatory system, is a crucial organ in human body that is responsible for nutrient transportation, oxygen and carbon dioxide transportation, temperature and pH stabilization, and homeostasis maintenance. Therefore, the understanding and monitoring of the vascular system is vital for the diagnosis and treatment of many diseases. An ideal fluorophore for vascular system research should possess both high photochemical stability, high fluorescence yield, and long blood circulation time.

Nowadays, ICG is the most commonly used fluorophore in angiography [14]. However, ICG still suffers from some limitations in vascular lymphatic imaging, such as the low photostability, rapid liver enrichment, and unsatisfactory spatial resolution. In 2014, polyethylene glycol (PEG)-modified Ag_2S QDs emitting at 1200 nm were successfully applied for whole-body blood pool imaging in mice (Fig. 5.2a). Due to the high quantum yield (15.5%) and long circulation time (circulation half-time of 4.1 h) of PEGylated Ag_2S QDs, a micrometer-level resolution (~100 μm) of the peripheral vasculature was achieved by NIR-II imaging

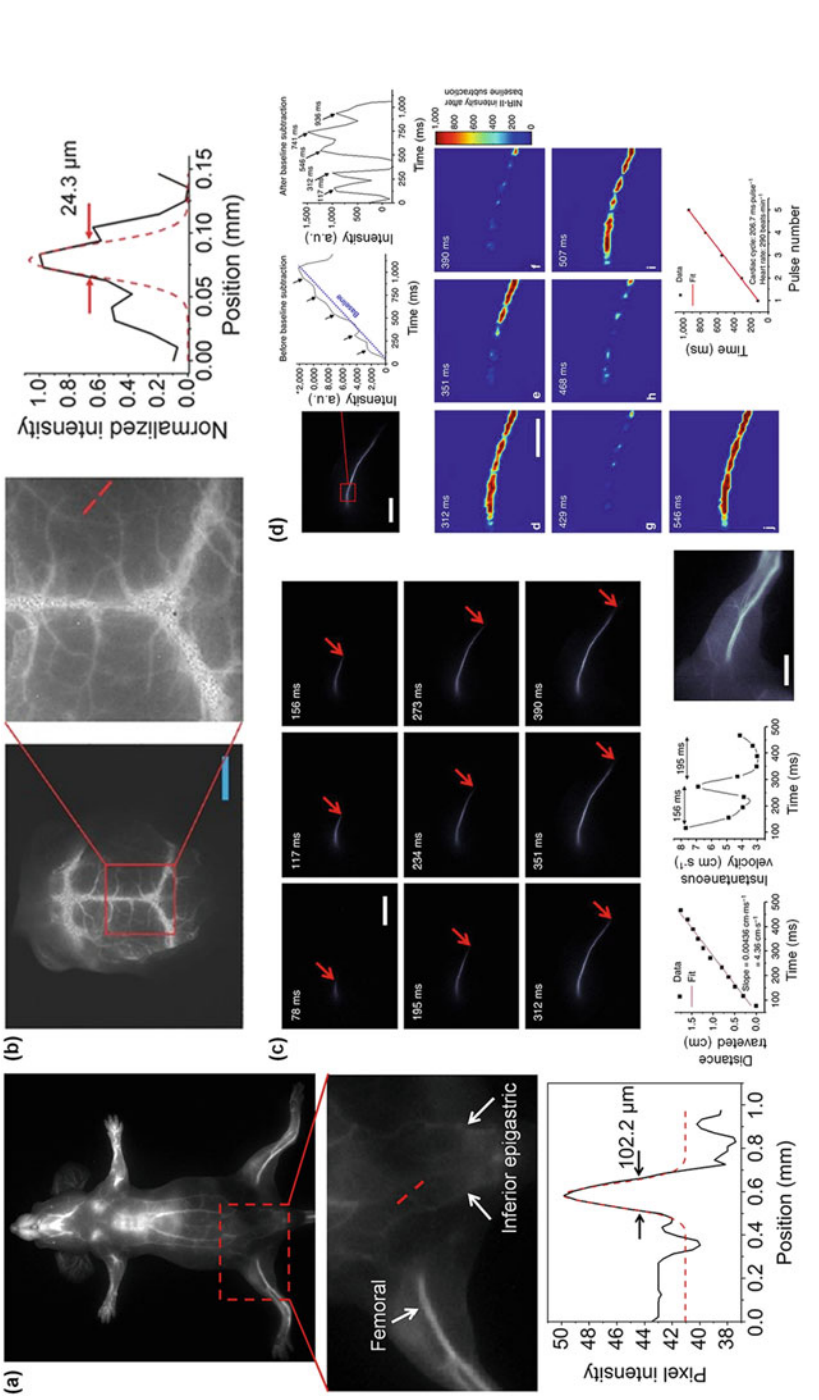

Fig. 5.2 NIR fluorescence imaging for whole-body vascular imaging and blood flow monitoring. (**a**) Whole-body blood pool imaging of the mouse by using PEGylated Ag_2S QDs (Ex: 808 nm, Em: 1200 nm) (reproduced with permission [10]; Copyright 2014, Elsevier). (**b**) In vivo NIR-II fluorescence image of the

[10]. In addition to Ag_2S QDs, SWCNTs, RE NPs, AIE dots, and other organic fluorophores also have been used for peripheral vasculature imaging [28, 32, 55].

In addition to peripheral vasculature imaging, brain vasculature imaging also has attracted numerous attentions in recent decades. For example, Li et al. synthesized a Gd-Ag_2S nanoprobe for in vivo whole-brain vasculature imaging (Fig. 5.2b). And a brain microvascular with a size of 24.3 μm was clearly observed in vivo [60]. Zhang et al. developed a novel NIR-II fluorophore, IR-E1, for traumatic brain injury (TBI) assessment [61]. In this study, the dynamic vascular changes in a mouse TBI model were systematically characterized by assessing the changes of initial transient hypoperfusion caused by TBI. This approach offers new opportunities to explore the pathogenesis of TBI at the morphological and cellular levels to better design TBI treatments. Another interesting application of fluorescence vascular imaging is tumor angiogenesis assessment [10]. Due to the high spatial and temporal resolution of NIR-II imaging, the development of new blood vessels around tumors can be real-time explored with a micrometer-level resolution (~40 μm). This study shows the promising of NIR imaging for monitoring and understanding the development of tumors, screening of anti-angiogenic drugs, and so on.

In addition to exploring the fine structure of blood vasculature, NIR-II imaging can also be used to real-time monitor the blood flow and heart rate. For example, Hong et al. synthesized a pDA dot emitting at 1047 nm for in vivo imaging of mouse arterial blood flow with a frame rate of >25 frames per second (FPS) [28]. Therefore, the blood velocities including the highest instantaneous blood velocity corresponding to the ventricular systolic phase and the lowest blood velocity corresponding to ventricular diastolic phase were accurately measured to be ~8 cm s^{-1} and ~2 cm s^{-1}, respectively (Fig. 5.2c). Furtherly, the heart rate of the mouse was also successfully measured to be 290 beats per minute by analyzing the NIR-II fluorescence oscillations per cardiac cycle (Fig. 5.2d). The capability of NIR-II imaging to in vivo measure the blood velocity and heart rate indicates its promise in diagnosing of various cardiovascular diseases and assessing of therapeutic effects.

5.3.2 Whole-Body Lymphatic System Imaging

The lymphatic system is a subsystem of the vascular system in the vertebrate body, which helps the body to maintain fluid balance, defend against infection, etc. Imaging the lymphatic system is important for numerous lymphatic system-related diseases including infection and tumor metastasis. The NIR fluorescence imaging

Fig. 5.2 (continued) brain vasculature in a nude mouse by the Gd-Ag_2S nanoprobe (reproduced with permission [60]; Copyright 2015, Wiley). (**c**) In vivo real-time NIR-II imaging of arterial blood flow using pDA-PEG (Ex: 808 nm, Em: 1047 nm). (**d**) Resolving waveform blood flow pattern by pDA. (Reproduced with permission [28]. Copyright 2014, Nature Publishing Group)

provides an ideal method for the detection of systemic lymphatic system including lymphatic vessels and lymph nodes [10, 24]. Similar to the blood vascular system, ICG is the primary probe for lymphatic system imaging both in fundamental biomedical research and clinical practice. And recently, new NIR-II fluorophores have offered greater penetration depth and clarity for imaging both lymphatic vessels and lymph nodes in vivo. For example, Antaris et al. developed an ultra-bright NIR-II emitting CH-4T-protein complexes for lymph node imaging (Fig. 5.3). In this study, the popliteal and sacral lymph nodes were clearly visualized by using CH-4T [24]. Moreover, a comparative study of CH-4T and ICG for deep lumbar lymph nodes imaging (at a depth of ~5–8 mm) clearly demonstrated the unique advantages of imaging deep anatomical features at the NIR-II window. In another example, Ag_2S QD-based NIR-II imaging was successfully used for imaging the lymphatic system during resection of sentinel lymph nodes, showing much higher resolution and better penetration depth than ICG-based NIR imaging [10]. All these studies suggested the whole-body NIR fluorescence imaging is promising for the diagnosis of lymphatic system-related diseases and surgical resection of lymph nodes.

5.4 NIR Fluorescence Imaging for Precision Cancer Theranostics

Cancer is one of the most deadly diseases in humans. Imaging techniques can help researchers explore the progress of tumor formation, vascularization, and metastasis, as well as help clinicians diagnose cancer and evaluate therapeutic efficacy. Among the available imaging techniques, NIR fluorescence imaging is an emerging imaging modality for cancer detection, imaging-guided drug delivery and drug screening, imaging-guided surgery in both fundamental researches and clinical applications [3, 5, 62]. In particular, the recently developed NIR-II imaging with unprecedented tissue penetration and spatiotemporal resolution has greatly aided the precision cancer theranostics [3, 5].

5.4.1 NIR Fluorescence Imaging for Early Tumor Diagnosis

Early diagnosis of cancer can greatly reduce the incidence of tumor metastasis and improve the cure rate of cancer. In the past several decades, a series of NIR fluorescence imaging techniques have been developed to detect tumor at its early stage with high sensitivity and high tumor-to-background ratio (TBR).

For example, 6PEG-Ag_2S QDs with fluorescence emission at 1200 nm were successfully applied for in vivo tumor detection. Because of the excellent biocompatibility and long circulation half-life (~4.37 h), 6PEG-Ag_2S QDs could be readily uptaken by tumors after intravenous injection via the enhanced permeability and retention (EPR) effect. Due to the high tumor retention property in combination with the high quantum yield (15.5%) of 6PEG-Ag_2S QDs, a high TBR was achieved in early diagnosis of the xenograft 4T1 tumors in mice [63].

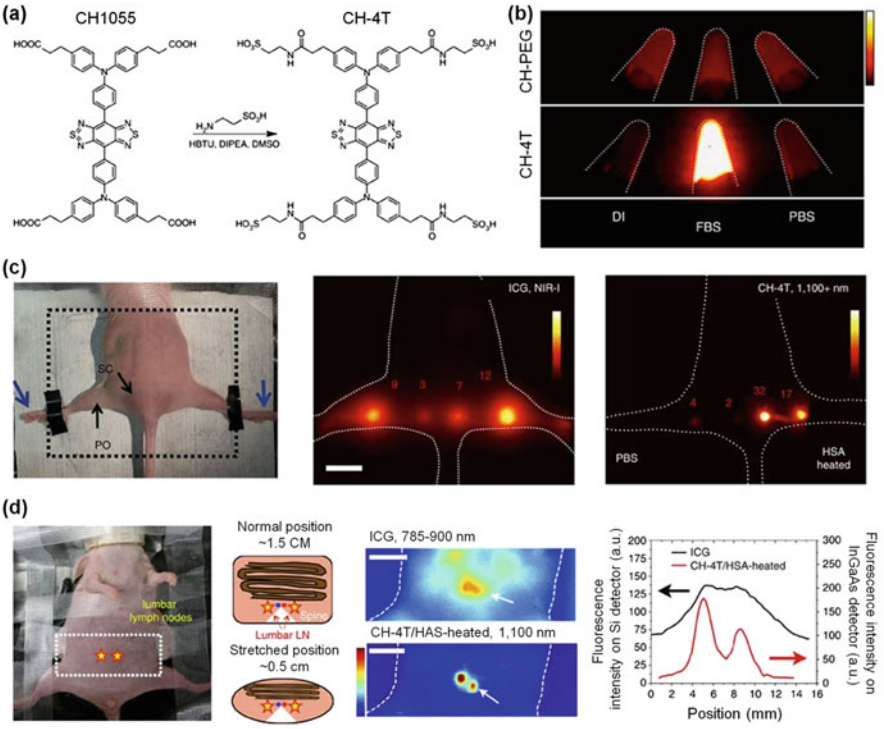

Fig. 5.3 Ultra-bright NIR-II emitting CH-4T-protein complexes and its application in lymph node imaging. (**a**) Synthesis method and chemical structure of CH-4T. (**b**) In vivo NIR imaging of popliteal and sacral lymph nodes by ICG and CH-4T. (**c**) In vivo NIR imaging of lumbar lymph nodes by ICG and CH-4T. (Reproduced with permission [24]. Copyright 2017, Nature Publishing Group)

In addition to passive targeting approaches by utilizing the EPR effect of tumor, numerous studies have shown that the enrichment of probe in tumor can be furtherly improved by conjugating specific tumor-targeting ligands on probes. For example, Antaris et al. synthesized a NIR-II emitting dye named CH1055 for tumor detection. After being conjugated with an anti-EGFR affibody, the CH1055@affibody conjugate can effectively target the squamous cell carcinoma tumors in mice. Thus, the tumor position signal can be distinguished to the normal tissue signal with a tumor-to-normal tissue ratio of approximately 15 [21]. In another example, NIR-II emitting SCH1100 was conjugated with RGD peptide to prepare an integrin αVβ3-targeted probe. This probe showed high affinity to integrin αVβ3-overexpression glioma and could be used to in vivo detect the glioma with high TBR [64].

Although the TBR ratio has been significantly improved by using NIR-II emitting probes and active targeting strategies, the interference signal of the background is still a big challenge for the aims of precise early detection. Thus, several activatable probes that can turn on their fluorescence in the tumor position have been developed

for cancer diagnosis [65]. For example, Tang et al. designed a dual-pathological-parameter cooperatively activatable NIR fluorescence nanoprobe (HISSNPs) for ultrahigh specific imaging of tumors. In HISSNPs, the fluorescence-quenched aggregation state of IR-1061 was double locked by hydrophilic hyaluronic acid (HA) and disulfide. In tumor microenvironments, the overexpressed hyaluronidase and thiols could fracture HA chains and disulfide bonds in HISSNPs to release IR-1061. Therefore, the fluorescence of self-quenched IR-1061 specifically turned "on" in the tumor position, and thus efficiently reduced nonspecific signals in the normal tissues. Due to this unique property, the activatable NIR probes may have great potential in precise early diagnosis of cancer and optical theranostics in biomedicine [26].

5.4.2 NIR Imaging-Guided Anti-tumor Drug Delivery and Drug Screening

Another important application of whole-body fluorescence imaging in cancer research is imaging-guided drug delivery and drug screening. It is known that inefficient drug utilization and the side effects of drugs are two key issues that need to be addressed in developing efficient anti-tumor drugs [60, 66–68]. The non-invasive whole-body fluorescence imaging offers the possibility to obtain the dynamic information of drugs and tumors, reporting the pharmacokinetics and therapeutic efficacy of drugs.

In a proof-of-concept study, Li et al. developed a novel strategy for monitoring the pharmacokinetics of a model protein nanocage (PNC) in vivo using NIR-II imaging. In this study, Ag_2S QDs (1200 nm) were encapsulated within a simian virus 40 (SV40) PNC, avoiding interference in PNC-host interactions [66]. Due to the deep penetration depth and high spatiotemporal resolution of NIR-II imaging, the dynamic distribution of the PNC in live mice could be imaged in real time without requiring a laparotomy. Furthermore, the novel imaging helps researchers in vivo explore the role of the surface property of the PNCs on their in vivo pharmacokinetics, showing the blood circulation time of PNC significantly prolonged from <5 to 476 min after surface modification by PEG. The feasible imaging strategy will facilitate the study of interactions between PNC-based drug and host body, facilitating the evaluation and development of future protein-based drugs.

In addition to analysis of the pharmacokinetics of drugs, whole-body fluorescence imaging can also be used for imaging-guided drug delivery and simultaneous therapeutic efficacy analysis. For instance, Song et al. developed a traceable probe nanodrug (T&D@RGD-Ag_2S) for imaging-guided tumor vasculature-targeted drug delivery [67]. In this system, PEG-Ag_2S QDs were used as NIR-II probe and drug carrier to encapsulate tumor angiogenesis inhibitor TNP-470 and the doxorubicin (DOX). And the cRGD peptide was conjugated on the surface of Ag_2S QDs for tumor vasculature targeting. In the U87-MG tumor-bearing mice, the dynamic accumulation of T&D@RGD-Ag_2S in the tumor position can be real-time reported with the NIR-II fluorescence of Ag_2S QDs. Moreover, the therapeutic effects of

T&D@RGD-Ag_2S on tumor sizes and vessel patterns also could be simultaneously monitored by NIR-II fluorescence imaging. This real-time drug monitoring and real-time therapeutic feedback by the whole-body fluorescence imaging method holds great promise for both imaging-guided drug delivery and anti-tumor drug screening.

5.4.3 Intraoperative NIR Image-Guided Surgery

Surgery is the most common strategy for treating solid tumors. Intraoperative optical image can help surgeons perform surgery faster, better, and less expensively, and thus it has been extensively used in clinical trials. At present, the FDA approved NIR-I organic dyes (ICG and MB) are the most commonly used fluorophores in image-guided surgery both in fundamental biomedical researches and clinical practices [16, 69]. More recently, a series of new NIR-II fluorophores and imaging strategies have been developed for image-guided surgery [3, 5].

For example, Wang et al. reported a NIR-II emitting down-conversion NPs (DCNPs) for the image-guided surgery of metastatic ovarian cancer [70]. In this study, DCNPs were modified with DNA and targeting peptides (FSHβ) to improve their tumor-targeting capability. Two NPs contain complementary DNA sequence, DCNPs-L1-FSHβ and DCNPs-L2-FSHβ were prepared. To specifically improve the retention of DCNPs in the tumor position, the DCNPs-L1-FSHβ was first injected into an ovarian tumor-bearing mouse and DCNPs-L2-FSHβ was injected into the same mouse 8 h later. Therefore, DCNPs-L1-FSHβ and DCNPs-L2-FSHβ assembled and were trapped in the tumor position, while dispersed NPs in the normal tissues were rapidly removed by renal excretion. By this way, a superior TBR was achieved to aid the elimination of the abdominal ovarian metastases using NIR-II bioimaging and metastases with $\leq$1 mm can be completely excised.

In another instance, Wen et al. constructed a NIR-II emitting APP-Ag_2S-RGD probe for intraoperative NIR image-guided surgery [71]. In this work, the APP-Ag_2S-RGD was first prepared by conjugating of NIR-II Ag_2S QDs and the RGD peptides in the self-assembly of an amphiphilic peptide (APP) nanochain (Fig. 5.4a). In comparison with RGD-functionalized Ag_2S QDs, APP-Ag_2S-RGD is more readily taken up by tumor cells to provide higher TBR (13.6). In a mouse model of peritoneal metastasis, a non-vascularized tiny tumor metastatic foci with a diameter of about 0.2 mm could be eliminated under NIR-II imaging guidance (Fig. 5.4b–d). With such unique merits, these novel NIR-II probes and imaging strategies may have great potential for future clinical preoperative diagnosis and intraoperative navigation.

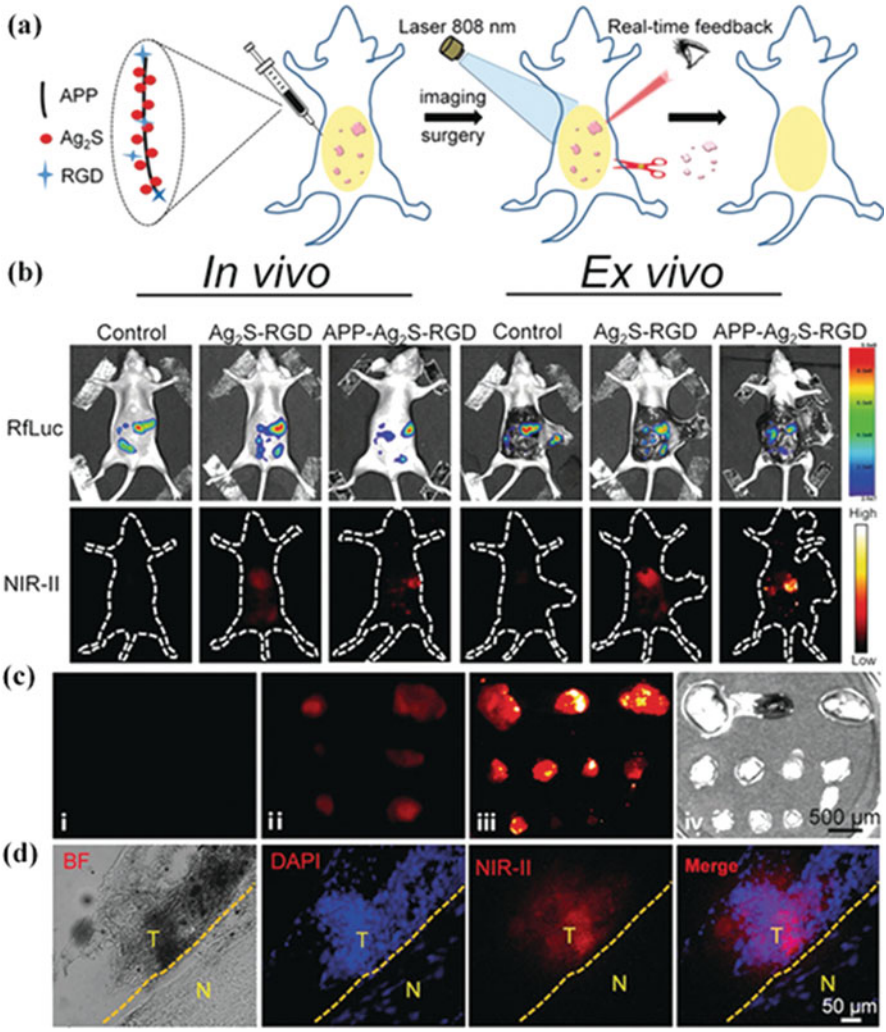

Fig. 5.4 NIR-II emitting APP-Ag_2S-RGD probe and its application in intraoperative NIR image-guided surgery. (**a**) Schematic illustration of intraoperative NIR image-guided surgery by APP-Ag_2S-RGD. (**b**) In vivo and ex vivo bioluminescence and NIR-II images after administration of either Ag_2S-RGD or APP-Ag_2S-RGD in tumor-bearing mice. (**c**) NIR-II fluorescence images of tumors excised by different methods (i: naked eye, ii: Ag_2S-RGD, iii: APP-Ag_2S-RGD, iv: bright-field image of iii). (**d**) Multichannel fluorescence microscope images of tumor nodules. *T* tumor tissue, *N* normal tissue. (Reproduced with permission [71]. Copyright 2019, Wiley)

5.5 NIR Fluorescence Imaging for Regenerative Medicine

In the past decades, stem cell-based regenerative medicine has shown great potential for treating numerous incurable diseases of human being, such as liver failure, bone defect, heart disease, neurodegenerative disease, cancer, and so forth. As a type of fast self-renewing and multipotential cells, stem cells can help to cure numerous diseases by damaged cell replacement, paracrine effect, etc. However, the therapeutic process, safety, and the fate of transplanted stem cells are not fully understood yet. Therefore, many efforts have been made to develop in vivo imaging methods for monitoring the translocation, viability, and differentiation ability of stem cells after transplantation to improve the therapeutic efficacy and safety of stem cell therapy [72]. Due to its deep tissue imaging capability with high spatiotemporal resolution, NIR fluorescence imaging has been widely used in stem cell-based regenerative medicine research. In particular, the applications of recently developed NIR-II imaging have not only improved our understanding of the role of stem cells played in tissue regeneration but also offered a great opportunity for imaging-guided development of stem cell therapy [4, 41, 51, 73–75].

5.5.1 Tracking the Biodistribution of Transplanted Stem Cells

NIR fluorescence imaging offers a great opportunity to in vivo real-time tracking the biodistribution of transplanted stem cells. For example, octa-arginine peptide-functionalized QDs (emitting at 655 or 800 nm) were successfully used for labeling and tracking adipose tissue-derived stem cells (ASCs) in living mice [36]. In this study, 0.5×10^5 ASCs could be detected after subcutaneous transplantation. In the mouse model of acute liver failure, the transplanted ASCs could be visualized by QDs800 without requiring a laparotomy. However, the QDs655-labeled ASCs were not able to be detected in vivo by fluorescence imaging, suggesting that fluorescence imaging with longer wavelengths has significant advantages than imaging with shorter wavelengths. And more recently, the first in vivo stem cell tracking in the NIR-II window was achieved by using the NIR-II emitting Ag_2S QDs (emitting at 1200 nm) [76]. After being conjugated with a cell penetration peptide (Tat peptide), the Tat-Ag_2S could effectively label mesenchymal stem cells (MSCs) without causing any adverse effects to MSCs (Fig. 5.5a–d). As compared with QDs800, a much better detection sensitivity of 1000 subcutaneously transplanted cells was achieved by using Ag_2S QDs. Moreover, the distribution of transplanted MSCs in the lung and liver could be clearly visualized by NIR-II imaging; offering a direct evidence of heparin helps MSCs to migrate from the lung to the liver. In addition, because of the extra high temporal resolution of NIR-II imaging, the real-time translocation of MSCs from the lung to the liver were successfully monitored with a temporal resolution of 100 ms (Fig. 5.5f). In another interesting study, Yang et al. synthesized NIR-II emitting PbS QDs for stem cell labeling and tracking in a mouse model of supraspinatus tendon tear. In their study, the spatiotemporal migration, biodistribution, and clearance processes of intra-articularly injected MSCs in the

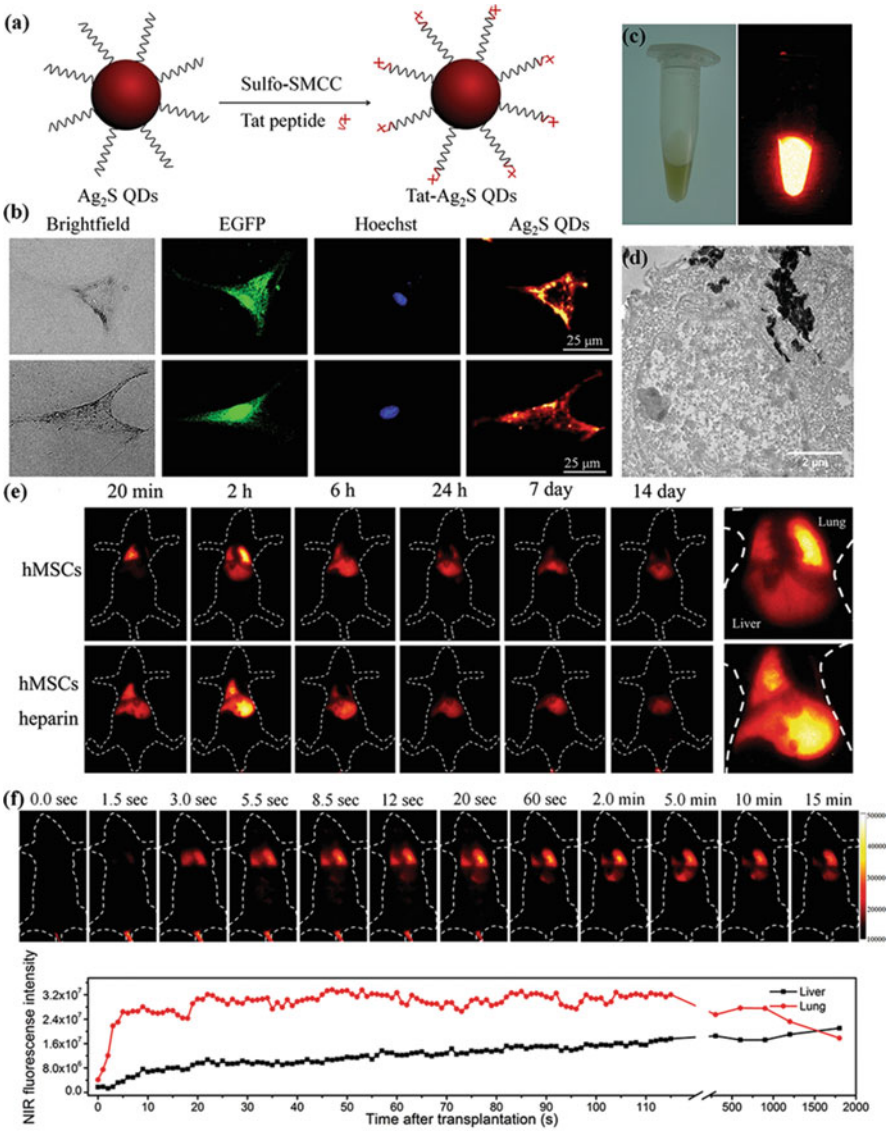

Fig. 5.5 In vivo tracking of the transplanted MSCs using Ag_2S QDs in the NIR-II window. (**a**) Schematic illustration of preparing Tat peptide-functionalized Ag_2S QDs. (**b**) NIR-II fluorescence images of Ag_2S QD-labeled MSCs obtained using a NIR-II fluorescence microscopy (reproduced with permission [74]; Copyright 2018, Wiley). (**c**) NIR-II fluorescence images of the Ag_2S QD-labeled MSCs. (**d**) The TEM image of Ag_2S QD-labeled MSCs. (**e**) In vivo tracking of Ag_2S QD-labeled MSCs in mice with acute liver failure. MSCs were intravenously transplanted with or without heparin and monitored up to 14 days (reproduced with permission [76]; Copyright 2014, Wiley). (**f**) In vivo real-time imaging the dynamic translocation of intravenously transplanted MSCs in mice. (Reproduced with permission [74]. Copyright 2018, Wiley)

mouse model of supraspinatus tendon tear was clearly visualized by using the PbS QD-based NIR-II imaging. These studies all suggested the promising of NIR-II imaging for monitoring the fine biodistribution of transplanted stem cells.

5.5.2 Tracking the Viability of Transplanted Stem Cells

The viability of transplanted stem cells is also a key factor involved in their therapeutic efficacy. Nowadays, the reporter gene-based methodologies are the most common methods for tracking the viability of stem cells, such as fluorescence proteins-based fluorescence imaging and luciferase-based bioluminescence imaging. Recently, exogenous probe-based NIR fluorescence imaging methods have also been found as promising methods for monitoring the viability of transplanted stem cells. For instance, Alam et al. synthesized self-illuminated QDs by coating firefly luciferase in QD800 [77]. In this system, the viability of cells can be monitored by using the methodology of bioluminescence resonance energy transfer (BRET), because the BRET signal intensity is highly depended on the ATP and oxygen (important indicators of cell viability) in cells. In a similar manner, the self-illuminated NIR-II emitting Luc-PbS QDs and self-illuminated NIR polymer dots (MEHPPV@NIR@PEG NPs) have also been developed for cell tracking [78, 79]. These self-illuminated NPs are promising NIR probes for monitoring the viability of transplanted stem cells, which is unachievable by traditional exogenous probes.

In another interesting study, a multi-layered nanoprobe (DL2) was synthesized for in vivo tracking the fate of human mesenchymal stem cells (hMSCs) by Lee and colleagues [80]. In this study, an Au NP core was coated by poly-D-lysine (PDL) with fluorescein isothiocyanate (FITC) and poly-L-lysine (PLL) with cy5.5 using a layer-by-layer deposition technique. In this system, the Au core could be used to quench the fluorescence of cy5.5 and FITC in the intact multi-layered nanoprobe. Once the probe was taken up by living cells, intracellular proteases will degrade the PLL and release cy5.5 to produce red fluorescence. For apoptotic and necrotic sensing, the over-produced ROS in cell will degrade the protease-resistant PDL and release FITC to produce green fluorescence. By this way, the DL2 could be readily used to monitor the fate of transplanted stem cell from live to dead. In a more recently study, a NIR-II/BLI multimodal imaging method was developed to monitor the fate of transplanted stem cells by distinguishing the live and dead cells in vivo [74]. In this study, MSCs were labeled by red-emitting firefly luciferase (RfLuc, 620 nm) reporter gene and Ag_2S QDs (1200 nm). In this imaging system, the RfLuc-based BLI were used to specifically report the living cells. And the Ag_2S QD-based NIR-II imaging was used to report the precise location of all transplanted stem cells. Thus, the living stem cells could be distinguished from dead stem cells in vivo by merging NIR-II signals with BLI signals in the same mouse. Thus, how the living stem cells help to liver regeneration and the fate of transplanted MSCs were clearly visualized.

5.5.3 Tracking the Differentiation Capability of Transplanted Stem Cells

In addition to the biodistribution and viability, the differentiation capability of stem cells is more important for their therapeutic efficacy. The endogenous reporter gene-based fluorescence imaging has been well developed for imaging the differentiation of stem cells. However, the available NIR fluorescent proteins are still quite limited. At present, several NIR fluorescence imaging methods using exogenous nanoprobes have been developed to explore the differentiation capability of transplanted stem cells. For example, Wang et al. developed a multifunctional nanocomplex for spatiotemporal imaging the dynamic expression of mRNA in neural stem cell during the differentiation process [81]. In this study, DNA oligonucleotides with a 5′ end fluorophore tag (Alexa 488; Cy3) were conjugated on the Au NP surface. Therefore, the fluorescence of the fluorophore was quenched by the Au NP in the intact nanocomplex. Upon reaction with the target mRNA, the oligonucleotides with fluorophore tags will release and produce NIR fluorescence to report the expression of target mRNA at their specific differentiation stages.

In another example, Wiraja et al. reported a dual-colored nanosensor to validate MSC osteogenesis. The dual-colored nanosensor contains two molecular beacon (MB) probes, an oligonucleotide-based probe detecting the mRNA of glyceraldehyde-3-phosphate dehydrogenase (GAPDH), and an oligonucleotide-based probe detecting the mRNA of alkaline phosphatase (ALP). Therefore, the dynamic expression of ALP was monitored by normalizing ALP-MB signal with GAPDH-MB signal, thus noninvasively reporting the osteogenic differentiation of MSCs [82].

More recently, an NIR-II fluorescence/dual BLI multiplexed imaging method was successfully developed for in vivo monitoring the distribution, viability, and osteogenic differentiation of transplanted hMSCs [75]. In this imaging system, the Ag_2S QD-based NIR-II imaging is used for detecting the long-term biodistribution of transplanted hMSCs. CMV promoter-driven RFLuc-based BLI and the collagen type 1 (Col1a1) promoter-driven Gaussia luciferase (GLuc)-based BLI were applied to report the viability and osteogenic differentiation statuses of hMSCs, respectively. Thus, the distribution, viability, and osteogenic differentiation of transplanted hMSCs were able to be simultaneously visualized by precisely integrating the three imaging channel signals in the same mouse. The novel multiplexed imaging strategy has a broad spectral detecting range from 400 to 1700 nm and can offer abundant imaging channels to in vivo report multiple functions of stem cells, which will have great promise for therapeutic efficacy evaluation, imaging-guided cell therapeutics, and so forth.

5.6 Clinical Applications of NIR Fluorescence Imaging

During the past several decades, fluorescence imaging has been applied in a series of clinical trials. NIR-I fluorophores, including ICG, MB, IRDye800CW, and fluorescent cRGDY PEG-Cy5.5 C dots, are the most widely used probes in these clinical

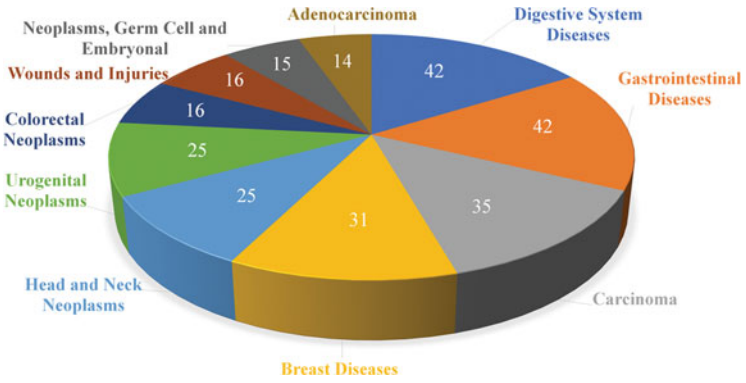

Fig. 5.6 Ten representative diseases that mostly studied by using fluorescence imaging in the clinical trials. White numbers indicate the number of clinical trials associated with each disease. (Data were collected from the public clinical trial database http://clinicaltrials.gov)

trials. By 20 September 2019, the clinical trial database http://clinicaltrials.gov showed 250 clinical trials using fluorescence imaging. Most of these trials are performed in the North American (119) and Europe (76), followed by East Asian (24), Middle East (3), South America (2), and Southeast Asia (2). These clinical trials also include a wide range of therapeutic applications (Fig. 5.6), such as lymphatic vessels imaging (NCT02154204), diagnosis and intraoperative detection of endometriosis (NCT03017989), hepatobiliary surgery (NCT03946761), thoracic surgery (NCT02611245), hepatocellular carcinoma detection (NCT03793322), sentinel lymph node biopsy for breast cancer and melanoma (NCT02316795), imaging in head and neck cancer (NCT03297957), bladder cancer detection (NCT03058705), sentinel lymph node mapping of oral cancer (NCT02478138), assessing tissue remodeling in the skin (NCT03535077), etc. At present, most of the clinical trials are associated with imaging-guided tumor surgery. Moreover, several completed clinical trials have proved the promising of NIR fluorescence imaging for indicating the accurate localization of tumor, and thus improving the surgical outcomes [16, 19].

For examples, Rosenthal et al. reported a clinical study of applying cetuximab conjugated IRDye800 for imaging-guided surgical resection of squamous cell carcinoma arising in the head and neck [19]. By using the intraoperative fluorescence imaging device, tumor was successfully differentiated from normal tissue with a high TBR of approximately 5.2 during resection. This study demonstrated that antibodies conjugated IRDye800 can be safely administered to humans to report tumors with sub-millimeter resolution, which has great potential to improve outcomes of surgery treatment. In another example, Newton et al. reported a clinical study of "intraoperative near-infrared imaging of thoracic malignancy" in 2019. In this clinical trial, 45 patients with biopsy-proven thoracic tumors or suspicious for malignancy were enrolled and supplied with ICG at different doses to identify the best TBR for each tumor type. This study demonstrated that lower dose ICG

(2–3 mg/kg) is superior for nonprimary lung cancers, and high dose ICG (4–5 mg/kg) is superior for lung cancers [16]. These clinical trials have shown that NIR fluorescence imaging has great potential to improve the therapeutic effects of various diseases, and more researches are still needed in the future to further promote the clinical applications of NIR fluorescence imaging.

5.7 Conclusions and Future Prospects

Due to its numerous advantages, including non-invasive, high spatiotemporal resolution, high sensitivity and easy to operate, NIR fluorescence imaging has been successfully applied in a wide range of fundamental researches and clinical practices. In particular, the recently developed NIR-II imaging has provided an unprecedented spatiotemporal resolution and tissue penetration for in vivo fluorescence imaging [1, 3, 6, 7]. However, the NIR-II imaging is still underexplored and many efforts are still necessary to further improve the NIR fluorescence imaging in various aspects.

First, although several NIR-I fluorescent probes have been tested in a wide range of clinical trials, clinical trials by using NIR-II fluorescent probes have not been achieved yet. Thus, more efforts are needed to promote the clinical application of NIR-II fluorescent probes in several aspects. (1) The safety of the probe is the most important factor for its clinical application. Thus, more systematic preclinical safety evaluation on large animals for the existing NIR-II probes are urgently needed to facilitate their clinical applications. In addition, the development of new safety probes with rapid renal clearance properties is also needed. (2) As compared with the visible and NIR-I fluorescent probes, the existing NIR-II fluorescent probes generally have low QYs (below 20%) [1, 11]. Therefore, there is still an urgent need to improve the QYs of both organic and inorganic fluorescent probes to improve the imaging sensitivity and reduce the dosage of probes administrated in vivo in their future clinical utilities. (3) Probes with efficient tissue targeting and tissue microenvironmental response activation properties can greatly improve the signal-to-noise ratio of in vivo fluorescence imaging [65]. Therefore, the development of targeted and activatable probes is also an important research direction for future clinical applications of NIR fluorescence imaging.

Second, in addition to the fluorescent probes, the development of new in vivo imaging systems is also important for the next-generation NIR fluorescence imaging. Nowadays, numerous NIR-I imaging systems have been developed for both animal modal researches (such as the PerkinElmer IVIS in vivo imaging system) and clinical practices (such as the fluorescence-assisted resection and exploration (FLARE) imaging system) [83, 84]. These imaging systems generally contain a silicon-based complementary metal oxide semiconductors (CMOS) or charge-coupled device (CCD) camera as the detector, which can't be used for NIR-II imaging studies. At present, only a few NIR-II imaging systems are commercially available for fundamental biomedical researches, such as the NIR-II in vivo imaging system developed by Suzhou NIR-Optics Technologies Co., Ltd., in China. The

NIR-II imaging system generally uses a shortwave infrared (SWIR) camera (such as InGaAs) as the detector to monitor fluorescence signals in the 900–1700 nm region. Thus, in the next few decades, more efforts are still needed to develop more NIR-II in vivo imaging systems for both fundamental researches and clinical practices.

Third, multimodal imaging by combining NIR-I imaging with magnetic resonance imaging (MRI), ultrasound imaging (US), photoacoustic imaging (PA), or positron emission computerized-tomography (PET) has shown great potential to imaging multiple molecule events in both biomedical research and clinical practices. However, the NIR-II imaging-based multimodal imaging has only been reported in a few cases in recent years. Therefore, the development of multimodal NIR-II probes and multimodal NIR-II imaging systems is still needed to support the clinical applications of next-generation NIR fluorescence imaging technologies.

References

1. Hong GS, Antaris AL, Dai HJ (2017) Near-infrared fluorophores for biomedical imaging. Nat Biomed Eng 1:0010
2. Kenry DY, Liu B (2018) Recent advances of optical imaging in the second near-infrared window. Adv Mater 30:e1802394
3. Zhu S, Tian R, Antaris AL et al (2019) Near-infrared-II molecular dyes for cancer imaging and surgery. Adv Mater 31:e1900321
4. Chen G, Zhang Y, Li C et al (2018) Recent advances in tracking the transplanted stem cells using near-infrared fluorescent nanoprobes: turning from the first to the second near-infrared window. Adv Healthc Mater 7:1800497
5. Li C, Wang Q (2019) Advanced NIR-II fluorescence imaging technology for in vivo precision tumor theranostics. Adv Therap 2:1900053
6. Wang H, Mu XY, Yang J et al (2019) Brain imaging with near-infrared fluorophores. Coord Chem Rev 380:550–571
7. Li CY, Wang QB (2018) Challenges and opportunities for intravital near-infrared fluorescence imaging technology in the second transparency window. ACS Nano 12:9654–9659
8. Smith AM, Mancini MC, Nie S (2009) Bioimaging: second window for in vivo imaging. Nat Nanotechnol 4:710–711
9. Ntziachristos V (2010) Going deeper than microscopy: the optical imaging frontier in biology. Nat Methods 7:603–614
10. Li C, Zhang Y, Wang M et al (2014) In vivo real-time visualization of tissue blood flow and angiogenesis using Ag_2S quantum dots in the NIR-II window. Biomaterials 35:393–400
11. He SQ, Song J, Qu JL et al (2018) Crucial breakthrough of second near-infrared biological window fluorophores: design and synthesis toward multimodal imaging and theranostics. Chem Soc Rev 47:4258–4278
12. Lu H, Carroll GM, Neale NR et al (2019) Infrared quantum dots: progress, challenges, and opportunities. ACS Nano 13:939–953
13. Deng G, Li S, Sun Z et al (2018) Near-infrared fluorescence imaging in the largely unexplored window of 900-1,000 nm. Theranostics 8:4116–4128
14. Tanaka E, Chen FY, Flaumenhaft R et al (2009) Real-time assessment of cardiac perfusion, coronary angiography, and acute intravascular thrombi using dual-channel near-infrared fluorescence imaging. J Thorac Cardiovasc Surg 138:133–140
15. Starosolski Z, Bhavane R, Ghaghada KB et al (2017) Indocyanine green fluorescence in second near-infrared (NIR-II) window. PLoS One 12:e0187563

16. Newton AD, Predina JD, Corbett CJ et al (2019) Optimization of second window indocyanine green for intraoperative near-infrared imaging of thoracic malignancy. J Am Coll Surg 228:188–197
17. Choi HS, Gibbs SL, Lee JH et al (2013) Targeted zwitterionic near-infrared fluorophores for improved optical imaging. Nat Biotechnol 31:148–153
18. Rosenthal EL, Warram JM, de Boer E et al (2015) Safety and tumor specificity of cetuximab-IRdye800 for surgical navigation in head and neck cancer. Clin Cancer Res 21:3658–3666
19. Warram JM, de Boer E, Korb M et al (2015) Fluorescence-guided resection of experimental malignant glioma using cetuximab-IRdye 800cw. Br J Neurosurg 29:850–858
20. Hyun H, Henary M, Gao T et al (2016) 700-nm zwitterionic near-infrared fluorophores for dual-channel image-guided surgery. Mol Imaging Biol 18:52–61
21. Antaris AL, Chen H, Cheng K et al (2016) A small-molecule dye for NIR-II imaging. Nat Mater 15:235–242
22. Lei Z, Sun C, Pei P et al (2019) Stable, wavelength-tunable fluorescent dyes in the NIR-II region for in vivo high-contrast bioimaging and multiplexed biosensing. Angew Chem Int Ed Engl 58:8166–8171
23. Tao ZM, Hong GS, Shinji C et al (2013) Biological imaging using nanoparticles of small organic molecules with fluorescence emission at wavelengths longer than 1000 nm. Angew Chem Int Ed Engl 52:13002–13006
24. Antaris AL, Chen H, Diao S et al (2017) A high quantum yield molecule-protein complex fluorophore for near-infrared II imaging. Nat Commun 8:15269
25. Zhu S, Yang Q, Antaris AL et al (2017) Molecular imaging of biological systems with a clickable dye in the broad 800- to 1,700-nm near-infrared window. Proc Natl Acad Sci U S A 114:962–967
26. Tang Y, Li Y, Hu X et al (2018) "Dual lock-and-key"-controlled nanoprobes for ultrahigh specific fluorescence imaging in the second near-infrared window. Adv Mater 30:e1801140
27. Chen L, Chen D, Jiang Y et al (2019) A bodipy-based donor/donor-acceptor system: towards highly efficient long-wavelength-excitable near-ir polymer dots with narrow and strong absorption features. Angew Chem Int Ed Engl 58:7008–7012
28. Hong GS, Zou YP, Antaris AL et al (2014) Ultrafast fluorescence imaging in vivo with conjugated polymer fluorophores in the second near-infrared window. Nat Commun 5:4206
29. Miao QQ, Pu KY (2018) Organic semiconducting agents for deep-tissue molecular imaging: second near-infrared fluorescence, self-luminescence, and photoacoustics. Adv Mater 30: e1801778
30. Guo B, Feng Z, Hu D et al (2019) Precise deciphering of brain vasculatures and microscopic tumors with dual NIR-II fluorescence and photoacoustic imaging. Adv Mater 31:1902504
31. Qi J, Sun C, Li D et al (2018) Aggregation-induced emission luminogen with near-infrared-II excitation and near-infrared-i emission for ultradeep intravital two-photon microscopy. ACS Nano 12:7936–7945
32. Qi J, Sun C, Zebibula A et al (2018) Real-time and high-resolution bioimaging with bright aggregation-induced emission dots in short-wave infrared region. Adv Mater 30:e1706856
33. Fu W, Yan C, Guo Z et al (2019) Rational design of near-infrared aggregation-induced-emission-active probes: in situ mapping of amyloid-beta plaques with ultrasensitivity and high-fidelity. J Am Chem Soc 141:3171–3177
34. Kim S, Lim YT, Soltesz EG et al (2004) Near-infrared fluorescent type II quantum dots for sentinel lymph node mapping. Nat Biotechnol 22:93–97
35. Zheng YG, Gao SJ, Ying JY (2007) Synthesis and cell-imaging applications of glutathione-capped CdTe quantum dots. Adv Mater 19:376–380
36. Yukawa H, Watanabe M, Kaji N et al (2012) Monitoring transplanted adipose tissue-derived stem cells combined with heparin in the liver by fluorescence imaging using quantum dots. Biomaterials 33:2177–2186
37. Du YP, Xu B, Fu T et al (2010) Near-infrared photoluminescent Ag_2S quantum dots from a single source precursor. J Am Chem Soc 132:1470–1471

38. Zhang Y, Hong G, Zhang Y et al (2012) Ag_2S quantum dot: a bright and biocompatible fluorescent nanoprobe in the second near-infrared window. ACS Nano 6:3695–3702
39. Dong B, Li C, Chen G et al (2013) Facile synthesis of highly photoluminescent Ag_2Se quantum dots as a new fluorescent probe in the second near-infrared window for in vivo imaging. Chem Mater 25:2503–2509
40. Gu YP, Cui R, Zhang ZL et al (2012) Ultrasmall near-infrared Ag_2Se quantum dots with tunable fluorescence for in vivo imaging. J Am Chem Soc 134:79–82
41. Yang Y, Chen J, Shang X et al (2019) Visualizing the fate of intra-articular injected mesenchymal stem cells in vivo in the second near-infrared window for the effective treatment of supraspinatus tendon tears. Adv Sci 6:1901018
42. Chen J, Kong YF, Wang W et al (2016) Direct water-phase synthesis of lead sulfide quantum dots encapsulated by beta-lactoglobulin for in vivo second near infrared window imaging with reduced toxicity. Chem Commun 52:4025–4028
43. Ma ZR, Zhang MX, Yue JY et al (2018) Near-infrared IIb fluorescence imaging of vascular regeneration with dynamic tissue perfusion measurement and high spatial resolution. Adv Funct Mater 28:1803417
44. Goswami N, Giri A, Kar S et al (2012) Protein-directed synthesis of NIR-emitting, tunable hgs quantum dots and their applications in metal-ion sensing. Small 8:3175–3184
45. Xie RG, Peng XG (2009) Synthesis of Cu-doped InP nanocrystals (d-dots) with ZnSe diffusion barrier as efficient and color-tunable NIR emitters. J Am Chem Soc 131:10645–10651
46. Miyazaki Y, Yukawa H, Nishi H et al (2013) Adipose tissue-derived stem cell imaging using cadmium-free quantum dots. Cell Med 6:91–97
47. Park JH, Gu L, von Maltzahn G et al (2009) Biodegradable luminescent porous silicon nanoparticles for in vivo applications. Nat Mater 8:331–336
48. Ma QA, Su XG (2010) Near-infrared quantum dots: synthesis, functionalization and analytical applications. Analyst 135:1867–1877
49. Zhao P, Xu Q, Tao J et al (2018) Near infrared quantum dots in biomedical applications: current status and future perspective. Wiley Interdiscipl Rev Nanomed Nanobiotechnol 10:e1483
50. Naczynski DJ, Tan MC, Zevon M et al (2013) Rare-earth-doped biological composites as in vivo shortwave infrared reporters. Nat Commun 4:2199
51. Zhao L, Kutikov A, Shen J et al (2013) Stem cell labeling using polyethylenimine conjugated (alpha-naybf4:Tm^{3+})/CaF2 upconversion nanoparticles. Theranostics 3:249–257
52. Gao N, Ling B, Gao Z et al (2017) Near-infrared-emitting nayf4:Yb,tm/mn upconverting nanoparticle/gold nanorod electrochemiluminescence resonance energy transfer system for sensitive prostate-specific antigen detection. Anal Bioanal Chem 409:2675–2683
53. He SQ, Chen S, Li DF et al (2019) High affinity to skeleton rare earth doped nanoparticles for near-infrared ii imaging. Nano Lett 19:2985–2992
54. Wang SF, Liu L, Fan Y et al (2019) In vivo high-resolution ratiometric fluorescence imaging of inflammation using NIR-II nanoprobes with 1550 nm emission. Nano Lett 19:2418–2427
55. Hong GS, Lee JC, Robinson JT et al (2012) Multifunctional in vivo vascular imaging using near-infrared II fluorescence. Nat Med 18:1841–1846
56. Ceppi L, Bardhan NM, Na Y et al (2019) Real-time single-walled carbon nanotube-based fluorescence imaging improves survival after debulking surgery in an ovarian cancer model. ACS Nano 13:5356–5365
57. Welsher K, Liu Z, Sherlock SP et al (2009) A route to brightly fluorescent carbon nanotubes for near-infrared imaging in mice. Nat Nanotechnol 4:773–780
58. Yu MX, Zhou JC, Du BJ et al (2016) Noninvasive staging of kidney dysfunction enabled by renal-clearable luminescent gold nanoparticles. Angew Chem Int Ed Engl 55:2787–2791
59. Biffi S, Petrizza L, Garrovo C et al (2016) Multimodal near-infrared-emitting plus silica nanoparticles with fluorescent, photoacoustic, and photothermal capabilities. Int J Nanomedicine 11:4865–4874

60. Li C, Cao L, Zhang Y et al (2015) Preoperative detection and intraoperative visualization of brain tumors for more precise surgery: a new dual-modality MRI and nir nanoprobe. Small 11:4517–4525
61. Zhang XD, Wang HS, Antaris AL et al (2016) Traumatic brain injury imaging in the second near-infrared window with a molecular fluorophore. Adv Mater 28:6872–6879
62. Vahrmeijer AL, Hutteman M, van der Vorst JR et al (2013) Image-guided cancer surgery using near-infrared fluorescence. Nat Rev Clin Oncol 10:507–518
63. Hong G, Robinson JT, Zhang Y et al (2012) In vivo fluorescence imaging with Ag_2S quantum dots in the second near-infrared region. Angew Chem Int Ed Engl 51:9818–9821
64. Sun Y, Ding M, Zeng X et al (2017) Novel bright-emission small-molecule nir-ii fluorophores for in vivo tumor imaging and image-guided surgery. Chem Sci 8:3489–3493
65. Tang Y, Pei F, Lu X et al (2019) Recent advances on activatable NIR-II fluorescence probes for biomedical imaging. Adv Opt Mater 7:1900917
66. Li C, Li F, Zhang Y et al (2015) Real-time monitoring surface chemistry-dependent in vivo behaviors of protein nanocages via encapsulating an NIR-II Ag_2S quantum dot. ACS Nano 9:12255–12263
67. Song C, Zhang Y, Li C et al (2016) Enhanced nanodrug delivery to solid tumors based on a tumor vasculature-targeted strategy. Adv Funct Mater 26:4192–4200
68. Li C, Zhang Y, Chen G et al (2017) Engineered multifunctional nanomedicine for simultaneous stereotactic chemotherapy and inhibited osteolysis in an orthotopic model of bone metastasis. Adv Mater 29:1605754
69. Verbeek FPR, Schaafsma BE, Tummers QRJG et al (2014) Optimization of near-infrared fluorescence cholangiography for open and laparoscopic surgery. Surg Endosc 28:1076–1082
70. Wang P, Fan Y, Lu L et al (2018) NIR-II nanoprobes in-vivo assembly to improve image-guided surgery for metastatic ovarian cancer. Nat Commun 9:2898
71. Wen Q, Zhang Y, Li C et al (2019) NIR-II fluorescent self-assembled peptide nanochain for ultrasensitive detection of peritoneal metastasis. Angew Chem Int Ed Engl 58:11001–11006
72. Naumova AV, Modo M, Moore A et al (2014) Clinical imaging in regenerative medicine. Nat Biotechnol 32:804–1121
73. Chen G, Tian F, Li C et al (2015) In vivo real-time visualization of mesenchymal stem cells tropism for cutaneous regeneration using NIR-II fluorescence imaging. Biomaterials 53:265–273
74. Chen G, Lin S, Huang D et al (2018) Revealing the fate of transplanted stem cells in vivo with a novel optical imaging strategy. Small 14:1702679
75. Huang D, Lin S, Wang Q et al (2019) An NIR-II fluorescence/dual bioluminescence multiplexed imaging for in vivo visualizing the location, survival, and differentiation of transplanted stem cells. Adv Funct Mater 29:1806546
76. Chen GC, Tian F, Zhang Y et al (2014) Tracking of transplanted human mesenchymal stem cells in living mice using near-infrared Ag_2S quantum dots. Adv Funct Mater 24:2481–2488
77. Alam R, Karam LM, Doane TL et al (2014) Near infrared bioluminescence resonance energy transfer from firefly luciferase--quantum dot bionanoconjugates. Nanotechnology 25:495606
78. Ma N, Marshall AF, Rao JH (2010) Near-infrared light emitting luciferase via biomineralization. J Am Chem Soc 132:6884–6885
79. Xiong LQ, Shuhendler AJ, Rao JH (2012) Self-luminescing bret-fret near-infrared dots for in vivo lymph-node mapping and tumour imaging. Nat Commun 3:1193
80. Lee SK, Mortensen LJ, Lin CP et al (2014) An authentic imaging probe to track cell fate from beginning to end. Nat Commun 5:5216

81. Wang Z, Zhang RL, Wang ZL et al (2014) Bioinspired nanocomplex for spatiotemporal imaging of sequential mrna expression in differentiating neural stem cells. ACS Nano 8:12386–12396
82. Wiraja C, Yeo DC, Chong MSK et al (2016) Nanosensors for continuous and noninvasive monitoring of mesenchymal stem cell osteogenic differentiation. Small 12:1342–1350
83. Troyan SL, Kianzad V, Gibbs-Strauss SL et al (2009) The flare intraoperative near-infrared fluorescence imaging system: a first-in-human clinical trial in breast cancer sentinel lymph node mapping. Ann Surg Oncol 16:2943–2952
84. Mieog JS, Troyan SL, Hutteman M et al (2011) Toward optimization of imaging system and lymphatic tracer for near-infrared fluorescent sentinel lymph node mapping in breast cancer. Ann Surg Oncol 18:2483–2491

Whole Murine Brain Imaging Based on Optical Elastic Scattering

6

Jian Ren and Brett E. Bouma

Abbreviations

CAST	Clearing assisted scattering tomography
CT	Computed tomography
DOF	Depth of focus
EM	Electron microscopy
FDOCT	Fourier domain optical coherence tomography
FWHM	Full wave half maximum
LM	Light microscopy
MRI	Magnetic resonance imaging
OFDI	Optical frequency domain imaging
RI	Refractive index

J. Ren (✉)
Wellman Center for Photomedicine, Massachusetts General Hospital, Harvard Medical School, Boston, MA, USA
e-mail: jren@mgh.harvard.edu

B. E. Bouma
Wellman Center for Photomedicine, Massachusetts General Hospital, Harvard Medical School, Boston, MA, USA

Institute for Medical Engineering and Science, Massachusetts Institute of Technology, Cambridge, MA, USA

X. Wei, B. Gu (eds.), *Optical Imaging in Human Disease and Biological Research*, Advances in Experimental Medicine and Biology 1355,
https://doi.org/10.1007/978-981-15-7627-0_6

6.1 Introduction

Today, neuroscientists have accumulated a rich body of knowledge of how a single neuron or a group of a few neurons work. Yet, it has been increasingly evident that the interactions among heterogeneous types of cells spanning the entire nervous system hold the key to numerous unanswered questions at the foundation of neuroscience. For instance, the unsettling discrepancy between pathology and cognitive decline in neurodegeneration could be better studied with a global perspective as cognitive and affective processes rely on multiple sets of neurons across various brain regions forming an extremely intricate network [1, 2]. Therefore, to enable such large-scale studies and reveal new insights, there has been sustained effort to develop new imaging methods for whole mammalian brains, particularly for application to murine models [3].

6.1.1 Macroscale Methods

With a spatial resolution from 1 mm to 100μm, magnetic resonance imaging (MRI) predominates macroscale studies. Being able to measure living subjects, MRI has revolutionized neuroscience by supporting investigations on cognitive and affective processes in vivo. Specialized MRI techniques have also been developed to enhance its utility. While functional MRI can monitor activities across various brain regions via blood flow, diffusion-weighted MRI infers brain connectivity using water molecule diffusion. Moreover, contrast agents have also being created for added specificity. Yet, because of its current resolution of one-cubic-millimeter, MRI is unable to directly resolve neural cells and axonal fibers thus limiting the "ground-truth" level investigation [4]. For those MRI systems with higher resolution, such as 100μm, longer acquisition time and stronger magnetic field are required, making this technology mainly suitable for ex vivo studies due to motion artifacts and subject safety. Compared to today's "Gold standard"—immunochemistry, the coverage and the specificity of available contrast agents are also limited.

6.1.2 Microscale Method

Electron microscopy (EM) can resolve structures as small as 30 nm or below. This resolution is beyond the diffraction limit of conventional optical methods and discloses the finest details of neurons, such as individual synaptic connection [5]. But this microscale method is only practical for small sample volumes because extensive specimen preparation and ultra-thin sectioning are required [6]. The large-scale morphological data reconstruction to assemble 2D EM images into 3D volumes adds another level of complexity. Therefore, there are serious challenges for this labor-intensive and costly technology to be used for large-cohort studies on whole murine brains.

6.1.3 Mesoscale Method

Ranging from ~1 μm to a few hundred nanometers, light microscopy (LM) offers a mesoscale resolution. Bridging the above two scales, it can reveal both local and long-range neural connections [7]. Especially, when used with neural tracers, such as genetically encoded fluorescent proteins introduced via viral injection, specific types of cells can be identified and investigated. Moreover, with a wide selection of immunofluorescent markers available, LM can be used to perform extensive cellular phenotyping and has facilitated successful acquisition of various mesoscale connectomes of mouse brains [8–10]. However, this type of approaches is also subject to serial sample sectioning, followed by labeling (if not genetically encoded), imaging, and reconstruction from 2D images to 3D volumes, a similar workflow to EM. Slicing samples has been necessary for two reasons. First, for those studies that don't have genetically encoded markers, the tissue penetration of large molecular probes is limited. Tissue sections of $<$50μm are normally used for this reason. Second, the strong light scattering in brain tissues restricts the optical imaging depth to about 150μm for typical confocal microscopy and 500–800μm for two-photon microscopy. Although these slices can be thicker than those used in EM (typical around 80 nm), LM methods still face technical challenges when used for whole murine brain imaging, including avoiding sample damage and deformation caused by mechanical disruption, precise co-registration and alignment of multiple sample sections, and efficient volumetric image reconstruction.

6.2 Controlling Light Scattering in Tissue

To overcome the difficulties encountered by LM methods, tissue clearing techniques have been developed and applied to whole murine brains [11]. Originated early twentieth century [12], these methods make biological samples optically transparent by reducing their light scattering. The major source of the scattering is the refractive index (RI) mismatch between lipid-rich membranes (RI $\approx$ 1.5) and water (RI $\approx$ 1.33). Therefore, efforts have been made toward balancing this RI discrepancy and/or replacing lipid out of tissue. Currently, there are three major types of clearing methods [13, 14]: (1) Hydrophobic clearing [15–18]. This type of clearing consists two major steps. First, samples are fully dehydrated to displace the water inside. Next, they are incubated in organic solvents for delipdation and RI matching. The key features of these approaches include fast clearing, high optical transparence, and good sample preservation—due to dehydration. But some organic solvents used in these methods quench fluorescence very rapidly and they may be toxic as well. (2) Hydrophilic clearing [19–22]. These methods are also referred as hyperhydration because they employ mild detergents and aqueous-based reagents to carry out lipid removal and RI matching. These processes are associated with better compatibility (for instance, less fluorescence quenching) and improved biosafety (reagents are less toxic). Yet, compared to the hydrophobic methods, they usually require longer processing time to render large tissues transparent. (3) Hydrogel-

embedding clearing [23, 24]. This type of clearing infuses monomers into tissues, then reinforces them by a following polymerization procedure. The resulted tissue-gel hybrid can preserve the sample both structurally and biochemically so that thorough delipidation can be performed to achieve high optical transparence. While all three of these methods have their advantages and disadvantages, the hydrogel-embedding methods are of particular benefit for optical imaging based on elastic scattering because light scattering from different tissue components can be better controlled by managing both lipid removal and the formation of tissue-gel hybrid.

6.3 Coherent Detection of Photons Scattered from Large Volumes

While tissue clearing now transforms whole mouse brains into transparent samples and light is scattered from various anatomical structures deep inside the samples, the next challenge becomes reading out the massive biological information in large tissue volumes. Multiple microscopy approaches have been developed to detect backscattered photons from a 3D volume. Compared to conventional 2D microscopes, these instruments offer depth sectioning or even depth encoding capabilities. The major objective is to locate and quantify the source of the scattered photons. Based on how photons are detected, these microscopy approaches can be divided into two categories: coherent and incoherent methods. Incoherent methods include confocal reflectance microscopy [25], reflectance light-sheet microscopy, structure illumination microscopy [26], and optical projection tomography [27]. To locate scattering signal, confocal and light-sheet based methods generate and scan a confined illumination and detection volume across samples. Regardless how these methods map the location of scatters, the scattered photons are detected by direct photon-counting.

In contrast, coherent methods, such as Fourier domain optical coherence tomography (FDOCT) and optical frequency domain imaging (OFDI), come with two unique features. First, due to their sensitive detection, these methods generally offer much higher throughput than incoherent methods. Scattered light is detected by interfering it with reference light. The interference signal detected by the same photon-counting mechanism as in incoherent detection is expressed below:

$$P_{\mathrm{d}} = [P_{\mathrm{s}} + P_{\mathrm{r}}] + \widehat{S}(\Delta x)[2\sqrt{P_{\mathrm{s}}P_{\mathrm{r}}}\cos(2\Delta x k_0)] \tag{6.1}$$

where P_{d} is the optical power received at the detector; P_{s} is the power of scattered photons received at the sample arm of the interferometer; P_{r} is the optical power received at the reference arm; $\hat{S}$ is the coherence envelop function of the light source; and k_0 is the center wavenumber of the source. The cross-correlation term of this equation clearly shows that the signal of scattered photons gets amplified by the reference light, which serves as a local oscillator. This coherent amplification is critical for detecting weak signals and results in a typical sensitivity of over 110 dB

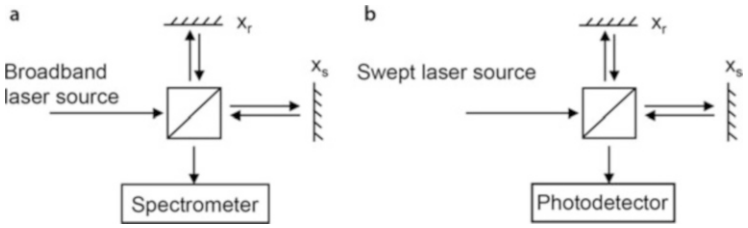

Fig. 6.1 The schematics of FDOCT and OFDI. (**a**) FDOCT. (**b**) OFDI (swept-source OCT)

for current OCT/OFDI systems [28–30]. This enormous sensitivity advantage of FDOCT/OFDI is directly translated to its throughput advantage over incoherent methods. Second, OCT and OFDI have their intrinsic depth encoding capability. From Eq. (6.1), one can see that the interference signal is also a function of the path length difference Δx, which indicates that the location information of the source of the scattered photons is now encoded onto the frequency of detected FDOCT/OFDI fringe signals. This tomographic mechanism is particularly beneficial for imaging volumetric samples, like whole mouse brains. Rather than rejecting the photons scattered from out-of-focus regions as confocal or light-sheet methods, coherent methods accept scattered photons from all regions and sort them out based on their location, leading to a higher imaging efficiency.

There are two major arguments calling the imaging throughput demand into questions. First, as samples are fixed before imaging, there appears no real constraints on the readout time. This is indeed true if the region of interest is 2D or a microscopic volume and the size of the cohort is small (a few brains). However, for whole brain studies on large groups of subjects, the imaging time can quickly mount up to an impractical duration of several months or even years. Next, the clearing process usually takes a few days to a week, which has already outrun the typical acquisition time for one whole mouse brain. This seems to suggest that the bottleneck of the overall throughput lies in tissue processing. Yet, tissue clearing can be performed in batches where a large number of brains can be processed in parallel, resulting in virtually unlimited sample yield. However, the imaging readout of these samples has to be conducted in serial, which in fact determines the overall throughput. Therefore, improving imaging throughput has a pivotal impact on today's neuroscience by enabling large-scale investigations that are simply impractical or impossible for conventional technologies.

To further illustrate coherent methods, an FDOCT and an OFDI imaging system are depicted in Fig. 6.1. It is not the intention of this chapter to elaborate on the operation principle of such systems. Instead, the major consideration when designing these systems for whole murine brain imaging is discussed there. First, the safety limit of the laser power is significantly relaxed for cleared tissues. This is owing to the lessened thermal effect resulting from the reduced light–tissue interaction. It is beneficial as higher power yields higher throughput in general. Second, because imaging through a cleared whole mouse brain is now achieved, the deeper penetration of longer wavelengths would not weight as heavily as for imaging uncleared

tissue. Instead, based on Gaussian beam propagation, shorter wavelength will improve the lateral resolution with the same depth of focus. This improvement is at a rate of square root of wavelength, as expressed by $w_0 = \sqrt{\frac{\lambda z_0}{\pi}}$, where w_0 is the beam waist (defines the lateral resolution); λ is the wavelength; and z_0 is the half of Rayleigh-range (related to the depth of focus). The axial resolution of these systems is usually determined by the center wavelength and the spectrum width. For a Gaussian-shape spectrum, the full-wave-half-maximum (FWHM) of the axial point spread function (PSF) Δz_{FWHM} scales with the inverse of the spectrum FWHM $1/\Delta\lambda_{\mathrm{FWHM}}$ and the square of the central wavelength λ_{c}^2, as expressed by

$$\Delta z_{\mathrm{FWHM}} = \frac{2\ln(2)\lambda_{\mathrm{c}}^2}{\pi\Delta\lambda_{\mathrm{FWHM}}} \tag{6.2}$$

From Eq. (6.2), one can appreciate that reducing the center wavelength increases the axial resolution in a quadratic manner. In fact, most commercial OCT systems centered at shorter wavelengths such as 850 nm have better overall resolution than the commercial systems at longer wavelengths, such as 1310 nm. Third, in order to image a whole mouse brain, the minimal imaging window width is about 10–12 mm. The imaging window or ranging depth of FDOCT/OFDI systems is largely determined by the coherent falloff. For swept-source based OCT/OFDI systems, this falloff is related to the instantaneous linewidth of the laser. Current wavelength-swept laser sources can offer an imaging window over several tens of centimeters [31]. By shifting the fringe frequency, the ranging depth of these systems can also be doubled, which provides plenty room for whole mouse brain imaging [32].

It is worth noting that all existing OFDI/OCT imaging on uncleared brain tissues are limited to 1–2 mm by scattering. Although deeper than confocal (tens of micron) [33] and two-photon microscopy (hundreds of micron) [34], this limitation prevents all these OFDI/OCT studies [35–37] from imaging through a whole intact mouse brain.

6.4 Clearing Assisted Scattering Tomography

Based on the previous discussions, it is well-reasoned that coherent tomography combined with optimized scattering through controlling tissue clearing could have some unique benefits for imaging whole mouse brains. First, the scattering contrast among various tissue types is intrinsic, i.e., no labeling needed. While immunostaining and reporter genes that most LM methods rely on do offer high molecular and cellular specificity, they all require substantial sample preparation. Immunolabeling offers a broad spectrum of biomarkers, however, staining large volumes of tissues uniformly has been very challenging owing to limited penetration of molecular probes [38]. As these macromolecules have to pass enormous molecular barriers, including protein cross-link and lipid bilayers, passive diffusion has

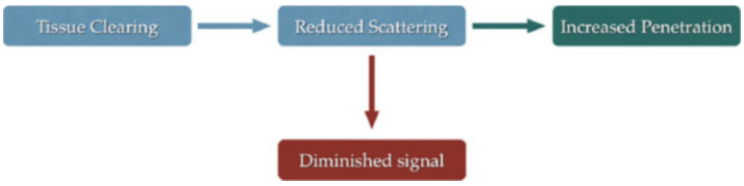

Fig. 6.2 The "paradox" of optimal clearing in scattering-based optical imaging

been shown to be extremely slow, i.e., multiple months for adult whole mouse brains [39]. While electrophoresis-based methods have been developed to accelerate this process [40], homogeneously labeled and fully cleared whole mouse brains are not yet easily accessible to neuroscience community. Genetic labeling is not limited by this macromolecule diffusion but constrained to transgenic models or viral vectors available. Second, the scattering contrast is stable. Immune to the photobleaching effect of fluorescence imaging, elastic scattering is a robust contrast mechanism for the prolonged exposure in large-scale imaging. More importantly, the unbleachable contrast is ideal for quantitative investigation of large tissue volumes.

Based on the above idea, a new imaging methodology was introduced, termed as Clearing Assisted Scattering Tomography (CAST) [41]. Instead of detecting the incoherent photons emitted from fluorophores, CAST employs coherent tomography such as OCT/OFDI to detect photons elastically scattered back from cleared tissues. Extending optical imaging depth by optimizing scattering through the clearing procedure, CAST enables high throughput imaging on whole mouse brains without the need for sectioning and labeling—significant advantages for large-scale investigation.

Although tissue clearing extends light penetration, it inevitably decreases OCT/OFDI signals because of the reduction of scattering. As illustrated in Fig. 6.2, the challenge now lies in whether there exists an optimal level of clearing so that CAST can image through whole mouse brains while maintaining sufficient contrast. By adjusting the degree of lipid removal in hydrogel-embedding clearing methods, it has been shown that this optimal balance can be achieved [41]. Figure 6.3a–d displays the OFDI cross-sections of a mouse brain with the optical focus at different depths. Figure 6.3e–h shows the cross-sections of the same sample after a controlled clearing based on SWITCH protocol [39], with the foci at the same locations as in Fig. 6.3a–d. When placing the focus deeper into the tissue, various anatomical structures at different depths emerged in the images of the sample after clearing. In comparison, only the shallow cortical region can be visualized in the images of the sample before clearing, regardless of the location of the focus. This result demonstrates that a sufficient number of scattered photons can be collected from various structures across the entire brain to form the CAST tomogram while many photons can penetrate through the entire brain.

To study what physiological structures in the cleared samples give rise to the scattering signal, immunostaining was performed on brain samples that had been previously imaged by CAST. As shown in Fig. 6.4, the OFDI images of a 1 mm

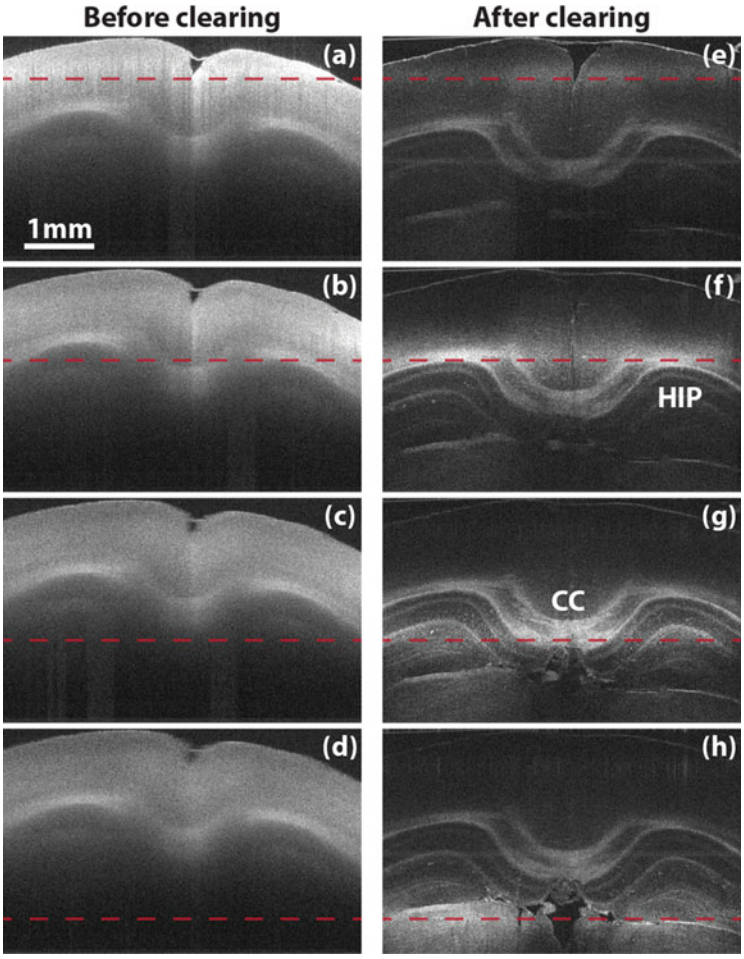

Fig. 6.3 Imaging penetration enhancement. (**a**–**d**) The coronal images of a fixed mouse brain while moving the optical focus deep by a step of 707μm. (**e**–**h**) The coronal images of the same section after clearing with the same location of focal plane, indicated by the dashed lines. All images share the same scale bar in (**a**). *CC* corpus callosum, *HIP* hippocampus. (From Ren et al. [41])

thick mouse brain coronal section before and after a controlled clearing process are compared. The scattering signals of different parts changed dramatically during the clearing. After CAST imaging, the same tissue was labeled with lectin (Fig. 6.4c) and SMI-312 (Fig. 6.4d) and imaged by a confocal fluorescence microscope. The blood vessels (lectin) and the neuronal fibers (SMI-312) highlighted in the fluorescence images correlate well to the structures with positive contrast in CAST images. With light scattering from most tissue components suppressed, the contrast of neuronal fiber bundles and blood vessels is generally enhanced across the entire

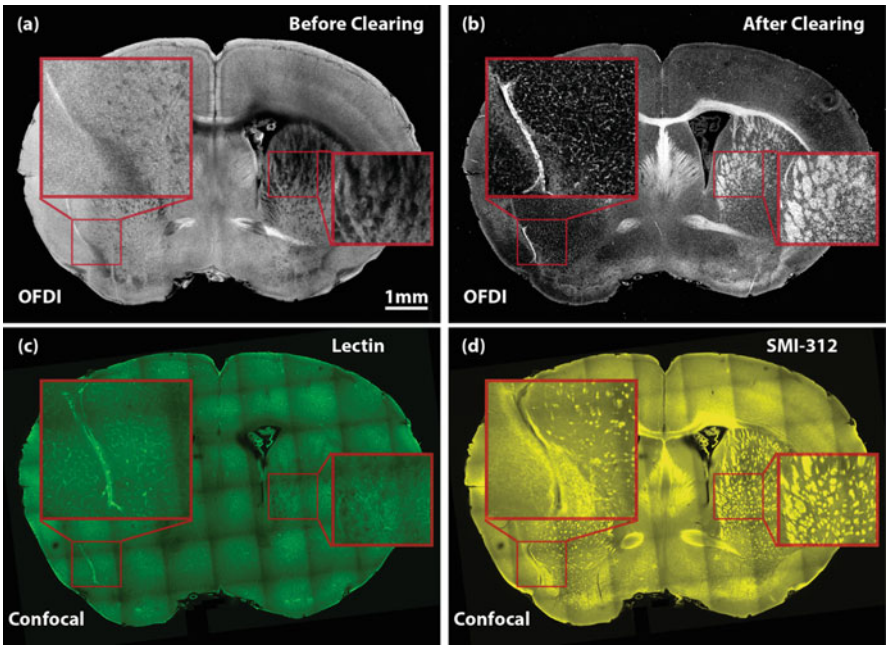

Fig. 6.4 Contrast validation. (**a**) The OFDI image of a mouse brain coronal section before clearing. (**b**) The OFDI image of the same section in (**a**) after clearing. (**c**) The confocal image of the same section stained by lectin. (**d**) The confocal image of the same section stained by SMI-312. All images share the same scale bar in (**a**). (From Ren et al. [41])

section, suggesting that CAST, through controlled tissue clearing, can selectively highlight some specific anatomical structures of mouse brains.

Upon the validation of its contrast, the volumetric and deep imaging capability of CAST was examined. Figure 6.5 displays the results of a 1 mm thick mouse brain coronal section, where various regions with high content of white matter tracts are clearly visualized, such as corpus callosum (CC) (Figs. 6.5d and 6.6c), caudoputamen (CP) (Figs. 6.5b, and 6.6c), thalamus (TH) (Fig. 6.5e), and globus pallidus (GP) (Fig. 6.5c). One of the most important cross-region brain connections is the thalamocortical radiations. This connection can be well appreciated in Fig. 6.5, where the fibers connecting between the thalamus and the cerebral cortex emerge from the thalamic basal ganglion, extend via the internal capsule (IC) into CP, and eventually project to the cortical layers. In addition, parts of the vascular network of the cortex were highlighted simultaneously. Some important grey matters were also captured, such as the layered structure of the hippocampus (HIP) (Fig. 6.6b), which is disclosed with some prominent vessels inside.

Figure 6.6 summarizes the results acquired from a right mouse brain hemisphere. A three-dimensional rendering of the hemisphere is shown in Fig. 6.6e. To validate the 3D structures observed by CAST, the sample was stained with lipophilic dye DiD to highlight the residual lipid and reveal the basic structure. After staining, the

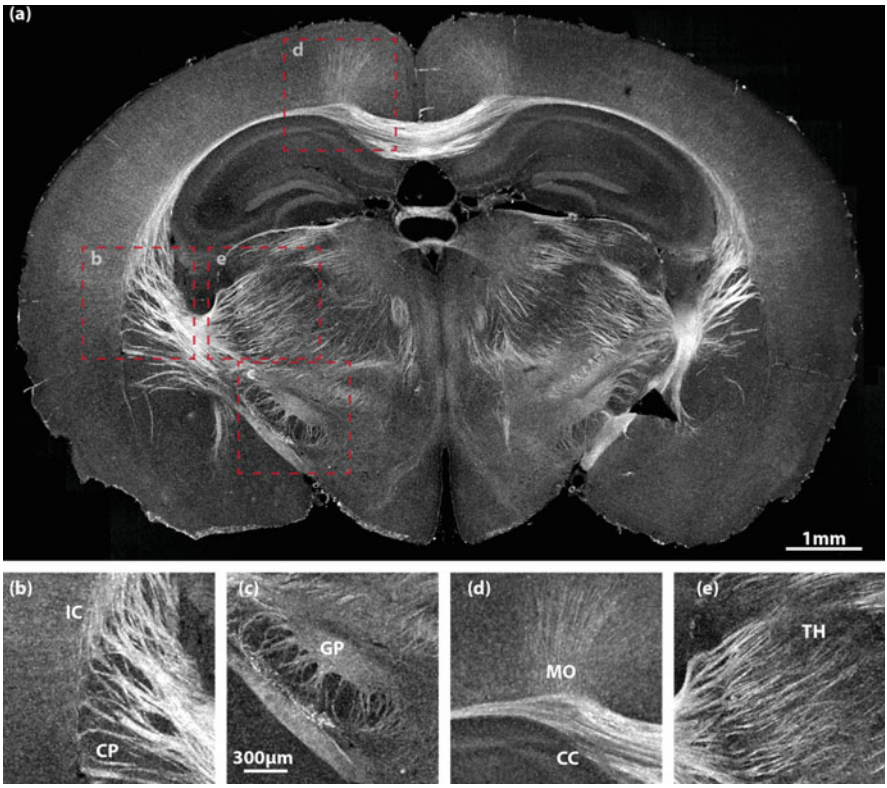

Fig. 6.5 CAST imaging of a 1 mm thick mouse brain section. (**a**) A coronal view of the section. (**b**–**e**) Magnified images of the boxed areas in (**a**). (**b**) Caudoputamen (CP) and internal capsule (IC); (**c**) Globus pallidus (GP); (**d**) Corpus callosum (CC) and cortical motor area (MO); (**e**) Thalamus (TH). (**b**–**e**) share the same scale bar in (**c**). (From Ren et al. [41])

sample was subsequently scanned by a light-sheet microscope. Displayed in Fig. 6.6f, the structures imaged by both methods agree well with each other. Figures 6.5 and 6.6 indicate that CAST enables deep imaging into whole mouse brains without exogenous contrast reporters and it is possible to use CAST to map both long-range connections and local projections at the mesoscale.

6.5 3D Image Stack Formation and Practical Considerations

Each CAST axial scan can retrieve sample information within certain depth range. This range is currently limited by the finite depth of focus (DOF), which is related to the lateral resolution of the system. For a typical mesoscale lateral resolution of 10μm, a reasonably useable section of the axial scan is about 200–300μm. Therefore, a large-field *en face* scan (about 10 mm by 10 mm along X and Y axes) covering a whole mouse brain in axial direction will essentially generate a very thin slab-shape

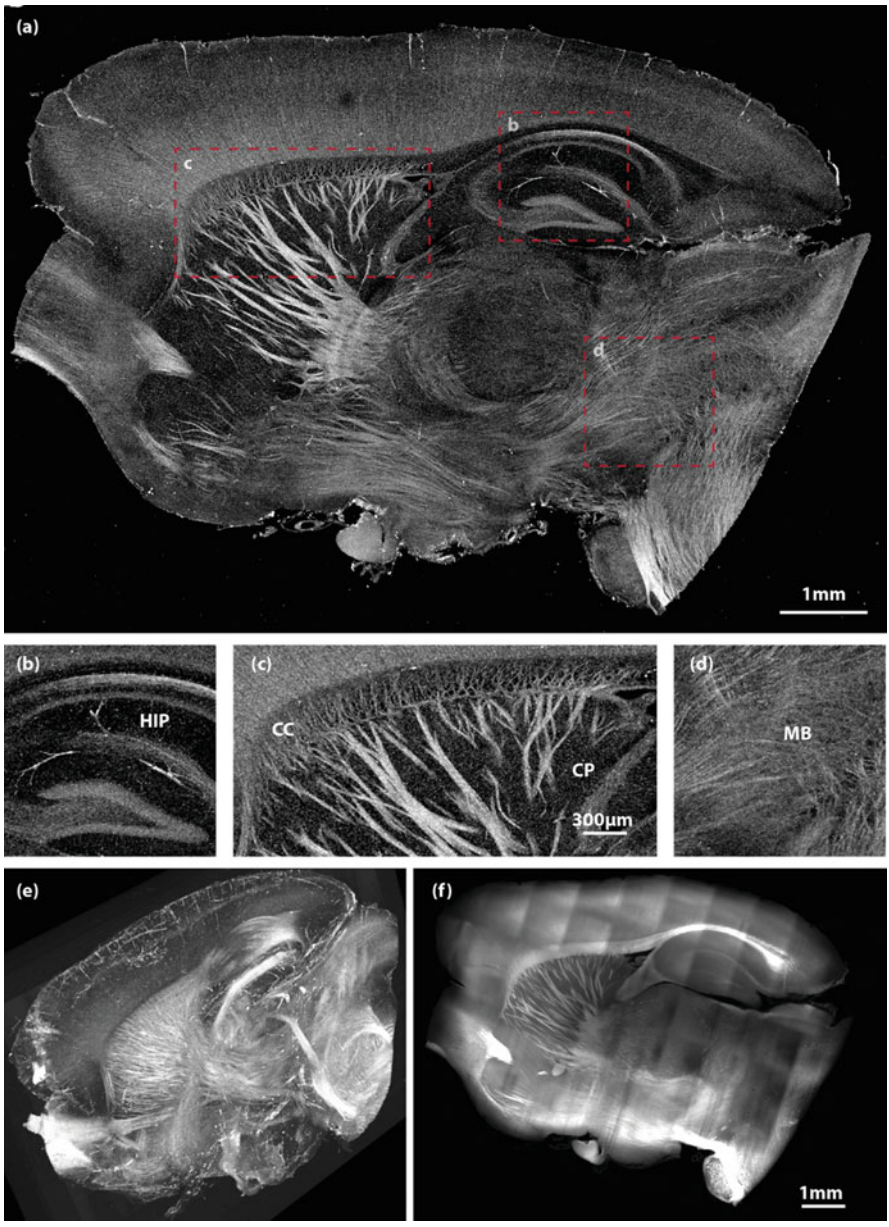

Fig. 6.6 CAST imaging of an intact mouse brain hemisphere. (**a**) A sagittal view of the hemisphere. (**b–d**) Magnified images of the boxed areas in (**a**). (**b**) Hippocampus (HIP); (**c**) Corpus callosum (CC) and caudoputamen (CP); (**d**) Midbrain (MB). (**e**) A three-dimensional rendering of the CAST volumetric image stack. (**f**) The corresponding sagittal image from a light-sheet microscope on the same hemisphere stained by DiD. (**b–d**) share the same scale bar in (**c**). (From Ren et al. [41])

in-focus image stack. To obtain datasets for a whole murine brain as large as $14 \times 14 \times 10$ mm^3 ($X \times Y \times Z$), special techniques beyond simple raster scans need to be developed.

One straightforward solution is to repeat 2D *en face* scans at different depths along Z to cover the entire brain sample, then stack these thin slab-shape datasets into one complete 3D image volume. Previous woks have successfully applied this idea to smaller optical coherence microscopy datasets [42]. However, there are some new and serious challenges when using this method to automatically process large CAST datasets. First, the hardware of the scanning system needs to provide user-controllable and precise axial displacement for the depth stepping. Common 2D optical raster scan apparatus can be used for the *en face* X and Y axes, such as galvanometer mirrors, polygon mirrors, and microelectromechanical systems mirrors. Current high-precision motorized stages are good candidates for Z stepping, with a typical accuracy ($<1\mu$m) and a bi-directional repeatability ($<0.1\mu$m) well below the targeted mesoscale resolution of a few microns. In addition, the automation and synchronization among all scan axes are essential for the acquisition throughput and quality of the datasets, which demands deliberate electro-mechanical engineering and thorough testing.

Second, the alignment of those datasets at different depths is critical for the success of the image fusion. The main goal of this alignment process is to co-register the axial scans in the *en face* plane, i.e., identify the axial scans in datasets at different depths but crossing the same location in XY plane. There are two common factors affecting this alignment: (1) the repeatability of the *en face* scanning and (2) the physical alignment between Z axis and the probing beam. Among them, the latter one is less detrimental as it causes a deterministic deformation of the image stack, which can be corrected during the image fusion process. Depending on the type of the 2D scanner, the former one can stem from various mechanisms, including the timing jitter of the synchronization among axes and acquisition, the mechanical jitter of scanning mirrors, and the repeatability of the motion if a motorized translation stage is used as the slow axis for the raster scan. This issue is often more problematic and difficult to compensate due to its random nature. One of the possible solutions would be to manually examine each dataset and use some distinct sample features as landmarks to align them. With extra computational efforts, this feature-tracking and alignment can be semi-automated or even fully automated using existing computer vision approaches, but the large size of 3D CAST datasets will require additional consideration and validation. After the XY co-registration is completed, the next step is to align the axial scans along Z direction. This alignment can be performed with the reflection signal from a calibration target that stays still relatively to the sample, such as the cover class, as a landmark to correlate the Z displacements among co-registered axial scans crossing the same *en face* location.

Third, upon obtaining volumetrically aligned axial scans, one needs to segment the in-focus range of each scan. These ranges are arrayed along Z direction covering the entire sample. Ideally, these ranges should have the same length and be centered at the same height for every axial scan within one depth-stepping dataset. However,

the focal plane of the raster scan might not be flat due to the finite field curvature. This effect is particularly evident when trying to maximize the scan field for large samples and the slab-shape in-focus area will deform to a dome area. Using two mechanical stages to translate the probing beam for the raster scan can solve this problem as the beam becomes stationary and maintains the same focal location relative to the optics. But this strategy usually dramatically slows down the acquisition process because the translating speed of mechanical stages is often far lower than the beam steering speed of scanning mirrors. Therefore, a reasonable compromise is to use high-speed scanning mirrors for the fast axis, such as *X*, and employ a translation stage for the slow axis, such as *Y*. This will result in a 1D-only deformation. Rather than a dome, the slab-shape area will now deform to a cylindrical shell. After scanner calibration, simple algorithms can be applied to compensate these systematic distortions during segmentation process. Although the clearing process has drastically reduced the aberration caused by the tissues between the optics and the focal plane, the optical heterogeneity of cleared tissues across the large scan field will still cause some sample-dependent transformation of in-focus ranges, including not only the shift of the focus but also the change of the range length. While manual segmentation can indeed cope with this problem, it becomes less practical for large CAST datasets. One automatic solution would be to employ a sharpness metric to quantify how well a local neighborhood is in-focus. After computing the axial profile of this metric for every aligned scan at the same *XY* location, computational algorithms can be developed to compare the metric profiles of the scans at adjacent depths. The axial location where the sharpness of the current scan drops to be equal to that of the next scan marks the end of the current in-focus range and the start of the next one, which is part of the adjacent depth-stepping axial scan.

Lastly, the segmented in-focus ranges of each axial scan at same *en face* location can be fused into one complete axial scan where the entire depth of the sample is in reasonably good focus. Practical consideration in this step is how to mitigate the stitching artifact caused by the system sensitivity drift among multiple *en face* scans. One technique is to estimate the system sensitivity globally, i.e., the entire dataset at one depth. Image intensity normalization based on this sensitivity estimation will balance out the brightness variance among the fused in-focus ranges and largely suppress the stitching artifact, although the difference of the signal to noise ratio cannot be compensated. Moreover, image blending methods can be applied to further smooth the transition from one range to the next and thus improve visual perception and subsequent image analysis.

6.6 Limitation and Future Directions

As demonstrated earlier in this chapter, CAST dramatically simplifies the conventional histopathology workflow when used in a label-free manner. While the scattering of axonal bundles can now be selectively highlighted in CAST, the number of tissue types that can be reliably differentiated is currently limited and the overall specificity needs significant improvement. A potential strategy that can still keep the

simplicity of label-free CAST is to leverage multiple measurements of light scattering during tissue clearing process. The basic hypothesis here is that the scattering of different tissue types decreases at different rates during clearing process. By recording how the scattering of various tissue types change through the clearing process, one can potentially build a library of scattering temporal decrease profiles. With these "tissue signatures," different tissue types might be identified. A potential difficulty of this strategy is that the profiles of various tissue types might be too similar to be reliably distinguished from each other. To this end, joint optimizing both the fixation/gelling and the clearing process might help maximize the difference among those "tissue signatures."

While coherent detection is more sensitive than normal photon-counting measurements, the current throughput of optical readout is still below optimal. Owing to the long coherence length of newly developed swept laser sources, the imaging window (or ranging depth) of today's coherent tomographic systems can extend as long as tens of centimeters and beyond. Systems with over 10 mm imaging window are now commercially available. These instruments are ideal for imaging cleared murine brains as the shortest dimension (axial direction) of a mouse brain is about 10 mm. This suggests that it is possible to image a whole mouse brain in a single volumetric acquisition through one raster scan across the transverse plane without any imaging stitching. However, as described previously, DOFs limited by the optics used in conventional microscopy are usually on the order of tens of microns at their maximum depending on the resolution. Much shorter than both the optical penetration depth offered by current clearing techniques and the coherent ranging depth of those available wavelength-swept lasers, DOF now becomes the major bottleneck of imaging throughput. This limitation appears very evident when we take a closer look at the cross-sectional CAST images in Fig. 6.3. Even with only 6 mm of ranging depth, the majority of the images were either out of focus or simply did not have signals—roughly only 90 out of 1024 pixels in each axial scan can be considered to have reasonable imaging fidelity. This marks a significant waste of measurements. While computational algorithms can work well enough to fuse multiple volumes at focal depth into a high-quality 3D dataset as described in the previous section, the ever-increasing acquisition reduces the effective readout throughput. To address these problems, future efforts in optical engineering is essential. First, a method to effectively confine photons along the entire ranging depth is needed to solve the low or no signal issues. A potential candidate would be beam engineering, where "non-diffracting" beams can be used to physically extend DOF. Next, the out-of-focus problem and/or the side lope pollution of the "non-diffracting" beams might be mitigated by numerical refocusing approaches.

Another important aspect of this method is the large amount of data acquired. Compared to EM methods, the lower resolution of this mesoscale approach will yield smaller datasets for a specific brain sample. However, the goal of CAST is to streamline large-cohort investigations of brain samples, where the amount of data increases proportional to the number of subjects. Data integration and correlation across multiple samples will further complicate data processing and management. While there have been many on-going efforts to develop computational methods for

other imaging modalities, both the unique physics and the application of this scattering-based coherent imaging procedure demand new developments for scalable and sustainable data processing. Current challenges include how to efficiently carry out large-scale image processing specific to coherent imaging, such as tomographic reconstruction, speckle reduction; how to analyze, abstract, and visualize the big data to address existing biological questions or even inspire new ones, such as tensor conversion for optical tractography [43], graph model based on "ground-truth" [44]. The rapid-growing performance of new hardware (such as graphic processing units) combined with the emerging deep learning techniques is expected to give a solid push to the large-scale data handling for CAST.

6.7 Conclusions

Investigating a fully assembled biological system, such as intact murine brains, holds the key to many unanswered biomedical questions. Recent advances in tissue clearing enabled optical access into these complex systems, so that light-based approaches can now play a vital role in bridging the macroscale studies, such as MRI and CT, and the microscale investigations, such as EM. While successful for numerous existing studies, traditional fluorescence-based methods have two fundamental limitations when facing large volumes of tissue samples, namely limited readout throughput due to finite fluorescence yield and unstable contrast due to photobleaching effect. Overcoming these constraints, elastic scattering is promised to be an alternative imaging mechanism for intact murine brains. Leveraging controlled tissue processing and coherent detection, current results have demonstrated the potential of this new type of method, with improved throughput and long-lasting contrast. Multidisciplinary efforts are required to fully harness the power of this new approach, including new biochemistry techniques to improve the tissue specificity of scattering, novel optical engineering to maximize image throughput, and customized computational methods to extract the hidden yet vital biological information.

References

1. Swanson LW (2012) Brain architecture: understanding the basic plan. Oxford University Press, Oxford
2. Sporns O, Tononi G, Kötter R (2005) The human connectome: a structural description of the human brain. PLoS Comput Biol 1(4):e42
3. Bohland JW et al (2009) A proposal for a coordinated effort for the determination of brainwide neuroanatomical connectivity in model organisms at a mesoscopic scale. PLoS Comput Biol 5 (3):e1000334
4. Craddock RC et al (2013) Imaging human connectomes at the macroscale. Nat Methods 10 (6):524–539
5. White JG, Southgate E, Thomson JN, Brenner S (1986) The structure of the nervous system of the nematode Caenorhabditis elegans. Phil Trans R Soc B Biol Sci 314(1165):1–340
6. Helmstaedter M (2013) Cellular-resolution connectomics: challenges of dense neural circuit reconstruction. Nat Methods 10(6):501–507

7. Osten P, Margrie TW (2013) Mapping brain circuitry with a light microscope. Nat Methods 10 (6):515–523
8. Li A et al (2010) Micro-optical sectioning tomography to obtain a high-resolution atlas of the mouse brain. Science 330(6009):1404–1408
9. Ragan T et al (2012) Serial two-photon tomography for automated ex vivo mouse brain imaging. Nat Methods 9(3):255–258
10. Oh SW et al (2014) A mesoscale connectome of the mouse brain. Nature 508(7495):207–214
11. Chung K, Deisseroth K (2013) CLARITY for mapping the nervous system. Nat Methods 10 (6):508–513
12. Spalteholz W et al (1914) Uber das Durchsichtigmachen von menschlichen und tierischen Praparaten und seine theoretischen Bedingungen, nebst Anhang. S. Hirzel, Leipzig
13. Richardson DSS, Lichtman JWW (2015) Clarifying tissue clearing. Cell 162(2):246–257
14. Ueda HR et al (2020) Tissue clearing and its applications in neuroscience. Nat Rev Neurosci 21:61
15. Dodt H-U et al (2007) Ultramicroscopy: three-dimensional visualization of neuronal networks in the whole mouse brain. Nat Methods 4(4):331–336
16. Ertürk A et al (2012) Three-dimensional imaging of solvent-cleared organs using 3DISCO. Nat Protoc 7(11):1983–1995
17. Renier N, Wu Z, Simon DJ, Yang J, Ariel P, Tessier-Lavigne M (2014) iDISCO: a simple, rapid method to immunolabel large tissue samples for volume imaging. Cell 159(4):896–910
18. Pan C et al (2016) Shrinkage-mediated imaging of entire organs and organisms using uDISCO. Nat Methods 13(10):859–867
19. Ke M-T, Fujimoto S, Imai T (2013) SeeDB: a simple and morphology-preserving optical clearing agent for neuronal circuit reconstruction. Nat Neurosci 16(8):1154–1161
20. Kuwajima T, Sitko AA, Bhansali P, Jurgens C, Guido W, Mason C (2013) ClearT: a detergent- and solvent-free clearing method for neuronal and non-neuronal tissue. Development 140 (6):1364–1368
21. Hama H et al (2011) Scale: a chemical approach for fluorescence imaging and reconstruction of transparent mouse brain. Nat Neurosci 14(11):1481–1488
22. Susaki EA et al (2014) Whole-brain imaging with single-cell resolution using chemical cocktails and computational analysis. Cell 157(3):726–739
23. Chung K et al (2013) Structural and molecular interrogation of intact biological systems. Nature 497(7449):332–337
24. Yang B et al (2014) Single-cell phenotyping within transparent intact tissue through whole-body clearing. Cell 158(4):945–958
25. Schain AJ, Hill RA, Grutzendler J (2014) Label-free in vivo imaging of myelinated axons in health and disease with spectral confocal reflectance microscopy. Nat Med 20(4):443–449
26. Neil MAA, Juškaitis R, Wilson T (1997) Method of obtaining optical sectioning by using structured light in a conventional microscope. Opt Lett 22(24):1905
27. Sharpe J et al (2002) Optical projection tomography as a tool for 3D microscopy and gene expression studies. Science 296(5567):541–545
28. Leitgeb R, Hitzenberger C, Fercher A (2003) Performance of fourier domain vs time domain optical coherence tomography. Opt Express 11(8):889
29. de Boer JF, Cense B, Park BH, Pierce MC, Tearney GJ, Bouma BE (2003) Improved signal-to-noise ratio in spectral-domain compared with time-domain optical coherence tomography. Opt Lett 28(21):2067
30. Choma M, Sarunic M, Yang C, Izatt J (2003) Sensitivity advantage of swept source and Fourier domain optical coherence tomography. Opt Express 11(18):2183
31. Jayaraman V et al (2011) OCT imaging up to 760 kHz axial scan rate using single-mode 1310nm MEMS-tunable VCSELs with >100nm tuning range. In: Quantum Electronics and Laser Science Conference, p PDPB2
32. Yun SH, Tearney GJ, de Boer JF, Bouma BE (2004) Removing the depth-degeneracy in optical frequency domain imaging with frequency shifting. Opt Express 12(20):4822

33. Conchello J-A, Lichtman JW (2005) Optical sectioning microscopy. Nat Methods 2 (12):920–931
34. Helmchen F, Denk W (2005) Deep tissue two-photon microscopy. Nat Methods 2(12):932–940
35. Ben Arous J (2011) Single myelin fiber imaging in living rodents without labeling by deep optical coherence microscopy. J Biomed Opt 16(11):116012
36. Magnain C et al (2014) Blockface histology with optical coherence tomography: a comparison with Nissl staining. NeuroImage 84:524–533
37. Wang H, Zhu J, Akkin T (2014) Serial optical coherence scanner for large-scale brain imaging at microscopic resolution. NeuroImage 84:1007–1017
38. Gleave JA, Lerch JP, Henkelman RM, Nieman BJ (2013) A method for 3D immunostaining and optical imaging of the mouse brain demonstrated in neural progenitor cells. PLoS One 8:e72039
39. Murray E et al (2015) Simple, scalable proteomic imaging for high-dimensional profiling of intact systems. Cell 163(6):1500–1514
40. Kim S-Y et al (2015) Stochastic electrotransport selectively enhances the transport of highly electromobile molecules. Proc Natl Acad Sci U S A 112(46):E6274–E6283
41. Ren J, Choi H, Chung K, Bouma BE (2017) Label-free volumetric optical imaging of intact murine brains. Sci Rep 7:46306
42. Rolland JP, Meemon P, Murali S, Thompson KP, Lee K (2010) Gabor-based fusion technique for optical coherence microscopy. Opt Express 18(4):3632
43. Wang H, Lenglet C, Akkin T (2015) Structure tensor analysis of serial optical coherence scanner images for mapping fiber orientations and tractography in the brain. J Biomed Opt 20 (3):036003
44. Bullmore E, Sporns O (2009) Complex brain networks: graph theoretical analysis of structural and functional systems. Nat Rev Neurosci 10(4):312–312

Label-Free Multimodal Multiphoton Intravital Imaging

7

Jaena Park, Haohua Tu, Marina Marjanovic, and Stephen A. Boppart

7.1 Introduction

Intravital microscopy (IVM) is an imaging technique for visualizing microstructural features and molecular and functional dynamics in a live animal. IVM visualizes the more natural, unperturbed biological state, and provides a more comprehensive picture of physiological processes compared to cell and tissue-culture models.

J. Park
Biophotonics Imaging Laboratory, University of Illinois at Urbana-Champaign, Urbana-Champaign, IL, USA

Beckman Institute for Advanced Science and Technology, University of Illinois at Urbana-Champaign, Urbana-Champaign, IL, USA

Department of Bioengineering, University of Illinois at Urbana-Champaign, Urbana-Champaign, IL, USA

H. Tu
Biophotonics Imaging Laboratory, University of Illinois at Urbana-Champaign, Urbana-Champaign, IL, USA

Beckman Institute for Advanced Science and Technology, University of Illinois at Urbana-Champaign, Urbana-Champaign, IL, USA

M. Marjanovic
Biophotonics Imaging Laboratory, University of Illinois at Urbana-Champaign, Urbana-Champaign, IL, USA

Beckman Institute for Advanced Science and Technology, University of Illinois at Urbana-Champaign, Urbana-Champaign, IL, USA

Department of Bioengineering, University of Illinois at Urbana-Champaign, Urbana-Champaign, IL, USA

Carle Illinois College of Medicine, University of Illinois at Urbana-Champaign, Urbana-Champaign, IL, USA

X. Wei, B. Gu (eds.), *Optical Imaging in Human Disease and Biological Research*, Advances in Experimental Medicine and Biology 1355,
https://doi.org/10.1007/978-981-15-7627-0_7

Depending on the size of the living organism being imaged, IVM can be used to image from the subcellular level up to the whole organism [1, 2]. It has been demonstrated and used to further our understanding of biological processes in immunology, dermatology, neuroscience, and cancer research, among many other scientific and medically related areas [2–4]. For example, IVM has been employed to show the heterogeneity in cell motility and the mode of cell migration, dynamic intercellular interaction, local cancer invasion, and distant metastases [2, 5]. It has also been used to characterize the dynamic interactions between cancer cells and the tumor-associated immune system in order to understand the influence of the tumor microenvironment on disease progression, metastasis, and treatment [6, 7]. Real-time insight in evaluating targets of drug treatment [8] or pharmacodynamics [9] and pharmacokinetics [10] can be provided by it. IVM also offers comparison data that were previously only available by histopathology, the current gold standard for diagnosing cancer and other diseases. A research study using intraoperative imaging for assessing tumor margins showed the potential for immediate diagnosis at the point-of-procedure, which could not only shorten the time that histopathology would require, but would also avoid the structural artifacts to the tissue that commonly arise from the histological sample preparation [11].

To enable in vivo studies, bright-field transillumination microscopy is not practical, and imaging platforms have shifted to laser scanning confocal or two-photon microscopy with epi-detection. Microscopic techniques such as fluorescence, confocal, and multiphoton microscopy are better suited for in vivo investigations. More specifically, second harmonic generation, third harmonic generation, two-photon excitation, three-photon excitation, optical coherence tomography, coherent anti-Stokes Raman scattering, and fluorescence lifetime imaging microscopy have all been developed and used for various in vivo imaging studies of intact tissue at high resolution. Each modality, however, based on the light–tissue interaction, reveals only a portion of signal that can be generated and collected from tissue. Since each modality is generated by different contrast mechanisms, combining them into

S. A. Boppart (✉)
Biophotonics Imaging Laboratory, University of Illinois at Urbana-Champaign, Urbana-Champaign, IL, USA

Beckman Institute for Advanced Science and Technology, University of Illinois at Urbana-Champaign, Urbana-Champaign, IL, USA

Department of Bioengineering, University of Illinois at Urbana-Champaign, Urbana-Champaign, IL, USA

Carle Illinois College of Medicine, University of Illinois at Urbana-Champaign, Urbana-Champaign, IL, USA

Department of Electrical and Computer Engineering, University of Illinois at Urbana-Champaign, Urbana-Champaign, IL, USA

Cancer Center at Illinois, University of Illinois at Urbana-Champaign, Urbana-Champaign, IL, USA
e-mail: boppart@illinois.edu

multimodal platforms allows for more comprehensive, integrated, and informative studies [12, 13]. Multimodal imaging platforms can be engineered to maintain both spatial and temporal co-registration between modalities, and given that cellular activity in a live animal is inherently dynamic, this multimodal image acquisition and co-registration facilitates high-dimensional data sets appropriate for machine-learning and deep-learning analysis.

Different imaging techniques can be utilized for different applications, depending on the depth of imaging. Near-infrared imaging or excitation wavelengths are preferred for imaging in thicker specimens because of reduced absorption and scattering. Multiphoton microscopy with ultrafast short-pulse NIR lasers and tightly focused beams can perform optical sectioning and generate three-dimensional volumes of image data. Multiphoton microscopy also outperforms laser scanning confocal microscopy in three-dimensional sectioning with less out-of-focus photobleaching, and without the need for a confocal pinhole that often can generate aberration [14–16].

Since the discovery of fluorescent proteins and their introduction as a marker for gene expression, the field of IVM has evolved to include them for imaging labeled live cells and tracking their spatiotemporal dynamics directly in vivo [17, 18]. In addition, considerable work has been done in molecular imaging with the use of targeted exogenous contrast agents or probes that are detectable with the aforementioned imaging modalities and localize to known receptors or targets on cells or in tissue. IVM images using exogenous probes or genetically expressed fluorescent proteins represent the three-dimensional spatial distribution of the targeted molecules within the tissue, can provide diagnostic information at the molecular level, and can reveal functional properties of cells. Even though these exogenous and genetically-expressed labels are advantageous for highlighting structural, biological, and chemical information, labeling multiple cell types using exogenous staining, cell/tissue transplantation, and genetic modification is difficult and laborious. These methods are also prone to disrupt or shift the natural biological processes or physiology of the microenvironment. By leveraging only endogenous tissue components like the extracellular matrix and cellular metabolites that have autofluorescent properties, label-free IVM provides a view of the natural unperturbed dynamics that can reveal fundamental principles in biological research, or diagnostic features and biomarkers for clinical applications.

In this chapter, we provide an overview of label-free IVM with multiple modalities that generate multiple forms of endogenous contrast. Applications in biological imaging and clinical human studies will be covered, along with the advantages and challenges faced when relying on truly label-free multimodal multiphoton microscopy techniques.

7.2 Label-Free Imaging Modalities and Contrast Mechanisms

While there have been many studies and reviews on IVM, relatively few have focused on truly label-free IVM, meaning not only free of exogenous probes, dyes, or labels, but also free of any genetic alterations that would produce genetically expressed fluorescent proteins as labels. By this definition, label-free microscopy makes use of inherent, natural, endogenous contrast mechanisms and is non-perturbative of the biological or physiological processes in the living organism. This is a significant advantage over imaging small molecular probes or dyes as such labeling or altered gene expression may significantly affect local biomolecular properties and often require site-specific targeting that may be incomplete, leading to either off-target labeling, or missed labeling of the target.

Multiphoton microscopy (MPM) allows the visualization of intact biological samples at high resolution. MPM is based on nonlinear optical processes such as two-photon and three-photon excited fluorescence (2PF, 3PF) and second and third harmonic generation (SHG, THG) (Fig. 7.1). Standard fluorescence imaging relies on 1-photon excited fluorescence where a single higher energy photon is absorbed, followed by emission of a lower energy photon. Nonlinear 2-photon (3-photon) excited fluorescence is based on the simultaneous absorption of two (three) lower energy photons. With 2PF or 3PF excitation, it is also possible to measure the lifetime of the endogenous autofluorescence using fluorescence lifetime imaging microscopy (FLIM) techniques. Second (third) harmonic generation is another nonlinear optical process where two (three) photons are converted to a single photon without losing any energy to the environment.

Most commonly, 2PF and 3PF are used to image endogenous autofluorescent molecules such as nicotinamide adenine dinucleotide (NADH), flavin adenine dinucleotide (FAD), retinol, riboflavin, and pyrilamine. These imaging modalities have been widely applied for biological investigations since the realization that these nonlinear optical signals can be generated from biological tissues [20, 21]. SHG generates contrast from the noncentrosymmetric organization of molecules. It has been applied to investigate structures such as collagen, myosin, and microtubules [22]. Third harmonic generation (THG) primarily occurs at water–lipid and water–protein interfaces, providing structural information such as defining cell morphology from the surrounding extracellular matrix. It is used to visualize the refractive index differences across cellular membranes and the interfaces of lipid droplets [23]. THG is often combined with autofluorescence-generating methods to obtain morphological and biochemical information [24]. Coherent anti-Stokes Raman scattering (CARS) microscopy probes the vibrational frequency of chemical bonds and can produce 3D vibrational contrast images with high spatial resolution (Fig. 7.1). Like spontaneous Raman, CARS, along with stimulated Raman scattering (SRS) probes vibrational modes in molecules and does not require the introduction of exogenous dyes or markers, which is advantageous in imaging small molecules, such as metabolites, for which labeling may significantly affect their molecular properties. CARS and SRS are commonly used for imaging lipid bilayers, cell membranes, adipocytes, DNA, and myelin sheaths [25].

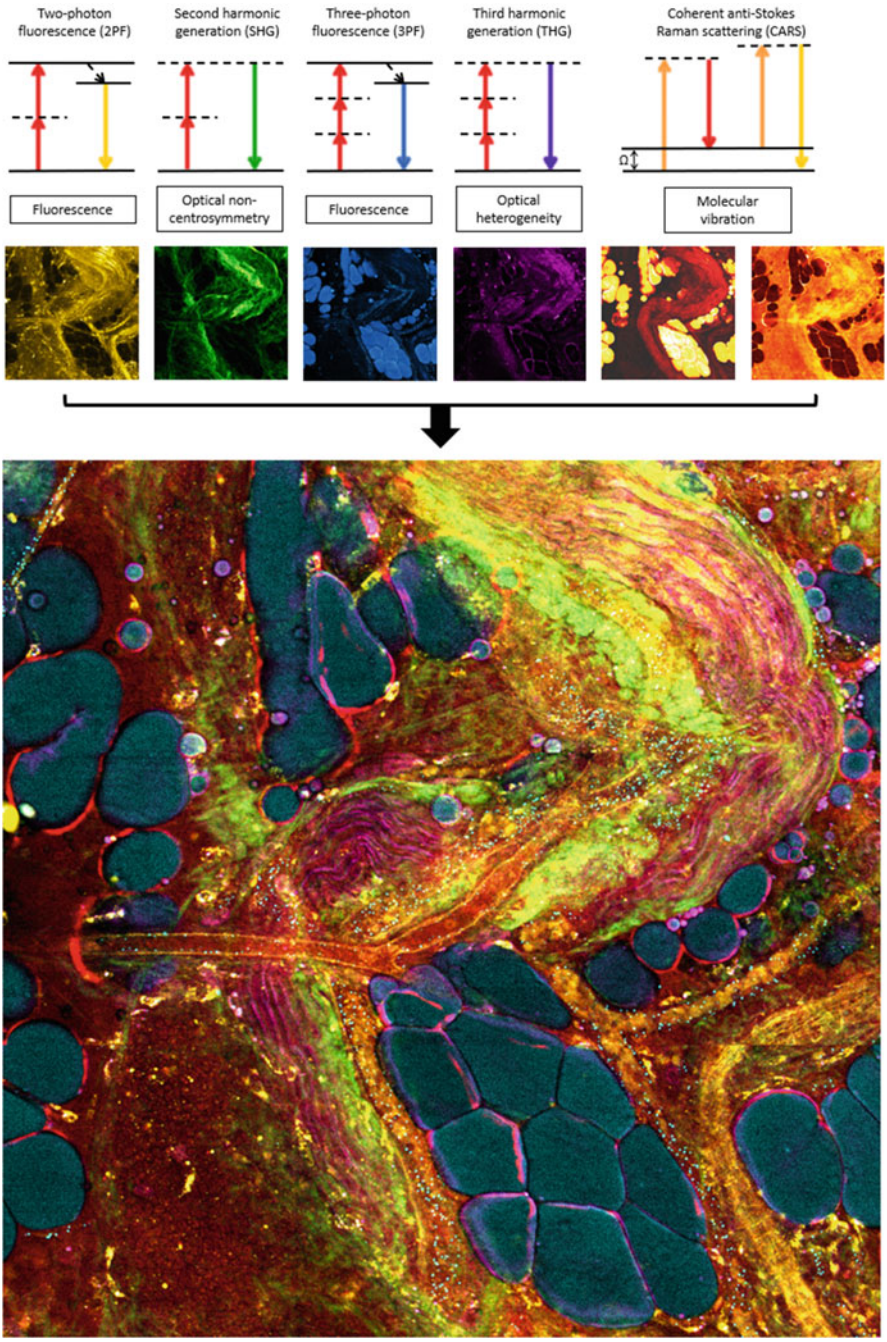

Fig. 7.1 (above) Co-registered multimodal MPM images, with energy level diagrams for different nonlinear optical processes. (below) A composite image obtained from label-free intravital imaging of a rat mammary tumor, when all images from individual modalities are combined with orthogonal contrast. (Adapted with permission from [19])

Due to the nonlinear processes in these modalities, multiphoton signal generation is essentially confined to the focal volume, giving high resolution without the need for spatial filtering as in confocal microscopy. Additionally, photobleaching of autofluorescent molecules outside the focus is virtually eliminated. Another important advantage of multiphoton absorption over single-photon absorption is that near-infrared light is used instead of visible wavelengths. Longer wavelength light experiences less scattering and absorption in biological tissue, allowing for deeper imaging penetration and relatively low phototoxicity. Relatively uniform diffraction-limited three-dimensional spatial resolution (~1 μm) can be obtained by near-infrared excitation of biological specimens, and deep imaging penetration (~1 mm) even in highly scattering thick specimens is possible using simple epi-detection [26].

The resulting coupled laser-imaging technology has made significant progress since the 1990s and has been highly valuable in in vitro and ex vivo studies to generate fundamentally new biological insights. However, a quarter century later, multiphoton microscopy remains largely restricted to a small number of optical laboratories or biological laboratories with engineering expertise, and these systems are operated more often by laser experts than by biologists [92]. These imaging modalities have previously been extensively reviewed in several dedicated papers [4, 19].

While many of these techniques are used individually, or combined with labeling techniques, the ability to combine these different modalities enables the full potential of these technologies to be realized. The unique configuration of an integrated microscope allows for the simultaneous acquisition of both anatomical (structural) and functional imaging information. The primary advantage of an integrated microscope over other imaging techniques is that it is well suited for imaging live, intact tissue. This enables high-resolution in situ visualization of tissues and organs, which is of great interest for both biological research and medical diagnostics.

7.3 Animal Model Selection for Intravital Microscopy

Due to limited light penetration, IVM requires an appropriate animal model. Without the use of any optical catheter, endoscope, or needle for imaging deep into larger animal models, IVM can largely only be used for imaging superficial (skin, ear, oral cavity) or transparent (retina, auricular mouse ear) tissues, or the surgically exposed tissues. An increasing number of genetically engineered cells and animals that express fluorescent protein reporters have become available, expanding the options for IVM [27, 28]. Mice and rats can be engineered with various exogenous agents to label specific cell types [29–31], including oncomice [32, 33] and fluorescent protein-expressing transgenic mice [34].

Targeted tissue can also be surgically exposed for short-term (hours) [17, 35, 36] or long-term (days or weeks) observation through chronic imaging windows [37, 38] implanted over the brain [39–43], spinal cord [44], dorsal skin [45], mammary gland [46], abdomen [47], ovary [48], or lung [49]. Optical imaging windows inserted in the skin and over the organ of interest provide a short-term alternative to surgically

exposed tissues, and enable repeated long-term imaging and expanded applications of IVM. Such optical windows have become a preferred approach for following tumor progression in mouse and rat cancer models [50–54].

Selection of a region for imaging is also important and depends on the purpose of the study. Imaging hairless skin regions, for example, will prevent the confounding signal from hair autofluorescence, and selecting a region that is the least affected by respiration and cardiac movements will enhance image quality by acquiring a more stable image free of motion artifacts [55]. Similarly, investigation of immune cells like dendritic cell subsets, Langerhans cells, T cells, and circulating leukocytes can be done on the hairless ear skin of a rodent [4].

7.4 Label-Free Intravital Microscopy in Preclinical Research

Long-term multimodal IVM imaging has provided deeper insight into carcinogenesis and tumor development using only label-free modalities, or in combination with exogenous labels (Table 7.1).

Observation of the tumor microenvironment is very important for cancer characterization including its invasiveness. Traditional fluorescence microscopy techniques [56–61], while highlighting specific features of tumor tissue by labeling, inherit the limitation of other applications of IVM, i.e., the inability to track the "content" of a targeted cell type under study in the comprehensive "context" of untargeted cell types in the stroma. Imaging of targeted cells such as tumor-associated fibroblasts [56], macrophages [58], melanoma cells [57], or other tumor cells [59–61] is often combined with label-free imaging of collagen and the vasculature to enhance molecular information (Table 7.1). However, labeling multiple cell

Table 7.1 Survey of long-term multiphoton intravital imaging of the invasion-metastasis cascade. FP denotes cell labeled with fluorescent protein

Window	Step in the cascade	Biological component (labeling agent or nonlinear contrast) at specific excitation wavelength	Ref.
Dorsal skin	Local matrix remodeling	Tumor-associated-fibroblast (FP), collagen (SHG) at 890 nm	[56]
Dorsal skin	Local invasion	Collagen (SHG), nerve/lipid/vesicle (THG), melanoma-cell (E2-Crimson) at 1180 nm	[57]
Mammary	Local invasion	Cytoplasm-NADH (2PF-FLIM) at 780 nm; cytoplasm-FAD (2PF)/macrophage (FP), collagen (SHG) at 890 nm	[58]
Mammary	Invasion, intravasation	Precancerous cell (FP), collagen (SHG), vasculature (dextran) at 880 nm	[59]
Cranial	Extravasation, metastasis	Tumor cell (FP), vasculature (dextran) at 750 nm	[60]
Abdominal	Extravasation, metastasis	Tumor cell (FP), collagen (SHG), vasculature (dextran) at 960 nm	[61]
Mammary	Local invasion	Cytoplasm (2PF-3PF-THG), extracellular matrix (SHG-2PF-3PF-THG) at 1110 nm	[62]

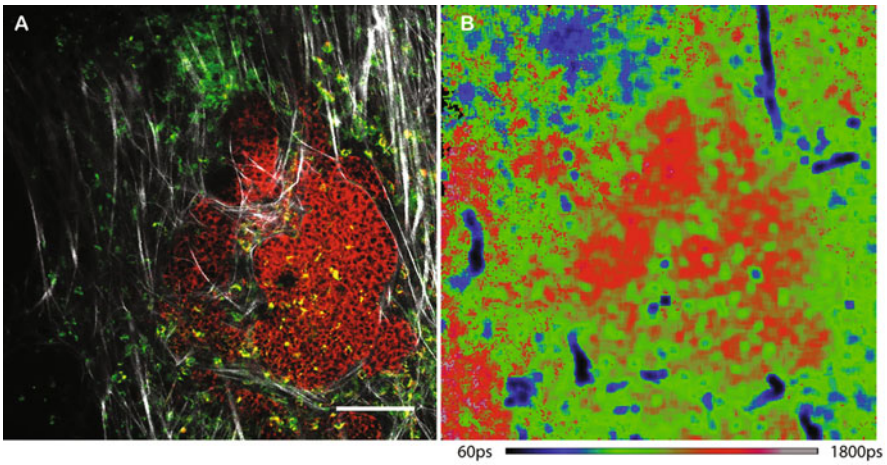

Fig. 7.2 Endogenous fluorescence of tumor cells in the breast microenvironment. (**a**) Composite of two label-free channels; red/green = FLIM, grayscale = SHG. (**b**) NADH-FLIM image of the same field-of-view as in (**a**). Scale bar: 100 μm. (Reprinted with permission from [58])

types using exogenous staining, cell/tissue transplantation, and/or genetic modification is not only labor intensive, but also prone to disruption of the tumor microenvironment. Even in the studies using novel multiplexed labeling, imaging all labeled cells simultaneously and in real time can be technically difficult [63–65]. Label-free multimodal multiphoton imaging, based on the intrinsic optical response of tumor tissue, is aiming to visualize various biological features in the tumor microenvironment, and resolve the long-standing challenge in IVM to discriminate different cell types label-free, and track them within their authentic tissue microenvironment.

Figure 7.2 shows SHG and FLIM images using IVM in a PyVT (MMTV-Polyoma Middle-T) animal model [58]. SHG is used for imaging fibrillar collagen to locate the tumor region, while FLIM provided an ability to discriminate specific cell types based on their metabolic signatures by using the endogenous population of FAD and NADH. PyVT tumor cells and stromal macrophages are distinguished by their metabolic signature matches [58]. In a similar study, a dorsal window model was used in IVM for deeper imaging penetration and a longitudinal study of collagen to reveal stromal cell–matrix interaction. The results showed that the matrix-modifying hormone relaxin increased tumor-associated fibroblast interaction [56]. Another study used type I collagen structure visualized by SHG as reference points for retracing subcellular accuracy. With this information, Wei et al. used an abdominal imaging window to investigate the biological processes related to tumor cell migration during pre-micrometastases in the mouse liver [61].

Currently, IVM is the only method that can obtain cellular-level spatiotemporal information in the system with functional circulation. One study, although not entirely label-free, used THG and SHG in combination with fluorescently labeled B15F10 melanoma cells in the dorsal skin-fold chamber model to visualize cellular-

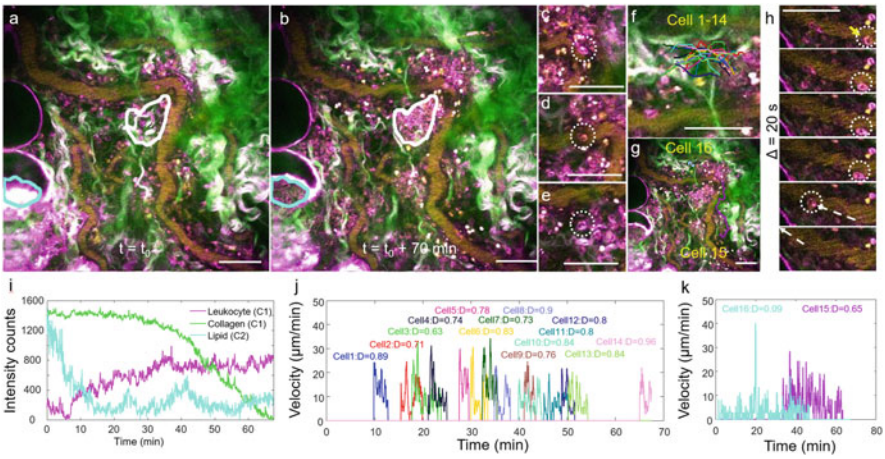

Fig. 7.3 Leukocyte-clustering visualized and characterized by SLAM microscopy. (**a**) Image acquired at the beginning and (**b**) at the end of the clustering, respectively, over a 70 min time period. Changes in cell density are noted in the circled areas. (**c**–**h**) Cell dynamics and tracking at a rate of 1 frame every 2 s. (**i**) Quantification of collagen clearance, cell accumulation, and lipid deformation within the marked clusters in (**a**) and (**b**) (C1 and C2). (**j, k**) Velocity and directionality map of Cells 1–16. The color of the curves matches the color of the traces in (**f**) and (**g**). *D* directionality; green: SHG, pink: THG, yellow: 2PF, blue: 3PF. Scale bar: 50 μm. (Modified with permission from [62])

level invasion along the interface with the dermis [57]. This study also imaged the presence and dynamics of tumor-associated microvesicles.

Recently, simultaneous label-free autofluorescence-multiharmonic (SLAM) microscopy was introduced [62]. This single excitation source and nonlinear imaging platform with low incident optical power (14 mW) was conducive for long-term label-free in vivo imaging. In a comprehensive IVM study, it was used to co-register 2PF, 3PF, SHG, and THG and longitudinally image an exposed rat mammary tumor [62, 66, 91]. SHG showed the collagen structure of the tumor microenvironment, THG distinguished individual cells, 2PF revealed vascular structures, and 3PF showed the vital phenomena in cells. A time-lapse study with a high-speed microscope ($\sim 10^5$ Hz pixel rate) revealed diapedesis of the cells, including rolling and crawling of leukocytes and their migration into and out of the perivascular tissue microenvironment and blood vessels (Fig. 7.3).

With increasing interest in extracellular vesicles (EVs) as vehicles in the cell–cell communication, both in healthy as well as in the diseased tissue, IVM can be used to track these small (100–1000 nm) and elusive particles. An investigational study of EVs with label-free multimodal multiphoton imaging was first done on ex vivo tissue. This generated a database of various contrasts from molecules and structures in both rat mammary and human breast tumor microenvironments [67]. Co-locally combined images of four individual modalities (2PF, 3PF, SHG, THG) showed the distribution of tumor cells, malignant adipocytes, stromal cells, and EVs. In the same study, IVM of tumor-bearing rats demonstrated label-free monitoring of EV

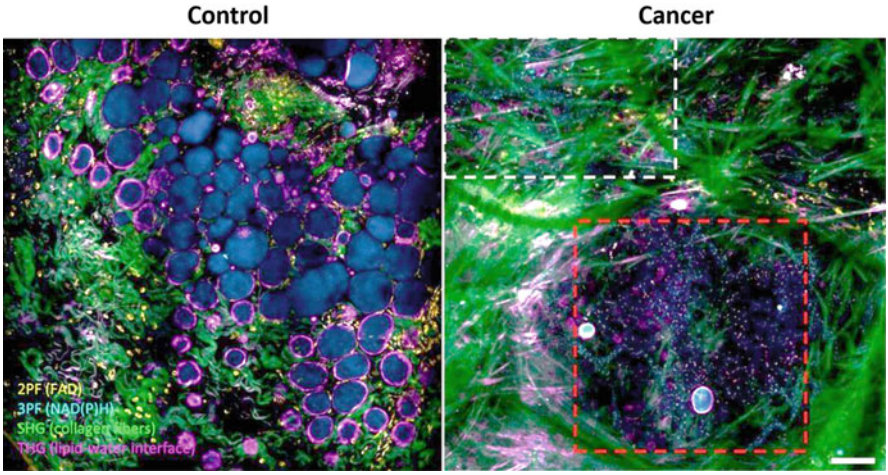

Fig. 7.4 In vivo visualization and characterization of extracellular vesicles in control rats (left) and tumor-bearing rats (right) by label-free intravital SLAM microscopy. The white and red dashed boxes indicate regions of normal collagen versus tumor nest, respectively, showing a high density of blue-colored NADH-rich EVs in the tumor nest. Scale bar: 100 μm. (Reprinted with permission from [67])

dynamics (Fig. 7.4). Label-free IVM, tracking, and quantitative analysis of EVs in a live rat revealed the correlation between NAD(P)H-rich EVs and cancer cells, suggesting the active metabolic role of EVs in cancer progression.

Cranial window models, such as the thinned-skull cranial window, open-skull glass window, and skull optical clearing window, are widely used for IVM of the brain to image deep inside the cortex [2], although very few studies are applying label-free approach. In one study, two-photon microscopy enabled longitudinal tracking of the bone engraftment process after surgery by implanting the calvarial window [40]. Temporal changes in the bone marrow microenvironment, such as the reconstitution of transplanted bone marrow cells and the recovery of vasculature, were followed. Combining THG with visible-wavelength reflectance confocal microscopy, label-free imaging of the mouse brain was demonstrated through a window, and down to ~1.3 mm depth, reaching the subcortical region [68]. This method offers high-resolution in vivo imaging and does not require expensive laser sources or a complicated optical setup. To investigate the capability of THG imaging for IVM of the mouse brain, high-contrast images could be obtained, but depths of only ~200 μm were achieved, which was limited by the laser power and the vasculature above the imaging site [69]. With the continuous development of multiphoton imaging capabilities and with the rise of BRAIN Initiative funding, in the U.S., the use of IVM in the brain is certain to be a focus for expanded research.

Due to its ready optical accessibility, the skin has been an obvious target for longitudinal IVM studies. The high resolution and multimodal framework allow for longitudinal visualization of both structural and metabolic changes [70], including

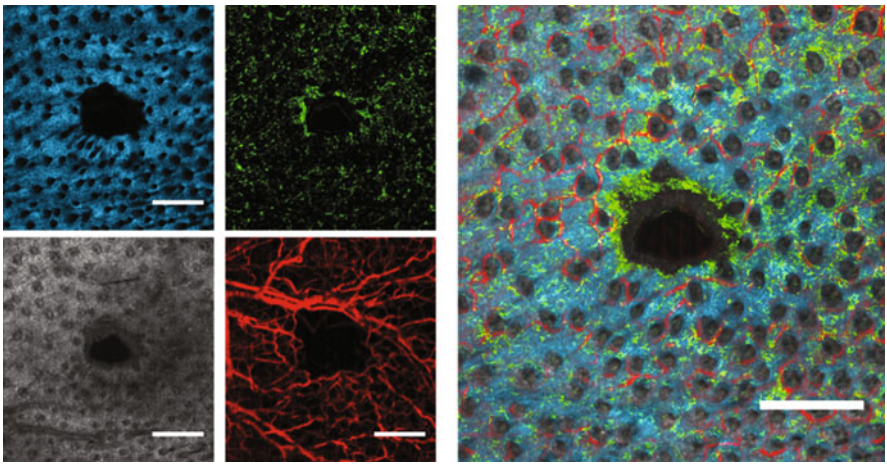

Fig. 7.5 In vivo multimodal *en face* images of a mouse ear 10 days after wounding. Left: SHG image of collagen structure (blue) and location of hair follicles (small black voids), 2PF image of GFP-labeled bone marrow-derived cells (green), OCT of epidermal structures (gray), and OCT phase-variance projection of the microvasculature (red). Right: Overlay of the four modalities. Scale bar: 500 μm. (Adapted with permission from [71])

specific biological events that occur in the skin such as early development of squamous cell carcinoma [54], wound healing [71, 72], the effect of pharmaceutical treatments [21, 73, 74], apoptosis [75], and collagen regeneration after thermal injury [76].

Skin regeneration processes often occur over long time periods, from weeks to months. In a time-lapse study, a novel non-rigid image registration algorithm was demonstrated and quantitatively evaluated for imaging cell dynamics during mouse wound healing and skin regeneration processes over a period of several months, including collagen synthesis, angiogenesis, structural repair, and wound contraction biomechanics [71]. Three-dimensional (3D) 2PF, SHG, structural OCT, and microvascular phase-variance OCT imaging were combined, in addition to a non-rigid image registration method that utilized hair follicle positions as reference landmarks between subsequent imaging sessions. In this study, IVM was complemented with GFP-labeled bone marrow-derived cells to establish the role of bone marrow cells in skin regeneration (Fig. 7.5). Another study used in vivo longitudinal tracking of collagen remodeling in diabetic wounds and found that a stem cell-treated group had a significantly faster rate of collagen remodeling than a non-treated group [72].

In other longitudinal studies, IVM was used to examine the effect of interleukin-12 [21] as well as angiogenesis-promoting [73] and steroid [74] topical treatments on collagen structure and cellular metabolic activity during skin wound healing. In another IVM study of hairless mouse skin revealed cellular-level metabolic differences between different cell death processes [75]. The metabolic response of mouse epidermal keratinocytes following induction of apoptosis and necrosis showed significantly elevated levels of both the mean autofluorescence lifetime of

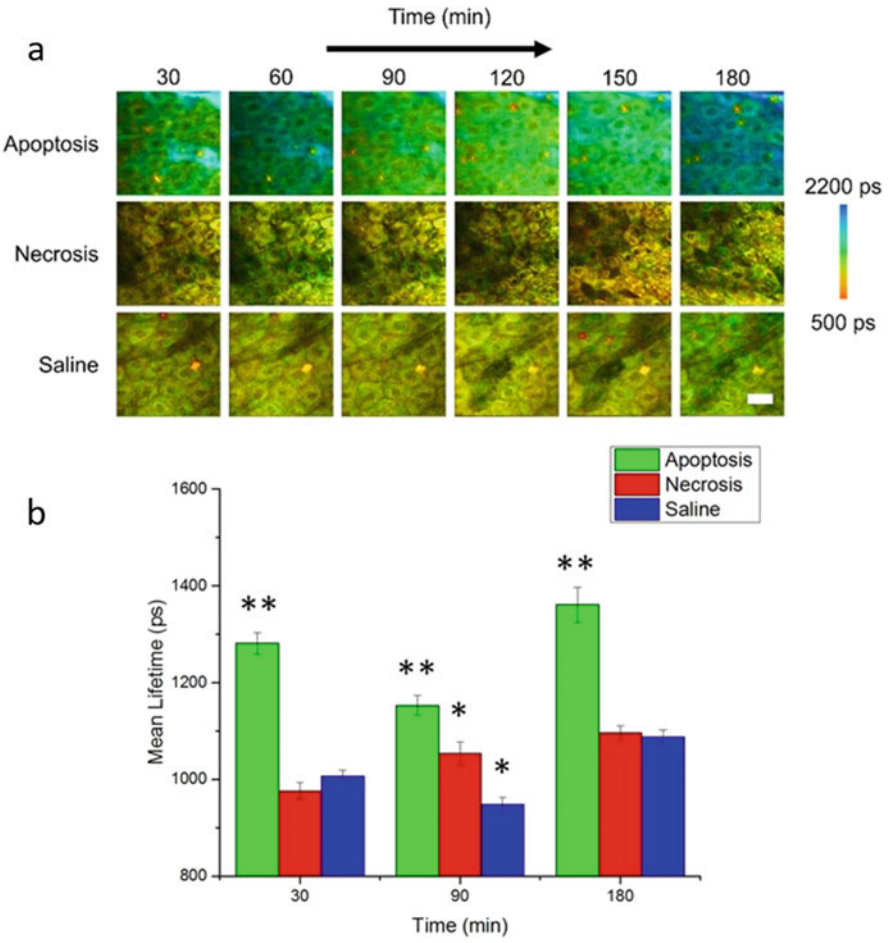

Fig. 7.6 In vivo mean autofluorescence lifetime dynamics in murine keratinocytes. (above) Images of the mean lifetime tracked between 30 and 180 min following treatment for inducing apoptosis or necrosis in epidermal keratinocytes. Saline-treated mice were used as a control. (below) Comparison of the mean lifetime across the entire observed cell population at 30, 90, and 180 min after the treatment. The mean lifetime in the keratinocytes with induced apoptosis was significantly different compared to the other two groups 30 min ($p < 0.01$) and 180 min ($p < 0.05$) after the treatment. Scale bar: 25 μm. (Reprinted with permission from [75])

NADH and the intracellular ratio of protein bound-to-free NADH in the apoptotic tissue compared to the necrotic tissue (Fig. 7.6). Finally, one in vivo study followed the effect of radiofrequency ablation of nude mice skin, demonstrating the disruption of the collagen structure due to thermal injury, and the subsequent collagen regeneration after 1-month post-treatment [76].

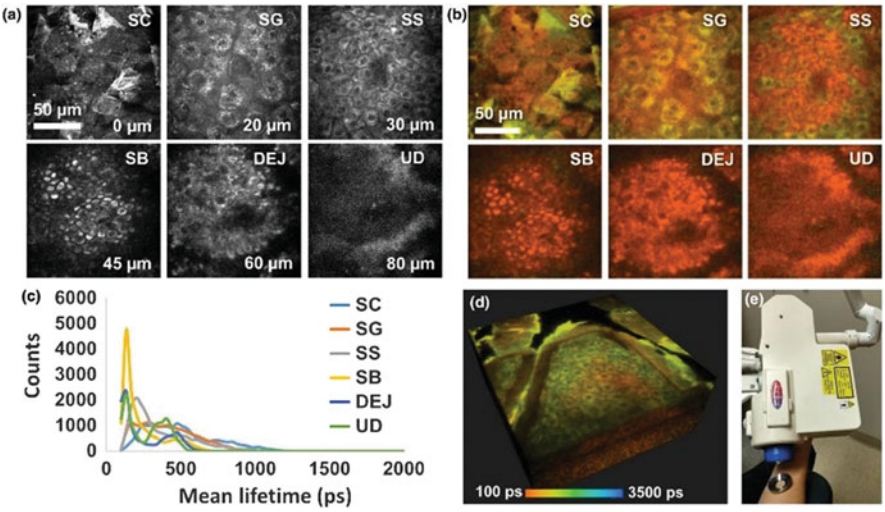

Fig. 7.7 In situ biodistribution and residency of a topical anti-inflammatory drug using fluorescence lifetime imaging microscopy (FLIM). (**a**) Two-photon excited fluorescence images of different skin layers. (**b**) FLIM images of different skin layers. (**c**) Mean lifetime distribution in different skin layers. (**d**) Three-dimensional rendering of skin from FLIM images. (**e**) Coupling the head of the optical tomography system to human skin for in vivo imaging. *SC* stratum corneum, *SG* stratum granulosum, *SS* stratum spinosum, *SB* stratum basale, *DEJ* dermal–epidermal junction, *UD* upper dermis. (Reprinted with permission from [78])

7.5 Label-Free Intravital Microscopy in Clinical Research

There are very few clinical studies attempting to use noninvasive, label-free IVM in human subjects. An early study demonstrated the use of multiphoton excitation microscopy at 730 and 960 nm to image the autofluorescence of in vivo human skin from the surface to a depth of about 200 µm [77]. It was suggested that the optical biopsy of in vivo human skin based on functional imaging of cellular metabolites may have diagnostic potential in dermatology.

In a clinical study with healthy participants, penetration, spatial distribution, and residency of two topical creams were evaluated longitudinally using a commercial MPM system [78]. Endogenous fluorophores, such as NADH, elastin, keratin, and melanin, enabled visualization of the structural organization and biochemical composition of different skin layers with multiphoton FLIM (Fig. 7.7). Cream distribution and residency were mapped and tracked from the FLIM images. Understanding the pharmacokinetic and pharmacodynamic properties of a newly developed drug is essential for its efficacy and for faster availability to patients. This study also demonstrated the potential for using multiphoton IVM in clinical studies in patients with skin diseases, including skin cancer, and longitudinally tracking responses to treatment in a completely noninvasive manner.

7.6 Technical Limitations and Translational Challenges

Several challenges are imposed on label-free intravital optical imaging. The greatest challenge is in acquiring high-quality images deep from within the animal tissue, and rapidly enough to avoid motion artifacts while still imaging the real-time dynamics of cells and tissue structures. Compared to in vitro environments, such as cell or tissue cultures, or ex vivo tissue specimens, imaging in vivo tissue consists of complex cellular and extracellular components undergoing dynamic interactions and biological processes. Providing access to tissue sites and generation of sufficient contrast to provide a comprehensive view of these tissue components in vivo represent other significant technical challenges. Technical barriers limiting in vivo biological multiphoton microscopy also originate from the optical sources, imaging platforms, and beam-delivery methods. Tradeoffs therefore exist, and often system designs and capabilities are dictated more by the targeted application of interest. Compromises must frequently be made between the medical or biological scientists and the questions they seek, and the laser physicists and optical engineers and the technology and performance that they can deliver.

Physically, the signal generation rate of multiphoton microscopy scales with $\psi(\lambda) P^n/(f\tau)^{n-1}$, where $\psi(\lambda)$ is the wavelength-dependent nonlinear response and n is the order of the nonlinear process ($n = 2$ for SHG or 2PF, and $n = 3$ for THG or 3PF) [16]. Thus, tuning λ to maximize $\psi(\lambda)$ is required to maximize the signal generation. However, the flexibility to tune λ comes with the steep price of operational instability against beam pointing drift, dispersion variations that elongates τ, and thermal or mechanical disturbance to the laser cavity.

Photodamage to biological samples also scales with $P^r/(f\tau)^{r-1}$, in which the nonlinear order r lies between 2 and 3 [79, 80]. This photodamage can be attributed to a combination of two- and three-photon absorption involving both photochemical and photoionization processes [81]. Within the scope of two-photon microscopy ($n = 2$), the mitigation of this highly nonlinear ($2 < r < 3$) photodamage demands a low duty-cycle inverse $(f\tau)^{-1}$ because $n < r$. This requires elongating τ [79] and/or increasing f [82]. Unfortunately, there exists another photodamage mechanism that includes two-photon absorption-induced photochemical damage ($r = 2$) [80] and one-photon absorption-induced photothermal damage ($r = 1$) [83]. Because $n \geq r$, the mitigation of this low-r photodamage demands a high duty-cycle inverse, which requires shortening τ [84] and/or lowering f [85]. Thus, the flexibility to vary f and tune τ below 80 fs is needed to either increase or decrease the duty-cycle inverse in imaging contrast generation, dependent on the specific biological sample and the photodamage mechanism. However, it has not been technically feasible to independently vary or tune all excitation parameters (f, λ, τ, and P). In particular, the *inflexibility* to adjust the duty-cycle inverse has prohibited the optimization of in vivo multiphoton imaging to maximize the signal-to-damage ratio.

Moreover, three-photon signals (3PF or THG) are typically much weaker than two-photon signals (2PF or SHG), and thus require a slower and separate scan for image acquisition, which prohibits the co-localization of the two contrast mechanisms or modalities in in vivo imaging. As a result, multiphoton microscopy

has rarely been employed for in vivo clinical diagnosis of superficial tissue (skin, ear, oral cavity, etc.) at the point-of-care or in surgically exposed tissues in the operative room. Improvement of harmonic generation signals has been done with sample thicknesses less than 200 μm, which may be limiting for some in vivo imaging applications [86].

Label-free multiphoton IVM has been limited by the relatively small set of endogenous target components [87]. For example, even though two-photon microscopy has become the preferred tool to study in vivo brain activity, routine experimental procedures have preferably used calcium-sensitive fluorescent proteins to image neural activity at different wavelengths between stimulation and recording.

Longitudinal in vivo imaging is also sensitive to motion artifacts, which can be removed or at least mitigated during imaging or by post-processing. For imaging dynamics of cell migration in tissues, the system has to be fast enough to capture these fast events. For skin applications, the autofluorescence from hair could mask weaker nonlinear signals from tissue. Careful hair removal procedures are important to help address this problem. For clinical research, portable MPM systems for IVM investigations require a bulky cart and often a special light-delivery articulated arm that makes the system complex and expensive. After obtaining high-resolution multi-dimensional images, high computational power is often needed but may not always be readily available, particularly for real-time processing, display, and visualization for point-of-procedure decision-making. Despite these limitations and challenges, there are significant opportunities and impactful end-goals that justify further technical advances for biological and medical investigations.

7.7 Conclusions and Future Prospects

In this chapter, we reviewed and demonstrated the potential of label-free multimodal multiphoton IVM of live cells and tissues with morphological and dynamic details from the neighboring cells, vasculature, and stroma. The use of more invasive and perturbative exogenous labeling, sample treatment, or genetic modification are no longer required to attain high-resolution real-time and longitudinal image data that is more biologically and medically relevant.

The ability to correlate animal (rodent) and human cells with similar optical phenotypes allows for the ready translation of in vivo histochemical knowledge from preclinical animal models to humans. For example, ex vivo human basal cell carcinoma has been investigated with label-free multimodal multiphoton imaging techniques. Similar to the IVM on preclinical animal models, SHG and multiphoton fluorescence imaging were able to differentiate cancer cells and adjacent cancer stroma from the normal dermis in ex vivo human samples. Morphological evidence of basal cell carcinoma as clusters of autofluorescent cells with large nuclei was shown [88]. FLIM and multiphoton laser tomography also differentiated basal cell carcinoma from other skin disorders [89], and this was further successfully used to image stratum corneum, upper epidermis, and lower epidermis in in vivo humans [90].

With this potential, we expect that future studies will find even broader applications of label-free multimodal multiphoton IVM not only in biological research, but also in clinical applications where it may be used as a tool for detecting disease and making a diagnosis, monitoring disease conditions, or tracking responses to drugs and treatment interventions in clinical settings.

Acknowledgements We thank all of our colleagues for their dedicated efforts to advance the field of IVM and its applications in biology and medicine. While this chapter has focused on the more narrowly defined topic of label-free IVM, we acknowledge that a more comprehensive review and inclusion of more results was not practical due to length limitations. This review was prepared with support in part from the National Institutes of Health (R01CA213149, R01EB023232, R01CA241618). Additional information can be found at: http://biophotonics.illinois.edu.

References

1. Pittet MJ, Weissleder R (2011) Intravital imaging. Cell 147:983–991
2. Nobis M, Warren SC, Lucas MC, Murphy KJ, Herrmann D, Timpson P (2018) Molecular mobility and activity in an intravital imaging setting–implications for cancer progression and targeting. J Cell Sci 131:jcs206995
3. Osswald M, Winkler F (2013) Insights into cell-to-cell and cell-to-blood-vessel communications in the brain: *in vivo* multiphoton microscopy. Cell Tissue Res 352:149–159
4. Secklehner J, Lo Celso C, Carlin LM (2017 Jul) Intravital microscopy in historic and contemporary immunology. Immunol Cell Biol 95(6):506–513
5. Zhao Z, Zhu X, Cui K, Mancuso J, Federley R, Fischer K, Teng GJ, Mittal V, Gao D, Zhao H, Wong ST (2016) *In vivo* visualization and characterization of epithelial–mesenchymal transition in breast tumors. Cancer Res 76(8):2094–2104
6. Hawkins ED, Duarte D, Akinduro O, Khorshed RA, Passaro D, Nowicka M, Straszkowski L, Scott MK, Rothery S, Ruivo N, Foster K (2016) T-cell acute leukemia exhibits dynamic interactions with bone marrow microenvironments. Nature 538(7626):518–522
7. Orth JD, Kohler RH, Foijer F, Sorger PK, Weissleder R, Mitchison TJ (2011) Analysis of mitosis and antimitotic drug responses in tumors by *in vivo* microscopy and single-cell pharmacodynamics. Cancer Res 71(13):4608–4616
8. Conway JR, Carragher NO, Timpson P (2014) Developments in preclinical cancer imaging: innovating the discovery of therapeutics. Nat Rev Cancer 14(5):314–328
9. Dubach JM, Kim E, Yang K, Cuccarese M, Giedt RJ, Meimetis LG, Vinegoni C, Weissleder R (2017) Quantitating drug-target engagement in single cells in vitro and *in vivo*. Nat Chem Biol 13(2):168–173
10. Miller MA, Weissleder R (2017) Imaging of anticancer drug action in single cells. Nat Rev Cancer 17(7):399–414
11. Orringer DA, Camelo-Piragua S (2017) Fast and slide-free imaging. Nat Biomed Eng 1:926–928
12. Rius C, Sanz MJ (2015) Intravital microscopy in the cremaster muscle microcirculation for endothelial dysfunction studies. In: Methods in mouse atherosclerosis. Humana Press, New York, NY, pp 357–366
13. Beaurepaire E, Moreaux L, Amblard F, Mertz J (1999) Combined scanning optical coherence and two-photon-excited fluorescence microscopy. Opt Lett 24:969–971
14. Tu H, Liu Y, Turchinovich D, Marjanovic M, Lyngsø JK, Lægsgaard J, Chaney EJ, Zhao Y, You S, Wilson WL, Xu B, Dantus M, Boppart SA (2016) Stain-free histopathology by programmable supercontinuum pulses. Nat Photon 10:534–540

15. Follain G, Mercier L, Osmani N, Harlepp S, Goetz JG (2017) Seeing is believing–multi-scale spatio-temporal imaging towards *in vivo* cell biology. J Cell Sci 130:23–38
16. Zipfel WR, Williams RM, Webb WW (2003) Nonlinear magic: multiphoton microscopy in the biosciences. Nat Biotechnol 21:1369–1377
17. Condeelis J, Segall JE (2003) Intravital imaging of cell movement in tumours. Nat Rev Cancer 3:921–930
18. Chalfie M, Tu Y, Euskirchen G, Ward WW, Prasher DC (1994) Green fluorescent protein as a marker for gene expression. Science 263:802–805
19. Tu H, Liu Y, Marjanovic M, Chaney EJ, You S, Zhao Y, Boppart SA (2017) Concurrence of extracellular vesicle enrichment and metabolic switch visualized label-free in the tumor microenvironment. Sci Adv 3(1):e1600675
20. Maiti S, Shear JB, Williams RM, Zipfel WR, Webb WW (1997) Measuring serotonin distribution in live cells with three-photon excitation. Science 275:530–532
21. Li J, Bower AJ, Vainstein V, Gluzman-Poltorak Z, Chaney EJ, Marjanovic M, Basile LA, Boppart SA (2015) Effect of recombinant interleukin-12 on murine skin regeneration and cell dynamics using *in vivo* multimodal microscopy. Biomed Opt Express 6(11):4277–4287
22. Campagnola PJ, Loew LM (2003) Second-harmonic imaging microscopy for visualizing biomolecular arrays in cells, tissues and organisms. Nat Biotechnol 21:1356–1360
23. Schießl IM, Castrop H (2016) Deep insights: intravital imaging with two-photon microscopy. Pflugers Arch 468(9):1505–1516
24. Barad Y, Eisenberg H, Horowitz M, Silberberg Y (1997) Nonlinear scanning laser microscopy by third harmonic generation. Appl Phys Lett 70:922–924
25. Cheng JX, Xie XS (2004) Coherent anti-Stokes Raman scattering microscopy: instrumentation, theory, and applications. J Phys Chem B 108(3):827–840
26. Theer P, Hasan MT, Denk W (2003) Two-photon imaging to a depth of 1000 μm in living brains by use of a Ti:Al2O3 regenerative amplifier. Opt Lett 28:1022–1024
27. Tsien RY (1998) The green fluorescent protein. Annu Rev Biochem 67:509–544
28. Chudakov DM, Matz MV, Lukyanov S, Lukyanov KA (2010) Fluorescent proteins and their applications in imaging living cells and tissues. Physiol Rev 90:1103–1163
29. Progatzky F, Dallman MJ, Lo Celso C (2013) From seeing to believing labelling strategies for *in vivo* cell-tracking experiments. Interface Focus 3:20130001
30. Zitvogel L, Pitt JM, Daillère R, Smyth MJ, Kroemer G (2016) Mouse models in oncoimmunology. Nat Rev Cancer 16:759–773
31. Kersten K, de Visser KE, van Miltenburg MH, Jonkers J (2017) Genetically engineered mouse models in oncology research and cancer medicine. EMBO Mol Med 9:137–153
32. Hanahan D, Wagner EF, Palmiter RD (2007) The origins of oncomice: a history of the first transgenic mice genetically engineered to develop cancer. Genes Dev 21:2258–2270
33. Politi K, Pao W (2011) How genetically engineered mouse tumor models provide insights into human cancers. J Clin Oncol 29:2273
34. Hoffman RM (2005) The multiple uses of fluorescent proteins to visualize cancer *in vivo*. Nat Rev Cancer 5:796–806
35. Gavins FN, Chatterjee BE (2004) Intravital microscopy for the study of mouse microcirculation in anti-inflammatory drug research: focus on the mesentery and cremaster preparations. J Pharmacol Toxicol Methods 49(1):1–4
36. Jain RK, Munn LL, Fukumura D (2002) Dissecting tumour pathophysiology using intravital microscopy. Nat Rev Cancer 2:266–276
37. Alieva M, Ritsma L, Giedt RJ, Weissleder R, van Rheenen J (2014) Imaging windows for long-term intravital imaging: general overview and technical insights. Intravital. 3:e29917
38. Prunier C, Chen N, Ritsma L, Vrisekoop N (2017) Procedures and applications of long-term intravital microscopy. Methods 128:52–64
39. Holtmaat A, Bonhoeffer T, Chow DK, Chuckowree J, De Paola V, Hofer SB, Hübener M, Keck T, Knott G, Lee WC, Mostany R (2009) Long-term, high-resolution imaging in the mouse neocortex through a chronic cranial window. Nat Protoc 4:1128–1144

40. Le VH, Lee S, Lee S, Wang T, Jang WH, Yoon Y, Kwon S, Kim H, Lee SW, Kim KH (2017) *In vivo* longitudinal visualization of bone marrow engraftment process in mouse calvaria using two-photon microscopy. Sci Rep 7:44097
41. Yang G, Pan F, Parkhurst CN, Grutzendler J, Gan WB (2010) Thinned-skull cranial window technique for long-term imaging of the cortex in live mice. Nat Protoc 5:201–208
42. Drew PJ, Shih AY, Driscoll JD, Knutsen PM, Blinder P, Davalos D, Akassoglou K, Tsai PS, Kleinfeld D (2010) Chronic optical access through a polished and reinforced thinned skull. Nat Methods 7:981–984
43. Kim TH, Zhang Y, Lecoq J, Jung JC, Li J, Zeng H, Niell CM, Schnitzer MJ (2016) Long-term optical access to an estimated one million neurons in the live mouse cortex. Cell Rep 17:3385–3394
44. Farrar MJ, Bernstein IM, Schlafer DH, Cleland TA, Fetcho JR, Schaffer CB (2012) Chronic *in vivo* imaging in the mouse spinal cord using an implanted chamber. Nat Methods 9:297
45. Palmer GM, Fontanella AN, Shan S, Hanna G, Zhang G, Fraser CL, Dewhirst MW (2011) *In vivo* optical molecular imaging and analysis in mice using dorsal window chamber models applied to hypoxia, vasculature and fluorescent reporters. Nat Protoc 6:1355–1366
46. Kedrin D, Gligorijevic B, Wyckoff J, Verkhusha VV, Condeelis J, Segall JE, Van Rheenen J (2008) Intravital imaging of metastatic behavior through a mammary imaging window. Nat Methods 5:1019–1021
47. Ritsma L, Steller EJ, Ellenbroek SI, Kranenburg O, Rinkes IH, Van Rheenen J (2013) Surgical implantation of an abdominal imaging window for intravital microscopy. Nat Protoc 8:583–594
48. Bochner F, Fellus-Alyagor L, Kalchenko V, Shinar S, Neeman M (2015) A novel intravital imaging window for longitudinal microscopy of the mouse ovary. Sci Rep 5:12446
49. Entenberg D, Voiculescu S, Guo P, Borriello L, Wang Y, Karagiannis GS, Jones J, Baccay F, Oktay M, Condeelis J (2018) A permanent window for the murine lung enables high-resolution imaging of cancer metastasis. Nat Methods 15:73–80
50. McCreery MQ, Balmain A (2017) Chemical carcinogenesis models of cancer: back to the future. Annu Rev Cancer Biol 1:295–312
51. Beerling E, Ritsma L, Vrisekoop N, Derksen PW, van Rheenen J (2011) Intravital microscopy: new insights into metastasis of tumors. J Cell Sci 124:299–310
52. Alexander S, Weigelin B, Winkler F, Friedl P (2013) Preclinical intravital microscopy of the tumour-stroma interface: invasion, metastasis, and therapy response. Curr Opin Cell Biol 25:659–671
53. Ellenbroek SI, van Rheenen J (2014) Imaging hallmarks of cancer in living mice. Nat Rev Cancer 14:406–418
54. Wang CC, Li FC, Lin SJ, Lo W, Dong CY (2007) Utilizing nonlinear optical microscopy to investigate the development of early cancer in nude mice *in vivo*. In: European Conference on Biomedical Optics. (paper 6630_33)
55. Obeidy P, Tong PL, Weninger W (2018) Research techniques made simple: two-photon intravital imaging of the skin. J Invest Dermatol 138(4):720–725
56. Perentes JY, McKee TD, Ley CD, Mathiew H, Dawson M, Padera TP, Munn LL, Jain RK, Boucher Y (2009) *In vivo* imaging of extracellular matrix remodeling by tumor-associated fibroblasts. Nat Methods 6:143–145
57. Weigelin B, Bakker GJ, Friedl P (2012) Intravital third harmonic generation microscopy of collective melanoma cell invasion: principles of interface guidance and microvesicle dynamics. IntraVital 1:32–43
58. Szulczewski JM, Inman DR, Entenberg D, Ponik SM, Aguirre-Ghiso J, Castracane J, Condeelis J, Eliceiri KW, Keely PJ (2016) *In vivo* visualization of stromal macrophages via label-free FLIM-based metabolite imaging. Sci Rep 6:25086
59. Harper KL, Sosa MS, Entenberg D, Hosseini H, Cheung JF, Nobre R, Avivar-Valderas A, Nagi C, Girnius N, Davis RJ, Farias EF, Condeelis J, Klein CA, Aguirre-Ghiso JA (2016) Mechanism of early dissemination and metastasis in Her2+ mammary cancer. Nature 540:7634

60. Kienast Y, von Baumgarten L, Fuhrmann M, Klinkert WE, Goldbrunner R, Herms J, Winkler F (2010) Real-time imaging reveals the single steps of brain metastasis formation. Nat Med 16:116–122
61. Ritsma L, Steller EJ, Beerling E, Loomans CJ, Zomer A, Gerlach C, Vrisekoop N, Seinstra D, van Gurp L, Schäfer R, Raats DA, de Graaff A, Schumacher TN, de Koning EJ, Rinkes IH, Kranenburg O, van Rheenen J (2012) Intravital microscopy through an abdominal imaging window reveals a pre-micrometastasis stage during liver metastasis. Sci Transl Med 4:ra145
62. You S, Tu H, Chaney EJ, Sun Y, Zhao Y, Bower AJ, Liu Y-Z, Marjanovic M, Sinha S, Pu Y, Boppart SA (2018) Intravital imaging by simultaneous label-free autofluorescence-multiharmonic microscopy. Nat Commun 9:2125
63. Livet J, Weissman TA, Kang H, Draft RW, Lu J, Bennis RA, Sanes JR, Lichtman JW (2007) Transgenic strategies for combinatorial expression of fluorescent proteins in the nervous system. Nature 450:56–62
64. Niehörster T, Löschberger A, Gregor I, Krämer B, Rahn HJ, Patting M, Koberling F, Enderlein J, Sauer M (2016) Multi-target spectrally resolved fluorescence lifetime imaging microscopy. Nat Methods 13:257–262
65. Wei L, Chen Z, Shi L, Long R, Anzalone AV, Zhang L, Hu F, Yuste R, Cornish VW, Min W (2017) Super-multiplex vibrational imaging. Nature 544:465–470
66. You S, Sun Y, Chaney EJ, Zhao Y, Chen J, Boppart SA, Tu H (2018) Slide-free virtual histochemistry (Part I): development via nonlinear optics. Biomed Opt Express 9:5240–5252
67. You S, Barkalifa R, Chaney EJ, Tu H, Park J, Sorrells JE, Sun Y, Liu YZ, Yang L, Chen DZ, Marjanovic M, Sinha S, Boppart SA (2019) Label-free visualization and characterization of extracellular vesicles in breast cancer. Proc Natl Acad Sci U S A 116(48):24012–24018
68. Xia F, Wu C, Sinefeld D, Li B, Qin Y, Xu C (2018) *In vivo* label-free confocal imaging of the deep mouse brain with long-wavelength illumination. Biomed Opt Express 9(12):6545–6555
69. Witte S, Negrean A, Lodder JC, De Kock CP, Silva GT, Mansvelder HD, Groot ML (2011) Label-free live brain imaging and targeted patching with third-harmonic generation microscopy. Proc Natl Acad Sci U S A 108(15):5970–5975
70. Lee JH, Rico-Jimenez JJ, Zhang C, Alex A, Chaney EJ, Barkalifa R, Spillman DR, Marjanovic M, Arp Z, Hood SR, Boppart SA (2019) Simultaneous label-free autofluorescence and multi-harmonic imaging reveals *in vivo* structural and metabolic changes in murine skin. J Biomed Opt 10(10):5431–5444
71. Graf BW, Chaney EJ, Marjanovic M, Adie SG, De Lisio M, Valero MC, Boppart MD, Boppart SA (2013) Long-term time-lapse multimodal intravital imaging of regeneration and bone-marrow-derived cell dynamics in skin. Technology 1(01):8–19
72. Li J, Pincu Y, Marjanovic M, Bower AJ, Chaney EJ, Jensen T, Boppart MD, Boppart SA (2016) *In vivo* evaluation of adipose-and muscle-derived stem cells as a treatment for nonhealing diabetic wounds using multimodal microscopy. J Biomed Opt 21(8):086006
73. Li J, Bower AJ, Arp Z, Olson EJ, Holland C, Chaney EJ, Marjanovic M, Pande P, Alex A, Boppart SA (2018) Investigating the healing mechanisms of an angiogenesis-promoting topical treatment for diabetic wounds using multimodal microscopy. J Biophotonics 11(3):e201700195
74. Bower AJ, Zane ZA, Zhao Y, Li J, Chaney EJ, Marjanovic M, Hughes-Earle AR, Boppart SA (2016) Longitudinal *in vivo* tracking of adverse effects following topical steroid treatment. Exp Dermatol 25(5):362–367
75. Bower AJ, Marjanovic M, Zhao Y, Li J, Chaney EJ, Boppart SA (2017) Label-free *in vivo* cellular-level detection and imaging of apoptosis. J Biophotonics 10(1):143–150
76. Tsai TH, Lin SJ, Lee WR, Wang CC, Hsu CT, Chu T, Dong CY (2012) Visualizing radiofrequency–skin interaction using multiphoton microscopy *in vivo*. J Dermatol Sci 65 (2):95–101
77. Masters BR, So PT, Gratton E (1997) Multiphoton excitation fluorescence microscopy and spectroscopy of *in vivo* human skin. Biophys J 72:2405–2412
78. Alex A, Frey S, Angelene H, Neitzel CD, Li J, Bower AJ, Spillman DR Jr, Marjanovic M, Chaney EJ, Medler JL, Lee W, Vasist Johnson LS, Boppart SA, Arp Z (2018) *In situ*

biodistribution and residency of a topical anti-inflammatory using fluorescence lifetime imaging microscopy. Br J Dermatol 179(6):1342–1350
79. Hopt A, Neher E (2001) Highly nonlinear photodamage in two-photon fluorescence microscopy. Biophys J 80:2029–2036
80. Koester HJ, Baur D, Uhl R, Hell SW (1999) Ca2+ fluorescence imaging with pico- and femtosecond two-photon excitation: signal and photodamage. Biophys J 77:2226–2236
81. Vogel A, Noack J, Hüttman G, Paltauf G (2005) Mechanisms of femtosecond laser nanosurgery of cells and tissues. Appl Phys B 81:1015–1047
82. Ji N, Magee J, Betzig E (2008) High-speed, low-photodamage nonlinear imaging using passive pulse splitters. Nat Methods 5:197–202
83. Masters B, So P, Buehler C, Barry N, Sutin J, Mantulin WW, Gratton E (2004) Mitigating thermal mechanical damage potential during two-photon dermal imaging. J Biomed Opt 9:1265–1270
84. Xi P, Andegeko Y, Weisel LR, Lozovoy VV, Dantus M (2008) Greater signal, increased depth, and less photobleaching in two-photon microscopy with 10 fs pulses. Opt Commun 281:1841–1849
85. Fu Y, Wang H, Shi R, Cheng JX (2006) Characterization of photodamage in coherent anti-Stokes Raman scattering microscopy. Opt Express 14:3942–3951
86. Rehberg M, Krombach F, Pohl U, Dietzel S (2010) Signal improvement in multiphoton microscopy by reflection with simple mirrors near the sample. J Biomed Opt 15(2):026017
87. Brown EB, Campbell RB, Tsuzuki Y, Xu L, Carmeliet P, Fukumura D, Jain RK (2001) *In vivo* measurement of gene expression, angiogenesis and physiological function in tumors using multiphoton laser scanning microscopy. Nat Med 7:864–868
88. Lin SJ, Hsu CJ, Wu RJ, Kuo CJ, Chen JS, Chan JY, Lin WC, Jee SH, Dong CY (2007) Quantitative multiphoton imaging for guiding basal-cell carcinoma removal. In: Proceedings from SPIE BiOS. Photonic Therapeutics and Diagnostics III, vol 6424, p 642404
89. Seidenari S, Arginelli F, Dunsby C, French P, König K, Magnoni C, Manfredini M, Talbot C, Ponti G (2012) Multiphoton laser tomography and fluorescence lifetime imaging of basal cell carcinoma: morphologic features for non-invasive diagnostics. Exp Dermatol 21(11):831–836
90. Graf BW, Boppart SA (2011) Multimodal *in vivo* skin imaging with integrated optical coherence and multiphoton microscopy. IEEE J Sel Top Quant Electron 18(4):1280–1286
91. You S, Sun Y, Chaney EJ, Zhao Y, Chen J, Boppart SA, Tu H (2018) Slide-free virtual histochemistry (Part II): detection of field cancerization. Biomed Opt Express 9:5253–5268
92. Boppart SA, You S, Li L, Chen J, Tu H (2019) Simultaneous label-free autofluorescence-multiharmonic microscopy and beyond. APL Photonics 4(10):100901

Photoacoustic Imaging

8

Li Lin and Lihong V. Wang

8.1 Introduction

With recent advances in photonics and optical molecular probes, optical imaging plays an increasingly important role in preclinical and clinical imaging. The manner in which light is scattered and absorbed in tissues can provide both structural and functional information in biomedical contexts. A fundamental constraint in pure optical imaging is light diffusion, which limits the spatial resolution in deep-tissue imaging. Consequently, pure optical imaging methods fall into two categories—ballistic optical microscopy and diffuse optical tomography. Limited to using only minimally scattered light, optical microscopy provides fine spatial resolution but with a low imaging depth (~1 mm) as defined by the optical diffusion limit in tissue [1]. In contrast, diffuse optical tomography can probe centimeters into tissue, but the scrambled paths of the diffuse photons render the image reconstruction mathematically ill-posed with poor spatial resolution [2]. Therefore, it remains a challenge for pure optical imaging to achieve fine spatial resolution at depths beyond the optical diffusion limit in tissue.

Fortunately, ultrasonic waves, which can be converted from photon absorption, scatter approximately 1000 times less than light in tissue. Based on the

L. Lin
Caltech Optical Imaging Laboratory, Andrew and Peggy Cherng Department of Medical Engineering, California Institute of Technology, Pasadena, CA, USA

L. V. Wang (✉)
Caltech Optical Imaging Laboratory, Andrew and Peggy Cherng Department of Medical Engineering, California Institute of Technology, Pasadena, CA, USA

Caltech Optical Imaging Laboratory, Department of Electrical Engineering, California Institute of Technology, Pasadena, CA, USA
e-mail: LVW@caltech.edu

X. Wei, B. Gu (eds.), *Optical Imaging in Human Disease and Biological Research*, Advances in Experimental Medicine and Biology 1355,
https://doi.org/10.1007/978-981-15-7627-0_8

Table 8.1 Comparison of various imaging modalities and their advantages and disadvantages (highlighted). *MRI* magnetic resonance imaging, *X-ray CT* X-ray computed tomography

Properties \ Modalities	X-ray CT	Ultrasound	MRI	Pure optical tomography	PAI
Functional imaging	No	No	Yes	Yes	Yes
Spatial resolution	Excellent	Good	Good	Poor	Good
Imaging speed	High	High	Low	High	High
Ionizing radiation	Yes	No	No	No	No

photoacoustic effect, absorption of photons by biomolecules thermoelastically induces a pressure rise which propagates as ultrasonic waves. The amplitude of the ultrasonic wave is proportional to the optical absorption. Photoacoustic imaging (PAI) forms high-resolution images by detecting the low-scattered ultrasonic waves and consequently revealing the optical absorption as the imaging contrast. Accordingly, PAI combines the advantages of both optical excitation and acoustic detection. This technology has undergone rapid development in the last decade, having become the largest conference topic at SPIE Photonics West in 2010. The conversion from optical to ultrasonic energy brings multiple inherent advantages: (1) the low acoustic scattering enables PAI to break through the optical diffusion limit and achieves multiscale high-resolution imaging of biological structures ranging in size from organelles to organs; (2) rich optical contrast based on chemical compositions, which express wavelength-dependent light absorption; (3) PAI images optical absorption with 100% sensitivity and provides background-free detection because non-absorbing tissue components present no background [3]; (4) PAI is speckle free [4].

PAI also has unique advantages when compared with other mainstream biomedical imaging modalities (Table 8.1), making a broad impact both in preclinical studies and clinical practice. Applications of PAI have been established in vascular biology, oncology, neurology, ophthalmology, dermatology, gastroenterology, and cardiology. Here, we first introduce the fundamentals and state-of-the-art embodiments of PAI with multi-scalability. Next, rich photoacoustic contrasts are shown for tissue anatomies and functions, as well as for metabolic, molecular, and genetic processes. Then, high-impact applications in preclinical studies and clinical practice are highlighted. Finally, we envision future technology development and discuss remaining challenges.

8.2 Fundamentals of Photoacoustic Imaging

In PAI, a short-pulsed (usually in nanoseconds) light source is typically used to irradiate the tissue. Following the temporally confined optical absorption, an initial temperature rise induces a pressure rise. The pressure rise is proportional to the temperature rise and propagates as an ultrasonic wave (i.e., photoacoustic wave). Approximately, a 1-mK temperature rise results in an 800-Pa pressure rise, which is

on the order of the noise level of a typical ultrasonic transducer. If the pulse duration is shorter than the thermal relaxation time and the stress relaxation time, the excitation satisfies both thermal and stress confinements and the initial pressure rise p_0 can be expressed as:

$$p_0 = \Gamma \eta_{\text{th}} \mu_{\text{a}} F, \tag{8.1}$$

Where Γ is the Gruneisen parameter (dimensionless) and η_{th} denotes the percentage of absorbed light converted into heat. They are usually approximated as constants, although Γ has been found to increase with equilibrium temperature, enabling PAI to image temperature with a sensitivity of 0.16 °C—useful for monitoring thermal therapy [5]. μ_{a} is the optical absorption coefficient (cm^{-1}) and F represents the local optical fluence (J/cm^2), also called radiant exposure. Therefore, if p_0 can be measured and F is known, μ_{a} can be recovered. Since p_0 is linearly proportional to the local optical fluence F, increasing the optical fluence within the safety limit is always preferable for obtaining higher signal-to-noise ratio (SNR) in photoacoustic images. Averaging photoacoustic signals will also improve the SNR, which, however, is proportional to the square root of the signal averaging times.

Starting from the initial pressure p_0, an acoustic wave propagates at the speed of sound (v_{s}) in the material. A general photoacoustic equation in the time-domain [6] can be used to describe the propagation in an inviscid medium:

$$\left(\nabla^2 - \frac{1}{v_{\text{s}}^2}\frac{\partial^2}{\partial t^2}\right) p\left(\vec{r}, t\right) = -\frac{\beta}{C_p}\frac{\partial H\left(\vec{r}, t\right)}{\partial t}, \tag{8.2}$$

where $p\left(\vec{r}, t\right)$ is the acoustic pressure at position $\vec{r}$ and time t. β and C_p denote the isothermal compressibility and specific heat capacity at constant pressure, respectively. $H\left(\vec{r}, t\right)$ is the heating function defined as the thermal energy converted per unit volume and per unit time; it is related to the optical fluence rate Φ by $H = \eta_{\text{th}}\mu_{\text{a}}\Phi$. Solving Eq. (8.2) with the Green's function approach, the delta heating response of an arbitrary absorbing object is:

$$p\left(\vec{r}, t\right) = \frac{1}{4\pi v_{\text{s}}^2}\frac{\partial}{\partial t}\left[\frac{1}{v_{\text{s}} t}\int \mathrm{d}\vec{r}' \, p_0\left(\vec{r}'\right)\delta\left(t - \frac{\left|\vec{r} - \vec{r}'\right|}{v_{\text{s}}}\right)\right]. \tag{8.3}$$

For an ideal point transducer placed at $\vec{r}_{\text{d}}$, the detected photoacoustic signal can be written by reforming Eq. (8.3) as:

$$p_{\mathrm{d}}\left(\vec{r}_{\mathrm{d}}, t\right) = \frac{\partial}{\partial t}\left[\frac{t}{4\pi}\iint\limits_{\left|\vec{r}_{\mathrm{d}}-\vec{r}\right|=v_{\mathrm{s}}t} p_0\left(\vec{r}\right)\mathrm{d}\Omega\right], \tag{8.4}$$

where $\mathrm{d}\Omega$ is the solid-angle element of $\vec{r}$ with respect to the point at $\vec{r}_{\mathrm{d}}$. Eq. (8.4) indicates that the detected pressure at time t comes from sources over a spherical shell centered at the detector position $\vec{r}_{\mathrm{d}}$ with a radius $v_{\mathrm{s}}t$. To reconstruct the optical absorption in biological tissue, we want to use the detected pressure $p_{\mathrm{d}}\left(\vec{r}_{\mathrm{d}}, t\right)$ to reveal the initial pressure distribution $p_0\left(\vec{r}\right)$, which can be obtained by inverting Eq. (8.4). The so-called universal back projection (UBP) algorithm for image reconstruction can be expressed in the temporal domain as [6, 7]:

$$p_0\left(\vec{r}\right) = \frac{1}{\Omega_0}\int\limits_S \mathrm{d}\Omega_0\left[2p_{\mathrm{d}}\left(\vec{r}_{\mathrm{d}}, t\right) - 2t\frac{\partial p_{\mathrm{d}}\left(\vec{r}_{\mathrm{d}}, t\right)}{\partial t}\right]\Bigg|_{t=\left|\vec{r}_{\mathrm{d}}-\vec{r}\right|/v_{\mathrm{s}}}. \tag{8.5}$$

Here, Ω_0 is the solid angle of the whole detection surface S with respect to a given source point at $\vec{r}$. Eq. (8.5) indicates that the initial pressure $p_0\left(\vec{r}\right)$ can be obtained by back projecting the filtered data, $\left[2p_{\mathrm{d}}\left(\vec{r}_{\mathrm{d}}, t\right) - 2t\frac{\partial p_{\mathrm{d}}\left(\vec{r}_{\mathrm{d}}, t\right)}{\partial t}\right]$, onto a collection of concentric spherical surfaces that are centered at each transducer location $\vec{r}_{\mathrm{d}}$, with $\mathrm{d}\Omega_0/\Omega_0$ as the weighting factor applied to each back projection. The first derivative with respect to time represents a ramp filter, which suppresses low-frequency signals. The UBP reconstruction algorithm is essentially a method for sophisticated triangulation of photoacoustic sources from the time-resolved acoustic signals [8]. We note that UBP assumes the medium is acoustically lossless and homogeneous. Significant acoustic inhomogeneity of the sample may introduce reconstruction distortions, which, however, may be corrected or minimized using modified algorithms that take into account the acoustic inhomogeneity [9].

8.3 Major Implementations of Multiscale Photoacoustic Imaging

The elegant marriage between light and sound endows PAI with the unique capability of scaling its spatial resolution and imaging depth across both optical and ultrasonic dimensions. Currently, PAI has three major implementations: photoacoustic microscopy (PAM), photoacoustic endoscopy (PAE), and photoacoustic computed tomography (PACT). While PAM and PAE generally aim to produce micrometer-scale resolution with millimeter imaging depth, PACT can be implemented to image centimeter deep at both mesoscopic and macroscopic resolution. Microwave-induced thermoacoustic tomography (TAT) is a macroscopic

imaging modality that bears resemblance to PACT. Instead of using light, TAT utilizes microwaves for excitation, providing deeper penetration with dielectric contrast.

8.3.1 Photoacoustic Microscopy (PAM)

Here, we define microscopy as an imaging modality with a spatial resolution finer than 50 μm, where the unaided eye can only discern features larger than approximately 50 μm. In PAM, both the optical excitation and ultrasonic detection are focused, and the dual foci are usually configured confocally to maximize sensitivity. Volumetric imaging is realized by two-dimensional (2-D) raster scanning of the dual foci of optical excitation and ultrasonic detection. At each scanning position, a laser pulse excites tissue predominantly along a line in the elevational direction and the ultrasonic transducer receives photoacoustic signals along the line and records the time-of-arrival, producing a one-dimensional (1D) depth-resolved image (A-line). Accordingly, a two-dimensional (2D) transverse scanning generates a 3D image. While the depth information is resolved by the acoustic time of flight, the lateral resolution is determined by the product of the point spread functions of the light illumination and acoustic detection. Depending on whether the optical or ultrasonic focus is finer, PAM is further classified into optical-resolution (OR) and acoustic-resolution (AR) PAM.

In OR-PAM, optical focusing can readily confine the photoacoustic excitation for high lateral resolution while maintaining substantial imaging depth (Fig. 8.1a). OR-PAM provides lateral resolution at the subcellular or cellular scale ranging from a few hundred nanometers to a few micrometers. However, the imaging depth is limited by optical diffusion to 1.2 mm in vivo [10]. At depths beyond the optical diffusion limit and up to a few millimeters, AR-PAM achieves high resolution by taking advantage of the much lower acoustic scattering (Fig. 8.1b). Despite the loosely focused laser beam, lateral resolution of tens of micrometers is achieved by diffraction-limited acoustic detection. In both PAM modalities, the axial resolution is given by the corresponding distance of the full width at half maximum (FWHM) of the temporal signal envelope. Accordingly, if the impulse response of the ultrasonic transducer has a Gaussian envelope, the axial resolution can be estimated as $0.88v_s/B$, where B is the ultrasonic transducer bandwidth which is generally proportional to the transducer's central frequency. Although a higher bandwidth improves the axial resolution of the imaging system, the greater acoustic attenuation at higher frequencies leads to a reduction in imaging depth.

To convert each photoacoustic signal to a depth-resolved image, the Hilbert transformation is normally used to extract the envelope of the short-pulsed photoacoustic signal. Because the transducer is focused in PAM and each signal acquired by the transducer directly represents a 1-D image after Hilbert transformation, UBP is usually not applied to PAM.

PAM is safe for human subjects since it delivers a transient fluence (mJ/cm^2) well within the American National Standard Institute (ANSI) safety standard on the skin

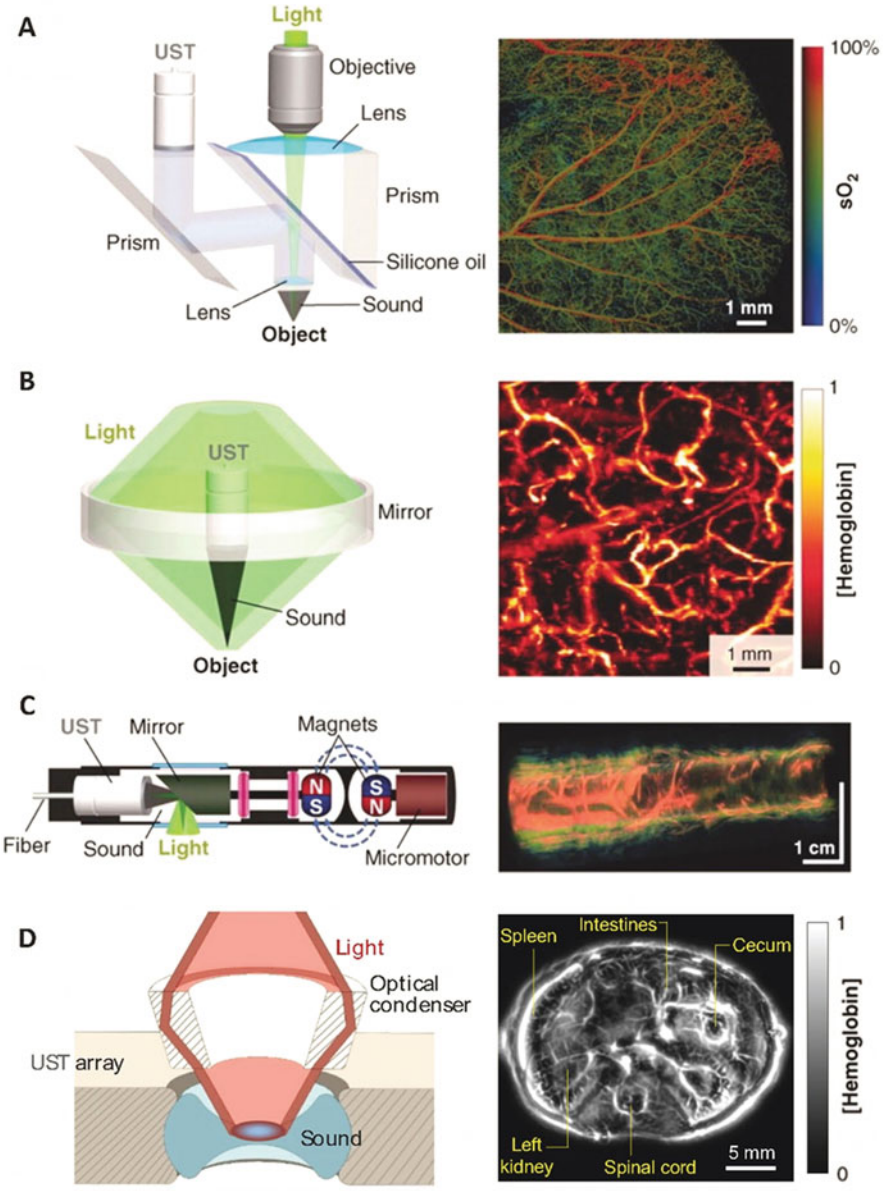

Fig. 8.1 Major implementations of PAI and representative in vivo images. (**a**) OR-PAM of a mouse ear showing hemoglobin oxygen saturation (sO_2) [12]. (**b**) AR-PAM of a human palm showing normalized total hemoglobin concentration [hemoglobin] [15]. (**c**) PAE of a rabbit esophagus and adjacent internal organs, including the trachea and lung [17]. (**d**) Circular-array PACT of a mouse abdominal cross section. *UST* ultrasonic transducer [23]

surface [11]. Since PAM works in raster scanning mode, the exposure duration of any given point on the skin surface is short.

8.3.1.1 Optical-Resolution Photoacoustic Microscopy (OR-PAM)

In OR-PAM, the laser beam is focused by a microscope objective to a diffraction-limited spot. The diameter of the spot depends on the optical wavelength (λ_{Opt}) and the numerical aperture (NA_{Opt}) of the optical focusing lens, and can range from several hundred nanometers to several micrometers. In typical OR-PAM, the objective forms an Airy diffraction pattern whose FWHM size determines the lateral resolution of OR-PAM ($R_{OR\text{-}PAM}$):

$$R_{OR\text{-}PAM} = 0.51\frac{\lambda_{Opt}}{NA_{Opt}}. \tag{8.6}$$

Relying on the tight optical focus, the penetration of an OR-PAM system is limited to about one transport mean free path in tissue. By using longer optical wavelengths, which have longer transport mean free paths, the penetration limit can be increased.

To maximize the imaging sensitivity, the optical and acoustic foci are often configured coaxially and confocally. In a representative OR-PAM system (Fig. 8.1a) [12], an optical-acoustic beam combiner is applied beneath the objective to confocally transmit the light and reflect the ultrasound. The combiner consists of two prisms sandwiching a thin layer of silicone oil, which has matched optical refractive indices but mismatched acoustic impedances. To provide focused acoustic detection, a concave lens is ground into the bottom of the combiner. An unfocused ultrasonic transducer with a broad bandwidth is attached to the top of the combiner.

Equipped with a water-immersible scanner (e.g., galvo mirror), modern high-speed OR-PAMs have achieved frame rates over a few hertz when imaging millimeter-scale 3D regions [13]. Capitalizing on its high spatial resolution, OR-PAM can image vasculature in the mouse ear (Fig. 8.1a), eye, brain, and human skin clearly. Other than imaging hemoglobin, OR-PAM can use ultraviolet light to excite and acquire histology-like images by label-free simultaneous sensing of DNA/RNA [14].

8.3.1.2 Acoustic-Resolution Photoacoustic Microscopy (AR-PAM)

The most mature version of AR-PAM is dark-field AR-PAM, in which a conical lens is used to transform the pulsed laser beam into a ring-shaped illumination pattern. The illumination is illumination and then is weakly focused into biological tissues to overlap the tight ultrasonic focus (Fig. 8.1b) [15]. Dark-field optical illumination minimizes the interference caused by strong photoacoustic signals from the tissue surface. Since the ultrasonic focus is smaller than the optical focus, the lateral resolution of AR-PAM is determined acoustically as

$$R_{\text{AR-PAM}} = 0.71 \frac{\lambda_{\text{Act}}}{\text{NA}_{\text{Act}}}, \tag{8.7}$$

where λ_{Act} and NA_{Act} denote the center wavelength of the acoustic wave and the numerical aperture of the ultrasonic detector, respectively. For instance, a lateral resolution of 48 μm can be achieved with a center frequency of 50 MHz and an NA_{Act} of 0.44. This resolution, although adequate for many biomedical applications, cannot resolve fine structures such as capillaries (diameter: 4–9 μm). To provide high resolution, the acoustic detector must have a wide bandwidth and a large NA. However, increasing the ultrasonic frequency immoderately can result in an undesirably small penetration depth since the ultrasonic attenuation in biological tissue generally increases linearly with the frequency (for example, 0.7–3 dB/(cm/MHz) for human skin [16]). Therefore, a large NA is essential for the desired resolution.

8.3.2 Photoacoustic Endoscopy (PAE)

To image internal organs such as the esophagus and colon, PAE has been intensively investigated in recent years. Because of the confinement in space, PAE often resorts to PAM. In a representative PAE design (Fig. 8.1c) [17], a multimode optical fiber is used to deliver pulsed laser light through the central hole of a ring transducer. A magnet-driven mirror rotates both the optical illumination and the acoustic detection to produce circumferential cross-sectional scanning. Volumetric imaging is achieved by pulling back the entire probe. While pure optical endoscopy has an imaging depth within the optical diffusion limit, PAE that is based on AR-PAM has shown a 7-mm imaging depth in the dorsal region of a rat colon ex vivo (Fig. 8.1c).

8.3.3 Photoacoustic Computed Tomography (PACT)

Rather than relying on raster scanning as in photoacoustic microscopy (PAM), PACT uses an ultrasonic transducer array to detect PA waves emitted from an object at multiple view angles simultaneously, allowing a much faster cross-sectional or volumetric imaging speed at the expense of system and computational costs. In PACT, the entire region of interest (ROI) is excited by an expanded laser beam for wide-field illumination.

After the acoustic waves are detected by the transducers, various reconstruction algorithms can be applied for PACT image formation [18]. The UBP based on Eq. (8.5) is commonly utilized because of its high accuracy and ease of implementation. In the reconstructed images, tissue interfaces are important for identifying organ boundaries. Because each boundary is composed of small flat segments and each segment transmits acoustic waves along the two opposite directions perpendicular to it, a boundary can be well-reconstructed if the local normal directions of the boundary pass through the transducers [19]. Therefore, the detection surface with

respect to the imaging object should be 4π steradians and 2π radians to exactly reconstruct an arbitrary boundary in 3D and 2D, respectively. For instance, placing the object at the center of a ring-shaped transducer array enables the generated photoacoustic signals within the imaging plane be detected at different receiving angles over a complete 2π-radian circle. In some practical measurements, however, only a limited space around the tissue sample is available for ultrasound detection. For example, clinical practices widely use linear-array transducers due to their versatility and free-hand guidance. However, the linear array can only detect photoacoustic signals from a limited range of view angles. The UBP reconstruction algorithm can be extended straightforwardly to the limited-angle view case, in which the reconstruction may be incomplete and reconstruction artifacts may occur. The solid-angle weighting factor in the UBP Eq. (8.5), however, can compensate for the variations in the detection views. Ultrasonic transducer arrays with various populating patterns, such as line, plane, half ring, full ring, and hemisphere, have been employed and demonstrated in both animal and clinical applications.

In linear-array PACT, a multimode optical fiber bundle is bifurcated to flank the handheld ultrasonic array for dark-field optical illumination with minimal signals from the tissue surface [20]. A single laser pulse—with a safe exposure to the tissue ($\leq$20 mJ/cm^2 in the visible spectral range)—yields a 2D image. The 2D resolutions in the imaging plane are derived from reconstruction, whereas the orthogonal resolution (imaging cross section thickness) comes from cylindrical acoustic focusing. The imaging plane can be further translated along the orthogonal dimension for 3D imaging.

Planar-view PACT uses either a 2D ultrasonic transducer array [21] or a Fabry–Perot interferometer (FPI) [22]. Using a 2D transducer array usually provides a higher frame rate, while FPI-based instruments generally have higher sensitivity and a larger receiving angle. In FPI-based system, the deformation of pressure-sensitive materials (e.g., polymer) is measured by optical resonance. By raster scanning the probe optical beam across the FPI surface, photoacoustic waves can be mapped in 2D.

Circular-array PACT (Fig. 8.1d) is designed to accommodate cylindrical objects and to provide panoramic detection within the field of view (FOV). Unlike the partial-view detection in linear-array PACT, all photoacoustic waves propagating in the imaging plane are detected by the circular array, regardless of propagation direction. The full-view detection provides high-quality images without missing boundaries. The merits of circular-array PACT was demonstrated by small-animal deep brain and whole-body imaging with high spatiotemporal resolution [23].

Rotational scanning of an arc-shaped [24] or hemispherical array [25] have been implemented for partial spherical-view coverage and dense sampling, providing isotropic 3D resolution. Since each transducer element has a flat surface with a size on the order of acoustic wavelength, 3D images can be reconstructed by projecting the photoacoustic signal into the 3D space. It must be noted that the light distribution in the object should not be disturbed during PACT scanning, otherwise the transducer array at different scanning positions would attempt to recover time-varying optical absorption distributions.

For all detection geometries, the axial resolution is spatially invariant and is primarily determined by the bandwidth of the ultrasonic transducer [26]. For a wideband transducer, the axial resolution, R_{axial}, approximates $0.6\lambda_c$, where λ_c is the acoustic wavelength at the high cutoff frequency. For spherical- and cylindrical-view PACTs, the lateral resolution can be characterized by $\sqrt{R_{\text{axial}}^2 + \left(\frac{r}{r_0}d\right)^2}$, where r is the distance between the imaging point and the scanning center, r_0 is the radius of the scan circle, and d is the width of each transducer element. For linear-array PACTs, the lateral resolution can be characterized by $\sqrt{R_{\text{axial}}^2 + d^2}$.

There are a few important factors a researcher/engineer should consider when building a PACT system: (1) Since PACT reconstruction assumes light has a uniform or predicable distribution, light illumination needs to be carefully designed. High optical fluence within the safety limit is preferable for high SNR; (2) A large view angle of the transducer array or detection aperture is helpful to minimize the loss of information and improve the image quality; (3) Since photoacoustic signals generated from the deep tissue could suffer both light and acoustic attenuation, analog preamplifiers connected between the array and data acquisition systems (DAQ) can amplify the weak photoacoustic signals before cable noise compromises the SNR; (4) In addition to the temporal Nyquist sampling law, one should also consider the spatial Nyquist sampling criterion [23]. Inadequate spatial sampling will result in limited FOV and undersampling artifacts; (5) High imaging speed is helpful to reduce the motion-induced artifacts. Although co-registration methods can partially mitigate the motion distortion, the non-rigidity of the biological tissue compromises the effectiveness; (6) Proper grounding of the metallic housing of the transducer array, preamplifiers, and DAQs is important to reduce noise. The motors are often well-shielded to eliminate electromagnetic interference.

8.3.4 Microwave-Induced Thermoacoustic Tomography (TAT)

The high imaging speed and deep penetration is the key advantage of PACT over PAM. For light incident upon a homogeneous scattering half-space, expression for light fluence can be readily simplified as $F = F_0 \cdot e^{-(\mu_{\text{eff}} \cdot z)}$ that is well known as Beer's law. $\mu_{\text{eff}} = \sqrt{3\mu_a(\mu_a + \mu_s')}$ is the effective absorption coefficient with a reduced scattering coefficient μ_s'. Using near-infrared (NIR) light, PACT can image blood vessels as deep as 4 cm in the human breast [27]. Nevertheless, deeper penetration is necessary for many clinical applications, including human brain or trunk imaging.

By simply replacing the laser with a pulsed microwave source and applying proper shielding of the transducers and electronics, microwave-induced TAT images can be generated using the same reconstruction algorithm. Different from visible light absorption in which heat is generated by non-radiative relaxation of excited electrons, microwaves generate heat through the electrical conductivity of tissues.

Molecular relaxation and ionic conduction dominate this response at microwave frequencies, which generally relate to water and salt content. Therefore, the difference in dielectric properties of biological tissues can be revealed by TAT.

Due to the long microwave wavelength, objects are usually placed in the near field of the antenna. Therefore, the positions and orientations of the antennas need to be configured to distribute the microwave energy homogeneously in the tissue. Several techniques have been developed for this purpose. For instance, researchers used a power divider to equally distribute the microwave energy from a source into multiple antennas located around the object, allowing for uniform energy distribution. Another approach is to use a high-permittivity immersion medium such as deionized water, which reduces the wavelength and extends the working distance of the tissue toward the far-field of the antenna.

8.3.5 Multiscale Photoacoustic Imaging

In OR-PAM, the lateral resolution and imaging depth are mainly determined by the optical wavelength and the numerical aperture (NA) of the optical objective. A higher NA improves the lateral resolution but decreases the depth of focus [28]. In AR-PAM, the spatial resolution is acoustically defined in the optically diffusive region. Considering the frequency-dependent acoustic attenuation, AR-PAM typically employs a transducer with a central frequency of a few tens of megahertz (MHz) to provide an imaging depth of several millimeters and a lateral resolution of a few tens of micrometers. In PACT, low-frequency ($<$10 MHz) transducers are commonly used to provide an imaging depth greater than 1 cm. For a low-frequency ultrasonic detection system, the imaging depth is mainly limited by light attenuation, which is the combined effect of optical absorption and scattering. With recent advances in microwave-induced TAT [29, 30], we expect the imaging depth can reach tens of centimeters in the tissue, and eventually human whole-body imaging will be achieved.

The imaging depth of OR-PAM is approximately proportional to the chosen lateral resolution within the optical diffusion limit. Beyond this limit, the imaging depth is primarily determined by the acoustic attenuation. Since both transducer center frequency and bandwidth are inversely proportional to the desired imaging depth, the lateral and axial resolutions are proportional to the imaging depth. For both regimes, the ratio of the imaging depth to the spatial resolution is roughly a constant of 200 [3], making PAI a high-resolution modality across all length scales. The optimal tradeoff between spatial resolution and imaging depth depends on the application.

8.4 Multi-Contrast Photoacoustic Imaging

PAI can be used for both functional and molecular imaging. Functional imaging is generally based on endogenous contrast (e.g., oxy- and deoxy-hemoglobin), whereas molecular imaging utilizes exogenous contrast (e.g., organic dyes) to stain biomarkers in vivo. Functional imaging reveals physiological activity usually at the organ or tissue level, while molecular imaging typically measures biological and pathophysiological processes at the molecular level.

With selected optical wavelengths, PAI can probe a wide variety of endogenous or exogenous absorbers to reveal the anatomy, function, metabolism, and molecular or genetic processes in biological systems in vivo. Because PAI is sensitive to optical absorption and each biological component has a distinct absorption spectrum, by tuning the excitation light to multiple wavelengths, the photoacoustic signal amplitude will vary according to the absorption spectrum of the target. Since anatomical structure may not be able to fully reflect the true physiological and pathological conditions, multi-contrast PAI can potentially provide more comprehensive information for diagnosis, staging, and treatment of diseases.

8.4.1 Endogenous Contrasts

Endogenously, DNA/RNA, hemoglobin, water, lipids, protein, and melanin provide important anatomical and functional contrast. Capitalizing on the strong ultraviolet absorption of DNA and RNA, OR-PAM can image individual cell nuclei without staining (Fig. 8.2a), providing a label-free substitute for ex vivo HE-staining histology [31]. This technology can potentially provide intraoperative demarcation of cancer. Hemoglobin, as a primary oxygen carrier, is essential to tissue metabolism. Using hemoglobin's predominant optical absorption in the visible and short-wavelength NIR regions (i.e., 380–1100 nm) over other absorbers, spectroscopic photoacoustic measurement separates the individual contributions from oxy-hemoglobin (HbO_2) and deoxy-hemoglobin (Hb) to the signal, and thus the total concentration (C_{Hb}) and oxygen saturation (sO_2) can be computed (Fig. 8.2b). These two factors are the most commonly used indices of blood perfusion and oxygenation, respectively. Abnormal concentrations of water, lipids, and protein can be important disease indicators [3]. Their relatively strong optical absorption in the long-wavelength NIR and mid-infrared (MIR) ranges allows PAI to map their distributions in vivo (Fig. 8.2c) [32]. Melanin, a major pigment in the skin and most melanomas, has broadband optical absorption, which can be spectroscopically distinguished from hemoglobin absorption. PAI of the melanoma anatomy and the surrounding vascular function provides an unprecedented opportunity for understanding the interactions between a tumor and its microenvironment and for noninvasively detecting and staging melanoma (Fig. 8.2d) [33].

In addition to the aforementioned static contrast agents, PAI can also image dynamic contrast, including hemodynamics (e.g., blood flow) and thermodynamics (e.g., temperature variation). PAI of blood flow is based on the photoacoustic

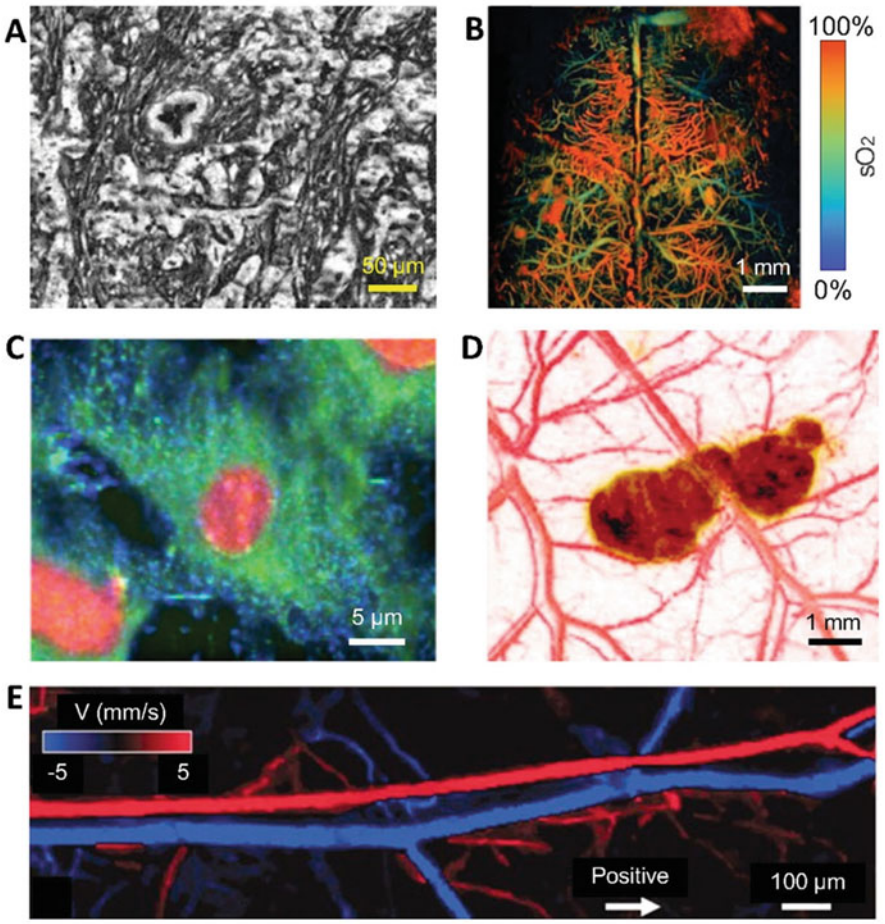

Fig. 8.2 Multi-contrast PAI with endogenous contrasts. (**a**) Ultraviolet OR-PAM of unstained breast tissue slice by excitation of DNA and RNA [31]. (**b**) OR-PAM of oxygen saturation of hemoglobin (sO_2) in the mouse brain cortex [13]. (**c**) Mid-infrared OR-PAM of lipids (blue), proteins (green) and nucleic acids (red) [32]. (**d**) AR-PAM of a subcutaneously inoculated B16 melanoma and the surrounding vasculature on the back of a living mouse [33]. (**e**) OR-PAM of blood flow velocity and direction in the ear of a living mouse [35]

Doppler effect [34]. Figure 8.2e shows both blood flow direction and velocity in a living mouse [35]. The high optical absorption contrast greatly increases imaging sensitivity, enabling the detection of intravascular blood. Furthermore, the excellent scalability of Doppler PAI bridges the spatial gap between scattering-based ultrasonic and optical technologies. The imaging of thermodynamic contrast is essential for thermal therapy. PAI is capable of high-resolution temperature imaging in deep tissue because the initial photoacoustic pressure depends on the equilibrium

temperature. Tissue phantom experiments showed that PAI has a sensitivity on the order of 0.1 °C [5].

PAI can be used for metabolic imaging, by imaging with both static and dynamic contrast. The measurement of vessel diameter, total hemoglobin concentration, sO_2, tissue volume of interest, and blood flow velocity allows PAI to evaluate the metabolic rate of oxygen (MRO_2) [36]. Because photoacoustic signal amplitude also depends on the local optical fluence, accurate laser fluence compensation is important for quantifying the absolute concentrations of components. To compensate the optical fluence in deep tissue, a potential solution is to incorporate PAI with diffuse reflectance spectroscopy [37] or diffuse optical tomography [38], which can quantify the tissue's optical properties or the fluence distribution.

8.4.2 Exogenous Contrasts

Exogenous contrast agents further extend PAI to molecular and genetic imaging. Organic dyes, nanoparticles, and reporter gene products are excellent photoacoustic contrast agents. The primary advantage of gold nanoparticles lies in their high absorption tuned to the optical window (~730 nm), minimizing endogenous absorption. Moreover, the bio-conjugation capability of nanoparticles enables biomarker targeting for both drug delivery and molecular imaging [39]. Recently, the utilization of iron oxide and gold-coupled core-shell nanoparticles as a photoacoustic contrast agent has led to the development of magnetomotive PAI [40], which suppresses the non-magnetomotive background and markedly improves the contrast and specificity of PAI. The relatively slow clearance of nanoparticles can be either an advantage or disadvantage in different applications.

While FDA has not approved the clinical usage of most nanoparticles, many organic dyes have been approved for human use. Because of their small molecular sizes (typically ~1 nm), organic dyes can clear rapidly from the body and some can penetrate the blood–brain barrier. Imaging exogenous contrast agents can help to reveal structures with low optical absorption at certain wavelengths (e.g., lymph nodes) and label pathological phenomena [41]. Spectral separation has also been attempted using indocyanine green (ICG), a dye approved by the FDA for human use. For example, vascular permeability changes in the tumor can be assessed by imaging the leakage of ICG [42].

Genetically encoded contrast in PAI is complementary to intrinsic contrast. The use of reporter genes expressing absorbing proteins enables the visualization of dynamic cellular and molecular processes. Chromoproteins can provide high photoacoustic signal generation efficiency, but have not yet been expressed efficiently in mammalian cells [43]. So far, PAI of photo-switchable proteins shows great potential for in vivo imaging since the signal difference between on and off states suppresses the background and improves the image contrast [44]. Reporter genes for PAI have the potential to be applied in a variety of fundamental biomedical studies that require high spatial resolution at extended penetration depths. To give an example, as the tumor grew, LacZ genes expressed into β-galactosidase, which

metabolized the locally injected lactose-like substrate into highly absorbing blue products, providing contrast for genetic PAI in vivo [45]. Applications include but are not limited to visualizing the expression of genes of interest, understanding signal transduction pathways and protein interactions, and longitudinal monitoring of tumor growth [22].

All molecules can potentially be imaged by PAI at appropriate wavelengths, whereas only a small subset of molecules are fluorescent. Even fluorescent proteins from reporter genes have been imaged in vivo by PAI [46]. Because most fluorophores have imperfect fluorescence quantum yields, PAI can rely on the thermal relaxation to achieve deeper penetration at high spatial resolution than its fluorescence counterpart.

8.5 Photoacoustic Imaging in Biological Research

To date, PAI is the only high-resolution optical imaging modality that breaks the optical diffusion limit. With its multiscale and multi-contrast imaging capability, PAI has irreplaceable advantages over other imaging modalities in biological research and has been applied in many different disciplines, including cardiology, dermatology, oncology, ophthalmology, gastroenterology, hematology, and neurology. PAI has been used for small-animal imaging of the brain, ear, eye, liver, intestine, and skin using anatomical, functional, molecular, and metabolic contrast. As for object size, PAI can detect objects ranging from organelles to human organs or the whole body of small animals. In this section, rather than covering details of all the applications, we will introduce the most recent advances and significant applications of PAI in biological research.

8.5.1 Mid-infrared Imaging with Ultraviolet-Localized OR-PAM

PAI using mid-infrared (MIR) excitation provides rich chemical and structural information of biological samples. Owing to optical diffraction, the long wavelengths of conventional MIR microcopy have limited the technique's lateral resolution; moreover, the strong MIR absorption of water results in high background and reduces the contrast when imaging fresh biological samples. A PAI modality called ultraviolet-localized MIR photoacoustic microscopy has overcome these limitations by combining the fine focus of the ultraviolet beam with MIR contrast (Fig. 8.2c) [32]. In this approach, a pulsed MIR laser thermally excites the sample at a focal spot, resulting in a transient temperature rise proportional to the magnitude of the MIR absorption. Ultraviolet laser beams photoacoustically detect the temperature rise by imaging the focal spot (confocally aligned with the MIR beam) before and after the MIR excitation. This temperature measurement method is based on the Gruneisen relaxation effect: photoacoustic signal amplitude rises with temperature [47]. While this imaging method reveals MIR absorption contrast, its lateral resolution is determined by the ultraviolet focus, which is an order of magnitude finer than

the MIR focus. In addition, ultraviolet wavelength light in the range of 200–230 nm is highly absorbed by most biomolecules [48] but is totally transmissive in water [49]. Thus, the ultraviolet signal suppresses the strong water background of MIR absorption. Such a method provides convenient high-resolution and high-contrast MIR imaging, which can benefit the diagnosis of fresh biological samples.

8.5.2 High-Speed PAI of Small-Animal Brain Functions

PAI has been extensively applied to brain studies. Using high-speed OR-PAM, optical-resolution mouse cortical images, i.e., at micrometer level resolution, were obtained (Fig. 8.2b). Using a full-ring array or scanned linear array, the cross-sections of the entire mouse/rat brain on the coronal plane have been imaged in vivo [23, 50]. Capitalizing on multiscale PAI with high imaging speed, researchers have imaged cerebral hemodynamics and oxygen metabolism.

Recently, a few high-speed PAM systems have been reported for mouse brain function imaging in action. Working as OR-PAM, one system utilizes a water-immersed microelectromechanical (MEMS) scanning mirror along with a 500 kHz repetition rate laser, achieving a 2D frame rate of 400 Hz over a 3-mm scanning range. By using a single-wavelength pulse-width-based method, the system can perform high-speed sO_2 imaging and visualizes the cortex vasculature in detail with the skull intact (Fig. 8.2b) [13].

Multi-wavelength OR-PAM has been reported to provide the quantification of two key metabolic parameters—oxygen extraction fraction (OEF) and the cerebral metabolic rate of oxygen ($CMRO_2$). This enables quantitative analysis of the hemodynamic and oxygen-metabolic responses of the mouse brain to isoflurane [51]. Side-by-side comparison of the awake and anesthetized brains suggests that isoflurane induces elevated blood flow, diameter-dependent arterial dilation, and reduced OEF in a dose-dependent manner. As a result of the combined effects, $CMRO_2$ is significantly reduced in the anesthetized brain, which suggests a mechanism for anesthetic neuroprotection.

Linear-array PACT has been used to map the microvascular network of a whole mouse brain and reveal its hemodynamic activities with the skull intact [50]. The linear array was scanned in the coronal plane to enlarge the view angle. Data collected from different angles was synthesized to form a full-view image in which vessels were clearly revealed (Fig. 8.3a). Neural activities during an epileptic seizure and the epileptic wave spreading around the injection were observed. To further increase the imaging speed, researchers used a full-ring transducer array with 512 elements to image the rat brain in the coronal plane [26]. Utilizing 1064-nm light, which suffers less scattering in the tissue than that of the visible light, PACT sees through the rat whole brain and detects the functional connectivity in the deep brain (up to 9.7 mm).

PACT with 2-NBDG and IRDye-800-2DG was used to study mouse brain metabolism [52]. Similar to the fluorodeoxyglucose used in PET, 2-NBDG and IRDye-800-DG are two glucose analogs which are transported into cells but cannot

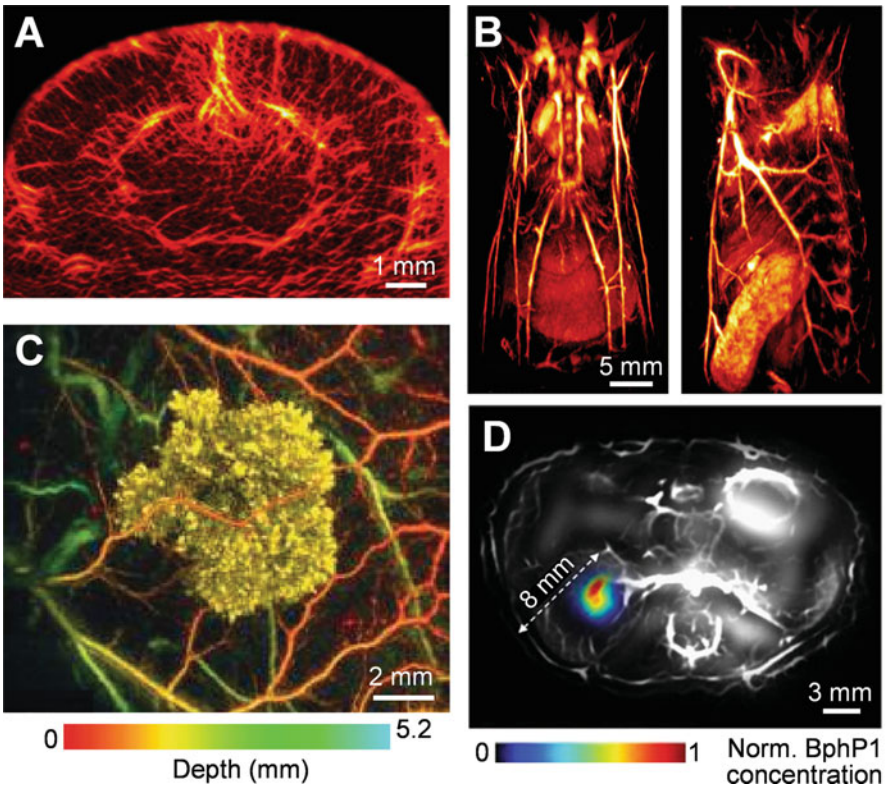

Fig. 8.3 PAI in biological research. (**a**) Coronal plane PACT image of a mouse brain through the intact skull (Bregma −1.0 mm) [50]. (**b**) Whole-body PACT images of a mouse trunk in 3D [25]. (**c**) In vivo PACT image of tyrosinase-expressing K562 cells (false-colored yellow) after subcutaneous injection into the flank of a nude mouse [22]. (**d**) An overlay of the U87 tumor (shown in color) in the left kidney and the blood-dominated OFF state image (shown in gray) [44]

be further metabolized. Therefore, the imaging of the trapped glucose analogs allows for the noninvasive quantification of the glucose uptake and thus the local glucose metabolism.

8.5.3 PACT of Small-Animal Whole-Body Dynamics

Imaging of small animals has played an indispensable role in preclinical research by providing high-dimensional physiological, pathological, and phenotypic insights with clinical relevance. Here, we highlight two representative PACT systems that can image small-animal whole body in vivo with full-view fidelity (for instance, no partial-view artifacts).

To achieve high imaging speed in 2D, researchers have invented a PACT system that employs 512-element full-ring acoustic detection with simultaneous one-to-one

mapped preamplification and analogue-to-digital sampling. This full-ring ultrasonic transducer array provides a 2D panoramic acoustic detection scheme, generating 125 μm isotropic in-plane resolution and forming a cross-sectional image with a single laser shot [23]. At a 50 Hz frame rate (limited by the laser's repetition rate), PACT noninvasively performs whole-body imaging of small animals and clearly resolves the sub-organ vasculatures and internal organ structures without the use of exogenous labeling (Fig. 8.1d). The high imaging speed enables PACT to clearly observe the biological dynamics associated with heartbeats and respiration without motion artifacts. In addition, the absorption spectral signatures of oxy-hemoglobin and deoxy-hemoglobin allow PACT to perform mouse brain and whole-body functional imaging. Since PACT uses nonionizing radiation, it can be used to monitor live animals for drug testing without the detrimental interference. PACT also demonstrates the capability of molecular imaging by showing the process of dye perfusion and melanoma circulation in both the mouse brain and internal organs.

In addition to the aforementioned PACT system designed for high-speed 2D imaging, researchers have developed PACT systems for 3D volumetric imaging [25]. To collect photoacoustic signals in 3D from as many locations (projections) around the imaged object as possible, most attempts for volumetric imaging are based on scanning a set of unfocused detectors around the imaged object such that signals are acquired for optimal 3D image reconstruction. However, the scanning-based approaches limit the imaging speed and suffer from motion artifacts. In response, one 3D PAI approach has been developed that utilizes a hemispherical array with a large number of unfocused elements distributed on the aperture. This configuration enables the collection of real-time data from a relatively small volume for each illumination pulse. It takes about 5 min to acquire an image of the mouse whole trunk by combining all images acquired along the entire spiral trajectory (Fig. 8.3b). The motion artifacts can be further mitigated by self-gated respiratory motion rejection [53]. 3D PACT has been applied to tracking contrast agent perfusion in entire organs, beat-by-beat imaging of the mouse heart, and monitoring the distribution of epileptic seizures in whole mouse brains.

8.5.4 PACT of a Tyrosinase-Based Genetic Reporter

Genetically encodable photoacoustic contrast allows selective labeling of cells. Researchers utilized a planar PACT scanner that is based on Fabry–Perot interferometer (FPI) to image a tyrosinase-based reporter that causes human cell lines to synthesize the absorbing pigment eumelanin, thus providing genetically encoded photoacoustic contrast [22]. Figure 8.3c shows a 3D image of xenografts formed of tyrosinase-expressing cells implanted in a live mouse. Multi-wavelength illumination was implemented to separate the signals from the hemoglobin and eumelanin due to their distinct absorption spectra. Such a scheme is powerful for studying cellular and genetic processes in deep tissues.

8.5.5 Multiscale PAI with Photo-Switchable Protein Contrast

Rhodopseudomonas palustris (BphP1), a reversibly switchable bacterial phytochrome, has been combined with PAI for deep molecular imaging with improved detection sensitivity. Upon absorption of 730- to 790-nm light, BphP1 undergoes a Pfr → Pr state photoconversion, while the inverse transformation Pr → Pfr occurs upon absorption of 630- to 690-nm light. Background absorbers, primarily hemoglobin, do not have the same photo-switchable properties, differential measurements can therefore be used to suppress the background and improve the detection of tumors labeled by BphP1 in deep tissue [44].

U87 human glioblastoma cells expressing BphP1 are observed by a circular-view PACT system with a noise-equivalent detection sensitivity of ~20. With the single-wavelength differential method, the CNR was about 34-times higher than the two-wavelength spectral unmixing method. After 20 cycles of photo-switching, the differential image showed the tumor in the mouse left kidney with high contrast (Fig. 8.3d). The same tumor could not be detected without photo-switchable protein labeling due to the overwhelming background signals from the hemoglobin.

Combined with a high NA OR-PAM system, the reversely switchable protein can also be used for super-resolution microscopy. Because the switching-off rate of BphP1 is proportional to the local excitation intensity, photoacoustic signals generated from the center of the light focus have a faster-decay rate than those generated from the periphery. A high-order coefficient can be extracted by fitting the nonlinear signal-decay process, and thus sub-diffraction resolution can be produced. The axial and lateral resolutions are 400 nm and 141 nm, respectively.

8.5.6 A Microrobotic System Guided by PACT

PACT has been applied to image micromotors in intestines in vivo. The micromotors enveloped in microcapsules are stable in the stomach and exhibit efficient propulsion in various biofluids once released. PACT can visualize the migration of micromotor capsules toward the targeted regions in the intestines in real time in vivo [54]. NIR light irradiation induces disintegration of the capsules to release the cargo-loaded micromotors. The intensive propulsion of the micromotors prolongs the retention in intestines. The integration of the newly developed microrobotic system and PACT enables precise control of the micromotors in vivo and promises practical biomedical applications such as drug delivery.

8.6 Technical Advantages from Bench to Bedside

Translational PAI has attracted growing interest in the past decade. Its major applications include, but are not limited to, intraoperative specimen analysis, skin imaging, vaginal examination, breast cancer screening, sentinel lymph node mapping, and Crohn's disease diagnosis. In this section, we review the recent

technical developments in these areas and discuss current progress toward other clinical uses.

8.6.1 Ultraviolet OR-PAM of Tumor Specimen

Breast-conserving surgery aims to completely remove all of the cancer. However, 20–60% of patients have to undergo second surgeries to achieve clear margins because no intraoperative tools can microscopically analyze the entire lumpectomy specimen. To address this critical need, ultraviolet OR-PAM has been developed for accurate intraoperative margin assessment [31]. Ultraviolet (UV) laser illumination has the advantage of highlighting cell nuclei, thus providing the same contrast as hematoxylin labeling used in conventional histology without the need for labels. Accordingly, ultraviolet OR-PAM achieves multilayered histology-like imaging of the tissue surface (Fig. 8.2a). The high correlation of the OR-PAM images to the conventional histologic images allows rapid computations of diagnostic features such as packing density and nuclear size, potentially identifying small clusters of cancer cells. Without the need for tissue processing or staining, ultraviolet OR-PAM can be performed promptly and intraoperatively, enabling immediate directed re-excision and reducing second surgeries. Such an imaging modality can be further applied for brain tumor, bone cancer, and lesions that require intraoperative assessment. The imaging speed can be further improved after applying faster lasers and scanning mechanisms.

8.6.2 OR-PAM and PACT of Human Skin

Skin is the largest organ in human and uses about 5% of the total blood flow to support its physiological functions. The cutaneous vasculature is the main target of pathologic processes in vasculopathies and vasculitis. It is also involved in common inflammatory skin diseases such as eczema and psoriasis. Current clinical examination techniques, however, cannot resolve the human vasculature with all plexus in a noninvasive manner.

Capitalizing on multiscale PAI, cutaneous vasculature at different depths can be visualized. To image capillaries under the skin surface (epidermis), OR-PAM has been minimized to a handheld probe which uses a newly developed two-axis water-immersible MEMS scanning mirror. In the OR-PAM probe, the optical and acoustic beams are confocally configured to maximize the SNR. The two beams are quickly scanned by the MEMS mirror, yielding a 3-D imaging rate of 2 Hz over a 2.5 (length) $\times$ 2.0 (width) $\times$ 0.5 (depth) mm^3 volume [55]. To image blood vessels embedded in the optical diffusive regime (dermis), a planar-view PACT based on FPI has been applied. The FPI sensor has several advantages for skin imaging. First, it allows transmission of the light and thus is compatible for other optical imaging modalities (e.g., optical coherence tomography). Second, the FPI sensor has a higher sensitivity and bandwidth than that of the traditional piezoelectric transducers. Third,

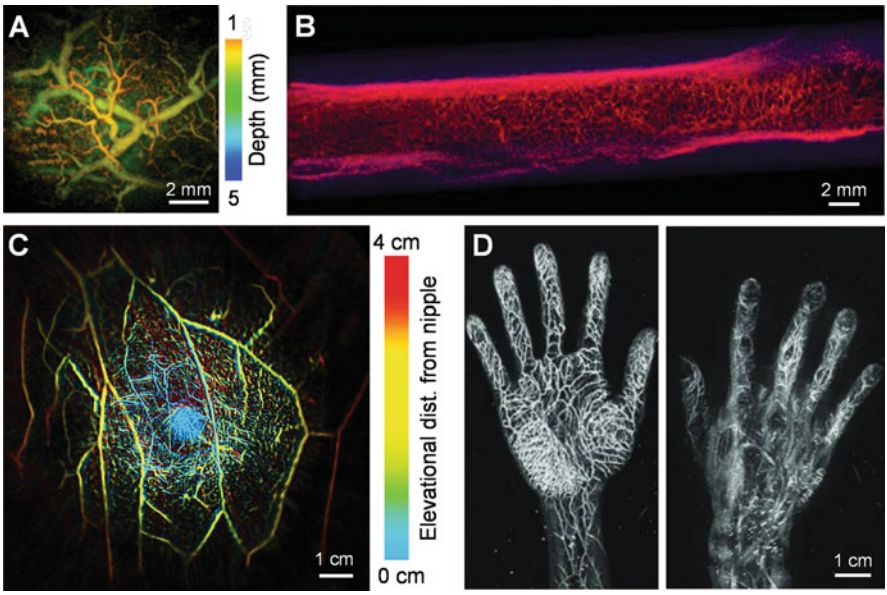

Fig. 8.4 Representative images of PAI toward clinical applications. (**a**) Color-encoded depth-resolved PACT image of the human skin [56]. (**b**) Label-free PAE image of a rat colorectum. The right-hand side corresponds to the anus [59]. (**c**) PACT of a healthy human breast acquired within a single breath-hold of 15 s [27]. (**d**) PACT image of a human palm (left) and back of the hand (right) [66]

the use of FPI sensor makes the system compact and easy to operate. The planar-view PACT can provide 3D imaging of human skin (Fig. 8.4a) [56] and has been used to image patients with nevus araneus, a surgical scar and basal cell carcinoma [57]. Vascular morphological and tortuosity parameters such as the vascular density, sum of angles metric, and inflection count metric have been quantified [58].

8.6.3 PAE of Internal Organs

At present, clinicians routinely apply ultrasound endoscopy in a variety of interventional procedures that provide treatment solutions for diseased organs. Ultrasound endoscopy not only produces high-resolution images, but is also safe for clinical use and is broadly applicable. However, for soft tissue imaging, its mechanical wave-based image contrast fundamentally limits its ability to provide physiologically specific functional information. By contrast, PAE possesses a unique combination of functional optical contrast and high spatial resolution at clinically relevant depths, ideal for imaging soft tissues. With these attributes, PAE can overcome the current limitations of ultrasound endoscopy. Moreover, the benefits of photoacoustic imaging do not come at the expense of existing ultrasound functions; PAE systems are

inherently compatible with ultrasound imaging, thereby enabling multimodality imaging with complementary contrast.

PAEs based on OR-PAM and AR-PAM were developed and tested on small animals before applying to humans. Researchers have shown the feasibility of PAE by imaging the microvasculature of a rat colorectum (Fig. 8.4b) [59], gastrointestinal tracts and esophagi of rabbits. Most recently, transvaginal PAE was developed to illustrate the vascular network in human ectocervix and uterine body. The longitudinal and cross-sectional differences of cervical vasculatures in pregnant women were studied [60]. PAE is promising for screening the visceral pathological changes associated with angiogenesis.

8.6.4 PACT of Breast Cancer

Breast cancer is the second most common cancer to affect women in the U.S. and is the second ranked cause of cancer-related deaths. The importance of early detection in improving breast cancer survival has been demonstrated by multiple large prospective clinical trials. PACT combines the functional optical contrast of diffuse optical tomography and the high spatial resolution of ultrasonography. This hybrid nature grants PACT unique advantages and makes it complementary to other mainstream imaging modalities in clinical practice: (1) Compared with X-ray mammography and positron emission tomography (PET), PACT is free of radioactive material and uses nonionizing illumination; (2) Compared with ultrasonic imaging, PACT has rich intrinsic and extrinsic optical contrasts and is free of speckle artifacts; (3) Compared with pure optical tomography techniques, such as diffuse optical tomography and fluorescence tomography, PACT can sustain high spatial resolution in the deep tissue; (4) Compared with magnetic resonance imaging (MRI), laser-based PACT provides higher spatial resolution and imaging speed at a lower cost, though it faces a challenge to penetrate the entire human body. Specifically, the cutting-edge PACT system can image the human breast in 15 s with full penetration (4 cm) and spatial resolution (0.26–0.4 mm) [27] that is finer than breast 3T-MRI.

In biological tissue, the optical absorption contrast of PACT is much higher than mammographic X-ray contrast. However, the $1/e$ attenuation coefficient for 1064-nm light in an average breast is around 0.9 cm^{-1}, which is slightly higher than that for X-rays (0.5–0.8 cm^{-1}) [61]. In the NIR region, hemoglobin is the principal optical absorber to provide PACT an endogenous contrast (i.e., blood vessel density and morphology, total hemoglobin concentration, oxygenation state, etc.), which is closely correlated with the tumor growth and metastasis [62]. The optical absorption contrast can also serve as an indicator of the breast cancer's response to treatment. Here, we present two breast PACT systems which have provided best images and attracted wide interest from the industry as a result.

Combining 1064-nm light illumination and a 2.25-MHz unfocused full-ring transducer array, researchers have developed a PACT system that achieved up to 4 cm imaging depth in human breast and a 255 μm in-plane resolution, which is approximately four times finer than that of contrast-enhanced MRI. The system is

equipped with one-to-one mapped signal amplification and data acquisition DAQ circuits, and therefore needs no multiplexing. The moderate divergence angle of acoustic detection in the elevational direction allows the system to perform both 2D imaging of a breast cross section and 3D imaging of the whole breast by scanning elevationally within a single breath-hold of 15 s (Fig. 8.4c) [27]. In a previous study, this PACT system clearly identified eight of nine breast tumors by delineation of angiographic anatomy. Taking advantage of the high imaging speed, PACT can detect stiffer tumors by assessing deformations caused by breathing and identifies the tumor missed in angiographic imaging. At such high spatiotemporal resolutions, PACT is able to differentiate arteries from veins by detecting blood flow-mediated arterial deformation at the heartbeat frequency. In this system, the high-speed 2D imaging capability was acquired by sacrificing the elevational resolution in the 3D imaging mode.

The other PACT breast imaging system, cooperatively developed by the Kyoto University and Canon, sacrifices the imaging speed (~2 min for one scan) but gains an isotropic 3D spatial resolution [63]. In this prototype, broadband capacitive micromachined ultrasound transducers (CMUTs) were utilized for high-resolution PACT and the ultrasonic B-mode imaging was incorporated to provide ultrasound images in the same coordinate. 3D images of breasts were obtained with fine blood vessel revealed. Arteries and veins were differentiated by spectroscopic PACT at two wavelengths. Tumor-related blood vessels were observed with high resolution. The 3D PACT system could be helpful to elucidate various mechanisms of vascular-associated diseases and events.

8.6.5 PACT of Sentinel Lymph Nodes

The detection of regional lymph node metastases is important in cancer staging because it guides the prognosis of the patient and the strategy for treatment. Sentinel lymph node (SLN) biopsy is a less invasive alternative to axillary lymph node dissection. Based on the SLN hypothesis, determining the status of the first lymph nodes that drain from the primary tumor can accurately predict the pathological status of the axilla. Ultrasonography permits the visualization of SLN. However, sonographic signs of metastatic disease sometimes overlap with those of benign reactive changes, resulting in an overall sensitivity of less than 50% in detecting the SLN and nodal involvement [64]. To identify the SLN, which is most likely to contain metastatic cancer cells, physicians use methylene blue dye and/or radiolabeled sulfur colloid. To reduce the surgery-caused morbidity and expenses, researchers combined photoacoustic and ultrasonic imaging modalities to noninvasively detect the methylene blue dye accumulated in SLNs [41]. This method can potentially guide percutaneous needle biopsies, providing a minimally invasive method for axillary staging of breast cancer.

8.6.6 PACT of Human Extremities

Vascular disease present in appendicular regions is among the most common, where its presence doubles the likelihood of a vascular related death [65]. Current clinical methods of angiographic imaging include digital subtraction angiography, computed tomography angiography, and magnetic resonance angiography, which either resort to ionizing radiation or exogenous contrast agent. PACT has been applied to image angiographic structures in human extremities, including hands (Fig. 8.4d), arms, legs, and feet [66]. PACT features deep penetration with high spatial and temporal resolutions, clearly showing the vascular network of each appendage. This highlights PACT's ability to image major and minor vasculatures without the use of an external contrast or ionizing radiation. Examples of potential applications include monitoring the response to drug therapy such as the perfusion of medication, providing preoperative imaging for reconstructive surgery planning, giving postoperative surveillance for procedures such as revascularization surgery, and screening for peripheral vascular disease and diabetic foot.

8.6.7 PACT of Crohn's Disease

In chronic inflammatory diseases, uncontrolled inflammation is associated with increased rates of hospitalization and death. There is an increased demand for new diagnostic approaches because of the potential severity of these conditions. Multispectral PACT allows the noninvasive quantification of hemoglobin-dependent tissue perfusion and oxygenation associate with inflammation. Physicians utilized multispectral PACT to perform transabdominal evaluation of intestinal inflammation in 108 patients with Crohn's disease [67]. They compared the distribution of PACT measurements between patients with active and nonactive Crohn's diseases and found that there were significant differences between active disease and nonactive disease for PACT values including total hemoglobin, oxy-hemoglobin, and deoxy-hemoglobin. This pilot study suggests that PACT-based assessment of hemoglobin levels in the intestinal wall has the potential to be used to distinguish active disease from remission in patients with Crohn's disease without the need for more invasive procedures.

8.7 Summary and Outlook

In this chapter, both the fundamental principles of PAI and its state-of-the-art implementation and applications were discussed. PAI has the following advantages: (1) PAI breaks through the current fundamental depth limit of high-resolution optical imaging modalities while maintaining the depth-to-resolution ratio greater than 100. The depth-to-resolution ratio remains approximately constant while the imaging depth and spatial resolution are scaled. On the one hand, the imaging depth can be scaled up to potentially a few centimeters (PACT), which is limited by the

penetration depth of diffuse light rather than ballistic light. On the other hand, the spatial resolution can be scaled down to micrometers, where the imaging depth is limited by the penetration depth of high-frequency ultrasound (PAM); (2) PAI is highly sensitive to optical absorption and provides functional imaging based on endogenous optical absorption contrast that is physiologically specific. Exogenous contrast agents also enable molecular or reporter gene imaging; (3) PAI provides speckle-free images; (4) PAI is safe for small animal and human subjects, and is ready for clinical application. In summary, PAI has broad applications from laboratory research to clinical patient care, yet additional work is still needed to further mature this technology.

As with any imaging technology, PAI has certain limitations. First, optical attenuation limits the penetration to ~5 cm when a resolution of less than 1 mm is desired in tissue without signal averaging [8]. Microwaves can be used for deeper excitation, although the contrast mechanisms differ. Second, due to the strong mismatch of acoustic impedances, ultrasound sustains strong reflection from gas/liquid interfaces. Therefore, ultrasound signals cannot efficiently penetrate through gas cavities or lung tissues. For the same reason, ultrasonic detection requires acoustic coupling between the ultrasonic transducers and the biological tissue. The development of non-contact optical detection for acoustic displacement is a potential solution to this problem [68]. Third, ultrasound suffers from attenuation and phase distortion in thick bones, such as the human skull. Fortunately, unlike pulse-echo ultrasound imaging, PAI involves only one-way acoustic attenuation/distortion through the skull. The remaining challenge is to compensate for the phase distortion introduced by the skull.

Another aspect of PAI that needs improvement relates to quantitative imaging, which is important for functional and molecular imaging. Light propagating in tissue attains a spectrum that varies with location due to wavelength-dependent fluence attenuation, which limits the quantification accuracy of spectroscopic PAI. To compensate the optical fluence in deep tissue, several solutions have been proposed by researchers. One method attempts to describe light fluence in the spectral domain and introduce eigenspectra multispectral PAI to account for wavelength-dependent light attenuation [69]; Another strategy models optical fluence distribution by diffuse optical tomography [38]. Researchers also resort to methods including acousto-optic modulation [70], fluence dependent chromophores [71], and Monte Carlo modeling [72]. However, most methods are not sufficiently reliable for clinical applications. Additional approaches are being invented to increase the accuracy of quantitative PAI.

PAI has been evolving rapidly over the last two decades toward higher spatial resolution, higher imaging speed, and higher detection sensitivity. The development of PAI has also triggered growing contributions from biology, chemistry, and nanotechnology. While PAI faces the aforementioned challenges, exciting PAI progress has already been made. Addressing these challenges will further improve the capability of PAI. The unique combination of optical absorption contrast and ultrasonic imaging depth and scalable resolution provide PAI irreplaceable

advantages for high-impact applications in both biomedical research and clinical practice.

References

1. Wang LV, Wu H-i (2012) Biomedical optics: principles and imaging. John Wiley & Sons, New York, NY
2. Culver J, Ntziachristos V, Holboke M, Yodh A (2001) Optimization of optode arrangements for diffuse optical tomography: a singular-value analysis. Opt Lett 26(10):701–703
3. Wang LV, Hu S (2012) Photoacoustic tomography: in vivo imaging from organelles to organs. Science 335(6075):1458–1462
4. Guo Z, Li L, Wang LV (2009) On the speckle-free nature of photoacoustic tomography. Med Phys 36(9 Part 1):4084–4088
5. Shah J, Park S, Aglyamov SR, Larson T, Ma L, Sokolov KV, Johnston KP, Milner TE, Emelianov SY (2008) Photoacoustic imaging and temperature measurement for photothermal cancer therapy. J Biomed Opt 13(3):034024
6. Xu M, Wang LV (2005) Universal back-projection algorithm for photoacoustic computed tomography. Phys Rev E 71(1):016706
7. Wang LV (2008) Tutorial on photoacoustic microscopy and computed tomography. IEEE J Select Top Quant Electronics 14(1):171–179
8. Wang LV (2009) Multiscale photoacoustic microscopy and computed tomography. Nat Photonics 3(9):503
9. Hristova Y, Kuchment P, Nguyen L (2008) Reconstruction and time reversal in thermoacoustic tomography in acoustically homogeneous and inhomogeneous media. Inverse Probl 24 (5):055006
10. Hu S, Wang LV (2013) Optical-resolution photoacoustic microscopy: auscultation of biological systems at the cellular level. Biophys J 105(4):841–847
11. American National Standards Institute (2000) American national standard for the safe use of lasers. ANSI Standard Z136.1. ANSI, New York, NY
12. Hu S, Maslov K, Wang LV (2011) Second-generation optical-resolution photoacoustic microscopy with improved sensitivity and speed. Opt Lett 36(7):1134–1136
13. Yao J, Wang L, Yang J-M, Maslov KI, Wong TT, Li L, Huang C-H, Zou J, Wang LV (2015) High-speed label-free functional photoacoustic microscopy of mouse brain in action. Nat Methods 12(5):407
14. Yao D-K, Maslov KI, Wang LV, Chen R, Zhou Q (2012) Optimal ultraviolet wavelength for in vivo photoacoustic imaging of cell nuclei. J Biomed Opt 17(5):056004
15. Favazza CP, Wang LV, Jassim OW, Cornelius LA (2011) In vivo photoacoustic microscopy of human cutaneous microvasculature and a nevus. J Biomed Opt 16(1):016015
16. Kothapalli S-R, Wang LV (2009) Ex vivo blood vessel imaging using ultrasound-modulated optical microscopy. J Biomed Opt 14(1):014015
17. Yang J-M, Maslov K, Yang H-C, Zhou Q, Shung KK, Wang LV (2009) Photoacoustic endoscopy. Opt Lett 34(10):1591–1593
18. Lutzweiler C, Razansky D (2013) Optoacoustic imaging and tomography: reconstruction approaches and outstanding challenges in image performance and quantification. Sensors 13 (6):7345–7384
19. Shu W, Ai M, Salcudean T, Rohling R, Abolmaesumi P, Tang S (2016) Broadening the detection view of 2D photoacoustic tomography using two linear array transducers. Opt Express 24(12):12755–12768
20. Kim C, Erpelding TN, Jankovic L, Pashley MD, Wang LV (2010) Deeply penetrating in vivo photoacoustic imaging using a clinical ultrasound array system. Biomed Opt Express 1 (1):278–284

21. Wang Y, Guo Z, Wang LV, Erpelding TN, Jankovic L, Robert J-L, David G (2012) In vivo three-dimensional photoacoustic imaging based on a clinical matrix array ultrasound probe. J Biomed Opt 17(6):061208
22. Jathoul AP, Laufer J, Ogunlade O, Treeby B, Cox B, Zhang E, Johnson P, Pizzey AR, Philip B, Marafioti T (2015) Deep in vivo photoacoustic imaging of mammalian tissues using a tyrosinase-based genetic reporter. Nat Photonics 9(4):239
23. Li L, Zhu L, Ma C, Lin L, Yao J, Wang L, Maslov K, Zhang R, Chen W, Shi J (2017) Single-impulse panoramic photoacoustic computed tomography of small-animal whole-body dynamics at high spatiotemporal resolution. Nat Biomed Eng 1(5):0071
24. Ermilov SA, Su R, Conjusteau A, Oruganti T, Wang K, Anis F, Anastasio MA, Oraevsky AA (2015) Three-dimensional laser optoacoustic and laser ultrasound imaging system for biomedical research. In: Photons plus ultrasound: imaging and sensing 2015. International Society for Optics and Photonics, Bellingham, WA
25. Deán-Ben XL, Fehm TF, Ford SJ, Gottschalk S, Razansky D (2017) Spiral volumetric optoacoustic tomography visualizes multi-scale dynamics in mice. Light-Sci Appl 6(4):e16247
26. Xu M, Wang LV (2017) Analysis of spatial resolution in photoacoustic tomography. In: Photoacoustic imaging and spectroscopy. CRC Press, Boca Raton, FL, pp 47–60
27. Lin L, Hu P, Shi J, Appleton CM, Maslov K, Li L, Zhang R, Wang LV (2018) Single-breath-hold photoacoustic computed tomography of the breast. Nat Commun 9(1):2352
28. Xia J, Yao J, Wang LV (2014) Photoacoustic tomography: principles and advances. Electromagn Waves (Camb) 147:1–22
29. Roggenbuck M, Walker R, Catenacci J, Patch S (2013) Volumetric thermoacoustic imaging over large fields of view. Ultrason Imaging 35(1):57–67
30. Yan A, Lin L, Liu C, Shi J, Na S, Wang LV (2019) Microwave-induced thermoacoustic tomography through an adult human skull. Med Phys 46(4):1793–1797
31. Wong TT, Zhang R, Hai P, Zhang C, Pleitez MA, Aft RL, Novack DV, Wang LV (2017) Fast label-free multilayered histology-like imaging of human breast cancer by photoacoustic microscopy. Sci Adv 3(5):e1602168
32. Shi J, Wong TT, He Y, Li L, Zhang R, Yung CS, Hwang J, Maslov K, Wang LV (2019) High-resolution, high-contrast mid-infrared imaging of fresh biological samples with ultraviolet-localized photoacoustic microscopy. Nat Photonics 13:609
33. Zhang HF, Maslov K, Stoica G, Wang LV (2006) Functional photoacoustic microscopy for high-resolution and noninvasive in vivo imaging. Nat Biotechnol 24(7):848
34. Fang H, Maslov K, Wang LV (2007) Photoacoustic Doppler effect from flowing small light-absorbing particles. Phys Rev Lett 99(18):184501
35. Yao J, Maslov KI, Shi Y, Taber LA, Wang LV (2010) In vivo photoacoustic imaging of transverse blood flow by using Doppler broadening of bandwidth. Opt Lett 35(9):1419–1421
36. Yao J, Maslov KI, Zhang Y, Xia Y, Wang LV (2011) Label-free oxygen-metabolic photoacoustic microscopy in vivo. J Biomed Opt 16(7):076003
37. Ranasinghesagara JC, Zemp RJ (2010) Combined photoacoustic and oblique-incidence diffuse reflectance system for quantitative photoacoustic imaging in turbid media. J Biomed Opt 15 (4):046016
38. Bauer AQ, Nothdurft RE, Culver JP, Erpelding TN, Wang LV (2011) Quantitative photoacoustic imaging: correcting for heterogeneous light fluence distributions using diffuse optical tomography. J Biomed Opt 16(9):096016
39. Kim C, Cho EC, Chen J, Song KH, Au L, Favazza C, Zhang Q, Cobley CM, Gao F, Xia Y (2010) In vivo molecular photoacoustic tomography of melanomas targeted by bioconjugated gold nanocages. ACS Nano 4(8):4559–4564
40. Jin Y, Jia C, Huang S-W, O'donnell M, Gao X (2010) Multifunctional nanoparticles as coupled contrast agents. Nat Commun 1:41
41. Garcia-Uribe A, Erpelding TN, Krumholz A, Ke H, Maslov K, Appleton C, Margenthaler JA, Wang LV (2015) Dual-modality photoacoustic and ultrasound imaging system for noninvasive sentinel lymph node detection in patients with breast cancer. Sci Rep 5:15748

42. Beziere N, Lozano N, Nunes A, Salichs J, Queiros D, Kostarelos K, Ntziachristos V (2015) Dynamic imaging of PEGylated indocyanine green (ICG) liposomes within the tumor microenvironment using multi-spectral optoacoustic tomography (MSOT). Biomaterials 37:415–424
43. Brunker J, Yao J, Laufer J, Bohndiek SE (2017) Photoacoustic imaging using genetically encoded reporters: a review. J Biomed Opt 22(7):070901
44. Yao J, Kaberniuk AA, Li L, Shcherbakova DM, Zhang R, Wang L, Li G, Verkhusha VV, Wang LV (2016) Multiscale photoacoustic tomography using reversibly switchable bacterial phytochrome as a near-infrared photochromic probe. Nat Methods 13(1):67
45. Li L, Zhang HF, Zemp RJ, Maslov K, Wang LV (2008) Simultaneous imaging of a lacZ-marked tumor and microvasculature morphology in vivo by dual-wavelength photoacoustic microscopy. J Innov Opt Health Sci 1(02):207–215
46. Razansky D, Distel M, Vinegoni C, Ma R, Perrimon N, Köster RW, Ntziachristos V (2009) Multispectral opto-acoustic tomography of deep-seated fluorescent proteins in vivo. Nat Photonics 3(7):412
47. Wang L, Zhang C, Wang LV (2014) Grueneisen relaxation photoacoustic microscopy. Phys Rev Lett 113(17):174301
48. Beaven G, Holiday E (1952) Ultraviolet absorption spectra of proteins and amino acids. In: Advances in protein chemistry. Elsevier, Amsterdam, pp 319–386
49. Quickenden T, Irvin J (1980) The ultraviolet absorption spectrum of liquid water. J Chem Phys 72(8):4416–4428
50. Zhang P, Li L, Lin L, Hu P, Shi J, He Y, Zhu L, Zhou Y, Wang LV (2018) High-resolution deep functional imaging of the whole mouse brain by photoacoustic computed tomography in vivo. J Biophotonics 11(1):e201700024
51. Cao R, Li J, Ning B, Sun N, Wang T, Zuo Z, Hu S (2017) Functional and oxygen-metabolic photoacoustic microscopy of the awake mouse brain. NeuroImage 150:77–87
52. Yao J, Xia J, Maslov KI, Nasiriavanaki M, Tsytsarev V, Demchenko AV, Wang LV (2013) Noninvasive photoacoustic computed tomography of mouse brain metabolism in vivo. NeuroImage 64:257–266
53. Ron A, Davoudi N, Deán-Ben XL, Razansky D (2019) Self-gated respiratory motion rejection for optoacoustic tomography. Appl Sci 9(13):2737
54. Wu Z, Li L, Yang Y, Hu P, Li Y, Yang S-Y, Wang LV, Gao W (2019) A microrobotic system guided by photoacoustic computed tomography for targeted navigation in intestines in vivo. Sci Robot 4(32):eaax0613
55. Lin L, Zhang P, Xu S, Shi J, Li L, Yao J, Wang L, Zou J, Wang LV (2016) Handheld optical-resolution photoacoustic microscopy. J Biomed Opt 22(4):041002
56. Liu M, Chen Z, Zabihian B, Sinz C, Zhang E, Beard PC, Ginner L, Hoover E, Minneman MP, Leitgeb RA, Kittler H, Drexler W (2016) Combined multi-modal photoacoustic tomography, optical coherence tomography (OCT) and OCT angiography system with an articulated probe for in vivo human skin structure and vasculature imaging. Biomed Opt Express 7(9):3390–3402
57. Chen Z, Rank E, Meiburger KM, Sinz C, Hodul A, Zhang E, Hoover E, Minneman M, Ensher J, Beard PC, Kittler H, Leitgeb RA, Drexler W, Liu M (2017) Non-invasive multimodal optical coherence and photoacoustic tomography for human skin imaging. Sci Rep 7(1):17975
58. Meiburger KM, Nam SY, Chung E, Suggs LJ, Emelianov SY, Molinari F (2016) Skeletonization algorithm-based blood vessel quantification using in vivo 3D photoacoustic imaging. Phys Med Biol 61(22):7994–8009
59. Yang JM, Li C, Chen R, Rao B, Yao J, Yeh CH, Danielli A, Maslov K, Zhou Q, Shung KK, Wang LV (2015) Optical-resolution photoacoustic endomicroscopy in vivo. Biomed Opt Express 6(3):918–932
60. Qu Y, Li C, Shi J, Chen R, Xu S, Rafsanjani H, Maslov K, Krigman H, Garvey L, Hu P, Zhao P, Meyers K, Diveley E, Pizzella S, Muench L, Punyamurthy N, Goldstein N, Onwumere O, Alisio M, Meyenburg K, Maynard J, Helm K, Slaughter J, Barber S, Burger T, Kramer C, Chubiz J, Anderson M, McCarthy R, England SK, Macones GA, Zhou Q, Shung KK, Zou J,

Stout MJ, Tuuli M, Wang LV (2018) Transvaginal fast-scanning optical-resolution photoacoustic endoscopy. J Biomed Opt 23(12):1–4
61. Durduran T, Choe R, Culver JP, Zubkov L, Holboke MJ, Giammarco J, Chance B, Yodh AG (2002) Bulk optical properties of healthy female breast tissue. Phys Med Biol 47 (16):2847–2861
62. Schneider BP, Miller KD (2005) Angiogenesis of breast cancer. J Clin Oncol 23(8):1782–1790
63. Matsumoto Y, Asao Y, Sekiguchi H, Yoshikawa A, Ishii T, Nagae K, Kobayashi S, Tsuge I, Saito S, Takada M, Ishida Y, Kataoka M, Sakurai T, Yagi T, Kabashima K, Suzuki S, Togashi K, Shiina T, Toi M (2018) Visualising peripheral arterioles and venules through high-resolution and large-area photoacoustic imaging. Sci Rep 8:14930
64. Diepstraten SC, Sever AR, Buckens CF, Veldhuis WB, van Dalen T, van den Bosch MA, Mali WP, Verkooijen HM (2014) Value of preoperative ultrasound-guided axillary lymph node biopsy for preventing completion axillary lymph node dissection in breast cancer: a systematic review and meta-analysis. Ann Surg Oncol 21(1):51–59
65. Ho CY, Shanahan CM (2016) Medial arterial calcification: an overlooked player in peripheral arterial disease. Arterioscler Thromb Vasc Biol 36(8):1475–1482
66. Nagae K, Asao Y, Sudo Y, Murayama N, Tanaka Y, Ohira K, Ishida Y, Otsuka A, Matsumoto Y, Saito S, Furu M, Murata K, Sekiguchi H, Kataoka M, Yoshikawa A, Ishii T, Togashi K, Shiina T, Kabashima K, Toi M, Yagi T (2018) Real-time 3D photoacoustic visualization system with a wide field of view for imaging human limbs. F1000Res 7:1813
67. Knieling F, Neufert C, Hartmann A, Claussen J, Urich A, Egger C, Vetter M, Fischer S, Pfeifer L, Hagel A, Kielisch C, Gortz RS, Wildner D, Engel M, Rother J, Uter W, Siebler J, Atreya R, Rascher W, Strobel D, Neurath MF, Waldner MJ (2017) Multispectral optoacoustic tomography for assessment of Crohn's disease activity. N Engl J Med 376(13):1292–1294
68. Buj C, Munter M, Schmarbeck B, Horstmann J, Huttmann G, Brinkmann R (2017) Noncontact holographic detection for photoacoustic tomography. J Biomed Opt 22(10):1–14
69. Tzoumas S, Nunes A, Olefir I, Stangl S, Symvoulidis P, Glasl S, Bayer C, Multhoff G, Ntziachristos V (2016) Eigenspectra optoacoustic tomography achieves quantitative blood oxygenation imaging deep in tissues. Nat Commun 7:12121
70. Steenbergen W, Molenaar R, Daoudi K (2011) Combined application of photoacoustic and acousto-optic imaging for model-free quantitative optical absorption mapping. J Acoust Soc Am 129:2641
71. Cox BT, Laufer JG, Beard PC (2010) Quantitative photoacoustic image reconstruction using fluence dependent chromophores. Biomed Opt Express 1(1):201–208
72. Liu Y, Jiang H, Yuan Z (2016) Two schemes for quantitative photoacoustic tomography based on Monte Carlo simulation. Med Phys 43(7):3987

Spontaneous Raman and Surface-Enhanced Raman Scattering Bioimaging

9

Li Lin and Jian Ye

9.1 Raman Imaging

9.1.1 Principles of Raman Spectroscopy and Raman Imaging

Raman spectroscopy, also named Raman scattering after its discoverer the Indian physicist Sir C. V. Raman, relies on the inelastic scattering of incident photons. Typically, when a radiation of frequency ω_0 is incident on the molecules of a sample, a certain number of scattered photons occur at all directions with varied frequencies (Fig. 9.1). Among them, the majority is the elastic scattered photons called Rayleigh scattering, without any change in frequency; and the inelastic scattered photons with a shifted frequency of $\omega_0 \pm \omega_\nu$ are the Raman scattering. The frequency ω_ν is found to be associated to the transitions between molecular rotational or vibrational levels, resulting in the energy of the incident photons being shifted up or down [1]. The Raman shifts for scattering with an energy loss (with a frequency of $\omega_0 - \omega_\nu$) are referred to as Stokes shift, and the others (with a frequency of $\omega_0 + \omega_\nu$) are as anti-Stokes shift.

The unit for expressing Raman shift (also reported as wavenumber) is the inverse centimeters (cm^{-1}), which is directly related to energy and can be converted to wavelength (λ, nm) by:

$$\text{Raman shift}\left(cm^{-1}\right) = \left(\frac{1}{\lambda_{\text{laser}}\ (nm)} - \frac{1}{\lambda_{\text{signal}}\ (\text{nm})}\right) \times 10^7$$

L. Lin · J. Ye (✉)
School of Biomedical Engineering, Shanghai Jiao Tong University, Shanghai, P. R. China
e-mail: yejian78@sjtu.edu.cn

X. Wei, B. Gu (eds.), *Optical Imaging in Human Disease and Biological Research*, Advances in Experimental Medicine and Biology 1355,
https://doi.org/10.1007/978-981-15-7627-0_9

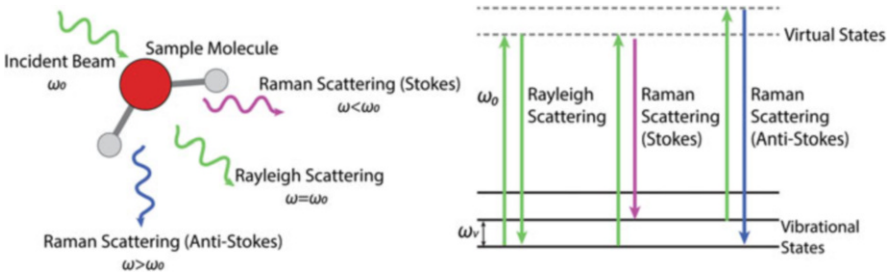

Fig. 9.1 Schematic illustration (left) and energy-level diagram (right) of Rayleigh and Raman scattering process

At present, Raman spectroscopy is widely used in chemistry to provide a molecular fingerprint by which molecules can be identified. The unique Raman shifts in energy offer the structural information of molecules and chemical components, allowing the researchers to detect analytes and obtain their relative concentrations. For the detection of biological samples, Raman spectroscopy provides favorable properties: (1) noninvasive detection capability and high specificity with a fingerprint spectrum, weakly influenced by the temperature or environments; (2) high compatibility with water, which enables the study of biomolecules under the active state in aqueous samples; (3) minimal volume/amount required for the measurement, typically with μL–mL of analytes.

Optical imaging based on Raman spectroscopy is further achieved by collecting and mapping Raman spectra in an area of interest. Either for fundamental studies or in clinical trials, Raman imaging has now been a powerful technique for generating structural images or monitoring minute chemical changes of biological samples such as tumor cells. Basically, Raman imaging can be performed through direct and indirect strategies: the former detects the target directly through the featured Raman spectra of targets; while the latter adopts a Raman label with characteristic peaks to tag and track the targets.

9.1.2 Spontaneous, Surface-Enhanced, and Coherent Anti-Stokes Raman Spectroscopy

If consider within the framework of the energy-level model, spontaneous Raman scattering could be regarded as a process where the perturbation of incident photons makes the molecules transit from the ground state (lowest energy state) to a virtual state, and then molecules spontaneously turn back to the lower state with the emission of new photons (Fig. 9.2). It should be noted that the virtual state does not correspond to any electronic levels, and it cannot be occupied but does allow for transitions between unoccupied real states [2]. This process doesn't literally involve the direct energy absorption. Instead, the role of the incident light is more likely to induce the possibility of the electronic transitions. Nowadays, many types of

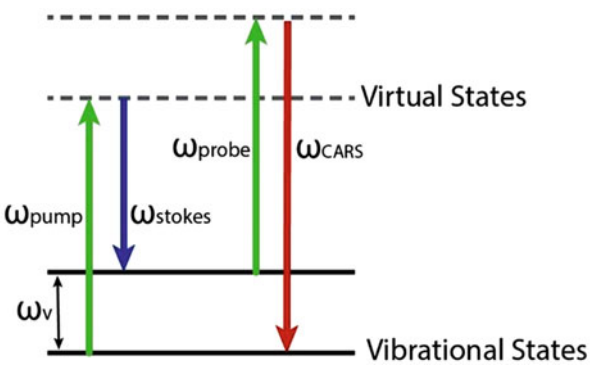

Fig. 9.2 Energy-level diagram of CARS process

spontaneous Raman spectroscopy techniques have been explored, such as correlative Raman imaging and the resonance Raman spectroscopy. Since Raman scattering highly relies on the chemical information of molecules and is nearly unaffected by the environment, the spontaneous Raman imaging can be used to qualitatively analyze the structure and concentrations of the targets, offering images of high sensitivity and resolution to reveal the details of biological samples.

However, the inherent cross-section (10^{-30} to 10^{-25} cm^2) of Raman scattering is small, compared to that of fluorescence spectroscopy (10^{-17} to 10^{-16} cm^2). This leads to a quiet weak spontaneous Raman signal, and largely limits its application in clinical imaging [3]. The techniques applied to overcome these limitations include the surface-enhanced Raman spectroscopy (SERS) and coherent anti-stokes Raman spectroscopy (CARS).

SERS is a surface-sensitive technique that can greatly amplify the intensity of Raman spectrum of molecules on or near the surface of plasmonic nanostructures. The enhancement factor (EF) can be as high as 10^{14} to 10^{15}, which opens the possibility for single-molecule detection [1, 4]. So far, SERS has been widely used in the field of chemical, biological, or clinical sensing and imaging. It has proven to be an effective and convenient way to amplify the Raman signal of either target or probe molecules. In addition, the capability to analyze each component from a multiplexed mixture on the nanoscale makes SERS superior in performing sensitive and quantitative detection of variant biomolecules, and in obtaining high-quality images of biological structures. The explicit introduction of SERS will be shown in Sect. 9.3.

The coherent nonlinear stimulation can effectively enhance the Raman signal, referred as coherent Raman scattering. One of the developed coherent Raman imaging techniques is based on CARS. As illustrated in the energy-level diagram (Fig. 9.2), the molecule is initially in the ground state, and the pump irradiation (ω_{pump}) excites the molecule to a virtual state. A Stokes beam (ω_{stokes}) is simultaneously present along with the pump, together inducing the energy coupling between the ground state and the vibrational state of the molecule. This coherence can be probed by a probe beam (ω_{probe}), which makes the molecule be excited to a virtual state, and fall back instantaneously to the ground state, leading to the

emission of an anti-stokes photon at the frequency of $\omega_{CARS} = \omega_{pump} + \omega_{probe} - \omega_{stokes}$. When ω_{probe} equals to ω_{pump} in practical application, the signal $\omega_{CARS} = 2\omega_{pump} - \omega_{stokes}$ is generated with the intensity dependence of a third-order nonlinear optical process [5]. By adjusting ω_{pump} and ω_{stokes} to couple with different molecular vibration energy, the anti-stokes signal can be coherently enhanced and benefit the detection of the corresponding chemical bonds. CARS technique is also label-free and noninvasive, has the capability to show three-dimensional images on molecular components of samples due to its sensitivity to chemical bonds and nonlinear effects. An alternative nonlinear technique is the stimulated Raman spectroscopy (SRS). Together with CARS, they have been studied and shown promises on small molecules tracking and visualization in biological samples. These two techniques are not the main focus in this chapter. Readers are encouraged to find detailed information in the relevant reference [6].

9.1.3 Instrumentation, Data Acquisition, and Spectral Analysis

9.1.3.1 Instrumentation

In a typical setup of Raman microscopic spectrometer, the sample is illuminated with a laser beam, and then the emitted photons from the illuminated spot are collected with a lens and pass through a monochromator. The collected light is dispersed onto a detector with Rayleigh scattering being filtered out using the notch or edge filters. The dispersive spectrographs paired with CCD detectors are commonly used. Among the applied excitation wavelengths for Raman measurements (514, 532, 615, 633, 785, 830 nm, etc.), 785 nm at the first near-infrared window (NIR-I), is the most frequently used in biomedical imaging due to the optimal light penetration depth and the minimization of autofluorescence from biological tissues.

9.1.3.2 Data Acquisition

The most applied method of acquiring spectra for Raman imaging is the pixel-by-pixel point scanning, which requires no technical upgrades on the basic Raman microscopes [7]. Although this strategy has shown enough time resolution to visualize the localization of analytes or nanoparticles (NPs), it leads to a relatively long acquisition time, usually 0.5–20 h for a single-cell imaging (50 × 50 pixels) if considering that of 0.5–30 s per spectrum.

There have been some techniques developed to accelerate the imaging process in commercial Raman spectrometers. One is the line-scanning method, adopted as the StreamLine™ (Renishaw). Line-scanning acquires spectra from a line of points through a linear laser spot, and can reduce the image acquisition time for the sufficient temporal resolution, rapidly generating high-resolution two-dimensional images of large sample areas in square centimeter scale. It can also prevent laser induced sample damage by illuminating with a line of laser beam, rather than an intense spot. Secondly, Raman imaging can be realized by rapid movement of the laser spot instead of mechanical movement of the sample stage, therefore greatly improving the imaging speed. For example, the Duoscan™ mode (Horiba) uses a

combination of two galvo mirrors that make the laser beam scan across a pattern, either a line for linear profiles or a two-dimensional mapping area. It can be used to generate a "macro laser spot" for a large area with a scanning step size down to 50 nm. Some other techniques, such as multifocus Raman imaging which arranges excitation beams throughout the field of view, or the selective scanning which takes advantages of spatial correlation within samples to reduce the number of spectra required, are also developed in Raman imaging studies to reduce overall acquisition time [7].

9.1.3.3 Spectral Analysis

The Raman spectra for imaging provide high-resolution spatial information of samples, and their raw data also contain spectral information of many interferents. Therefore, it is usually necessary to perform data processing and spectral analysis to deal with the complex dataset for diagnosis and imaging [8].

Spectral preprocessing refers to the treatment before the data are effectively analyzed, aiming to eliminate the interferences of nontarget signals such as autofluorescence background, noise, substrate-generated and other unwanted signals from the sample itself [9]. It could be performed in the following steps: (1) Spectrum smooth. It is applied to a set of Raman spectral data to smooth the high-frequency components without distorting the signal tendency. Savitzky–Golay filter is one of the most popular digital filters applied, which fits successive subsets of adjacent data points with a local polynomial, and can be adjusted by selecting the degrees of polynomials [10]. (2) Background removal, i.e., baseline subtraction. The non-Raman background can be determined and removed while preserving characteristic Raman peaks originating from the sample, by using the polynomial fitting, a wavelet transform, etc. (3) Normalization. Different Raman spectra are often obtained under different experimental conditions and time instruments. The purpose of normalization is to ensure that the Raman spectra of the same materials are as consistent as possible under different test conditions. The common normalizations are based on peak intensity or peak area of a standard material, e.g., a silicon substrate.

After acquiring a group of Raman data with spatial and spectral information (x, y, and Raman shift), a variety of methods can be used to transform them into an image, from direct display of band intensities to more advanced statistical methods [7]. The univariate imaging is a simple way to visualize the locations and relative concentrations of target molecules in the samples, by displaying the intensity of a specific Raman band at each pixel. Advanced multivariate analysis can be further used for complicated samples with multiple components. It exploits the whole spectrum of Raman data rather than relying on a single Raman mode, simultaneously using multiple peaks to display molecular properties and to extract effective information from complex variables. In this case, the minor variations in the spectrum that are unobservable to the naked eyes could convey valuable information. A variety of multivariate analysis methods can be combined and optimized based on the goals of analysis: (1) Data generalization and model construction. For example, principal component analysis (PCA) captures a set of linearly uncorrelated variables

called as principal components to represent the entire dataset, then generates PCA images by plotting the principal components scores at each pixel. (2) Classification. The cluster analysis is adopted to group the sets of similar spectra by assigning colors to each cluster. The average spectrum of each cluster can be analyzed to extract chemical information throughout the sample. (3) Regression to make predictions. The two groups of variables can be correlated and quantified to form a regression model. In this process the coefficients define the relationship between each independent variable and the dependent variable.

9.2 Spontaneous Raman in Biomedical Imaging

9.2.1 Raman Contrast and Label

Spontaneous Raman spectroscopy is capable to provide specific vibrational information of chemical bonds in biomolecules (e.g., lipids, nucleic acids, proteins) as a direct imaging method. The intrinsic bonds with characteristic Raman modes are chosen as label-free chemical contrast in biomedical imaging, such as C–H (2800–3000 cm^{-1}), C=O (1680–1820 cm^{-1}), C–C (stretching mode at 1000–1200 cm^{-1}), and C=C (stretching mode at approximately 1500–1700 cm^{-1}), as shown in Fig. 9.3 [11]. The common biomolecules and their corresponding chemical contrast information can be found in Table 9.1.

Still, spontaneous Raman imaging is hindered by the low sensitivity and weak signals. Some specialized Raman labels have thus been developed to enhance imaging contrast and track molecules. The requirements for the Raman labels are that their bands are easily distinguishable and should not overlap with intrinsic signals of the target molecules. Two excellent candidates are the stable isotope

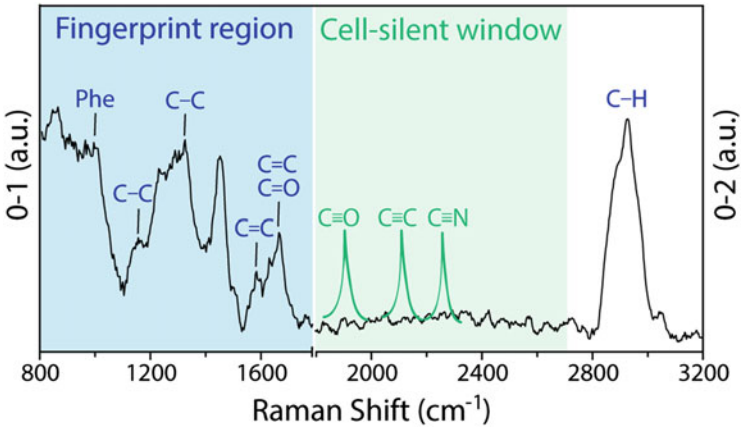

Fig. 9.3 The contrast bands (blue) and label bands (green). The Raman spectrum is measured on an MDA-MB-231 breast cancer cell. The labels exhibit instinct Raman bands in the cell-silent window

Table 9.1 Biomolecules, corresponding contrast and Raman bands, with data adapted from ref. [12, 13]

Biomolecule	Contrast	Raman band (cm^{-1})
Phospholipid	PO_4^{2-}	1090
Lipid	Cholesterol	607, 700, 1440, 1674
	C–C	1065, 1129
	C=C	1660
	C=O	1740
	CH_2 deformation	1300, 1440
	$N(CH_3)_3$	716, 875
Protein	Amide I	1655–1666
	Amide III	1255
	CH_3 deformation	1320, 1450
	Peptide C–C_α	898, 935
	Phenylalanine	622, 1004, 1030, 1159, 1208, 1607
	Tyrosine	644, 830, 855, 1175, 1617
	Tryptophan	757, 1159, 1340, 1555, 1617
Nucleic acid	Adenine	727, 1490, 1580
	Cytosine	785
	backbone	830, 1093–1100
	DNA backbone	680, 1490, 1580
	Guanine	667, 757, 780, 1277
	Thymine	

labels and alkyne labels. The stable isotopes (e.g., ^2H, ^{13}C, ^{15}N) are used to replace their primordial isotopes (^1H, ^{12}C, ^{14}N) [14]. The heavier isotope can lower the vibrational energies of the associated chemical bond, leading to the shifted Raman bands. As the isotope labels can be nondestructively tagged into cellular genomics by cell co-incubation, they enable the direct studies of single-cell metabolism, cell–cell transition and functional properties of microbial communities [14]. Another promising Raman label is the alkyne structure (C≡C), which shows a strong band in the spectral cell-silent window (1800–2800 cm^{-1}). Considering that the 600–1800 cm^{-1} region is generally crowded with intrinsic Raman bands, and the high-frequency C–H stretching mode (2800–3200 cm^{-1}) lacks specificity, the cell-silent window is free from the interference of endogenous cellular background (Fig. 9.3). Also, being small enough not to affect the properties of target molecules, the alkyne structures have been applied to design a kind of alkyne-tagged cell proliferation probes, EdU (5-ethynyl-2′-deoxyuridine), for live cell imaging [15]. Both the stable isotope and alkyl-based Raman label can provide a way with minimal labeling to distinguish the molecules of interest in the spectrum, greatly enhancing the specificity of Raman images.

9.2.2 Spontaneous Raman in Biological Studies

Spontaneous Raman spectroscopy has been shown to measure the slight chemical changes and relative concentrations of components in a single cell, or even at a subcellular level. The visualization of various factors, including the uptake of drugs, bioactive compounds or non-chemical stressors can be obtained [16]. So far, Raman imaging has been be used to study metabolites such as (deoxy)nucleotides, lipids, proteins, amino acids and sugars, playing an important role in fundamental studies of biology, pharmaceutical and medical sciences [11, 17].

9.2.2.1 Nucleic Acid and Proteins Tracking

Nucleic acids and proteins are both essential components in biological cells. The commonly applied imaging method is by staining morphologically preserved fixed cells and tissues. The Raman technique provides an investigation on them in live cells with minimal labels. Sodeoka et al. put forward with the strategies of using alkynes in nucleic acid and proteins visualization [15, 18]. They successfully designed an alkyne-tagged cell proliferation probe, 5-ethynyl-2′-deoxyuridine (EdU), which was readily incorporated into DNA as a mimic of thymidine during DNA replication and can accumulate in nucleus. Thus, the localization of DNA in live cells can be visualized. Alkyne-tagged coenzyme Q (CoQ) analogues were imaged in the same way and their cellular concentrations be semiquantitatively estimated. A simultaneous imaging of the two small molecules, EdU and a CoQ analogue, was also demonstrated. This strategy should be applicable to image a variety of small molecules, such as lipids and drug candidate molecules.

It is noteworthy that in recent years, this method is more adopted by nonlinear Raman imaging techniques, which offers faster image acquisition and greater sensitivity. For example, the alkyne-tagged deoxyribonucleoside ethynyl-deoxyuridine has been used to elucidate DNA synthesis and cell proliferation by SRS [19].

9.2.2.2 Medial Vascular Calcification Imaging

Medial calcification accumulated in the human aorta induces a weakened arterial compliance and is known to comprise a number of diseases. Stevens et al. studied the mechanism of cardiovascular calcification, especially its relationship to atherosclerosis, by using Raman imaging methods [20]. They revealed a biochemical distribution in the aorta by characterizing the Raman spectroscopy of proteins, cholesterol and predominant minerals. Spectral unmixing algorithms were adopted to distinguish between the major biomolecules (apatite, whitlockite, β-carotene, cholesterol ester, triglyceride, elastin, collagen, actin). Raman images of 200 mm × 200 mm with a step size of 0.8 mm × 0.8 mm were acquired using 785-nm laser, 100 mW power and 1 s integration time. For the first time they demonstrated that Raman spectroscopy can be used to quantify the spatial distribution of the mineral species in aortic tissues.

9.2.2.3 Study on Endoplasmic Reticulum (ER) Changes

ER is a cellular compartment where proteins undergo folding and being transported to other parts of a cell or outside cell. The exposure to stressors induces a decreased ER capacity of protein folding and thus an accumulation of unfolded proteins. Majzner et al. have used Raman confocal imaging to monitor biochemical alterations in single endothelial cells under stress stimulated by tunicamycin (Tu) [21]. A 532 nm laser was used with a power of ~15–20 mW at the sample. Raman imaging was performed on cells with a 0.5 s integration time and a sampling step size of 0.5 μm. They found that Tu accumulation led to the enlarged size of the ER and a decrease of the phospholipid content in the corresponding area. The increased intensity of bands at 790, 1098, 1206, 1342, and 1380 cm^{-1} observed in the ER spectra after Tu treatment indicated that the content of nucleic acids is also bigger. Overall, the application of Raman imaging enabled the studies on the minute chemical information within a single endothelial cell.

9.2.3 Spontaneous Raman in Disease Diagnostics

9.2.3.1 Brain Tumor Biopsy

Limited by the long exposure time, spontaneous Raman imaging is rarely used in vivo or in clinical applications. Still, it can be used on tissues ex vivo for the visualization of tumor sites. J. Popp et al. demonstrate the diagnostic prospects of Raman imaging to probe the cell density and nucleic acid of brain primary tumor metastases [22]. They collected Raman images of human brain tumor tissue sections and analyzed the data using the multivariate vector vertex component analysis (VCA). The results were compared with the gold-standard histopathological assessment, which uses H&E staining on abnormal tissues to show what type of brain lesion (abscess, tumor) is and whether it is malignant or not. A good agreement of Raman imaging results with H&E staining results was reached after spectral demultiplexing. The morphology obtained in lots of Raman images could be interpreted in a similar way as the H&E staining biopsy. Moreover, it was impressive that the spatial resolution was high enough that individual cell nuclei could be resolved in the Raman images. This work demonstrated the prospects of spontaneous Raman imaging as a biopsy tool for direct vision without labeling.

9.2.3.2 Biochemical Study of Heart Tissues

The biochemical study of heart tissues is important to provide information on infarct and related heart disease. Conventional histological examinations such as hematoxylin and eosin staining is capable of elucidating morphological information on fixed tissues, but cannot be applied in vivo. Takamatsu et al. demonstrated a high-speed spontaneous Raman imaging on rat heart tissues with resonance Raman effect of heme proteins [23]. In their findings, the cardiomyocytes and blood vessels in intact hearts can be visualized via cytochromes from oxy- and deoxyhemoglobin, while those in infarct hearts via cytochromes from collagen type-I. By using spectra extracted by PCA, they imaged the intact and infarcted myocardial sections at the

cellular level without further staining. Their work has shown the potential of spontaneous Raman imaging for studying morphological and biochemical changes of heart tissue based on the molecular components, and is prospective toward in vivo monitoring of cardiac microcirculation and fibrosis.

9.3 SERS in Biomedical Imaging

9.3.1 Mechanism and Advantages of SERS

SERS was firstly discovered by Fleischmann et al. in 1974, when they adsorbed pyridine molecules on the surface of roughened silver electrode and obtained the enhanced Raman spectra of pyridine molecules [24]. It was found that the pyridine Raman signal was enhanced by nearly six orders of magnitude. The observed enhancement cannot be explained simply by the increase in the number of molecules, which turned out to be an enhancement effect associated with rough plasmonic surfaces referred as the SERS effect. Its mechanism has been studied throughout decades, with the contributions of EF usually separated into two main categories [1, 2]:

9.3.1.1 Electromagnetic (EM) Enhancement

It is due to an enhanced electric field near the surface of metallic nanostructures, which is affected by their material, size and shape. When metal NPs are irradiated with incident light, the collective oscillations of conduction electrons at the boundary of NPs are excited as localized surface plasmon resonance (LSPR). This process results in a large local field enhancement near NP surfaces, referred to as EM hot spot regions. The Raman signal of molecules located in hot spots can be greatly enhanced, through the coupling of metallic NPs with both the incident field and the re-emitted (scattered) Raman field: the LSPR firstly amplifies the intensity of incident field which excites the Raman scattering of the molecules, thus increasing the signal; then, the Raman scattering signal is further amplified due to the same mechanism, bringing an increase in total EF. The electric field is enhanced as $|E|^2$ at each stage. When both the incident light and the scattering resonate with plasmon frequency, the maximum enhancement can be obtained as the fourth power of the incident field $|E|^4$. EM is thought to be the main contribution to SERS EF, and is nonselective that gives the same enhancement to all types of molecules on the surfaces either through chemisorption or physisorption.

9.3.1.2 Chemical Enhancement (CE)

It is due to the electronic interaction between chemically adsorbed molecules and metallic surfaces. CE can be understood in a way that the interaction induces the formation of intermediates which have a larger scattering cross-section than that of original molecules. The most widely accepted explanation for this is the so-called charge transfer (CT), which can be from the highest occupied molecular orbital (HOMO) of molecules to the Fermi level of metal, and the Fermi level of metal to the

lowest unoccupied molecular orbital (LUMO). Yet researchers have not reached an agreement on the mechanisms and enhancement contributions of CT effect, of which the reported EF was in a wide range of 10 to as high as 10^7 to 10^8 [25]. Also, there are different explanations for the CT effect, including the vibronic coupling model based on the selection rule [26], tunneling or electron transport at metal–molecule–metal interface [27, 28].

9.3.2 Fabrication of SERS Probes

In SERS imaging, the Raman labels with characteristic spectrum are designed to attach to biological tissues or cells through bio-recognition. Then targets can be evaluated by reading the spectra of labels, as an indirect imaging strategy. These Raman labels are named as SERS probes (or SERS tags), which consist of metallic NPs, Raman reporters, protective layers and targeting ligands [29, 30]. In the fabrication process of a typical SERS probe (Fig. 9.4), each step follows certain strategies and principles of design, aiming to improve the intensity, sensitivity, stability, targeting efficiency and binding ability of the SERS probes.

9.3.2.1 Metal NPs

As the core of a SERS probe, the metal NP serves as a substrate to enhance the Raman signal of the molecules adsorbed on the surface. In recent years, plasmonic nanostructures with different sizes and shapes have been intensively studied such as nanospheres, nanorods, nanostars, hollow nanocages and core-shell particles with interior nanogaps. Among them, three types of NPs reported to have ultrahigh EF are: (1) the ones with sharp tips (e.g., nanostars), (2) the assembled NP aggregates with large numbers of hot spots (e.g., NP dimers or trimers), (3) NPs with interior nanogaps as built-in hot spots (e.g., Au core/gap/Au shell NP). Still, Au or Ag nanospheres are the most commonly applied NPs because of their convenient synthetic routes.

9.3.2.2 Raman Reporters

These reporter molecules attached onto the metal NPs endow SERS probes with unique Raman spectra. Generally, the metallic NPs and Raman reporters are the

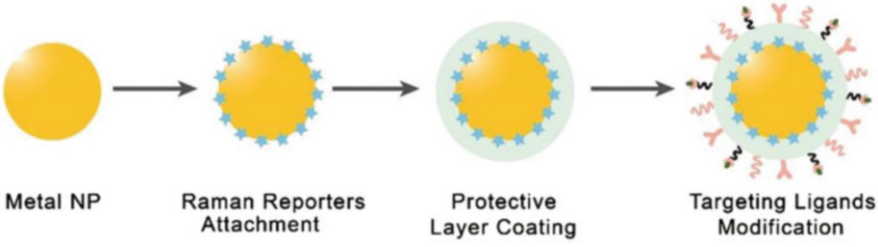

Fig. 9.4 Fabrication process of a typical SERS probe

basic unit of a SERS probe to provide the strong and characteristic Raman signals, being decisive on the specificity and sensitivity of SERS imaging. There are several strategies to choose suitable Raman reporters [29, 30]: (1) molecules are with a large scattering cross-section for obtaining strong Raman signals, which typically feature aromatic rings or π-conjugated systems; (2) molecules can be easily adsorbed onto metal substrates through physisorption or chemisorption, e.g., molecules with sulfhydryl groups, amino groups, and carboxyl groups; (3) molecules should have, but not too many, characteristic Raman bands to minimize the band overlap with other molecules in a multiplexing analysis; (4) molecules with an electronic transition band in resonant with the incident laser are beneficial for the surface-enhanced resonant Raman scattering (SERRS) effect, gaining additional 10- to 100-fold enhancement [31].

9.3.2.3 Protective Layer

The compound of metal NP-Raman reporter is the core of a SERS probe, but this simple structure lacks stability and its Raman signal is easily interfered by the surrounding environment. The protective layer is thus adopted to: (1) enhance the stability and biocompatibility of NPs by replacing the original stabilizers or surfactants on their surface; (2) offer the anchoring sites for targeting ligands; (3) protect Raman reporters from directly contacting and being affected by the solution medium. The materials of protective layers can be silica, mesoporous silica, polymers (including polyethylene glycol, polyvinylpyrrolidone, polydiacetylenes), dihydrolipoic acid, *etc*. Nowadays, silica is mostly adopted due to its easy fabrication, and has been applied in commercial Nanoplex™ biotags—a type of silica coated Au NP SERS probes.

9.3.2.4 Targeting Ligands

In the final step of fabrication, the ligands are conjugated to the surface of SERS probes. This step is of critical effects in imaging specificity since the interaction between ligands and targets leads SERS probes to migrate to specific sites. The selection of ligands, including proteins, nucleic acids, aptamers, and small biomolecules, depends on the types of target molecules, e.g., receptors on the tumor cell surface.

The SERS probes facilitate the researches and applications of Raman-based imaging and detections owing to its impressive advantages over conventional optical labels (e.g., organic fluorescent dyes and quantum dots) [32]:

1. High sensitivity down to the single-NP detection level.
2. The narrow bandwidth (usually ~10 cm^{-1}) much smaller than that of fluorescent dyes (~50 nm), which minimizes the peak overlapping for various Raman molecules in the multiplex assays.
3. High photostability under continuous laser irradiation.
4. The selectable excitation wavelength by adjusting the morphology of the SERS substrate and choosing a specific Raman molecule.

9.3.3 SERS Imaging in Biological Studies

9.3.3.1 Cell Imaging

The in vitro cell bioimaging yields information on the cellular biomarkers' expression, intracellular organelles, interactions and dynamics, thus being widely applied and playing a critical role in fundamental biological studies. SERS probes are of intrinsic photostability and multiplexing capability, and the surface coating further brings in high specificity and targeting efficiency, making them ideal optical agents. SERS probes can identify cancer cells via the recognition between specific membrane cancer marker and targeting ligands, such as anti-epidermal growth factor receptor (EGFR) antibodies.

As a nondestructive and sensitive detection technique for chemical components in living cells, SERS cell imaging can be applied for studying the biomarker expression on cell membrane. Additionally, it can be adopted to study and visualize the local chemistry and changes in cell micro environment. The main principle for this type of measurement is to use the target-sensitive Raman reporters. For example, in order to detect the dynamic detection of local pH in living cells, the molecules with pH-dependent spectra are favorable, such as 4-mercaptobenzoic acid (MBA) or 2-aminobenzenethiol (ABT) whose carboxyl or amino groups can be protonated at low pH [32]. Typically, the signal ratios of 1423 cm^{-1} mode (COO- stretching mode) to 1076 cm^{-1} (aromatic ring vibration) of MBA molecules can be applied to sense pH variation. Similarly, to detect the cholesterol in living cells, the Au/Ag NPs modified with 4-mercaptophenylboronic acid (MPBA) on the shell surface was developed [33]. MPBA can react with H_2O_2 and convert into 4-hydroxybenzenethiol (HBT), inducing a change in SERS signal. These NPs can be used to quantify and map the intracellular cholesterol via the produced H_2O_2 in cholesterol oxidation process, proving a reliable SERS mapping analysis of intracellular H_2O_2 and cholesterol at single-cell level.

9.3.3.2 Multiplexing Imaging

The multiplexing imaging has also been intensively studied using SERS probes, which is of multiplexing capability of detecting cancer biomarker on the cell membrane, and the concentration of the biomarkers could be calculated through data processing of individual Raman spectrum, demonstrating the potential for high throughput mapping of cancer cells. For example, researchers have applied the ultrasensitive SERS probes as intracellular imaging agents, which can be embedded with different Raman reporters, and modified with different types of targeting ligands: cell-penetrating peptide, mitochondria-targeting peptide, nucleus-targeting peptide. Their characteristic Raman spectrum can be separated to obtain the location of each type of SERS probes in cells. The multiplexing live-cell imaging is achieved in high-speed (10 ms/pixel) with 200 μW laser power and 785 nm excitation [34]. This work demonstrates promising subcellular organelle targeting and multiplexed capabilities for informative SERS cell imaging, also reveals a great potential for the high throughput SERS imaging of living subjects in the future.

9.3.4 SERS Imaging in Disease Diagnostics

9.3.4.1 Tumor Imaging

SERS has emerged as a powerful tool for in vivo imaging and overcomes several limitations of other imaging methods. The biosafety of SERS probes is expected that no evidence of significant toxicity was observed 2-week after administration in mice [35]. The photostability of SERS probes surpasses the fluorophores. Also, they can be used with adjustable laser excitation and allow multiplexing imaging without strong autofluorescence background interference of tissues.

Starting from one decade ago, researchers have achieved in vivo tumor detection on the mice model. In 2008, Nie et al. using polyethylene glycol coated Au NPs as SERS probes with crystal violet molecules as Raman molecules, which can attach to xenograft tumor models by EGFR biomarkers on human cancer cells [36]. Similar experiments were reported by Kircher et al. using carbon nanotubes as SERS substrate [37]. Following these pioneered works, plenty of progress has been made toward in vivo tumor SERS imaging, mainly to reduce acquisition time by developing brighter SERS probes, improving target specificity, and optimizing Raman system and methodologies [29]. So far, different SERS tags have been developed like Au NPs, nanostars, nanorods, gap-enhanced Raman tags (GERTs) and carbon NPs, with a potential for multiplexing tumor imaging, showing broad research interest in engineering and medicine [29, 38, 39].

Researchers have also begun to integrate SERS with other imaging modalities, such as fluorescence, photoacoustic imaging, PET, CT, and MRI. Gambhir et al. has invented a unique triple modal agent for magnetic resonance imaging, photoacoustic imaging and SERS imaging. This tri-modality agent can help delineate the margins of brain tumors in living mice both preoperatively and intraoperatively, showing the promise for precise brain tumor imaging and resection [40]. Similarly, a type of core-shell Au nanorods embedded with fluorophores of high Raman cross-sections was designed as fluorescence-Raman bimodal nanoprobes by Kircher et al. [41]. Their dual-mode imaging has achieved the visualization of tumor sites on mice models of subcutaneous ovarian cancer or the glioblastoma. The work demonstrates the potential of the integrated fluorescence-Raman technique in cancer imaging.

9.3.4.2 Lymph Node Localization

The sentinel lymph node (SLN) is considered as the first station for metastatic tumors to spread to other parts of the body through the lymphatic system. The presence or absence of cancer cells in SLN could be critical in determining the stage of cancers. As a result, the SLN identification is a key step in the investigation procedure for lymphatic metastasis of tumor sites, in which the optical imaging technique is usually applied. The SERS probes can fulfill the requirement as an SLN imaging agent. In recent years, Ye et al. developed the core-shell structured GERTs [42, 43], which is reported to have strong EF, high photostability, long retention time (24 h) in lymph node, convenient usage (injection 2 h before surgery), and good imaging depth (over 2 mm). They not only allow the high-contrast and deep imaging, but provide the dynamic migration trace of SERS probes into the SLN.

The high-resolution three-dimensional margin of SLN can be visualized through quantitative volumetric Raman imaging data processing. It is also possible to apply a portable Raman spectrometer to locate the SLN, proving a promising potential for convenient preclinical applications.

9.3.4.3 SERS Image-Guided Surgery

Despite major advances in targeted drug and radiation therapies, surgery is still the most effective treatment for localized tumors. Benefited from the development and application of portable Raman scanners and Raman endoscopes, precision cancer surgery guided by intraoperative Raman imaging has been explored in biomedical studies [44]. A SERS probe with high brightness, good targeting capability and specificity can be beneficial for the complete tumor resection surgery of the primary tumor, draining lymph nodes and metastatic sites. Ye et al. developed a type of sensitive core-shell SERS NPs with embedded Raman reporters, showing a detection limit of 20 fM in aqueous solution under laser power density of 10^5 W/cm^2 and 1.86 s integration time [38, 45]. These SERS probes can be applied to identify the tumor margin and locations of micro satellite metastases, as demonstrated in mice for the successful diagnostics of disseminated ovarian cancers, as well as the treatment of the prostate tumors, opening the possibility for more complete tumor resection.

Since SERS probes have large surface areas for functionalization, it is also possible to incorporate other therapy methodologies, including photodynamic therapy, photothermal therapy, and chemotherapeutic delivery, to achieve an image-guided therapy. For example, plasmonic NPs can be served as photothermal agents due to their intrinsic EM enhancement ability. Under continuous irradiation, the SERS probes can have high-enough temperature as the therapeutic agents for image-guided photothermal ablation of tumors [46]. Also, by loading drugs in the surface coating layer of SERS probes, one can perform the Raman-guided chemo-photothermal synergistic therapy [47]. This can be designed for the SERS probes to precisely bind to tumor sites, revealing tumor margin, releasing drugs under the irradiation, killing tumor cells in high temperature, and thus minimizing the side effects on normal tissues. It proves that SERS probes are a robust platform for the intraoperative diagnosis and treatment of tumors.

9.4 Perspective and Conclusions

Raman imaging, including spontaneous Raman and SERS microscopic imaging technique, have been explored to provide the high-resolution noninvasive molecular analysis of biological samples, and shows a breakthrough potential for the diagnoses on human diseases.

Spontaneous Raman imaging is capable to obtain label-free chemical images of samples especially in vitro. Various strategies have been adopted to optimize its performance, such as developing advanced instruments, or enhancing contrast by attaching Raman labels. However, it is still far from clinical application due to the limitations of imaging speed. Huge research opportunities exist in its data acquisition

techniques, spectral processing and analysis methodologies. For example, Raman systems should be updated by reducing either the scanning or data collecting time for high-speed and wide-field imaging. A small-animal Raman imaging system with a speed of 1.5 min for a 5 mm × 5 mm area was reported, showing a tenfold and 240-fold improvement in scan time compared with the Streamline™ (Renishaw) and the normal scan mode, respectively [48].

In contrast, SERS imaging possesses several advantages over spontaneous Raman imaging with reduced time, better photostability, sensitivity, and capability of multiplexing imaging, and has achieved huge progress during the past decade. Nevertheless, the most threatening impediment to its general application is still the imaging speed, particularly compared to that of fluorescence imaging. Its typical exposure time on a single cell is in minutes, which may damage the biological samples and hinder the high-resolution live cell imaging. Efforts have been devoted in two aspects to circumvent this problem. The first is to develop advanced Raman spectrometers, which can also be used for spontaneous Raman imaging. The second is to invent brighter SERS probes. A series of work has been undertaken so far. For example, a type of core-shell probes with the embedded Raman reporters and the petal-like Au shells were reported to have a 10^9 EF and the single-NP detection sensitivity. They allowed the high-resolution cell imaging within 6 s in an area of 50 × 50 pixels, under a 370 μW laser by using the commercial confocal Raman microscopy. In vivo imaging on mice models using the same power and an acquisition time of 0.7 ms per pixel on an area of 3.2 × 2.8 cm^2 was also achieved, which enables high-contrast Raman imaging with a signal-to-background ratio up to ~80 [49].

Like other optical imaging techniques, the tissue penetration in SERS imaging is limited by the absorption and scattering of photons. This hinders the deep tissue imaging on large animals or whole-body scanning on humans. Attempts to circumvent this problem including the development of SERS probes for the second near-infrared window (NIR-II). The NIR-II region of 1000–1700 nm has drawn much attention in bioimaging due to its high improvement in penetration depth and spatial resolution by reducing scattering, absorption, and autofluorescence of tissues. Researches on a direct comparison between NIR-I and NIR-II SERS have demonstrated that the latter provides more favorable optical conditions on biological tissues than the former [50]. It thus would be a great benefit for the studies and applications of SERS imaging with suitable NIR-II probes. Other efforts have been put on the development of multimodal SERS probes, which integrates SERS with other imaging techniques (such as photoacoustic imaging, PET, CT, and MRI) to overcome the limitations of tissue penetration in optical imaging.

Finally, although a variety of fascinating SERS probes have been developed, there are still many obstacles needed to overcome for clinical application, which requires the regulatory approval of the inert NPs based on the knowledge of the pharmacokinetics and toxicity related to metallic, inorganic, and polymeric materials.

References

1. Langer J, Jimenez De Aberasturi D, Aizpurua J, Alvarez-Puebla RA, Auguié B et al (2020) Present and future of surface enhanced Raman scattering. ACS Nano 14:28
2. Le Ru E, Etchegoin P (2008) Principles of surface-enhanced Raman spectroscopy: and related plasmonic effects. Elsevier, Amsterdam
3. Kneipp J, Kneipp H, Kneipp K (2008) SERS—a single-molecule and nanoscale tool for bioanalytics. Chem Soc Rev 37:1052
4. Lane LA, Qian X, Nie S (2015) SERS nanoparticles in medicine: from label-free detection to spectroscopic tagging. Chem Rev 115:10489–10529
5. Zhang Y, Zhen Y, Neumann O, Day JK, Nordlander P et al (2014) Coherent anti-stokes Raman scattering with single-molecule sensitivity using a plasmonic Fano resonance. Nat Commun 5:4424
6. Cheng J, Xie XS (2016) Coherent Raman scattering microscopy. CRC press, Boca Raton, FL
7. Durrant B, Trappett M, Shipp D, Notingher I (2019) Recent developments in spontaneous Raman imaging of living biological cells. Curr Opin Chem Biol 51:138–145
8. Tan Z, Zhang Y, Thackray BD, Ye J (2019) Improvement of surface-enhanced Raman scattering detection and imaging by multivariate curve resolution methods. J Appl Phys 125:173101
9. Byrne HJ, Knief P, Keating ME, Bonnier F (2016) Spectral pre and post processing for infrared and Raman spectroscopy of biological tissues and cells. Chem Soc Rev 45:1865–1878
10. Člupek M, Matějka P, Volka K (2007) Noise reduction in Raman spectra: finite impulse response filtration versus Savitzky-Golay smoothing. J Raman Spectrosc 38:1174–1179
11. Shen Y, Hu F, Min W (2019) Raman imaging of small biomolecules. Annu Rev Biophys 48:347–369
12. Krafft C, Schie IW, Meyer T, Schmitt M, Popp J (2016) Developments in spontaneous and coherent Raman scattering microscopic imaging for biomedical applications. Chem Soc Rev 45:1819–1849
13. Thomas GJ (1999) Raman spectroscopy of protein and nucleic acid assemblies. Annu Rev Biophys Biomol Struct 28:1–27
14. Wang Y, Huang WE, Cui L, Wagner M (2016) Single cell stable isotope probing in microbiology using Raman microspectroscopy. Curr Opin Biotechnol 41:34–42
15. Yamakoshi H, Dodo K, Okada M, Ando J, Palonpon A et al (2011) Imaging of EdU, an alkyne-tagged cell proliferation probe, by Raman microscopy. J Am Chem Soc 133:6102–6105
16. Kaczor A, Marzec KM, Majzner K, Kochan K, Pacia MZ et al (2018) Raman imaging of biomedical samples. In: Confocal Raman microscopy. Springer, New York, NY
17. Gomes Da Costa S, Richter A, Schmidt U, Breuninger S, Hollricher O (2019) Confocal Raman microscopy in life sciences. Morphologie 103:11–16
18. Yamakoshi H, Dodo K, Palonpon A, Ando J, Fujita K et al (2012) Alkyne-tag Raman imaging for visualization of mobile small molecules in live cells. J Am Chem Soc 134:20681–20689
19. Jin Q, Fan X, Chen C, Huang L, Wang J et al (2019) Multicolor Raman beads for multiplexed tumor cell and tissue imaging and in vivo tumor spectral detection. Anal Chem 91:3784–3789
20. You A, Bergholt MS, St-Pierre JP, Kit-Anan W, Pence IJ et al (2017) Raman spectroscopy imaging reveals interplay between atherosclerosis and medial calcification in the human aorta. Sci Adv 3:e1701156
21. Bik E, Mielniczek N, Jarosz M, Denbigh J, Budzynska R et al (2019) Tunicamycin induced endoplasmic reticulum changes in endothelial cells investigatedin vitro by confocal Raman imaging. Analyst 144:6561
22. Krafft C, Belay B, Bergner N, Romeike BF, Reichart R et al (2012) Advances in optical biopsy--correlation of malignancy and cell density of primary brain tumors using Raman microspectroscopic imaging. Analyst 137:5533–5537

23. Ogawa M, Harada Y, Yamaoka Y, Fujita K, Yaku H et al (2009) Label-free biochemical imaging of heart tissue with high-speed spontaneous Raman microscopy. Biochem Biophs Res Commun 382:370–374
24. Fleischmann M, Hendra PJ, McQuillan AJ (1974) Raman spectra of pyridine adsorbed at a silver electrode. Chem Phys Lett 26:163–166
25. Park W, Kim ZH (2010) Charge transfer enhancement in the SERS of a single molecule. Nano Lett 10:4040–4048
26. Lombardi JR, Birke RL (2009) A unified view of surface-enhanced Raman scattering. Acc Chem Res 42:734–742
27. Lin L, Zapata M, Xiong M, Liu Z, Wang S et al (2015) Nanooptics of plasmonic nanomatryoshkas: shrinking the size of a core–shell junction to subnanometer. Nano Lett 15:6419–6428
28. Lin L, Zhang Q, Li X, Qiu M, Jiang X et al (2018) Electron transport across plasmonic molecular nanogaps interrogated with surface-enhanced Raman scattering. ACS Nano 12:6492–6503
29. Jiang C, Wang Y, Song W, Lu L (2019) Delineating the tumor margin with intraoperative surface-enhanced Raman spectroscopy. Anal Bioanal Chem 411:3993–4006
30. Wang Z, Zong S, Wu L, Zhu D, Cui Y (2017) SERS-activated platforms for immunoassay: probes, encoding methods, and applications. Chem Rev 117:7910–7963
31. McNay G, Eustace D, Smith WE, Faulds K, Graham D (2011) Surface-enhanced Raman scattering (SERS) and surface-enhanced resonance Raman scattering (SERRS): a review of applications. Appl Spectrosc 65:825–837
32. Wang Y, Yan B, Chen L (2013) SERS tags: novel optical nanoprobes for bioanalysis. Chem Rev 113:1391–1428
33. Jiang X, Tan Z, Lin L, He J, He C et al (2018) Surface-enhanced Raman nanoprobes with embedded standards for quantitative cholesterol detection. Small Methods 2:1800182
34. Kang JW, So PTC, Dasari RR, Lim D (2015) High resolution live cell Raman imaging using subcellular organelle-targeting SERS-sensitive gold nanoparticles with highly narrow intra-nanogap. Nano Lett 15:1766–1772
35. Thakor AS, Luong R, Paulmurugan R, Lin FI, Kempen P et al (2011) The fate and toxicity of Raman-active silica-gold nanoparticles in mice. Sci Transl Med 3:33r–79r
36. Qian X, Peng X, Ansari DO, Yin-Goen Q, Chen GZ et al (2008) In vivo tumor targeting and spectroscopic detection with surface-enhanced Raman nanoparticle tags. Nat Biotechnol 26:83–90
37. Zavaleta C, de la Zerda A, Liu Z, Keren S, Cheng Z et al (2008) Noninvasive Raman spectroscopy in living mice for evaluation of tumor targeting with carbon nanotubes. Nano Lett 8:2800–2805
38. Zhang Y, Liu Z, Thackray BD, Bao Z, Yin X et al (2018) Intraoperative Raman-guided chemo-photothermal synergistic therapy of Aadvanced disseminated ovarian cancers. Small 14:1801022
39. Davis RM, Kiss B, Trivedi DR, Metzner TJ, Liao JC et al (2018) Surface-enhanced Raman scattering nanoparticles for multiplexed imaging of bladder cancer tissue permeability and molecular phenotype. ACS Nano 12:9669–9679
40. Kircher MF, de la Zerda A, Jokerst JV, Zavaleta CL, Kempen PJ et al (2012) A brain tumor molecular imaging strategy using a new triple-modality MRI-photoacoustic-Raman nanoparticle. Nat Med 18:829–834
41. Pal S, Ray A, Andreou C, Zhou Y, Rakshit T et al (2019) DNA-enabled rational design of fluorescence-Raman bimodal nanoprobes for cancer imaging and therapy. Nat Commun 10:1926
42. Bao Z, Zhang Y, Tan Z, Yin X, Di W et al (2018) Gap-enhanced Raman tags for high-contrast sentinel lymph node imaging. Biomaterials 163:105–115

43. Zhang Y, Qiu Y, Lin L, Gu H, Xiao Z et al (2017) Ultraphotostable mesoporous silica-coated gap-enhanced Raman tags (GERTs) for high-speed bioimaging. ACS Appl Mater Interfaces 9:3995–4005
44. Karabeber H, Huang R, Iacono P, Samii JM, Pitter K et al (2014) Guiding brain tumor resection using surface-enhanced Raman scattering nanoparticles and a hand-held Raman scanner. ACS Nano 8:9755–9766
45. Qiu Y, Zhang Y, Li M, Chen G, Fan C et al (2018) Intraoperative detection and eradication of residual microtumors with gap-enhanced Raman tags. ACS Nano 12:7974–7985
46. Jin X, Khlebtsov BN, Khanadeev VA, Khlebtsov NG, Ye J (2017) Rational design of ultrabright SERS probes with embedded reporters for bioimaging and photothermal therapy. ACS Appl Mater Interfaces 9:30387–30397
47. Gandra N, Portz C, Singamaneni S (2014) Multifunctional plasmonic nanorattles for spectrum-guided locoregional therapy. Adv Mater 26:424–429
48. Bohndiek SE, Wagadarikar A, Zavaleta CL, Van de Sompel D, Garai E et al (2013) A small animal Raman instrument for rapid, wide-area, spectroscopic imaging. Proc Natl Acad Sci 110:12408–12413
49. Zhang Y, Gu Y, He J, Thackray BD, Ye J (2019) Ultrabright gap-enhanced Raman tags for high-speed bioimaging. Nat Commun 10:1–12
50. Lane LA, Xue R, Nie S (2018) Emergence of two near-infrared windows for in vivo and intraoperative SERS. Curr Opin Chem Biol 45:95–103

Optical Coherence Tomography for Ophthalmology Imaging

10

Jia Qin and Lin An

10.1 Introduction

Optical Coherence Tomography (OCT) is a noncontact, noninvasive biomedical imaging technology which developed rapidly in recent years [1–3]. It is able to achieve ~1 to 15 μm imaging resolution for biological tissue. The basic principle of OCT is based on a technique called low coherence interferometry, which was used to measure the eye-length by Fercher in 1988 [4]. In 1991, researchers lead by James Fujimoto demonstrated that [1] by scanning the imaging beam along lateral direction, the low coherent imaging system could achieve microlevel optical biopsy of human tissue, which is named as Optical Coherence Tomography. Since then, tremendous efforts have been made by scientists all around the world [5–14]. The imaging performance of OCT system, such as imaging resolution [7, 8, 15, 16], imaging speed [9, 11, 17, 18], imaging depth [12, 13, 19], etc., has been improved impressively. Nowadays, OCT has been used in several clinical applications, such as ophthalmology [20–22], cardiology [23], dermatology [24, 25].

Compared with other imaging techniques, such as ultrasonic imaging, nuclear magnetic resonance imaging (MRI), X-ray computerized tomography (CT), OCT technology has much higher resolution (several microns), which is able to offer much more detailed information for researchers and physicians. As to the imaging depth, it is able to penetrate ~1 to 2 mm in biological tissue, which is much deeper compared with confocal microscopy (multiphoton microscopy) [26, 27]. Considering the delicate structure and clear optical pathway, the human eye is a perfect match for OCT. Nowadays, OCT has become a routine diagnostic procedure for ophthalmic

J. Qin (✉) · L. An
Innovation and Entrepreneurship Teams Project of Guangdong Pearl River Talents Program, Guangdong Weiren Meditech Co., Ltd, Foshan, Guangdong, People's Republic of China

X. Wei, B. Gu (eds.), *Optical Imaging in Human Disease and Biological Research*, Advances in Experimental Medicine and Biology 1355,
https://doi.org/10.1007/978-981-15-7627-0_10

diseases, such as Glaucoma [21, 28], Macular Degeneration [29–31], Retinal Detachment [20, 32], and so on.

In the past almost 30 years, the developments of OCT could be roughly divided into three stages. For each stage, the OCT system was able to substantially change the manage strategy of different types of ocular diseases. From 1991 to 2003, the OCT system is based on time domain setup, which obtain the subsurface information by scanning the reference arm [7, 15, 33]. Although it is difficult for the time domain system to achieve high-speed imaging in vivo, the attractive features demonstrated by this type of system make it become a popular tool in ophthalmic clinicians [34]. For example, it is the first time for ophthalmic physicians to check the ocular disease from the axial direction [8, 34]. The thickness of different layers of retina had become new biomarkers for several ocular diseases, such as diabetic retinopathy (DR) [34] and glaucoma [35], etc. The second stage of OCT is called Fourier Domain OCT (FD-OCT), which captured the interference signal by either a high-speed spectrometer or a swept source [36, 37]. Due to the elimination of mechanical scanning requirements of reference arm, the FD-OCT system is able to achieve much faster imaging speed than TD-OCT system [6]. With the improved imaging speed, the new version OCT could deliver 3D images and *en face* images of different depth from the pathological region. The third stage of OCT developments starts recently. After Optovue launched OCT angiography (OCTA) device in Europe in 2014 and Carl Zeiss Meditec received FDA clearance for OCTA system in 2015, OCTA has become a powerful tool for diagnosis of lots of ocular diseases [38]. Because OCTA is noninvasive and noncontact, it has substantially changed the way in which some ocular diseases have been diagnosed and managed, for example, age-related macular degeneration (AMD) [39, 40].

In this chapter, we will roughly review the three stages of ophthalmic OCT techniques. Several representative systems which have made significant contributions to OCT developments will be reviewed in detail respectively. For each system, the principle and setup configuration will be illustrated first followed by a brief introduction of their clinical applications. The review concludes with discussions on potential directions of OCT developments and clinical applications as well as the expectations for further improvements of OCT imaging capabilities.

10.2 Time Domain OCT

In 1991, the researchers in Fujimoto's group, David Huang, etc., demonstrated that a novel imaging modality could be achieved by scanning the imaging beam of a low coherence interferometer [1]. The system diagram is illustrated in Fig. 10.1. It is an optical analog of ultrasound B-mode imaging mode. For ultrasound, the system can detect the sound echo reflected from different depth of the imaging sample sequentially. Because the speed of light is much higher than ultrasound, the detection of light echo is achieved by a coherence gate which is generated by a broad band light source. When the coherence gate was scanned by moving the reference arm along axial direction, the light reflected from the layers which matching the optical path

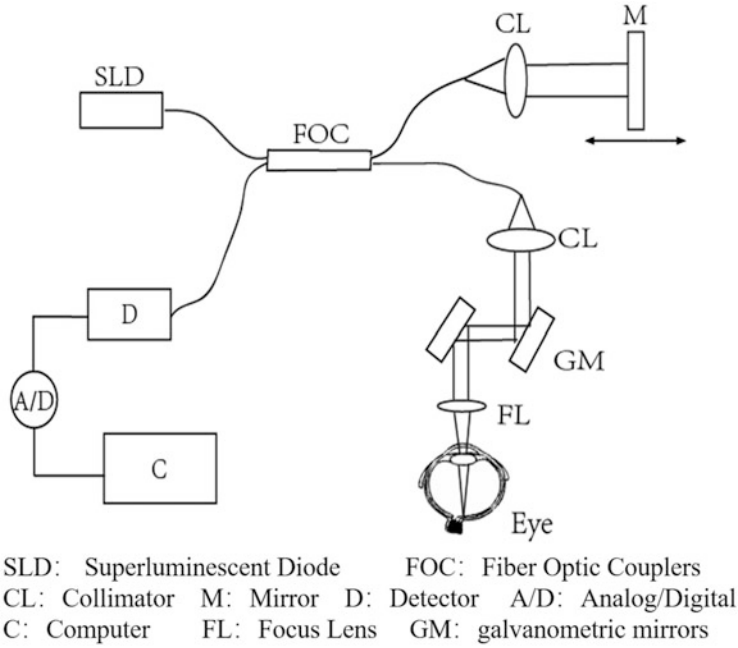

Fig. 10.1 System schematic of time domain OCT system

length could be detected sequentially to form the depth profile of the sample, which was called A-line. This technology was called low coherence interferometry [41], which has been widely used in lots of applications, such as temperature [42], pressure [43] and strain [44]. If the imaging beam was scanned along the lateral direction, a B-scan image could be generated when all the A-lines were captured during scanning. Because the lateral resolution is determined by the coherent gate of the light source, when a light source with wide bandwidth was used, the OCT system could achieve much higher lateral resolution (e.g., ~15 μm) compared to other types of optical imaging modalities, such as confocal microscopy. The OCT images were also called as "optical biopsy" [45].

For TD-OCT system, how to achieve reference mirror scanning speed upon required imaging depth is one of the most important technical issue to resolve. The higher the scanning speed of the reference mirror could achieve, the faster imaging speed the system could reach. For the first OCT system demonstrated in [1], the system uses a translation stage for referencing scanning. The imaging time is ~190 s for one cross-sectional image, which severely restrict its clinical applications. In 1996, 2 years after Zeiss acquire Advanced Optical Device (AOD), the first commercialized OCT system, OCT1, was launched [46]. Compared to the first demo system, OCT1 could achieve 100 frames per second due to implementation of high sensitivity interferometric receivers, optical fiber and galvanometric beam steering devices. Although the system was able to produce in vivo two dimensional

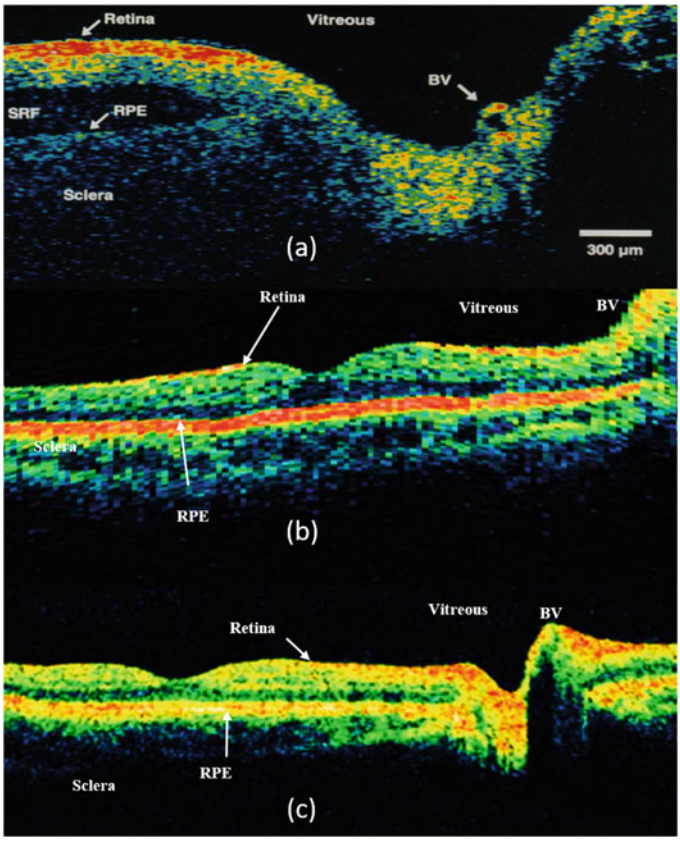

Fig. 10.2 (**a**) In vitro human retinal images obtained by the first OCT system demonstrated in [1]. (**b**) In vivo human retinal images captured by the first commercial ophthalmic OCT system, OCT1, launched by the Zeiss; (**c**) In vivo human retinal images captured by the third generation TD-OCT system, Stratus. Based on a fast scanning optical delay line, it can reach 400 frames per second and were accepted by ophthalmic clinicians. *RPE* retinal pigment epithelium, *BV* blood vessel

human retinal images, it was not widely accepted by the clinicians because of the poor image quality. From 1996 to 2002, only several hundreds of OCT system were sold all over the world. Until 2002, Zeiss launched its third generation OCT system Stratus which could reach 400 frames per second based on a technology named as fast scanning optical delay line. At that time, the OCT technique could provide clinical valuable images and be accepted as an important ophthalmic diagnostic tool all over the world.

In Fig. 10.2, three images captured from the systems mentioned above (the first OCT system, OCT1 and Stratus) were presented to demonstrate the improvements of OCT images produced by different generations of TD-OCT systems. From

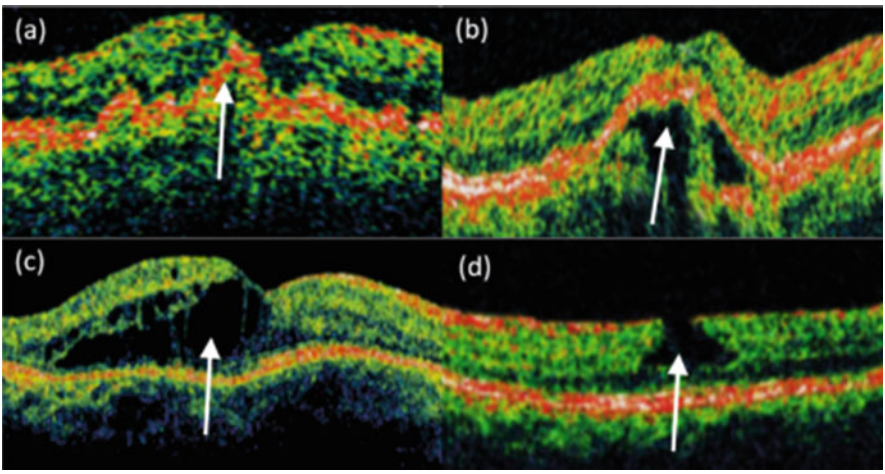

Fig. 10.3 Representative OCT images captured by Stratus system from different patients. (**a**) AMD patient with soft drusen; (**b**) AMD patient with pigment epithelium detachment (PED); (**c**) the image of patient with diabetic cystoid macular edema; (**d**) the image of patient with macular hole

Fig. 10.2a–c, the image quality was improved dramatically. For the first OCT system (as demonstrated in Fig. 10.2a), limited by the imaging speed, it was only able to capture images from in vitro sample. Due to the poor spatial resolution, it could only resolve obvious retinal morphology features, such as RPE. The detailed microstructures in the layers of retina could not be identified. For the first commercialized ophthalmic OCT system, OCT1, the imaging speed had been dramatically improved, it only took ~1.5 s to capture one cross-sectional image, which make it possible to directly achieve in vivo human retina imaging. As illustrated in Fig. 10.2b, the image could present similar retinal features compared to the first system, such as retina layer, RPE and blood vessels. However, there were two issues that restricts it from widely clinical applications. The first is the slow imaging speed, which generates severe motion artifacts. Another one is the poor spatial resolution, which makes it difficult to resolve micro features of the lesion region. In 2002, Zeiss launched the third generation TD-OCT system, Stratus. Based on a technology called fast scanning optical delay lines, it can reach 400 frames per second. Compared to OCT1, the Stratus system effectively reduces the motion artifacts and improves the image quality. Small lesion features could be successfully identified. Stratus was the first commercial system that was widely accepted by the clinical ophthalmic doctors all over the world. Until 2006, more than 6000 systems were utilized in clinical applications and over 20 million ophthalmic OCT procedures were performed.

For better illustration that the Stratus could be widely accepted as a useful diagnostic tool, several representative lesion images captured with stratus system were demonstrated in Fig. 10.3. Figure 10.3a is the image captured from an 84 years

old male patient with AMD. As shown in Fig. 10.3a, several excrescences of the hyper-reflective RPE could be easily identified. Also, it is easy to be observed that the RPE layer (pointed by the white arrow) was elevated because of the accumulation of drusen material. Figure 10.3b is an image captured from a 76 years old male AMD patient with Stratus system. In this image, the elevation of RPE layers with low scattering region could be easily observed (pointed by the white arrow). Its appearance is consistent with an RPE detachment. Figure 10.3c shows a typical OCT retinal image with cystoid macular edema (CME). It was captured from a 45 years old female patient. The low intensity region with round or oval appearance (pointed by the white arrow) is the district cystic foveal legions, which were revealed clearly by OCT images. Figure 10.3d shows OCT image captured from a patient with lamellar macular hole. The loss of retinal tissue could be clearly revealed (pointed by the white arrow).

In a short summary, TD-OCT is the first generation of OCT system. It is able to offer in vivo micro-structure cross-sectional images for human retina. With this capability, TD-OCT could reveal pathology patterns which match with clinical study for clinical diagnosis. Compared to traditional ophthalmic diagnostic tools, such as fundus camera and FA, it is the first time that the doctors can manage the diagnosis and treatment progress from the depth dimension. TD-OCT system has achieved great success both on commercial and academic point of view. However, the imaging speed is not high enough because of the utilization of slow mechanical scanning component, which makes it difficult to achieve in vivo 3D or en face images of human retina.

10.3 Frequency domain OCT

With further developments on scanning components of reference arm, TD-OCT system is able to achieve 2 kHz imaging speed [47]. Still, the imaging speed is not high enough to capture 3D data of human retina in vivo. A novel technique, called Frequency Domain OCT, could dramatically improve the imaging speed as well as imaging sensitivity [6, 36, 37]. With FD-OCT system setup, the interference signal between the reference arm and sample arm could be detected directly without moving the reference mirror. The depth information encoded interferometric fringes were recorded by FD-OCT system according to the wave number. By applying Fast Fourier Transform, the depth profile of one A-line could be directly obtained. Another huge advantage that could be gained from FD-OCT setup is the sensitivity improvement [6, 37]. Usually, one A-line was calculated from more than 1000 points of data, which make it possible to achieve ~20 dB higher sensitivity than TD-OCT system. With sensitivity advantage, FD-OCT could achieve more than 10 times faster than TD-OCT system without image quality loss [11, 48, 49].

According to how the interferometric signal was captured, the FD-OCT system could be divided into Spectral Domain OCT (SD-OCT) and Swept-Source OCT (SS-OCT) systems, the system schematics are illustrated in Fig. 10.4a, b respectively. For SD-OCT system [17, 36], the interference signal between the reference

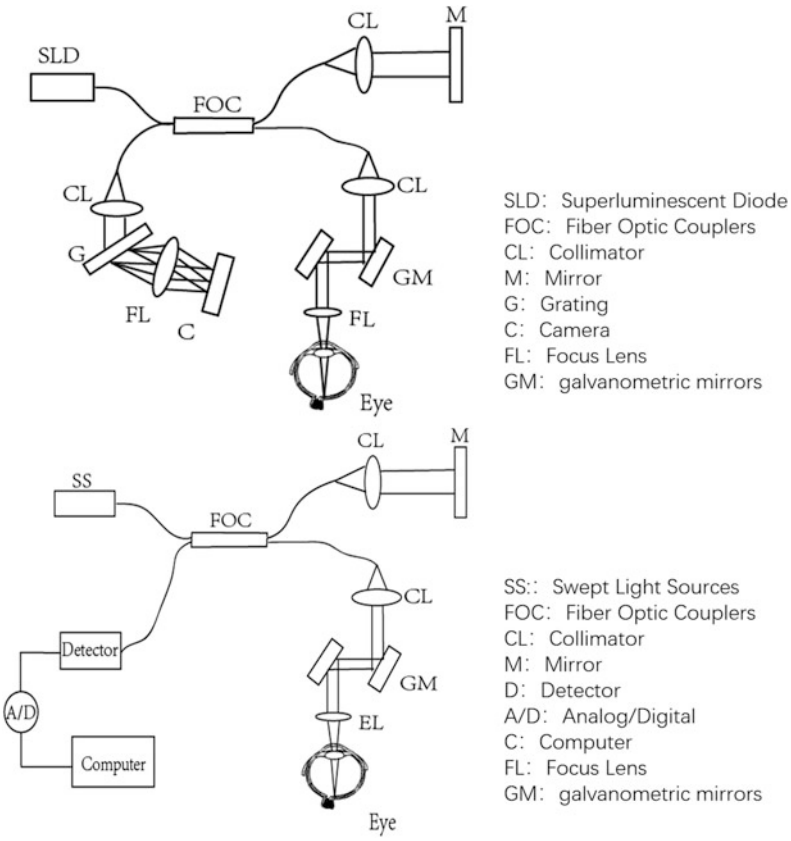

Fig. 10.4 System schematic of SD-OCT system and SS-OCT system

arm and sample arm were separated by a grating into different wavenumber and were captured by a high-speed line scan camera in parallel. For SS-OCT [50–53], the single wavelength light is emitted from the light source sequentially. After interfered between the sample and reference arm, the signal will be detected through a high balance detector. Although both system setups can achieve high speed for clinical applications, the SD-OCT system is more popular for clinical ophthalmic commercial system from the cost-effective point of view. In 2003, an American company, Optovue, launched its first commercial ophthalmic SD-OCT system, the imaging speed of which could reach 27 kHz. It is ~70 times higher than the imaging speed of Stratus system. Since then, Zeiss, Topcon, Heidelberg et al., have also launched their own SD-OCT systems, with imaging speed ranged from 25 to 80 kHz. Moreover, with improved imaging speed, the SD-OCT system is able to capture several B-scan images from the same location in a short time, which make it easier for further improving imaging quality with using an averaging procedure [54]. For better

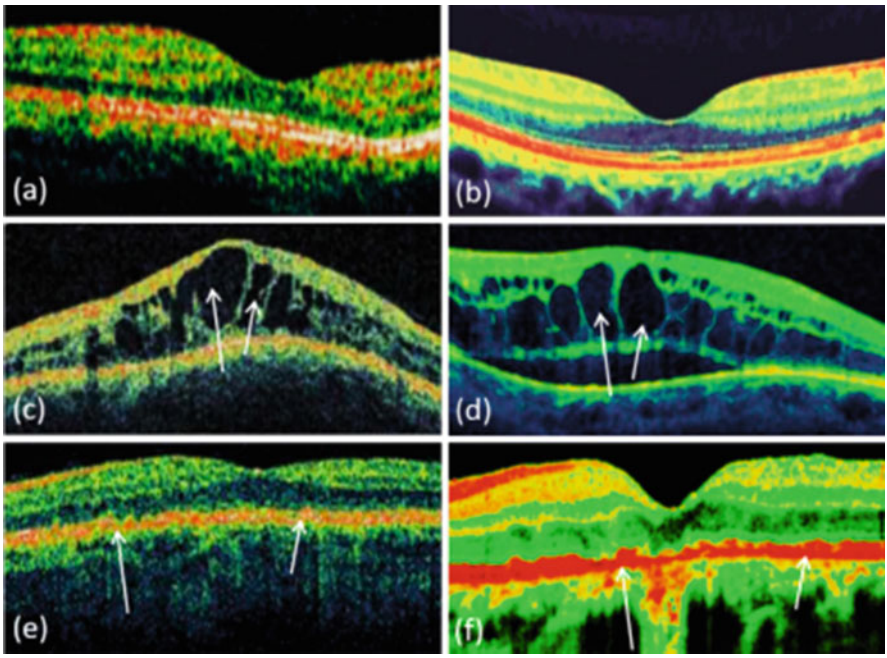

Fig. 10.5 (**a**–**f**) Comparison of OCT cross-sectional images captured from TD-OCT system, the left column, and FD-OCT system, the right column. The images were captured from normal people (the first row), people with diabetic macular edema (the middle row) and AMD patient with drusen (the bottom row)

illustration, several representative comparison images captured by Stratus and Cirrus OCT systems were demonstrated in Fig. 10.5.

Figure 10.5 shows several OCT images captured by the Status system and Cirrus system from the normal people (top row), people with diabetic macular edema (middle row) and people with dry AMD with drusen (bottom row). As illustrated by Fig. 10.5, although images captured by TD-OCT system is able to reveal clinical micro morphological features, such as cystic patterns (pointed by white arrows in Fig. 10.5c) for diabetic people, drusen (pointed by the white arrow in Fig. 10.5e) for AMD people, the overall image quality is much lower than FD-OCT system (Fig. 10.5b, d, f). First, FD-OCT could achieve higher imaging speed, which could suppress most of the inevitable eye movements of patients and make the images smoother compared to TD-OCT system. Second, also because of the higher imaging speed, the FD-OCT system is able to capture several images at the same location. By averaging these frames, the imaging quality could be dramatically improved. In [55, 56], researchers make detailed comparison between TD-OCT and FD-OCT systems, which demonstrated that FD-OCT is a better diagnostic tool for clinical applications.

With faster imaging speed and higher imaging sensitivity, the imaging capability of FD-OCT could be expanded significantly. Several useful features could be

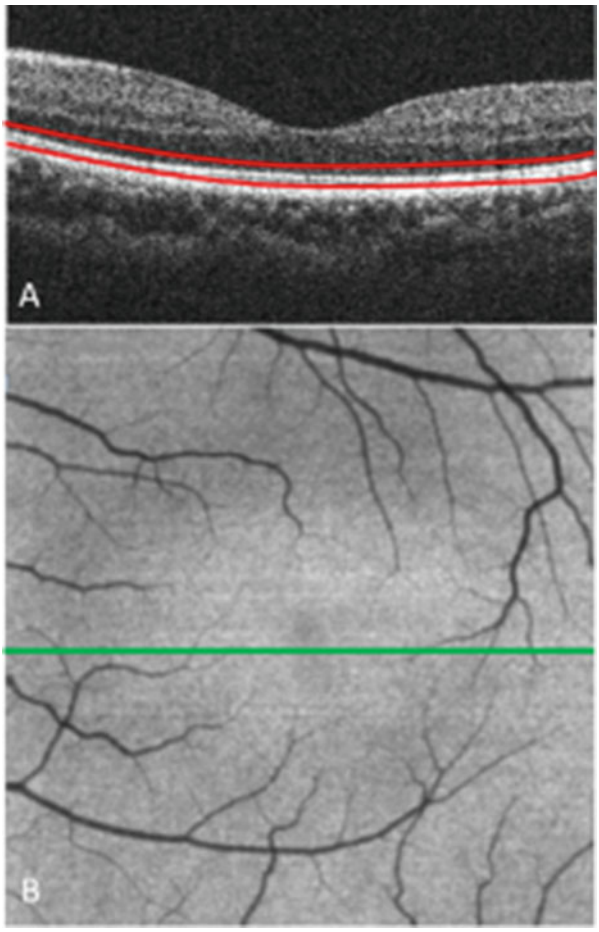

Fig. 10.6 OCT en face image visualization obtained by segmenting out the region of interest from cross-sectional B-scan images (**a**) and averaging the intensity values along depth direction (**b**)

developed through volumetric scans, which are difficult for TD-OCT system to produce high quality images. For example, the OCT en face images [57–59] of the required depth region and the high definition thickness map [60–62] of the region of interest usually require the OCT system to capture several hundreds of B-scans within several seconds for in vivo scans. While for TD-OCT system, only dozens of B-scan could be captured, which severely restricts the imaging quality and the diagnosis results [63]. The representative imaging results were illustrated in Figs. 10.6 and 10.7.

In vivo *en face* imaging is a technique developed based on the high-speed imaging capability of FD-OCT system, which make it possible for ophthalmic clinicians to make detailed diagnosis for a region of interest along lateral direction of a specific depth layer in the eye. Typically, it requires the system to perform a volumetric scan over a region of interest, which could capture several hundred

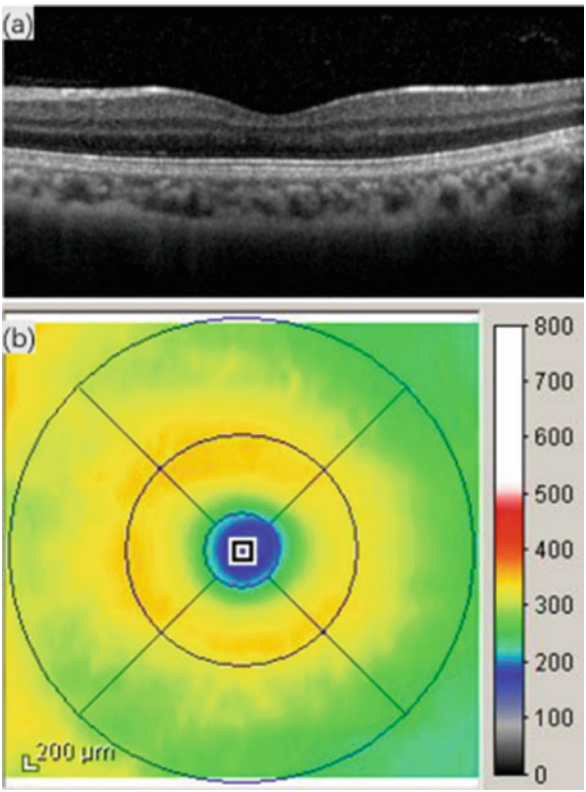

Fig. 10.7 Retinal OCT cross-sectional image captured from normal subject (**a**) and (**b**) the corresponding typical high definition retinal thickness map

B-scan images within few seconds. For each B-scan, the segmentation algorithm was performed to segment out the desired layers according to the imaging features. Then, the segmented A-line values were projected along the *z*-direction by performing an operation algorithm, such as averaging, maximizing, and minimizing. For example, for each A-line, the lowest intensity value could be selected to form an en face image, which could be a useful tool for visualizing cystic pocked for diabetic macular edema patients. In Fig. 10.6, a typical OCT en face slab is demonstrated, which could be used to visualize inner segment/outer segment (IS/OS) of a healthy subject. Figure 10.6a is the B-scan image obtained from the location marked by the green line in Fig. 10.6b. The two red curves are used to segment out the IS/OS layer, which were obtained first by segmenting the RPE layer and then moving up 20 μm and 40 μm respectively. To obtain Fig. 10.6b, the intensity values of each segmented A-lines were averaged to one value. The volumetric scan could be projected to a 2D en face slab.

Nowadays, OCT en face images have become an important diagnostic tool for ophthalmic clinical applications. Compared to the traditional fundus camera image or auto fluorescence images, et al., OCT en face images are able to visualize the lesion region according to the depth position, which could reveal more

morphological information with detail. In [64], researchers demonstrated several detailed comparison results between OCT fundus images with color fundus and autofluorescence fundus images. According to their comparison, OCT en face images are able to reveal similar clinical information for geographic atrophy diagnosis. In addition, combining with the OCT B-scan images, OCT en face images are able to locate the depth position of the lesion region precisely. It indicates that OCT is able to play more important roles in future ophthalmic clinical applications.

The high definition thickness map is also an important biomarker for diagnosis of several diseases, such as diabetic retinopathy [65], age-related macular degeneration [66] and Glaucoma [67]. Figure 10.7 demonstrates a typical retinal thickness map, which is obtained by segmenting out the retinal layers from a 3D volumetric scan of a normal subject. Figure 10.7a is the corresponding B-scan cross-sectional images, based on which the inner limit membrane (ILM, the top red curve in Fig. 10.7a) and the retina pigment epithelium layer (RPE, the bottom red curve in Fig. 10.7b) could be segmented. By calculating the distance between two segmented curves for all the B-scans of the captured 3D data, the thickness map of the scanned area could be obtained. The thickness map could offer important clinical information for typical retinal diseases diagnosis and treatment managements. For example, for wet AMD patients, the retinal thickness would be measured before and after the treatment. The retinal thickness could be a useful biomarker for clinicians to determine whether the treatment process is effective for the patients [68].

Briefly speaking, the FD-OCT system has much faster imaging speed and higher imaging sensitivity compared to TD-OCT system. FD-OCT system has become a standard procedure for ocular diseases by offering better B-scan images, en face view images as well as thickness maps for human retina.

10.4 Optical Coherence Tomography Angiography

With high speed and imaging sensitivity, FD-OCT is able to deliver high definition OCT images for clinical application, which make it a standard diagnostic tool for several ocular diseases. However, to achieve better diagnosis and treatment results, ophthalmic clinicians usually combine OCT images with vasculature imaging modalities, such as fluorescence angiography to visualize the microvasculature of diseased eyes, such as AMD [69], DR [70], Branched Retinal Vein Occlusion (BRVO) [71] etc. Due to the side effects caused by the injection of fluorescence dye, the utilization of FA as a diagnosis procedure is restricted by regulation requirements. With traditional angiography imaging modalities, such as FA or Indocyanine Green Angiography (ICG), it is difficult for clinicians to obtain vasculature imaging results at the early stage of ocular diseases for the same patients at repeated examinations in a short period. A technique called OCT angiography was developed by several research groups. For examples, researcher from University of Washington developed a vasculature imaging technique, called Optical Micro Angiography (OMAG), which based on complex signal analysis [72–75]. With OMAG, UW researchers demonstrated the capabilities of OCTA which is able to

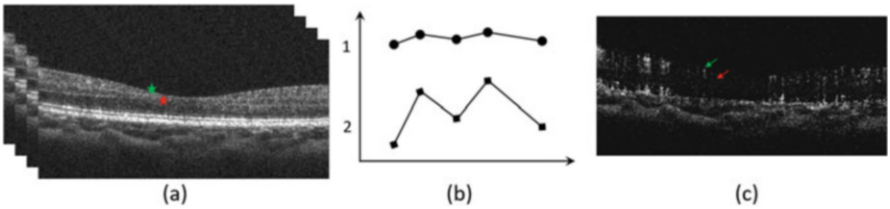

Fig. 10.8 Illustration of the processing of OCTA images. (**a**) OCT B-scan images captured from the same location; (**b**) The signal patterns from static tissue region (signal 1) and blood vessel region (signal 2); (**c**) OCTA cross-sectional image

noninvasively achieve micro vasculature imaging for several ocular diseases, such as AMD [76], DR [77], Glaucoma [78], etc.

In 2015, Carl Zeiss Meditec releases an OCTA imaging platform, AngioPlex, based on the collaboration with UW researchers. It is the first commercial OCTA imaging system that got FDA clearance. In the same year, Optovue released another ophthalmic microvasculature imaging platform, called Angiovue. Although the two systems were based on two different vasculature extracting algorithms, they both use the intrinsic signal generated by the moving red blood cells to produce vasculature images. Compared to FA or ICGA, it doesn't rely on the injection of extrinsic imaging dye as contrast agent, which makes it much safer for patients. Since the OCT is a confocal technique, OCTA could deliver better imaging resolution than FA and ICGA. Third, since OCTA is inherited from OCT technique, it is also be able to achieve depth-resolved capability, which enables OCTA to localize the position of lesion region precisely. Due to the advantages mentioned above, OCTA has become a hot topic in the ophthalmic diagnostic market since it was released, even though it was restricted by the imaging field and imaging capability of blood leakage [79].

Although the principles of the developed different vasculature contrast extracting algorithms are similar, most of the methods are based on analyzing motion signal from two or more B-scan images captured from the same position. In order to reduce the motion artifacts introduced by the inevitable movements of human eye for in vivo imaging, the frame rate of the OCTA system would be set at hundreds of frames per second. For better illustration the endogenous signal generated by the moving blood cells, a sketch of how OCTA was processed was demonstrated in Fig. 10.8.

Figure 10.8a illustrated the B-scan images sequence captured from the location around the fovea region. The position marked by the green star reveals a typical static tissue, while the position marked by the red star denotes a typical micro blood vessel. It is difficult to identify the micro blood vessel from the structure B-scan images because of the similar performance. However, if the signal value could be recorded from each frame sequentially from a B-scan sequence, the signal profile would be like Fig. 10.8b. As illustrated by Fig. 10.8b, the signal from position 2 (corresponding to the green star position) has much larger variation compared to the signal from position 1 (corresponding to the red star position). It is because when

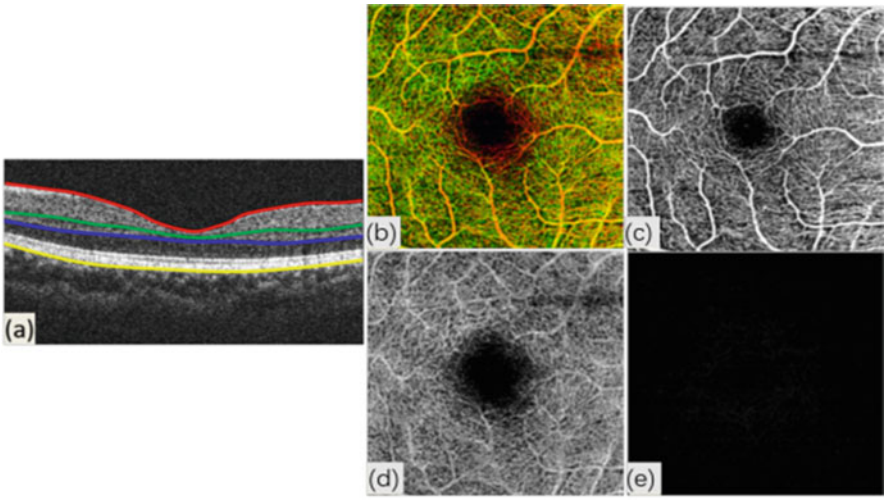

Fig. 10.9 Typical OCTA images obtained from desired layers. (**a**) OCT B-scan image from which the OCT layers were segmented. Red, green, blue and yellow curves marked the inner limiting membrane (ILM), inner nuclear layer (INL), outer plexiform layer (OPL) and RPE layer. (**b**) is the color coded OCTA image with the superficial retinal layer (**c**) coded with red, deeper retinal layer (**d**) coded with green and outer retinal layer (**e**) coded with blue color

the blood cells move across the imaging beam, the reflected light would be modulated. The demodulated signal could be used as the contrast agent to image the micro vasculature of human retina. Based on the signal characteristic of the OCT data used by the OCTA algorithms, they could fall into three categories, phase [80, 81], intensity [82, 83] and complex [72, 73] analysis algorithm. In this chapter, the complex based algorithm was used to generate vasculature contrast, which is supposed to have better blood vessel visualization sensitivity. The result was demonstrated in Fig. 10.8c. Obviously, after applying the OCTA algorithm, the signal from the background tissue was significantly compressed while the signal from blood vessels was enhanced. The blood vessels (as pointed by the green arrow) could be directly identified from the background.

To visualize the retinal vasculature from the lateral direction, a volumetric scan could be performed over the region of interest. After applying the vasculature imaging algorithm, the blood vessel signal could be projected onto a 2D image. Furthermore, the vasculature map from different layers could be identified when the OCTA data was segmented based on the OCT B-scan images features. For example, in Fig. 10.9a, the inner limiting membrane (ILM), inner nuclear layer (INL), outer plexiform layer (OPL) and RPE layer could be segmented and marked by red, green, blue and yellow curves. By projecting the OCTA signal from layers between red and green, green and blue, blue and yellow for all the B-scan images, three vasculature map could be produced and could be named as superficial retinal layer (SRL), deeper retinal layer (DRL) and outer retinal layer (ORL) respectively (demonstrated as Fig. 10.9c–e respectively). To demonstrate the depth-resolved capability of OCTA,

the three maps could be overlapped together, and color coded with different colors (red for SPL, green for DRL and blue for ORL).

Since release, OCTA has made deep impact on ocular diseases diagnosis, with selecting typical treatment strategies and disease progress managements for lots of ocular diseases, such as AMD, DR and so on. OCTA has also become a useful tool to assist the researchers and clinicians for better understanding the mechanisms of those diseases and their progressions.

AMD is a very common medical condition for people at 50 years of age and older in developed country. It is the leading cause of vision loss for these people [84]. Usually it affects the central vision of the vision field (the macular region) which results in blurring and the decay of vision gradually. For better understanding the progression of AMD, researchers from different groups have demonstrated that OCTA is able to achieve detailed visualization for vasculature abnormalities from the eyes of AMD patients [85–87]. For example, in [88], researchers examined the progression of Type II neovascularization of AMD patients with OCTA. By comparing with FA imaging, OCTA is able to reveal more detailed neovascular features with better imaging contrast. Similarly, OCTA could also be used as a diagnostic tool for subclinical type I neovascularization of AMD as demonstrated in [87]. As reported in [87], the imaging results delivered by OCTA is comparable or even better compared to FA or ICGA images. Besides the qualitative evaluation, the OCTA is also able to achieve quantitative results because of the higher imaging contrast and resolution. In [89], researchers demonstrate that the treatment could reduce the size of blood vessels and density of vessel maps of the lesion regions by 45% and 50%.

Diabetic retinopathy is another medical complication caused by diabetes. It is another vasculature related ocular diseases. Reported in [90], DR is the leading cause of blindness for people at working age. Precise evaluation for retinal microvasculature could help clinicians to achieve early diagnosis for DR patients. For the early stage of DR, patients are usually not found with obvious symptoms. But the abnormal features of microvasculature, such as non-perfusion, microaneurysms, irregular and/or enlarged foveal avascular zone, diabetic macular edema, could be treated as biomarkers for early diagnosis of DR. However, due to the side effect of FA, it cannot be used as the routine diagnostic tool for early stages of DR patients. Alternatively, OCTA has great potential for early and routine diagnosis imaging modality of DR due to the noninvasive, noncontact, high-resolution, and depth-resolved features. It was reported that OCTA is not only able to qualitatively evaluate the vasculature abnormalities of DR patients, such as microaneurysms, vascular loop, neovascularization, and so on, but also quantify the vasculature features as the biomarkers for diagnosis of DR [91–95]. For example, the capillary perfusion density calculated from the OCTA vasculature maps for DR patients were found to be significantly lower than normal subjects [92]. Another research result [96] demonstrated that the size of FAZ from DR patients is significantly larger than those from normal subjects, even at very early phase of DR progression.

OCTA has also demonstrated advanced imaging capabilities for other ocular diseases. Several pilot researches have shown that OCTA could also be able to reveal valuable information for Glaucoma [97], Macular Telangiectasia Type 2 [98],

retinal artery and vein occlusions [99, 100], and so on. Further developments of OCTA could improve the image qualities of vasculature maps. For examples, with improved imaging speed, OCTA system is able to produce larger field of view vasculature maps or higher imaging contrast by repeating more in the location to produce each B-frames. With high speed 1 μm (wavelength) swept source system, OCTA is able to produce better imaging qualities for deeper tissue since the 1 μm light has lower scattering coefficient than traditional 840 nm light.

10.5 Conclusion

Since proposed in 1991, OCT technique has been developed dramatically because of the efforts made by researchers all over the world over the past 30 years. It has generated great impacts and become a valuable imaging tool for many fields, such as ophthalmology, intravascular and dentistry. Especially for ophthalmology, OCT has changed the diagnosis procedure because of the 3D imaging capability. Compared to traditional imaging modalities (e.g., color fundus, slit lamp) used in ophthalmology diagnosis, OCT is able to examine the diseases from the depth direction, which give better understanding of the disease progression for clinicians. Furthermore, the newest development of OCT and OCTA could provide vasculature information of the examined biological tissue, which could further extend the imaging capability of OCT. According to the estimation of clinicians, they were able to achieve good enough diagnosis for most of the retinal diseases with OCT technique (including OCTA). In future, the further developments on imaging speed, contrast, resolution, and field of view, could make OCT deliver more precise diagnosis information and make it more popular for ophthalmic diagnosis over the world.

References

1. Huang D, Swanson EA, Lin CP, Schuman JS, Stinson WG, Chang W, Hee MR, Flotte T, Gregory K, Puliafito CA et al (1991) Optical coherence tomography. Science 254:1178–1181
2. Fercher AF (2010) Optical coherence tomography- development, principles, applications. Z Med Phys 20:251–276
3. Tomlins PH, Wang RK (2005) Theory, developments and applications of optical coherence tomography. J Phys D Appl Phys 38:17
4. Fercher AF, Mengedoht K, Werner W (1988) Eye-length measurement by interferometry with partially coherent light. Opt Lett 13:186–188
5. de Boer JF, Cense B, Park BH, Pierce MC, Tearney GJ, Bouma BE (2003) Improved signal-to-noise ratio in spectral-domain compared with time-domain optical coherence tomography. Opt Lett 28:2067–2069
6. Leitgeb R, Hitzenberger C, Fercher A (2003) Performance of fourier domain vs. time domain optical coherence tomography. Opt Express 11:889–894
7. Drexler W, Morgner U, Kartner FX, Pitris C, Boppart SA, Li XD, Ippen EP, Fujimoto JG (1999) *In vivo* ultrahigh-resolution optical coherence tomography. Opt Lett 24:1221–1223
8. Drexler W, Morgner U, Ghanta RK, Kartner FX, Schuman JS, Fujimoto JG (2001) Ultrahigh-resolution ophthalmic optical coherence tomography. Nat Med 7:502–507

9. An L, Li P, Shen TT, Wang R (2011) High speed spectral domain optical coherence tomography for retinal imaging at 500,000 Alines per second. Biomed Opt Express 2:2770–2783
10. An L, Guan G, Wang RK (2011) High-speed 1310 nm-band spectral domain optical coherence tomography at 184,000 lines per second. J Biomed Opt 16:060506
11. Wieser W, Biedermann BR, Klein T, Eigenwillig CM, Huber R (2010) Multi-megahertz OCT: high quality 3D imaging at 20 million A-scans and 4.5 GVoxels per second. Opt Express 18:14685–14704
12. An L, Wang RK (2007) Use of a scanner to modulate spatial interferograms for *in vivo* full-range Fourier-domain optical coherence tomography. Opt Lett 32:3423–3425
13. Baumann B, Pircher M, Gotzinger E, Hitzenberger CK (2007) Full range complex spectral domain optical coherence tomography without additional phase shifters. Opt Express 15:13375–13387
14. Tsai TH, Potsaid B, Tao YK, Jayaraman V, Jiang J, Heim PJ, Kraus MF, Zhou C, Hornegger J, Mashimo H, Cable AE, Fujimoto JG (2013) Ultrahigh speed endoscopic optical coherence tomography using micromotor imaging catheter and VCSEL technology. Biomed Opt Express 4:1119–1132
15. Hartl I, Li XD, Chudoba C, Ghanta RK, Ko TH, Fujimoto JG, Ranka JK, Windeler RS (2001) Ultrahigh-resolution optical coherence tomography using continuum generation in an air-silica microstructure optical fiber. Opt Lett 26:608–610
16. Kowalevicz A, Ko T, Hartl I, Fujimoto J, Pollnau M, Salathe R (2002) Ultrahigh resolution optical coherence tomography using a superluminescent light source. Opt Express 10:349–353
17. Yun S, Tearney G, Bouma B, Park B, de Boer J (2003) High-speed spectral-domain optical coherence tomography at 1.3 mum wavelength. Opt Express 11:3598–3604
18. Srinivasan VJ, Wojtkowski M, Witkin AJ, Duker JS, Ko TH, Carvalho M, Schuman JS, Kowalczyk A, Fujimoto JG (2006) High-definition and 3-dimensional imaging of macular pathologies with high-speed ultrahigh-resolution optical coherence tomography. Ophthalmology 113:2054.e2051–2054.e2014
19. Wojtkowski M, Kowalczyk A, Leitgeb R, Fercher AF (2002) Full range complex spectral optical coherence tomography technique in eye imaging. Opt Lett 27:1415–1417
20. Baba T, Hirose A, Kawazoe Y, Mochizuki M (2003) Optical coherence tomography for retinal detachment with a macular hole in a highly myopic eye. Ophthalmic Surg Lasers Imaging 34:483–484
21. Chen HY, Wang TH, Lee YM, Hung TJ (2005) Retinal nerve fiber layer thickness measured by optical coherence tomography and its correlation with visual field defects in early glaucoma. J Formos Med Assoc 104:927–934
22. Ho J, Witkin AJ, Liu J, Chen Y, Fujimoto JG, Schuman JS, Duker JS (2011) Documentation of intraretinal retinal pigment epithelium migration via high-speed ultrahigh-resolution optical coherence tomography. Ophthalmology 118:687–693
23. Yonetsu T, Bouma BE, Kato K, Fujimoto JG, Jang IK (2013) Optical coherence tomography - 15 years in cardiology. Circ J 77:1933–1940
24. Gambichler T, Moussa G, Sand M, Sand D, Altmeyer P, Hoffmann K (2005) Applications of optical coherence tomography in dermatology. J Dermatol Sci 40:85–94
25. Pierce MC, Strasswimmer J, Park BH, Cense B, de Boer JF (2004) Advances in optical coherence tomography imaging for dermatology. J Invest Dermatol 123:458–463
26. Patel DV, McGhee CN (2013) Quantitative analysis of *in vivo* confocal microscopy images: a review. Surv Ophthalmol 58:466–475
27. Patel DV, Zhang J, McGhee CN (2019) In vivo confocal microscopy of the inflamed anterior segment: a review of clinical and research applications. Clin Exp Ophthalmol 47:334–345
28. Mumcuoglu T, Wollstein G, Wojtkowski M, Kagemann L, Ishikawa H, Gabriele ML, Srinivasan V, Fujimoto JG, Duker JS, Schuman JS (2008) Improved visualization of glaucomatous retinal damage using high-speed ultrahigh-resolution optical coherence tomography. Ophthalmology 115:782–789.e782

29. Chen Y, Vuong LN, Liu J, Ho J, Srinivasan VJ, Gorczynska I, Witkin AJ, Duker JS, Schuman J, Fujimoto JG (2009) Three-dimensional ultrahigh resolution optical coherence tomography imaging of age-related macular degeneration. Opt Express 17:4046–4060
30. Ebneter A, Gekkiev B, Chanana B, Wolf S, Zinkernagel MS (2015) The presence of intra- or subretinal fluid during the loading phase in the treatment of exudative age-related macular degeneration with intravitreal ranibizumab assessed by optical coherence tomography. Ophthalmologica 234:61–66
31. Pieroni CG, Witkin AJ, Ko TH, Fujimoto JG, Chan A, Schuman JS, Ishikawa H, Reichel E, Duker JS (2006) Ultrahigh resolution optical coherence tomography in non-exudative age related macular degeneration. Br J Ophthalmol 90:191–197
32. Wang Y, Li SY, Zhu M, Chen SJ, Liu Y, Men XH, Gillies M, Larsson J (2005) Metamorphopsia after successful retinal detachment surgery: an optical coherence tomography study. Acta Ophthalmol Scand 83:168–171
33. Fujimoto JG, Boppart SA, Tearney GJ, Bouma BE, Pitris C, Brezinski ME (1999) High resolution in vivo intra-arterial imaging with optical coherence tomography. Heart 82:128–133
34. Strom C, Sander B, Larsen N, Larsen M, Lund-Andersen H (2002) Diabetic macular edema assessed with optical coherence tomography and stereo fundus photography. Invest Ophthalmol Vis Sci 43:241–245
35. Giovannini A, Amato G, Mariotti C (2002) The macular thickness and volume in glaucoma: an analysis in normal and glaucomatous eyes using OCT. Acta Ophthalmol Scand Suppl 236:34–36
36. Wojtkowski M, Leitgeb R, Kowalczyk A, Bajraszewski T, Fercher AF (2002) In vivo human retinal imaging by Fourier domain optical coherence tomography. J Biomed Opt 7:457–463
37. Choma M, Sarunic M, Yang C, Izatt J (2003) Sensitivity advantage of swept source and Fourier domain optical coherence tomography. Opt Express 11:2183–2189
38. Spaide RF, Fujimoto JG, Waheed NK (2015) Optical coherence tomography angiography. Retina 35:2161–2162
39. Nehemy MB, Brocchi DN, Veloso CE (2015) Optical coherence tomography angiography imaging of quiescent choroidal neovascularization in age-related macular degeneration. Ophthalmic Surg Lasers Imaging Retina 46:1056–1057
40. Kuehlewein L, Dansingani KK, de Carlo TE, Bonini Filho MA, Iafe NA, Lenis TL, Freund KB, Waheed NK, Duker JS, Sadda SR, Sarraf D (2015) Optical coherence tomography angiography of type 3 neovascularization secondary to age-related macular degeneration. Retina 35:2229–2235
41. Danielson BL, Boisrobert CY (1991) Absolute optical ranging using low coherence interferometry. Appl Opt 30:2975–2979
42. Gerges AS, Jackson DA (1991) A fibre-optic based high temperature probe illuminated by a multimode laser diode. Opt Commun 80:5
43. Rao YJ, Jackson DA (1994) Prototype fiber-optic-based ultrahigh pressure remote sensor with built-in temperature compensation. Rev Sci Instrum 65:4
44. Vikram Bhatia KA, Murphy RO, Claus ME, Jones JL, Grace TA, Tran JAG (1996) Optical fibre based absolute extrinsic Fabry–Perot interferometric sensing system. Meas Sci Technol 7:4
45. Brezinski ME, Tearney GJ, Bouma B, Boppart SA, Pitris C, Southern JF, Fujimoto JG (1998) Optical biopsy with optical coherence tomography. Ann N Y Acad Sci 838:68–74
46. Fujimoto J, Swanson E (2016) The development, commercialization, and impact of optical coherence tomography. Invest Ophthalmol Vis Sci 57:OCT1–OCT13
47. Tearney GJ, Bouma BE, Fujimoto JG (1997) High-speed phase- and group-delay scanning with a grating-based phase control delay line. Opt Lett 22:1811–1813
48. Cense B, Nassif N, Chen T, Pierce M, Yun SH, Park B, Bouma B, Tearney G, de Boer J (2004) Ultrahigh-resolution high-speed retinal imaging using spectral-domain optical coherence tomography. Opt Express 12:2435–2447

49. Cense B, Chen TC, Nassif N, Pierce MC, Yun SH, Park BH, Bouma BE, Tearney GJ, de Boer JF (2006) Ultra-high speed and ultra-high resolution spectral-domain optical coherence tomography and optical Doppler tomography in ophthalmology. Bull Soc Belge Ophtalmol (302):123–132
50. Zhang J, Rao B, Chen Z (2005) Swept source based fourier domain functional optical coherence tomography. Conf Proc IEEE Eng Med Biol Soc 7:7230–7233
51. Davis AM, Choma MA, Izatt JA (2005) Heterodyne swept-source optical coherence tomography for complete complex conjugate ambiguity removal. J Biomed Opt 10:064005
52. Choma MA, Hsu K, Izatt JA (2005) Swept source optical coherence tomography using an all-fiber 1300-nm ring laser source. J Biomed Opt 10:44009
53. Nielsen F, Thrane L, Black J, Bjarklev A, Andersen P (2005) Swept wavelength source in the 1 microm range. Opt Express 13:4096–4106
54. Spaide RF, Koizumi H, Pozzoni MC (2008) Enhanced depth imaging spectral-domain optical coherence tomography. Am J Ophthalmol 146:496–500
55. Folgar FA, Jaffe GJ, Ying GS, Maguire MG, Toth CA, G. Comparison of Age-Related Macular Degeneration Treatments Trials Research (2014) Comparison of optical coherence tomography assessments in the comparison of age-related macular degeneration treatments trials. Ophthalmology 121:1956–1965
56. Gupta V, Gupta P, Singh R, Dogra MR, Gupta A (2008) Spectral-domain Cirrus high-definition optical coherence tomography is better than time-domain Stratus optical coherence tomography for evaluation of macular pathologic features in uveitis. Am J Ophthalmol 145:1018–1022
57. Srinivasan VJ, Adler DC, Chen Y, Gorczynska I, Huber R, Duker JS, Schuman JS, Fujimoto JG (2008) Ultrahigh-speed optical coherence tomography for three-dimensional and en face imaging of the retina and optic nerve head. Invest Ophthalmol Vis Sci 49:5103–5110
58. van Velthoven ME, Verbraak FD, Garcia PM, Schlingemann RO, Rosen RB, de Smet MD (2005) Evaluation of central serous retinopathy with en face optical coherence tomography. Br J Ophthalmol 89:1483–1488
59. van Velthoven ME, Verbraak FD, Yannuzzi LA, Rosen RB, Podoleanu AG, de Smet MD (2006) Imaging the retina by en face optical coherence tomography. Retina 26:129–136
60. Mujat M, Chan R, Cense B, Park B, Joo C, Akkin T, Chen T, de Boer J (2005) Retinal nerve fiber layer thickness map determined from optical coherence tomography images. Opt Express 13:9480–9491
61. Bagci AM, Shahidi M, Ansari R, Blair M, Blair NP, Zelkha R (2008) Thickness profiles of retinal layers by optical coherence tomography image segmentation. Am J Ophthalmol 146:679–687
62. Loduca AL, Zhang C, Zelkha R, Shahidi M (2010) Thickness mapping of retinal layers by spectral-domain optical coherence tomography. Am J Ophthalmol 150:849–855
63. Sung KR, Kim DY, Park SB, Kook MS (2009) Comparison of retinal nerve fiber layer thickness measured by Cirrus HD and Stratus optical coherence tomography. Ophthalmology 116:1264–1270. 1270.e1261
64. Nunes RP, Gregori G, Yehoshua Z, Stetson PF, Feuer W, Moshfeghi AA, Rosenfeld PJ (2013) Predicting the progression of geographic atrophy in age-related macular degeneration with SD-OCT en face imaging of the outer retina. Ophthalmic Surg Lasers Imaging Retina 44:344–359
65. Sikorski BL, Malukiewicz G, Stafiej J, Lesiewska-Junk H, Raczynska D (2013) The diagnostic function of OCT in diabetic maculopathy. Mediat Inflamm 2013:434560
66. Menke MN, Dabov S, Knecht P, Sturm V (2011) Reproducibility of retinal thickness measurements in patients with age-related macular degeneration using 3D Fourier-domain optical coherence tomography (OCT) (Topcon 3D-OCT 1000). Acta Ophthalmol 89:346–351
67. Leung CK, Lam S, Weinreb RN, Liu S, Ye C, Liu L, He J, Lai GW, Li T, Lam DS (2010) Retinal nerve fiber layer imaging with spectral-domain optical coherence tomography: analysis of the retinal nerve fiber layer map for glaucoma detection. Ophthalmology 117:1684–1691

68. Witkin AJ, Vuong LN, Srinivasan VJ, Gorczynska I, Reichel E, Baumal CR, Rogers AH, Schuman JS, Fujimoto JG, Duker JS (2009) High-speed ultrahigh resolution optical coherence tomography before and after ranibizumab for age-related macular degeneration. Ophthalmology 116:956–963
69. Henschel A, Spital G, Lommatzsch A, Pauleikhoff D (2018) Optical coherence tomography in neovascular age-related macular degeneration compared to fluorescein angiography and visual acuity. Eur J Ophthalmol 19:5
70. Jain A, Desai RU, Charalel RA, Quiram P, Yannuzzi L, Sarraf D (2009) Solar retinopathy: comparison of optical coherence tomography (OCT) and fluorescein angiography (FA). Retina 29:1340–1345
71. Papadia M, Misteli M, Jeannin B, Herbort CP (2014) The influence of anti-VEGF therapy on present day management of macular edema due to BRVO and CRVO: a longitudinal analysis on visual function, injection time interval and complications. Int Ophthalmol 34:1193–1201
72. An L, Qin J, Wang RK (2010) Ultrahigh sensitive optical microangiography for in vivo imaging of microcirculations within human skin tissue beds. Opt Express 18:8220–8228
73. An L, Shen TT, Wang RK (2011) Using ultrahigh sensitive optical microangiography to achieve comprehensive depth resolved microvasculature mapping for human retina. J Biomed Opt 16:106013
74. Wang RK, An L, Francis P, Wilson DJ (2010) Depth-resolved imaging of capillary networks in retina and choroid using ultrahigh sensitive optical microangiography. Opt Lett 35:1467–1469
75. Wang RK, An L (2011) Multifunctional imaging of human retina and choroid with 1050-nm spectral domain optical coherence tomography at 92-kHz line scan rate. J Biomed Opt 16:050503
76. Keiner CM, Zhou H, Zhang Q, Wang RK, Rinella NT, Oldenburg CE, Duncan JL, Schwartz DM (2019) Quantifying choriocapillaris hypoperfusion in patients with choroidal neovascularization using swept-source OCT angiography. Clin Ophthalmol 13:1613–1620
77. Zhang Q, Rezaei KA, Saraf SS, Chu Z, Wang F, Wang RK (2018) Ultra-wide optical coherence tomography angiography in diabetic retinopathy. Quant Imaging Med Surg 8:743–753
78. Richter GM, Sylvester B, Chu Z, Burkemper B, Madi I, Chang R, Reznik A, Varma R, Wang RK (2018) Peripapillary microvasculature in the retinal nerve fiber layer in glaucoma by optical coherence tomography angiography: focal structural and functional correlations and diagnostic performance. Clin Ophthalmol 12:2285–2296
79. Kashani AH, Chen CL, Gahm JK, Zheng F, Richter GM, Rosenfeld PJ, Shi Y, Wang RK (2017) Optical coherence tomography angiography: a comprehensive review of current methods and clinical applications. Prog Retin Eye Res 60:66–100
80. Fingler J, Schwartz D, Yang C, Fraser SE (2007) Mobility and transverse flow visualization using phase variance contrast with spectral domain optical coherence tomography. Opt Express 15:12636–12653
81. Kim DY, Fingler J, Werner JS, Schwartz DM, Fraser SE, Zawadzki RJ (2011) In vivo volumetric imaging of human retinal circulation with phase-variance optical coherence tomography. Biomed Opt Express 2:1504–1513
82. Hong Y, Makita S, Yamanari M, Miura M, Kim S, Yatagai T, Yasuno Y (2007) Three-dimensional visualization of choroidal vessels by using standard and ultra-high resolution scattering optical coherence angiography. Opt Express 15:7538–7550
83. Jia Y, Tan O, Tokayer J, Potsaid B, Wang Y, Liu JJ, Kraus MF, Subhash H, Fujimoto JG, Hornegger J, Huang D (2012) Split-spectrum amplitude-decorrelation angiography with optical coherence tomography. Opt Express 20:4710–4725
84. Ratnapriya R, Chew EY (2013) Age-related macular degeneration-clinical review and genetics update. Clin Genet 84:160–166
85. Jia Y, Bailey ST, Wilson DJ, Tan O, Klein ML, Flaxel CJ, Potsaid B, Liu JJ, Lu CD, Kraus MF, Fujimoto JG, Huang D (2014) Quantitative optical coherence tomography angiography of

choroidal neovascularization in age-related macular degeneration. Ophthalmology 121:1435–1444
86. Miere A, Querques G, Semoun O, El Ameen A, Capuano V, Souied EH (2015) Optical coherence tomography angiography in early type 3 neovascularization. Retina 35:2236–2241
87. Roisman L, Zhang Q, Wang RK, Gregori G, Zhang A, Chen CL, Durbin MK, An L, Stetson PF, Robbins G, Miller A, Zheng F, Rosenfeld PJ (2016) Optical coherence tomography angiography of asymptomatic neovascularization in intermediate age-related macular degeneration. Ophthalmology 123:1309–1319
88. El Ameen A, Cohen SY, Semoun O, Miere A, Srour M, Quaranta-El Maftouhi M, Oubraham H, Blanco-Garavito R, Querques G, Souied EH (2015) Type 2 neovascularization secondary to age-related macular degeneration imaged by optical coherence tomography angiography. Retina 35:2212–2218
89. Kuehlewein L, Sadda SR, Sarraf D (2015) OCT angiography and sequential quantitative analysis of type 2 neovascularization after ranibizumab therapy. Eye (Lond) 29:932–935
90. Mohamed Q, Gillies MC, Wong TY (2007) Management of diabetic retinopathy: a systematic review. JAMA 298:902–916
91. de Carlo TE, Chin AT, Bonini Filho MA, Adhi M, Branchini L, Salz DA, Baumal CR, Crawford C, Reichel E, Witkin AJ, Duker JS, Waheed NK (2015) Detection of microvascular changes in eyes of patients with diabetes but not clinical diabetic retinopathy using optical coherence tomography angiography. Retina 35:2364–2370
92. Agemy SA, Scripsema NK, Shah CM, Chui T, Garcia PM, Lee JG, Gentile RC, Hsiao YS, Zhou Q, Ko T, Rosen RB (2015) Retinal vascular perfusion density mapping using optical coherence tomography angiography in normals and diabetic retinopathy patients. Retina 35:2353–2363
93. Matsunaga DR, Yi JJ, De Koo LO, Ameri H, Puliafito CA, Kashani AH (2015) Optical coherence tomography angiography of diabetic retinopathy in human subjects. Ophthalmic Surg Lasers Imaging Retina 46:796–805
94. Ishibazawa A, Nagaoka T, Takahashi A, Omae T, Tani T, Sogawa K, Yokota H, Yoshida A (2015) Optical coherence tomography angiography in diabetic retinopathy: a prospective pilot study. Am J Ophthalmol 160:35–44.e31
95. Hwang TS, Jia Y, Gao SS, Bailey ST, Lauer AK, Flaxel CJ, Wilson DJ, Huang D (2015) Optical coherence tomography angiography features of diabetic retinopathy. Retina 35:2371–2376
96. Takase N, Nozaki M, Kato A, Ozeki H, Yoshida M, Ogura Y (2015) Enlargement of foveal avascular zone in diabetic eyes evaluated by en face optical coherence tomography angiography. Retina 35:2377–2383
97. Chansangpetch S, Lin SC (2018) Optical coherence tomography angiography in glaucoma care. Curr Eye Res 43:1067–1082
98. Roisman L, Rosenfeld PJ (2016) Optical coherence tomography angiography of macular telangiectasia type 2. Dev Ophthalmol 56:146–158
99. Bonini Filho MA, Adhi M, de Carlo TE, Ferrara D, Baumal CR, Witkin AJ, Reichel E, Kuehlewein L, Sadda SR, Sarraf D, Duker JS, Waheed NK (2015) Optical coherence tomography angiography in retinal artery occlusion. Retina 35:2339–2346
100. Kashani AH, Lee SY, Moshfeghi A, Durbin MK, Puliafito CA (2015) Optical coherence tomography angiography of retinal venous occlusion. Retina 35:2323–2331

Tissue Optical Clearing for Biomedical Imaging: From In Vitro to In Vivo

11

Tingting Yu, Dongyu Li, and Dan Zhu

11.1 Introduction

Biomedical photonics is currently one of the fastest-growing fields of life sciences, connecting research in physics, optics and electrical engineering coupled with medical or biological applications. It allows structural and functional analysis of tissues and cells with resolution and contrast unattainable by any other method. Advanced optical methods combined with the various contrast agents pave the way toward real molecular imaging within living cells. However, the major challenges are associated with the need to enhance imaging resolution even further to the subcellular level for larger tissue blocks or organs as well as for in vivo studies. The high scattering of turbid tissues limits the penetration of visible and near-infrared light, and then both the imaging resolution and contrast decrease as light propagates deeper into the tissue [1]. To perform deeper tissue imaging, several optical imaging techniques have been developed [2]. Alternatively, reducing scattering and absorption of tissues could also significantly enhance optical imaging of deep-tissue structures [3, 4]. For example, White created a transparent adult zebra fish, which has been applied to study cancer pathology and development in real-time [5], but this method is unsuitable for studies in other animals or human.

In contrast, a tissue optical clearing (TOC) method, proposed by Tuchin, provides an innovative way to perform deep-tissue imaging by reducing the scattering of tissue and making the tissue more transparent by using immersion of tissues into

T. Yu · D. Li · D. Zhu (✉)
Britton Chance Center for Biomedical Photonics, Wuhan National Laboratory for Optoelectronics, Huazhong University of Science and Technology, Wuhan, Hubei, China

MoE Key Laboratory for Biomedical Photonics, School of Engineering Sciences, Huazhong University of Science and Technology, Wuhan, Hubei, China
e-mail: dawnzh@mail.hust.edu.cn

X. Wei, B. Gu (eds.), *Optical Imaging in Human Disease and Biological Research*, Advances in Experimental Medicine and Biology 1355,
https://doi.org/10.1007/978-981-15-7627-0_11

optical clearing agents (OCAs) [1, 3, 4]. It is well known that tissues are densely packed with many types of substances, including scattering particles with higher refractive index, i.e., collagen, elastic fibers, cells and cell compartments, and surrounding media with lower refractive index, i.e., interstitial fluid and/or cytoplasm. Usually, the scattering particles have a higher refractive index (1.39–1.52), and the surrounding media have a lower refractive index (1.33–1.37). The mismatch of the refractive index between the scattering particles and background medium results in the strong scattering of tissue [3]. When some chemical agents with high refractive index penetrate into tissue, and/or hyperosmolarity agents provide a water flux from tissue, the refractive index of background medium will increase, which enhances the refractive index matching in tissue, and reduces the scattering of tissue.

In this chapter, the mechanisms of tissue optical clearing were briefly introduced, and then the in vitro and in vivo tissue optical clearing methods and their applications on biomedical optical imaging were demonstrated.

11.2 Tissue Optical Clearing Mechanisms

The refractive index matching in tissue reduces the scattering of tissue and makes tissue transparent, which has been regarded as the essential foundation of tissue optical clearing. According to the refractive index matching mechanism of tissue optical clearing, the optical clearing agents (OCAs) with higher refractive indices should have better optical clearing efficacy on biological tissues. After examining the clearing capabilities in the two tissue types, striated muscle and tendon, LaComb et al. supported this mechanism [6]. However, Choi et al. [7] and Mao et al. [8] indicated that optical clearing efficacy of skin did not correlate with OCAs' refractive indices by topical treatment of OCA on in vitro skin epidermal side. In order to clarify the mechanism of tissue optical clearing, some other views were proposed. Mao et al. found that the optical clearing effect of skin induced by alcohols is positively correlated to the number of hydroxyl groups [8], which could be explained by the dissociation of collagen caused by glycerol [9]. Tuchin and collaborators have proved that the dehydration induced by OCAs is the important mechanism of tissue optical clearing [1, 10]. The variety of optical clearing mechanisms under discussion should be due to complex interactions between agents and tissues, such as diffusion of agents into tissue and water out, and other changes in tissue structure caused by chemical reaction. Therefore, the mechanism of optical clearing might be multiple factors affected, the following will introduce the mechanisms of tissue optical clearing from physical and chemical aspects, respectively.

11.2.1 Physical Mechanisms

Since tissues have their structures, the interactions between tissues and different OCAs are very complex and prevent understanding of the optical clearing mechanisms. The tissue-simulating phantom with high homogeneity and stability

should be an available and adequate model to block the biological effect of tissues and give a direct answer to the physical mechanism of optical clearing. Among the different types of tissue-simulating phantom, Intralipid, one of the aqueous suspension phantoms, is most suitable in the research. On the one hand, the scattering caused by lipid bilayer vesicles of Intralipid is just close to that by lipid bilayer membrane structures of cells, and the scattering property of Intralipid can be predicted based on the distribution of particle sizes. On the other hand, when this aqueous suspension phantom is applied to study the optical clearing effect, the diffuse process of agents can be neglected [11].

In order to explain the physical mechanism of optical clearing, Wen et al. applied three methods, direct observation, Mie theory prediction and spectral measurement, to investigate the change in the optical properties of Intralipid caused by different OCAs [12]. Several commonly used OCAs, i.e., dimethyl sulfoxide (DMSO), glycerol, 1,4-butanediol, 1,2-propanediol, poly-ethylene glycol 200 (PEG200), and poly-ethylene glycol 400 (PEG400) at different concentrations, were mixed with Intralipid, respectively. The results indicated that 5% Intralipid mixed with four kinds of OCAs, respectively, could keep the solution uniform, and the optical clearing effect increased gradually in the order of 1,2-propanediol, 1,4-butanediol, glycerol, and DMSO. The refractive index of the above agents increased gradually. Their optical clearing effect increased in the same way, which suggested the refractive index matching dominated the optical clearing process. Meanwhile, they also observed that the mixtures of 5% Intralipid with PEG200 or PEG400 were no longer uniform, which demonstrated some aggregation of particles. This suggests that the mechanism of refractive index matching is suitable for pure physical interaction between tissue phantom and OCA.

To make the tissue phantom accessible for theory prediction, the scattering particle size distribution of lipid droplets in Intralipid was counted in electron microscope images after fixing and staining process for the lipid droplets. And then, Mie theory calculation was used to quantitatively predict the scattering property of Intralipid solution before and after the mixing with OCAs according to the refractive index of the background medium. Meanwhile, the transmittance and reflectance of the solution in a fixed thickness sample cell were measured. Then inverse adding doubling method was employed to get the scattering coefficients of the Intralipid solution before and after the mixing with different OCAs with different concentrations. The theoretical prediction was consistent with the experimentally measured scattering coefficient, which showed the refractive index of the background medium directly affected optical clearing. And the refractive index of the background medium can be directly derived from the refractive index of the OCA used and the mixing ratio with Intralipid.

In addition, Wen et al. [12] further investigated the relationship between the reduced scattering coefficient and the refractive index of the above agents with different concentrations, and found that the scattering of the mixture decreased with the increase of the background refractive index, and Mie theory predicted values matched well with the measurements. The correlation coefficient between the reduced scattering coefficient and the background refractive index was about

0.97. This result reveals that increasing the background refractive index makes the refractive index matching of mixture. This conclusion is inconsistent with the results on skin optical clearing from Choi [7] and Mao [8]. It should be the reason that for tissue phantom, we need not consider the diffusion of agents, nor the interaction between Intralipid and OCAs, while the concentration of OCAs in tissue is related to the penetrative ability of agents, water flux, even chemical reaction between OCAs and some molecules of tissue.

11.2.2 Chemical Mechanisms

In the view of physical principle, the main mechanism of tissue optical clearing is to increase the refractive index matching to reduce the light scattering of tissue, while their chemical strategies used are variant [13, 14]. It is well known that there are various components in a tissue. Tissue optical clearing can be realized by removing lipid, dissociating collagen, and dehydration et al., and then adding agents with high refractive index to increase the refractive index match. Among the numerous chemicals, sugar alcohols are widely applied to make the tissue optical clearing. Hirshburg et al. used molecular dynamics (MD) simulations to study the interaction between collagen and alcohols, and predicted the optical clearing potential and indicated that the propensity of OCAs to form hydrogen bonds and bridges determines their ability to destabilize higher-order structures of collagen by disrupting water bridges and the hydration shell [9]. Note that sugars also have hydroxyl groups, Zhu's group paid attention to saccharides and disaccharides, including fructose, glucose, ribose, sucrose, and maltose, to evaluate their optical clearing potential by the MD simulation according to its propensity to form hydrogen bonds and bridges [15, 16]. Among the saccharides, fructose has the strongest ability to disrupt the water bridges and hydration shell around collagen [15, 16], but still less than disaccharides [15, 16]. Except for collagen, the lipid is also the source of tissue scattering, and removing lipid is usually achieved by dissolving in organic solvents. Notably, for the hard bone tissue, its mineral compositions make its refractive index higher (1.55–1.65) than the other tissue components [17], therefore decalcification is indispensable for high transparency of bone clearing or whole-body clearing. In addition, in many tissues, there are some pigments such as heme, melanin, and lipofuscin [18], which have strong absorption of light and can weaken the fluorescence signal. Hence, decolorizing is important for clearing of large tissues to achieve deep detection in tissues.

According to the chemical processes, the tissue optical clearing methods can be divided into two categories: hydrophobic clearing method (i.e., solvent-based clearing method) and hydrophilic clearing method. Figure 11.1 briefly summarizes their main clearing processes.

For solvent-based clearing methods, the clearing steps mainly include dehydration, delipidation/bleaching, and refractive index (RI) matching, as shown in Fig. 11.1a. The dehydration is mainly based on alcohol reagents, such as methanol [19, 20], ethanol [21–25], 1-propanediol [26], *tert*-butanol [26–28], tetrahydrofuran

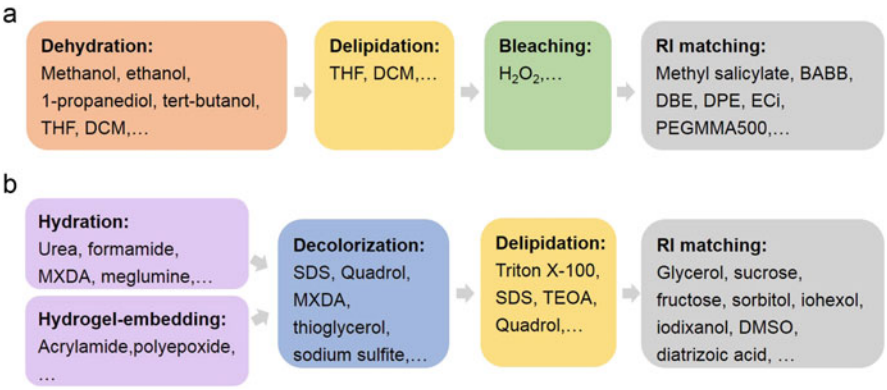

Fig. 11.1 Overview of the main processes of (**a**) the solvent-based clearing method and (**b**) the hydrophilic-reagents-based clearing method

(THF) [29–31], and so on. The delipidation mainly uses THF and dichloromethane (DCM) [30]. Some methods that do not care about endogenous fluorescent protein also need to bleach the samples, mainly using hydrogen peroxide [32]. The refractive index matching reagents are mainly based on ether reagents, such as methyl salicylate, benzyl alcohol-benzyl benzoate (1:2, BABB) [26], dibenzyl ether (DBE) [30, 33], diphenyl ether (DPE) [27], ethyl-3-phenylprop-2-enoate (ECi) [24, 25], PEGMMA500 [28], and so on. These reagents are miscible with organic solvents and have a high refractive index ($n \approx 1.56$), so they can effectively infiltrate into tissues and play a role of homogenization for optical clearing.

For hydrophilic reagents-based clearing methods, the main steps involve the delipidation/decolorization, and refractive index matching, as shown in Fig. 11.1b. The delipidation is mainly based on detergents, such as Triton X-100 [34–37], triethanolamine [36, 37], Quadrol [36, 37], sodium dodecyl sulfate (SDS) [38, 39], *m*-xylylenediamine (MXDA) [40], etc. And the decolorization is achieved by Quadrol [28, 36, 37], SDS [41], MXDA [40], and thioglycerol [42] or sodium sulfite [43] which can inhibit oxidation reaction. The refractive index matching solutions are mainly high concentration of sugars, sugar alcohols or contrast agents with high refractive indices, such as glycerol [38], sucrose [37, 44], fructose [42, 45], sorbitol [39, 40, 46], iohexol [39, 47–49], iodixanol [50], DMSO [46], diatrizoic acid [51], etc. This category of the method can be subdivided into three types: one is simple immersion with merely refractive index matching using a gradient concentration of sugar or sugar alcohol solutions for clearing; the other is based on the hyperhydration of urea or urea-like chemicals to increase the permeability of tissue, combined with the use of delipidation/decolorizing reagents, and finally performing refractive index matching; another type is based on hydrogel embedding to increase the stability of tissue structures, combined with SDS reagents (as well as electrophoresis, temperature rise) for delipidation/decolorization, and followed by refractive index matching with high refractive index reagents to achieve clearing [13, 52].

Additionally, decalcification is a critical step to achieve high transparency of bone tissues due to their mineral compositions. Generally, to clear bone tissues or whole bodies, decalcification was carried out prior to the other steps for both clearing methods. The decalcification can be achieved by ethylene diamine tetraacetic acid (EDTA) [41, 47] and some organic acids, such as nitric acid, hydrochloric acid, formic acid, etc. [53].

The following will first introduce a variety of in vitro tissue optical clearing methods for tissue or whole-organ imaging in these two aspects.

11.3 In Vitro Tissue Optical Clearing Methods for Tissue or Whole-Organ Imaging

The mapping of three-dimensional (3D) structures of intact tissues or whole organs with high resolution is essential for many biological researches. The development of modern optical imaging and fluorescent labeling techniques has provided powerful tools for obtaining 3D structural information. However, the strong scattering and absorption of biological tissues limit the light penetration depth in tissue, and further limit the imaging depth of optical imaging technologies [13]. In recent years, dozens of tissue optical clearing methods have emerged to overcome this problem by employing a variety of physical and chemical means, providing a new perspective for 3D imaging of large tissues and organs. As described above, current in vitro tissue optical clearing methods mainly include solvent-based and hydrophilic reagents-based clearing methods. The following will introduce the up-to-date clearing methods from the two aspects.

11.3.1 The Solvent-Based Clearing Methods

11.3.1.1 The Older Tissue Clearing Technique

About a century ago, Spalteholz proposed a method to make large tissues or intact organs transparent by using organic solvents for the anatomical study of human and animal organs [54]. But this method has complicated steps requiring a series of dehydration, tissue bleaching, and clearing treatment. At that time, it was an unprecedented technique to obtain transparent organs for sample preparation. It provided a new method for observation of the internal structures of tissues and organs, and also greatly promoted the development of anatomy. However, this method can destroy the tissue structures of a few centimeters on the surface and cannot preserve the fluorescence signal, so it can only be used for clearing of very large samples and cannot be used for fluorescence imaging. In 2001, Steinke et al. modified the Spalteholz's clearing protocol to preserve the external structures of the tissues and applied it to clear human larynx and observe the structures such as blood vessels, muscles, cartilage, and thyroid gland [55].

In recent years, with the development of 3D fluorescence microscopes, and data acquisition and storage technologies, 3D imaging of large tissue samples has become

possible. To improve the imaging depth of optical imaging technology, the researchers began to reconsider the tissue optical clearing technology originally proposed by Spalteholz.

11.3.1.2 The Emergence of 3DISCO Clearing Method

In recent years, Dodt's group has made a lot of efforts on the solvent-based clearing method. Initially, they used ethanol as the dehydration reagent and BABB as refractive index matching reagent to transparentize different tissues and organs [21–23, 56], and combined with a light-sheet microscopy to perform 3D imaging, which has opened the door for the rapid 3D imaging of large tissues with the combination of tissue optical clearing and light-sheet microscopy. Aided by the BABB clearing method, the researchers realized 3D imaging of different organs, such as mouse lung fibrosis and human airways [19, 57].

However, this method based on ethanol or methanol and BABB can severely quench the signal of endogenous fluorescent protein (such as GFP). To overcome this problem, Dodt's group selected THF from thousands of chemicals for dehydration instead of ethanol [29]. This improved the fluorescence preservation to a certain extent and has been applied to the evaluation of axon regeneration after spinal cord injury (SCI) (Fig. 11.2) and peripheral nerve injury [31, 58]. Further, to obtain a higher transparency and fluorescence signal, DBE was used to replace BABB for refractive index matching, thus 3DISCO method was developed [30]. Combined with the light-sheet microscopy, it has been applied to kinds of studies, such as the neuronal and vascular networks in the whole mouse brain and spinal cord, distribution of tumors in the lung, and mammary glands [30].

3DISCO is featured by a high level of tissue transparency, fast clearing speed, tissue shrinkage, and simple operation. However, it can still quench the endogenous

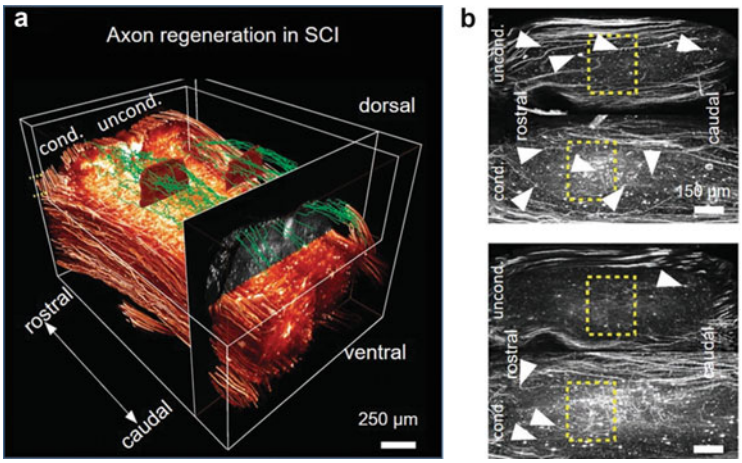

Fig. 11.2 Application of 3DISCO in the SCI mouse model. (**a**) 3D imaging of spinal cord to assess axon regeneration after SCI by 3DISCO. (**b**) Projections from the indicated regions in A. (Images adapted from ref. [31])

fluorescence signal rapidly, for example, GFP can only be preserved for 1–2 days [30], which has limited the applicability of 3DISCO.

11.3.1.3 A Series of Optimized Methods Based on 3DISCO

To solve the problem of rapid fluorescence quenching of 3DISCO cleared samples, the researchers have carried out related work from several aspects, providing different options for long-term preservation of fluorescence after clearing.

On the one hand, the researchers improved the fluorescence preservation by screening fluorescence-friendly dehydration and refractive index matching reagents. For example, FluoClearBABB proposed used 1-propanol or *tert*-butanol for dehydration [26], and Ethanol-ECi used pH-adjusted ethanol for dehydration, which has been used to quantify the glomerular number and creatinine clearance rate in a kidney disease model—nephrotoxic nephritis [24]. The uDISCO method [27] developed by the Ertürk's group used *tert*-butanol for dehydration, BABB and DPE mixture for refractive index matching, and introduced antioxidants such as vitamin-E to preserve the fluorescent protein signal for several months. The latest PEGASOS [28] by Zhao's group introduced EDTA and Quadrol for decalcification and decolorization, used Quadrol to adjust the pH of *tert*-butanol for dehydration, and introduced PEGMMA500 and benzyl benzoate to match the refractive index, which can effectively clear both soft and hard tissues, such as mouse brain and human dental tissues. Both uDISCO and PEGASOS have been applied for clearing and imaging of 1-mm thick archival human brain samples [27, 28]. The researchers have also used uDISCO for interrogating of BMSCs in the entire body [27], showing its potential for application in transplantation studies.

On the other hand, some studies demonstrated improved fluorescence preservation by adjusting the conditions in the clearing process. For example, Zhu's group proposed a modified clearing method, named FDISCO [33], by adjusting the temperature and pH of clearing reagents. This method retained the advantages of the 3DISCO, such as high clearing capability, meanwhile effectively overcame the problem of fluorescence quenching. FDISCO had been applied to high-resolution 3D imaging and reconstruction of neuronal and vascular networks in various tissues and organs (Fig. 11.3), and showed a potential for use in the imaging of fluorescent proteins with low expression. This modification based on pH adjustment is also applicable to other methods. For instance, Zhu et al. optimized uDISCO to develop a-uDISCO [59], and increased the fluorescence signal by about two times. These optimized protocols provided better alternatives for tissue clearing of large samples.

11.3.1.4 Whole-Mount Immunostaining Based on DISCO

Most tissue optical clearing methods were developed with an eye to endogenous fluorescence of proteins, such as GFP, which is valuable but not essential because it can be achieved by immunolabeling. The iDISCO developed by Renier et al. is a simple and rapid immunolabeling method of large tissue samples for volume imaging [32]. Liebmann et al. used iDISCO to visualize the amyloid plaques together with tau, microglia, and vasculature in Alzheimer's disease (AD) mouse model [60]. To better preserve the morphology and size of samples, Renier et al.

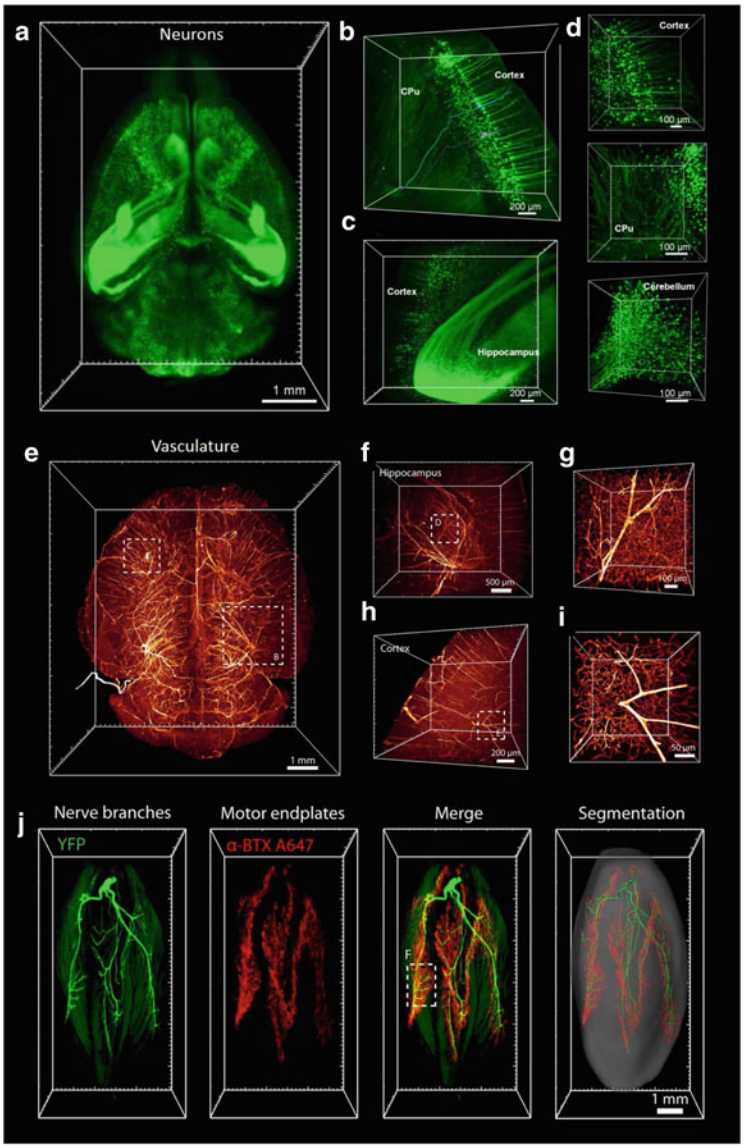

Fig. 11.3 Applications of FDISCO in 3D visualization of neuronal and vascular structures. (**a**–**d**) Reconstruction of neurons in *Thy1*-YFP-H mouse brain. (**e**–**i**) The vasculature in the mouse brain labeled with anti-CD31-Alexa Fluor 647. (**j**) 3D reconstruction and segmentation of nerve branches and motor endplates of the gastrocnemius muscle in *Thy1*-YFP-16 mouse. (Images adapted from ref. [33])

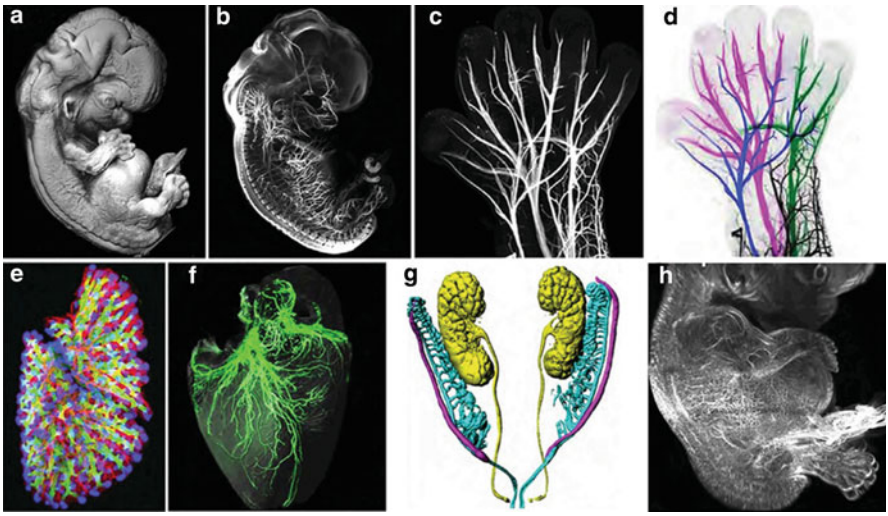

Fig. 11.4 3D visualization of the early human development by 3DISCO/iDISCO+, including (**a**–**d**) developing peripheral nervous, (**e**, **f**) cardiopulmonary, (**g**) urogenital, and (**h**) vascular systems. (Images adapted from ref. [62])

further improved the iDISCO protocol, termed iDISCO+ method [61]. The iDISCO and iDISCO+ have been applied to conduct imaging studies of intact rodent organs (such as the brain, kidney), rodent embryos, and even human tissues, such as the human prostate [20]. Belle et al. used iDISCO+ to label and clear human embryonic and fetal specimens, and obtained 3D images of peripheral nerves, blood vessels, cardiopulmonary, urogenital system, and other systems during early human development [62], as shown in Fig. 11.4.

Ertürk's group developed a nanobody-based whole-body immunolabeling technology, named vDISCO [63], to boost the intensity of fluorescent proteins. It can enhance the fluorescent signals more than 100 times and thereby allow panoptic imaging of the whole body at subcellular resolution. vDISCO has been applied to visualize whole-body neuronal projections and assess central nervous system trauma effects on neuronal projections (Fig. 11.5a) and inflammatory processes in the entire mouse body [63]. Pan et al. applied the vDISCO method to image cancer metastasis at single-cell resolution and to reveal the efficacy of therapeutic antibody targeting in entire mice (Fig. 11.5b) [64].

However, clearing and labeling of large adult human tissues or organs remained challenging. Recently, they published an approach, SHANEL [65], based on a new tissue permeabilization, to clear and deeply label intact human organs. This technique enables deep molecular labeling and clearing of centimeters-sized human organs, such as the human brain and kidney. Figure 11.6 showed an intact uncleared human brain before and after SHANEL clearing, and demonstrated the labeling and imaging of large brain blocks, which indicated that the differences in microglia density and morphology were evident throughout the gray matter and white matter.

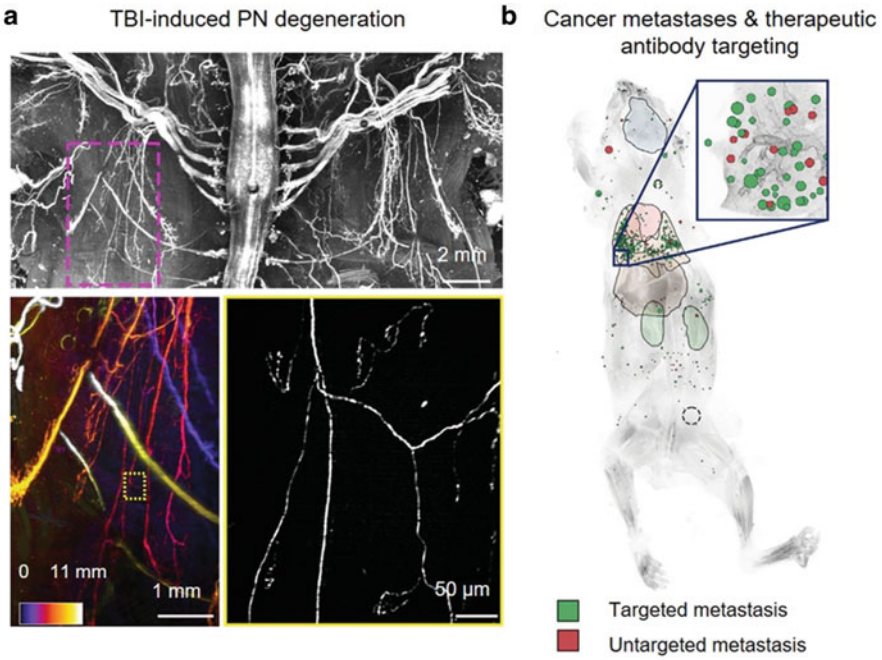

Fig. 11.5 Applications of vDISCO in mouse models of different human diseases. (**a**) TBI-induced peripheral nerve (PN) degeneration by vDISCO. (**b**) vDISCO panoptic imaging of cancer metastases and therapeutic antibody targeting. (Images adapted from refs. [63, 64])

SHANEL is promising to be widely used for the physiological and pathological conditions of human tissues in the future.

Roebroeck et al. also reported a simple, fast, and low-cost method for cytoarchitectonic labeling of human brain tissues, MASH, which is based on methanol pretreatment and hydrogen peroxide bleaching [66]. MASH suitable for large formalin-fixed adult brain samples (4–5 cm thick) and compatible with small organic dyes, such as acridine orange, methylene blue, methyl green, or neutral red.

11.3.2 The Hydrophilic Reagents-Based Clearing Methods

Except for the solvent-based clearing methods mentioned above, the other category is the hydrophilic reagents-based clearing methods, which are mainly based on three methodologies, including simple immersion, hyperhydration, and gel-embedding.

11.3.2.1 Simple Immersion-Based Clearing Methods

Some clearing methods used hydrophilic reagents with high refractive index to replace the water in tissues through simple immersion, to match the refractive index of tissues to achieve transparency for small-volume samples.

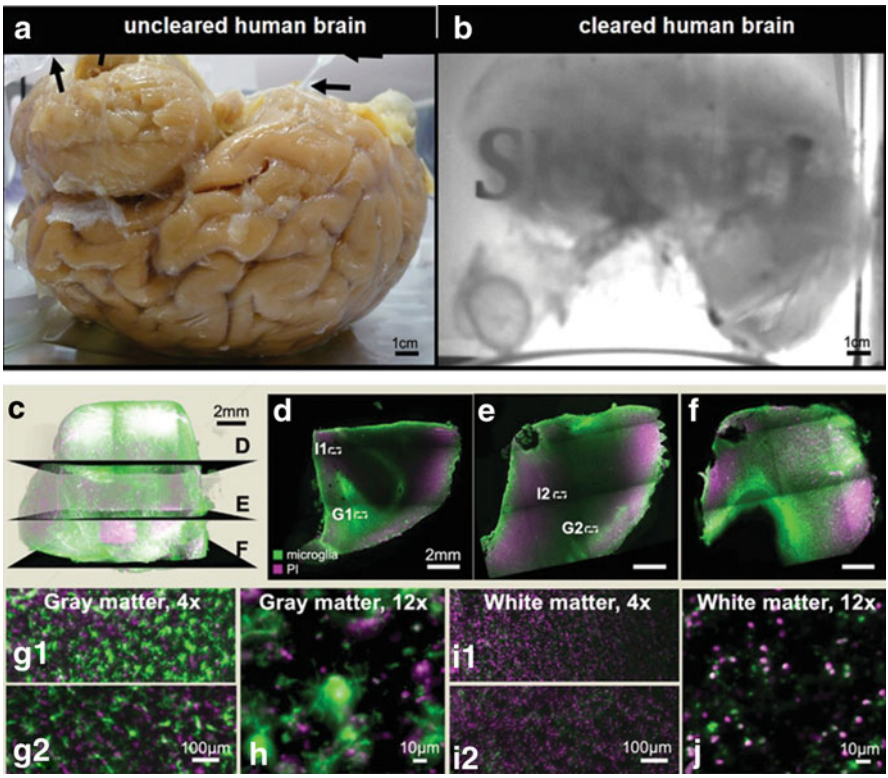

Fig. 11.6 SHANEL clearing of intact adult human brain and imaging of brain blocks. (**a**) Uncleared whole human brain. (**b**) Cleared whole human brain. (**c**–**j**) Iba1 microglia (green) and propidium iodide (PI) (magenta) labeling of postmortem human brain tissue. (Images adapted from ref. [65])

FocusClear, developed by Chiang's group, mainly used a mixture of DMSO, diatrizoic acid, glucosamine, and other chemicals as clearing reagents [67]. FocusClear has been applied for clearing of a variety of tissues, including Drosophila, plants, zebrafish, mice, etc., but limited to small or thin tissue samples. Hua et al. applied it to reveal the 3D neurohistology of tongue in health and injury [68].

After sucrose solutions had been used to clear 1–2 mm brain blocks [44], Ke et al. used gradient concentrations of fructose to enhance the clearing effect and proposed SeeDB (see deep brain) [42]. With good transparency and fine morphology preservation on mouse embryos, young brains, and adult brain slices, it has been applied for studies in development and brain circuits [42]. However, the high-concentration fructose solution used in SeeDB has a high viscosity. The FRUIT combined fructose and urea effectively solved the problem of high viscosity [45]. Recently, Zhu et al. developed a fast clearing protocol FOCM for thin tissue slices by combining urea with sorbitol and DMSO [69]. Subsequently, to obtain super-resolution images of

thick tissues, Ke et al. developed SeeDB2 by replacing fructose with iohexol, adding saponin and Tris-EDTA buffer to the clearing agent, and achieved super-resolution mapping of neuronal circuitry on the thick tissues of Drosophila and mouse brain blocks [48].

Costantini et al. developed a clearing method based on TDE and demonstrated the 3D imaging of hippocampal combined with STP, and also applied the protocol to human brain samples removed from a patient with drug-resistant epilepsy due to hemimegalencephaly [70]. Economo et al. used DMSO and sorbitol to clear mouse brain tissues and combined with STP to conduct whole-brain imaging, which realized tracing of neuronal axons through the whole brain [46].

11.3.2.2 Hyperhydration-Based Clearing Methods

The hyperhydration-based clearing methods mainly benefit from the high hydration of urea or urea-like chemicals, which can enhance the penetration of clearing reagents into the tissues, to achieve better transparency.

Miyawaki's group firstly used this principle and developed Sca*l*e by using urea for hydration, glycerol for refractive index matching, and the surfactant Triton X-100 to increase tissue permeability [71]. It obtained good transparency on mouse brain and intact embryo, but required weeks or even months for clearing a whole mouse brain and would cause obvious swelling and fragility, which make the imaging operation and morphology maintenance difficult. They further proposed Sca*l*eS [72], by introducing agents such as sorbitol and DMSO, and using gradient concentration to enhance the penetration. It not only accelerated the clearing process, but also showed excellent preservation of ultrastructure. It has been applied to aged and diseased brains in AD mouse models [72], including mapping of 3D networks of amyloid plaques, neurons, and microglia, and human clinical samples from AD patients for 3D pathology analysis (Fig. 11.7a). However, the clearing effect of Sca*l*eS on intact organs, such as the whole mouse brain, is still limited.

At the same time, Ueda' group developed CUBIC [37] based on Sca*l*e. In this method, amino-alcohol, Triton X-100, and urea were mixed to produce Sca*l*eCUBIC-1 to remove lipids, loose tissue structure, and then Sca*l*eCUBIC-2 with high RI was used to match the refractive index of tissue. It can render the whole mouse brain transparent in about 2 weeks, and it is also applicable to clearing and 3D imaging of marmoset brain tissues, normal and diseased human lung and lymph node tissues [37, 73]. Following CUBIC, a series of modified protocols have been proposed, such as CB-Perfusion using cardiac perfusion to deliver clearing reagents into the whole body of adult mouse [36]; CUBIC-cancer using immersion of *N*-butyldiethanolamine and antipyrine/nicotinamide for whole-body profiling of cancer metastasis [35]; and CUBIC-X based on imidazole and antipyrine reagents to expand the sample, thereby achieving efficient clearing of the whole brain, and is used to construct the 3D whole-brain atlas at single-cell resolution [74]. The group also described some other CUBIC cocktails and a series of CUBIC protocols (I–IV) [34], which enables the 3D imaging of mouse body and large marmoset brain, and human organ blocks, such as human heart, kidney, and brain tissues. Figure 11.7b

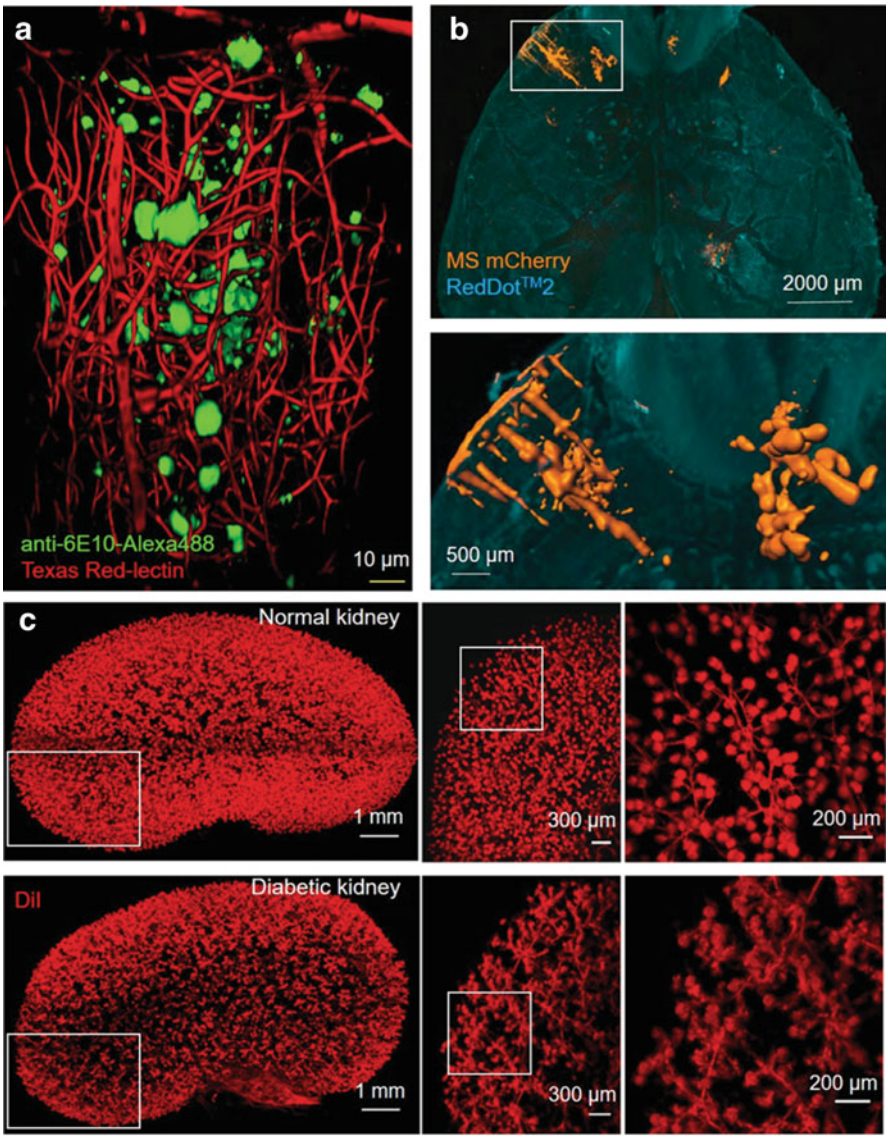

Fig. 11.7 Hyperhydration-based clearing methods facilitate 3D pathology of tissues in different disease models. (**a**) 3D mapping of amyloid plaques and blood vessels in AD mouse by Sca*l*eS. (**b**) The metastasis of human breast cancer cells in mouse brain by CUBIC (protocol I). (**c**) The pathology of glomeruli in diabetic kidney by MACS. (Images adapted from refs. [34, 40, 72])

shows the metastasis of human breast cancer cells in the mouse brain by CUBIC protocol I [34].

There are some other urea or urea analogs-based aqueous methods, such as UbasM [75], C_e3D [49], *Clear*$^{T/T2}$ [76], RTF [77], and OPTIClear [78]. In these

methods, OPTIClear is a tissue clearing solution optimized for fresh and archival human brain tissues [78], containing *N*-methylglucamine, 2,2′-thiodiethanol, and iohexol. Recently, Zhu's group has developed MACS [40] with ultrafast clearing speed, robust compatibility, and fine morphology maintenance. It can clear the whole brain of an adult mouse in 2.5 days, which is more than four times faster than the commonly used aqueous clearing methods, such as CUBIC. MACS is compatible with a variety of fluorescent probes, especially the lipophilic dyes, such as DiI. Combined with light-sheet microscopy, MACS allows 3D imaging and visualization of various organs, such as the rodent brain, spinal cord, spleen and intestine, and achieves 3D pathology of diabetic kidneys with DiI labeling (Fig. 11.7c).

11.3.2.3 Gel-Embedding-Based Clearing Methods

Distinct from the above methods, CLARITY is the first method based on hydrogel embedding to achieve tissue clearing [38, 79]. First, acrylamide hydrogel and tissue protein molecules are cross-linked and polymerized to form a physical framework to protect tissue proteins and structures, and then sodium dodecyl sulfate (SDS) is used to remove lipids in the tissue that are not cross-linked by the hydrogel. By adding a unidirectional electric field, a voltage difference was formed on the two sides of the tissue to speed up lipid removal. Finally, the samples were immersed in a refractive index matching solution to achieve final transparency.

Although CLARITY is an active delipidation method, it is still limited by the slow clearing speed and the risk of sample destruction. It has been optimized in several ways, including controlling temperature [80], improving the ETC chamber [81], or modifying conditions of tissue-hydrogel formation and tissue electrophoresis (ACT-PRESTO) [82]. Chung's group introduced stochastic electrotransport (SE) [83], a method using a random electric field to clear and stain intact tissues. It can render transparency of mouse organs in a short time (about 1–3 days) but requires complex customized devices. The MAP protocol [84] expands the tissues four- to fivefold for super-resolution imaging through hydrogel embedding, tissue denaturation, and expansion, which is also compatible with SE. There are some other CLARITY derivatives focused on interrogating the biological information in RNA, such as EDC-CLARITY [85], or bone tissues, such as Bone CLARITY [41].

In recent years, Chung's group proposed SHIELD [43], which stabilized the tissue structure by polyepoxides and degreased by SDS immersion or combined with SE, followed by refractive index matching reagents. Its advantage is that it can preserve protein fluorescence and antigenicity, transcription products, and tissue structures under harsh conditions, and has been used for studying human brain tissues and metastasis of breast cancer cells in mouse kidneys [43] (Fig. 11.8a). The latest eFLASH method first fixed tissue structures based on SHIELD, uses SE for lipid removal and 3D labeling [86]. By adjusting the pH of the labeling solution and the concentration of sodium deoxycholate to control the binding affinity of the probe-target, it can quickly realize the complete and uniform labeling of various tissues, including mouse organs, marmoset brain tissues, and brain organoids (Fig. 11.8b).

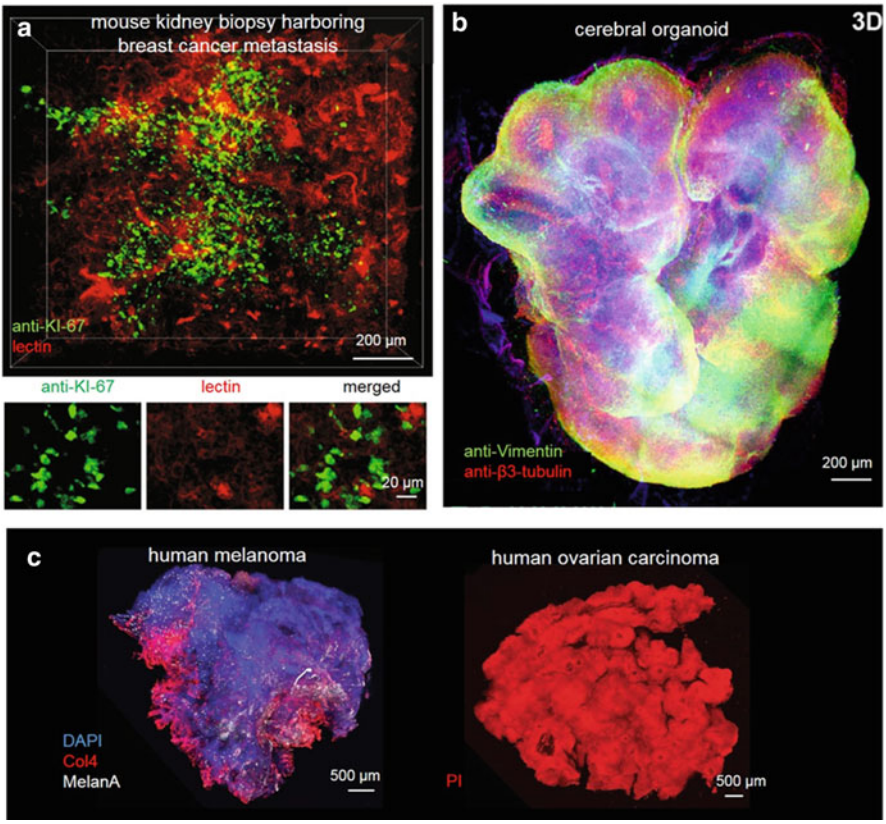

Fig. 11.8 Applications of gel-embedding-based clearing methods. (**a**) Distribution of cancer metastases in a mouse kidney biopsy by SHIELD. (**b**) 3D mapping of cerebral organoid by eFLASH staining. (**c**) 3D visualization of human cancer specimens (melanoma and ovarian carcinoma) by biphasic CLARITY. (Images adapted from refs. [43, 93, 94])

Due to the complexity of the ETC device, some gel-embedding-based clearing methods that do not require ETC were reported. PACT is a passive CLARITY method [39], which relies on passive delipidation by immersion to make the sample transparent. There are many optimization methods based on PACT [87–90], such as SCM [89], FASTClear [88], which have demonstrated the applications in imaging of human skin cancer tissue samples, human brain tissues, human gut samples. CLARITY derivatives have been applied to human brain tissues to aid neuropathological investigations, such as the 3D visualization of amyloid-beta plaques in Alzheimer's brain tissues [91] and pathological investigations of post mortem Parkinson's disease brain tissues [92]. PARS [39] is also based on CLARITY but uses the cardiac circulation and cerebrospinal fluid circulation system to deliver the reagents to the whole body or whole brain, to achieve rapid clearing and labeling. The SWITCH method [50] also does not require special equipment. By using glutaraldehyde as a

cross-linking agent to preserve tissue structure and molecular components, using high temperature to accelerate the clearing process, it allows dozens of rounds of molecular labeling and clearing [50]. However, it cannot preserve endogenous fluorescence, and has been used for neuronal or vascular labeling and imaging of mouse brain, rat brain, marmoset, and even formalin-fixed human brain tissues. Hsueh et al. developed biphasic CLARITY for irregular clinical samples and biopsies, with specific focus on developing and diseased pancreatic islets, also demonstrated that it could be used for visualization and demarcation of complex 3D tumor boundaries (Fig. 11.8c) [93].

In summary, there are a variety of tissue optical clearing methods, and different methods have certain applicability and characteristics. Generally, the solvent-based clearing methods show advantages in clearing speed, tissue transparency. Although BABB and 3DISCO developed in the early stage are not conducive to the preservation of endogenous fluorescent signals, the subsequent optimized methods, such as FDISCO and PEGASOS, overcame the problem of fluorescence quenching. The hydrophilic reagents-based clearing methods are more friend to fluorescence than 3DISCO with minimal size change, but it usually takes a long time (several weeks) to obtain high transparency, or partially requires specific devices (such as electrophoresis devices), while the newly reported MACS has addressed the problem of slow clearing speed along with fine compatibility with lipophilic dyes.

With the constantly emerging tissue optical clearing methods, as well as the development of fluorescence labeling, 3D imaging and data processing techniques, the applications of in vitro clearing methods have been developed rapidly. From the early 3D imaging of Drosophila and zebra fish [51, 95, 96], as well as the brain, spinal cord and other rodent organs (such as rat and mouse) [27, 28, 31, 33, 40, 97], it has developed into the imaging research of human tissues and organs [65, 78, 86], and even human organoids [62]. The scientific problems ranged from observing the 3D structure of normal tissues (such as the single-cell-level brain atlas [74] and whole-brain vasculature [98]) to studying of the corresponding structural changes of the pathological process (such as the progress of AD [60]), cancer metastasis in the entire body [35, 64], ischemic stroke [63, 99], to the evaluation of the effects of interventional treatment of diseases (such as the efficacy of stem cell transplantation [27]), and even the early development of human embryos [62] and adult human intact organs [34, 65], etc., involving a wide range of aspects. It is expected to play an important role in fundamental researches and clinical diagnosis, and greatly promote the development and progress of life science.

11.4 In Vivo Tissue Optical Clearing Window for Cell and Vascular Imaging

Over the last decade, various noninvasive and minimally invasive optical imaging modalities have been widely used in biomedical imaging with promising resolution, including laser speckle contrast imaging (LSCI) [100, 101], hyperspectral imaging (HSI) [102, 103], optical coherence tomography (OCT) [104, 105], photoacoustic

imaging [106, 107], confocal imaging [108, 109] and multiphoton imaging [110–114], etc. In order to image cutaneous or cortical cells or vasculature, various surgery-based window models such as the dorsal skin chamber [115–117], exposed cortex [118, 119], and cranial skull windows [120–123] have been developed, but surgical operation inevitably causes side effects.

With the development of tissue optical clearing techniques, in vivo tissue optical clearing provides a window for optical imaging techniques to obtain dynamic cellular and vascular information, not only in skin but also in cortex in vivo [124–129].

11.4.1 Skin Optical Clearing for Cell and Vascular Imaging

It is well known that skin is not only the largest organ of the body, but also the most important route for foreign compounds entering the body. In addition, skin is the first barrier to in vivo optical imaging or laser-targeted therapy, so skin optical clearing attracts more attention. Generally, skin roughly consists of three major layers from the outmost, epidermis, dermis, and subcutaneous adipose tissue. Dermis is the main scattering source of skin for rich collagen.

To make the skin transparent, high-refractive agents, such as alcohol or sugars agents with hydroxyl groups, introduced into dermis could disassociate collagen and dehydrate. The agents with more hydroxyl groups, the stronger propensity of OCAs to form hydrogen bonds and bridges, which determines their ability to destabilize higher-order structures of collagen by disrupting water bridges and the hydration shell [12, 15, 130–134]. For in vivo application, the skin is usually topically treated with OCAs since direct injection of OCAs into dermis would cause edema, suppuration, and even scarring [135]. In order to enhance the penetration of OCAs into dermis, physical and chemical methods are introduced. The physical enhancement methods mainly include laser irradiation [130, 132], ultrasound application [136], sandpaper grinding [137], microneedle rolling [138], and tape stripping [139], which could interrupt stratum corneum. In addition, massage was also proved to be helpful for OCAs trans-epidermal delivery [140]. Futhermore, chemical penetration enhancers, such as azone [141], oleic acid (OA) [142], DMSO [143], propylene glycol (PG) [140], and thiazone [134], could change the structure of epidermis tissue and enhance the optical clearing effect as well.

Considering differences in components and structures of skin in different parts of rodent, various skin optical clearing agents (SOCAs) have been developed, respectively, including dorsal skin optical clearing agents (DSOCA) [134, 140, 144–147], ear skin optical clearing agents (ESOCA) [148, 149] and footpad skin optical clearing agents (FSOCA) [125, 150] to make the relative skins transparent, which have been used for cutaneous cellular and vascular imaging.

11.4.1.1 In Vivo Dorsal Skin Optical Clearing for Microvascular Imaging

Dysfunction of skin microcirculation is an advanced indicator that represents peripheral vascular disease. Recently, in vivo SOCA provides a noninvasive skin window

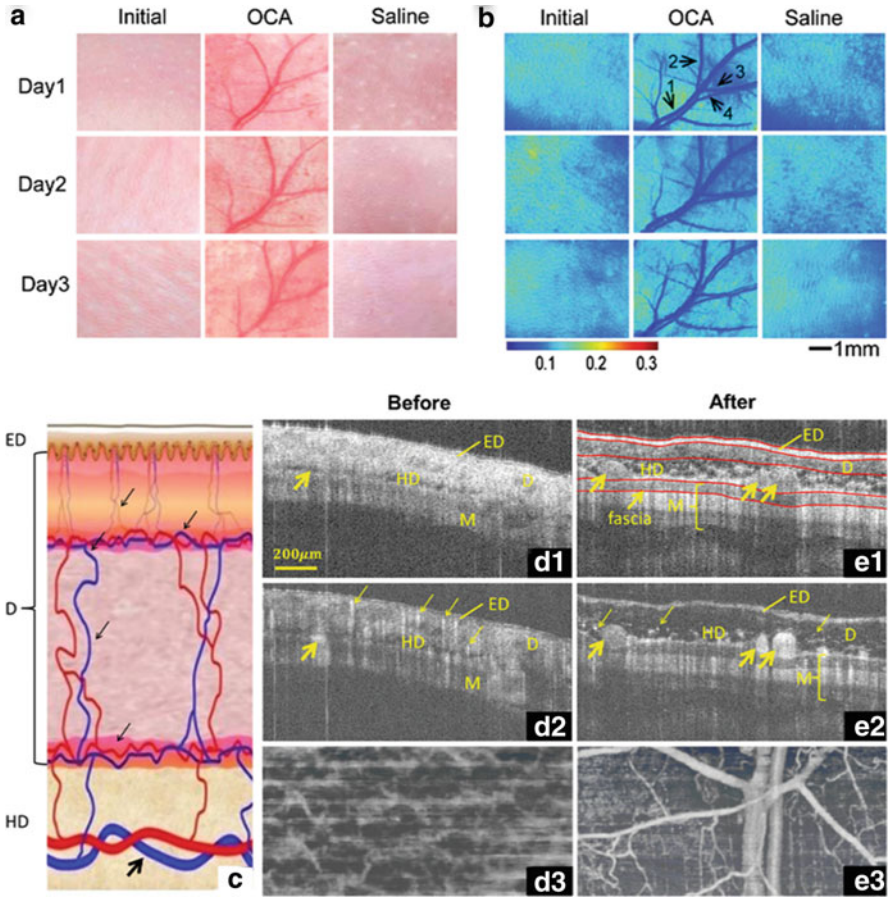

Fig. 11.9 (**a**, **b**) Typical visual photos (**a**) and corresponding laser speckle temporal contrast images (**b**) of in vivo rat skin. The arrows 1–4 indicate the interested blood vessels, whose diameters were measured each day after skin optical clearing [147]. (**c–e**) Representative OCT structural and angiographic images of mouse dorsal skin in vivo, before (column **d**) and after (column **e**) FPT treatment, respectively. (**a**) Cross-sectional schematic of the layered skin. (**d1**) and (**e1**) Structural cross-sections. (**d2**) and (**e2**) Cross-sectional angiograms. (**d3**) and (**e3**) Projection view of 3-D angiography. *ED* epidermis, *D* dermis, *HD* hypodermis, *M* muscles. Thin arrows indicate small vessels. Bold arrows indicate big vessels [145]

for various optical imaging systems to obtain cutaneous microvascular structural and functional information.

In 2010, Zhu et al. [134] firstly developed a DSOCA to make the rat dorsal skin transparent in vivo with topical treatment of PEG-400 and thiazone for several minutes. Together with laser speckle contrast imaging (LSCI) technique, they obtained blood flow distribution in dermis. Wang et al. [147] further proved the safety of DSOCA by repeated imaging without affecting the structure and flow distribution of dermal blood vessels (Fig. 11.9a, b), as well as the body weight and

organ coefficients. Li et al. [145] applied a mixture of saturated fructose, PEG-400 and thiazone on mice dorsal skin to increase the imaging depth and quality of optical coherence tomography angiography (OCTA). After optical clearing, the imaging depth and contrast were significantly improved, and the boundaries of epidermis, dermis, subcutaneous, and even muscle under the skin were able to be distinguished (Fig. 11.9d, e), suggesting skin optical clearing technique allowed OCTA not only to see the dermis, but also to obtain tissue information beneath the skin. Feng et al. [150] applied a mixture of PEG-400, thaizone and saccharose to dorsal skin of type 1 diabetic mice and investigated the dysfunction of microcirculation response to noradrenaline (NE). With the help of skin optical clearing procedure, the changes of blood flow and blood oxygen saturation in skin vasculature were clearly obtained with LSCI and HSI technique. The results demonstrated that the blood flow and blood oxygen responses of skin vasculature to NE had changed dramatically with the development of diabetes. Their further study [129] showed the responses to sodium nitroprusside and acetyl choline also interrupted with the development of diabetes.

11.4.1.2 In Vivo Ear Skin Optical Clearing and Its Applications

Although the mouse ear provides an available window, the residual scattering of ear skin still influences the imaging quality. The in vivo tissue optical clearing technique presents a new opportunity to decrease the scattering of skin, and enhance the imaging contrast or imaging depth of optical methods.

Wang et al. [149] applied a mixture of PEG-400, fructose, and thaizone to mouse ear, and found it could significantly increase the transparency of ear (Fig. 11.10). They also demonstrated that the topical application of ESOCA on ear skin in vivo could improve the imaging contrast of cutaneous blood vessels and blood flow without changing the structure and blood flow of vasculature. Compared with the intact case, the contrast-to-noise ratios (CNRs) of speckle contrast images increased by $128 \pm 21\%$ and $49 \pm 7\%$ after application of ESOCA when the diameter of blood vessels is between 25 μm and 30 μm, or 50 μm and 80 μm, respectively.

Ding et al. [148] applied ESOCA to rat ear. Ten minutes after optical treatment of ESOCA, the transmittance of the ear skin increased significantly while the glycerol only made a slight enhancement. Especially, three wavelengths were chosen to quantitatively evaluate the optical clearing efficacy: the LED (535 ± 15 nm) was used for visualizing the blood vessels in the rat ear; 635 and 665 nm were the excited wavelength and the emitted wavelength for IVFC measurement. As shown in Table 11.1, there were significant differences between the intact and ESOCA-treated skin ($p < 0.01$) at the three wavelengths, but no differences between the intact and glycerol-treated or saline-washed skin.

They next performed in vivo flow cytometry (IVFC) in the ear blood vessels, with the red blood cells labeled by DiD (1,1′-Dioctadecyl-3,3,3′,3′-Tetramethylindodicarbocyanine Perchlorate). Peak intensity, peak number, and signal-to-noise ratio of IVFC at each depth from 80 to 330 μm during a 6-min measurement were used to evaluate the optical clearing effect of ESOCA, and the

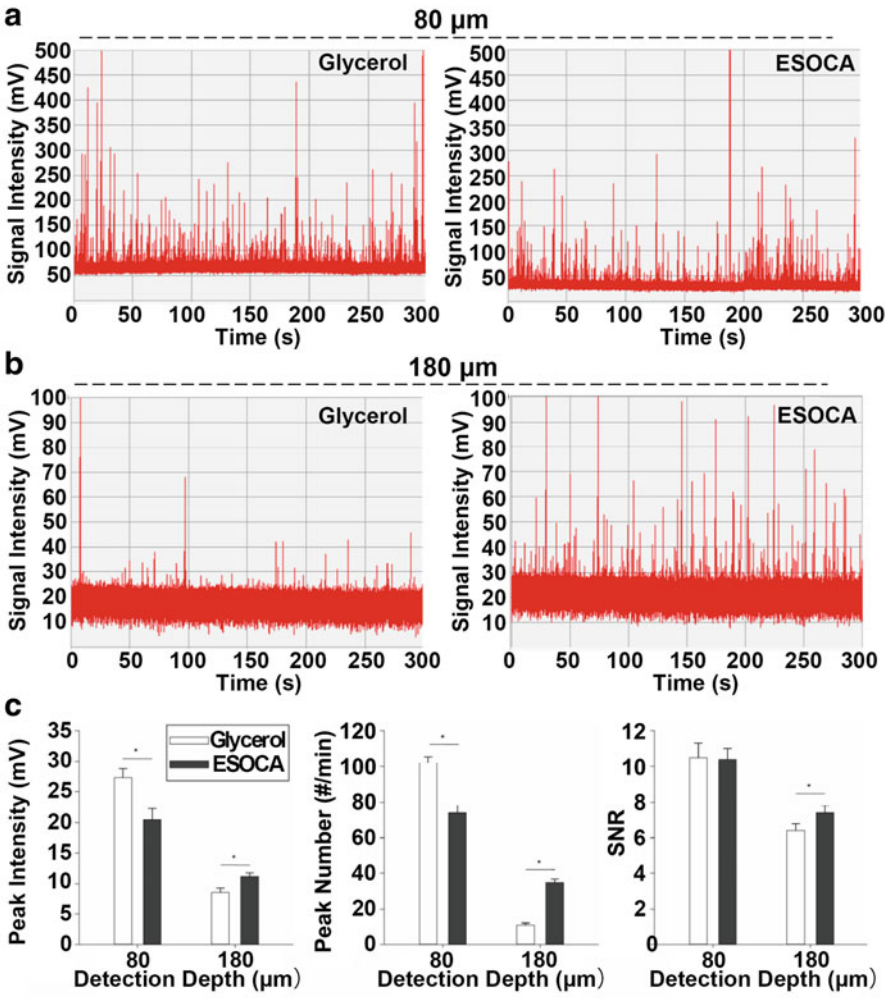

Fig. 11.10 (**a**, **b**) IVFC signals of DiD-labeled red blood cells (left: treated by glycerol; right: treated by ESOCA). The signals were recorded at the depth of 80 μm (**a**), and 180 μm (**b**) for 6 min. Each peak represented a DiD-labeled cell traversing the excitation slit. (**c**) Comparison of signal peak properties after the treatment with glycerol or ESOCA, respectively (a.u.: arbitrary unit, $p < 0.05$ *) [148]

results are stated in Fig. 11.10. Not surprisingly, at a deeper depth of 180 μm in the skin, the mean intensity increased by 31.04% after the application of ESOCA, and the peak number and SNR of ESOCA-treated group here was also higher than glycerol-treated group.

Table 11.1 Transmittance of rat ear at different wavelengths before or after the treatment of agents ($p < 0.01$**) [148]

Treatment	535 nm (%)	635 nm (%)	665 nm (%)
Intact	18.03 ± 2.93	31.44 ± 3.52	33.72 ± 3.99
Glycerol for 10 min	20.08 ± 3.13	34.62 ± 4.32	37.33 ± 4.37
Saline washed	19.04 ± 2.17	31.91 ± 4.64	34.01 ± 4.1
ESOCA for 10 min	35.59 ± 6.1**	49.05 ± 4.81**	52.07 ± 6.46**

11.4.1.3 In Vivo Footpad Skin Optical Clearing for Monocyte/Macrophage Dynamic Observation

Footpad provides a classical physiological site for monitoring cellular behavior during inflammation, but limited to the superficial dermis due to the strong scattering of footpad.

Shi et al. [125] established a switchable footpad skin optical clearing window with a FSOCA, composed of fructose, ethanol, DMSO, PEG-400, and thiazone. As shown in Fig. 11.11a, the performances of the cutaneous blood flow imaging were greatly improved after topical treatment with FSOCA, and the saline treatment could eliminate this effect. In addition, combined with confocal microscopy, monocyte/macrophage (MM) imaging was performed through the footpad skin window. They used C57BL/6 mice expressing GFP under the control of endogenous Cx3cr1 locus in MMs. For transparent footpad skin, a remarkable increase in the number of MM was observed (Fig. 11.11b), and fluorescence imaging depth increased 2.5-fold in average, compared to the turbid footpad skin (Fig. 11.11c). In addition, the repeated imaging experiments demonstrated that the distributions of monocytes at 4 h (cyan border) was almost the same as that at 0 h, and that at 72 h also had no noticeable changes in distributions of MMs, indicating the repeated optical clearing treatments did not lead to an inflammatory response.

In the further study, Shi et al. [150] monitored the recruitment and motility of monocyte/macrophage at different depths in skin tissue around delayed-type hypersensitivity (DTH) foci with the development of type 1 diabetes (T1D). Figure 11.12a–d shows typical maximum intensity projection (MIP) images about MM infiltration and recruitment at various time points in mice with different T1D disease durations. The number of MM recruiting to the imaging area and the distributional density of MMs become increasingly larger with time after heat-aggregated ovalbumin (AOVA) injection, as well as with the development of T1D for the same time point after AOVA injection (Fig. 11.12e, f). Furthermore, MMs were imaged at each indicated time point in a large-scale imaging area, and the result also showed progressive T1D leads to the much stronger MM recruitment, and even the formation of some dense cellular clusters (Fig. 11.12g).

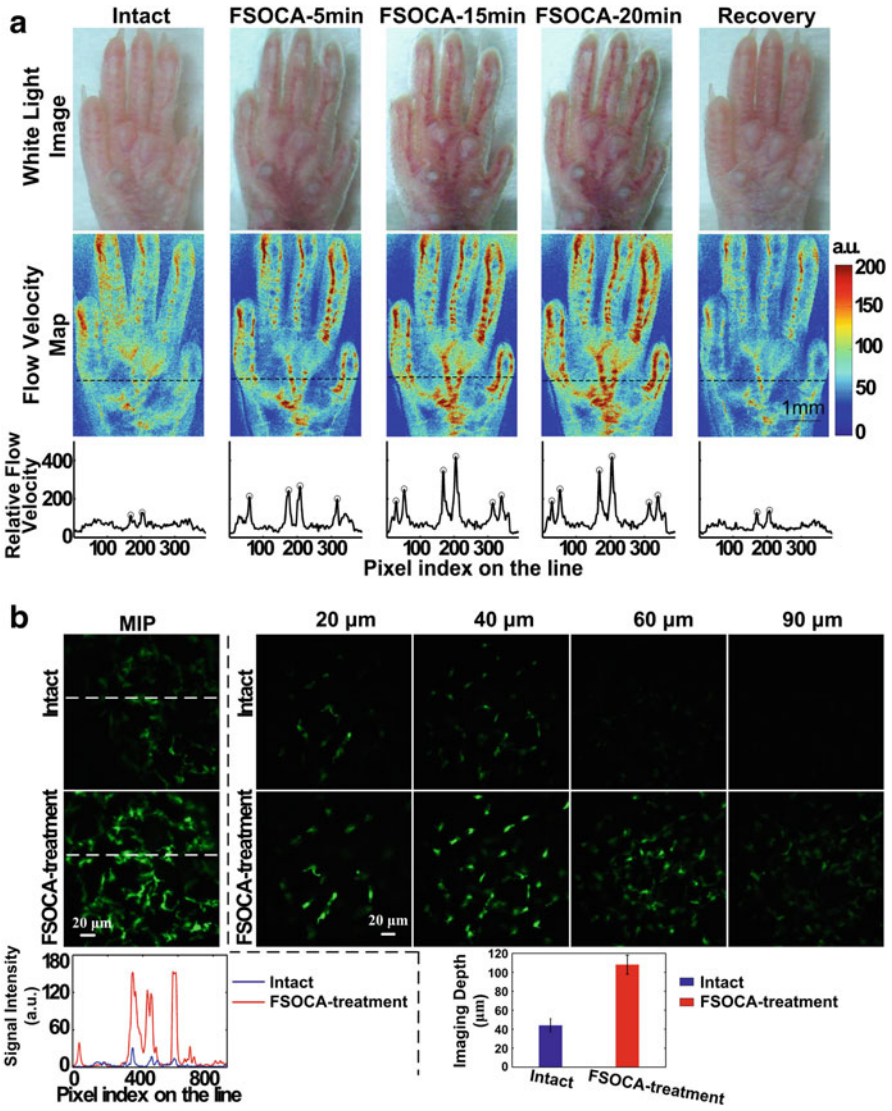

Fig. 11.11 (**a**) White-light images (top row), relative blood flow velocity maps (middle row) and profiles of blood flow index along the dashed line (bottom row) through the intact, FSOCA-5 min, FSOCA-15 min, FSOCA-20 min, and recovered footpad skin. The circles indicate the blood vessels of interest. (**b**) Maximum intensity projection (MIP) maps imaged by confocal microscopy through the intact (top row) and transparent footpad skin (middle row), and profiles of fluorescence signal intensity along the dashed line (bottom row). (**c**) Depth-resolved fluorescence images (the first two rows) and the imaging depth (the third row) before and after FSOCA treatment. (Data are expressed as mean ± SEM [125])

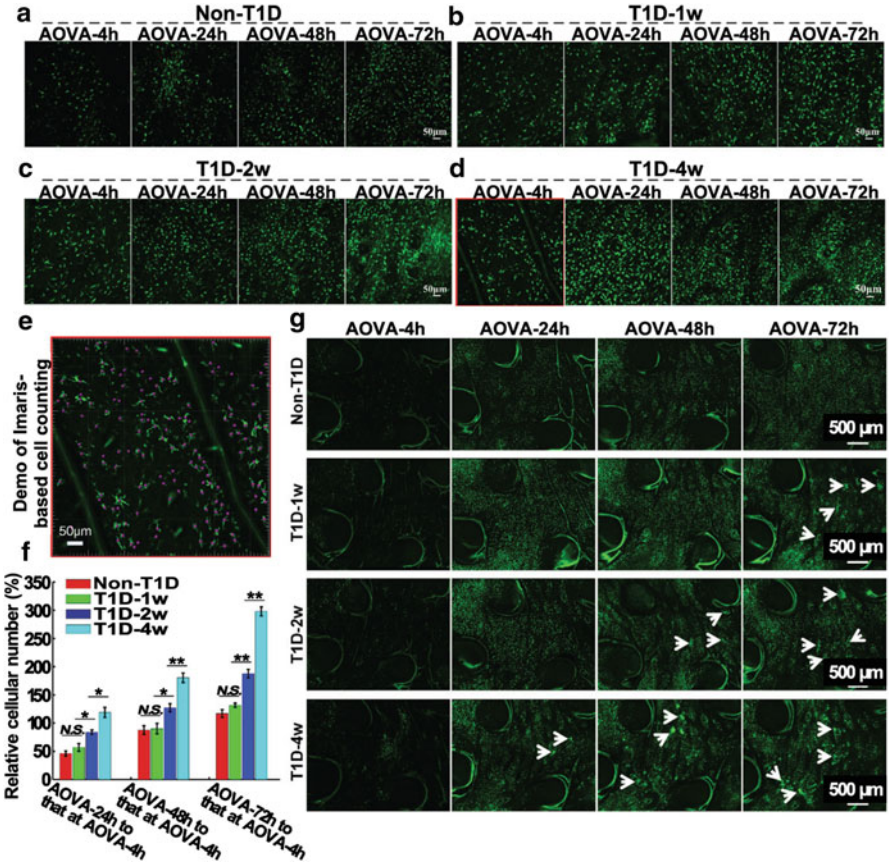

Fig. 11.12 Cell recruitment Single-imaging field demonstrates MM recruitment at AOVA-4 h, AOVA-24 h, AOVA-48 h and AOVA-72 h on non-T1D (**a**), T1D-1 week (**b**), T1D-2 weeks (**c**) and T1D-4 weeks (**d**) mice. (**e**) Demo of Imaris-based cell counting, and (**f**) Relative cellular number in single-imaging field at AOVA-24 h, AOVA-48 h and AOVA-72 h to that at AOVA-4 h. (**g**) Large-scale imaging at each indicated time point demonstrates the shifting ahead of time for forming the dense cellular accumulated clusters as progressive T1D develops. Mean values ± SEM (data were pooled from six mice per group). N.S., *, and ** refer to no significant difference, $p < 0.05$ and $p < 0.01$, respectively [150]

11.4.2 Skull Optical Clearing for Cortical Neuron and Vasculature Imaging

It is crucial to obtain information of in vivo brain in its natural environment to better understand the function of vasculature and neural networks, as well as various diseases related to the dysfunction of brain [100, 151, 152]. Optical imaging techniques, such as LSCI, HSI, photoacoustic imaging, optical coherent tomography (OCT), can provide vascular structure and function with low invasiveness in cortex

[100, 110–114]. The development of transgenic technology and multiphoton microscopy promises us to image neurons, glia, and microvasculature in live mice with high resolution, which has become a powerful tool to explore brain function and disease [153–162]. However, the strong scattering caused by the skull over the cortex hinders the observation of fluorescently labeled neuronal structures and microvasculature [163, 164]. To overcome this obstacle, various cranial window methods were developed, including the open-skull glass window [120, 121], the thinned-skull cranial window [122, 123], and their variant [122, 165, 166], but all of them cannot circumvent the problems, the associated inflammatory response, or the complexities in surgical procedures and high skill requirements for laboratory personnel.

The tissue optical clearing technique can reduce the scattering of tissue [30, 31] and has great potential for solving this problem. According to the components of skull, calcium hydroxyapatite (16%), collagen (16%), lipids (54%), and water (14%) [167], some agents can be selected specifically to decrease the scattering of these components by dissolving the collagen, lipid, or removing hydroxyapatite. In 2012, Wang et al. [168] developed a skull optical clearing solution (SOCS), including laurinol, dimethyl sulfoxide, sorbitol, alcohol, and glucose, which could make the skull transparent within 25 min. Combined with skull optical clearing method with LSCI, they firstly realized in vivo cortical blood flow imaging without craniotomy; combined with photoacoustic microscopy, the imaging performance for cerebral microvasculature was enhanced [169]. However, the safety and repeatability had not been proved systematically. According to the need for cortical imaging, the newly reported skull optical clearing methods optimized the effect of optical clearing skull window from two aspects, including imaging resolution and long-term observing capability. Meanwhile, the safety for in vivo application was demonstrated [170, 171].

11.4.2.1 In Vivo Skull Optical Clearing Window for In Vivo Imaging of Mouse Cortex at Synaptic Resolution

Zhao et al. [170] developed a skull optical clearing window (SOCW), which allowed to repeatedly image neurons, microglia, and microvasculature of mice with synaptic resolution. In their study, since components of the skull change with age, various clearing methods were developed for mice of different ages. For infantile mice aged postnatal day 15 (P15)–P20, the intact skull was topically treated with collagenase; for mice aged P21–P30, the reagent was replaced by EDTA disodium; for mice older than P30, the skull has to be thinned to approximately 100 μm before clearing and then treat it with EDTA disodium. After 5–10 min of treatment, the first reagent was removed and glycerol was applied to match the refractive index.

Two-photon laser scanning microscopy (TPLSM) combined with transgenic mice (*Thy1*-YFP-H) was performed to assess the optical clearing efficacy through the SOCW. The results demonstrated that the image quality, depth and contrast were considerably improved and sufficient for imaging the dendritic spines without craniotomy. Furthermore, the SOCW technique is proved to be compatible with various fluorescent proteins and dyes, including GFP, YFP, RFP, FITC, and tetramethylrhodamine, for various cortical structures, including dendrites, microglia, and blood vessels.

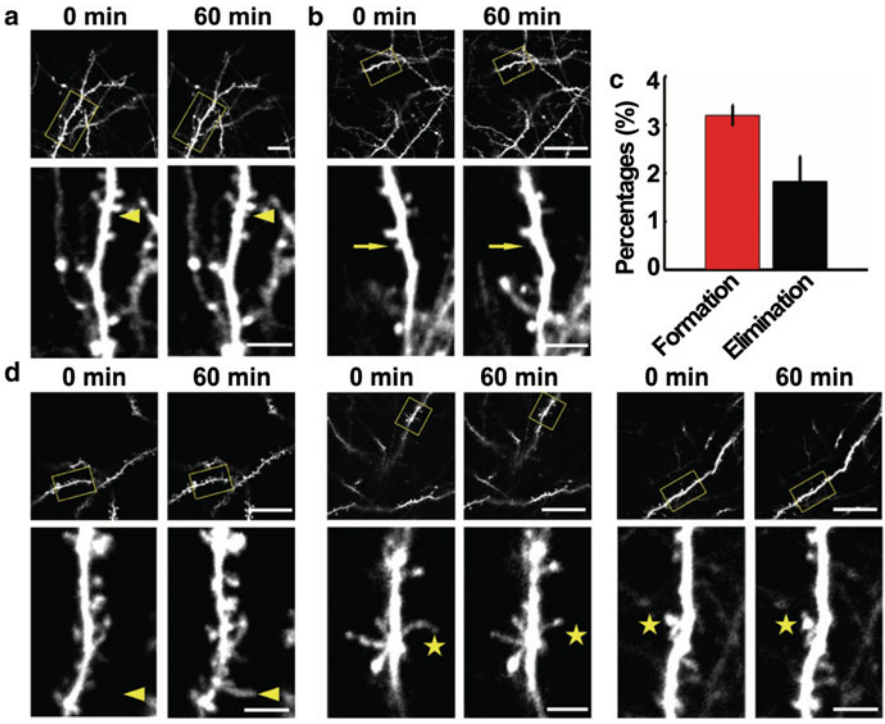

Fig. 11.13 Dynamical monitoring of the plasticity of dendritic protrusions in infantile mice (P19) through the SOCW. Time-lapse images of dendritic branches over an hour (60 min). (**a**, **b**) Dendritic spines can (**a**) appear and (**b**) disappear within an hour. (**c**) Percentage of spines formed and eliminated within an hour, according to the SOCW technique ($n = 6$ mice). (**d**, **e**) Filopodia can also (**d**) appear and (**e**) convert into a spine-like protrusion within an hour. (**f**) The morphology of dendritic spines can change within an hour. The triangle, arrow and asterisk show appearance, disappearance and morphological changes, respectively. Scale bar = 25 μm (above) and 5 μm (below) [170]

They next applied this method to dynamically monitor the plasticity of dendritic protrusions in critical periods in immature mice. It was found that dendritic spines of infantile mice had morphological changes within 1 h, including appearance (Fig. 11.13a) and disappearance (Fig. 11.13b) of spines and changes of shape (Fig. 11.13f), which points to changes in the wiring of neuronal circuits. Figure 11.13c shows that the formation of spines was more than elimination during 1 h. Compared with dendritic spines, filopodia exhibited higher motility (Fig. 11.13d, e). In addition, filopodia could even convert into spine-like protrusions, demonstrating that filopodia are likely to be the precursors of dendritic spines. These results indicate that the plasticity of dendritic protrusions during the third week is very intense.

In addition, Zhao et al. tested the repeatability and safety of the SOCW technique. The results showed the skull could return to the opaque state very quickly after

treatment with saline, and retreatment with OCAs made the skull re-clear very quickly. Besides, the optical clearing skull window could be repeatedly open and close during 3 days. Both in vivo and ex vivo safety assessment showed the SOCW technique did not affect the microenvironment.

11.4.2.2 In Vivo Skull Optical Clearing Window for Long-Term Imaging

Zhao's skull optical clearing window has not only obvious advantage, but also disadvantage, such as lack of repeats, and age-dependent skull optical clearing methods. Zhang et al. [171] developed a urea-based skull optical clearing agent (USOCA), which had advantages of making an easy-to-handle, large, switchable, and safe optical clearing skull window for repeated cortical vascular observation for as long as 7 months. USOCA consists of two kinds of mixture, named S1 and S2, respectively. S1 is a saturated supernatant solution of 75% (vol/vol) ethanol and urea. S2 is a high-concentration sodium dodecylbenzenesulfonate (SDBS) solution. When the skull was exposed, S1 was firstly applied to skull for about 10 min, making the skull gradually turn transparent. During this time, the skull could be gently rubbed with a swab to accelerate the clearing. Then, S1 was removed, and S2 was added to the same area for further clearing within 5 min. The skull should be covered by S2 to stay transparent, and the optical clearing skull window could be closed by scrubbing with phosphate-buffered saline. The study also demonstrated that the USOCA was valid for mice at different ages from 2- to 8-month-old.

Repeated treatment with USOCA permitted to establish the optical clearing skull window in the same area again with the clearing efficacy similar to that of the first time. In their study, the optical clearing skull window was efficiently and repeatedly established once a month on mice as they aged from 2- to 7-month-old. In addition, the vascular network was maintained relatively well, indicating its safety (Fig. 11.14).

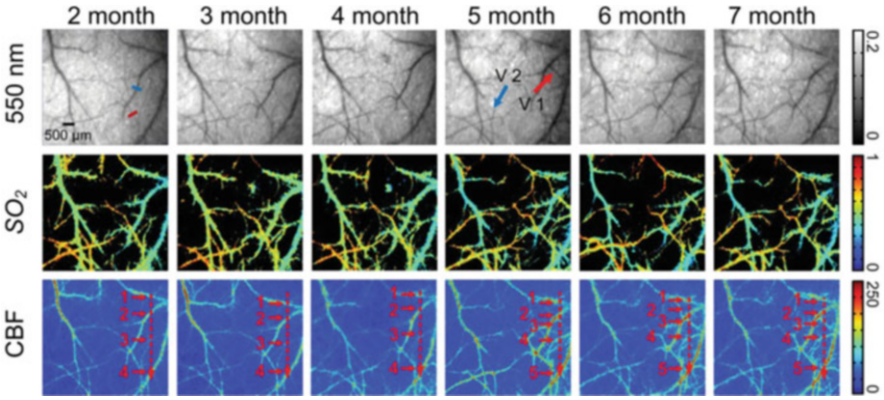

Fig. 11.14 Optical clearing skull window was established and cleared once a month over 6 months on the same mouse to image cortical vessels. Red and blue arrows indicate newly formed vessels and vessels that "disappeared," respectively [171]

The USOCA was proved compatible with various optical imaging systems, including LSCI, HSI, and TPLSM. In the TPLSM experiment, before clearing, the imaging depth was about 120 μm, and only a few large vessels (67.5 ± 7.9 μm) could be barely detected, while with the optical clearing skull window, the imaging depth increased to about 300 μm, and both those large vessels and microvessels (4.5 ± 0.31 μm) could be distinguished. LSCI and HSI were used to measure the cerebral blood flow (CBF) and oxygen saturation (SO_2) of cortical vasculature, respectively. When PBS was applied on the skull, the imaging quality slightly improved for the 2- and 4-month-old mice but not for the 6- and 8-month-old mice. However, with the application of USOCA, abundant cortical vessels were clearly observed, and the contrast and resolution of the CBF and SO_2 maps were greatly enhanced and were almost comparable to those obtained in all four age groups with the skull removal. In addition, USOCA was applied to bi-hemispheric skull and achieve a large clearing skull window for monitoring the dynamic changes in CBF and SO_2 of bi-hemispheric cortex after MCAO surgery.

In the further study, USOCA was not only used for cortical imaging, but also used for cortical manipulation. Zhang et al. [127] successfully open the blood-brain barrier (BBB) by introducing photodynamic (PD) effect through the optical clearing window. Thirty minutes after intravenous injection of 5-ALA, a 635-nm laser was used to irradiate cortex to trigger PD effect and observed if high weight molecules were able to leak from the blood vessels. Their study indicates that optical clearing skull window is a promising tool for non-invasive PD-related BBB opening for high weight molecules and liposomes that provides a novel, useful tool for brain drug delivery and treatment of brain diseases. They further investigated the age differences in PD-related BBB opening and found that the PD-related increase in the BBB permeability to high weight molecules (EBd and FITC-dextran) and solutes (vasogenic edema) was more pronounced in 4-week-old mice than in 8-week-old mice [126].

11.4.2.3 In Vivo Skull Optical Clearing Window for Deep Cortical Imaging

Although optical clearing skull window allows light to assess to the cortex with little attenuation of scattering, the scattering of the cortical tissue itself still limits the optical imaging technique into the superficial layer. Even using two-photon microscopy, the imaging depth under the transparent skull was only 300 μm [170, 171]. To further enhanced the imaging depth, Chen et al. [172] combined optical clearing skull window with three-photon microscopy and blood vessels down to a depth of 850 μm were still visible.

In their study, coherent Raman scattering microscopy detected the component changes in skull with topical treatment of USOCA [171] or SOCW [170]. The results demonstrated that USOCA only degraded the protein-rich composition, mainly collagenous fibers on the surface of the skull and proteins embedded in the bone. EDTA, the main component of SCOW, was able to homogenize the proteins and effectively decompose the matrix of inorganic phosphates by chelating the calcium

ions and significantly reduces both the thickness and density of inorganic minerals in the skull.

Since the skull optical clearing principles of USOCA and SOCW were different, they combined the two methods. First, USOCA was topically applied to the exposed skull for 25 min and removed. Ten percent EDTA was then topically applied for 25 min and removed. Finally, the skull was treated by 80% glycerol for 5 min and the mouse cortex was observed with three-photon microscopy with glycerol covered.

SOCW and USOCA can be combined to establish an even more transparent skull for deep cortical vascular imaging with the penetration depth of 850 μm [172]. Thanks to the double enhancement of the two skull optical clearing methods, deep cortical 3D vasculature imaging was eventually realized under skull (Fig. 11.15).

In summary, tissue optical clearing technique has been widely used for in vivo applications. It provides a minimally invasive skin window and skull window, allowing optical system to perform cellular and vascular imaging in skin and cortex. In vivo tissue optical clearing technique makes it possible to obtain cutaneous and cortical cellular and vascular imaging without surgery, and has enormous potential for applications of diagnosis and therapy.

It is worth mentioning that, apart from rodents, SOCA has also been preliminarily used for human vasculature imaging. It was found that topical treatment of dehydrated glycerol [173] and fructose solution [174] was beneficial for transmission imaging and correlation mapping optical coherence tomography (cmOCT) on human proximal interphalangeal joints and arms, respectively. Thus, in vivo skin optical clearing technique has great potential in biological and clinical research.

11.5 Summary

Tissue optical clearing technique provides an innovative perspective to perform deep-tissue imaging in biological researches. This chapter first introduced the mechanisms of tissue optical clearing from physical to chemical aspects, then described the in vitro tissue optical clearing methods for tissue or whole-organ imaging, including the solvent-based and the hydrophilic reagents-based clearing methods, and finally presented the in vivo tissue optical clearing techniques for minimally invasive skin window and skull window for cell and vascular imaging. These clearing methods enable not only 3D imaging of the structures of physiological and pathological tissues with high resolution in vitro, but also allow deep detection of cutaneous or cortical cell and vascular structure and function without surgical window in vivo, playing important roles in biomedical imaging.

In the future, with the ongoing development of tissue optical clearing methods, as well as the progress of labeling and imaging techniques, tissue optical clearing is expected to have more and more applications and play an increasingly significant role in both biomedical researches and disease diagnosis and treatment, to greatly promote the development and progress of life science.

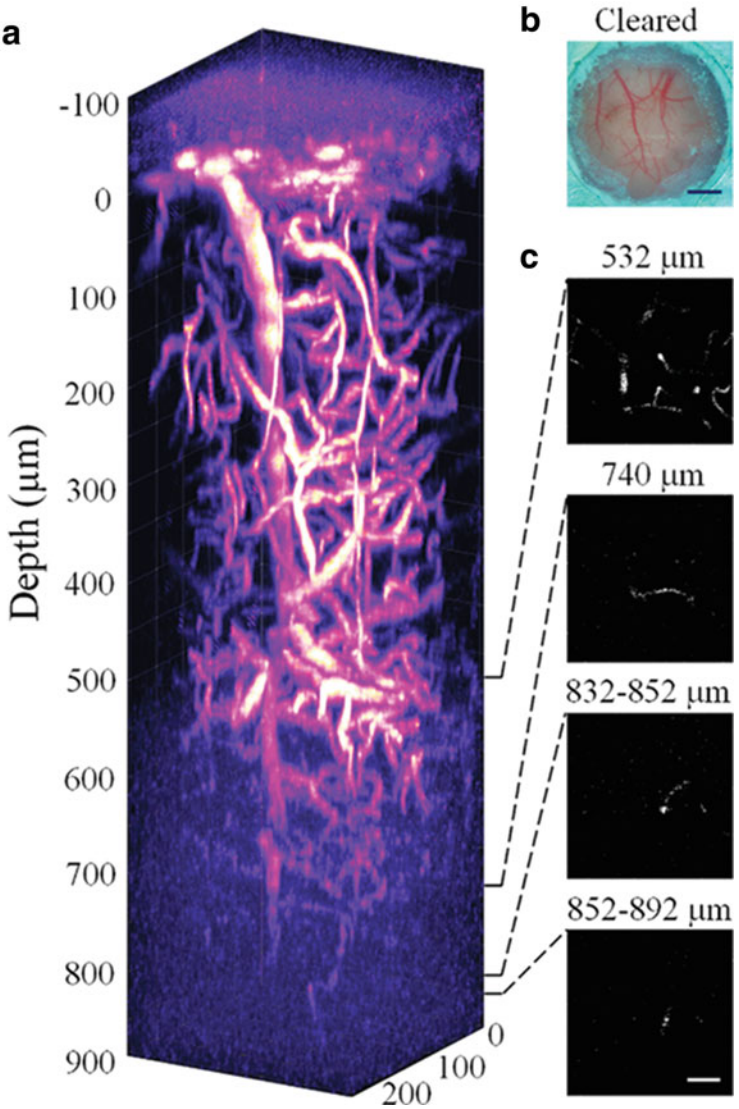

Fig. 11.15 Three-photon excitation imaging of mouse vasculature through the transparent skull window. (**a**) 3D reconstruction of the vasculature of the mouse brain with Texas Red-labeled (BALB/c mouse, 26 g, 8 weeks old; similar results for $n = 3$). (**b**) Photographed image of the mouse skull after optical clearing. (**c**) Three-photon excitation images at various depths. Scale bars, 1 mm (**b**) and 50 μm (**c**) [172]

References

1. Tuchin VV, Maksimova IL, Zimnyakov DA, Kon IL, Mavlyutov AH et al (1997) Light propagation in tissues with controlled optical properties. J Biomed Opt 2(4):401–417
2. Gratton E (2011) Deeper tissue imaging with total detection. Science 331(6020):1016–1017
3. Tuchin VV (2006) Optical clearing of tissues and blood. PM154. SPIE Press, Bellingham WA
4. Zhu D, Larin KV, Luo Q, Tuchin VV (2013) Recent progress in tissue optical clearing. Laser Photonics Rev 7(5):732–757
5. Wenner M (2009) The most transparent research. Nat Med 15(10):1106–1109
6. LaComb R, Nadiarnykh O, Carey S, Campagnola PJ (2008) Quantitative second harmonic generation imaging and modeling of the optical clearing mechanism in striated muscle and tendon. J Biomed Opt 13(2):021109
7. Choi B, Tsu L, Chen E, Ishak TS, Iskandar SM et al (2005) Determination of chemical agent optical clearing potential using in vitro human skin. Lasers Surg Med 36(2):72–75
8. Mao ZZ, Zhu D, Hu YT, Wen X, Han ZZ (2008) Influence of alcohols on the optical clearing effect of skin in vitro. J Biomed Opt 13(2):021104
9. Hirshburg J, Choi B, Nelson JS, Yeh AT (2007) Correlation between collagen solubility and skin optical clearing using sugars. Lasers Surg Med 39(2):140–144
10. Yu TT, Wen X, Tuchin VV, Luo QM, Zhu D (2011) Quantitative analysis of dehydration in porcine skin for assessing mechanism of optical clearing. J Biomed Opt 16(9):095002
11. Tuchin VV (2002) Handbook of optical biomedical diagnostics. SPIE Optical Engineering Press, Bellingham, WA
12. Wen X, Tuchin VV, Luo Q, Zhu D (2009) Controling the scattering of intralipid by using optical clearing agents. Phys Med Biol 54(22):6917–6930
13. Richardson DS, Lichtman JW (2015) Clarifying tissue clearing. Cell 162(2):246–257
14. Tainaka K, Kuno A, Kubota SI, Murakami T, Ueda HR (2016) Chemical principles in tissue clearing and staining protocols for whole-body cell profiling. Annu Rev Cell Dev Biol 32:713–741
15. Wang J, Ma N, Shi R, Zhang Y, Yu TT et al (2014) Sugar-induced skin optical clearing: from molecular dynamics simulation to experimental demonstration. IEEE J Sel Top Quant 20 (2):256–262
16. Feng W, Shi R, Ma N, Tuchina DK, Tuchin VV et al (2016) Skin optical clearing potential of disaccharides. J Biomed Opt 21(8):081207
17. Ohmi M, Ohnishi Y, Yoden K, Haruna M (2000) In vitro simultaneous measurement of refractive index and thickness of biological tissue by the low coherence interferometry. IEEE Trans Biomed Eng 47(9):1266–1270
18. Tuchin VV (2015) Tissue optics and photonics: light-tissue interaction. J Biomed Photonics Eng 1(2):98–134
19. Scott GD, Blum ED, Fryer AD, Jacoby DB (2014) Tissue optical clearing, three-dimensional imaging, and computer morphometry in whole mouse lungs and human airways. Am J Respir Cell Mol Biol 51(1):43–55
20. van Royen ME, Verhoef EI, Kweldam CF, van Cappellen WA, Kremers GJ et al (2016) Three-dimensional microscopic analysis of clinical prostate specimens. Histopathology 69 (6):985–992
21. Dodt H-U, Leischner U, Schierloh A, Jahrling N, Mauch CP et al (2007) Ultramicroscopy: three-dimensional visualization of neuronal networks in the whole mouse brain. Nat Methods 4(4):331–336
22. Becker K, Jahrling N, Kramer ER, Schnorrer F, Dodt H-U (2008) Ultramicroscopy: 3D reconstruction of large microscopical specimens. J Biophotonics 1(1):36–42
23. Jahrling N, Becker K, Dodt H-U (2009) 3D-reconstruction of blood vessels by ultramicroscopy. Organogenesis 5(4):227–230

24. Klingberg A, Hasenberg A, Ludwig-Portugall I, Medyukhina A, Mann L et al (2017) Fully automated evaluation of total glomerular number and capillary tuft size in nephritic kidneys using lightsheet microscopy. J Am Soc Nephrol 28(2):452–459
25. Masselink W, Reumann D, Murawala P, Pasierbek P, Taniguchi Y et al (2019) Broad applicability of a streamlined ethyl cinnamate-based clearing procedure. Development 146 (3):dev166884
26. Schwarz MK, Scherbarth A, Sprengel R, Engelhardt J, Theer P et al (2015) Fluorescent-protein stabilization and high-resolution imaging of cleared, intact mouse brains. PLoS One 10 (5):e0124650
27. Pan CC, Cai RY, Quacquarelli FP, Ghasemigharagoz A, Lourbopoulos A et al (2016) Shrinkage-mediated imaging of entire organs and organisms using uDISCO. Nat Methods 13(10):859–867
28. Jing D, Zhang S, Luo W, Gao X, Men Y et al (2018) Tissue clearing of both hard and soft tissue organs with the PEGASOS method. Cell Res 28(8):803–818
29. Becker K, Jahrling N, Saghafi S, Weiler R, Dodt H-U (2012) Chemical clearing and dehydration of GFP expressing mouse brains. PLoS One 7(3):e33916
30. Erturk A, Becker K, Jahrling N, Mauch CP, Hojer CD et al (2012) Three-dimensional imaging of solvent-cleared organs using 3DISCO. Nat Protoc 7(11):1983–1995
31. Erturk A, Mauch CP, Hellal F, Forstner F, Keck T et al (2012) Three-dimensional imaging of the unsectioned adult spinal cord to assess axon regeneration and glial responses after injury. Nat Med 18(1):166–171
32. Renier N, Wu Z, Simon DJ, Yang J, Ariel P et al (2014) iDISCO: a simple, rapid method to immunolabel large tissue samples for volume imaging. Cell 159(4):896–910
33. Qi Y, Yu T, Xu J, Wan P, Ma Y et al (2019) FDISCO: advanced solvent-based clearing method for imaging whole organs. Sci Adv 5(1):eaau8355
34. Tainaka K, Murakami TC, Susaki EA, Shimizu C, Saito R et al (2018) Chemical landscape for tissue clearing based on hydrophilic reagents. Cell Rep 24(8):2196–210.e9
35. Kubota SI, Takahashi K, Nishida J, Morishita Y, Ehata S et al (2017) Whole-body profiling of cancer metastasis with single-cell resolution. Cell Rep 20(1):236–250
36. Tainaka K, Kubota SI, Suyama TQ, Susaki EA, Perrin D et al (2014) Whole-body imaging with single-cell resolution by tissue decolorization. Cell 159(4):911–924
37. Susaki EA, Tainaka K, Perrin D, Kishino F, Tawara T et al (2014) Whole-brain imaging with single-cell resolution using chemical cocktails and computational analysis. Cell 157 (3):726–739
38. Chung K, Wallace J, Kim SY, Kalyanasundaram S, Andalman AS et al (2013) Structural and molecular interrogation of intact biological systems. Nature 497(7449):332–337
39. Yang B, Treweek JB, Kulkarni RP, Deverman BE, Chen CK et al (2014) Single-cell phenotyping within transparent intact tissue through whole-body clearing. Cell 158 (4):945–958
40. Zhu J, Yu T, Li Y, Xu J, Qi Y et al (2020) MACS: rapid aqueous clearing system for 3D mapping of intact organs. Adv Sci 7(8):1903185
41. Greenbaum A, Chan KY, Dobreva T, Brown D, Balani DH et al (2017) Bone CLARITY: clearing, imaging, and computational analysis of osteoprogenitors within intact bone marrow. Sci Transl Med 9(387):eaah6518
42. Ke MT, Fujimoto S, Imai T (2013) SeeDB: a simple and morphology-preserving optical clearing agent for neuronal circuit reconstruction. Nat Neurosci 16(8):1154–1161
43. Park Y-G, Sohn CH, Chen R, McCue M, Yun DH et al (2019) Protection of tissue physicochemical properties using polyfunctional crosslinkers. Nat Biotechnol 37(1):73–83
44. Tsai PS, Kaufhold JP, Blinder P, Friedman B, Drew PJ et al (2009) Correlations of neuronal and microvascular densities in murine cortex revealed by direct counting and colocalization of nuclei and vessels. J Neurosci 29(46):14553–14570
45. Hou B, Zhang D, Zhao S, Wei M, Yang Z et al (2015) Scalable and DiI-compatible optical clearance of the mammalian brain. Front Neuroanat 9:1–19

46. Economo MN, Clack NG, Lavis LD, Gerfen CR, Svoboda K et al (2016) A platform for brain-wide imaging and reconstruction of individual neurons. elife 5:e10566
47. Treweek JB, Chan KY, Flytzanis NC, Yang B, Deverman BE et al (2015) Whole-body tissue stabilization and selective extractions via tissue-hydrogel hybrids for high-resolution intact circuit mapping and phenotyping. Nat Protoc 10(11):1860–1896
48. Ke MT, Nakai Y, Fujimoto S, Takayama R, Yoshida S et al (2016) Super-resolution mapping of neuronal circuitry with an index-optimized clearing agent. Cell Rep 14(11):2718–2732
49. Li W, Germain RN, Gerner MY (2017) Multiplex, quantitative cellular analysis in large tissue volumes with clearing-enhanced 3D microscopy (Ce3D). Proc Natl Acad Sci U S A 114(35): E7321–E7E30
50. Murray E, Cho JH, Goodwin D, Ku T, Swaney J et al (2015) Simple, scalable proteomic imaging for high-dimensional profiling of intact systems. Cell 163(6):1500–1514
51. Lin HH, Lai JS, Chin AL, Chen YC, Chiang AS (2007) A map of olfactory representation in the Drosophila mushroom body. Cell 128(6):1205–1217
52. Ariel P (2017) A beginner's guide to tissue clearing. Int J Biochem Cell Biol 84:35–39
53. Susaki EA, Ueda HR (2016) Whole-body and whole-organ clearing and imaging techniques with single-cell resolution: toward organism-level systems biology in mammals. Cell Chem Biol 23(1):137–157
54. Spalteholz W (1914) Über das Durchsichtigmachen von menschlichen und tierischen Präparaten und seine theoretischen Bedingungen. S. Hirzel, Leipzig
55. Steinke H, Wolff W (2001) A modified Spalteholz technique with preservation of the histology. Ann Anat 183(1):91–95
56. Jährling N, Becker K, Kramer ER, Dodt H-U (2008) 3D-visualization of nerve fiber bundles by ultramicroscopy. Med Laser Appl 23(4):209–215
57. Ochoa LF, Kholodnykh A, Villarreal P, Tian B, Pal R et al (2018) Imaging of murine whole lung fibrosis by large scale 3D microscopy aided by tissue optical clearing. Sci Rep 8(1):13348
58. Jung Y, Ng JH, Keating CP, Senthil-Kumar P, Zhao J et al (2014) Comprehensive evaluation of peripheral nerve regeneration in the acute healing phase using tissue clearing and optical microscopy in a rodent model. PLoS One 9(4):e94054
59. Li Y, Xu J, Wan P, Yu T, Zhu D (2018) Optimization of GFP fluorescence preservation by a modified uDISCO clearing protocol. Front Neuroanat 12:67
60. Liebmann T, Renier N, Bettayeb K, Greengard P, Tessier-Lavigne M et al (2016) Three-dimensional study of Alzheimer's disease hallmarks using the iDISCO clearing method. Cell Rep 16(4):1138–1152
61. Renier N, Adams EL, Kirst C, Wu Z, Azevedo R et al (2016) Mapping of brain activity by automated volume analysis of immediate early genes. Cell 165(7):1789–1802
62. Belle M, Godefroy D, Couly G, Malone SA, Collier F et al (2017) Tridimensional visualization and analysis of early human development. Cell 169(1):161–73.e12
63. Cai R, Pan C, Ghasemigharagoz A, Todorov MI, Forstera B et al (2019) Panoptic imaging of transparent mice reveals whole-body neuronal projections and skull-meninges connections. Nat Neurosci 22(2):317–327
64. Pan C, Schoppe O, Parra-Damas A, Cai R, Todorov MI et al (2019) Deep learning reveals cancer metastasis and therapeutic antibody targeting in the entire body. Cell 179(7):1661–76. e19
65. Zhao S, Todorov MI, Cai R, Maskari RA, Steinke H et al (2020) Cellular and molecular probing of intact human organs. Cell 180(4):796–812.e19
66. Hildebrand S, Schueth A, Herrler A, Galuske R, Roebroeck A (2019) Scalable labeling for cytoarchitectonic characterization of large optically cleared human neocortex samples. Sci Rep 9(1):10880
67. Chiang AS (2002) Aqueous tissue clearing solution. United States Patent US 6472216 B1
68. Hua TE, Yang TL, Yang WC, Liu KJ, Tang SC (2013) 3-D neurohistology of transparent tongue in health and injury with optical clearing. Front Neuroanat 7:36

69. Zhu X, Huang L, Zheng Y, Song Y, Xu Q et al (2019) Ultrafast optical clearing method for three-dimensional imaging with cellular resolution. Proc Natl Acad Sci U S A 116 (23):11480–11489
70. Costantini I, Ghobril JP, Di Giovanna AP, Allegra Mascaro AL, Silvestri L et al (2015) A versatile clearing agent for multi-modal brain imaging. Sci Rep 5:9808
71. Hama H, Kurokawa H, Kawano H, Ando R, Shimogori T et al (2011) Scale: a chemical approach for fluorescence imaging and reconstruction of transparent mouse brain. Nat Neurosci 14(11):1481–1488
72. Hama H, Hioki H, Namiki K, Hoshida T, Kurokawa H et al (2015) ScaleS: an optical clearing palette for biological imaging. Nat Neurosci 18(10):1518–1529
73. Nojima S, Susaki EA, Yoshida K, Takemoto H, Tsujimura N et al (2017) CUBIC pathology: three-dimensional imaging for pathological diagnosis. Sci Rep 7(1):9269
74. Murakami TC, Mano T, Saikawa S, Horiguchi SA, Shigeta D et al (2018) A three-dimensional single-cell-resolution whole-brain atlas using CUBIC-X expansion microscopy and tissue clearing. Nat Neurosci 21(4):625–637
75. Chen L, Li G, Li Y, Li Y, Zhu H et al (2017) UbasM: an effective balanced optical clearing method for intact biomedical imaging. Sci Rep 7(1):12218
76. Kuwajima T, Sitko AA, Bhansali P, Jurgens C, Guido W et al (2013) ClearT: a detergent- and solvent-free clearing method for neuronal and non-neuronal tissue. Development 140 (6):1364–1368
77. Yu T, Zhu J, Li Y, Ma Y, Wang J et al (2018) RTF: a rapid and versatile tissue optical clearing method. Sci Rep 8(1):1964
78. Lai HM, Liu AKL, Ng HHM, Goldfinger MH, Chau TW et al (2018) Next generation histology methods for three-dimensional imaging of fresh and archival human brain tissues. Nat Commun 9(1):1–12
79. Tomer R, Ye L, Hsueh B, Deisseroth K (2014) Advanced CLARITY for rapid and high-resolution imaging of intact tissues. Nat Protoc 9(7):1682–1697
80. Epp JR, Niibori Y, Liz Hsiang HL, Mercaldo V, Deisseroth K et al (2015) Optimization of CLARITY for clearing whole-brain and other intact organs. eNeuro 2(3):ENEURO.0022-15.2015
81. Bastrup J, Larsen PH (2017) Optimized CLARITY technique detects reduced parvalbumin density in a genetic model of schizophrenia. J Neurosci Methods 283:23–32
82. Lee E, Choi J, Jo Y, Kim JY, Jang YJ et al (2016) ACT-PRESTO: rapid and consistent tissue clearing and labeling method for 3-dimensional (3D) imaging. Sci Rep 6:18631
83. Kim SY, Cho JH, Murray E, Bakh N, Choi H et al (2015) Stochastic electrotransport selectively enhances the transport of highly electromobile molecules. Proc Natl Acad Sci U S A 112(46):E6274–E6283
84. Ku T, Swaney J, Park JY, Albanese A, Murray E et al (2016) Multiplexed and scalable super-resolution imaging of three-dimensional protein localization in size-adjustable tissues. Nat Biotechnol 34(9):973–981
85. Sylwestrak EL, Rajasethupathy P, Wright MA, Jaffe A, Deisseroth K (2016) Multiplexed intact-tissue transcriptional analysis at cellular resolution. Cell 164(4):792–804
86. Yun DH, Park Y-G, Cho JH, Kamentsky L, Evans NB et al (2019) Ultrafast immunostaining of organ-scale tissues for scalable proteomic phenotyping. bioRxiv:660373
87. Woo J, Lee M, Seo JM, Park HS, Cho YE (2016) Optimization of the optical transparency of rodent tissues by modified PACT-based passive clearing. Exp Mol Med 48(12):e274
88. Xu N, Tamadon A, Liu Y, Ma T, Leak RK et al (2017) Fast free-of-acrylamide clearing tissue (FACT)-an optimized new protocol for rapid, high-resolution imaging of three-dimensional brain tissue. Sci Rep 7(1):9895
89. Sung K, Ding Y, Ma J, Chen H, Huang V et al (2016) Simplified three-dimensional tissue clearing and incorporation of colorimetric phenotyping. Sci Rep 6:30736
90. Liu AKL, Lai HM, Chang RC, Gentleman SM (2017) Free of acrylamide sodium dodecyl sulphate (SDS)-based tissue clearing (FASTClear): a novel protocol of tissue clearing for

three-dimensional visualization of human brain tissues. Neuropathol Appl Neurobiol 43 (4):346–351
91. Ando K, Laborde Q, Lazar A, Godefroy D, Youssef I et al (2014) Inside Alzheimer brain with CLARITY: senile plaques, neurofibrillary tangles and axons in 3-D. Acta Neuropathol 128 (3):457–459
92. Liu AK, Hurry ME, Ng OT, DeFelice J, Lai HM et al (2016) Bringing CLARITY to the human brain: visualization of Lewy pathology in three dimensions. Neuropathol Appl Neurobiol 42 (6):573–587
93. Hsueh B, Burns VM, Pauerstein P, Holzem K, Ye L et al (2017) Pathways to clinical CLARITY: volumetric analysis of irregular, soft, and heterogeneous tissues in development and disease. Sci Rep 7(1):5899
94. Albanese A, Swaney JM, Yun DH, Evans NB, Antonucci JM et al (2020) Multiscale 3D phenotyping of human cerebral organoids. Sci Rep 10(1):21487
95. Lai JS, Lo SJ, Dickson BJ, Chiang AS (2012) Auditory circuit in the Drosophila brain. Proc Natl Acad Sci U S A 109(7):2607–2612
96. Frétaud M, Rivière L, Job ÉD, Gay S, Lareyre J-J et al (2017) High-resolution 3D imaging of whole organ after clearing: taking a new look at the zebrafish testis. Sci Rep 7:43012
97. Zygelyte E, Bernard ME, Tomlinson JE, Martin MJ, Terhorst A et al (2016) RetroDISCO: clearing technique to improve quantification of retrograde labeled motor neurons of intact mouse spinal cords. J Neurosci Methods 271:34–42
98. Todorov MI, Paetzold JC, Schoppe O, Tetteh G, Shit S et al (2020) Machine learning analysis of whole mouse brain vasculature. Nat Methods 17(4):442–449
99. Lugo-Hernandez E, Squire A, Hagemann N, Brenzel A, Sardari M et al (2017) 3D visualization and quantification of microvessels in the whole ischemic mouse brain using solvent-based clearing and light sheet microscopy. J Cereb Blood Flow Metab 37(10):3355–3367
100. Draijer M, Hondebrink E, van Leeuwen T, Steenbergen W (2009) Review of laser speckle contrast techniques for visualizing tissue perfusion. Lasers Med Sci 24(4):639–651
101. Boas DA, Dunn AK (2010) Laser speckle contrast imaging in biomedical optics. J Biomed Opt 15(1):011109
102. Khaodhiar L, Dinh T, Schomacker KT, Panasyuk SV, Freeman JE et al (2007) The use of medical hyperspectral technology to evaluate microcirculatory changes in diabetic foot ulcers and to predict clinical outcomes. Diabetes Care 30(4):903–910
103. Yudovsky D, Nouvong A, Schomacker K, Pilon L (2011) Monitoring temporal development and healing of diabetic foot ulceration using hyperspectral imaging. J Biophotonics 4 (7–8):565–576
104. Chen S, Qi L, Xiao S, Soetikno B, Hao FZ (2016) Imaging hemodynamic response after ischemic stroke in mouse cortex using visible-light optical coherence tomography. Biomed Opt Express 7(9):3377–3389
105. Yang SS, Liu KZ, Ding HJ, Gao H, Zheng XX et al (2019) Longitudinal in vivo intrinsic optical imaging of cortical blood perfusion and tissue damage in focal photothrombosis stroke model. J Cereb Blood Flow Metab 39(7):1381–1393
106. Zhang HF, Maslov K, Stoica G, Wang LV (2006) Functional photoacoustic microscopy for high-resolution and noninvasive in vivo imaging. Nat Biotechnol 24(7):848–851
107. Yao JJ, Wang LHV (2010) Transverse flow imaging based on photoacoustic Doppler bandwidth broadening. J Biomed Opt 15(2):021304
108. Semwogerere D, Weeks ER (2005) Confocal microscopy. Encycl Biomater Biomed Eng 23:1–10
109. Dickie R, Bachoo RM, Rupnick MA, Dallabrida SM, Deloid GM et al (2006) Three-dimensional visualization of microvessel architecture of whole-mount tissue by confocal microscopy. Microvasc Res 72(1–2):20–26
110. Liu H, Deng X, Tong S, He C, Cheng H et al (2019) In vivo deep-brain structural and hemodynamic multiphoton microscopy enabled by quantum dots. Nano Lett 19(8):5260–5265

111. Wang S, Xi W, Cai F, Zhao X, Xu Z et al (2015) Three-photon luminescence of gold nanorods and its applications for high contrast tissue and deep in vivo brain imaging. Theranostics 5 (3):251–266
112. Wang Y, Han X, Xi W, Li J, Roe AW et al (2017) Bright AIE nanoparticles with F127 encapsulation for deep-tissue three-photon intravital brain angiography. Adv Healthc Mater 6 (21):1700685
113. Wang T, Ouzounov DG, Wu C, Horton NG, Zhang B et al (2018) Three-photon imaging of mouse brain structure and function through the intact skull. Nat Methods 15(10):789–792
114. Prevedel R, Verhoef AJ, Pernia-Andrade AJ, Weisenburger S, Huang BS et al (2016) Fast volumetric calcium imaging across multiple cortical layers using sculpted light. Nat Methods 13(12):1021–1028
115. Papenfuss HD, Gross JF, Intaglietta M, Treese FA (1979) A transparent access chamber for the rat dorsal skin fold. Microvasc Res 18(3):311–318
116. Lehr HA, Leunig M, Menger MD, Nolte D, Messmer K (1993) Dorsal skinfold chamber technique for intravital microscopy in nude mice. Am J Pathol 143(4):1055–1062
117. Sorg H, Krueger C, Vollmar B (2007) Intravital insights in skin wound healing using the mouse dorsal skin fold chamber. J Anat 211(6):810–818
118. Olesen SP (1987) Leakiness of rat brain microvessels to fluorescent probes following craniotomy. Acta Physiol Scand 130(1):63–68
119. Klijn E, Hulscher HC, Balvers RK, Holland WP, Bakker J et al (2013) Laser speckle imaging identification of increases in cortical microcirculatory blood flow induced by motor activity during awake craniotomy. J Neurosurg 118(2):280–286
120. Holtmaat A, Bonhoeffer T, Chow DK, Chuckowree J, De Paola V et al (2009) Long-term, high-resolution imaging in the mouse neocortex through a chronic cranial window. Nat Protoc 4(8):1128–1144
121. Levasseur JE, Wei EP, Raper AJ, Kontos AA, Patterson JL (1975) Detailed description of a cranial window technique for acute and chronic experiments. Stroke 6(3):308–317
122. Yang G, Pan F, Parkhurst CN, Grutzendler J, Gan WB (2010) Thinned-skull cranial window technique for long-term imaging of the cortex in live mice. Nat Protoc 5(2):201–208
123. Yu X, Zuo Y (2014) Two-photon in vivo imaging of dendritic spines in the mouse cortex using a thinned-skull preparation. J Vis Exp 87:e51520
124. Mao Z, Wen X, Wang J, Zhu D (2009) The biocompatibility of the dermal injection of glycerol in vivo to achieve optical clearing. In: Proceedings of SPIE, vol 7519. The International Society for Optical Engineering, Bellingham, WA, p 75191N-N-9
125. Shi R, Feng W, Zhang C, Zhang Z, Zhu D (2017) FSOCA-induced switchable footpad skin optical clearing window for blood flow and cell imaging in vivo. J Biophotonics 10 (12):1647–1656
126. Feng W, Zhang C, Yu TT, Semyachkina-Glushkovskaya O, Zhu D (2019) In vivo monitoring blood-brain barrier permeability using spectral imaging through optical clearing skull window. J Biophotonics 12(4):e201800330
127. Zhang C, Feng W, Vodovozova E, Tretiakova D, Boldyrevd I et al (2018) Photodynamic opening of the blood-brain barrier to high weight molecules and liposomes through an optical clearing skull window. Biomed Opt Express 9(10):4850–4862
128. Zhang C, Feng W, Li Y, Kürths J, Yu T et al (2019) Age differences in photodynamic therapy-mediated opening of the blood-brain barrier through the optical clearing skull window in mice. Lasers Surg Med 51(7):625–633
129. Feng W, Liu S, Zhang C, Xia Q, Yu T et al (2019) Comparison of cerebral and cutaneous microvascular dysfunction with the development of type 1 diabetes. Theranostics 9 (20):5854–5868
130. Liu CH, Zhi ZW, Tuchin VV, Luo QM, Zhu D (2010) Enhancement of skin optical clearing efficacy using photo-irradiation. Lasers Surg Med 42(2):132–140
131. Hirshburg J, Choi B, Nelson JS, Yeh AT (2006) Collagen solubility correlates with skin optical clearing. J Biomed Opt 11(4):040501

132. Stumpp O, Welch A, Milner T, Neev J (2005) Enhancement of transepidermal skin clearing agent delivery using a 980 nm diode laser. Lasers Surg Med 37(4):278–285
133. Tuchin VV, Altshuler GB, Gavrilova AA, Pravdin AB, Yaroslavsky IV (2006) Optical clearing of skin using flashlamp-induced enhancement of epidermal permeability. Lasers Surg Med 38(9):824–836
134. Zhu D, Wang J, Zhi Z, Wen X, Luo Q (2010) Imaging dermal blood flow through the intact rat skin with an optical clearing method. J Biomed Opt 15(2):026008
135. Mao Z, Han Z, Wen X, Luo Q, Zhu D (2009) Influence of glycerol with different concentrations on skin optical clearing and morphological changes in vivo. In: Photonics and Optoelectronics Meetings (POEM) 2008: Fiber Optic Communication and Sensors. SPIE, Bellingham, WA
136. Xu X, Zhu Q (2008) Sonophoretic delivery for contrast and depth improvement in skin optical coherence tomography. IEEE J Sel Top Quant 14(1):56–61
137. Stumpp O, Chen B, Welch AJ (2006) Using sandpaper for noninvasive transepidermal optical skin clearing agent delivery. J Biomed Opt 11(4):041118
138. Son T, Yoon J, Ko C-Y, Lee Y-H, Kwon K et al (2008) Contrast enhancement of laser speckle skin image: use of optical clearing agent in conjunction with micro-needling. In: Photonic Therapeutics and Diagnostics IV. SPIE, Bellingham, WA
139. Mcnichols RJ, Fox MA, Gowda A, Tuya S, Bell B et al (2005) Temporary dermal scatter reduction: quantitative assessment and implications for improved laser tattoo removal. Lasers Surg Med 36(4):289–296
140. Wen X, Jacques SL, Tuchin VV, Zhu D (2012) Enhanced optical clearing of skin in vivo and optical coherence tomography in-depth imaging. J Biomed Opt 17(6):066022
141. Xu X, Zhu Q (2007) Evaluation of skin optical clearing enhancement with Azone as a penetration enhancer. Opt Commun 279(1):223–228
142. Jiang J, Wang RK (2004) Comparing the synergistic effects of oleic acid and dimethyl sulfoxide as vehicles for optical clearing of skin tissue in vitro. Phys Med Biol 49 (23):5283–5294
143. Moulton K, Lovell F, Williams E, Ryan P, Lay DC et al (2006) Use of glycerol as an optical clearing agent for enhancing photonic transference and detection of Salmonella typhimurium through porcine skin. J Biomed Opt 11(5):054027
144. Shi R, Chen M, Tuchin VV, Zhu D (2015) Accessing to arteriovenous blood flow dynamics response using combined laser speckle contrast imaging and skin optical clearing. Biomed Opt Express 6(6):1977–1989
145. Guo L, Shi R, Zhang C, Zhu D, Ding Z et al (2016) Optical coherence tomography angiography offers comprehensive evaluation of skin optical clearing in vivo by quantifying optical properties and blood flow imaging simultaneously. J Biomed Opt 21(8):081202
146. Bai YY, Gao X, Wang YC, Peng XG, Chang D et al (2014) Image-guided pro-angiogenic therapy in diabetic stroke mouse models using a multi-modal nanoprobe. Theranostics 4 (8):787–797
147. Wang J, Shi R, Zhu D (2013) Switchable skin window induced by optical clearing method for dermal blood flow imaging. J Biomed Opt 18(6):061209
148. Ding Y, Wang J, Fan Z, Wei D, Shi R et al (2013) Signal and depth enhancement for in vivo flow cytometer measurement of ear skin by optical clearing agents. Biomed Opt Express 4 (11):2518
149. Jing W, Rui S, Yang Z, Dan Z (2013) Ear skin optical clearing for improving blood flow imaging. Photonics Lasers Med 2(1):37–44
150. Shi R, Feng W, Zhang C, Yu T, Fan Z et al (2018) In vivo imaging the motility of monocyte/macrophage during inflammation in diabetic mice. J Biophotonics 11(5):e201700205
151. McGonigle P (2014) Animal models of CNS disorders. Biochem Pharmacol 87(1):140–149
152. Wiesmann M, Zinnhardt B, Reinhardt D, Eligehausen S, Wachsmuth L et al (2017) A specific dietary intervention to restore brain structure and function after ischemic stroke. Theranostics 7 (2):493–512

153. Li P, Ni S, Zhang L, Zeng S, Luo Q (2006) Imaging cerebral blood flow through the intact rat skull with temporal laser speckle imaging. Opt Lett 31(12):1824–1826
154. Jeffcoate WJ, Clark DJ, Savic N, Rodmell PI, Game FL (2015) Use of HSI to measure oxygen saturation in the lower limb and its correlation with healing of foot ulcers in diabetes. Diabet Med 32(6):798–802
155. Radrich K, Ntziachristos V (2016) Quantitative multi-spectral oxygen saturation measurements independent of tissue optical properties. J Biophotonics 9(1–2):83–99
156. Wang KH, Majewska A, Schummers J, Farley B, Hu CC et al (2006) In vivo two-photon imaging reveals a role of arc in enhancing orientation specificity in visual cortex. Cell 126 (2):389–402
157. Wagner N, Norlin N, Gierten J, de Medeiros G, Balazs B et al (2019) Instantaneous isotropic volumetric imaging of fast biological processes. Nat Methods 16(6):497
158. Zheng Z, Li D, Liu Z, Peng H-Q, Sung HHY et al (2019) Aggregation-induced nonlinear optical effects of AIEgen nanocrystals for ultradeep in vivo bioimaging. Adv Mater 31 (34):1904799
159. Kobat D, Horton NG, Xu C (2011) In vivo two-photon microscopy to 1.6-mm depth in mouse cortex. J Biomed Opt 16(10):106014
160. Kobat D, Durst ME, Nishimura N, Wong AW, Schaffer CB et al (2009) Deep tissue multiphoton microscopy using longer wavelength excitation. Opt Express 17 (16):13354–13364
161. Zhang H, Alifu N, Jiang T, Zhu Z, Wang Y et al (2017) Biocompatible aggregation-induced emission nanoparticles with red emission for in vivo three-photon brain vascular imaging. J Mater Chem B 5(15):2757–2762
162. Horton NG, Wang K, Kobat D, Clark CG, Wise FW et al (2013) In vivo three-photon microscopy of subcortical structures within an intact mouse brain. Nat Photonics 7(3):205–209
163. Kneipp M, Turner J, Estrada H, Rebling J, Shoham S et al (2016) Effects of the murine skull in optoacoustic brain microscopy. J Biophotonics 9(1–2):117–123
164. Fan XF, Zheng WT, Singh DJ (2014) Light scattering and surface plasmons on small spherical particles. Light-Sci Appl 3:e179
165. Thrane VR, Thrane AS, Plog BA, Thiyagarajan M, Iliff JJ et al (2013) Paravascular microcirculation facilitates rapid lipid transport and astrocyte signaling in the brain. Sci Rep 3:2582
166. Dorand RD, Barkauskas DS, Evans TA, Petrosiute A, Huang AY (2014) Comparison of intravital thinned skull and cranial window approaches to study CNS immunobiology in the mouse cortex. Intravital. 3(2):e21978
167. Genina EA, Bashkatov AN, Tuchin VV (2008) Optical clearing of cranial bone. Adv Opt Technol 2008:267867
168. Wang J, Zhang Y, Xu T, Luo Q, Zhu D (2012) An innovative transparent cranial window based on skull optical clearing. Laser Phys Lett 9(6):469
169. Yang X, Zhang Y, Zhao K, Zhao Y, Liu Y et al (2016) Skull optical clearing solution for enhancing ultrasonic and photoacoustic imaging. IEEE Trans Med Imaging 35(8):1903–1906
170. Zhao Y-J, Yu T-T, Zhang C, Li Z, Luo Q-M et al (2018) Skull optical clearing window for in vivo imaging of the mouse cortex at synaptic resolution. Light-Sci Appl 7(2):17153
171. Zhang C, Feng W, Zhao YJ, Yu TT, Li PC et al (2018) A large, switchable optical clearing skull window for cerebrovascular imaging. Theranostics 8(10):2696–2708
172. Chen Y, Liu S, Liu H, Tong S, Tang H et al (2019) Coherent Raman scattering unravelling mechanisms underlying skull optical clearing for through-skull brain imaging. Anal Chem 91 (15):9371–9375
173. Kolesnikova EA, Kolesnikov AS, Zabarylo U, Minet O, Genina EA et al (2014) Optical clearing of human skin for the enhancement of optical imaging of proximal interphalangeal joints. In: Saratov Fall Meeting 2013: Optical Technologies in Biophysics and Medicine XV; and Laser Physics and Photonics XV. SPIE, Bellingham, WA

174. Enfield J, McGrath J, Daly SM, Leahy MJ (2016) Enhanced in vivo visualization of the microcirculation by topical application of fructose solution confirmed with correlation mapping optical coherence tomography. J Biomed Opt 21(8):081212

Tissue Imaging and Quantification Relying on Endogenous Contrast

12

Zhiyi Liu, Jia Meng, Kyle P. Quinn, and Irene Georgakoudi

12.1 Introduction

Cell-matrix interactions are critical for normal development and aging. Conversely, disruption of cell-matrix interactions is associated with a wide range of disorders, including cancer, osteoarthritis, fibrosis, and neurodegenerative diseases [1–3]. Modified interactions have major effects upon key functional cellular features including cytoskeletal structure, gene regulation, differentiation, and cell growth control, all of which are closely related to cellular metabolism [4–6]. Disrupted cell-matrix interactions also influence matrix biophysical and biochemical properties, including collagen fiber organization and mechanical properties [7]. Therefore, improved characterization of these structure–function connections, including both cell and extracellular matrix aspects, may have important implications for our understanding of tissue growth, development, and disease initiation and progression.

Cellular metabolism is responsible for all the life-sustaining chemical processes that support cellular function through molecular and energetic transformations [8]. Metabolic responses can be highly dynamic and spatially heterogeneous across a tissue [9]. Conventional imaging tools for assessing metabolic activity in vivo,

Z. Liu (✉) · J. Meng
State Key Laboratory of Modern Optical Instrumentation, College of Optical Science and Engineering, International Research Center for Advanced Photonics, Zhejiang University, Hangzhou, Zhejiang, China
e-mail: liuzhiyi07@zju.edu.cn

K. P. Quinn
Department of Biomedical Engineering, University of Arkansas, Fayetteville, AR, USA

I. Georgakoudi
Department of Biomedical Engineering, Tufts University, Medford, MA, USA

Sackler School of Graduate Biomedical Sciences, Tufts University, Medford, MA, USA

X. Wei, B. Gu (eds.), *Optical Imaging in Human Disease and Biological Research*, Advances in Experimental Medicine and Biology 1355,
https://doi.org/10.1007/978-981-15-7627-0_12

including functional magnetic resonance imaging and positron-emission tomography [10, 11], typically require the addition of exogenous agents and have limited resolution and sensitivity. More sensitive metabolic assays, such as those based on mass spectrometry and carbon labeling [12, 13], cannot be performed with live cells and require cell and tissue homogenization. Fluorescence imaging-based approaches that rely on exogenous fluorescent probes to stain for mitochondrial membrane potential or oxidative stress overcome the latter limitations [14], but require cellular manipulations and can be confounded by artifacts related to the distribution of the fluorophores. Two-photon excited fluorescence (TPEF) imaging that relies on endogenous fluorophores, such as NAD(P)H and FAD [15–17], has emerged as a powerful tool for high-resolution, label-free, and sensitive assessments of metabolic activity and cellular responses in vitro and in vivo through quantitative optical biomarkers [18–20].

It is becoming increasingly clear, that the extracellular matrix (ECM) plays an important role in determining cellular and overall tissue function [21]. Collagen is a major ECM component, whose content and organization has been shown to affect significantly mechanical tissue properties. Mechanosensitive signaling pathways are one important means of communication between cells and the surrounding environment and methods that enable us to understand tissue biomechanical properties, especially at the microscopic level within three-dimensional tissues are of great interest. With the development of optical imaging approaches, including confocal and multi-photon microscopy [22, 23], especially second harmonic generation (SHG), high-resolution 3D images of collagen fibers have become more readily accessible. However, quantitative analysis algorithms for their orientation and organization have largely remained limited to analysis of 2D images [24–26]. Even though, efforts to take advantage of the 3D information that is available are expanding [27–29], and methods that are highly quantitative, flexible and sensitive in terms of their implementation are emerging [30, 31].

This chapter examines specific applications of optical imaging to assess both the cellular metabolism and collagen fiber organization within biological tissues using endogenous sources of contrast. Regarding cellular metabolism, we start with a discussion of the relevant endogenous chromophores that provide fluorescence contrast, as well as the type of functional information that can be extracted, followed by applications in different disease models. In addition, we summarize current methods used for the extraction of collagen fiber orientation, including both two-dimensional (2D) and three-dimensional (3D) ones, and present corresponding applications. Label-free, high-resolution imaging and quantification of tissues are presented particularly in the context of wound healing, adipose tissue function, osteoarthritis, and cancer. We close with a summary and our perspective on potential future directions.

12.2 Assessing Cellular Metabolism via Non-invasive, Multi-Parametric Imaging of Autofluorescence

12.2.1 Role of NADH and FAD in Key Metabolic Pathways

Reduced nicotinamide adenine dinucleotide (NADH) and flavin adenine dinucleotide (FAD) are directly involved in cellular metabolism as an electron carrier and play a critical role in adenosine triphosphate (ATP) production through oxidative phosphorylation. They exist in either reduced (NADH/$FADH_2$) or oxidized (NAD^+/FAD) forms. However, only NADH and FAD yield significant fluorescence [32–34], which can be measured with high spatial and temporal resolution to assess metabolic activity. Understanding the roles that NADH and FAD play in cellular respiration is critical to properly interpreting the relationship between fluorescence-based measures and cellular metabolism.

Through cellular respiration, substrates (e.g., glucose) are systematically broken down to produce ATP, which is used as a source of energy for enzymes throughout the cell. Numerous catabolic pathways, including glycolysis, the tricarboxylic acid (TCA) cycle, oxidative phosphorylation, and lipid oxidation, can be utilized to produce ATP. Coenzymes NADH and FAD serve as electron carriers during these ATP-producing catabolic processes [16, 33, 35] (Fig. 12.1). During glycolysis, NAD^+ molecules gain electrons and are reduced to NADH, producing a net gain of two ATP molecules. After shuttling into the mitochondria, pyruvate can be converted to acetyl-coenzyme A (acetyl-CoA) by pyruvate dehydrogenase (PDH) complex, reducing an FAD molecule bound to lipoamide dehydrogenase (LipDH) to $FADH_2$ [36, 37], which can then be oxidized to reduce NAD^+ to NADH [38]. During the ensuing TCA cycle, NAD^+ is reduced to NADH thrice for every acetyl-CoA molecule (Fig. 12.1). In addition to LipDH, numerous different dehydrogenase complexes in the mitochondria play a direct role in regulating the NAD^+/NADH ratio and maintaining a pool of NADH that can be used for oxidative phosphorylation [17, 36]. In oxidative phosphorylation, these NADH molecules donate their electrons to Complex I of the electron transport chain (ETC) and revert back to their oxidized form, NAD^+. The electrons are further handed off to other enzyme complexes in the ETC which combine to pump protons into the mitochondrial intermembrane space. Ultimately, oxygen serves as the terminal acceptor of these donated electrons. The proton gradient across the inner membrane of the mitochondria then powers the production of ATP through ATP synthase (Fig. 12.1). This process of oxidative phosphorylation is by far the most efficient mode of producing ATP. The ratio of reduced to oxidized electron carriers provides insight into the metabolic state of a cell and is referred to as the redox ratio. Since NADH and FAD are the only forms of these electron carriers that exhibit endogenous fluorescence, a ratio of FAD/NADH fluorescence, or in the normalized form of FAD/(FAD + NADH), is usually termed as optical redox ratio and can be used to estimate the metabolic profile of a cell or tissue [39, 40].

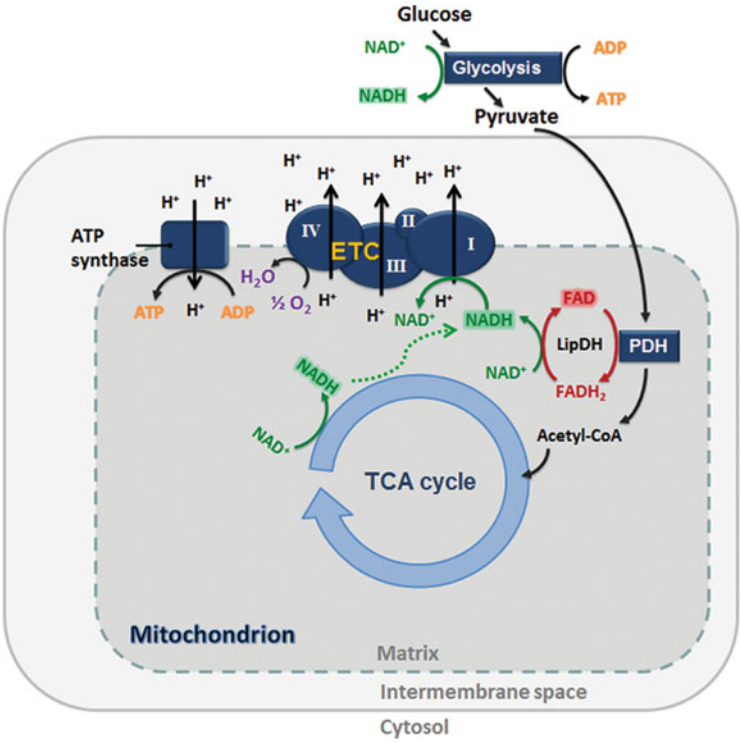

Fig. 12.1 Schematic relating changes in NADH and FAD concentrations to metabolic pathway of oxidative phosphorylation. ADP, adenosine diphosphate; ATP, adenosine triphosphate; PDH, pyruvate dehydrogenase; LipDH, lipoamide dehydrogenase; ETC, electron transport chain; acetyl-CoA, acetyl-coenzyme A; TCA, tricarboxylic acid. (Reprinted/adapted with permission from ref. [41])

12.2.2 Development of Optical Biomarkers for Quantifications of Cellular Metabolism

Given the complexity of metabolic pathways, using a single optical metabolic readout is potentially limited both in terms of its sensitivity and specificity to specific metabolic perturbations. Fortunately, there are different and complementary optical metrics of metabolic activity. We will highlight three optical biomarkers commonly used to examine metabolic function. The optical redox ratio is calculated using fluorescence intensities as: FAD/(FAD + NADH) (Fig. 12.2a–c). Although both NADH and NADPH may have contributed to the signal that we attribute to NADH, it has been shown by mass spectrometry that the optical redox ratio is highly correlated with the corresponding ratio assessed based on the corresponding concentrations of NADH and FAD [42, 43]. Only the cell cytoplasm, the material within a living cell excluding the nucleus, is selected for redox ratio quantification. Pixel-wise redox ratio maps are generated by color-coding each pixel with a redox

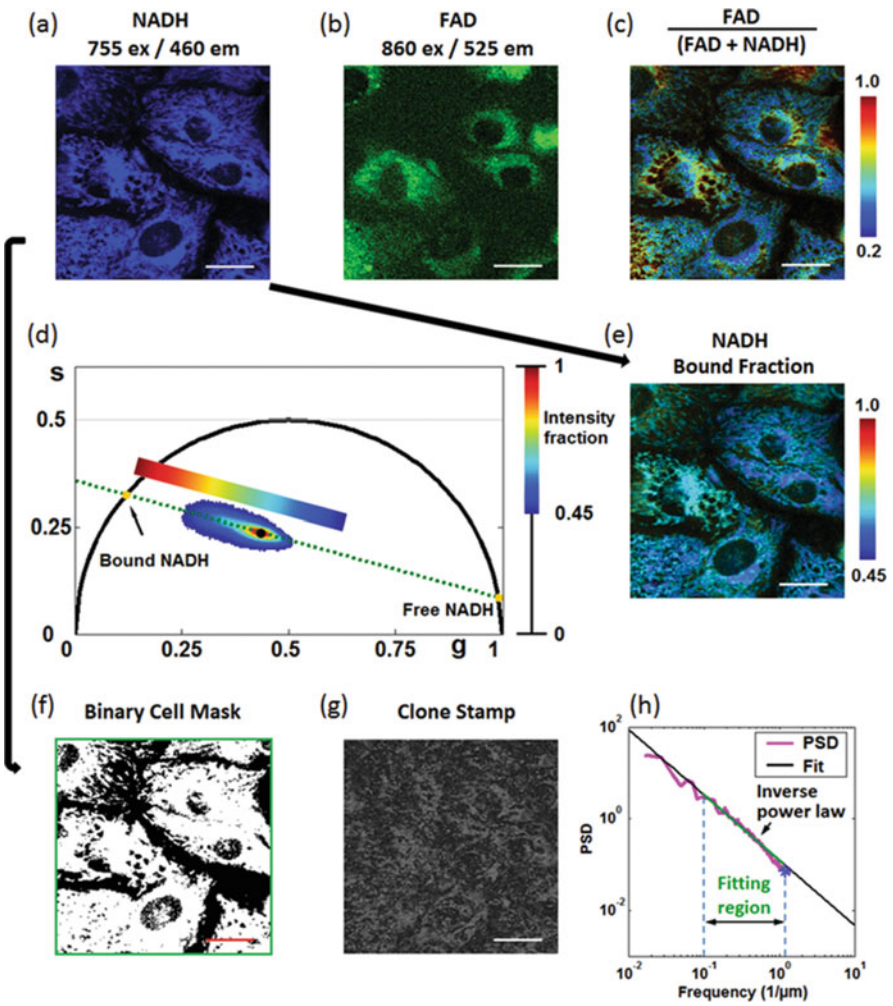

Fig. 12.2 Schematic of integrated analysis processing [41]. (**a**) Raw NADH image. (**b**) Raw FAD image. (**c**) Optical redox ratio map acquired from NADH and FAD images. (**d**) Phasor plot showing the distribution of fluorescence lifetimes within an NADH image, according to the time decay at each pixel. (**e**) NADH bound fraction map acquired from the phasor analysis. (**f**) To assess the spatial clustering of mitochondria, first a binary mask of NADH image selecting the cytoplasm region of cells is obtained. (**g**) Clone-stamped image of the NADH intensity signals within binary mask shown in (**f**). (**h**) PSD curve of the clone-stamped image along with fitting curve allows for a quantitative measure of mitochondrial clustering. Scale bar: 30 μm. (Reprinted/adapted with permission from ref. [41])

ratio value and then multiplied by merged gray scale intensity images of NADH and FAD for visualization purposes [42, 43] (Fig. 12.2c).

NADH fluorescence lifetime has also been used as a metabolic indicator because it depends on whether NADH is in its free or bound state. Free NADH found

typically in the cytosol has a lifetime that is approximately 400 ps [44]. Longer characteristic lifetimes varying over ~1 to 6 ns correspond to the bound NADH state, typically found in mitochondrial [45, 46], and the exact lifetime depends on the specific complex to which NADH is bound and other factors that affect the molecular microenvironment [47, 48]. Conventional analysis approaches to fluorescence time decay rely on the exponential fitting, which could be time-consuming and difficult for instantaneous applications. In contrast, phasor is a more sophisticated method of analysis in the time domain, without the need for nonlinear fitting [18, 48]. In the phasor representation we can easily recognize the presence of different molecular species in a pixel. After acquiring the NADH fluorescence decay $I_{m,n}$ at each pixel of an image (where (m, n) is the pixel location), Fourier transform is performed on the exponential time decay curve. The real and imaginary parts of the Fourier transform of the decay curve at each pixel are used to determine the x and y axis coordinates (i.e., g and s axis in this case) of a phasor [18, 48] (Fig. 12.2d). A phasor is generally defined as a vector, whose direction relative to the x axis represents the phase of a wave and whose length represents the amplitude. Using this approach, fluorescence lifetime spectra characterized by a mono-exponential decay will map onto a point that falls on the universal semi-circle (Fig. 12.2d), while more complicated decay curves are represented by points within the semi-circle. The phasors of spectra described well by a bi-exponential decay fall on a line within the semicircle, with the two points where the line intersects the semi-circle representing the short and long lifetime components. The relative distance of the point on that line provides an estimate of the fractional contributions of the free (short lifetime) and bound (long lifetime) NADH components (Fig. 12.2d). The bound NADH fraction is estimated based on the location of the centroid of an ellipse that represents the distribution of the detected fluorescence decay data. The fractional contribution can be quantified per pixel, yielding the color-coded bound NADH fraction maps [41] (Fig. 12.2e).

Finally, the third optical biomarker is related to the spatial organization of mitochondria. Mitochondria dynamically fuse and fission throughout the life of a cell to optimize energy production and distribution or to protect the cell from insult [49]. Using a binary mask (Fig. 12.2f), low intensity regions, which mainly correspond to background or weakly fluorescent nuclei, are excluded and only cell cytoplasmic regions are used for this analysis. The selected image intensity patterns are then digitally cloned and randomly positioned in the background space of the image to create a new image without distinct cell borders, so that only cytoplasmic mitochondrial patterns span the entire image [50, 51] (Fig. 12.2g). This clone-stamping approach leads to a more accurate assessment of the mitochondrial organization than using the raw image by eliminating artifacts caused by cell borders [50]. The power spectral density (PSD) of the 2D Fourier transform of an image is fit to an inverse power law at high spatial frequencies ($>0.1\ \mu m^{-1}$) (Fig. 12.2h). The value of the exponent, β, is an indicator of the frequency distributions of the intensity fluctuation patterns within the NADH images, and is referred to as mitochondrial clustering. Increased clustering values typically represent more fissioned/fragmented mitochondrial organizations [50, 51].

12.2.3 TPEF Imaging and Quantitative Characterization of Adipose Tissue Function

TPEF imaging of the cellular coenzymes NADH and FAD, along with highly quantitative characterizations, have been applied to assessments of metabolic activity associated with changes in tissue function and disease progression. For example, Alonzo et al. demonstrated that steady-state and time-resolved intrinsic two-photon excited fluorescence from NADH, FAD and lipid droplets can distinguish the functional states of excised white, brown, and cold-induced beige adipose tissues [52]. NADH was acquired using 755 nm excitation and 460 ± 20 nm emission, while FAD was acquired using 860 nm excitation and 525 ± 25 nm emission. They acquired redox and fluorescence lifetime images from the interscapular brown adipose tissue (BAT), subcutaneous inguinal white adipose tissue (scWAT), and epididymal white adipose tissue (epiWAT) from C57BL/6 mice [52]. Interscapular fat in mice is recognized as classical BAT with robust thermogenic response to cold. EpiWAT is often taken as a non-thermogenic control tissue as it is resistant to tissue browning [53, 54]. In contrast, scWAT exhibits beige adipose tissue (BeAT) formation in some mouse strains, although such susceptibility is low in C57BL/6 mice [54]. Contrast between adipose tissue depots was further demonstrated in a transgenic mouse model, the corticotropin-releasing hormone gene knockout (*Crh*−/−) mice. This mutation has increased cold-induced BeAT formation in scWAT, contributing both to thermogenesis and to total body energy expenditure [55]. Smaller-sized lipid droplets in BAT (Fig. 12.3a) compared to scWAT (Fig. 12.3e) and epiWAT (Fig. 12.3i) were immediately evident. More importantly, the images showed higher redox ratio, i.e., more oxidized state, in BAT (yellow-orange) compared to both WAT depots (cyan). This is a reflection of both higher mitochondrial density, and higher turnover rates in the electron transport chain (ETC) in BAT compared to WAT. Note that only the cytoplasmic regions, excluding the lipid droplets, were color-coded to demonstrate the cellular redox ratio levels (Fig. 12.3). Consistent with increased ETC activity during thermogenesis, even higher redox was observed in BAT from cold exposed mice (Fig. 12.3b) compared to BAT from mice kept at room temperature (Fig. 12.3a). Meanwhile, there were no obvious temperature effects on the redox ratio in either WAT depot (Fig. 12.3f, j). However, in the *Crh*−/− mice, increased optical redox ratio with cold exposure was evident not only in BAT (Fig. 12.3c, d), but also in some scWAT images (Fig. 12.3g, h). Redox in epiWAT remained insensitive to cold exposure (Fig. 12.3k, l).

Besides fluorescence from cell cytoplasm, intrinsic TPEF from lipid droplets has also been reported recently [56]. The fluorescence lifetime was analyzed using the phasor approach, from which the long lifetime intensity fraction (LLIF) was extracted, representing the fractional contribution to emission intensity from the long lifetime component (i.e., the bound NADH or long lifetime fluorescent component in lipid droplets in this case). It is worth mentioning that we color-coded the entire image in the LLIF map (Fig. 12.4) compared with the redox ratio one (Fig. 12.3), because both NADH and certain components within lipid droplets have fluorescence under the NADH-acquisition channel (i.e., 755 nm excitation/

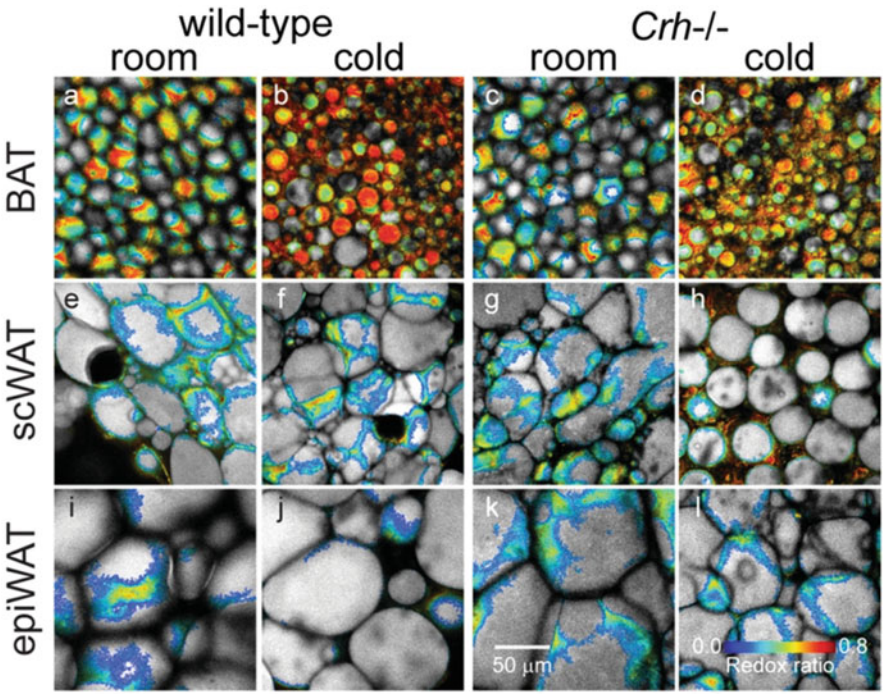

Fig. 12.3 (**a–l**) Redox ratio maps of different adipose tissue types [52]. The different adipose tissue types as well as different treatments are labeled in the figure. Notice that only the cytoplasm region was color-coded by redox ratio values. (Reprinted/adapted with permission from ref. [52])

460 ± 20 nm emission). Parallel to increases in redox ratio, BAT showed lower NADH fluorescence lifetime (Fig. 12.4a–d) relative to scWAT (Fig. 12.4e–h) and epiWAT (Fig. 12.4i–l). Further lifetime decreases were observed under cold treatment in BAT (Fig. 12.4b, d) and some *Crh*−/− scWAT depots (Fig. 12.4h). A lower redox ratio and a higher fluorescence lifetime might be associated with a preference of de novo fatty acid synthesis in WAT. In particular, increased flux through glycolysis, pyruvate dehydrogenase complex (PDC), and TCA cycle pathways relative to low ETC utilization leads to net accumulation of NADH relative to FAD, thus lowering the redox ratio [42], and the associated long fluorescence lifetime in these tissues indicates that NADH is accumulating primarily in its bound form [45, 47]. Meanwhile, expression of UCP1 in BAT and BeAT induces a proton leak in the inner mitochondrial membrane, compensated by increased electron flux via Complexes I through IV of the ETC [57]. This depletes enzyme-bound NADH in the mitochondria, thus increasing the optical redox ratio and lowering the fluorescence lifetime. Taken together, these images demonstrate that functional metabolic imaging via TPEF of endogenous NADH and FAD not only distinguish different functional types of adipose tissue, i.e., BAT vs. WAT, but can also indicate activation of thermogenic function in BAT and BeAT.

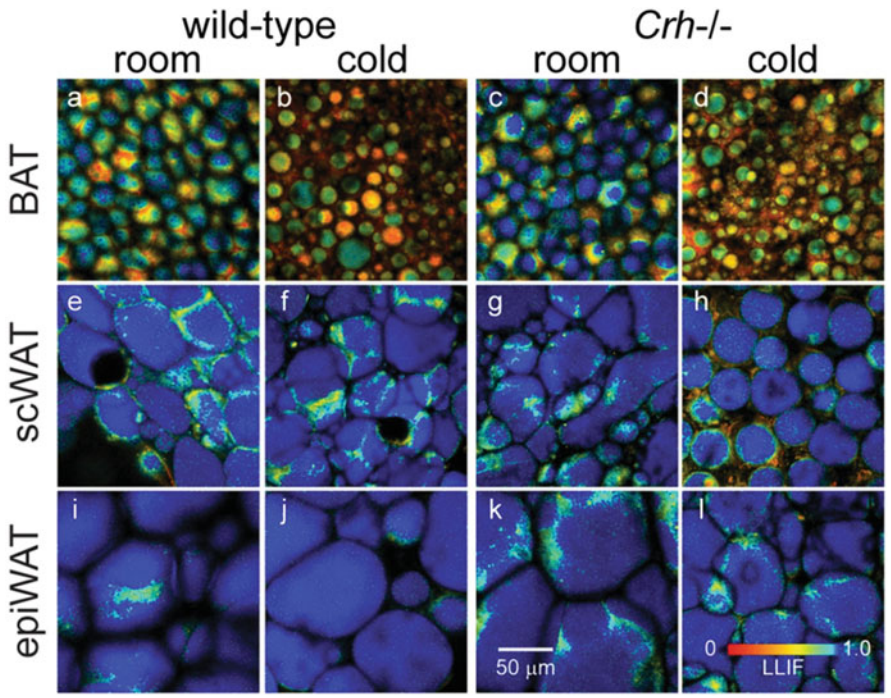

Fig. 12.4 (**a**–**l**) Long lifetime intensity fraction (LLIF) maps of different adipose tissue types [52]. The different adipose tissue types as well as different treatments are labeled in the figure. (Reprinted/adapted with permission from ref. [52])

12.2.4 In Vivo Imaging of Malignant Lesions in Human Skin as Revealed Through Mitochondrial Organization

In vivo TPEF images have been acquired throughout the depth of normal and cancerous human skin tissues [49]. In this study, the excitation wavelength was tuned to 765 nm and NADH fluorescence was detected over a broad spectral range (410–650 nm). Due to the wide spectral characteristics of the clinical emission filter, fluorescence was collected from NADH as well as from keratin, melanin, and collagen/elastin (Fig. 12.5), and the images were pre-processed to minimize the non-NADH signals before the acquisition of mitochondrial clustering levels (Fig. 12.5) [49]. In addition, to normal human skin, images were acquired from melanoma and basal cell carcinoma lesions. The quantitative analysis revealed that healthy epidermis displayed consistent, depth-dependent morphological and mitochondrial organization patterns that varied significantly with histological stratification, while these consistent patterns were absent in cancerous skin lesions (Fig. 12.5, the depth-dependent graphs at the right side). They then exploited these differences to successfully differentiate healthy from cancerous tissues using a predictive classification approach. Collectively, these results demonstrate that label-free, near

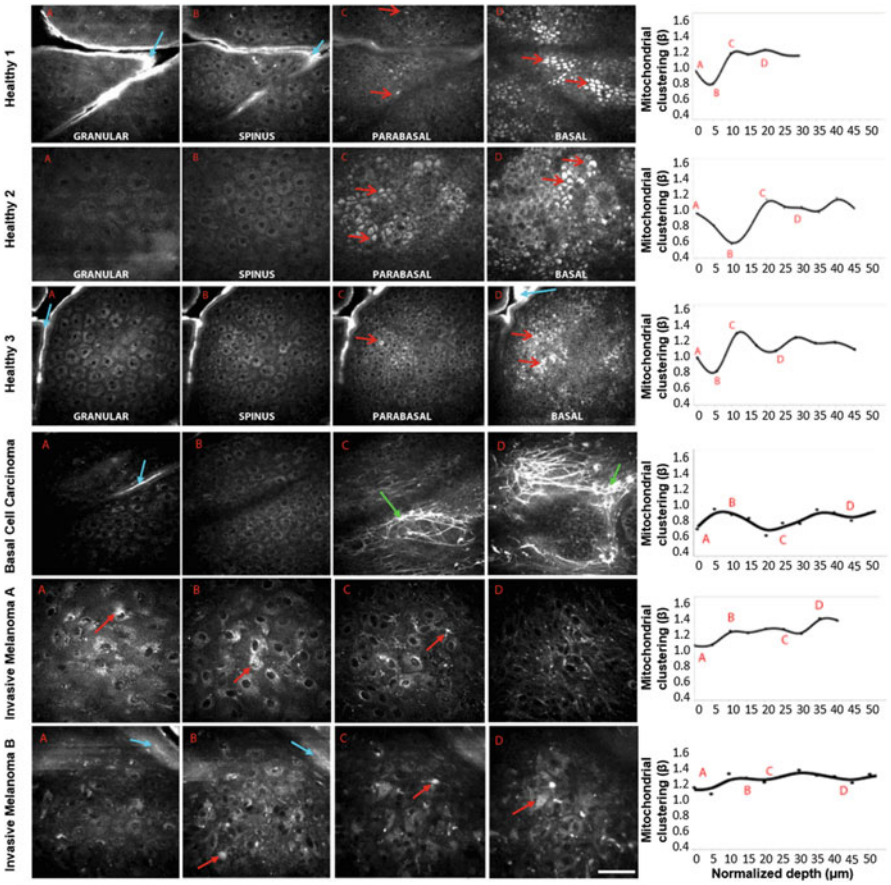

Fig. 12.5 Differences in morphology and function are detected in in vivo endogenous TPEF images of normal and cancerous human epithelia [49]. Left: representative raw images obtained at different depths from healthy and diseased epithelial tissues. Right: the corresponding mitochondrial clustering values as a function of depth. Labels A, B, C, D within the mitochondrial clustering graphs represent the mitochondrial clustering values extracted from the panel's respective labeled images. Open-head red arrows in raw images designate the melanin caps, which intensify above and regress below the nuclei of the basal cells. Closed-head red arrows designate melanin in melanoma tissues. Cyan and green arrows indicate keratin and collagen/elastin contributions, respectively. Scale bar, 50 μm. (Reprinted/adapted with permission from ref. [49])

real-time assessments of mitochondrial organization, relying completely on endogenous contrast, could be useful for accurate, non-invasive in vivo diagnosis of skin cancers, and might be more applicable to clinical translation compared with invasive techniques or the ones in need of mitochondria-specific dyes [58–60].

12.2.5 Complementary Insights into Cellular Metabolism and Underlying Biological Mechanisms by Combining Different Biomarkers

Due to the complex nature of cellular metabolism, application of an individual optical biomarker will likely not be sufficient to provide an accurate or sensitive description of the nature of the specific metabolic pathway change that led to a given optical change. It is also possible, that changes in more than one metabolic pathway occur further complicating interpretation of optical results. Therefore, in a recent study multi-parametric analysis of all the three optical biomarkers, including cellular redox state, NADH fluorescence lifetime, and mitochondrial clustering, was performed within intact, living cells and three-dimensional tissues [41]. These biomarkers were monitored within cells and tissues subjected to metabolic perturbations that triggered changes in distinct metabolic processes, including glycolysis and glutaminolysis, extrinsic and intrinsic mitochondrial uncoupling, and fatty acid oxidation and synthesis [41]. Representative maps of these three biomarkers of human foreskin keratinocytes (HFKs) in response to hypoxia and glucose starvation are shown in Fig. 12.6. Hypoxia selectively inhibits oxidative phosphorylation and enhances glycolytic flux, whereas glucose starvation in these

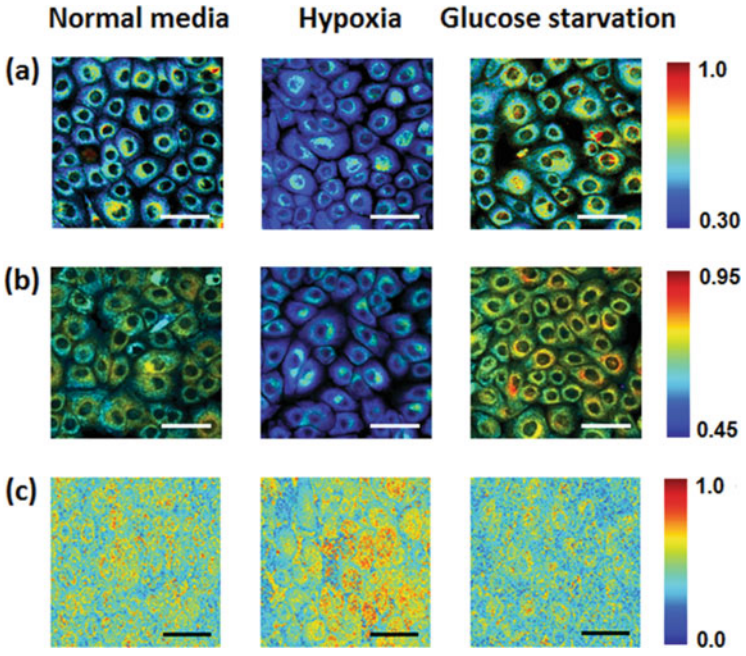

Fig. 12.6 Optical readouts of HFKs under metabolic pathways of glycolysis or glutaminolysis [41]. (**a**) Representative maps of redox ratio. (**b**) Representative NADH fluorescence lifetime maps as represented by bound NADH fraction. (**c**) Representative images of clone-stamped mitochondria. Scale bars, 50 μm. (Reprinted/adapted with permission from ref. [41])

cells enhances glutaminolysis [43]. As a result, hypoxia led to a decrease in the optical redox ratio (Fig. 12.6a), accompanied by a corresponding decrease in the NADH bound fraction (Fig. 12.6b) and enhanced mitochondrial clustering (Fig. 12.6c). This decrease in redox ratio upon the onset of hypoxia is consistent with previous studies and is expected as the lack of oxygen abolishes the mitochondrial oxidative capacity and shifts cellular metabolism to an enhanced glycolytic profile [16, 61]. Thus, the cytosolic and mitochondrial pools of NADH increase (Fig. 12.1), leading to the observed decreased redox ratio. A dominant contribution from the cytosolic, free, NADH pool is also consistent with the observed reduction in the NADH bound fraction. The detected increase in mitochondrial clustering is consistent with mitochondrial fragmentation, resulting from the hypoxia-driven disengagement of ETC and the corresponding decrease in mitochondrial membrane potential [49].

Glucose starvation treatment was achieved by culturing HFKs in the media prepared in-house with the same glutamine concentration as keratinocyte serum-free medium (KSFM), but with no glucose. Glucose starvation led to the exact opposite combination of changes in the optical metabolic readouts compared with those observed during hypoxic insult (Fig. 12.6). As the glycolytic flux is diminished, mitochondrial bioenergetic adaptation is required to support cellular homeostasis, and glutamine uptake is elevated [43]. Glutamine enters the mitochondria and is ultimately converted to a-ketoglutarate to fuel the TCA cycle [43]. The abrogation of the cytosolic, free, NADH pools and the increased mitochondrial oxidative flux yield an increase of the mitochondrial, NADH bound fraction, as well as an increase in the overall cellular redox ratio. The observed decrease in mitochondrial clustering relative to the control population is supported by previous studies [51, 62], showing that nutrient starvation can lead to a more fused mitochondrial organization. The latter has been associated with prevention of mitochondrial autophagy and increased oxidative efficiency to maintain ATP levels [43, 51, 63].

After acquiring all the optical readouts in response to different metabolic perturbations in the context of different cell cultures or intact tissues, Liu et al. mapped the field-based (Fig. 12.7a) or cell-based (Fig. 12.7b) data into the 3D space, with each axis representing one of the three biomarkers. The classification potential at the cellular level was quantified, since cellular heterogeneity represents one of the challenges in deciphering biological function and response to treatment [64]. The three-metric combination produced the best separation for different metabolic perturbations and quantitatively yielded the highest original (91.6%) and cross-validated accuracy (91.6%) in classifying all the cells into distinct experimental perturbations examined, including glycolysis and glutaminolysis, extrinsic and intrinsic mitochondrial uncoupling, and fatty acid oxidation and synthesis. In contrast, the utilization of only one or two metrics at a time yielded varying accuracies ranging from 35.5% to 70.9% (with only one metric) or 66.5–87.8% (with two metrics). Taken together, these findings show that multi-parametric TPEF imaging of endogenous contrast within cells is a valuable investigational approach that enables quantitative and non-invasive assessments of metabolic alterations at either the single-cell or the tissue level, and demonstrate that significant insights can be

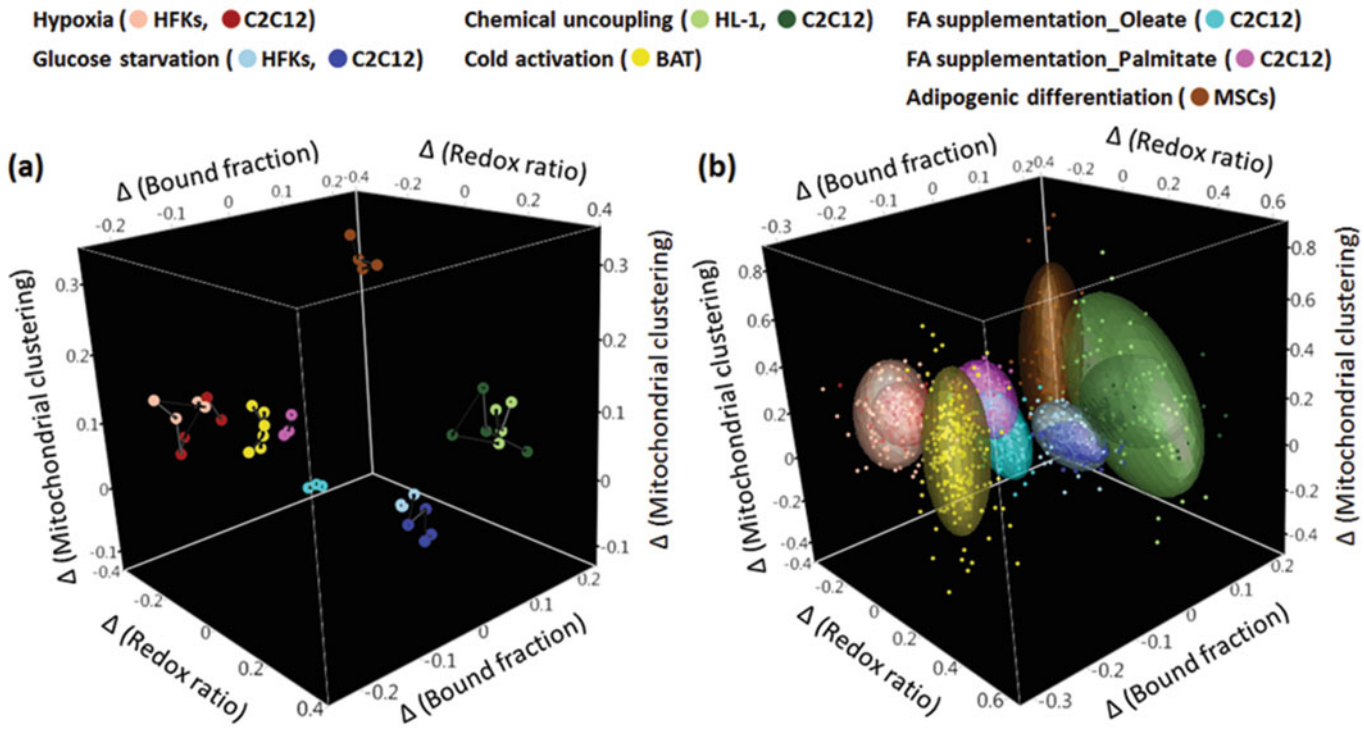

Fig. 12.7 Holistic visualization of all data sets by combining three optical metrics [41]. (**a**) Combining relative changes of the redox ratio, NADH bound fraction, and mitochondrial clustering at the biological replicate level. Different colors are used for representation of different perturbations and biological specimens (shown on top). Light and dark hues are used to differentiate between biological specimens for the perturbations where data from multiple cell lines are shown. (**b**) Combining relative changes of these three metrics at the cell level. Ellipsoids represent 70% of data coverage. Color representation is the same as in (**a**). (Reprinted/adapted with permission from ref. [41])

obtained into not only the presence of metabolic changes but also the nature of the metabolic processes that are altered.

12.3 Quantitative Imaging and Characterization of the Spatial Organization of the Extracellular Matrix Collagen Fibers

12.3.1 Definition of Angles for 2D and 3D Description of Fiber-Like Structures

In addition to cellular metabolism, changes in collagen fiber organization are another important characteristic of disrupted cell-matrix interactions, and an accurate description of these organizational alterations is critical to achieve a better understanding of disease initiation and progression. In order to describe an orientation in 2D space, an azimuthal angle θ is needed [65] (Fig. 12.8a). As can be seen from this schematic, θ is defined as the angle between the fiber (blue line) and the x axis, ranging between 0° and 180°. To depict an orientation in 3D space, both an azimuthal angle θ and a polar angle φ need to be determined [30] (Fig. 12.8b). θ is defined as the angle between the projection of the fiber (blue line) on the xy plane and the x axis, and φ is defined as the angle between the fiber and the $-z$ axis (Fig. 12.8b). For axial fiber data, both θ and φ range between 0° and 180°. A certain orientation in 2D or 3D space, can be fully described by the angles, along with the angular ranges mentioned above.

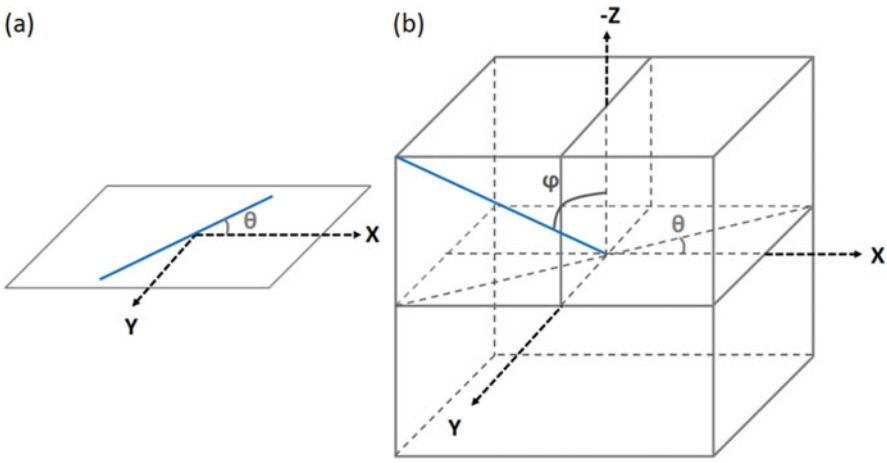

Fig. 12.8 Schematic of spatial orientations for fiber-like structures. (**a**) The 2D orientation of fiber is described by a single azimuthal angle θ; (**b**) The 3D orientation is described by both azimuthal angle θ and polar angle φ

12.3.2 2D Analysis Methods for Quantifying Collagen Fiber Organization

With the development of confocal and multi-photon microscopy, especially second harmonic generation (SHG) and two-photon excited fluorescence (TPEF), the necessary axial resolution has been achieved to capture fine collagen features within the extracellular matrix in a 3D context [22, 23]. However, even as high-resolution 3D images of collagen fibers become more readily accessible, quantitative analysis algorithms for their orientation and organization have largely remained limited to analysis of 2D images. Sivaguru et al. acquired SHG images of horse tendon (Fig. 12.9a), and calculated the 2D orientation of collagen fibers by means of Fourier transform of the SHG image [66] (Fig. 12.9b). This method could be applied to the entire image, or a certain region of interest (ROI). In this manner, the ROI-based orientation distribution of the corresponding SHG image can be obtained (Fig. 12.9c). However, the computational time of these Fourier-based approaches is dependent on the number of ROI locations over which the Fourier transform is computed. As a result, a more detailed mapping of localized fiber directions comes, at the expense of more computational time needed. Moreover, such techniques generally require a square image size and can be prone to systematic measurement errors produced by large-scale features such as the absence of fibers in irregularly

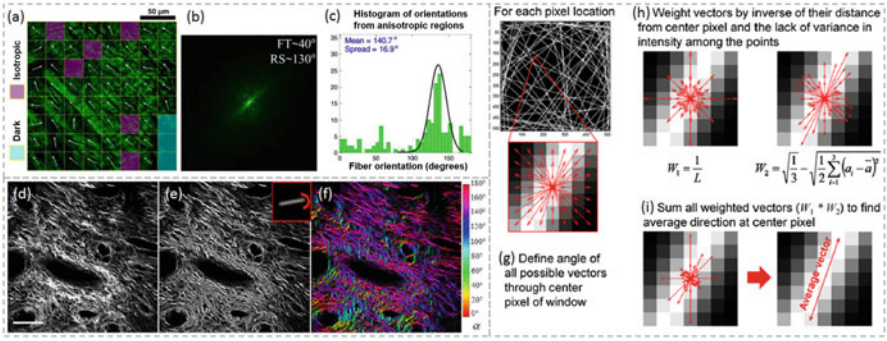

Fig. 12.9 Two-dimensional (2D) orientation analysis approaches for fiber-like structures. (**a**–**c**) Approach based on 2D Flourier transform [66]; (**d**–**f**) Approach based on opening operator [67]; (**g**–**i**) Approach based on weighted vector summation [65]. (**a**) The representative SHG image of collagen fibers from the horse tendon, which are divided into a number of regions of interest (ROIs), with the white arrow in each ROI corresponding to the fiber direction; (**b**) The 2D Fourier transform of the entire SHG image; (**c**) The ROI-based orientation distribution of this representative SHG image; (**d**) SHG image of collagen fibers from cervical biopsy section. Scale bar: 100 μm; (**e**) Fibers demonstrate the maximum intensity if they align parallel to the direction of the opening operator; (**f**) The acquired orientation map from the opening operator; (**g**) In the simulated fiber image, the orientation of a certain pixel is calculated starting from defining a window size surrounding this pixel and obtaining all the vectors; (**h**) All the vectors are weighted by two factors considering the vector length and the intensity fluctuations along each vector direction; (**i**) The orientation of the center pixel is finally acquired by the summation of all the weighted vectors. (Reprinted/adapted with permission from refs. [65–67])

shaped subregions within the image. Bancelin et al. obtained the collagen fiber images from histological slides of uterine cervical tissues collected from patients via SHG (Fig. 12.9d) for the generation of orientations using morphological operators [67]. Specifically, a morphological operator "opening" is applied using a structuring element (Strel) that is a line 10.5 μm long (see inset in Fig. 12.9e), in order to extract the orientation of the structuring element. As the structuring element rotates, a collection of openings by this rotatable line results in a stack of images, each corresponding to different Strel directions. By comparing the pixel-wise intensity along the third dimension of the stack, the maximum intensity of each pixel, corresponding to a certain Strel direction, could be identified (Fig. 12.9e). In this manner, the Strel direction realizing this maximum provides the pixel-wise orientation of fibers (Fig. 12.9f). However, there is a trade-off between the length of the structuring element and the orientation determination accuracy. A longer element gives a more precise measure since more angles are available; however its length is bounded by the local curvature of the fibers inside which the structuring element needs to fit.

In addition to the two approaches mentioned above, Quinn et al. developed "weighted vector summation" method for the generation of 2D fiber orientation maps [65] (Fig. 12.9g–i). Upon selecting a square window size to evaluate the patterns surrounding each pixel, all possible vectors passing through the center pixel in the window are defined, and the angles associated with these orientation vectors are calculated (Fig. 12.9g). Next, for each pixel location, the orientation vectors are weighted based on vector length and intensity variability (Fig. 12.9h). Typically there is a lower variation in intensity along the direction of the fiber than along the direction perpendicular to the fiber. Once the weighted vector lengths are computed for a given pixel, all the vectors are summed to determine an average direction (Fig. 12.9i), which is assumed as the orientation of the center pixel within the window. This approach offers advantages in computational efficiency over Fourier transform-based methods to map local fiber orientations, and is particularly suitable for generating orientations of curvy fibers [65].

12.3.3 Applications of 2D Organizational Quantification of Collagen Fibers

The 2D organizational characterization of collagen fibers has been applied to assessments of different diseases, such as wound healing and osteoarthritis. Quinn et al. assessed structural changes of extracellular matrix (ECM) after myocardial infarction (MI) [68]. To enhance optical imaging depths within the heart and isolate the ECM, whole organ decellularization was performed [69] in rat MI model. Both SHG images (red) of collagen fibers (acquired by 800 nm excitation and 400 ± 10 nm emission), and TPEF images at two distinct channels (blue: acquired by 740 nm excitation and 400 ± 10 nm emission; green: acquired by 740 nm excitation and 525 ± 25 nm emission), assumed to be related to crosslinks, were acquired from healthy or infarcted hearts at 1, 2, 4 and 8 weeks post-MI

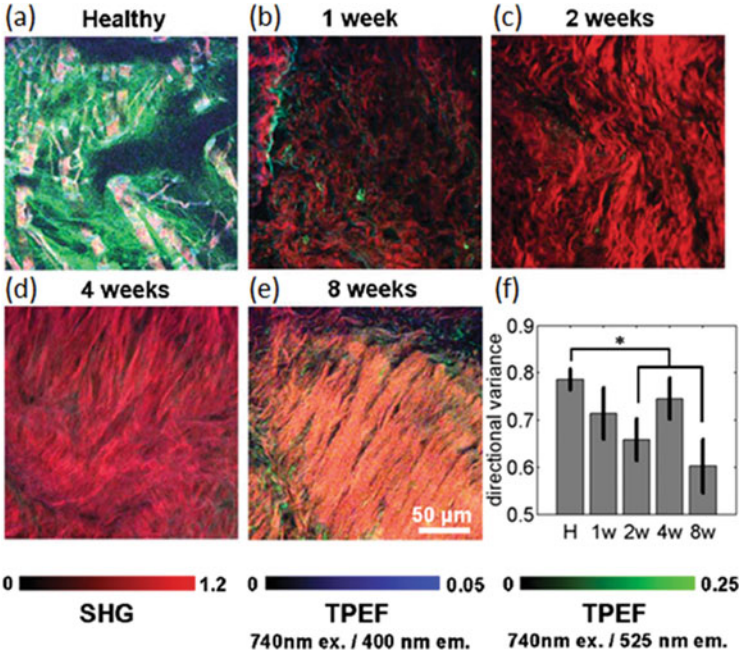

Fig. 12.10 Applications of 2D orientation analysis in rat myocardial infarction model [68]. The multi-photon images of the rat heart (**a**) before or (**b**) 1, (**c**) 2, (**d**) 4, (**e**) 8 weeks post-infarction. (**f**) Mean and standard deviation of 2D directional variance, indicating that fibers become more and more aligned as a function of time. (Reprinted/adapted with permission from refs. [68])

(Fig. 12.10a–e). Qualitative examination of these images revealed that decellularized healthy hearts were characterized by a sparse arrangement of relatively large diameter collagen fibers that were visible through SHG imaging, while the scar of infarcted samples consisted of a dense network of aligned, small diameter collagen fibers (Fig. 12.10a–e). Then the spatial organization of these collagen fibers was quantified by 2D directional variance metric, which was generated based on the 2D orientations obtained from SHG signals. Analogous to variance in linear data which measures how far a set of numbers is spread out, directional variance extends this measure to a set of orientations. It ranges between 0 and 1, with 0 corresponding to perfectly parallel fiber alignment, while 1 corresponding to completely randomly oriented fibers. Collagen fibers of the scar region were more aligned with each other than the mature collagen fibers of the healthy tissue as quantified by the significantly lower 2D directional variance on Week 2 and Week 8 relative to healthy tissue (Fig. 12.10f).

In addition to evaluating scar formation in the myocardium following infarction, Quinn et al. also assessed the remodeling of scars in rat skin following thermal burns directly from Masson's trichrome-stained histological sections [70]. Six-week-old female Sprague-Dawley rats were utilized, and full-thickness third-degree burns (1 cm^2) were created on the dorsum by pressing a brass block preheated to

approximately 95 °C to the skin for 10 s. Tissues were harvested 6 months after burn injury, stained and imaged using Hamamatsu's NanoZoomer Digital Pathology System, and then analyzed by custom code in Matlab. Automated colorimetric analysis of each pixel enabled the identification of collagen-containing pixels, and collagen fiber density measurements indicated significantly higher values within the scar compared to the adjacent uninjured region. To compliment measures of fiber density, a decrease in 2D directional variance was also able to delineate the scar region 6 months after burn injury, corresponding to a more aligned status of collagen fibers.

Mingalone et al. applied the 2D directional variance analysis to the assessment of collagen fibers within cartilage at the end of the tibia in a mouse model during the onset of osteoarthritis [71]. As shown in the schematic (Fig. 12.11a) and a representative image (Fig. 12.11b) of mouse articular cartilage, this tissue is divided into four zones: superficial, transitional, radial and calcified zone [72]. The chondrocytes and collagen fibers are oriented parallel to the articular surface in the superficial zone, while perpendicularly to this surface in the radial zone. In the transitional zone, the chondrocytes are oriented at an angle to the surface, surrounded by territorial matrix composed of sheets of collagen fibers. After acquiring the pixel-wise orientation of collagen fibers relying on SHG images, the 2D directional variance map can be generated accordingly (Fig. 12.11c). Throughout this study, cartilage samples were harvested from three groups for SHG imaging: destabilization of the medial meniscus (DMM) mimicking osteoarthritis, sham surgery with ligament exposed but not severed (Sham), and non-surgery control (NS-Ctrl). The representative 2D directional variance maps corresponding to these three groups are shown in Fig. 12.11d, with the hues indicating the fiber organization in response to different treatments. Quantitative assessments of the 2D variance values in DMM and Sham animals normalized to corresponding NS-Ctrl animal values were performed at distinct cartilage zones. The DMM joint showed significantly higher directional variance of collagen fibers compared to that of the sham joint in the superficial zone (Fig. 12.11e), indicating that the collagen degradation and disorganization might initiate within the superficial layer of cartilage. Interestingly, an opposite trend is found for the DMM group in the radial zone, which exhibited a lower variance (higher level of alignment) than the control group (Fig. 12.11e). Overall, these results reveal that changes in collagen fibers take place not only in the superficial layer but also in the deep layer of the articular cartilage during early stages of osteoarthritis [71].

12.3.4 3D Analysis Methods for Quantifying Collagen Fiber Organization

Given that collagen fibers extend naturally through all the tissue dimensions, 2D analysis approaches have limitations in accurately determining their spatial organization, as well as corresponding alterations during disease progression. A few truly 3D analysis approaches have been reported and applied to collagen fiber

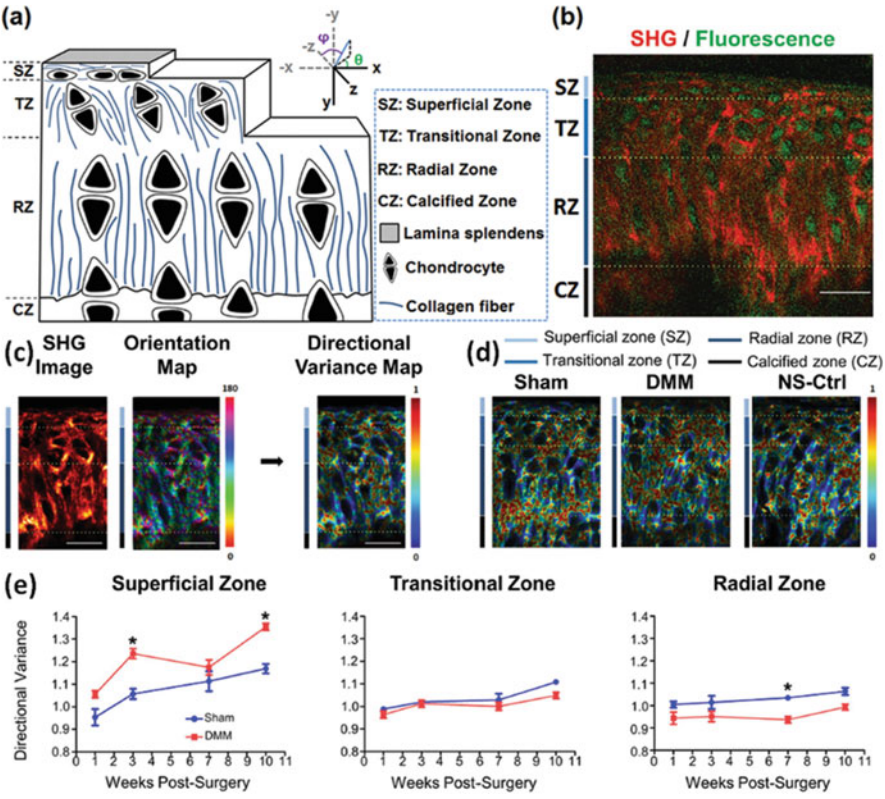

Fig. 12.11 Application of orientation analysis in osteoarthritis of mice [31, 71]. DMM: Destabilization of the medial meniscus (osteoarthritis model); Sham: Ligament being exposed but not severed; NS-Ctrl: Non-surgery control. (**a**) Schematic of the cartilage with layered structures; (**b**) A representative multi-photon image of cartilage, with the red signal corresponding to SHG image of collagen fibers; (**c**) Based on the 2D orientations generated from SHG images, the 2D directional variance map is acquired accordingly. (**d**) The representative 2D directional variance maps for different groups; (**e**) A comparison of 2D directional variance values between DMM and Sham at different layers. Scale bar: 25 μm. *, $p < 0.05$. (Reprinted/adapted with permission from refs. [31, 71])

characterization in recent years. Lau et al. acquired 3D SHG image stacks from horse tendon (Fig. 12.12a, b) and used Fourier transform-based analysis to quantify 3D orientations of collagen fibers at discrete ROIs [73] (Fig. 12.12c). The overall 3D orientation within each ROI is determined by the filter bank method. The filter bank consists of different 3D orientation filters constructed in the Fourier space, and the filter orientation that corresponds to the maximum likelihood to the Fourier transform is selected as the fiber orientation for each ROI (Fig. 12.12c). By acquiring 3D orientations (including both the azimuthal angle θ and the polar angle φ) at each ROI, a distribution of either φ (Fig. 12.12d) or θ (Fig. 12.12e) can be generated accordingly, revealing the overall angular characteristics of the 3D image stack. Note

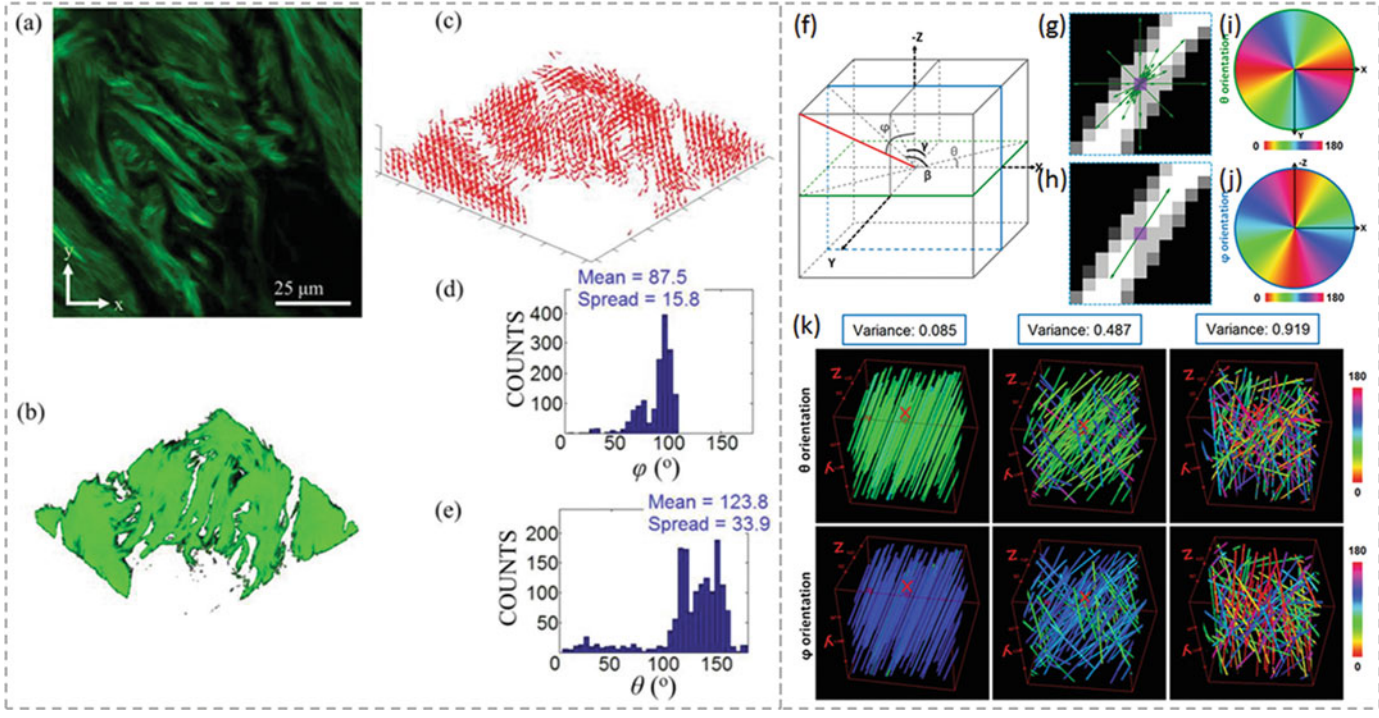

Fig. 12.12 Three-dimensional (3D) orientation analysis approaches for fiber-like structures. (**a**–**e**) Approach based on 3D Fourier transform [73]; (**f**–**k**) Approach based on weighted vector summation [31]. (**a**) Representative SHG image of porcine tendon; (**b**) 3D reconstruction of SHG images; (**c**) The calculated 3D orientation in each ROI; Distribution histograms of (**d**) φ and (**e**) θ of this representative 3D SHG image stack; (**f**) Definition of angles in 3D space; (**g**) Illustration of weighted vector summation algorithm; (**h**) The calculated orientation based on this weighted vector summation algorithm; The (**i**) θ and (**j**) φ orientation maps for the planes marked in green or blue in (**f**); (**k**) The 3D directional variance is acquired based on the 3D orientations, which quantifies the spatial organization of simulated fiber-like structures with different levels of alignment in a 3D context. (Reprinted/adapted with permission from refs. [31, 73])

that a 90° of the polar angle φ indicates an orientation of collagen fibers parallel to the optical section (typically the xy plane in Fig. 12.8b). Similar to the limitations regarding the 2D Fourier-based approach, the ROI size selection results in a trade-off between determination accuracy and computational time.

Liu et al. proposed a 3D weighted orientation vector summation algorithm, which was a generalization of the previously reported 2D vector summation technique aimed at quantifying collagen fiber orientations simultaneously at each voxel of an image stack [30]. In this approach, the determination of θ is achieved by projecting fibers to a fixed 2D plane, i.e., the xy plane (Fig. 12.12f), which means that the calculation of θ still obeys the 2D vector summation rules. However, according to the definition of φ which is the angle between the fiber of interest and the $-z$ axis, there is no fixed 2D plane that can be projected to for the determination of all the possible φ orientations. Therefore, two extra angles β and γ, which are symmetrical to the azimuthal angle θ, are defined to solve this problem (Fig. 12.12f). β is the angle between the projection of the fiber (red line) in the zx plane and the x axis, and γ is the angle between the projection in the yz plane and the $-y$ axis. Then the polar angle φ is determined according to the relationship: $\tan^2\varphi = \frac{1}{\tan^2\beta} + \frac{1}{\tan^2\gamma}$. The determination of angles θ, β and γ can be achieved by the summation of weighted vectors (Fig. 12.12g, h), as described for the determination of the azimuthal angle θ in 2D case (Fig. 12.9g–i). Orientation maps of two typical planes, as marked by green and blue (Fig. 12.12f), are plotted in Fig. 12.12i, j, respectively, which serve as a reference for assessing the orientation values. 3D directional variance, a generalization of the 2D directional variance for three-dimensional image analysis, is then developed to indicate the spatial organization of fiber-like structures. To test the 3D directional variance algorithm, three simulated fiber stacks were prepared with varying levels of alignment [31]. The voxel-wise orientations of these fibers were acquired by the weighted vector summation algorithm, and the false-colored orientation maps for θ (top) and φ (bottom) were prepared accordingly (Fig. 12.12k). 3D directional variance was then calculated based on the entire image stack (shown on top of the orientation maps), considering the contributions from all the fibers (Fig. 12.12k). As expected, the 3D directional variance is close to 0 for the stack image with parallel fibers (left), while it is close to 1 for the one with randomly distributed fibers (right). The stack with intermediate fiber organization has a moderate directional variance value (middle). These results illustrate the capability of this approach to provide a simple but highly quantitative metric of 3D organization of fiber-like structures.

12.3.5 Applications of 3D Organizational Quantification of Collagen Fibers

The 3D characterization of spatial orientation and organization of collagen fibers has been shown to have great potential in achieving a better understanding of diseases, such as cancers [31]. The peritoneal cavity acts as a common target for metastatic

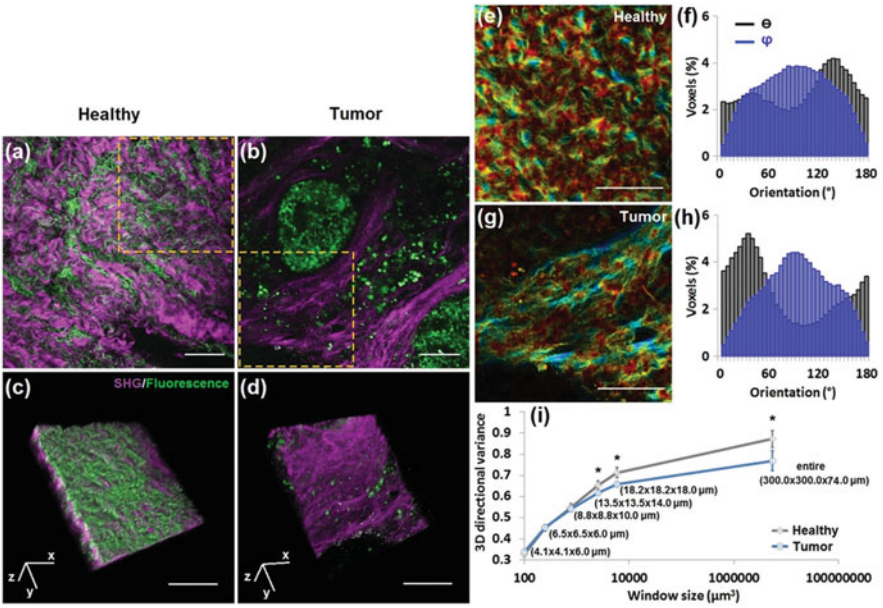

Fig. 12.13 Application of 3D orientation analysis in human peritoneal metastases [31]. Representative multi-photon images of (**a**) healthy parietal peritoneum and (**b**) pancreatic neoplastic tissue; 3D reconstructions of multi-photon images of (**c**) healthy parietal peritoneum and (**d**) pancreatic neoplastic tissue; 3D directional variance maps of (**e**) healthy parietal peritoneum and (**g**) pancreatic neoplastic tissue; 3D orientation distributions of (**f**) healthy parietal peritoneum and (**h**) pancreatic neoplastic tissue; (**i**) A comparison of 3D directional variance between healthy parietal peritoneum and pancreatic neoplastic tissue using different window sizes. Scale bar: 100 μm; *, $p < 0.05$. (Reprinted/adapted with permission from ref. [31])

lesions of gastrointestinal cancers [74], including pancreatic cancer; therefore, detecting such metastatic lesions with high sensitivity is important for proper cancer staging and subsequent treatment decisions [75]. Liu et al. applied the 3D analysis to images of collagen fibers within freshly excised biopsies from healthy parietal peritoneum (Fig. 12.13a, c) and primary pancreatic neoplastic tissues [31] (Fig. 12.13b, d), which served as surrogates of pancreatic peritoneal metastases since prior knowledge of metastasis prohibits surgical intervention [76]. Green TPEF signals correspond to cell clusters and blood vessels, while magenta SHG signals originate from collagen fibers. After acquiring voxel-wise 3D orientations of collagen fibers, 3D directional variance maps corresponding to the healthy peritoneum (Fig. 12.13e) and the neoplastic tissue (Fig. 12.13g) were generated accordingly. Bluer hues were observed within the directional variance map of the neoplastic tissue (Fig. 12.13g) compared with the healthy peritoneum (Fig. 12.13e), representing a lower level of directional variance (i.e., higher level of alignment). As can be seen from the θ (black) and φ (blue) distribution histograms of all the fibers within the representative frames (Fig. 12.13f, h), one single peak of θ at ~35° (notice that 0° is equal to 180° for fiber-like data) is observed from the tumor

tissue (Fig. 12.13h), in comparison to a wider, possibly bimodal distribution in the healthy peritoneum (Fig. 12.13f). In this study, the 3D directional variance was assessed quantitatively at different window sizes, which provide readouts of spatial organization at different scales (Fig. 12.13i). Beyond a certain window size, significantly lower directional variance is observed for the pancreatic neoplastic tissue than the normal parietal peritoneum (Fig. 12.13i), which is consistent with 3D orientation distribution histograms, as well as the visually apparent presence of more highly aligned fibers in the neoplastic tissue.

Besides peritoneal metastases, Liu et al. considered 3D directional variance as a quantitative metric of collagen fiber organization in normal and cancerous mouse mammary gland tissues [31]. Representative large-scale images combining TPEF and SHG signals for both normal and cancerous breast tissues are shown in Fig. 12.14a, b, and the 3D reconstructions of a certain region within the large-scale image are shown in Fig. 12.14c, f. 3D directional variance was calculated based on the SHG-only images. Collagen fibers were found to be "cross-hatched" in the normal tissues, while highly regular helical structures were observed in the tumor specimens (as indicated by the schematic illustrations shown in insets of Fig. 12.14d, g), consistent with observations from breast cancers by other groups [77, 78]. Relatively bluer hues are observed in the 3D directional variance map corresponding to the mammary tumor than the normal tissue (Fig. 12.14e, h), indicating a higher level of alignment. These visual observations were further validated by quantitative analysis of 3D directional variance (Fig. 12.14i). In this study, they use two types of window size for the organizational assessment. The localized window assessments, with its size dependent on the characteristics of the fibers, such as their diameter, waviness and tissue level organization, provided insights into the localized, fiber-to-fiber alignment. On the other hand, a full image stack window was used to assess the overall fiber alignment of the tissue at a larger scale. Significant differences were observed between normal and tumor breast tissues assessed using both the localized and the full image stack window, indicating organizational disparities at both length scales. The presence of more highly aligned fibers within tumors is consistent with previous studies which assessed collagen organization in breast tissues [79].

Mammary epithelial cells grown in 3D cultures recapitulate numerous features of the breast epithelium in vivo, adequately bridging the gap between complex whole animal models and simple 2D cultures [80–82]. Liu et al. assessed the hormonal regulation of matrix reorganization in a 3D breast tissue culture model using 3D directional variance to characterize the organization of collagen fibers [83]. These 3D engineered breast tissue models, consisting of human breast epithelial T47D cells and collagen, were treated with 17β-estradiol (E2) alone, and E2 in combination with either promegestone, a progestogen, or prolactin. TPEF images of Carmine Alum stained T47D cells were acquired and reconstructed in 3D to resolve the cell morphology (Fig. 12.15a). Different patterns of epithelial organization in response to different hormone treatments were observed in 3D cultures. Briefly, with the addition of physiological concentrations of E2 alone, cells typically formed slightly elongated (Fig. 12.15a) or rounded structures. In contrast, with the addition of E2

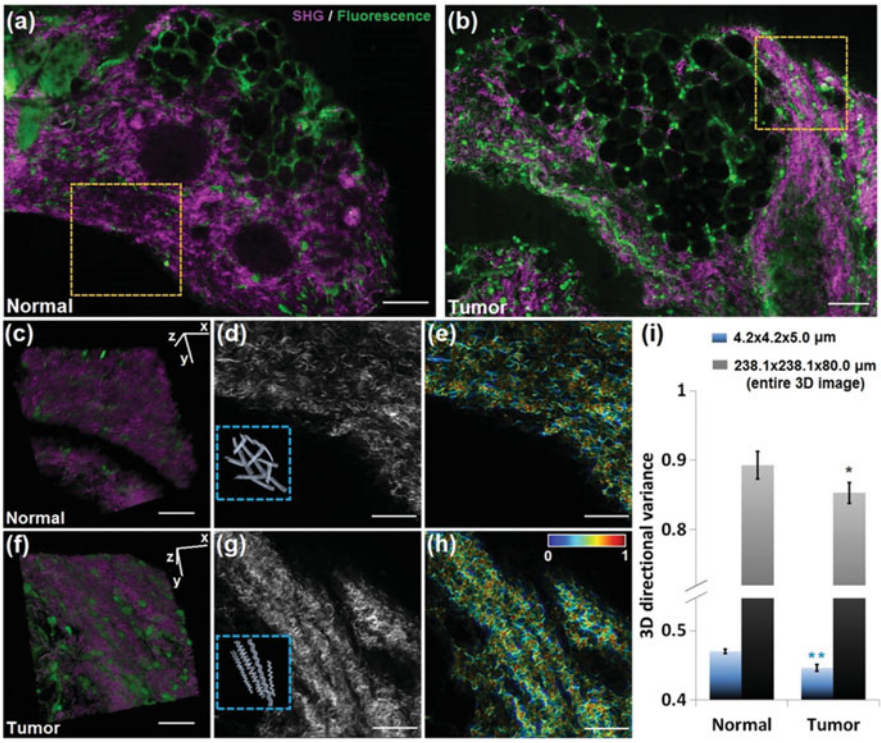

Fig. 12.14 Application of 3D orientation analysis in the breast cancer in mice model [31]. Representative multi-photon images of (**a**) normal and (**b**) tumor breast tissues; 3D reconstructions of (**c**) normal and (**f**) tumor multi-photon images with combined SHG and TPEF signals; Representative collagen SHG intensity images of (**d**) normal and (**g**) tumor tissues; Representative 3D directional variance maps of (**e**) normal and (**h**) tumor tissues. (**i**) Mean and standard deviation of 3D directional variance assessed by two different window sizes, indicating that the collagen fibers are more aligned in tumor than in normal tissues. Scale bar in (**a**) and (**b**): 100 μm, otherwise: 50 μm; **, $p < 0.001$, *, $p < 0.05$. (Reprinted/adapted with permission from ref. [31])

combined with the synthetic progestogen, promegestone, elongated structures were formed with multiple cellular projections simulating side-branching [84] (Fig. 12.15a). E2 in combination with prolactin led to the appearance of budding structures, which were spoon-like shapes observed at the tip of the ducts [85] (Fig. 12.15a). They acquired SHG images of collagen fibers surrounding cell clusters, with 3D reconstructions combining cells and collagen fibers shown in Fig. 12.15b. 3D orientations of collagen fibers were calculated to acquire the voxel-wise 3D directional variance. Representative images (Fig. 12.15c) within each 3D stack are shown along with distribution histograms (Fig. 12.15d), corresponding to the region within 23 μm from the cell structure edge. Compared to treatments with the addition of prolactin or promegestone, the E2 alone group showed a relatively sharper θ orientation distribution (black), with peaks close to

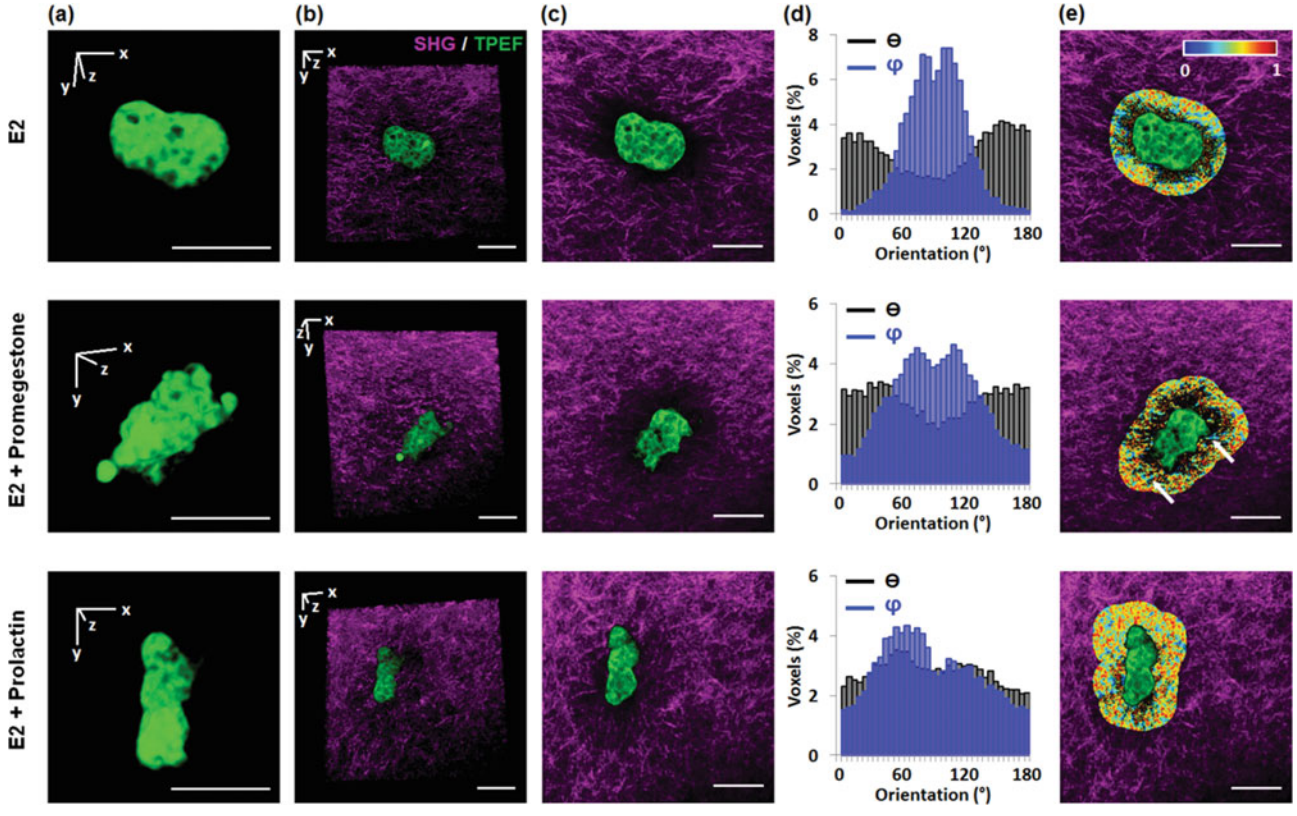

Fig. 12.15 Application of 3D orientation analysis in the study of hormone effects in engineered breast tissues [83]. (**a**) The 3D reconstructions of TPEF images of cell spheroids in response to different hormone treatments; (**b**) 3D reconstructions of engineered breast tissues including both cells and collagen fibers; (**c**) One representative frame from the 3D constructions; (**d**) Distribution histograms of 3D orientations under different hormone treatments; (**e**) The 3D directional variance maps of collagen fibers surrounding cell spheroids. Scale bar: 50 μm. (Reprinted/adapted with permission from ref. [83])

0° and 180°. These orientations features were consistent with the apparent directions of collagen fibers visualized in 2D and 3D images (Fig. 12.15b, c). Regarding the φ distributions, there was an even more dramatic difference among these groups. E2 alone treatment led to a single and sharp peak at ~90°, revealing that the majority of collagen fibers within this region were aligned primarily parallel to the optical sections. In contrast, there were relatively broader distributions for both θ and φ orientations in the prolactin and promegestone treatments, which revealed that collagen fibers were more randomly aligned in response to these treatments. 3D directional variance of collagen fibers was then acquired (Fig. 12.15e). E2 alone treatment showed bluer hues than the other two treatments, while E2 in combination with promegestone led to even redder hues (corresponding to a higher variance level) than E2 plus prolactin treatment. Interestingly, there were limited but clear blue hues at the tips of a few branches (as pointed by arrows in the E2 plus promegestone image), consistent with previous observations which indicated that collagen fibers were thickening and highly organized at the tip of the ducts [81, 86].

These differences as observed from color-coded variance maps (Fig. 12.16a), were further tested and validated by statistical analysis (Fig. 12.16d). The E2 alone treatment led to significantly lower mean directional variance than both the prolactin and promegestone groups, and the prolactin group showed a significantly lower directional variance relative to promegestone group. To demonstrate the sensitivity enhancement achieved by using 3D analysis, these results were compared with those acquired by two typical 2D analysis methods. In the first 2D approach (Fig. 12.16b), the entire 3D stack was projected along the z dimension, followed by 2D variance analysis within the 23 μm region from the cell structure edge. Although similar trends (Fig. 12.16e) were observed in the mean directional variance as for the 3D analysis, large standard deviations in the corresponding measurements were acquired, leading to non-significant differences among different treatments. The other 2D analysis approach is based on estimating the 2D directional variance frame-by-frame (Fig. 12.16c). As can be seen from the analysis results (Fig. 12.16f), there were subtle differences in the mean values among different treatments, and as in the previous case no statistical differences were identified. These comparison results confirmed an enhanced sensitivity by means of true 3D analysis versus 2D approaches.

12.4 Summary and Perspectives

In this chapter, recent advances in quantitative imaging of both the cellular metabolism and collagen fiber organization within biological tissues relying on endogenous sources of contrast are summarized. Regarding metabolism assessments, TPEF imaging of endogenous coenzymes NADH and FAD serves as a label-free, high-resolution tool that is able to assess cellular heterogeneity in a dynamic manner, important metabolic features that are not easily captured by conventional approaches. Assessing adipose tissue functions and identifying malignant lesions have been shown as examples of applications of such assessments. Moreover,

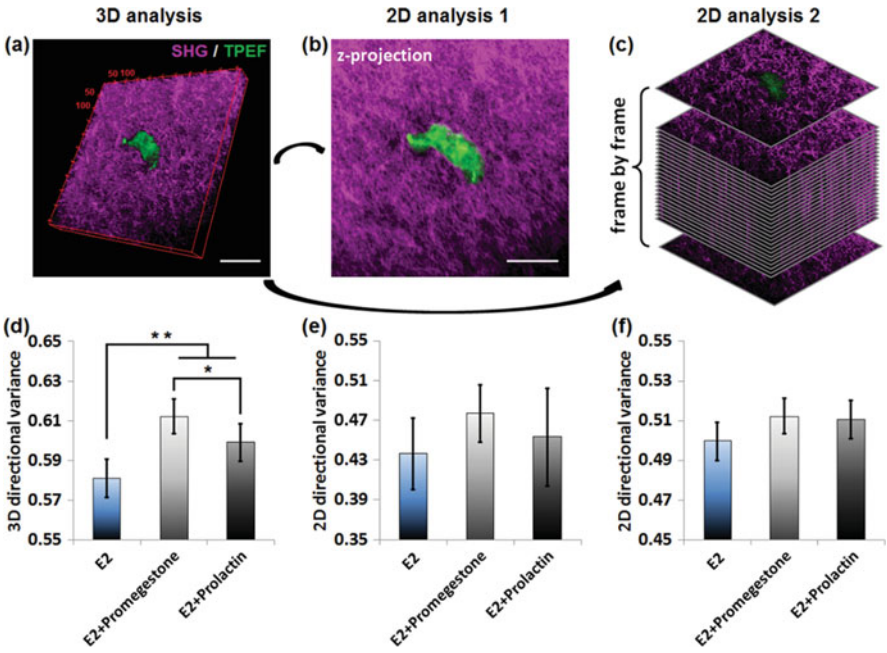

Fig. 12.16 3D directional variance analysis shows enhanced sensitivity compared with typical 2D analysis approaches [83]. (**a**) Schematic of 3D analysis approach. (**b**) Schematic of a typical 2D analysis approach, which projects the 3D stack into a 2D image along the z direction, followed by 2D variance calculation. (**c**) Schematic of another 2D analysis approach which quantifies the collagen fiber alignment frame-by-frame via 2D directional variance. Mean and standard deviation of analysis results corresponding to (**d**) 3D directional variance, (**e**) z-projection 2D analysis and (**f**) frame-by-frame 2D analysis. There are three samples under each hormone treatment, and totally nine stack images per treatment (three per sample) for 3D or 2D analysis. Scale bar: 50 μm *, $p < 0.05$; **, $p < 0.01$. (Reprinted/adapted with permission from ref. [83])

multi-parametric analysis was presented as a means to gain significant insights into not only the presence of metabolic changes but also the nature of the metabolic processes that are altered. Thus, we expect that TPEF imaging of endogenous contrast, along with multi-parametric, quantitative analysis, will be an important new platform for characterizing metabolic activity in physiologically relevant contexts (that is, live cells and tissues) that can be used to understand and detect diseases or monitor the metabolic impact of new treatments.

Quantifications of collagen fiber organization have been developed for 2D and 3D analysis, with the latter having improved sensitivity and accuracy since they capture the detailed collagen fiber arrangements within tissues. A lower 3D directional variance was observed in both examples of cancer tissues compared to healthy tissues discussed in this chapter. However, it is important to note that changes in collagen organization are likely dependent on cancer type. For example, Birk et al. examined human colon biopsies with SHG imaging, and the anisotropy parameter

generated by the SHG intensity at orthogonal polarizations indicated that the normal tissue consists of more aligned collagen fibers than high-grade dysplasia tissues [87].

Despite the successes that have been achieved in high-resolution imaging and highly-accurate characterization of cellular metabolism respectively, few studies have reported a direct combination of these two aspects and applications in disease detection. Quantitative assessments of cells and extracellular matrix simultaneously could be an important future direction, providing not only complementary information regarding disease initiation and progression, but also insights into cell-matrix interactions, which ultimately determine tissue function.

Acknowledgments This study was supported by National Natural Science Foundation of China (61905214); the Zhejiang Provincial Natural Science Foundation of China (LR20F050001); the Fundamental Research Funds for the Central Universities (2019QNA5004); the National Institutes of Health (NIH R21EB019079 to I. G.; NIH R01AG056560 to K.P.Q); the American Cancer Society (RSG-09-174-01-CCE); the National Science Foundation (NSF 1846853); the Avon Foundation (02-2011-095); Tufts University (Tufts Collaborates awards); Raymond & Beverly Sackler Convergence Lab; the Breast Cancer Research Foundation and the Alexander S. Onassis Foundation.

References

1. Geiger B, Bershadsky A, Pankov R, Yamada KM (2001) Transmembrane crosstalk between the extracellular matrix--cytoskeleton crosstalk. Nat Rev Mol Cell Biol 2:793–805
2. Egeblad M, Werb Z (2002) New functions for the matrix metalloproteinases in cancer progression. Nat Rev Cancer 2:161–174
3. Abbott NJ, Ronnback L, Hansson E (2006) Astrocyte-endothelial interactions at the blood-brain barrier. Nat Rev Neurosci 7:41–53
4. Discher DE, Mooney DJ, Zandstra PW (2009) Growth factors, matrices, and forces combine and control stem cells. Science 324:1673–1677
5. Frisch SM, Francis H (1994) Disruption of epithelial cell-matrix interactions induces apoptosis. J Cell Biol 124:619–626
6. Zamir E, Katz M, Posen Y, Erez N, Yamada KM, Katz BZ et al (2000) Dynamics and segregation of cell-matrix adhesions in cultured fibroblasts. Nat Cell Biol 2:191–196
7. Butcher DT, Alliston T, Weaver VM (2009) A tense situation: forcing tumour progression. Nat Rev Cancer 9:108–122
8. DeBerardinis RJ, Thompson CB (2012) Cellular metabolism and disease: what do metabolic outliers teach us? Cell 148:1132–1144
9. Slack MD, Martinez ED, Wu LF, Altschuler SJ (2008) Characterizing heterogeneous cellular responses to perturbations. Proc Natl Acad Sci U S A 105:19306–19311
10. Golman K, Zandt RI, Lerche M, Pehrson R, Ardenkjaer-Larsen JH (2006) Metabolic imaging by hyperpolarized 13C magnetic resonance imaging for in vivo tumor diagnosis. Cancer Res 66:10855–10860
11. Marchal G, Serrati C, Rioux P, Petit-Taboue MC, Viader F, de la Sayette V et al (1993) PET imaging of cerebral perfusion and oxygen consumption in acute ischaemic stroke: relation to outcome. Lancet 341:925–927
12. Hiller K, Metallo CM, Kelleher JK, Stephanopoulos G (2010) Nontargeted elucidation of metabolic pathways using stable-isotope tracers and mass spectrometry. Anal Chem 82:6621–6628
13. Shestov AA, Lee SC, Nath K, Guo L, Nelson DS, Roman JC et al (2016) (13)C MRS and LC-MS flux analysis of tumor intermediary metabolism. Front Oncol 6:135

14. Hung YP, Albeck JG, Tantama M, Yellen G (2011) Imaging cytosolic NADH-NAD(+) redox state with a genetically encoded fluorescent biosensor. Cell Metab 14:545–554
15. Denk W, Strickler JH, Webb WW (1990) Two-photon laser scanning fluorescence microscopy. Science 248:73–76
16. Georgakoudi I, Quinn KP (2012) Optical imaging using endogenous contrast to assess metabolic state. Annu Rev Biomed Eng 14:351–367
17. Huang S, Heikal AA, Webb WW (2002) Two-photon fluorescence spectroscopy and microscopy of NAD(P)H and flavoprotein. Biophys J 82:2811–2825
18. Stringari C, Cinquin A, Cinquin O, Digman MA, Donovan PJ, Gratton E (2011) Phasor approach to fluorescence lifetime microscopy distinguishes different metabolic states of germ cells in a live tissue. Proc Natl Acad Sci U S A 108:13582–13587
19. Skala MC, Riching KM, Gendron-Fitzpatrick A, Eickhoff J, Eliceiri KW, White JG et al (2007) In vivo multiphoton microscopy of NADH and FAD redox states, fluorescence lifetimes, and cellular morphology in precancerous epithelia. Proc Natl Acad Sci U S A 104:19494–19499
20. Kolenc OI, Quinn KP (2019) Evaluating cell metabolism through autofluorescence imaging of NAD(P)H and FAD. Antioxid Redox Signal 30:875–889
21. Lu P, Takai K, Weaver VM, Werb Z (2011) Extracellular matrix degradation and remodeling in development and disease. Cold Spring Harb Perspect Biol 3:a005058
22. Zipfel WR, Williams RM, Webb WW (2003) Nonlinear magic: multiphoton microscopy in the biosciences. Nat Biotechnol 21:1369–1377
23. Campagnola PJ, Loew LM (2003) Second-harmonic imaging microscopy for visualizing biomolecular arrays in cells, tissues and organisms. Nat Biotechnol 21:1356–1360
24. Brown E, McKee T, diTomaso E, Pluen A, Seed B, Boucher Y et al (2003) Dynamic imaging of collagen and its modulation in tumors in vivo using second-harmonic generation. Nat Med 9:796–800
25. Bayan C, Levitt JM, Miller E, Kaplan D, Georgakoudi I (2009) Fully automated, quantitative, noninvasive assessment of collagen fiber content and organization in thick collagen gels. J Appl Phys 105:102042
26. Robertson C, Ikemura K, Krasieva TB, George SC (2013) Multiscale analysis of collagen microstructure with generalized image correlation spectroscopy and the detection of tissue prestress. Biomaterials 34:6127–6132
27. Schriefl AJ, Zeindlinger G, Pierce DM, Regitnig P, Holzapfel GA (2012) Determination of the layer-specific distributed collagen fibre orientations in human thoracic and abdominal aortas and common iliac arteries. J R Soc Interface 9:1275–1286
28. Altendorf H, Decenciere E, Jeulin D, De Sa Peixoto P, Deniset-Besseau A, Angelini E et al (2012) Imaging and 3D morphological analysis of collagen fibrils. J Microsc 247:161–175
29. Napadow VJ, Chen Q, Mai V, So PT, Gilbert RJ (2001) Quantitative analysis of three-dimensional-resolved fiber architecture in heterogeneous skeletal muscle tissue using nmr and optical imaging methods. Biophys J 80:2968–2975
30. Liu Z, Quinn KP, Speroni L, Arendt L, Kuperwasser C, Sonnenschein C et al (2015) Rapid three-dimensional quantification of voxel-wise collagen fiber orientation. Biomed Opt Express 6:2294–2310
31. Liu Z, Pouli D, Sood D, Sundarakrishnan A, Hui Mingalone CK, Arendt LM et al (2017) Automated quantification of three-dimensional organization of fiber-like structures in biological tissues. Biomaterials 116:34–47
32. Mayevsky A, Chance B (1982) Intracellular oxidation-reduction state measured in situ by a multichannel fiber-optic surface fluorometer. Science 217:537–540
33. Chance B, Schoener B, Oshino R, Itshak F, Nakase Y (1979) Oxidation-reduction ratio studies of mitochondria in freeze-trapped samples. NADH and flavoprotein fluorescence signals. J Biol Chem 254:4764–4771
34. Rice WL, Kaplan DL, Georgakoudi I (2010) Two-photon microscopy for non-invasive, quantitative monitoring of stem cell differentiation. PLoS One 5:e10075

35. Quistorff B, Haselgrove JC, Chance B (1985) High spatial resolution readout of 3-D metabolic organ structure: an automated, low-temperature redox ratio-scanning instrument. Anal Biochem 148:389–400
36. Saks VA, Veksler VI, Kuznetsov AV, Kay L, Sikk P, Tiivel T et al (1998) Permeabilized cell and skinned fiber techniques in studies of mitochondrial function in vivo. Mol Cell Biochem 184:81–100
37. Perham RN (1991) Domains, motifs, and linkers in 2-oxo acid dehydrogenase multienzyme complexes: a paradigm in the design of a multifunctional protein. Biochemistry 30:8501–8512
38. Brautigam CA, Chuang JL, Tomchick DR, Machius M, Chuang DT (2005) Crystal structure of human dihydrolipoamide dehydrogenase: NAD+/NADH binding and the structural basis of disease-causing mutations. J Mol Biol 350:543–552
39. Shiino A, Haida M, Beauvoit B, Chance B (1999) Three-dimensional redox image of the normal gerbil brain. Neuroscience 91:1581–1585
40. Stuntz E, Gong Y, Sood D, Liaudanskaya V, Pouli D, Quinn KP et al (2017) Endogenous two-photon excited fluorescence imaging characterizes neuron and astrocyte metabolic responses to manganese toxicity. Sci Rep 7:1041
41. Liu Z, Pouli D, Alonzo CA, Varone A, Karaliota S, Quinn KP et al (2018) Mapping metabolic changes by noninvasive, multiparametric, high-resolution imaging using endogenous contrast. Sci Adv 4:eaap9302
42. Quinn KP, Sridharan GV, Hayden RS, Kaplan DL, Lee K, Georgakoudi I (2013) Quantitative metabolic imaging using endogenous fluorescence to detect stem cell differentiation. Sci Rep 3:3432
43. Varone A, Xylas J, Quinn KP, Pouli D, Sridharan G, McLaughlin-Drubin ME et al (2014) Endogenous two-photon fluorescence imaging elucidates metabolic changes related to enhanced glycolysis and glutamine consumption in precancerous epithelial tissues. Cancer Res 74:3067–3075
44. Vergen J, Hecht C, Zholudeva LV, Marquardt MM, Hallworth R, Nichols MG (2012) Metabolic imaging using two-photon excited NADH intensity and fluorescence lifetime imaging. Microsc Microanal 18:761–770
45. Blinova K, Levine RL, Boja ES, Griffiths GL, Shi ZD, Ruddy B et al (2008) Mitochondrial NADH fluorescence is enhanced by complex I binding. Biochemistry 47:9636–9645
46. Bower AJ, Marjanovic M, Zhao Y, Li J, Chaney EJ, Boppart SA (2017) Label-free in vivo cellular-level detection and imaging of apoptosis. J Biophotonics 10:143–150
47. Lakowicz JR, Szmacinski H, Nowaczyk K, Johnson ML (1992) Fluorescence lifetime imaging of free and protein-bound NADH. Proc Natl Acad Sci U S A 89:1271–1275
48. Digman MA, Caiolfa VR, Zamai M, Gratton E (2008) The phasor approach to fluorescence lifetime imaging analysis. Biophys J 94:L14–L16
49. Pouli D, Balu M, Alonzo CA, Liu Z, Quinn KP, Rius-Diaz F et al (2016) Imaging mitochondrial dynamics in human skin reveals depth-dependent hypoxia and malignant potential for diagnosis. Sci Transl Med 8:367ra169
50. Xylas J, Quinn KP, Hunter M, Georgakoudi I (2012) Improved Fourier-based characterization of intracellular fractal features. Opt Express 20:23442–23455
51. Xylas J, Varone A, Quinn KP, Pouli D, McLaughlin-Drubin ME, Thieu HT et al (2015) Noninvasive assessment of mitochondrial organization in three-dimensional tissues reveals changes associated with cancer development. Int J Cancer 136:322–332
52. Alonzo CA, Karaliota S, Pouli D, Liu Z, Karalis KP, Georgakoudi I (2016) Two-photon excited fluorescence of intrinsic fluorophores enables label-free assessment of adipose tissue function. Sci Rep 6:31012
53. Wu J, Bostrom P, Sparks LM, Ye L, Choi JH, Giang AH et al (2012) Beige adipocytes are a distinct type of thermogenic fat cell in mouse and human. Cell 150:366–376
54. Guerra C, Koza RA, Yamashita H, Walsh K, Kozak LP (1998) Emergence of brown adipocytes in white fat in mice is under genetic control. Effects on body weight and adiposity. J Clin Invest 102:412–420

55. Nedergaard J, Cannon B (2013) UCP1 mRNA does not produce heat. Biochim Biophys Acta 1831:943–949
56. Datta R, Alfonso-Garcia A, Cinco R, Gratton E (2015) Fluorescence lifetime imaging of endogenous biomarker of oxidative stress. Sci Rep 5:9848
57. Harms M, Seale P (2013) Brown and beige fat: development, function and therapeutic potential. Nat Med 19:1252–1263
58. Giedt RJ, Yang C, Zweier JL, Matzavinos A, Alevriadou BR (2012) Mitochondrial fission in endothelial cells after simulated ischemia/reperfusion: role of nitric oxide and reactive oxygen species. Free Radic Biol Med 52:348–356
59. Liu X, Hajnoczky G (2011) Altered fusion dynamics underlie unique morphological changes in mitochondria during hypoxia-reoxygenation stress. Cell Death Differ 18:1561–1572
60. Ghose P, Park EC, Tabakin A, Salazar-Vasquez N, Rongo C (2013) Anoxia-reoxygenation regulates mitochondrial dynamics through the hypoxia response pathway, SKN-1/Nrf, and stomatin-like protein STL-1/SLP-2. PLoS Genet 9:e1004063
61. Kim JW, Tchernyshyov I, Semenza GL, Dang CV (2006) HIF-1-mediated expression of pyruvate dehydrogenase kinase: a metabolic switch required for cellular adaptation to hypoxia. Cell Metab 3:177–185
62. Rambold AS, Kostelecky B, Elia N, Lippincott-Schwartz J (2011) Tubular network formation protects mitochondria from autophagosomal degradation during nutrient starvation. Proc Natl Acad Sci U S A 108:10190–10195
63. Amaravadi R, Kimmelman AC, White E (2016) Recent insights into the function of autophagy in cancer. Genes Dev 30:1913–1930
64. Brooks MD, Burness ML, Wicha MS (2015) Therapeutic implications of cellular heterogeneity and plasticity in breast cancer. Cell Stem Cell 17:260–271
65. Quinn KP, Georgakoudi I (2013) Rapid quantification of pixel-wise fiber orientation data in micrographs. J Biomed Opt 18:046003
66. Sivaguru M, Durgam S, Ambekar R, Luedtke D, Fried G, Stewart A et al (2010) Quantitative analysis of collagen fiber organization in injured tendons using Fourier transform-second harmonic generation imaging. Opt Express 18:24983–24993
67. Bancelin S, Nazac A, Ibrahim BH, Dokladal P, Decenciere E, Teig B et al (2014) Determination of collagen fiber orientation in histological slides using Mueller microscopy and validation by second harmonic generation imaging. Opt Express 22:22561–22574
68. Quinn KP, Sullivan KE, Liu Z, Ballard Z, Siokatas C, Georgakoudi I et al (2016) Optical metrics of the extracellular matrix predict compositional and mechanical changes after myocardial infarction. Sci Rep 6:35823
69. Ott HC, Matthiesen TS, Goh SK, Black LD, Kren SM, Netoff TI et al (2008) Perfusion-decellularized matrix: using nature's platform to engineer a bioartificial heart. Nat Med 14:213–221
70. Quinn KP, Golberg A, Broelsch GF, Khan S, Villiger M, Bouma B et al (2015) An automated image processing method to quantify collagen fibre organization within cutaneous scar tissue. Exp Dermatol 24:78–80
71. Hui Mingalone CK, Liu Z, Hollander JM, Garvey KD, Gibson AL, Banks RE et al (2018) Bioluminescence and second harmonic generation imaging reveal dynamic changes in the inflammatory and collagen landscape in early osteoarthritis. Lab Investig 98:656–669
72. Hughes LC, Archer CW, Ap Gwynn I (2005) The ultrastructure of mouse articular cartilage: collagen orientation and implications for tissue functionality. A polarised light and scanning electron microscope study and review. Eur Cell Mater 9:68–84
73. Lau TY, Ambekar R, Toussaint KC (2012) Quantification of collagen fiber organization using three-dimensional Fourier transform-second-harmonic generation imaging. Opt Express 20:21821–21832
74. Schnelldorfer T, Ware AL, Sarr MG, Smyrk TC, Zhang L, Qin R et al (2008) Long-term survival after pancreatoduodenectomy for pancreatic adenocarcinoma: is cure possible? Ann Surg 247:456–462

75. Li D, Xie K, Wolff R, Abbruzzese JL (2004) Pancreatic cancer. Lancet 363:1049–1057
76. Whatcott CJ, Diep CH, Jiang P, Watanabe A, LoBello J, Sima C et al (2015) Desmoplasia in primary tumors and metastatic lesions of pancreatic cancer. Clin Cancer Res 21:3561–3568
77. Provenzano PP, Eliceiri KW, Campbell JM, Inman DR, White JG, Keely PJ (2006) Collagen reorganization at the tumor-stromal interface facilitates local invasion. BMC Med 4:38
78. Provenzano PP, Inman DR, Eliceiri KW, Knittel JG, Yan L, Rueden CT et al (2008) Collagen density promotes mammary tumor initiation and progression. BMC Med 6:11
79. Ambekar R, Lau TY, Walsh M, Bhargava R, Toussaint KC Jr (2012) Quantifying collagen structure in breast biopsies using second-harmonic generation imaging. Biomed Opt Express 3:2021–2035
80. Krause S, Maffini MV, Soto AM, Sonnenschein C (2010) The microenvironment determines the breast cancer cells' phenotype: organization of MCF7 cells in 3D cultures. BMC Cancer 10:263
81. Dhimolea E, Maffini MV, Soto AM, Sonnenschein C (2010) The role of collagen reorganization on mammary epithelial morphogenesis in a 3D culture model. Biomaterials 31:3622–3630
82. Weigelt B, Bissell MJ (2008) Unraveling the microenvironmental influences on the normal mammary gland and breast cancer. Semin Cancer Biol 18:311–321
83. Liu Z, Speroni L, Quinn KP, Alonzo C, Pouli D, Zhang Y et al (2018) 3D organizational mapping of collagen fibers elucidates matrix remodeling in a hormone-sensitive 3D breast tissue model. Biomaterials 179:96–108
84. Sternlicht MD (2006) Key stages in mammary gland development: the cues that regulate ductal branching morphogenesis. Breast Cancer Res 8:201
85. Brisken C (2002) Hormonal control of alveolar development and its implications for breast carcinogenesis. J Mammary Gland Biol Neoplasia 7:39–48
86. Barnes C, Speroni L, Quinn KP, Montevil M, Saetzler K, Bode-Animashaun G et al (2014) From single cells to tissues: interactions between the matrix and human breast cells in real time. PLoS One 9:e93325
87. Birk JW, Tadros M, Moezardalan K, Nadyarnykh O, Forouhar F, Anderson J et al (2014) Second harmonic generation imaging distinguishes both high-grade dysplasia and cancer from normal colonic mucosa. Dig Dis Sci 59:1529–1534

In Vivo Flow Cytometry

13

Xi Zhu, Qi Liu, Yuting Fu, Fuli Zhang, Zhengqin Gu, Bobo Gu, and Xunbin Wei

13.1 Introduction

Hematologic examination that looks for abnormalities in the numbers and/or structure of cells in blood circulation is widely applied in the diagnosis of various types of diseases. Current methods for blood cell analysis require obtaining blood from patients and animals followed by secondary assays, such as hematology analysis and flow cytometry. However, the random sampling of several milliliters of blood may underestimate the true levels of indicators, especially for rare cells, such as circulating tumor cells (CTCs), including the following:

1. The preparation of blood samples may lead to a considerable loss of cells [1].
2. The sampling volume is too limited to acquire enough cells.

X. Zhu · Q. Liu · Y. Fu · F. Zhang
State Key Laboratory of Oncogenes and Related Genes, Shanghai Cancer Institute, Med-X Research Institute and School of Biomedical Engineering, Shanghai Jiao Tong University, Shanghai, China

Z. Gu
Department of Urology, Xinhua Hospital, School of Medicine, Shanghai Jiao Tong University, Shanghai, China

B. Gu
School of Biomedical Engineering, Shanghai Jiao Tong University, Shanghai, China

X. Wei (✉)
State Key Laboratory of Oncogenes and Related Genes, Shanghai Cancer Institute, Med-X Research Institute and School of Biomedical Engineering, Shanghai Jiao Tong University, Shanghai, China

Biomedical Engineering Department, Peking University, Beijing, China
e-mail: xwei01@sjtu.edu.cn

X. Wei, B. Gu (eds.), *Optical Imaging in Human Disease and Biological Research*, Advances in Experimental Medicine and Biology 1355,
https://doi.org/10.1007/978-981-15-7627-0_13

3. The cells may enter the blood in a noncontinuous way, and the circulating cells may not be homogenously distributed, so a random single sample is not representative [2].
4. Rare cells are difficult to isolate because they are mixed with billions of erythrocytes and millions of leukocytes.

How can we solve these problems and decrease false-negative results for rare circulating cell detection? Drawing blood from tumor-draining vessels could increase the blood volume for evaluating CTCs [3]. However, it is not practical for clinical screening use because of the location of the tumor. Therefore, a noninvasive technique that can continuously monitor CTCs within a large blood volume is needed to realize true "liquid biopsy." In vivo flow cytometry (IVFC), which was first reported by Lin et al. in 2004, allows circulating cells to be detected in vivo [4]. This technique is expected to be used in the clinic with many innovative setups that have been developed in recent years. The purpose of this chapter is to introduce the principles and applications of various types of IVFC technologies.

13.2 Principle of Fluorescence-Based IVFC

The first generation of IVFC technique was developed based on fluorescence [4, 5]. Such strategies made use of the principle of conventional flow cytometry in which fluorescently labeled cells are suspended in fluid and pass one by one through a set of lasers. Light scattered from the cells is detected by a photomultiplier tube (PMT) to determine its characteristics and function. Fluorescence IVFC utilizes blood flow instead of flow fluid, and fluorescently labeled cells circulating in the blood can be detected in vivo (Fig. 13.1a). Figure 13.1b shows a schematic of the fluorescence-based IVFC setup. Animals are anesthetized and fixed on the sample stage with their ear adhered to a microscope slide. The excitation laser is reshaped to a slit by a cylindrical lens and focused by a microscope objective. Blood vessels are

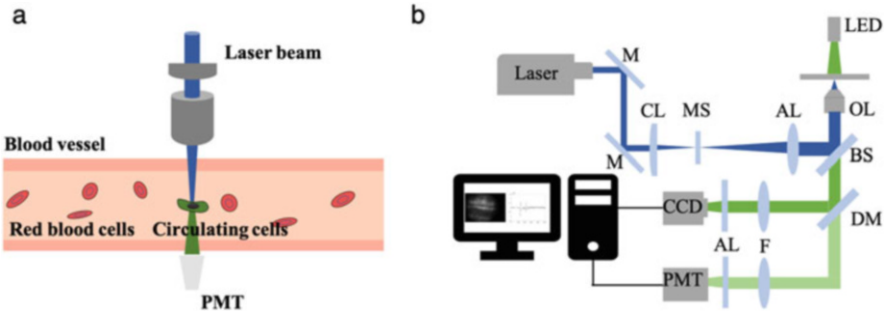

Fig. 13.1 The principle (**a**) and a schematic (**b**) of fluorescence IVFC. *M* mirror, *F* filter, *AL* achromatic lens, *BS* beam splitter, *DM* dichroic mirror, *CCD* charge-coupled device, *CL* cylindrical lens, *DAQ* data acquisition, *MS* mechanical slit, *OL* objective lens

lighted by a 532 nm LED that provides ideal contrast due to hemoglobin absorption. The focused laser slit directs light across the selected blood vessel. When a fluorescently labeled cell passes through the slit, the emitted fluorescence is detected by a PMT, and signals are sampled by a data acquisition card at a rate of 100 kHz. Signals are easily identified as high peaks compared to the background noise. Fluorescence-based IVFC has now been extended to six channels that can detect most of the fluorophores in the visible spectrum and the near-infrared spectrum [6].

Multiphoton microscopy-based IVFC was developed to improve the penetration depth of IVFC and acquire morphology information of circulating cells. He et al. detected CTCs directly via two-photon microscopy by applying one-dimensional line scanning rather than two-dimensional scanning to enhance the speed of date acquisition [7]. Zhong et al. established and modified a two-photon excitation system to form two excitation regions [8]. Rather than detecting circulating cells in anesthetized animals, Chang et al. used a two-photon fluorescence fiber that can be directly inserted into the blood vessel to monitor circulating cells in awake mice [9]. The spatial information would be lost with one-dimensional line scanning. By integrating standard two-photon microscopy with an optical phase-locked ultrasound lens (OPLUL), Kong et al. improved the cross-sectional frame rate to 2 kHz to precisely capture the morphological information of cells [10].

Other advanced IVFC technologies, such as retinal flow cytometry (RFC) [11], computer vision IVFC (CV-IVFC) [12] and diffuse fluorescence in vivo flow cytometry (DiFC) [13], have been proposed and demonstrated to increase the sampling volume to detect lower-abundance target cell populations. By circularly scanning a laser spot quickly around the optic nerve head, RFC could simultaneously detect five pairs of arteries and veins in the mouse eye and yielded a count rate approximately five times higher than that achieved by the original IVFC strategy in the ear. By using widefield fluorescence imaging and an automated computer vision algorithm, CV-IVFC could enumerate and track circulating cells in an approximately 5×5 mm^2 area in the ear of a mouse in vivo. It could sample about 10–15μL of blood per minute [14], which is an order of magnitude greater than microscopy-based IVFC. By detecting diffuse fluorescent light from relatively large blood vessels in vivo, DiFC could interrogate relatively large bulk tissue volumes, and the sensitivity was improved by several orders of magnitude compared to previous approaches.

13.3 Fluorescent Labeling and Applications of Fluorescence-Based IVFC

Cell dynamics in the circulation could be monitored by IVFC after labeling with extrinsic fluorescent dyes or fluorescent proteins, such as Vybrant DiD, DiR, FITC, and GFP [4, 5, 15, 16]. For example, Spikins et al. applied IVFC to investigate the molecular mechanism of leukemia cell homing. They blocked CXCR4 with stromal-cell-derived factor 1 (SDF-1) or AMD3100. Then, they labeled Nalm-6 cells (an acute lymphoblastic leukemia cell line) with DiD and injected the cells into

mice via tail injection. They found out that Nalm-6 cells remained in the peripheral circulation, which indicated that the homing of Nalm-6 cells was inhibited by blocking SDF-1 [17]. This study demonstrated that IVFC was helpful for developing molecular targeted drugs for cancer.

IVFC is most widely used in monitoring cancer progression. In this case, cells should be labeled with fluorescent proteins and subcutaneously or orthotopically injected into the mouse, and then the metastasis and treatment efficacy can be monitored by IVFC via changes in CTC numbers [18–20]. For instance, Fan et al. explored CTC dynamics in mice before and after tumor resection. They used the HCCLM3 cell line to establish a lung cancer mouse model with high lung metastatic potential. They first evaluated whether a subcutaneous model or orthotopic model could describe the CTC dynamics in clinical situations more accurately. The results showed that CTCs increased notably with increasing lung tumor size in an orthotopic model. However, in the subcutaneous model, CTC numbers remained at a relatively low level regardless of the increase in tumor size. Hence, the orthotopic model was chosen in further studies. By using IVFC, they found out that CTCs decreased significantly following tumor resection [18].

Circulating cells can also be labeled by directly targeting specific cell surface receptors using fluorophores conjugated with antibodies and detected by IVFC. For example, white blood cells in the circulation could be labeled using CD45 monoclonal antibody injected via the tail vein [4]. Hematopoietic stem cells could be labeled using antibodies targeting c-kit and sca-1 in vivo [15].

Researchers also used endogenous contrast to detect target cells by IVFC. Zeng et al. identified white blood cells by using two-photon excited NADH signals [21]. Li et al. used tryptophan for intrinsic contrast in a two-photon technique to monitor leukocyte reactions during inflammation [22]. In vivo photoacoustic flow cytometry using melanin to provide a high-sensitivity endogenous contrast will be discussed below.

IVFC has also been applied in nanoparticle tracking. Wei et al. demonstrated that IVFC could detect nanoparticle concentration by identifying the amplitude of the baseline (Fig. 13.2a–e) [23]. If the nanoparticles form aggregates, IVFC would detect pulse-like signals (Fig. 13.2d, e). By monitoring the different sizes of nanoparticles, they revealed that nanoparticles with smaller sizes could stay longer in circulation. Moreover, Polyethylene glycol (PEG)-modification could reduce the aggregation of nanoparticles and prolong their circulating time. The abilities of nanoparticles with different modifications to target CTCs in the circulation were also detected by double-channel IVFC [24–26]. For example, Zhang et al. used double-channel IVFC to investigate the CTC-targeting ability of PSN (P-selectin targeting peptide)-modified micelles. CFSE-labeled MDA-MB-231 cells and BODIPY-labeled unmodified micelles, PSN-modified micelles or unmodified micelles were injected sequentially into the mice via tail injection. When CTCs were recognized and captured by micelles, IVFC detected double-positive signals (Fig. 13.3a–d). After injection of unmodified micelles, IVFC detected 3 ± 1 double-positive signals in 1 h (Fig. 13.3a, b), while after injection of PSN-modified micelles, 18 ± 8 double-positive signals were detected in 1 h (Fig. 13.3c, d). The results

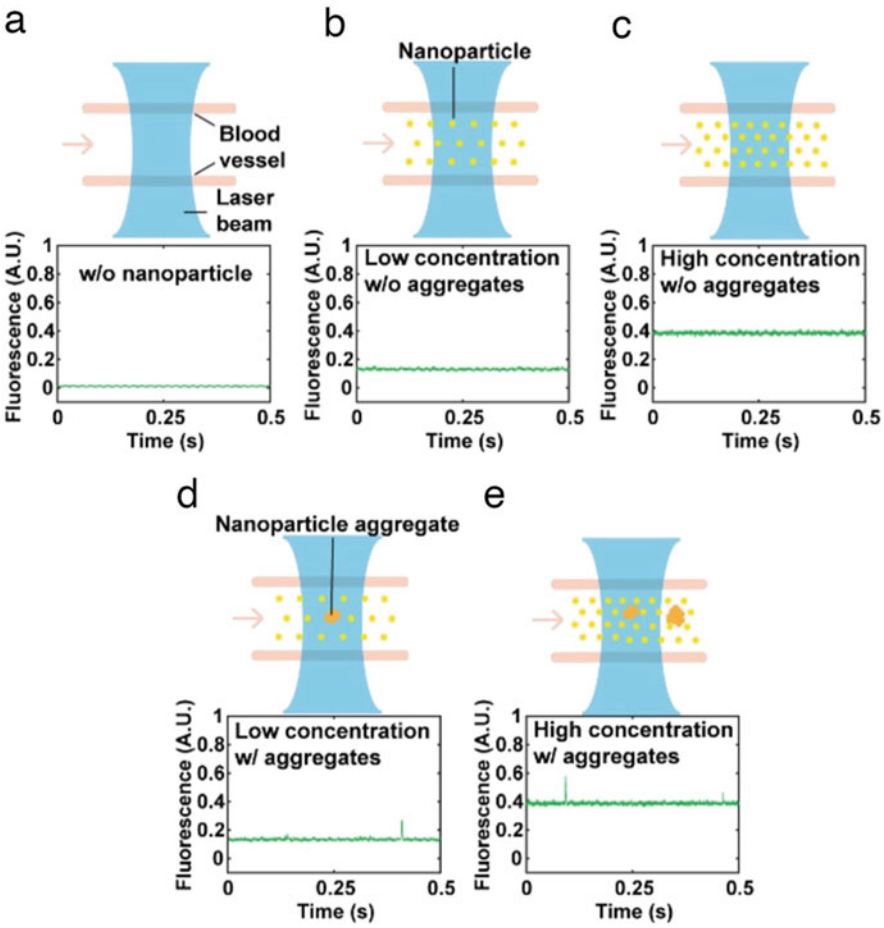

Fig. 13.2 Nanoparticle concentration and aggregates detected by IVFC. (**a**) Baseline signal detected by IVFC from blood without nanoparticles. (**b**) Baseline signal detected by IVFC from low-concentration nanoparticles. (**c**) Baseline signal detected by IVFC from high-concentration nanoparticles. (**d**) Baseline signal detected by IVFC from low-concentration nanoparticles with nanoparticle aggregates. (**e**) Baseline signal detected by IVFC from high-concentration nanoparticles with nanoparticle aggregates. *A.U.* arbitrary unit. (Reused with permission from [23])

showed that the PSN-modified micelles captured CTCs more efficiently than unmodified micelles.

Recent findings have shown that CTC clusters present up to 50-fold increased metastatic potential compared with single CTCs [27]. Hence, the dynamic CTC clusters may reflect metastasis better than single CTCs. Suo et al. proposed to identify CTC clusters by their multiple peak signal patterns on IVFC (Fig. 13.4a, b). The average time width of CTC clusters was significantly larger than that of single CTCs (Fig. 13.4c). They investigated the dynamics of CTC clusters in a liver

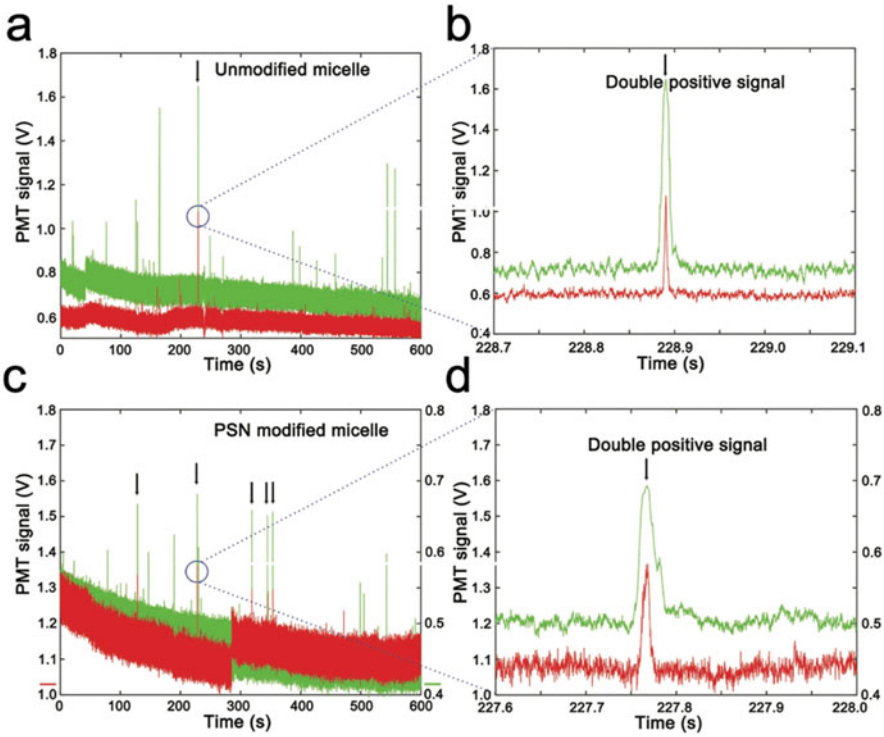

Fig. 13.3 PSN-modified micelles capture CTCs in vivo. Real-time monitoring of the interaction of breast cancer CTCs and unmodified micelles (**a**) and PSN-modified micelles (**c**) by IVFC. The double-positive signal represents CTCs recognized and captured by micelles. (**b**, **d**) Augmented double-positive signal. (Reused with permission from [24])

cancer model and a prostate cancer model. The results showed that the proportion of CTC clusters in total CTC events reached 27.7 ± 5.3% and 36.7 ± 7.2% at the late stage of liver cancer and prostate cancer, respectively.

In addition, with the improvements mentioned above, IVFC has acquired greater potential to be applied to detect a wider range of rare cells in in vivo biological or clinical models. For example, RFC can be applicable for the simultaneous detection of multiple cell populations in fundus examination by taking advantage of the transparent media of the eye. In addition to cell counting, CV-IVFC can also reconstruct the cell trajectory, which may be applied to automatic recognition of in vivo homing and docking events in the future. DiFC also has significant potential utility in a wide range of applications. In mice, DiFC has been used for multiple myeloma (MM) and mesenchymal stem cell (MSC) detection in the hind leg or tail [28]. In humans, DiFC was theoretically used to probe superficial blood vessels in the forearm or wrist.

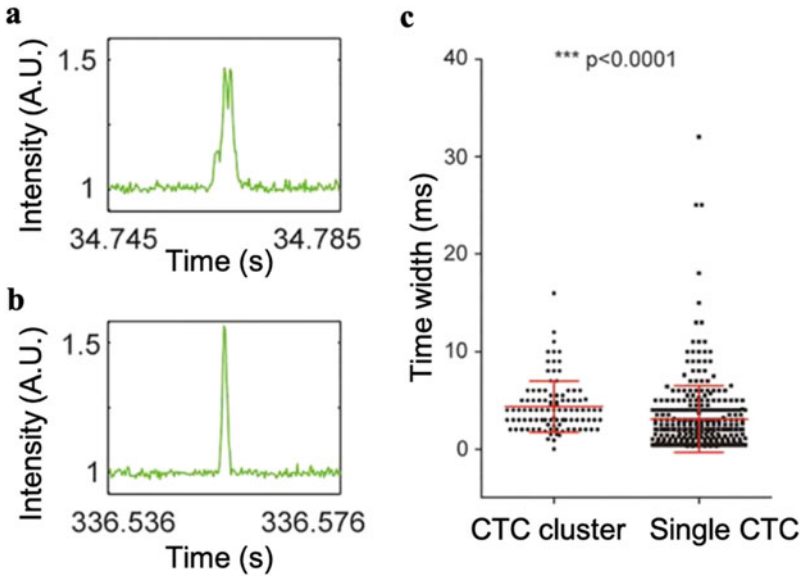

Fig. 13.4 Signal patterns of CTC clusters (**a**) and single CTCs (**b**) detected by IVFC. (**c**) The time width of multipeak signals and single-peak signals. (Reused with permission from [1])

13.4 Sensitivity of Fluorescence-Based IVFC

Ex vivo labeling by nonspecific dyes, such as CFSE, DiD and CellTrace, produces the highest number of fluorophores per cell. The efficiency of fluorescent proteins and direct antibody labeling may depend on the type of cell lines, transfection efficiency, probe binding efficiency, receptor density, etc. [29]. Lin et al. previously reported that the lower limit of fluorophores per cell for a Cy5.5-conjugated antibody for IVFC detection is 10^3 [30].

CTC counts detected by IVFC over time t are given by the following formula:

$$N = V_s \times P_d \times C_s \tag{13.1}$$

where V_s is the blood volume sampled by IVFC per minute, P_d is the proportion of cells that can be detected by IVFC, and C_s is the concentration of the target cells in 1 mL of blood. V_s is different for different IVFC methods. For microscopy-based IVFC, V_s ranges from 0.1 to 1 L/min; for CV-IVFC, V_s ranges from 1 to 10 L/min; for DiFC, V_s ranges from 10 to 100 L/min. P_d is determined by factors such as the fluorophore concentration.

13.5 Principle of Photoacoustic IVFC

In vivo flow cytometry can also be achieved based on the photoacoustic effect, namely, photoacoustic flow cytometry (PAFC). For the photoacoustic effect, light absorption of molecules and cells in biological tissue can lead to a temperature increase in endogenous or exogenous structures. The thermal expansion of heated zones induces a transient thermoelastic expansion leading to the generation of acoustic waves detected by ultrasonic transducers [31]. In PAFC, a high-frequency pulsed laser is shaped and focused by optical elements. A strip of light spot is formed on the orthogonal surface of the blood vessel. When molecules and cells with endogenous or exogenous contrast pass through the light spot, they are excited to generate photoacoustic waves. By analyzing the collected photoacoustic signals, real-time dynamic monitoring of the objects flowing through the blood can be conducted.

Compared with exogenous contrast agents, endogenous contrast agents have more potential for clinical diagnosis, and PAFC can achieve label-free detection of CTCs such as melanoma cells due to the high optical absorption of melanin [32]. Based on the analysis of the signal waveform, single cells and clusters can also be distinguished. To improve the sensitivity and specificity of PAFC, exogenous contrast agents such as magnetic nanoparticles can be used to label and enrich target cells [33]. Compared to the 500 μm penetration depth for fluorescence-based IVFC, PAFC benefiting from the weak acoustic attenuation in biological tissue can penetrate deeper tissues and monitor blood vessels up to a 1–3 mm depth, which meets the depth requirements for clinical diagnosis [34].

PAFC is usually divided into two modes, namely, optical resolution photoacoustic flow cytometry (OR-PAFC) and acoustic resolution photoacoustic flow cytometry (AR-PAFC). The design principle is shown in Fig. 13.5. Capillaries are distributed in the dermis, while arteries and veins are distributed in the

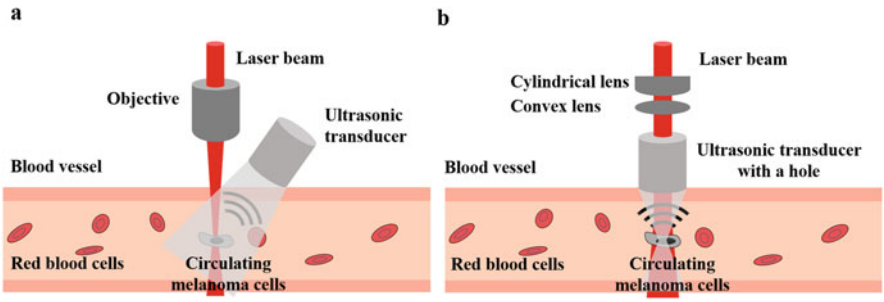

Fig. 13.5 Two kinds of designs for monitoring CTCs by PAFC. (**a**) The design of the optical resolution mode. The laser beam is focused on vessels, and the nonfocused transducer receives photoacoustic signals. (**b**) The design of the acoustic resolution mode. A nonfocused laser radiates on vessels, and a focused transducer detects photoacoustic signals. When a CTC passes through the laser slit, it generates ultrasonic waves by the photoacoustic effect, which are received by the transducer with a certain central frequency

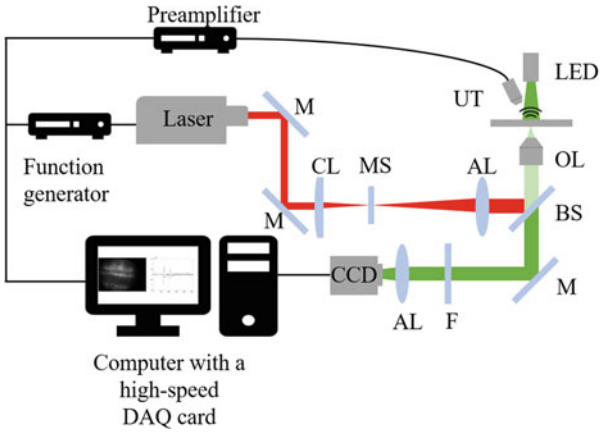

Fig. 13.6 General schematic of PAFC. *M* mirror, *F* filter, *AL* achromatic lens, *BS* beam splitter, *CCD* charge-coupled device, *CL* cylindrical lens, *DAQ* data acquisition, *MS* mechanical slit, *OL* objective lens, *UT* ultrasonic transducer

subcutaneous tissue. Typically, the irradiated blood vessels are arteries and veins. The left figure shows the principle of OR-PAFC in which the shaped laser is focused on the blood vessel and the ultrasound transducer is nonfocused [35, 36]. The design has better detection resolution and lower detection depth than the original PAFC method, leading to OR-PAFC being suitable for superficial thin blood vessels. The right figure shows the principle of AR-PAFC. Target cells irradiated by the unfocused laser generate photoacoustic waves, which are received by a focused ultrasound transducer [37]. The detection resolution of this mode is lower than that of OR-PAFC. However, sound attenuation is less than light attenuation due to light scattering in biological tissues, and unfocused spots can cover larger blood vessels. Therefore AR-PAFC is more suitable for thicker blood vessels in deeper tissues than OR-PAFC.

The general schematic of PAFC is shown in Fig. 13.6 [38]. A nanosecond or picosecond pulsed laser is usually used for photoacoustic excitation. The laser beam is shaped and focused to a narrow slit (5 μm × 70 μm) by a cylindrical lens and an objective. An LED with a central wavelength of 530 nm is used to irradiate the sample to provide considerable contrast between blood vessels and other tissues. A beam splitter separates the lasers and transmitted light, which is collected by a CCD. With the guidance of CCD imaging, the lasers can be directed to the region of interest. Photoacoustic signals are amplified with a preamplifier and recorded by a DAQ card. To analyze the data collected, signals generated from CTCs are counted with customized software on the MATLAB platform.

The photoacoustic signal is related to the thermal relaxation time and pressure relaxation time. The thermal relaxation time depends on the size and thermal diffusion rate of the excited target, while the pressure relaxation time depends on the size and sound velocity of the excited target. The pulse width (t_p) of the PAFC laser is much smaller than the thermal relaxation time and pressure relaxation time, resulting in negligible heat conduction and pressure propagation during the short single-pulse heating process, so that the initial sound pressure is only related to the temperature change, thermal expansion coefficient and isothermal compression rate

[39]. For typical conditions, a $t_p \leq 10$ ns and a $t_p \leq 0.5$ ns are typical for $R_{CTC} = 8$ μm (size of a whole B16 melanoma cell) and $R_M = 0.4$ μm (approximate size of a melanosome or NP cluster), respectively [40].

PAFC is generally equipped with a pulsed laser (532, 820, 905, or 1064 nm) as the excitation source when monitoring CTCs, especially circulating melanoma cells. The 532 nm pulsed laser is commonly used in photoacoustic angiography, although the light absorption of melanin is not significantly higher than that of blood vessels at this wavelength. The near-infrared window defines the range of wavelengths (700–900 nm, 1000–1700 nm) where light has the maximum depth of penetration in biological tissue. Besides, the absorption of melanin is higher than that of other substances in this window [41]. Therefore, a near-infrared pulsed laser at 1064 nm is used as the excitation light source for melanoma cell detection and can ensure a higher penetration depth.

To be able to detect CTCs without missing data, the laser pulse repetition rate f in PAFC is a critical parameter that also determines the throughput of PAFC. The time for a CTC to flow through the excitation laser beam t_c is calculated by the following formula:

$$t_c = (D_c + D_t)/V \tag{13.2}$$

Here, D_c is the cell diameter, while D_t is the laser beam width. V represents the blood flow speed at the point of detection. To be able to excite the CTC, the lower limit of laser pulse repetition rate f, which is determined by the following formula:

$$f \geq 1/t_c \tag{13.3}$$

The average diameter D_c is ~10 μm for typical B16 melanoma cells. For the typical laser beam width used in PAFC, D_t is also ~10 μm. For typical blood flow velocities of ~10 mm/s in mouse ear arteries and ~50 mm/s in human arm arteries, the minimum required laser pulse repetition rates are 500 Hz and 2.5 kHz, respectively. In practical applications, a higher laser pulse repetition rate will be used to ensure multiple excitations for each exposed CTC to avoid omissions and improve the signal-to-noise ratio [42–45].

13.6 Applications of Photoacoustic IVFC

Real-time in vivo photoacoustic flow cytometry was first built to detect single cells in blood or lymph flow by Zharov's group at the University of Arkansas. Based on this technique, cells with different optical absorption properties, such as melanoma and red blood cells, can be detected without markers, and the number or survival status of individual cells after treatments can be easily evaluated [46]. Since then, PAFC has expanded its range of applications, including ultrafast CTC detection with a high laser pulse repetition rate, two-color and multispectral PAFC with improved CTC detection sensitivity, in vivo magnetic enrichment and detection of CTCs,

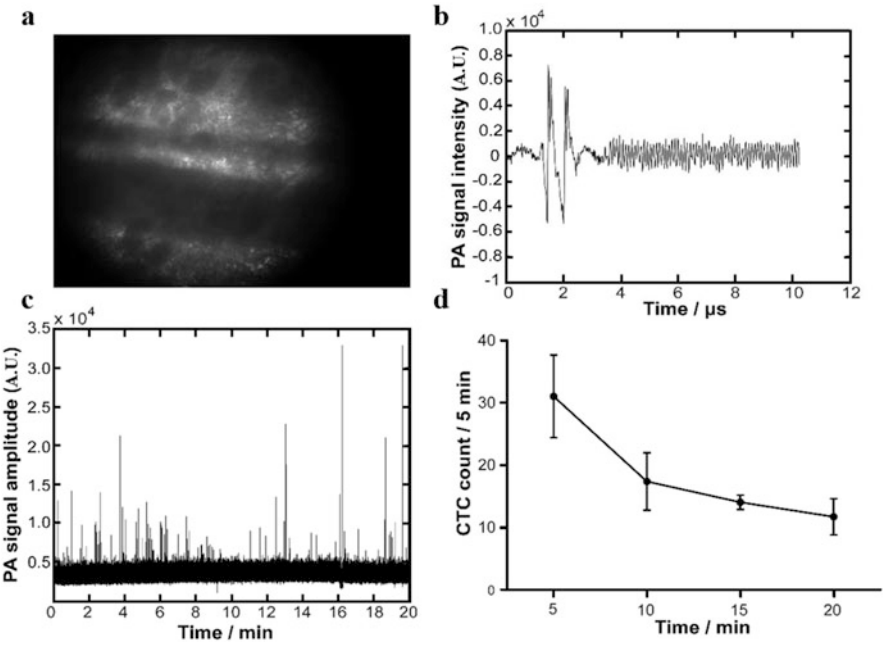

Fig. 13.7 Clearance of melanoma cells after intravenous injection. (**a**) CCD image of mouse ear vessels. (**b**) PA signal from a single cell. (**c**) PA signals of B16-F10 cells within 20 min. (**d**) Clearance rate of melanoma cells after intravenous injection. (Reused with permission from [38])

time-of-flight velocity measurement of a single CTC and the PAFC-based Cytophone diagnostic platform in clinical diagnosis.

Based on the "seed and soil theory" [47], tumor metastasis can be partially characterized by the number of CTCs in the blood. To solve the problem of insufficient sensitivity of in vitro blood collection and toxicity of CTC labels in vivo, Zharov's group constructed a noninvasive, label-free detection photoacoustic flow cytometry method using a two-color mode with pulses at wavelengths of 639 and 865 nm [48]. Due to the differences in the absorption spectra of RBCs and melanoma cells, different amplitudes and different time periods of photoacoustic signals were generated at the two wavelengths, which greatly improved the measurement accuracy. In addition, this PAFC platform was also used for deep vascular CTC monitoring and photothermal ablation of CTCs in vessels through photoacoustic guidance to achieve the early diagnosis and treatment of melanoma.

Wei's group also built an in vivo PAFC mechanisms and verified the stability of the system by tail intravenous injection [38]. As shown in Fig. 13.7, the number of melanoma cells detected in vivo tended to decrease within 20 min, which suggested that some melanoma cells were cleared by the immune system and retained in the lung.

To further improve the sensitivity and specificity of PAFC, Zharov's group adopted a method of magnetic enrichment in which immunomagnetic microbeads and magnetic nanoparticles (MNPs) were specifically targeted to breast cancer cells in the blood circulation under the attraction of magnets for detection in the system. In another way, gold-plated carbon nanotubes (GNTs) [33] conjugated with folic acid were used as a second contrast agent for photoacoustic detection, which is called multiplex targeting [49]. Combined with multicolor (639 and 900 nm) detection of tumor cells, multiplex targeting can effectively solve the problem of detecting fast-moving CTCs in the bloodstream by photoacoustic imaging. According to the PAFC setup, the laser beam is delivered either close to the external magnet or through a hole in the magnet using a fiber-based delivery system. MNPs and GNTs provide better photoacoustic contrast at 639 nm and 900 nm in normal blood, respectively, which means more accurately for detecting two PA signals from the same tumor cell.

In vivo measurements of nanoparticles were constructed by injecting MNPs and GNTs separately through the mouse tail vein at concentrations of 1×10^{11} nanoparticles mL^{-1} in 10 mL PBS, which showed that the half-life of both nanoparticles in circulation was 15–20 min. In addition, Zharov's group also demonstrated that nanoparticles can target tumor cells in vivo, and they can be cleared after injection for 60–90 min. This technology, duplexed molecular targeting of CTCs with functionalized nanoparticles followed by their capture using dual magnetic-photoacoustic flow cytometry, is feasible for the detection of CTCs in the bloodstream, in vivo, and in real time.

Another application of PAFC is to detect the properties of objects by measuring the time and amplitude through laser beams, which is called the PAFC time-of-flight technique [50]. This PAFC technique involves high-pulse-repetition-rate lasers and multiple laser beams to measure the velocity of individual cells and microparticles in vivo, which can be used for their identification. The object linear velocity (V_c) can be calculated from the following equation:

$$V_c = (D + d)/t_l \tag{13.4}$$

Where D represents the diameter of the object, d represents the width of the laser beam and t_l is the lifetime of the object in the laser volume. Thus, the flow velocity of the cells can be determined. Based on this method, cells could be identified with a two-parameter plot representing PA peak amplitude and peak width. In the scatter plot, area I represents signals from individual cells. Area II includes aggregates of several cells, and Area III suggests possible rolling cells (Fig. 13.8).

Therefore, multiparameter analysis of PA data may provide a criterion for distinguishing aggregates, which often have higher metastatic potential than individual rolling cells.

At present, real-time in vivo detection of melanoma cells by PAFC has made great progress. Zharov et al. proposed using PT technology to destroy the cell membrane and intracellular structure of CTCs through the photomechanical effect introduced by microbubbles while detecting CTCs to achieve the effect of simultaneous diagnosis and treatment in the clinic [51, 52]. In 2009, Zharov's group built a

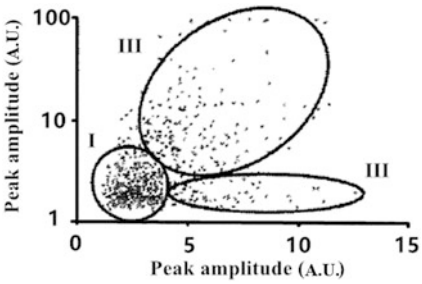

Fig. 13.8 Scatter plot of height and width of peaks for label-free PAFC detection of circulating B16-F10 cells in mouse ear arteriole (1064 nm). (Reused with permission from [50])

flow cytometry platform for the detection and killing of circulating cancer stem cells, which have strong autophagy, tumorigenicity, and multipotentiality associated with drug and radiation resistance and can lead to the progression of metastasis [52]. MNP-folate and GNT-CD44 were separately injected into a vein in the mouse tail at 4 weeks after tumor inoculation. Magnetically guided MNPs bound to individual tumor cells, directly amplifying the photoacoustic signal by approximately 10 times, were integrated with targeted PT eradication of individual stem CTCs. The PAFC system, which solves problems of marker toxicity and patient pain, has been applied in clinical diagnosis in an unlabeled and real-time manner. These advantages will make it an auxiliary means for the early diagnosis and treatment of tumors in the future.

Recently, Zharov's group applied the PAFC system to clinical diagnosis and verified the clinical effect of PAFC through a Cytophone-based blood testing platform. The results found that no CTC-related signal was found in 19 healthy volunteers, and 27 of 28 melanoma patients showed signals consistent with single, clustered, and rolling CTCs [51]. According to the patients' PA traces, single or clustered melanoma CTCs could produce sharp positive single or multiple PA peaks due to the high melanin absorption. Cells with much lower absorption such as CBCs could produce negative PA peaks. A peak with combined positive-negative contrast (the shape of the waveform like "N") is produced from CTC-CBC aggregates. Healthy volunteers versus those with melanoma were compared by the PAFC system and six in vitro verifications, including another set of in vitro PAFC detection systems, a cocktail of two antibodies conjugated to fluorescein isothiocyanate (FITC) to target the melanoma markers chondroitin sulfate proteoglycan (MCSP) and CD146, magnetic-activated cell sorting (MACS) using MCSP, fluorescence imaging, etc. The results from in vivo PAFC were consistent with clinical outcome, including a CTC photoacoustic signal peak appearing repeatedly, with a detection accuracy of 1 CTC/L of blood.

This Cytophone-based blood testing platform combines diagnosis and treatment by exposing the cubital vein under a laser for 1 h, with the institutional review board (IRB)-approved laser energy strength leading to a 48-fold reduction in a patient. After the therapeutic procedure, the CTC counts decreased to 2.8–11-fold, confirming its theranostic potential. The PAFC-based Cytophone diagnostic platform has the capability to improve the detection limit by ~1000 times compared to

existing methods and is the first of the methods to be applied in real-time, in vivo, noninvasive detection of photoacoustic signals for clinic diagnosis, suggesting its broad application prospects.

13.7 Conclusions and Future Prospects

IVFC is a real-time and noninvasive technique to detect circulating cells directly in the circulation. IVFC has been widely used in preclinical studies, especially in cancer studies, and it also shows great potential in clinical applications. This field will grow consistently with improvements in penetration depth, sensitivity and imaging speed. The largest barrier for fluorescence-based IVFC to be used in clinic is the use of a fluorescence label. There are some fluorescent molecules that are approved by the FDA for use in humans, such as 5-aminolevulinic acid (ALA) and indocyanine green (ICG). Unlike fluorescence-based in vivo flow cytometry, PAFC not only has the advantages of being a real-time and noninvasive method for IVFC that allows monitoring of a large sample volume with no labeling but also has the advantage of deep penetration because of ultrasonic signal transmission. It has recently been largely and stably used to detect melanoma cells in vivo for clinical diagnosis as well as for the treatment of melanoma cells.

Improving the sensitivity of IVFC technique is the most important and difficult problem in this filed. The minimum cell concentration and fluorophore concentration are the determinants of the sensitivity. If the object is not bright as expected, it should be abundant to be detected. If the object is lower abundant, it should be brightly labeled to be detected. Techniques that can detect larger blood volume have higher sensitivity than techniques that only use on mouse ear, such as DiFC and PAFC. The PAFC sensitivity has been improved 1000-fold (1 CTC/1000 mL) by the examination of a larger blood volume in humans, which is unachievable using existing assays. The potential clinical applications of this noninvasive, label-free, real-time and high-sensitivity detection method may include early blood CTC screening, drug intervention effect evaluation and tumor metastasis diagnosis [53]. However, due to the limitations of the in vivo environment and instrument hardware conditions, only melanoma cells have a higher absorption contrast than blood cells and can thus currently be used for the detection of completely unlabeled somatic cells. Nontoxic and unlabeled methods for a wider range of tumor cells still need further study.

References

1. Suo Y et al (2017) Proportion of circulating tumor cell clusters increases during cancer metastasis. Cytometry Part A 91(3):250–253
2. Atkin G, Chopada A, Mitchell I (2005) Colorectal cancer metastasis: in the surgeon's hands? Int Semin Surg Oncol 2:5
3. Murlidhar V et al (2017) Poor prognosis indicated by venous circulating tumor cell clusters in early-stage lung cancers. Cancer Res 77(18):5194–5206

4. Novak J et al (2004) In vivo flow cytometer for real-time detection and quantification of circulating cells. Opt Lett 29(1):77–79
5. Georgakoudi I et al (2004) In vivo flow cytometry: a new method for enumerating circulating cancer cells. Cancer Res 64(15):5044–5047
6. Suo Y et al (2015) Near infrared in vivo flow cytometry for tracking fluorescent circulating cells. Cytometry Part A 87(9):878–884
7. He W et al (2007) In vivo quantitation of rare circulating tumor cells by multiphoton intravital flow cytometry. Proc Natl Acad Sci 104(28):11760–11765
8. Zhong C et al (2008) Quantitative two-photon flow cytometry—in vitro and in vivo. J Biomed Opt 13(3):034008
9. Chang Y-C et al (2010) Fiber-optic multiphoton flow cytometry in whole blood and in vivo. J Biomed Opt 15(4):047004
10. Kong L, Tang J, Cui M (2016) Multicolor multiphoton in vivo imaging flow cytometry. Opt Express 24(6):6126–6135
11. Alt C et al (2007) Retinal flow cytometer. Opt Lett 32(23):3450–3452
12. Markovic S et al (2013) A computer vision approach to rare cell in vivo fluorescence flow cytometry. Cytometry Part A 83(12):1113–1123
13. Zettergren EW et al (2012) Instrument for fluorescence sensing of circulating cells with diffuse light in mice in vivo. J Biomed Opt 17(3):037001
14. Markovic S, Li S, Niedre MJ (2015) Performance of computer vision in vivo flow cytometry with low fluorescence contrast. J Biomed Opt 20(3):035005
15. Boutrus S et al (2007) Portable two-color in vivo flow cytometer for real-time detection of fluorescently-labeled circulating cells. J Biomed Opt 12(2):020507
16. Hwu D et al (2011) Assessment of the role of circulating breast cancer cells in tumor formation and metastatic potential using in vivo flow cytometry. J Biomed Opt 16(4):040501
17. Sipkins DA et al (2005) In vivo imaging of specialized bone marrow endothelial microdomains for tumour engraftment. Nature 435(7044):969
18. Fan Z-C et al (2012) Real-time monitoring of rare circulating hepatocellular carcinoma cells in an orthotopic model by in vivo flow cytometry assesses resection on metastasis. Cancer Res 72 (10):2683–2691
19. Pang K et al (2018) Monitoring circulating prostate cancer cells by in vivo flow cytometry assesses androgen deprivation therapy on metastasis. Cytometry Part A 93(5):517–524
20. Runnels JM et al (2011) Optical techniques for tracking multiple myeloma engraftment, growth, and response to therapy. J Biomed Opt 16(1):011006
21. Zeng Y et al (2014) In vivo micro-vascular imaging and flow cytometry in zebrafish using two-photon excited endogenous fluorescence. Biomed Opt Express 5(3):653–663
22. Li C et al (2010) Imaging leukocyte trafficking in vivo with two-photon-excited endogenous tryptophan fluorescence. Opt Express 18(2):988–999
23. Wei D et al (2018) Noninvasive monitoring of nanoparticle clearance and aggregation in blood circulation by in vivo flow cytometry. J Control Release 278:66–73
24. Zhang Y et al (2019) Activated platelets-targeting micelles with controlled drug release for effective treatment of primary and metastatic triple negative breast cancer. Adv Funct Mater 29 (13):1806620
25. Kang T et al (2017) Nanoparticles coated with neutrophil membranes can effectively treat cancer metastasis. ACS Nano 11(2):1397–1411
26. Yao J et al (2017) Neovasculature and circulating tumor cells dual-targeting nanoparticles for the treatment of the highly-invasive breast cancer. Biomaterials 113:1–17
27. Aceto N et al (2014) Circulating tumor cell clusters are oligoclonal precursors of breast cancer metastasis. Cell 158(5):1110–1122
28. Pera VE et al (2017) Diffuse fluorescence fiber probe for in vivo detection of circulating cells. J Biomed Opt 22(3):037004

29. Hartmann C et al (2017) Fluorescence detection, enumeration and characterization of single circulating cells in vivo: technology, applications and future prospects. Phys Med Biol 63 (1):01TR01
30. Runnels JM et al (2006) Imaging molecular expression on vascular endothelial cells by in vivo immunofluorescence microscopy. Mol Imaging 5(1):31
31. Wang LV, Hu S (2012) Photoacoustic tomography: in vivo imaging from organelles to organs. Science 335(6075):1458–1462
32. Galanzha EI, Zharov VP (2013) Circulating tumor cell detection and capture by photoacoustic flow cytometry in vivo and ex vivo. Cancer 5(4):1691–1738
33. Kim J-W et al (2009) Golden carbon nanotubes as multimodal photoacoustic and photothermal high-contrast molecular agents. Nat Nanotechnol 4(10):688
34. Tuchin VV, Tárnok A, Zharov VP (2011) In vivo flow cytometry: a horizon of opportunities. Cytometry Part A 79(10):737–745
35. Hu S, Maslov K, Wang LV (2011) Second-generation optical-resolution photoacoustic microscopy with improved sensitivity and speed. Opt Lett 36(7):1134–1136
36. Lin L et al (2016) Handheld optical-resolution photoacoustic microscopy. J Biomed Opt 22 (4):041002
37. Zhang HF et al (2006) Functional photoacoustic microscopy for high-resolution and noninvasive in vivo imaging. Nat Biotechnol 24(7):848
38. Zhou Q et al (2018) Label-free counting of circulating cells by in vivo photoacoustic flow cytometry. In: Biophotonics and immune responses XIII. International Society for Optics and Photonics, Bellingham, WA
39. Zhou Y, Yao J, Wang LV (2016) Tutorial on photoacoustic tomography. J Biomed Opt 21 (6):061007
40. Galanzha EI, Zharov VP (2012) Photoacoustic flow cytometry. Methods 57(3):280–296
41. Deán-Ben X et al (2017) Advanced optoacoustic methods for multiscale imaging of in vivo dynamics. Chem Soc Rev 46(8):2158–2198
42. Fu Y et al (2019) Photoacoustic signal classification for in vivo photoacoustic flow cytometry based on support vector machine. In: Optics in health care and biomedical optics IX. International Society for Optics and Photonics, Bellingham, WA
43. Niu Z et al (2015) Improving the signal analysis for in vivo photoacoustic flow cytometry. In: Biophotonics and immune responses X. International Society for Optics and Photonics, Bellingham, WA
44. Zhou H et al (2018) Improving label-free detection of circulating melanoma cells by photoacoustic flow cytometry. In: Biophotonics and immune responses XIII. International Society for Optics and Photonics, Bellingham, WA
45. Wang Q et al (2017) Optimized signal detection and analysis methods for in vivo photoacoustic flow cytometry. In: Biophotonics and immune responses XII. International Society for Optics and Photonics, Bellingham, WA
46. Zharov VP et al (2006) In vivo photoacoustic flow cytometry for monitoring of circulating single cancer cells and contrast agents. Opt Lett 31(24):3623–3625
47. Fidler IJ (2003) The pathogenesis of cancer metastasis: the 'seed and soil' hypothesis revisited. Nat Rev Cancer 3(6):453
48. Galanzha EI et al (2009) In vivo, noninvasive, label-free detection and eradication of circulating metastatic melanoma cells using two-color photoacoustic flow cytometry with a diode laser. Cancer Res 69(20):7926–7934
49. Galanzha EI et al (2009) In vivo magnetic enrichment and multiplex photoacoustic detection of circulating tumour cells. Nat Nanotechnol 4(12):855

50. Sarimollaoglu M et al (2011) In vivo photoacoustic time-of-flight velocity measurement of single cells and nanoparticles. Opt Lett 36(20):4086–4088
51. Galanzha EI et al (2019) In vivo liquid biopsy using Cytophone platform for photoacoustic detection of circulating tumor cells in patients with melanoma. Sci Transl Med 11(496): eaat5857
52. Galanzha EI, Kim JW, Zharov VP (2009) Nanotechnology-based molecular photoacoustic and photothermal flow cytometry platform for in-vivo detection and killing of circulating cancer stem cells. J Biophotonics 2(12):725–735
53. Nedosekin DA et al (2011) In vivo ultra-fast photoacoustic flow cytometry of circulating human melanoma cells using near-infrared high-pulse rate lasers. Cytometry Part A 79(10):825–833

Correction to: Optical Imaging in Human Disease and Biological Research

Xunbin Wei and Bobo Gu

Correction to:
X. Wei, B. Gu (eds.), *Optical Imaging in Human Disease and Biological Research*, Advances in Experimental Medicine and Biology 1355
https://doi.org/10.1007/978-981-15-7627-0

This book was inadvertently published with the incorrect volume number. The volume number has been updated to 1355 with this erratum.

The updated online version of the book can be found at
https://doi.org/10.1007/978-981-15-7627-0

X. Wei, B. Gu (eds.), *Optical Imaging in Human Disease and Biological Research*, Advances in Experimental Medicine and Biology 1355,
https://doi.org/10.1007/978-981-15-7627-0_14